PPG-821
UCLA-ENG-84-30

FINESSE

A Study of Issues, Experiments and Facilities for Fusion Nuclear Technology Research & Development

Interim Report

Volume III

October 1984

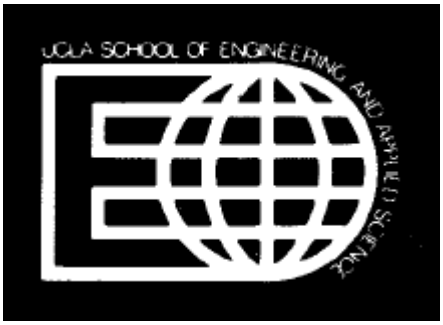

Center for Plasma Physics and Fusion Engineering
University of California, Los Angeles
Los Angeles, California

Printed in the United States of America

Available from:

National Technical Information Service
U.S. Department of Commerce
5285 Port Royal Road
Springfield, Virginia 22161

Price: Printed Copy
Microfiche A01

Distribution Category:
Magnetic Fusion (UC-20)

University of California, Los Angeles
PPG-821
UCLA-ENG-84-30

FINESSE: A Study of the Issues, Experiments and Facilities for Fusion Nuclear Technology Research and Development

Interim Report

Volume III

Contributors

M. Abdou, UCLA
C. Baker, ANL
T. Bauer, ANL
G. Bell, TRW
D. Berwald, TRW
M. Billone, ANL
J. Blanchard, UCLA
R. Burke, HEDL
R. Conn, UCLA
J. Crocker, EG&G
J. Davis, MDAC
G. Deis, EG&G
R. DiMelfi, UCLA
J. Doggett, LLNL
M. Fenstermacher, TRW
J. Garner, TRW
P. Gierszewski, UCLA/CFFTP
J. Gordon, TRW
S. Grotz, UCLA
J. Grover, HEDL
C. Gung, UCLA
G. Hollenberg, HEDL
J. Holmes, HEDL
D. Jassby, PPPL
K. KLeefeldt, UCLA/KfK
T. Kraft, ANL
Y. Lui, ANL
H. Madarame, UCLA/U. of Tokyo
L. Masson, EG&G
L. Miller, EG&G
G. D. Morgan, MDAC
R. Nygren, ANL
E. Opperman, HEDL
G. Orient, UCLA
Y. Oyama, UCLA/JAERI
M. Perrin, MDAC
R. Puigh, HEDL
D. Reuster, MDAC
D. Rose, ANL
Y. Seki, UCLA/JAERI
K. Shin, UCLA/Kyoto U.
W. Steele, TRW
J. Straalsund, HEDL
J. Szabo, UCLA
K. Taghavi, UCLA
K. Thomassen, LLNL
M. Tillack, UCLA
R. Whitley, TRW
M. Youssef, UCLA

October 1984

FINESSE: A Study of the Issues, Experiments and Facilities for Fusion Nuclear Technology Research and Development

Interim Report

Volume III

Task Leaders

M. Abdou, UCLA: Principal Investigator

D. Berwald, TRW: Development Scenarios, Mirror Facilities

M. Billone, ANL: Tritium Extraction Modelling

J. Davis, MDAC: Failure Modes

G. Deis, EG&G: Fission Reactor Utilization

P. Gierszewski, UCLA/CFFTP: Testing Needs, Testing Requirements

G. Hollenberg, HEDL: Solid Breeders

J. Holmes, HEDL: Point Neutron Sources

D. Jassby, PPPL: Tokamak Facilities

G. Morgan, MDAC: Reference Generic Designs

R. Nygren, ANL: Non-Neutron Test Stands

J. Straalsund, HEDL: Materials, Interactive Effects

M. Tillack, UCLA: Issues, Testing Requirements

R. Whitley, TRW: Availability Modelling

VOLUME III

TABLE OF CONTENTS

CHAPTER 5

ANALYSIS AND ENGINEERING SCALING OF SOLID BREEDER BLANKETS

TABLE OF CONTENTS

5 ANALYSIS AND ENGINEERING SCALING OF SOLID BREEDER BLANKETS

5.1 Introduction

A full technology development program encompasses tests ranging from property measurements to component verification. The integrated or component tests are particularly important since these are the first opportunity to verify the design concept and performance under full or near full operating conditions. This is a crucial step in identifying unknowns or unexpected behavior, and reducing the safety, economic and possibly political risk in committing to commercial production and operation.

However, the cost of a fusion reactor to test breeding blankets under commercial reactor conditions is very high. This makes it necessary to consider how the test requirements can be relaxed while still meeting the need for breeding blanket performance and lifetime verification.

5.1.1 Objective

In this chapter, the limits under which full component behavior can be achieved under changed test conditions are explored. In particular, such tests must be designed to act like the real module in a full device in order to bring out actual blanket performance and unknowns.

This involves determining important phenomena, considering how these could be retained under scaled test facility conditions and identifying conflicts between preserving the different phenomena. Also, although hard to quantify, a healthy respect must be retained for the many unknown or uncalculated effects. Issues to be addressed include, for example, the loss of information as test conditions are changed, the relative importance of the various test facility parameters, and the differences between tokamaks and mirrors as test facilities. Ultimately the analysis leads to requirements, for the integrated testing of solid breeder blankets, on both the test facility and the test articles.

The characterization of these test requirements for integrated testing, combined with the other needs identified in Chapter 4, contributes to the overall test matrix and test plan for the understanding and development of fusion nuclear technology.

5.1.2 Engineering Scaling

Although routinely done in modern industry, identifying a test program to take a concept from scientific possibility to commercial reality is more an art than a science. There is no definitive methodology or theory for performing this task. A general description of the approach developed in this chapter is given below, along with the terminology adopted, as applied to the testing of fusion blankets in a test device.

Device parameters are the characteristics of the test device that affect the behavior of the test module. Major device parameters, with a strong influence on blanket test module conditions and test device cost, include:

- surface heat flux;
- neutron wall load;
- neutron fluence;
- minimum continuous operating time;
- burn/dwell times;
- available test surface area;
- available test volume depth;
- steady magnetic field strength;
- transient magnetic field strength.

These parameters will drive the test module into some operating conditions or blanket conditions (e.g., temperature, stress, tritium generation rate, accumulated swelling) and may activate blanket phenomena (e.g., sintering of solid breeder, generation of global eddy currents in liquid breeders). Reference conditions includes the device parameters, blanket conditions and blanket phenomena under normal operation of the full component in a commercial reactor.

Models or parametric relations may be developed relating device parameters, blanket conditions and blanket phenomena. For example, the first wall temperature rise, ΔT (a blanket condition), due to surface heating, q_s (a device parameter), is given by the parametric relation $\Delta T_{fw} \sim q_s d_{fw}/k$, where d_{fw} is the first wall thickness and k its thermal conductivity.

A scaled test is a particular test module design that seeks to preserve aspects of reactor blanket behavior (conditions or phenomena) under non-reference operating conditions. Such tests are used when full operating

conditions (e.g., 5 MW/m^2 neutron wall load) are not available and/or when the conditions can be achieved but only in a reduced volume (e.g., wind tunnel tests of aircraft aerodynamics). This may be accomplished, for example, by reducing all test module dimensions. Other methods are given in Table 5.1-1. There is often no unique scaled test, it depends on what is considered important and on the methods for preserving these. A set of *scaled test options* or *scaling options* may be identified.

Engineering scaling is the process of developing a scaled test. This process is based on: 1) identifying important features (conditions or phenomena) worth preserving; 2) understanding the relationships between the device parameters and the blanket features; 3) evaluating methods for preserving these features under changed device parameters; and 4) balancing conflicting requirements for test conditions. This process leads to an understanding of how the usefulness of a test changes with device parameters. It may be possible to identify *test requirements*, or limits on how far the device parameters can be changed before the tests lose their value. These indications of test usefulness and test requirements can then be balanced against the test cost to determine an optimum test program.

5.1.3 Reference Blankets

In order to quantify the usefulness of scaled tests and determine test requirements, it is necessary to consider specific blanket designs. These need not be considered in the sense that they represent the best designs, or even proven workable designs. Rather, they serve as tools to identify the problems of scaling plausible solid breeder blankets so as to reproduce the reference component behavior in a scaled test.

In the Blanket Comparison and Selection Study,[1] a large number of potential blanket designs were considered and the characteristics of the better candidates identified. Based on this study, two representative solid breeder blankets were chosen as "reference" designs. These are a Li_2O/He/HT-9 and a $LiAlO_2$/H_2O/PCA/Be design, as described in Appendix D. Figures 5.1-1 and -2 illustrate these designs for tokamaks. Small modifications are necessary for mirrors that do not affect the design concept. These blankets cover a range of design features of general interest, such as plate versus breeder-outside-tube geometry, that are summarized in Table 5.1-2. It is hoped that

basing calculations on these blanket designs, as necessary to quantify results, will lead to conclusions on engineering scaling and test requirements that are applicable to a large class of candidate solid breeder blankets.

5.1.4 Organization

The remainder of this chapter is organized into four sections plus a summary. The purpose of Section 5.2, Analysis of Blanket Behavior, is to understand the conditions and phenomena that may occur under reference conditions. Potentially important phenomena are identified and analyzed were possible. For those that are considered, the modelling, limits of applicability and results for reference conditions are given - particularly the significance of the effect.

In Section 5.3, Requirements for Scaled Testing, the variation of phenomena and conditions with a limited number of device parameters or other factors is considered through the models or parametric relations just established. The purpose is to understand the changes under scaled test conditions and whether there are methods that will preserve the effect. Transitions in behavior and gradual loss of relevance between the test article and full component performance lead to requirements on the test conditions.

However, the test requirements cannot be considered in isolation. For example, modifications to preserve some aspect of breeder behavior may also affect the first wall behavior. To identify conflicts and understand the nature of the scaled test article, the parametric design of a test module is considered in Section 5.4, Test Module Design. This is not a detailed design, but rather identifies the general features of a test module, based on the scaling approaches from Section 5.3, under arbitrary device parameters.

The test requirements are examined collectively in Section 5.5, Engineering Scaling. The importance of finding the "unknowns" is emphasized. Conflicting requirements may be resolvable by alternate scaling methods, or may be fundamentally irreconcilable and lead to multiple test modules or additional limits on the device parameters. The results of the chapter are summarized to determine an overall sense of the test facility requirements for conducting useful integrated tests of solid breeder blankets.

Table 5.1-1 Methods for Scaled Testing

Method	Examples
Adjusting dimensions	Decreasing size to reduce test volume requirements
Adding impurities	Fissile material to enhance heating
Changing the isotope composition	^{6}Li enrichment to enhance tritium
Changing the material	Substituting high swelling alloy to study swelling interactions
Varying inlet conditions	Coolant temperature, pressure, flow rate, composition
Varying boundary conditions	Structural support rigidity; Location of neutron reflectors, multipliers and absorbers
Adding active hardware	Neutral beam surface heating; Resistive bulk heating; Local magnetic field coils
Altering basic design features	Cylindrical pellets rather than blocks
Pre-processing of the component	Prior irradiation in a fission reactor to simulate high fluence conditions

Table 5.1-2 Solid Breeder Reference Blanket Characteristics

	Li_2O/He/HT-9	$LiAlO_2$/H_2O/PCA/Be
Breeder	- Lithium oxide - high swelling - LiOT formation - high T diffusivity - Layered - Collapsed clad - Sintered blocks - No multiplier - Natural lithium - Plate breeder and coolant channels - Radial coolant flow	- Ternary ceramic - low swelling - accumulation of metal oxides - low T diffusivity - Breeder-outside-tube - Rigid structure - Sphere-pack - Beryllium multiplier - Enriched ^6Li - Double-walled tube coolant channels - Axial coolant flow
Coolant	- Helium	- Water
Structure	- HT-9 ferritic steel - low swelling	- PCA austenitic steel - low magnetic field interaction
First wall	- Lobe - Azimuthally cooled (symmetric) - Grooves in tokamak - Finned channels - First wall coolant also cools breeder region	- Lobe - Azimuthally cooled (asymmetric) - Grooves in tokamak - Simple channels - Separate first wall and breeder coolant flow

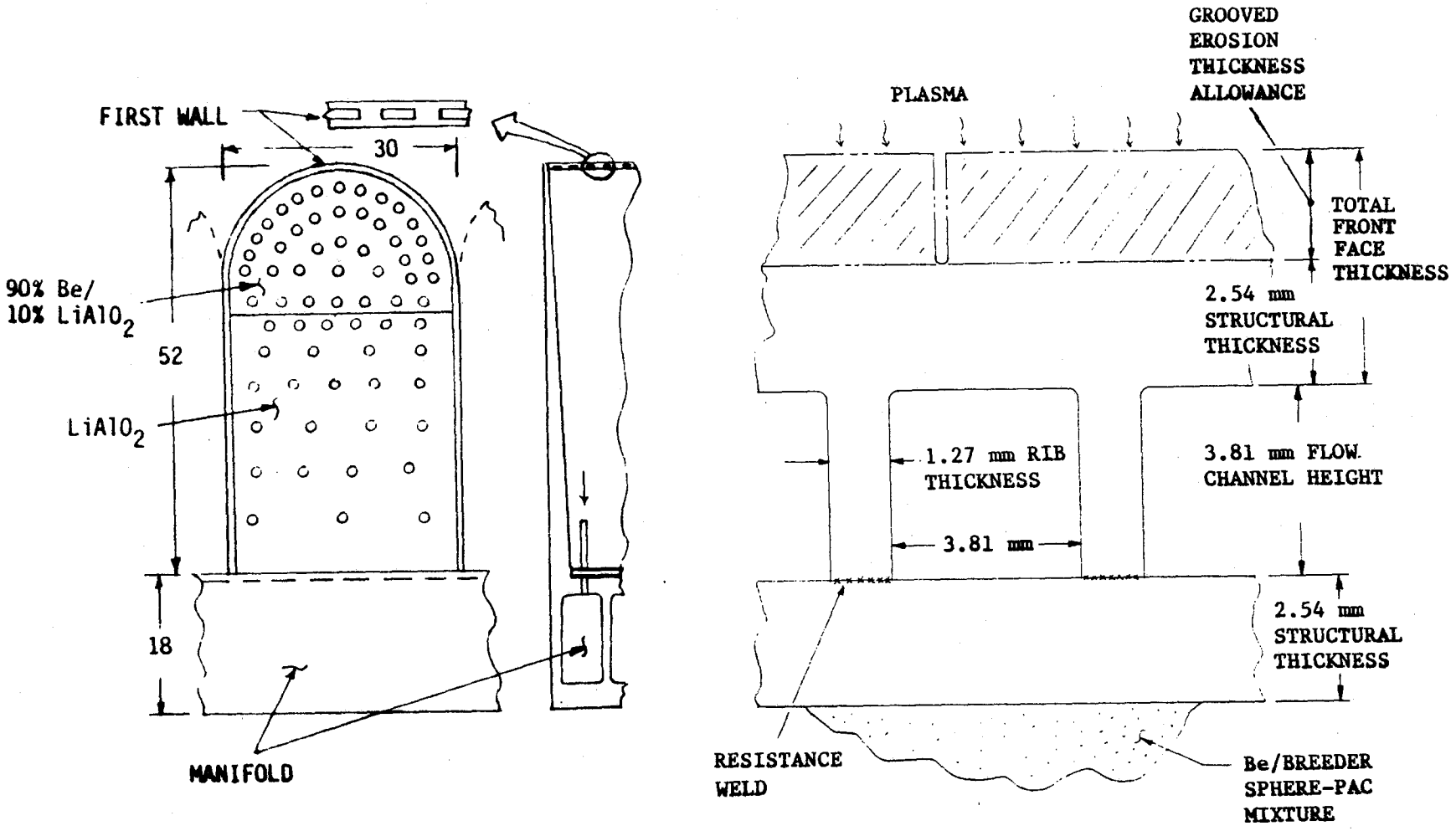

Figure 5.1-1 Reference $LiAlO_2/H_2O$/PCA/Be tokamak blanket

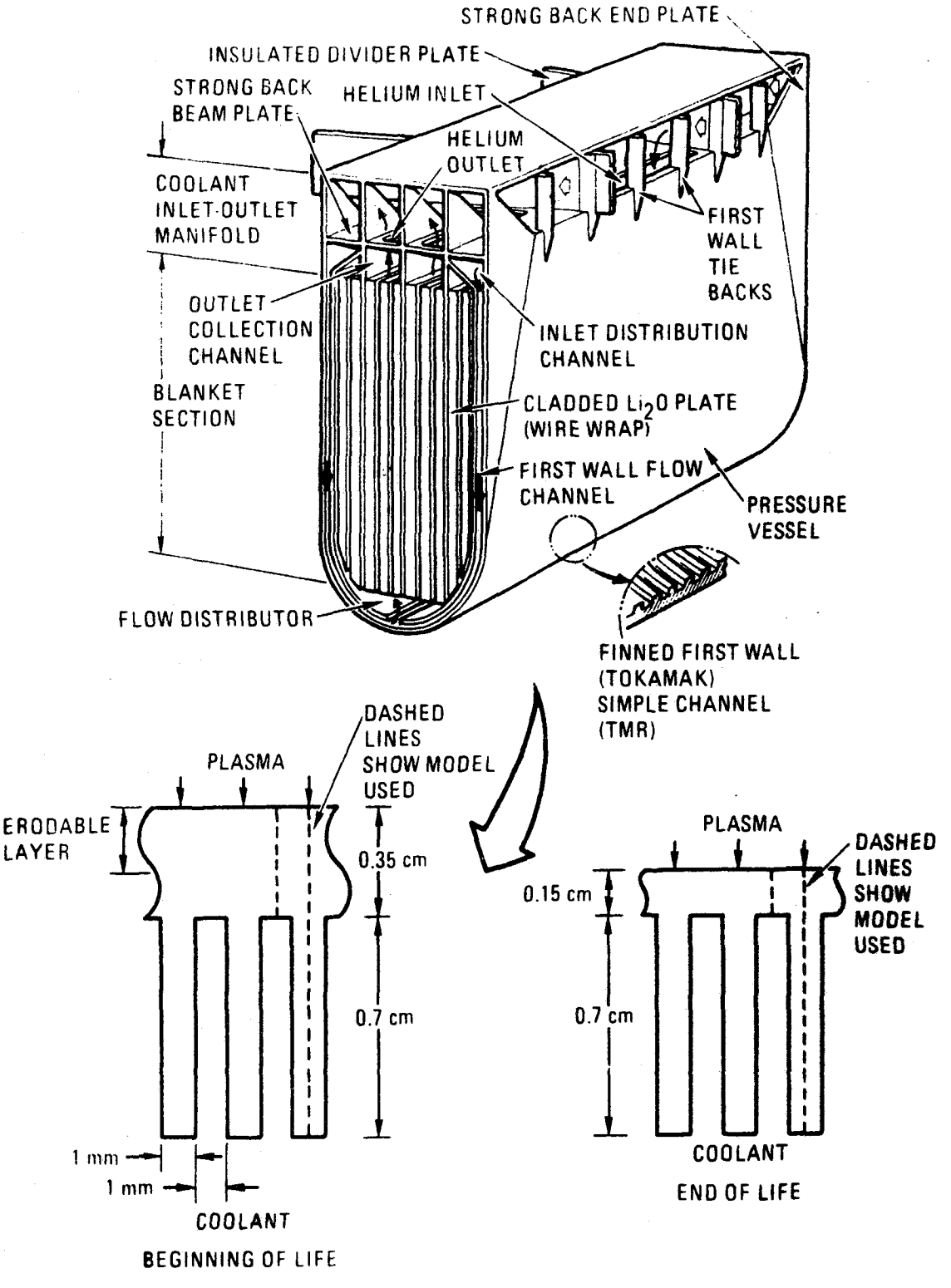

Figure 5.1-2 Reference Li_2O/He/HT-9 tokamak blanket

5.2 Analysis of Blanket Behavior

5.2.1 Neutronics

5.2.1.1. Introduction

The neutronics performance of the blanket will be characterized by the absolute value and profiles of tritium production, nuclear heating and radiation damage, i.e., atomic displacement (dpa), hydrogen production and helium production rates. Absolute values are important since they determine the fluence lifetime of the blanket, and since some processes such as the swelling or creep rate are dependent upon flux. Profiles are important since they may lead to interactions between different regions, or because different phenomena have different profiles. For example, He production is more dependent on high energy neutrons than dpa so will attenuate faster in the blanket, potentially affecting any structural behaviour that is sensitive to the He/dpa ratio.

Detailed results for the overall blanket neutronics performance are given in Appendix D, including neutron and gamma ray spectra in the blanket, total tritium breeding ratio, energy multiplication, as well as the parameters mentioned above.

Two representative solid breeder blankets were considered: the GA Li_2O-helium-cooled blanket with ferritic steel (HT-9) structure, Li_2O/He/FS,[1] and the BCSS $LiAlO_2$ water-cooled blanket with ferritic steel structure and beryllium neutron multiplier, $LiAlO_2/H_2O$/FS/Be.[1] Since natural lithium is used in the Li_2O/He/FS blanket, its heating and tritium production rates will be sensitive to both high and low energy neutrons. However, the $LiAlO_2/H_2O$/FS/Be blanket contains enriched lithium (90%^{6}Li enrichment) and beryllium, so the heating and tritium production will be controlled by the low energy neutrons.

It may be noted that the reference $LiAlO_2$ blanket uses PCA steel for structural material. However, the neutronics performance of the blanket will not be affected by the replacement of PCA by HT-9 except with respect to certain damage indicators. PCA contains nickel, which will result in slight increase (about 30%) in the helium and hydrogen production rates in the structure.

A tokamak reactor is considered as a reference reactor throughout this section. The neutronics parameters will be slightly affected by reducing the device size from the tokamak to a mirror reactor, and by differences in the first wall thickness.

The outline of this section is as follows. Methods of analysis and modelling assumptions are described in Section 5.2.1.2. A one-dimensional model is used here. In Section 5.2.1.3, the tritium production rate is described, and the differences between the two reference blankets shown. Section 5.2.1.4 shows the nuclear heating rate. The importance of high energy neutrons is appreciable for the heating rate in the Li_2O blanket as compared to that in the $LiAlO_2$ blanket. The first wall thickness effect is small for both the heating and tritium production rates. The radiation damage indicators are discussed in Section 5.2.1.5. Since the damage parameters are energy sensitive, these profiles reflect the distribution of the high energy neutron flux.

5.2.1.2. Calculational Method

The neutronics calculations were performed with one-dimensional cylindrical model of the blankets. The material arrangement of the Li_2O/He/FS tokamak blanket is shown in Fig. 5.2.1-1. The first wall is a curved, 10.8 mm thick HT-9 composite structure, which was homogenized over the corresponding one-dimensional region. In the breeder zone, the Li_2O plates, cladding, and module side walls were also homogenized. The assumed density of Li_2O is 85% of the theoretical value. Stainless steel (type 316) is used for the shield material. No coolant was assumed in the shield, but this does not affect the results. Since the shield thickness was decreased to 30 cm, a 30% albedo condition was imposed at the shield outer surface in the radiation transport calculation to compensate for the increased leakeage. The detailed atomic density of each region is given in Table D.2.2-1 of Appendix D.

The corresponding material configuration of the $LiAlO_2/H_2O$/FS/Be blanket is shown in Fig. 5.2.1-2. The first wall material is similar in both the Li_2O and $LiAlO_2$ blankets, but the volume fraction of the material in the $LiAlO_2$ blanket is about twice as much as compared to that in the Li_2O blanket. The water coolant channel requires thicker walls due to the higher coolant pressure. The breeding zone is broken into three subzones, Blanket 1, Blanket 2 and Blanket 3. Blanket 1 contains 45 volume % beryllium neutron multiplier at 87% theoretical density (TD), with a small amount of $LiAlO_2$ at 87% TD. The shield material is Fe1422, which is selected because of its low activation level. The water cooling concept resulted in relatively high volume fractions

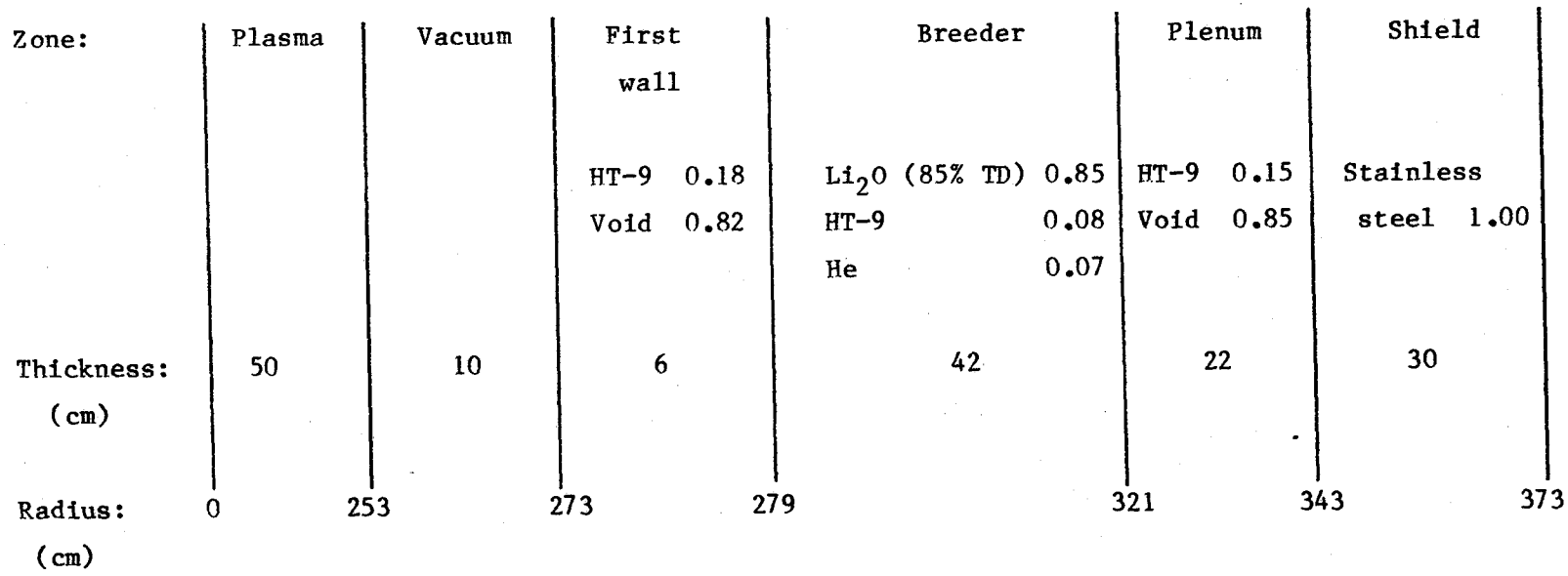

Figure 5.2.1-1 One-dimensional Model for the Li_2O Helium-Cooled Tokamak Blanket with HT-9 Structure (Li_2O/He/FS)

Zone:	Plasma	Vacuum	First wall	Blanket-1	Blanket-2	Blanket-3	Coolant manifold	Shield
			HT-9 0.32	HT-9 0.195	HT-9 0.125	HT-9 0.07	HT-9 0.33	Fe1422 0.8
			H_2O 0.07	H_2O 0.215	H_2O 0.115	H_2O 0.04	H_2O 0.17	H_2O 0.2
			Void 0.61	$LiAlO_2$* 0.70	$LiAlO_2$* 0.70	$LiAlO_2$* 0.84	Void 0.50	
				Be^+ 0.45	Void 0.06	Void 0.05		
				Void 0.06				
Thickness: (cm)	194	20	5	20	7	20	18	30
Radius: (cm)	0	194	214	219	239	246	266	284	314

(* $LiAlO_2$ is 87% T.D., 0% ^6Li; $^+$ Be is 87% T.D.)

Figure 5.2.1-2 One Dimensional Model for the $LiAlO_2/H_2O$/FS/Be Tokamak Blanket

of stucture and coolant in the breeder. Neutrons will be lost also through oxygen and aluminum reactions in the breeding material. To keep the required tritium breeding ratio, a ^{6}Li enrichment of 90% is assumed. The detailed atomic density of each region is tabulated in Table D.2.6-1. At the outer surface of the shield, a 30% albedo condition was imposed in the radiation transport calculations.

The neutronics analyses were performed by one dimensional S_N code ANISN[2] using 41 group (25n-21q) cross-section library. The group structure of the cross section is tabulated in Table D.2.1-1 in Appendix D. The library data was collapsed from the VITAMIN-C/DLC-41B library[3], which were derived from the ENDF/B-IV nuclear data library.[4] The ANISN calculation was done using 8 discrete directions (S_8) and the third order Legendre expansions (P_3) in the cylindrical geometry. All results were normalized to 5 MW/m^2 wall load. The one dimensional calculation method is well established, so errors originating from the calculational method are very small. The main sources of errors in the results are modeling of the blanket system, and cross-section data used in the analysis. It is expected that one-dimensional modeling of the multidimensional system will give rise to relatively large errors in the local profiles as compared to the cross-section data uncertainties. However, evaluating this error is very difficult.

5.2.1.3. Tritium Production Rate

Profiles for the total tritium production rate and the contributions from ^{6}Li and ^{7}Li on the Li_2O/He/FS blanket are shown in Fig. 5.2.1-3. Note that the reference blanket of Fig. 5.2.1-1 has a 10.8 mm thick first wall (with an 18% structural volume fraction). Near the front edge of the breeder, the contribution from the $^{7}Li(n,n'a)T$ reactions is about one-third of the total tritium produciton rate. Its fractional contribution decreases gradually with increasing depth because this reaction takes place through high energy neutrons; hence its reaction rate directly reflects the high energy neutron flux attenuation. Consequently, ^{6}Li reactions becomes more important with increasing depth.

The contribution from ^{6}Li to the total tritium production is 77%. The atomic density of ^{6}Li in the breeder is 7.4% of the total lithium density. It means the burnup of ^{6}Li proceeds about 40 times as fast as that of the ^{7}Li

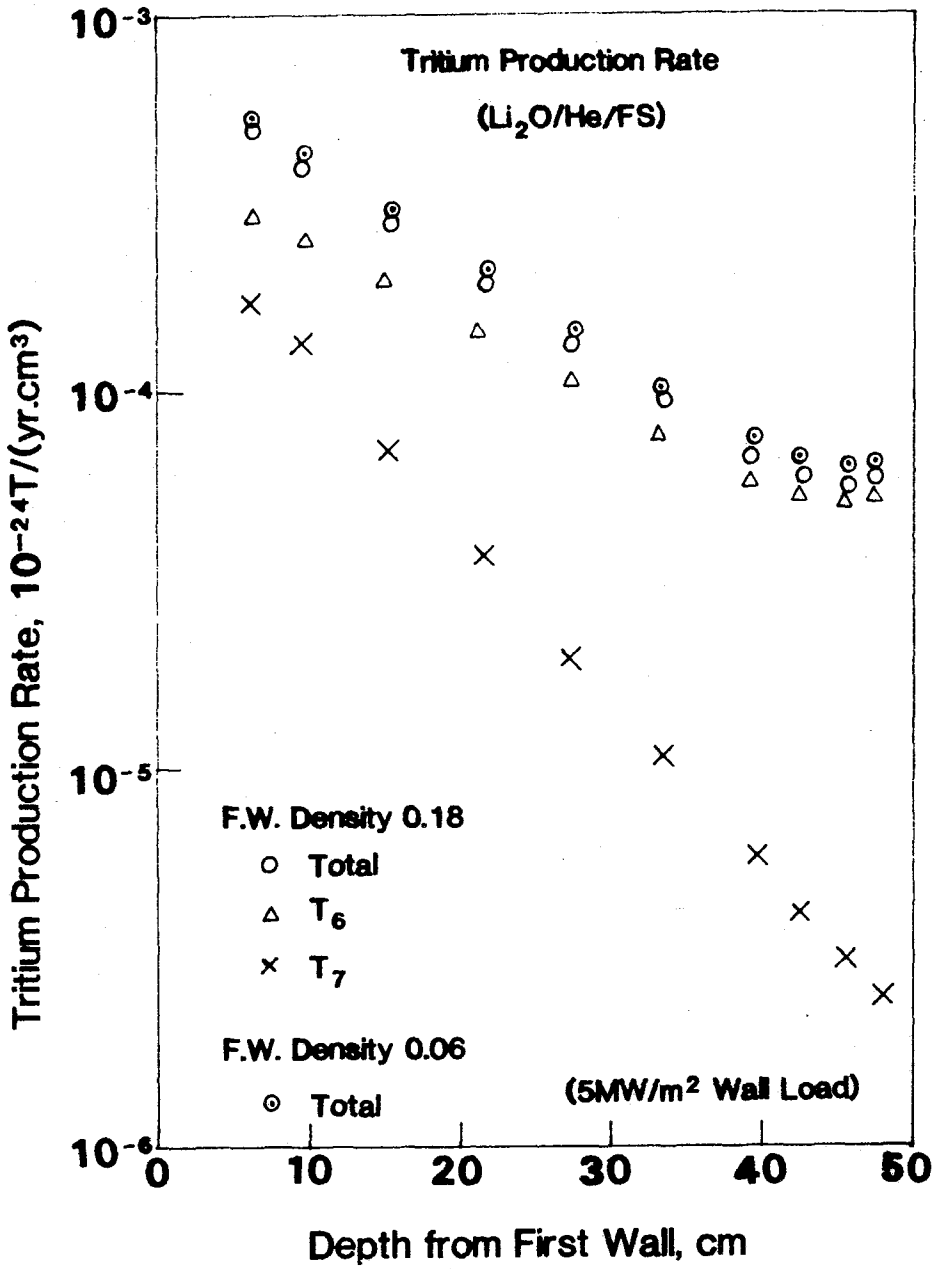

Figure 5.2.1-3 Profiles for tritium production rate and contributions from ^{6}Li and ^{7}Li in the Li_2O/He/FS blanket.

atoms. Figure 5.2.1-4 shows burnup rates of lithium nuclei through the tritium producing reactions. At the front edge of the breeder, the burnup rate of ^6Li is 7%/yr at 5 MW/m^2.

In order to analyze the effect of different first wall designs on the tritium production rate, the first wall thickness was decreased to one-third of the original thickness. Results for the total tritium production rate is shown in Fig. 5.2.1-3. The tritium production rate was increased by f 6%, while the relative profiles were scarcely affected. Consequently the above discussion for the 10.8 mm first wall case is still valid.

Figure 5.2.1-5 shows the corresponding profile of total tritium production rate in the $LiAlO_2/H_2O/Be/FS$ blanket, and Fig. 5.2.1-6 shows the burnup rate of lithium nuclei. Due to the 90% ^6Li enrichment and the softer energy spectrum from the neutron multiplier, the total tritium production is almost completely dominated by ^6Li. Since each blanket zone has different material compositions, the profile for the total tritium production rate is discontinuous at the zone boundaries. Although the volume fraction of the $LiAlO_2$ in the Blanket 1 region (mostly multiplier) is very small, its contribution to the total tritium production is very high. The neutron flux is enhanced by Be(n,2n) reactions in the Blanket 1 zone, and suppressed in the Blanket 2 zone by the absorption by ^6Li nuclei (see Fig. 5.2.1-6.). This resulted in relatively low tritium production rate in Blanket 2. Note that a very high volume fraction of $LiAlO_2$ was assumed there. The highest lithium burnup rate is observed at the front edge of Blanket 1, as much as 55%/yr.

5.2.1.4. Nuclear Heating Rate

Profiles of the total nuclear heating rate and the contributions from neutron and gamma ray heating are shown in Fig. 5.2.1-7 for the $Li_2O/He/FS$ blanket. The heating rate in the first wall is smaller than in the breeder because of the 18% first wall structural volume fraction. The actual heat deposition in the first wall structure is f 46 W/cm^3 at the front edge of the first wall. The gamma ray heating rate is about twice as high as that of neutrons in the first wall.

In the breeding zone, the contribution from neutrons is about four times as high as that from gamma rays. However, the relative profiles of the

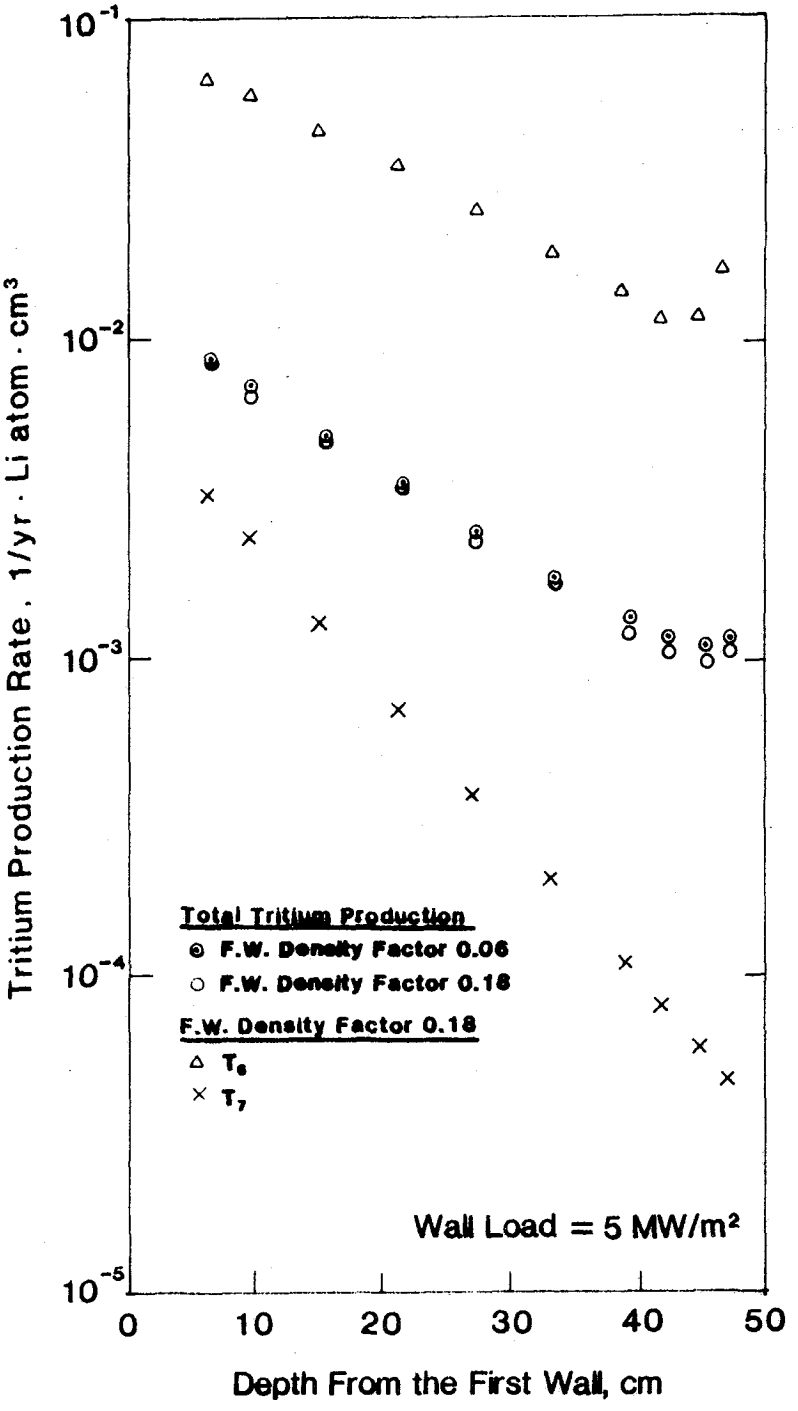

Figure 5.2.1-4 Burnup rate of lithium in the Li_2O/He/FS blanket.

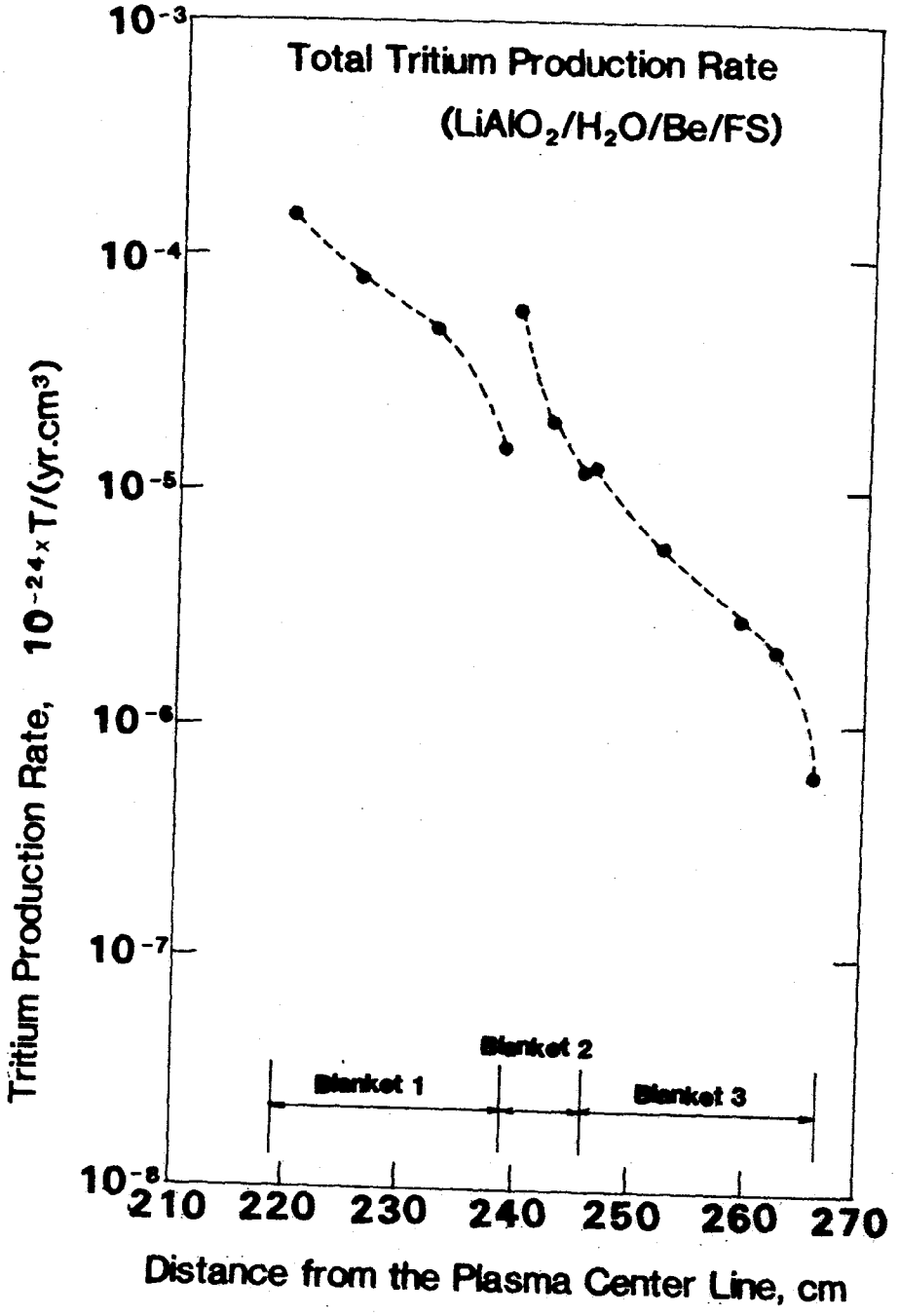

Figure 5.2.1-5 Profile of total tritium production rate in the $LiAlO_2/H_2O$/FS/Be blanket.

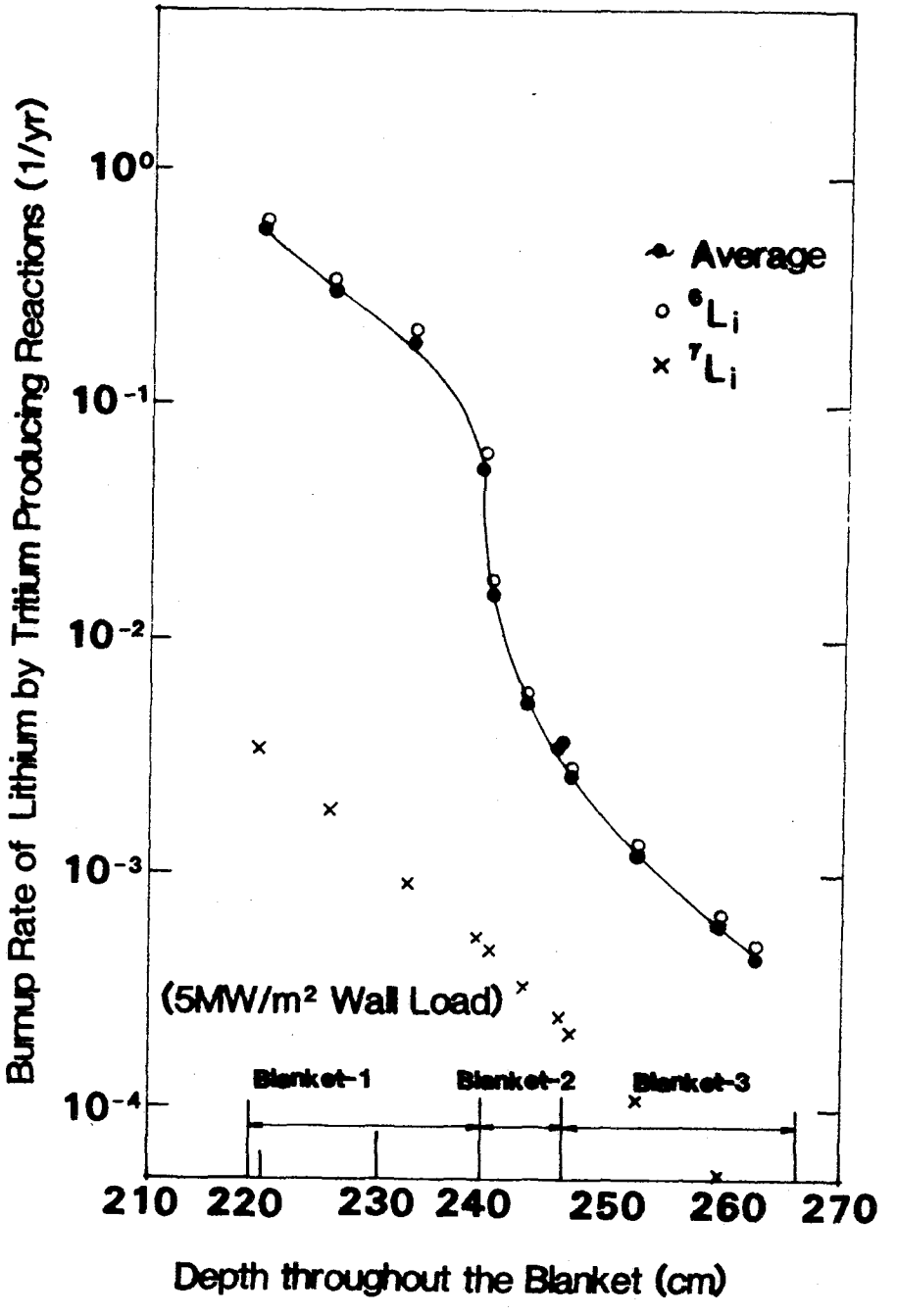

Figure 5.2.1-6 Burnup rate profile of lithium atom by tritium producing reactions in the $LiAlO_2/H_2O$/FS/Be blanket.

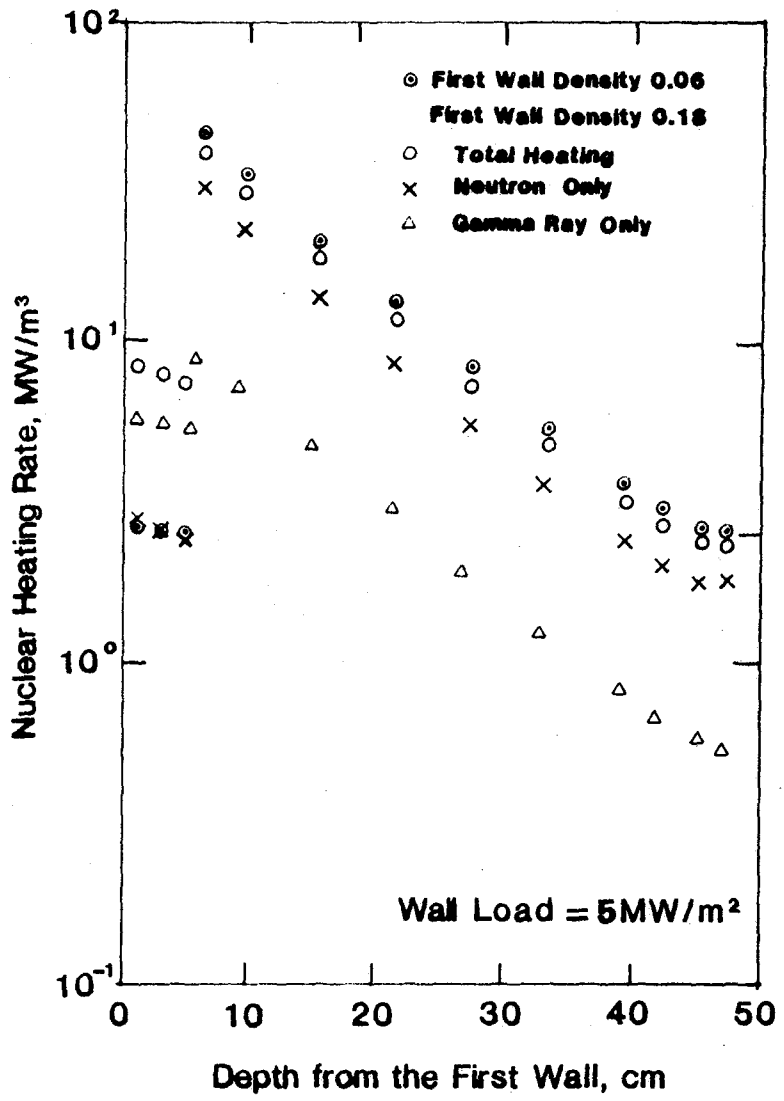

Figure 5.2.1-7 Heat deposition rate in the Li_2O/He/FS blanket.

neutron and gamma ray heating rates are similar to each other. When the gradient of the total heating rate in the breeder is compared with that of the tritium production rates from ^{6}Li and ^{7}Li, which represent the attenuation of low energy neutrons and high energy neutrons, respectively, the heating rate is seen to attenuate faster than the ^{6}Li tritium production rate but slower than the ^{7}Li rate. If the ^{7}Li rate is multiplied by a factor of four and added to the ^{6}Li curve in the Fig. 5.2.1-3, this reproduces the shape of the heating rate profile as shown in Fig. 5.2.1-8. This indicates that at the front edge, most of the heating comes from high energy neutrons, while low energy neutrons dominate at the back of the breeder.

When the first wall thickness is decreased to one-third of the original value, the total heating rate in the breeder is increased by f 18%, but the shape of the profile is not affected (Fig. 5.2.1-7).

Figure 5.2.1-9 shows profiles for the total heating rate and the contribution to the total heating from gamma rays and neutrons in the $LiAlO_2/H_2O/$-FS/Be blanket. In the first wall, the gamma ray heating rate is higher than the neutron heating. The maximum heating rate, at the front edge of the first wall, is f 55 W/cm^3 after correction for the structural density factor. This is higher than the corresponding value for the Li_2O/He/FS because of the Be neutron multiplier just behind the $LiAlO_2$ first wall.

In the breeder zone, neutron heating dominates the total heating rate, as was observed in the Li_2O blanket. As with the tritium production rate, the heating rate profile also changes at the boundary of blanket zones 1 and 2. The total heating rate in Fig. 5.2.1-9 may be broken down into two components: a high energy neutron contribution as indicated by the ^{7}Li curve in Fig. 5.2.1-6, and a low energy neutron contribution as indicated from the curve for total tritium production rate in Fig. 5.2.1-5. Note that gamma ray heating in Fig. 5.2.1-9 looks like the ^{7}Li curve in Fig. 5.2.1-6. These profiles may be combined as shown in Fig. 5.2.1-10 to match the calculated heating rate profile. This comparison indicates that the low energy and high energy components contribute about equally to the total heating rate at the front edge. The reason is that the $LiAlO_2$ blanket is rich in low energy neutrons.

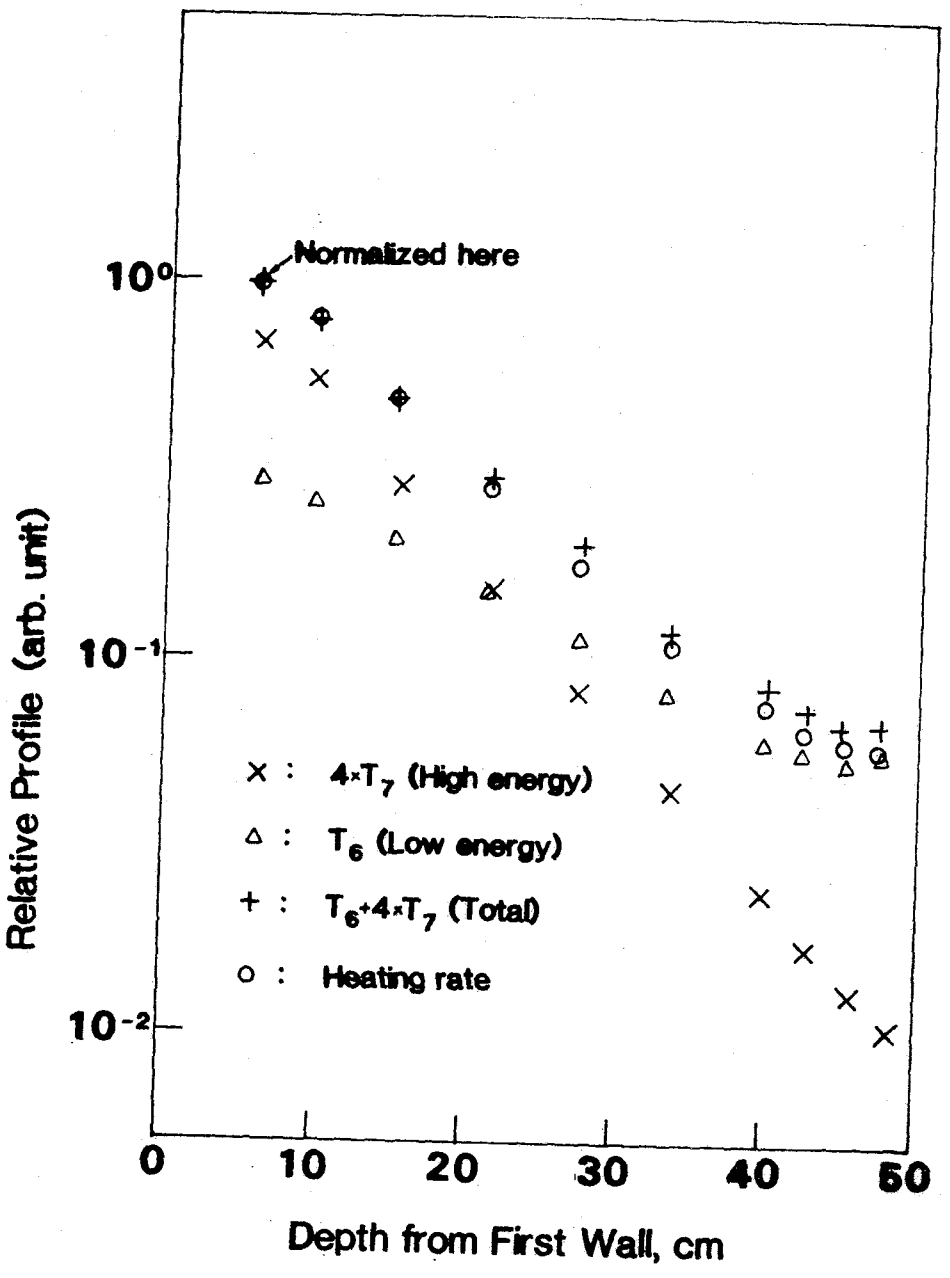

Figure 5.2.1-8 Break down of total heating rate in Li_2O/He/FS blanket into contributions from high energy neutrons and low energy neutrons.

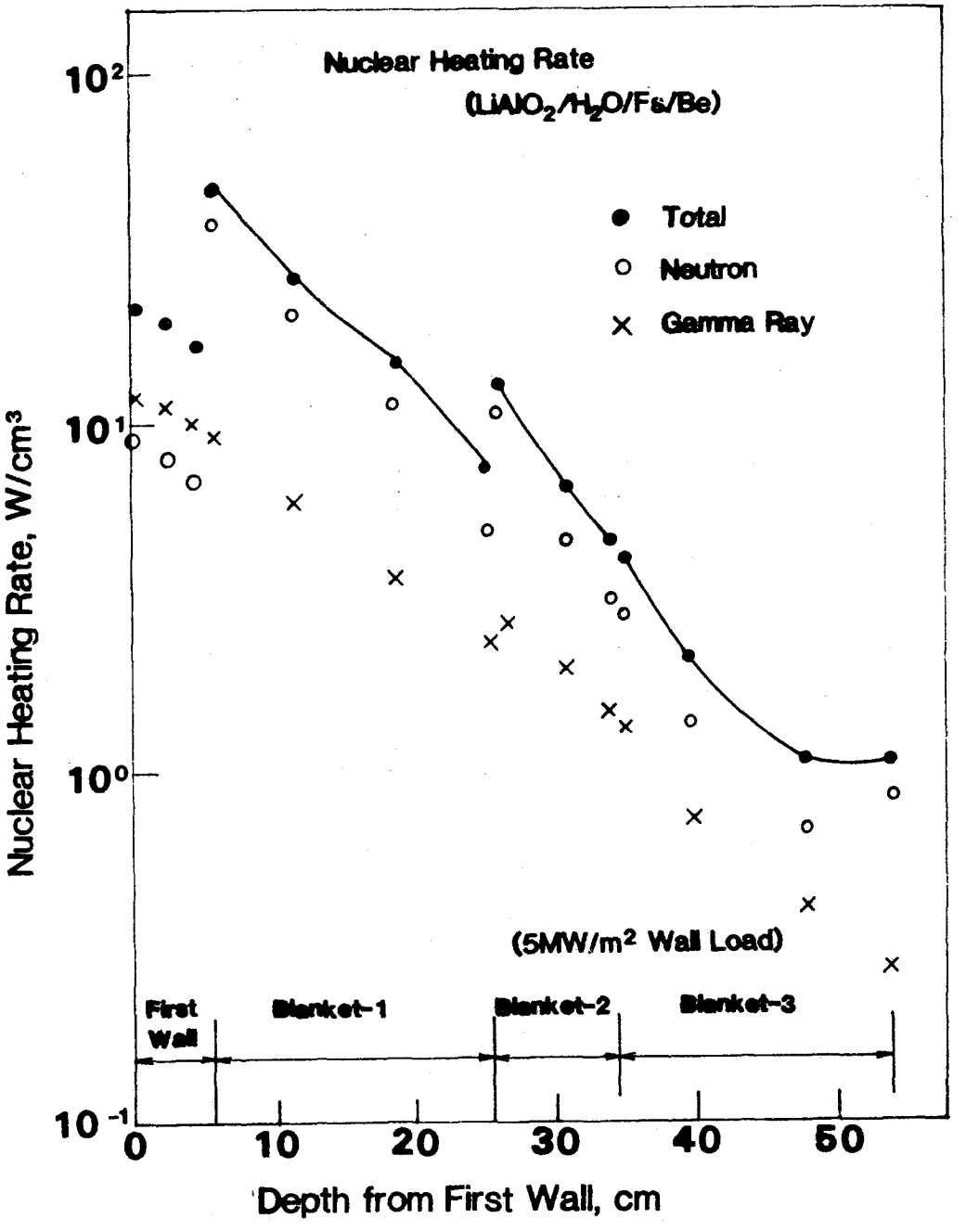

Figure 5.2.1-9 Depth profiles of nuclear heating rates in the $LiAlO_2/H_2O/FS/Be$ blanket.

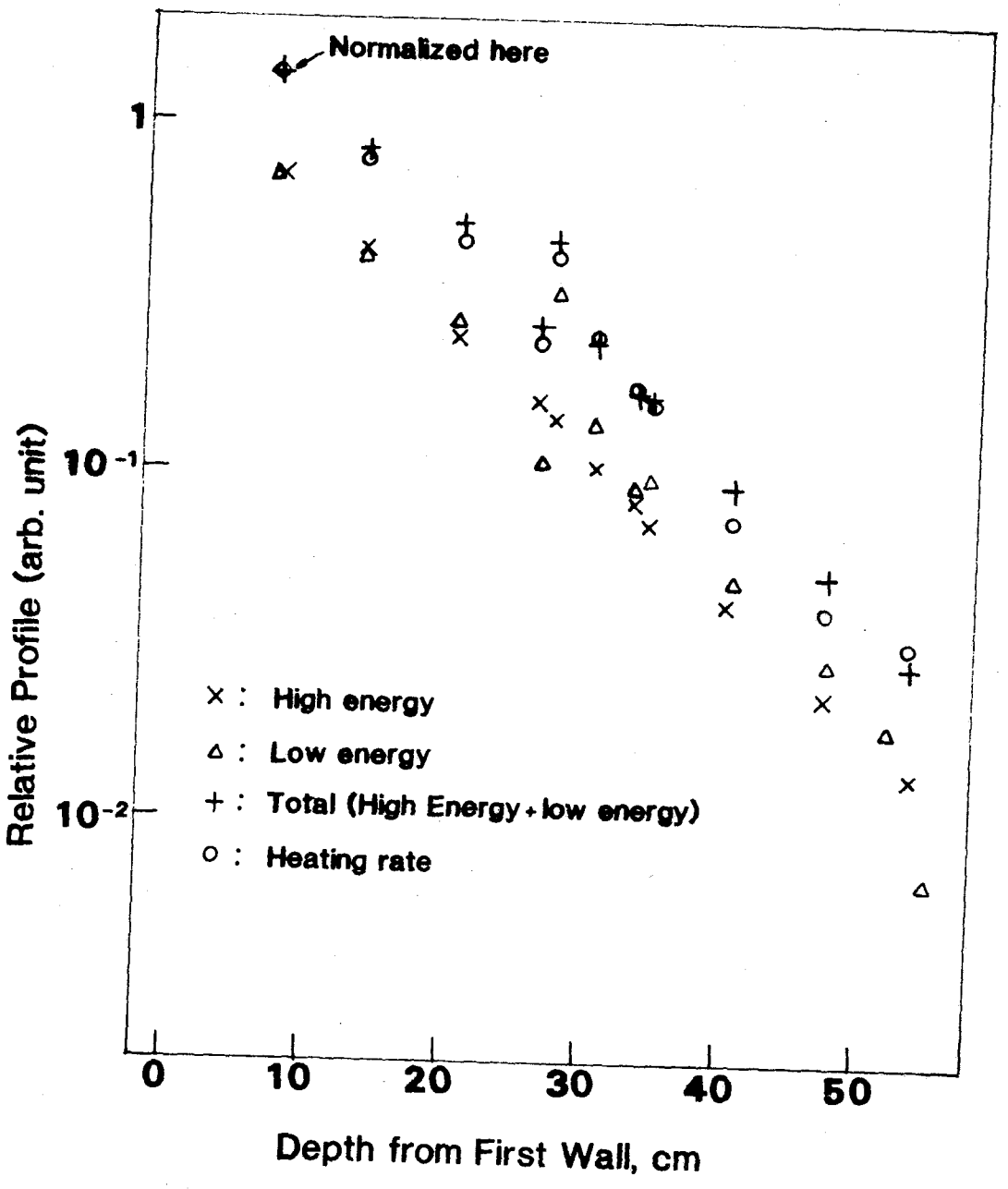

Figure 5.2.1-10 Breakdown of total heating rate in the $LiAlO_2/H_2O$/FS/Be blanket into contributions from high energy neutrons and low energy neutrons.

5.2.1.5 Radiation Damage Indicators

Figure 5.2.1-11 shows profiles for the radiation damage parameters of dpa, hydrogen production rate, and He production rate for the main elements (Fe and Cr) of the HT-9 steel, as well as the mixture average weighted by the relative density of iron and chromium in HT-9, for the Li_2O/He/FS blanket. The profiles for hydrogen and He production rates of each element looks very similar. Both of these reactions with the structure material have a high energy threshold. The maximum values for the dpa, hydrogen and helium production rate are observed at the front edge of the first wall. The peak HT-9 mixture values are 58 dpa/yr, 2200 ppm/yr and 620 ppm/yr, respectively.

Since a lower material density factor (0.18) was assumed in the first wall, the gradient of the profiles is more moderate than in the breeding zone. However, if the attenuation coefficient γ is defined by

$$g_1 = g_0 \, e^{-\gamma \varepsilon d_{fw}} \qquad (5.2.1\text{-}1)$$

where g_0, g_1 are the values at the first wall front and back for the neutronics parameter of interest (e.g., dpa), ε is the structural density factor (ε=0.18), and d_{fw} is the first wall thickness, then the attenuation rate in the first wall is larger than the corresponding rate in the breeding zone. For example, γ is 0.17 and 0.11 for the hydrogen production rate in the first wall and the breeding zone, respectively. High energy neutrons are attenuated more effectively by HT-9 steel than by Li_2O.

The dpa rate is related to the total energy deposition by neutrons, so it depends on both high and low energy neutrons. The profile of the dpa is more moderate than other radiation damage indicators. The dpa rates for the structural elements are similar.

Unfortunately, there are no systematic displacement cross-sections for Li_2O or similar ceramics. However, H. Heinisch[5] estimated the spectral-averaged cross-section using a method developed primarily for metals. Among spectra he considered, a helium-cooled lithium breeder concept may give similar spectrum as in the present Li_2O/He/FS blanket. From his estimates,

$$\sigma_{DPA}/\sigma_T = 1567 \qquad (5.2.1\text{-}2)$$

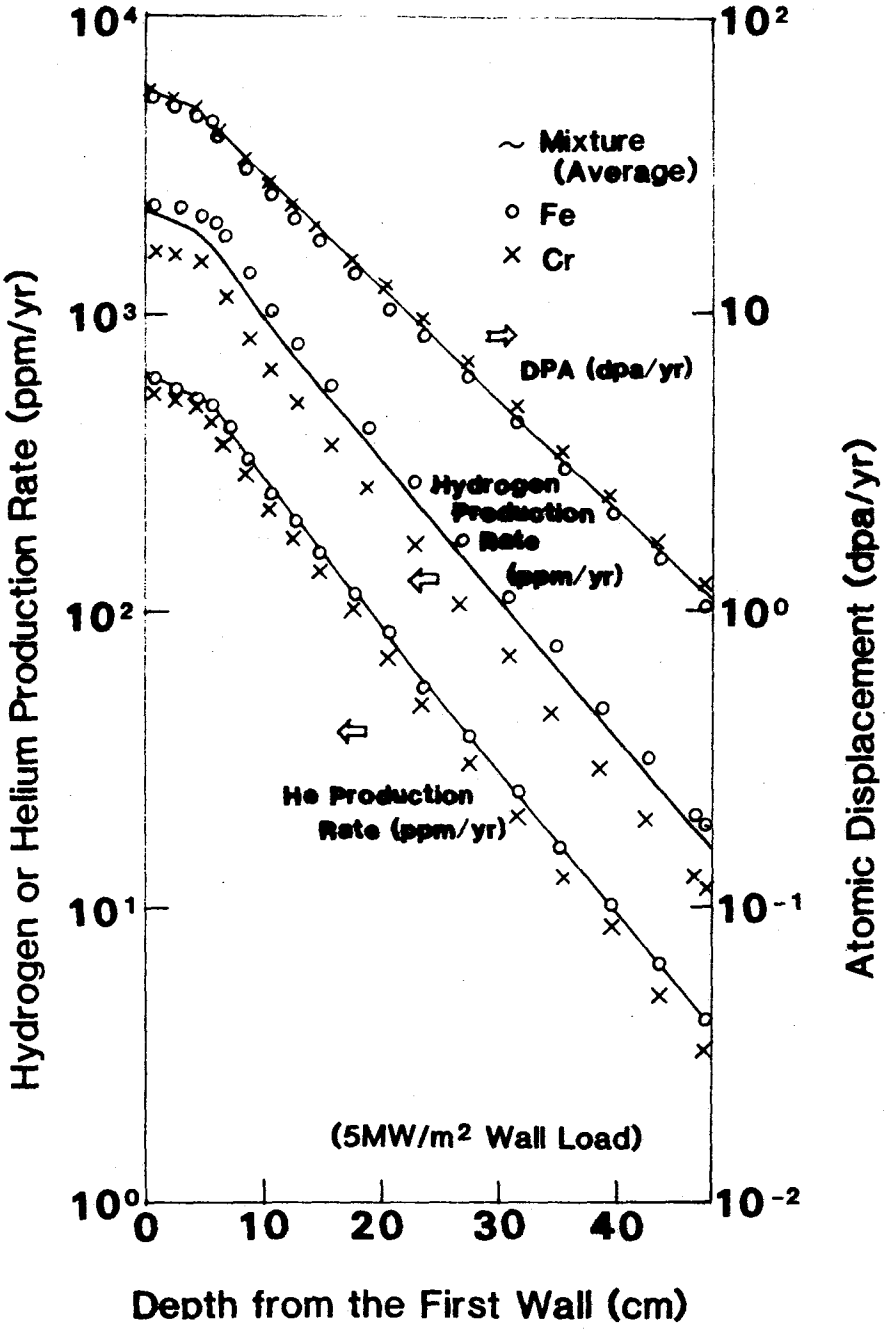

Figure 5.2.1-11 Atomic displacement rate, hydrogen and helium production rates in the Li_2O/He/FS blanket.

where σ_{DPA} is the dpa cross-section and σ_T is the tritium production cross-section. From this relation, the dpa rate in Li_2O at the front of the breeder is about 13.8 dpa/yr, using the burnup rate at the same position in Fig. 5.2.1-4. This is about one-third of the corresponding value for the structure.

Figure 5.2.1-4 also indicates the hydrogen and helium production rate from lithium through the $^6Li(n,\alpha)T$ and $^7Li(n,n'\alpha)T$ reactions. The corresponding contribution from oxygen is small. So the hydrogen and helium production rate (per atom) for the Li_2O would be two-thirds of the values in Fig. 5.2.1-4, or 5.9×10^3 ppm/yr at the front of the breeder. This is about a factor of three larger than the hydrogen production rate in the structure, and about one order of magnitude higher than the helium production rate in the structure.

Figure 5.2.1-12 shows profiles of damage parameters for the main elements of the HT-9 steel (Fe and Cr) in the $LiAlO_2/H_2O$/FS/Be blanket. The profiles of both the hydrogen and the helium production rates are very similar. The features of these curves are almost the same as was noted for the Li_2O/He/FS blanket because the same ferritic steel was assumed in both blankets.

The corresponding values for the aluminum in the breeding material are also shown in Fig. 5.2.1-12. Since the cross sections of $Al(n,\alpha)$ reactions are very large, the He production rate of aluminum is about 2.5 times as large as compared to the other elements. However, its relative profile is also determined by the fast neutron flux distribution, so it resembles the other curves.

Figure 5.2.1-13 shows the damage parameters for the HT-9 structure in the front of the blanket, which were obtained by averaging the data for each element over all elements in the alloy in the $LiAlO_2/H_2O$/FS/Be blanket. The maximum values are 55 dpa/yr, 2500 ppm/yr and 600 ppm/yr at the front edge of the first wall for the atomic displacement, hydrogen production rate and helium production rate, respectively at 5 MW/m^2 wall load.

A rough estimate of the maximum hydrogen and helium production rates in the breeder can be made using the tritium, and hence helium, production rates from Fig. 5.2.1-6. This gives a very high value of 1.2×10^5 ppm/yr, because of the very high local lithium burnup rate. Cross-sections for the atomic displacement are not available for $LiAlO_2$, so the dpa rate was not estimated.

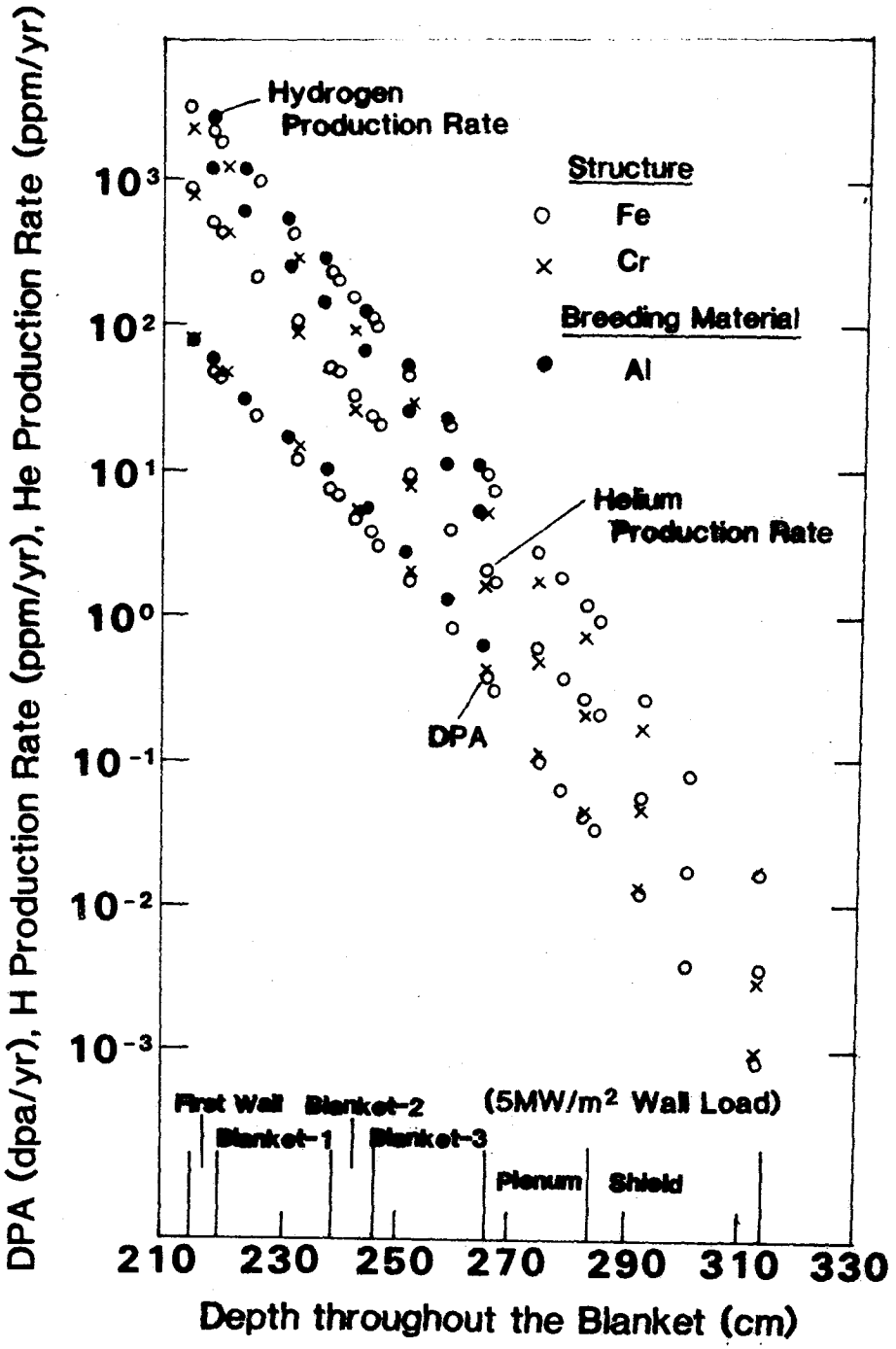

Figure 5.2.1-12 Profiles for the atomic displacement, hydrogen production and helium production rates in the $LiAlO_2/H_2O$/FS/Be blanket.

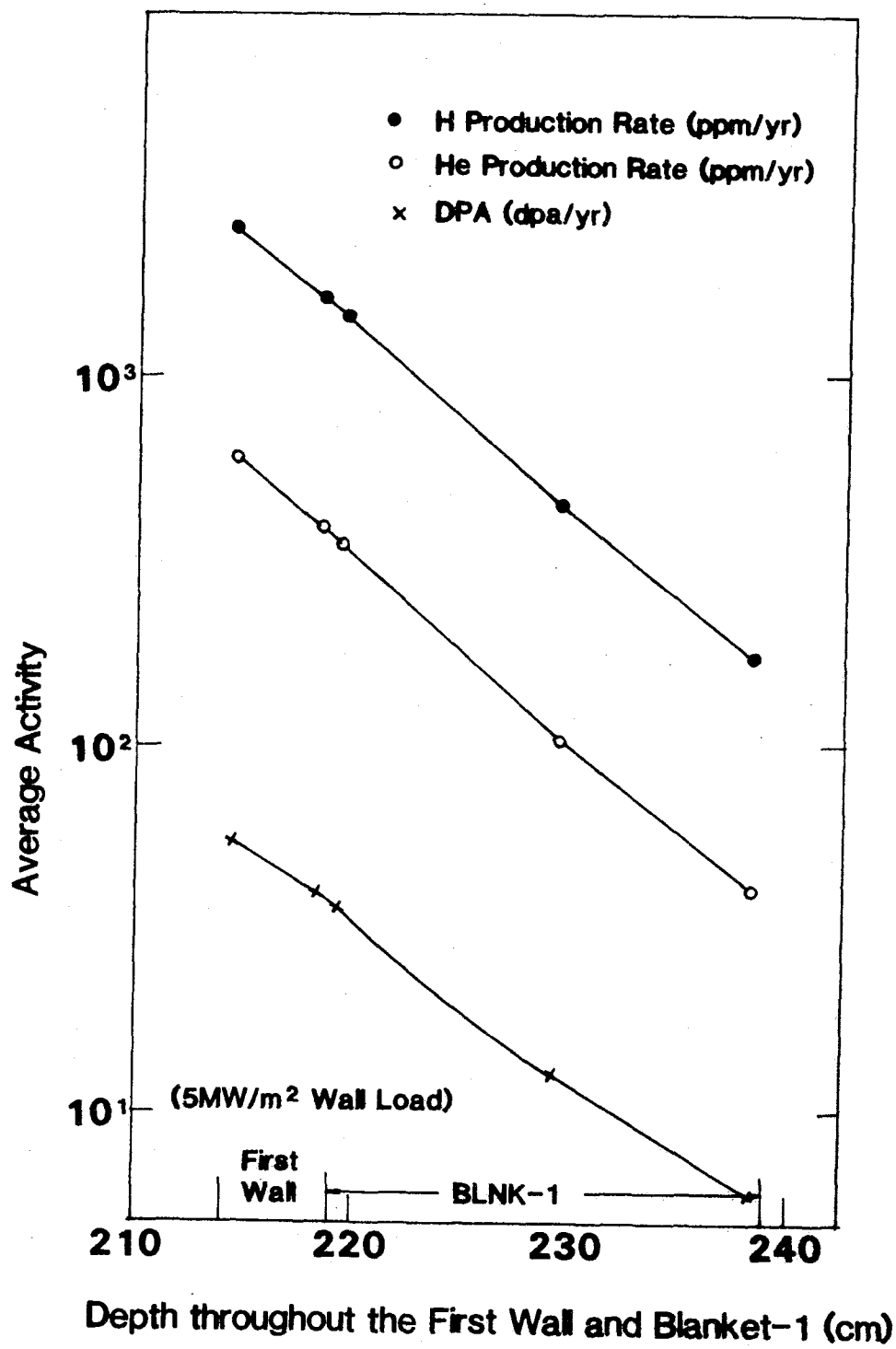

Figure 5.2.1-13 Activities (DPA, hydrogen and helium production rate) for HT-9 averaged over the Fe, Cr and Mo constituents in the $LiAlO_2/H_2O$/FS blanket.

References for Section 5.2.1

1. M. Abdou et al., "Blanket Comparison and Selection Study, Interim Report", Vol. I and II, Argonne National Laboratory, ANL/FPP-83-1 (October 1983).

2. W. W. Engle, Jr., "A User's Manual for ANISN", Oak Ridge National Laboratory, RSIC-CCC-82 (July 1973).

3. "VITAMIN-C: 171 Neutrons, 36 Gamma Group Cross-section Library in AMPX Interface Format for Fusion Neutronics Studies", Oak Ridge National Laboratory, Pkg DLC-41 (1978).

4. "ENDF/B Summary Documentation", BNL-NCS-17541, 2nd. ed. (1975).

5. H. Heinisch and G. Hollenberg, "Neutron Spectral Sensitivity of Displacement Damage in Lithium Oxide Solid Breeder Material", presented in FINESSE project meeting (May 1984).

5.2.2 Thermal Analysis

5.2.2.1 Introduction

Thermal analysis of a fusion blanket is essential to its design and proper operation. Blanket temperatures are very important for structural behavior, material properties, radiation damage, and tritium inventory. In this section, the first wall temperature distribution, breeder temperature distribution (including pulsing), flow hydraulics (including instabilities) and corrosion are considered. The intent is to understand the thermal-hydraulic behavior under normal conditions and to suggest important aspects to be considered under scaled test conditions. Table 5.2.2-1 summarizes some specific concerns related to the thermal behavior.

5.2.2.2 First Wall Temperature Distribution

The thermal analysis of water or gas-cooled first walls for solid breeder blankets is generally a well-understood problem of conduction, convective heat transfer, and fluid flow. The resulting temperature profile is important for structural behavior (influencing properties, thermal stresses, creep and swelling) and tritium permeation. Some specific uncertainties are in the actual surface and volumetric heat load profile, heat transfer to helium for $2000 < Re \lesssim 10000$, heat transfer at stagnant points near module tips, the presence and influence of flow oscillations, geometric effects (curved pipes, entry lengths), and effects of radiation and corrosion on bulk and surface properties. In this section, the basic characteristics of the first wall temperature profile are calculated assuming standard conduction and heat transfer models.

Most solid breeder first wall designs incorporate an array of tubes or channels carrying high velocity liquids or gas coolant. The physical arrangement varies from flat arrays (e.g., STARFIRE[1]) to cylindrical pods (e.g., FINESSE reference blankets). The basic temperature distribution may be characterized in general by a bulk coolant temperature rise, ΔT_{bulk}, a film rise, ΔT_{film}, and the surface layer temperature rise, ΔT_{fw}; although the exact exact profile will depend on details such as the presence of supports and the heating profile.

For the reference blankets, these temperature characteristics are

Table 5.2.2-1. Issues for Solid Breeder Thermal Behavior

First Wall Temperature Distribution

- Steady-state temperature profile
- Azimuthal surface and volumetric heat source profiles
- Heat transfer at module tip in symmetrically cooled designs
- Heat transfer to helium for $3000 < Re < 10000$
- Heat transfer from breeder region

Solid Breeder Temperature Distribution

- Steady-state temperature profile
- Effects of axial conduction, heat source asymmetries, geometrical asymmetries
- Pulsing effects on temperature profile
- Breeder/clad gap conductance
- Breeder intrinsic thermal conductivity changes with fluence
- Breeder effective thermal conductivity changes with fluence, mass redistribution, cracking, chemistry changes
- Effective thermal conductivity of porous and sphere-pack breeder

Flow Conditions

- Flow distribution
- Strength and frequency of flow-induced vibrations
- Thermal breeder/coolant instability
- Module pressure drop
- Entry lengths for heat transfer

Corrosion

- Impurity effects on corrosion rate of candidate coolant/alloys
- Mass transfer and corrosion by LiOT
- Materials compatibility concerns at high burnup regions
- Magnetic field effects on corrosion
- High-energy neutron effects on corrosion
- Corrosion effects on surface heat transfer

$$\Delta T_{fw} = \frac{d_{fw}}{k_{fw}} \left(q_s + \frac{\dot{Q}_v d_{fw}}{2}\right) \qquad (5.2.2\text{-}1)$$

$$\Delta T_{film} = \frac{d_{fc}(q_s + \dot{Q}_v d_{fw})}{Nu_{fw} k_c} \simeq C\,(q_s + \dot{Q}_v d_{fw}) \frac{d_{fc}^{0.2}}{U_{fw}^{0.8}} \qquad (5.2.2\text{-}2)$$

where d_{fc} is the channel hydraulic diameter; $Nu \simeq 0.023\ Pr^{0.4} Re^{0.8}$; and C contains numerical constants and materials properties; and

$$\Delta T_{bulk} = \int \frac{(q_s + \overline{\dot{Q}_v d} + q_{br})(d_{fc} + d_{fs})}{c_{pc} \rho_c U_{fw} \pi\, d_{fc}^2/4}\, ds \qquad (5.2.2\text{-}3)$$

where s is the length along the channel; c_{pc} and ρ_c are coolant specific heat and density; U_{fw} is the coolant velocity; the volumetric heating term $\overline{\dot{Q}_v d}$ includes contributions from the full first wall structure, including neutron attenuation effects; and q_{br} is the net heat flux from the breeder region.

For a uniform surface heat flux outwards from the plasma, small heat transfer from the breeder and pod geometry, the temperature rise from the edge to the center is

$$\Delta T_{bulk} \simeq C\,(q_{so} + \frac{\pi}{2} \dot{Q}_{vo} d_{fw} + \cdots) \frac{R_{fw}\,(d_{fc} + d_{fs})}{U_{fw} d_{fc}^2} \qquad (5.2.2\text{-}4)$$

where R_{fw} is the radius of the first wall lobes; and q_{so}, $\dot{Q}_{vo}$ are the peak heat source values.

The largest geometric perturbation to this simple description is due to the presence of channel support walls, which may act as fins and locally cool the first wall or act as heat sources from internal nuclear heating. However, in either case, the maximum perturbation of the first wall temperature in the vicinity of the fins is limited by conduction through the first wall, so

$$\frac{\Delta T_{fin}}{\Delta T_{fw}} \lesssim \frac{(q_s + \dot{Q}_v d_{fw})\ d_{fs}/k_{fw}}{(q_s + \dot{Q}_v d_{fw}/2\ )\ d_{fw}/k_{fw}} \qquad (5.2.2\text{-}5)$$

The variation of the heat source is also important for the temperature

distribution. There are three contributions: plasma side heat flux, volumetric neutron heating, and breeder side heat flux.

Plasma heating of the first wall is primarily in the form of radiation (less than 10% direct particle interaction). Taking the plasma to be a uniform radiator, then the surface heating flux varies with the angle of incidence,

$$q_s \simeq q_{so} \, |\sin \theta| \qquad (5.2.2\text{-}6)$$

where q_{so} is the peak heat flux at the tip of the module, and θ is the azimuthal angle of the lobe first wall ($\theta = 90°$ marks the module tip) away from the inlet.

Volumetric heating exponentially decreases through the first wall, although the attenuation is small in the reference blanket designs. The azimuthal variation in volumetric heating (discussed in Section 5.3.1) around the module first wall are related to the neutron source and reflection characteristics of the plasma chamber.

Heating from the breeder depends on the design details. The gas gap in the Li_2O/He/HT-9 reference design acts as insulation, while the adjacent solid breeder in the $LiAlO_2$/H_2O/PCA/Be could lead to appreciable heat transfer.

To incorporate these contributions into an overall temperature profile, a set of 2-D calculations were made. The first considered the temperature variation through a cross-section of the first wall, i.e., around the coolant channels, using the conduction code TAC02D.[2] The first wall temperature profile is shown in Fig. 5.2.2-1 for a Li_2O/He/HT-9 blanket. As expected, the variation is dominated by the ΔT across the first wall, with little effect due to the supporting walls.

The second analysis considered the temperature variation around the first wall along the coolant channels. The azimuthal variation is shown in Figs. 5.2.2-2 to -4. for the parameters given in Table 5.2.2-2. The results show the rapid rise in first wall surface temperature towards the module tip. This rise drops as the first wall is thinned by plasma erosion. The importance of surface heating is illustrated by the small change in first wall temperature in the Li_2O/He/HT-9 tokamak blanket, and the large change in the corresponding

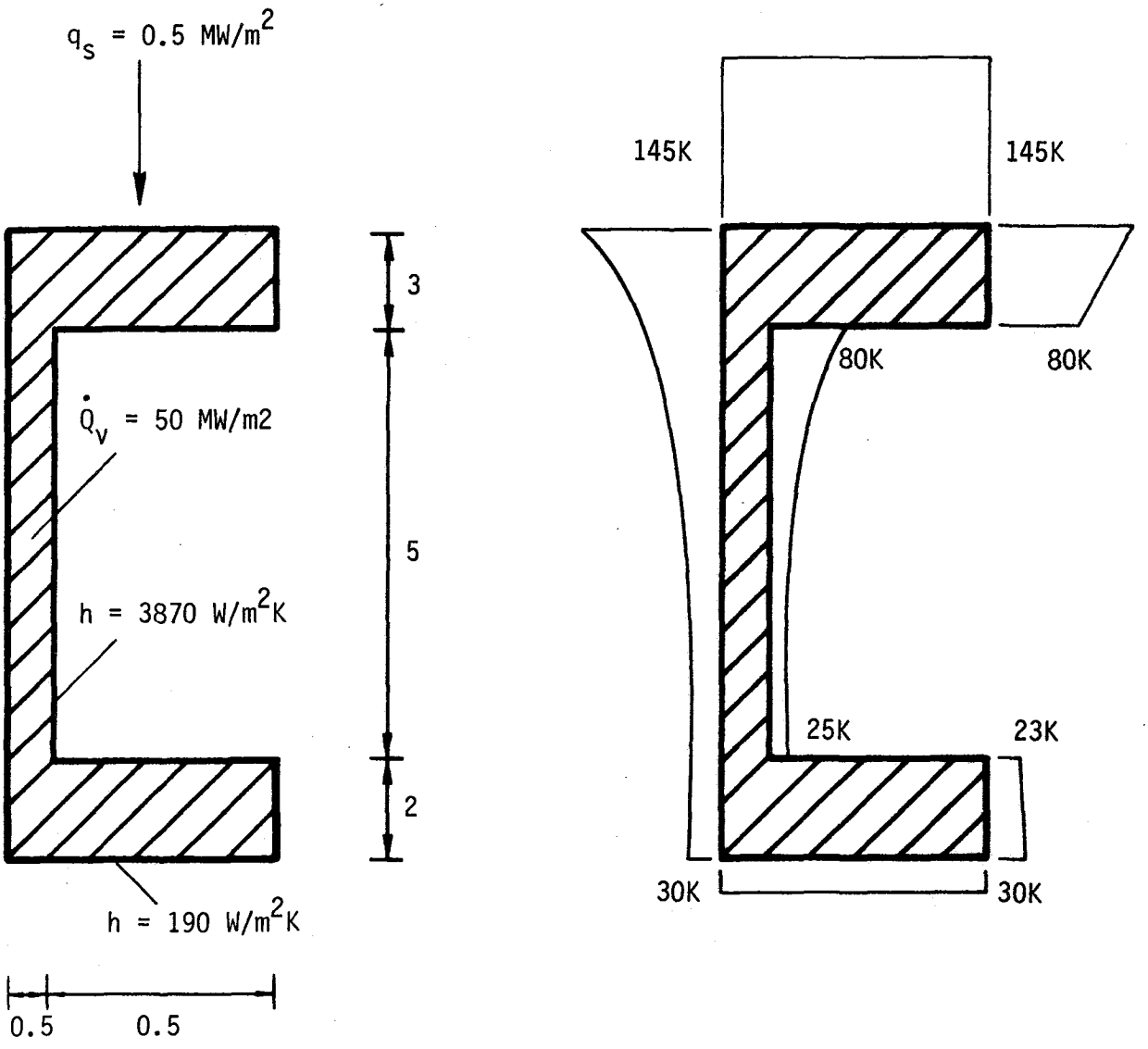

(Numbers in millimeters)

(Numbers are temperature difference between the structure and the coolant)

Figure 5.2.2-1 Temperature profiles in a rib supported first wall channel.

Table 5.2.2-2 First Wall Design Parameters

	Li_2O/He/HT-9 Tokamak	Li_2O/He/HT-9 Mirror	$LiAlO_2$/H_2O/PCA/Be Tokamak
Peak surface heat flux, MW/m^2	1.0	0.05	1.0
Neutron wall load, MW/m^2	5.0	5.0	5.0
Peak volumetric heating, MW/m^3	50	50	50
Back wall heat flux, MW/m^2	0	0	0.25
Neutron attenuation length, mm	70	70	70
Distance to plasma center, m	1.6	0.6	1.6
Lobe first wall radius, m	0.15	0.15	0.15
First wall thickness, mm	3.5	6.0	5.54
Coolant channel width, mm	1.0	5.0	3.81
Coolant channel height, mm	7.0	5.0	3.81
First wall (fin) support thickness, mm	1.0	1.0	2.54
Back wall thickness, mm	0.3	0.3	2.54
Coolant inlet temperature, °C	275	275	285
Coolant inlet velocity, m/s	60	31	2.5
Reynold's number	15000	22100	74100
Inlet heat transfer coefficient, $W/m^2 \cdot K$	5800	2770	24500

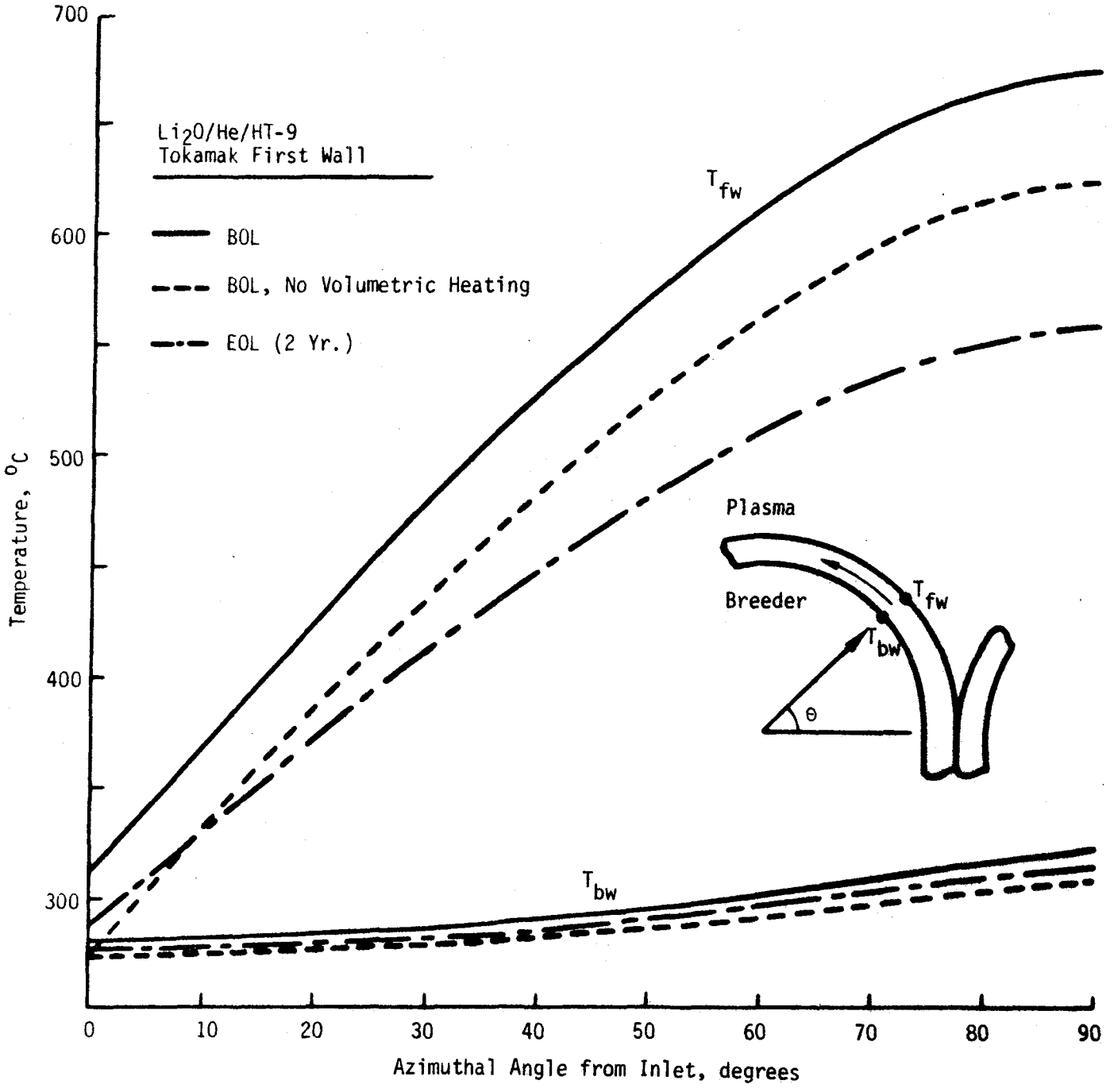

Figure 5.2.2-2 Li_2O/He/HT-9 tokamak reactor first wall temperature profiles at a peak surface heat flux q_s= 1 MW/m^2 and a peak volumetric heat load $\dot{Q}_v$= 50 MW/m^3.

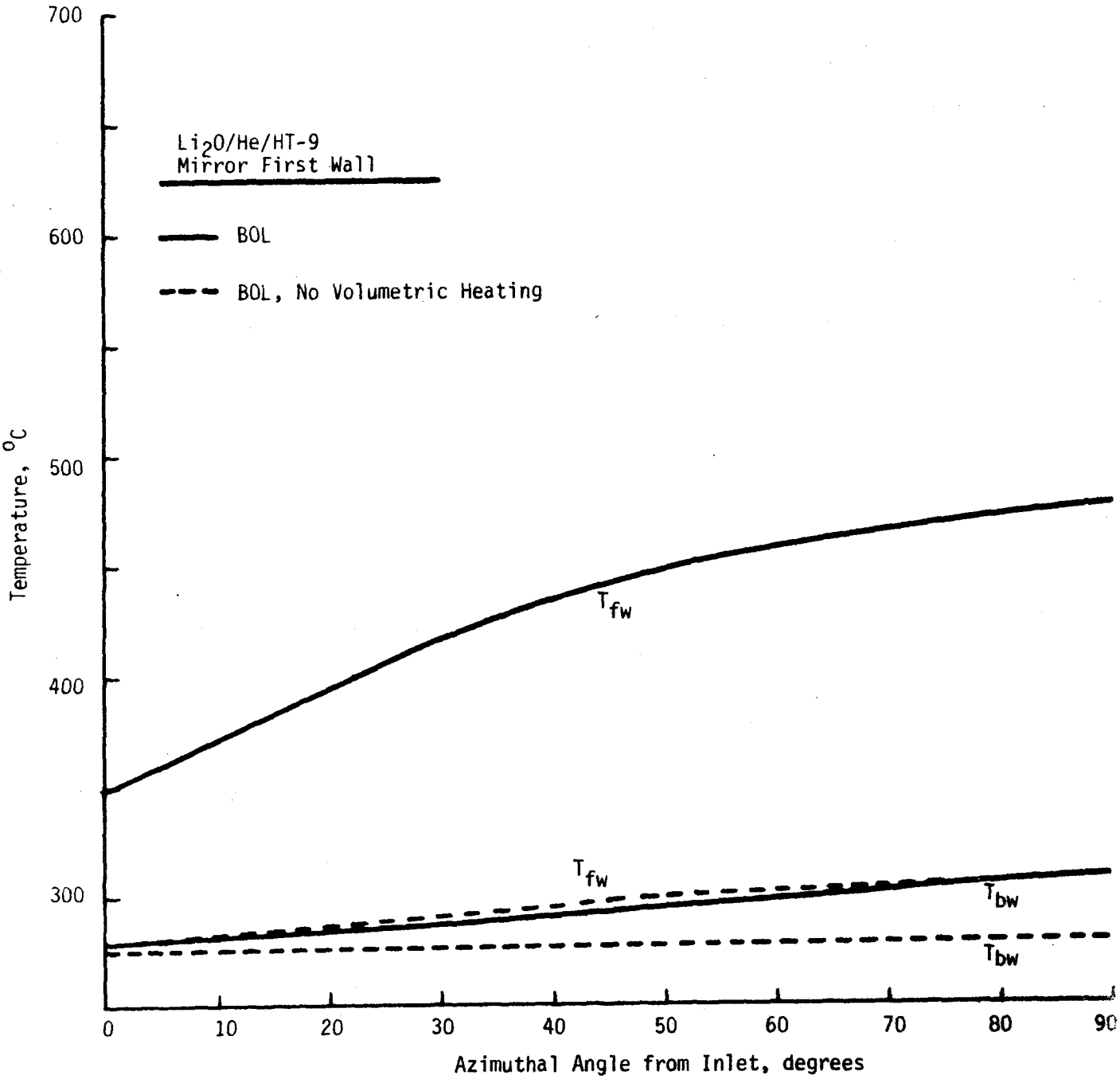

Figure 5.2.2-3 Li_2O/He/HT-9 mirror reactor first wall temperature profiles at a peak surface heat flux q_s = 0.05 MW/m^2 and a peak heat load $\dot{Q}_v$ = 50 MW/m^3.

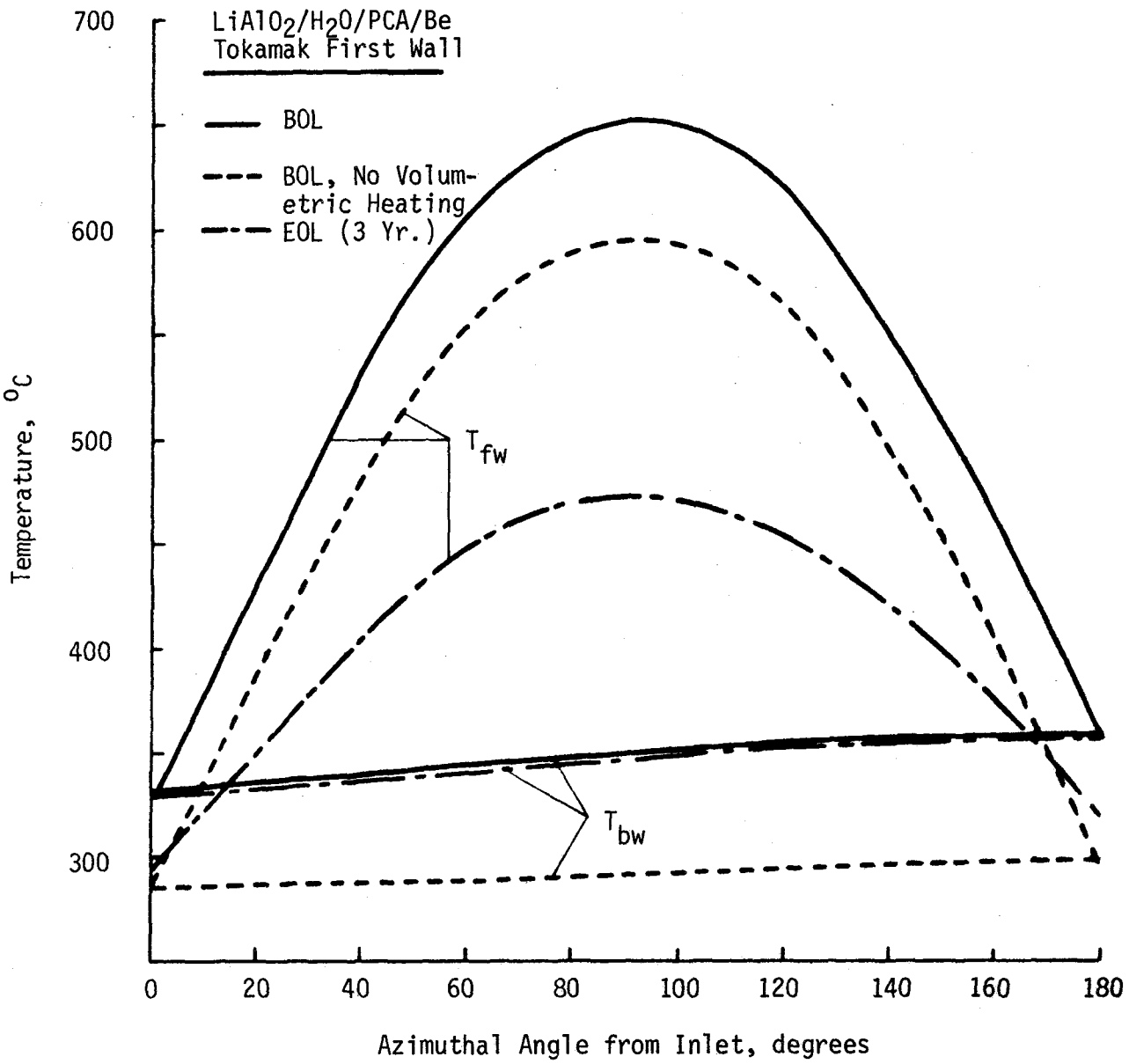

Figure 5.2.2-4 $LiAlO_2/H_2O$/PCA/Be tokamak reactor first wall temperature profile at a peak surface heat flux q_s = 1 MW/m^2 and a peak volumetric heat load $\dot{Q}_v$ = 50 MW/m^3.

mirror, as the volumetric heating is reduced. The $LiAlO_2/H_2O$/PCA/Be first wall has the same overall behavior. Although the coolant flow is from one side, the heating rate is symmetric about the module center leading to a largely symmetric first wall temperature.

5.2.2.3 Breeder Region Temperature Distribution

The breeder temperature profile is important for many phenomena, particularly related to tritium recovery and breeder mechanical behavior. Figure 5.2.2-5 illustrates the strong dependence of some of these processes on temperature. However, the breeder temperature distribution is not precisely known since it is affected by many uncertain factors, including the breeder thermal conductivity (both intrinsic and porosity effects), gap conductance, coolant flow distribution and their variation with time. Table 5.2.2-1 lists many of the phenomena that contribute to the breeder temperature profile.

Steady-State Temperature Profile in Solid Breeders: Layered Design

The reference Li_2O breeder design has a slab geometry, with coolant flowing between the breeder plates and heat generated in the breeder in a nonuniform manner (Figure 5.2.2-6). The assumptions made in analyzing the model are:

1. No conduction in z (radial) direction. This will allow solving for temperature profile in one dimension (x-direction) with Q_v varying in the z-direction. This conduction will be considered later

2. Since the cladding is very thin (0.25 mm) and has high thermal conductivity, the clad temperature drop is small and predictable. Instead, the boundary heat transfer coefficient is the sum of contributions from the gap, cladding and coolant, or

$$1/h_{eq} = 1/h_{gap} + (d/k)_{cladding} + 1/h_{coolant} \qquad (5.2.2\text{-}7)$$

3. Steady-state heat generation. Pulsing is considered later.

The energy equation governing the temperature profile is

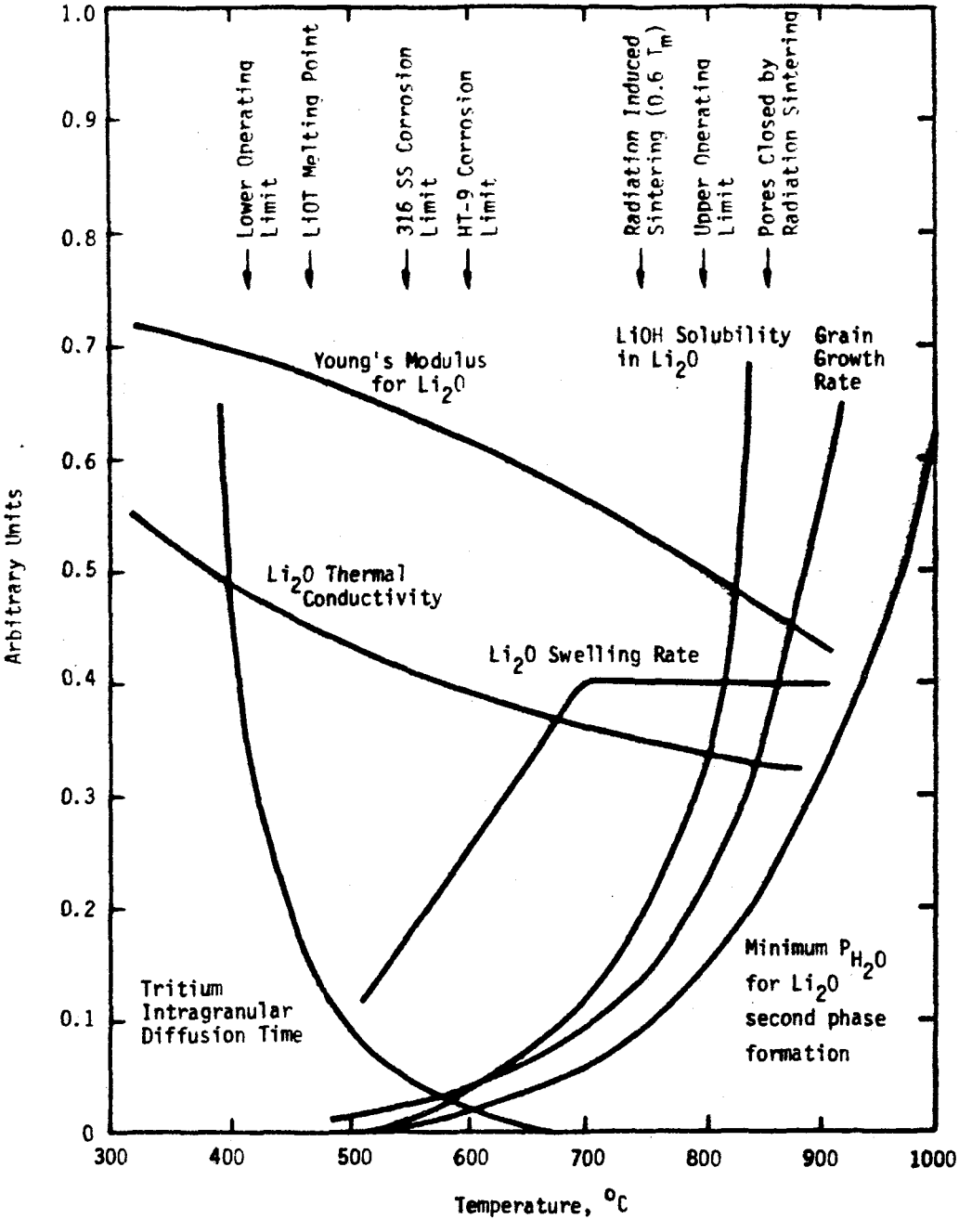

Figure 5.2.2-5 Temperature dependence of various phenomena occuring in Li_2O under irradiation

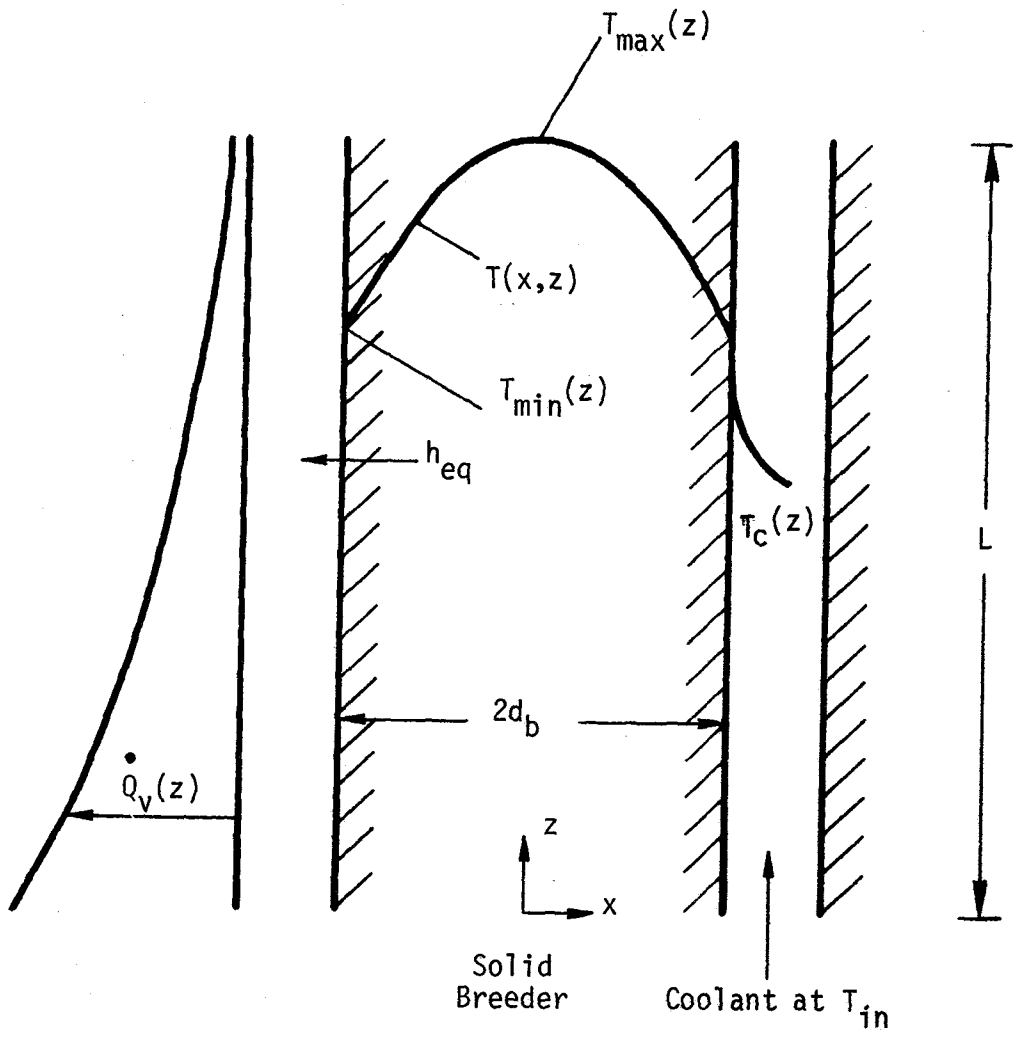

Figure 5.2.2-6 Layered solid breeder theoretical model.

$$k_b(\partial^2 T/\partial x^2) + \dot{Q}_v = 0 \qquad (5.2.2\text{-}8)$$

where

$$\partial T/\partial x = 0 \qquad \text{at } x = 0 \qquad (5.2.2\text{-}9)$$

and

$$-k_b \partial T/\partial x = h_{eq}(T - T_c) \qquad \text{at } x = d_b \qquad (5.2.2\text{-}10)$$

The coolant temperature is calculated by an energy balance as

$$\dot{m}_c' \, c_{pc} dT_c = \dot{Q}_v d_b dz \qquad (5.2.2\text{-}11)$$

where

$$T_c = T_{in} \qquad \text{at } z = 0 \qquad (5.2.2\text{-}12)$$

A set of dimensionless parameters are defined as

$$\xi = x/d_b \qquad (5.2.2\text{-}13)$$

$$\zeta = z/L_b \qquad (5.2.2\text{-}14)$$

$$q(z) = \dot{Q}_v(z)/\dot{Q}_{v,a} \qquad (5.2.2\text{-}15)$$

where $\dot{Q}_{v,a}$ is the heat generation averaged over the entire breeder volume. Equations (5.2.2-8) through (5.2.2-13) are solved to obtain the temperature profile in the entire breeder.

$$T_c = T_{in} + (2d_b L_b \dot{Q}_{v,a} / \dot{m}_c' c_{pc}) \int_0^{\zeta} d\zeta q(\zeta) \qquad (5.2.2\text{-}16)$$

$$T_{min} = T_c + \dot{Q}_{v,a} d_b q(\zeta)/h_{eq} \qquad (5.2.2\text{-}17)$$

$$T = T_{min} + (\dot{Q}_{v,a} d_b^2/2k_b)(1 - \xi^2) q(\zeta) \qquad (5.2.2\text{-}18)$$

An average breeder temperature at each z-location may be defined by

$$T_{avg}(\zeta) = (1/d_b) \int_0^{d_b} T(x,z)\, dx = \int_0^1 T(\xi,\zeta)\, d\xi \qquad (5.2.2\text{-}19)$$

or, from Eq. (5.2.2-18),

$$T_{avg}(\zeta) = T_{min} + (\dot{Q}_{v,a} d_b^2/3k_b)\, q(\zeta) \qquad (5.2.2\text{-}20)$$

The maximum breeder temperature occurs on the centerline, x = 0, where

$$T_{max}(\zeta) = T_{min} + (\dot{Q}_{v,a} d_b^2/2k_b)\, q(\zeta) \qquad (5.2.2\text{-}21)$$

Breeder Maximum and Minimum Temperatures The breeder temperature extremes are important for several reasons. For example, the entire breeder must be within some temperature window limited by high tritium inventory at low temperatures and sintering (and other phenomena) at high temperatures. The absolute maximum temperature occurs at the point with the highest heat generation and farthest from the coolant, i.e., the breeder centerline towards the plasma:

$$T_{max}^{abs} = T(\xi = 0, \zeta = 0)$$

$$= T_{in} + \dot{Q}_{v,a} d_b q(0)/h_{eq} + (\dot{Q}_{v,a} d_b^2/2k_b)\, q(0) \qquad (5.2.2\text{-}22)$$

The location of the minimum temperature, however, is not so simply specified, other than that it occurs adjacent to the coolant (ξ = 1). At ζ = 0, the coolant is the coldest but heat generation is highest. Conversely, at ζ = 1, the back of the breeder, the heat generation is lowest but the coolant is the hottest. From Eqs. (5.2.2-16) and (5.2.2-17)

$$T_{min}(\zeta) = T_{in} + (2d_b L_b \dot{Q}_{v,a}/\dot{m}'_c c_{pc}) \int_0^{\zeta} d\zeta q(\zeta)$$

$$+ \dot{Q}_{v,a} d_b q(\zeta)/h_{eq} \qquad (5.2.2\text{-}23)$$

It is clear that the location of the absolute minimum breeder temperature depends on many parameters and could be anywhere between ζ = 0 and 1.

For the special case of exponential heat generation

$$q(\zeta) = q(0)\,[q(1)/q(0)]^{\zeta} \qquad (5.2.2\text{-}24)$$

where q(0) and q(1) are the values of function q at $\zeta = 0$ and 1. Now Eq. (5.2.2-23) may be differentiated with respect to ζ while using Eq. (5.2.2-24). It is seen that the differential of T_{min} is dependent on ζ meaning that $T_{min}(\zeta)$ must vary monotonically, leading to the following conclusion for the location of absolute minimum temperature, $z_{min} = L_b\zeta_{min}$,

$$\zeta_{min} = 0 \qquad \text{if } 2L_b h_{eq}/\dot{m}'_c c_{pc} > \ln[q(0)/q(1)] \qquad (5.2.2\text{-}25)$$

$$\zeta_{min} = 1 \qquad \text{if } 2L_b h_{eq}/\dot{m}'_c c_{pc} < \ln[q(0)/q(1)] \qquad (5.2.2\text{-}26)$$

$$T_{min}(\zeta) \neq fn(\zeta) \qquad \text{if } 2L_b h_{eq}/\dot{m}'_c c_{pc} = \ln[q(0)/q(1)] \qquad (5.2.2\text{-}27)$$

The latter equation gives the condition for constant minimum temperature along the coolant channel. This case have design applications since it utilizes the breeder temperature window more efficiently than the other cases.

Axial Conduction in Layered Solid Breeders

The nuclear heat source decreases with depth into the breeder, leading to overall temperature gradients from breeder front to back, in addition to the larger gradients through the breeder thickness towards the coolant. The steady-state temperature distribution of a solid breeder plate was earlier obtained neglecting axial heat conduction due to this temperature difference. This assumption is studied here.

Analysis To estimate the size of the effect, it is assumed that axial conduction in the ζ (z)-direction does not change the shape of the temperature profile in the ξ (x)-direction, but rather changes the magnitude of the temperature differences. Therefore, a correction function is defined, $g(\zeta)$, which in effect accounts for the axial conduction. The results for temperature profiles from Eqs. (5.2.2-16) through (5.2.2-18), using the correction function may now be written as

$$T_c = T_{in} + (2d_b L_b \dot{Q}_{v,a}/\dot{m}'_c c_{pc}) \int_0^{\zeta} d\zeta\; q(\zeta)g(\zeta) \qquad (5.2.2\text{-}28)$$

$$T_{min} = T_c + \dot{Q}_{v,a} d_b q(\zeta) g(\zeta) / h_{eq} \qquad (5.2.2\text{-}29)$$

$$T = T_{min} + (\dot{Q}_{v,a} d_b^2 / 2k_b)\ (1 - \xi^2)\ q(\zeta) g(\zeta) \qquad (5.2.2\text{-}30)$$

$$T_{avg}(z) = T_{min} + (\dot{Q}_{v,a} d_b^2 / 3k_b)\ q(\zeta) g(\zeta) \qquad (5.2.2\text{-}31)$$

The other way to look at this is that an effective heat generation has been defined as

$$\dot{Q}_{v,eff}(\zeta) = \dot{Q}_v(\zeta) g(\zeta) \qquad (5.2.2\text{-}32)$$

The problem is to find $g(\zeta)$. Based on a fin type analysis, the energy balance equation may be written as

$$\partial^2 T_{avg} / \partial \zeta^2 = (h_{eq} L_b^2 / d_b k_b)\ (T_{min} - T_c) - \dot{Q}_v L_b^2 / k_b \qquad (5.2.2\text{-}33)$$

Equations (5.2.2-28, -29 and -31) are used to substitute for T_{avg}, T_{min}, and T_c in Eq. (5.2.2-33) to obtain an ordinary differential equation for $g(\zeta)$:

$$\frac{d^2(qg)}{d\zeta^2} + a \frac{d(qg)}{d\zeta} - b(qg) = -bq \qquad (5.2.2\text{-}34)$$

where

$$a = (6k_b L_b / \dot{m}'_c c_{pc} d_b) / (1 + 3k_b / d_b h_{eq}) \qquad (5.2.2\text{-}35)$$

$$b = (3L_b^2 / d_b^2) / (1 + 3k_b / d_b h_{eq}) \qquad (5.2.2\text{-}36)$$

This can be solved to obtain

$$qg = C_1 e^{m_1 \zeta} + C_2 e^{m_2 \zeta} + [b^{m_1 \zeta} / (m_2 - m_1)] \int_0^{\zeta} d\zeta e^{-m_1 \zeta} q(\zeta)$$

$$+ [b e^{m_2 \zeta} / (m_1 - m_2)] \int_0^{\zeta} d\zeta e^{-m_2 \zeta} q(\zeta) \qquad (5.2.2\text{-}37)$$

where m_1 and m_2 are the roots of

$$m^2 + am - b = 0 \qquad (5.2.2\text{-}38)$$

The constants C_1 and C_2 are determined from boundary conditions. A logical choice is that of insulated boundary at $\zeta = 0$ and 1,

$$dT_{avg}/d\zeta = 0 \quad \text{at} \quad \zeta = 0,1 \qquad (5.2.2\text{-}39)$$

The average temperature can be calculated from Eqs. (5.2.2-28, -29 and -31) as

$$T_{avg} = T_{in} + (2d_b L_b \dot{Q}_{v,a}/\dot{m}' c_{pc}) \int_0^{\zeta} d\zeta q(\zeta) g(\zeta)$$

$$+ (\dot{Q}_{v,a} d_b^2/3k_b)\,(1 + 3k_b/d_b h_{eq})\, qg \qquad (5.2.3\text{-}40)$$

Substitution of Eq. (5.2.2-40) in boundary condition Eq. (5.2.2-39) yields:

$$d(qg)/d\zeta + a(qg) = 0 \quad \text{at} \quad \zeta = 0,1 \qquad (5.2.2\text{-}41)$$

The constants C_1 and C_2 can be calculated by substituting qg from Eq. (5.2.2-37) into Eq. (5.2.2-41).

Axial Conduction Results To carry out the calculations, a quantitative expression is needed for the heat generation profile in the solid breeder. An exponential fit is used here as

$$\dot{Q}_v = \dot{Q}_{v,a}(c_1 + c_2 e^{-\gamma\zeta}) \qquad (5.2.2\text{-}42)$$

where

$$\dot{Q}_{v,a} = 14.3\ MW/m^2,\ c_1 = 3.267,\ c_2 = 0.1006,\ \gamma = 3.526 \qquad (5.2.2\text{-}43)$$

Figure 5.2.2-7 shows the correction function $g(\zeta)$ as a function of the location along the breeder while constant b is varied parametrically. It is seen that generally the correction function starts at somewhat less than unity at the front of the breeder, quickly goes to a region of a constant value generally above unity, then increases rapidly towards the back of the breeder. Thus, the front is colder and the back hotter due to axial conduc-

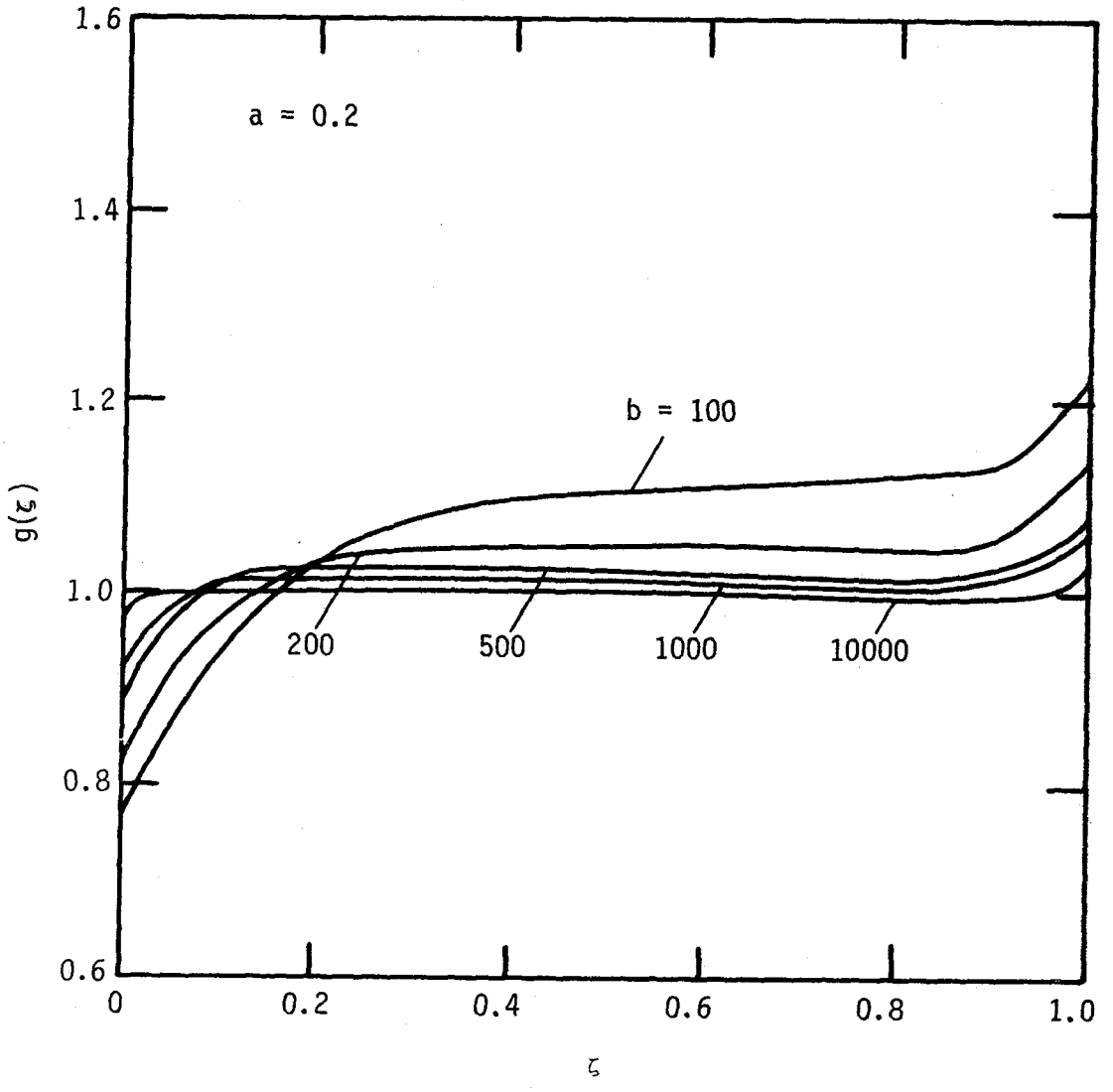

Figure 5.2.2-7 Correction function $g(\zeta)$ due to axial conduction.

tion. These points are of particular interest since the minimum and maximum temperatures occur here, so Figs. 5.2.2-8 and -9 show the correction function at the front and the back of the breeder as a function of constants a and b. It is seen from these figures that the correction decreases as the breeder becomes shorter and thicker (smaller b).

Thermal Results for Layered Solid Breeder The temperature distribution was obtained through 2-D analytical considerations as discussed above. A 2-D numerical code was also employed to confirm the analytical models and to have computational capabilities for those cases where an analytical solution is either too complicated or does not exist. A sample numerical result is shown in Fig. 5.2.2-10, illustrating the breeder geometry with contours of constant temperature. The temperatures obtained from the analytical results are also indicated on several locations on the breeder. For each of these points, the plain numbers include the effects of axial conduction while the numbers in the parenthesis do not. As can be seen, the results are fairly close and the inclusion of axial conduction has generally reduced the gap between the analytical and numerical results.

As has been mentioned, the breeder temperature distribution is very important in the design and operation of solid breeder blankets. It is not simply the average or the extreme temperatures that matter, but the entire distribution. Figure 5.2.2-11 shows the mass-weighted "temperature density" in the steady-state operation of the reference blanket Li_2O/He/HT-9. The temperature density function, f(T), is defined such that f(T)dT is the fraction of breeder between T and T+dT. The minimum and maximum breeder temperatures (510°C and 745°C respectively) in this figure correspond to the Li_2O/He-/HT-9 reference blanket.[1] The minimum temperature matches exactly with the refernce design. The maximum temperature, however, is about 50°C less than the reference design. The difference is believed to be due to the inclusion of hot spot factor in the reference design calculation. It is easily seen that most of the blanket is at colder temperatures. This is significant since the tritium diffusive inventory is dominated by the cold blanket regions. It is also noticeable from Fig. 5.2.2-10 that most of the blanket hot temperature is at the front of the breeder near the plasma.

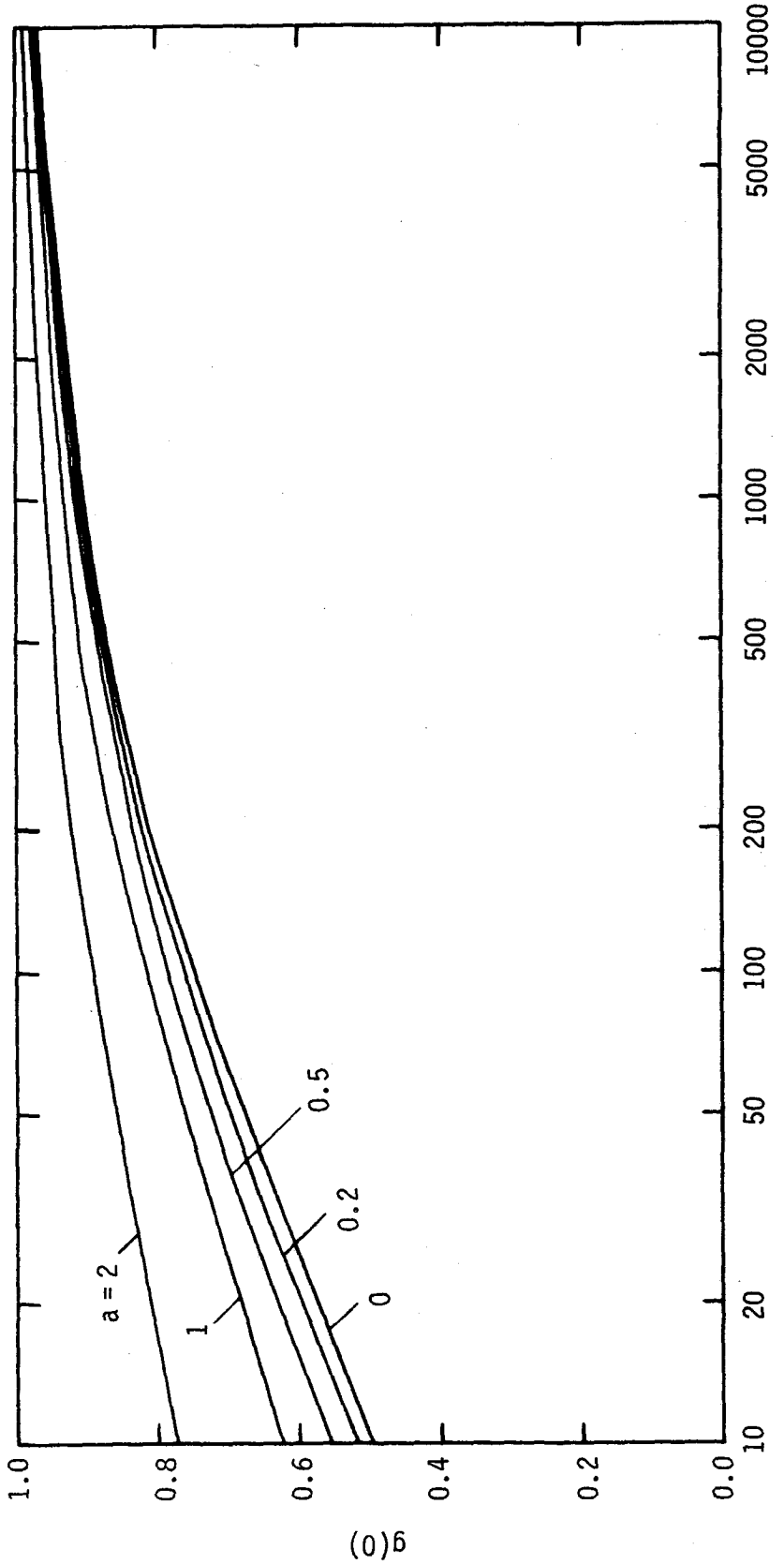

Figure 5.2.2-8 Axial conduction correction to temperature profile at the front of the breeder.

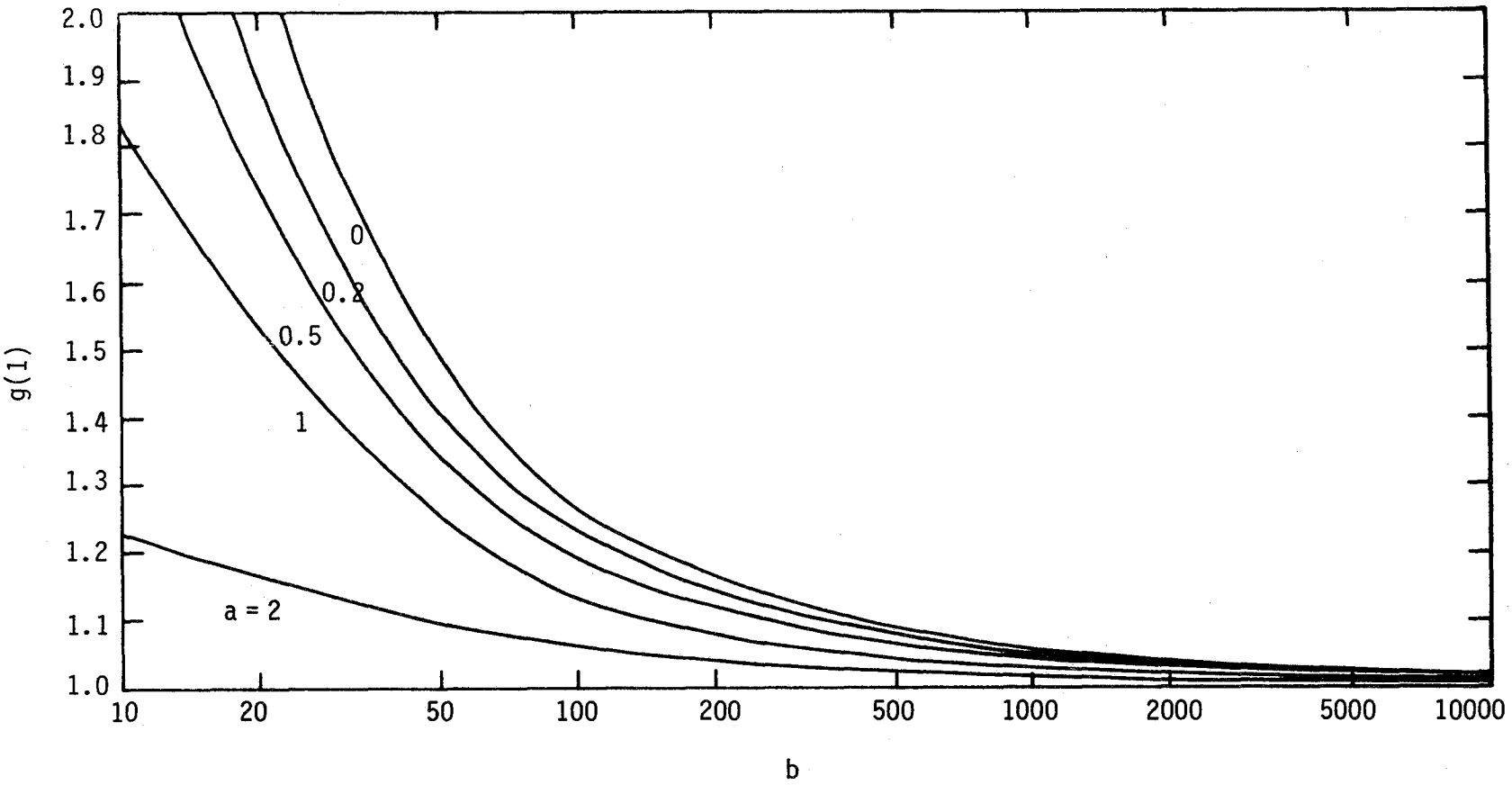

Figure 5.2.2-9 Axial conduction temperature profile at the back of the breeder.

Plain Numbers Numerical Solution

( ) Analytical Solution, Without Axial Conduction

[ ] Analytical Solution, With Axial Conduction

All Numbers in ^{o}C

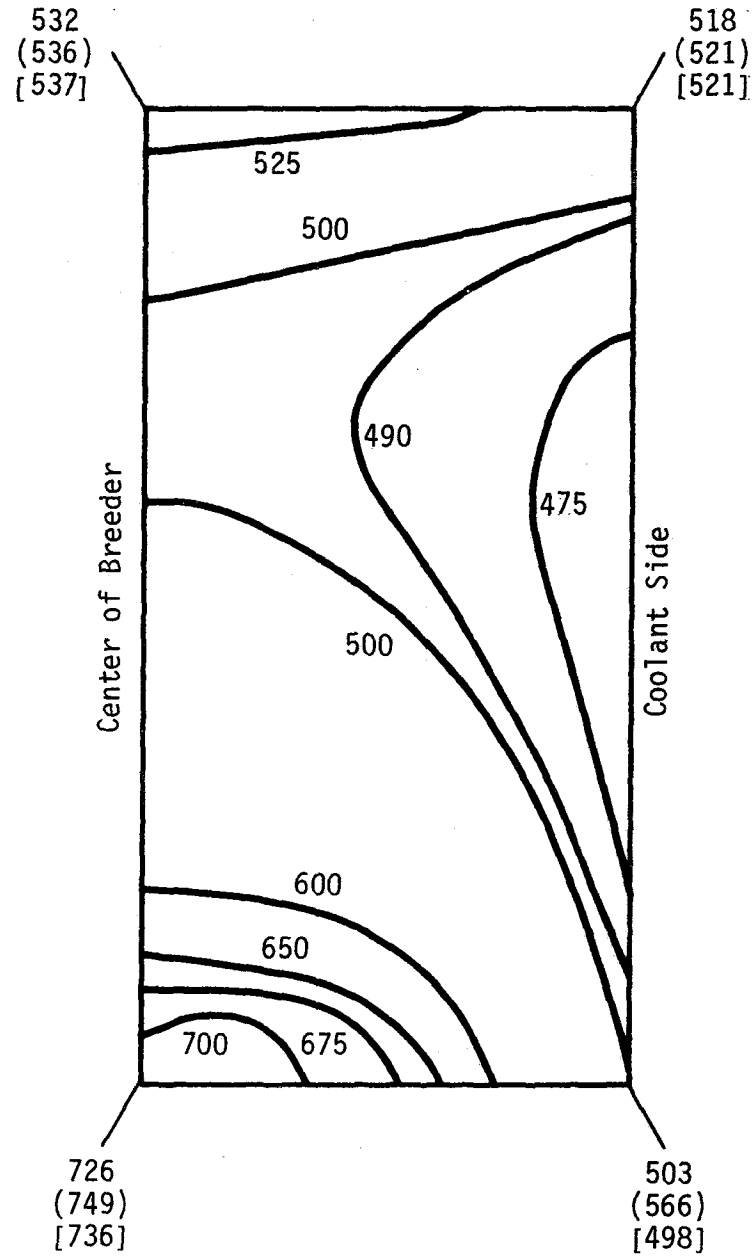

Figure 5.2.2-10 Comparison of numerical solution and analytical results for breeder temperature distribution in Li_2O/He/HT-9 reference blanket.

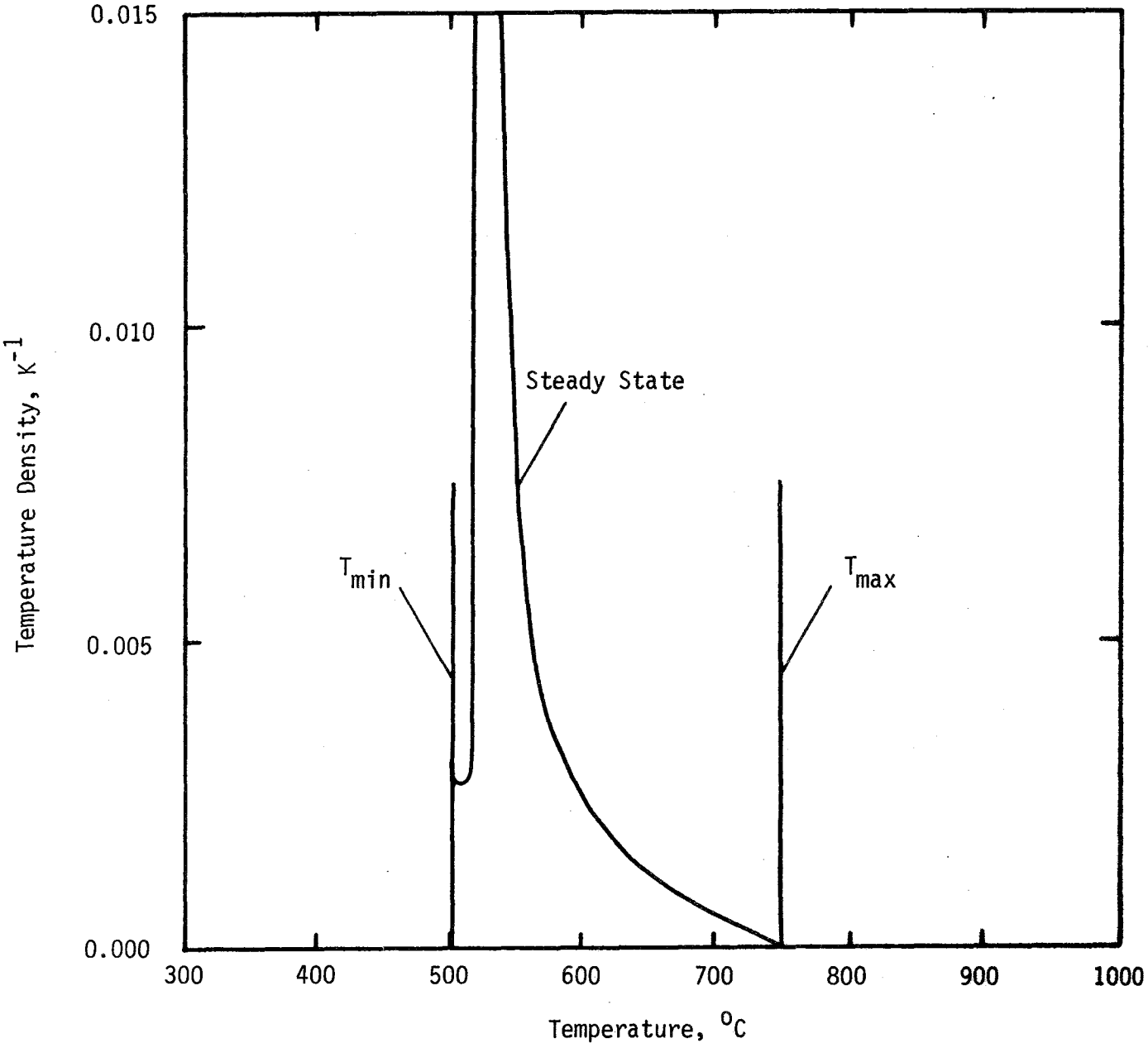

Figure 5.2.2-11 Steady state solid breeder temperature density in Li_2O/He/HT-9 reference blanket.

Steady-State Temperature Profile in Solid Breeders: Breeder-Out-of-Tube Design

A schematic of a sector of the blanket with the breeder-out-of-tube (BOT) design is shown in Fig. 5.2.2-12. The coolant, in this case water, flows through the tubes while cooling the breeder. The breeder consists of 85% dense γ-$LiAlO_2$ sphere-pack.

Analysis The following simplifying assumptions are made in order to carry out the thermal analysis of a BOT blanket design:

1. The blanket is operating under steady state. The effects of pulses will be considered later.

2. A unit cylindrical shape is chosen for analysis. Figure 5.2.2-13 shows such a unit cell. The outer radius of the unit cell may be modelled in two ways:

   (a) To preserve the longest distance from the coolant tube. In this case, a circle is fitted to the square surrounding a tube such that the four corners of the square lay on the cylinder (Fig. 5.2.2-12 shows such a square). The outer radius of the cylinder is then

$$r_o = (2n_t)^{-1/2} \qquad (5.2.2\text{-}44)$$

   where n_t is the density of tubes per unit area. This method has been used in design calculations performed by ANL.[3] The advantage is that it best models the maximum temperature in the solid breeder.

   (b) To preserve the total area and heat generation. In this case, a circle is chosen such that its area equals the area of the square;

$$r_o = (\pi n_t)^{-1/2} \qquad (5.2.2\text{-}45)$$

   The advantage of this method is that the total breeder mass and heat generation has been preserved.

3. Changes along the coolant flow direction are neglected.

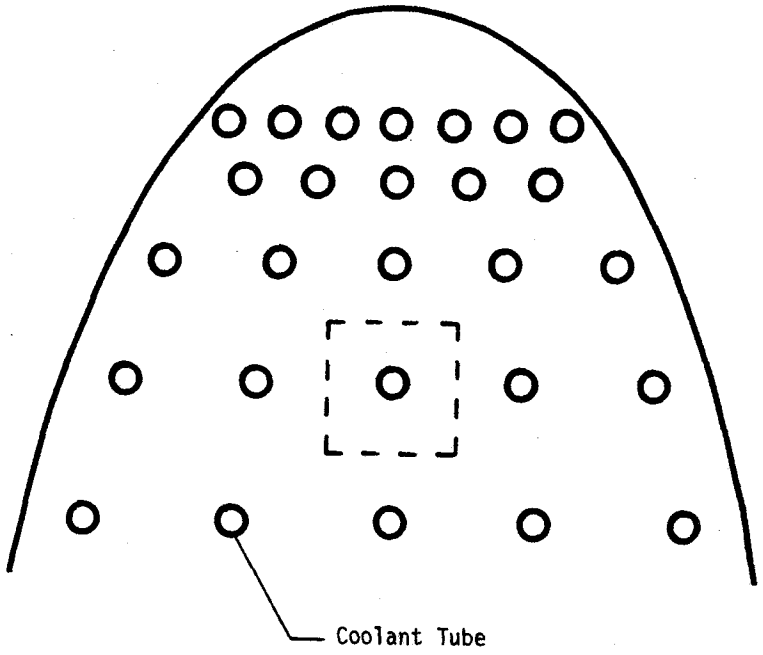

Figure 5.2.2-12 Schematic of breeder-outside-tube concept

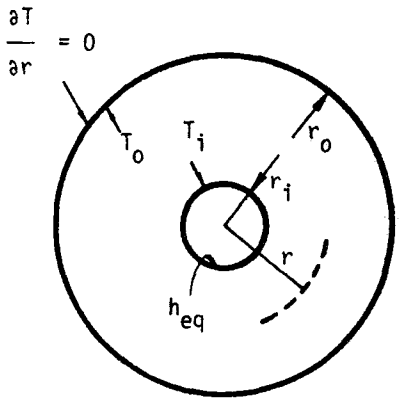

Figure 5.2.2-13 A cylindrical unit cell in the $LiAlO_2$/H_2O/PCA/Be reference blanket

4. Conduction in θ-direction is neglected. This allows a 1-D analysis even with θ-dependent heat generation.

5. A heat generation rate averaged over the unit cell is used. The effect of varying heat generation rate will be studied later.

6. The tube wall has been neglected. An equivalent heat transfer coefficient has been defined to account for the tube wall and any possible gap resistance:

$$1/h_{eq} = 1/h_{gap} + (d/k)_{tube} + 1/h_{coolant} \qquad (5.2.2\text{-}46)$$

The energy equation in cylindrical coordinates is:

$$\frac{k_b}{r}\frac{\partial}{\partial r}\left(r\frac{\partial T}{\partial r}\right) + \dot{Q}_{v,a} = 0 \qquad (5.2.2\text{-}47)$$

with the boundary conditions:

$$T = T_i \text{ at } r = r_i \qquad (5.2.2\text{-}48)$$

$$\partial T/\partial r = 0 \text{ at } r = r_o \qquad (5.2.2\text{-}49)$$

The temperature profile is calculated as:

$$T - T_i = \frac{\dot{Q}_{v,a}}{4k_b}\left[r_o^2 \ln(r^2/r_i^2) - (r^2 - r_i^2)\right] \qquad (5.2.2\text{-}50)$$

The maximum temperature of the breeder may now be calculated as

$$T_o - T_i = (\dot{Q}_{v,a} r_i^2/4k_b)\,(\beta \ln\beta - \beta + 1) \qquad (5.2.2\text{-}51)$$

where

$$\beta = r_o^2/r_i^2. \qquad (5.2.2\text{-}52)$$

Equation (5.2.2-51) relates the size of the cell, r_o [or, in effect, the density of the tubes, see Eqs. (5.2.2-44) and (5.2.2-45)] to the temperature

window in the breeder. In fact, to fully utilize the breeder volume, Eq. (5.2.2-51) is used to calculate r_o (or the tube density n_t) in the blanket.

It is useful here to calculate the average temperature of each unit cell.

$$T_{avg} = (2 \int_{r_i}^{r_o} dr\ rT)/(r_o^2 - r_i^2) \qquad (5.2.2\text{-}53)$$

Substituting for T from Eq. (5.2.2-50) and using Eq. (5.2.2-51) yields the following for the average temperature

$$T_{avg} = f_\beta T_o + (1 - f_\beta)\ T_i \qquad (5.2.2\text{-}54)$$

where

$$f_\beta = \frac{\beta}{\beta-1} - \frac{\beta-1}{2(\beta \ln\beta - \beta + 1)} \qquad (5.2.2\text{-}55)$$

The inside temperature, T_i, is related to coolant temperature through equivalent heat transfer coefficient as

$$T_i - T_c = (\beta - 1)\ (\dot{Q}_{v,a} r_i / 2h_{eq}). \qquad (5.2.2\text{-}56)$$

Temperature Density The temperature density function, f(T), for the cylindrical breeder may be calculated analytically since the temperature varies only in the r-direction. If F(T) is the cumulative distribution function, or the fraction of breeder between temperatures 0 and T, then

$$f(T) = \frac{dF}{dT} \qquad (5.2.2\text{-}57)$$

For a strictly monotonic radial temperature profile,

$$dF = \frac{2rdr}{r_o^2 - r_i^2}\ . \qquad (5.2.2\text{-}58)$$

Equations (5.2.2-57) and (5.2.2-58) may be combined to obtain

$$f(T) = \frac{dF}{dr}\frac{dr}{dT} = \frac{1}{\beta - 1}\frac{d}{dT}\left(\frac{r^2}{r_i^2}\right) \qquad (5.2.2\text{-}59)$$

The relation between r-coordinate and temperature is the temperature profile,

$$T - T_i = \frac{\dot{Q}_{v,a} r_i}{4k_b} \left[\beta \ln \frac{r^2}{r_i^2} - \left(\frac{r^2}{r_i^2} - 1\right)\right] \qquad (5.2.2\text{-}60)$$

From Eq. (5.2.2-60)

$$\frac{dT}{d(r^2/r_i^2)} = \frac{\dot{Q}_{v,a} r_i^2}{4k_b} \left[\frac{\beta r_i^2}{r^2} - 1\right] \qquad (5.2.2\text{-}61)$$

Equations (5.2.2-59) and (5.2.2-61) are combined to give

$$f(T) = \frac{4k_b}{\dot{Q}_{v,a} r_i^2 (\beta - 1)\ (\beta r_i^2/r^2 - 1)} \qquad (5.2.2\text{-}62)$$

It is not possible to further eliminate the r-coordinate from Eq. (5.2.2-62) and still have a general closed form solution. However, Eq. (5.2.2-62) together with the temperature profile Eq. (5.2.2-60) is adequate for calculating temperature density. Figure 5.2.2-14 shows the temperature density for a BOT solid breeder at steady state operation. It is observed that, unlike the layered solid breeder design, most of the breeder is at higher temperatures.

Cylindrical Asymmetry in Breeder-Out-of-Tube Designs

One of the assumptions made in the steady state analysis of this breeder was that the heat generation is averaged over the unit cell. In reality, the heat generation decreases away from the plasma. The effect of the varying heat generation is considered here for two reasons:

1. To obtain an improved distribution criterion for the coolant tube spacing such that the temperature variations in all the unit cells are equal, resulting in better utilization of the breeder.

2. To scale the temperature difference between points in the unit cell at the same radial distance from the cooling tube but at different azimuthal locations (e.g., the points closest to and farthest from the plasma). This temperature difference should increase with unit cell size, as from the breeder module front to back unit cells or with the proposed breeder test modules operating under reduced neutron wall load.

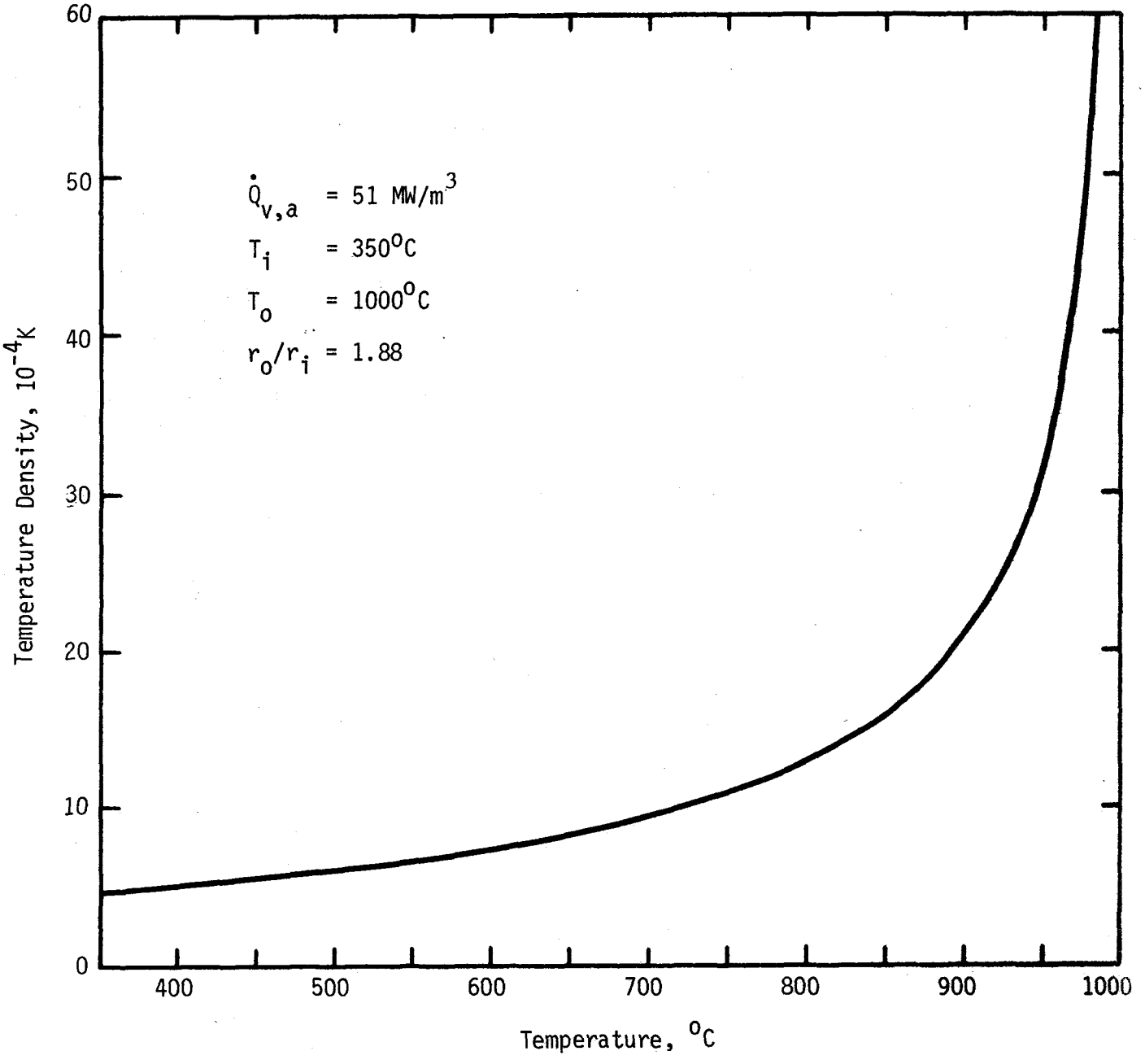

Figure 5.2.2-14 Solid breeder temperature density for the breeder out of tube $LiAlO_2/H_2O$/PCA/Be reference blanket.

Analysis Figure 5.2.2-15 shows a unit cell under nonuniform heat generation. A linear approximation for heat generation is used. This allows the results to be obtained in closed form, which is useful in understanding the parametric behavior of the problem

$$\dot{Q}_v = \dot{Q}_{v,0} (1 + r \cos \theta/d_q) \qquad (5.2.2\text{-}63)$$

where $\dot{Q}_{v,0}$ is the heat generation at the center of the unit cell and d_q is estimated by comparing Eq. (5.2.2-63) with actual heat generation profile. The scaling length d_q is different for each unit cell.

The energy equation and boundary conditions here are the same as those used earlier except for $\dot{Q}_v$ which is given by Eq. (5.2.2-63). The temperature at the outer radius of the cell is calculated as

$$\frac{k_b(T_o - T_i)}{\dot{Q}_{v,0} r_i^2} = \beta^2\left(\frac{1}{2} + \frac{\beta}{3}\frac{r_i}{d_q}\cos\theta\right)\ln\beta - (\beta^2 - 1)\left(\frac{1}{9}\frac{r_i}{d_q}\cos\theta + \frac{1}{4}\right) \qquad (5.2.2\text{-}64)$$

Three points of special interest are marked as a,b and c on Fig. 5.2.2-15. The maximum temperature difference occurs between the unit cell front and back region, or from Eq. (5.2.2-64):

$$\frac{k_b(T_a - T_b)}{\dot{Q}_{v,0} r_i^2} = \frac{2r_i}{3d_q}\left[\beta^3 \ln\beta - (\beta^2 - 1)/3\right] \qquad (5.2.2\text{-}65)$$

Cylindrical Asymmetry Results One way to arrange the coolant tubes in the breeder is to try to have as uniform temperature as possible on the outer radius of each cell since otherwise a large part of the breeder may be shifted to colder temperatures due to a few hot locations. It is clear that the temperature is not uniform for the case of $r_a = r_b = r_c$. But the radii r_a, r_b and r_c may be chosen such that $T_a = T_b = T_c$. The result is a spacing formula for the density of the coolant tubes in both the radial and poloidal directions. Unfortunately the results for such r_a, r_b and r_c may not be shown in closed form and have to be presented numerically.

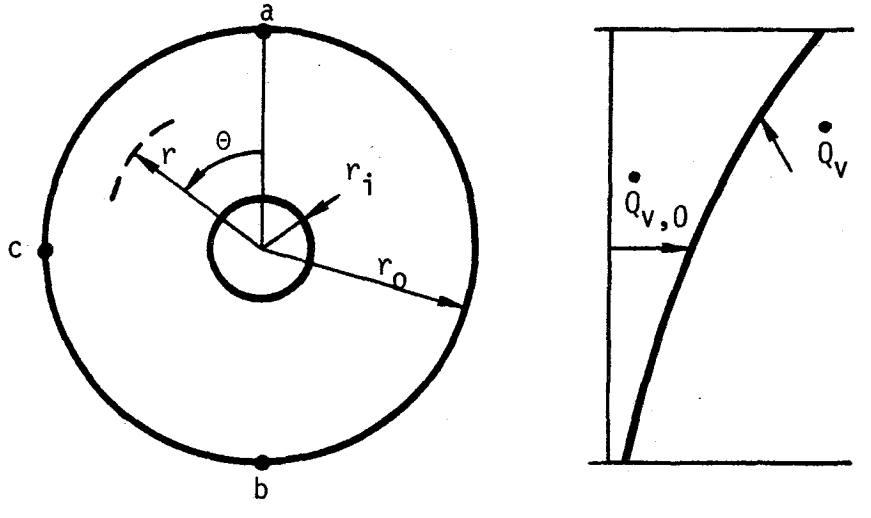

Figure 5.2.2-15 A solid breeder unit cell with non-uniform heat generation.

As an example, the temperature difference between points a and b of the second bank tubes in the reference blanket has been calculated. It is seen that the difference can be as high as 200 K if the radii r_a and r_b are chosen to be equal. On the other hand, if one decides to modify the spacing (that is r_a and r_b) to achieve uniform temperatures at points a and b, a moderate ratio of $r_b/r_a = 1.04$ is sufficient. The sample calculation here has been done for the second bank of tubes where the heat generation gradient is large, and thus so is the temperature difference. A general observation is that the temperature is very sensitive to the spacing and only small perturbation in the sizes can control large temperature differences. Alternately, however, small differences in tube location due to manufacturing tolerances may give rise to substantial local hot spots.

Pulsing Effects

While a reactor is intended to operate in steady-state, it is likely that a blanket test facility will be pulsed. This power cycling may lead to many consequences, but in particular the resulting temperature fluctuations and reduced average temperatures may be very significant.[4] In this section, the effect of pulsing on the solid breeder (both planar and cylindrical geometry) thermal behavior are studied.

Analysis The temperature profiles for the planar and cylindrical solid breeder geometries under steady state have already been obtained. These steady state solutions are denoted by superscript ss in this section.

The analysis performed here is of the "lumped capacitance" type in which it is assumed that the temperature profile at each time is that of steady-state conditions. In other words, "quasi-equilibrium" condition holds. This assumes that conduction within the solid breeder takes place faster than the pulse time scale. Obviously this assumption holds better for breeders with higher thermal conductivity and smaller sizes. Therefore it is expected that the results obtained here apply favorably to the layered solid breeder design which has a relatively small thickness.

An energy balance for a solid breeder of any geometry may be written as

$$\rho_b V_b c_{pb} \frac{dT_{avg}}{dt} = -h_{eq} A_c (T_{min} - T_c) + \dot{Q}_v V_b \qquad (5.2.2\text{-}66)$$

with the initial condition

$$T_{avg} = T_c \quad \text{at } t = 0 \tag{5.2.2-67}$$

Equation (5.2.2-66) equates the rate of increase of the internal energy of the solid breeder to the heat generated in the breeder minus the heat transferred to the coolant. In Eq. (5.2.2-66), V_b is the volume of the breeder and A_c is the area available for heat transfer to the coolant. Define:

$$\theta = T - T_c \tag{5.2.2-68}$$

and

$$C_{min} = (T_{min} - T_c)/(T_{avg} - T_c) \tag{5.2.2-69}$$

The parameter C_{min} may be thought as thermal shape factor and can be obtained from steady state analysis of each breeder geometry. Equation (5.2.2-59) is rewritten as

$$\frac{\rho_b V_b c_{pb}}{h_{eq} A_c C_{min}} \frac{d\theta_{avg}}{dt} + \theta_{avg} = \frac{V_b}{h_{eq} A_c C_{min}} \dot{Q}_v \tag{5.2.2-70}$$

It is clear that the solution to Eq. (5.2.2-70) is an exponential with a characteristic time of

$$t_c = \frac{\rho_b V_b c_{pb}}{h_{eq} A_c C_{min}} \tag{5.2.2-71}$$

Equation (5.2.2-63) may now be written in a general format of

$$d\theta/d\tau + \theta = S \tag{5.2.2-72}$$

where a dimensionless time has been defined as

$$\tau = t/t_c \tag{5.2.2-73}$$

and S is the general source term. It is useful to note that for a constant source, S is also the steady state value for θ.

The heat generation term in Eq. (5.2.2-70), in general, is time-dependent and usually periodic. Fortunately, Eq. (5.2.2-70) is linear with respect to heat generation and the principle of a superposition can be used. In particular, a pulse may be treated as the sum of two step functions - one positive, the other negative and delayed with respect to the first. Therefore, the fundamental solution needed is the response to a step function. The governing equations for a step function may be written from Eq. (5.2.2-72) as

$$d\theta/d\tau + \theta = \theta(\infty) \qquad (5.2.2\text{-}74)$$

with

$$\theta = \theta(0) \quad \text{at } \tau = 0 \qquad (5.2.2\text{-}75)$$

and where the source term has been replaced by the steady-state solution. The solution for θ is obtained as

$$\theta = \theta(\infty) + [\theta(0) - \theta(\infty)]e^{-\tau} \qquad (5.2.2\text{-}76)$$

Figure 5.2.2-16 shows a typical temperature response to a pulsed source with magnitude varying between 0 and 1. The response to this unity step source is denoted by u. As expected the response starts from zero and oscillates around an average value that increases and approaches its saturation value with an exponential pace. The quasi-equilibrium values of u_{max}, u_{min} and u_{avg} are of interest, where u_{avg} is defined as the time average of u over one cycle after quasi-equilibrium has been reached.

Quasi-Equilibrium Condition Quasi-equilibrium is reached when two consecutive peaks differ by only a small amount. The value of the u_{max} and u_{min} at quasi-equilibrium state, therefore, may be calculated by equating the magnitude of two consecutive temperature peaks, say u_1 and u_3. Between points 1 and 2, the source is turned off for some time $\tau_d = t_d/t_c$ where t_d is the dwell time and t_c is the characteristic thermal time given by Eq. (5.2.2-71). Noting that the steady-state solution of a system with a zero source is zero, then from Eq. (5.2.2-76):

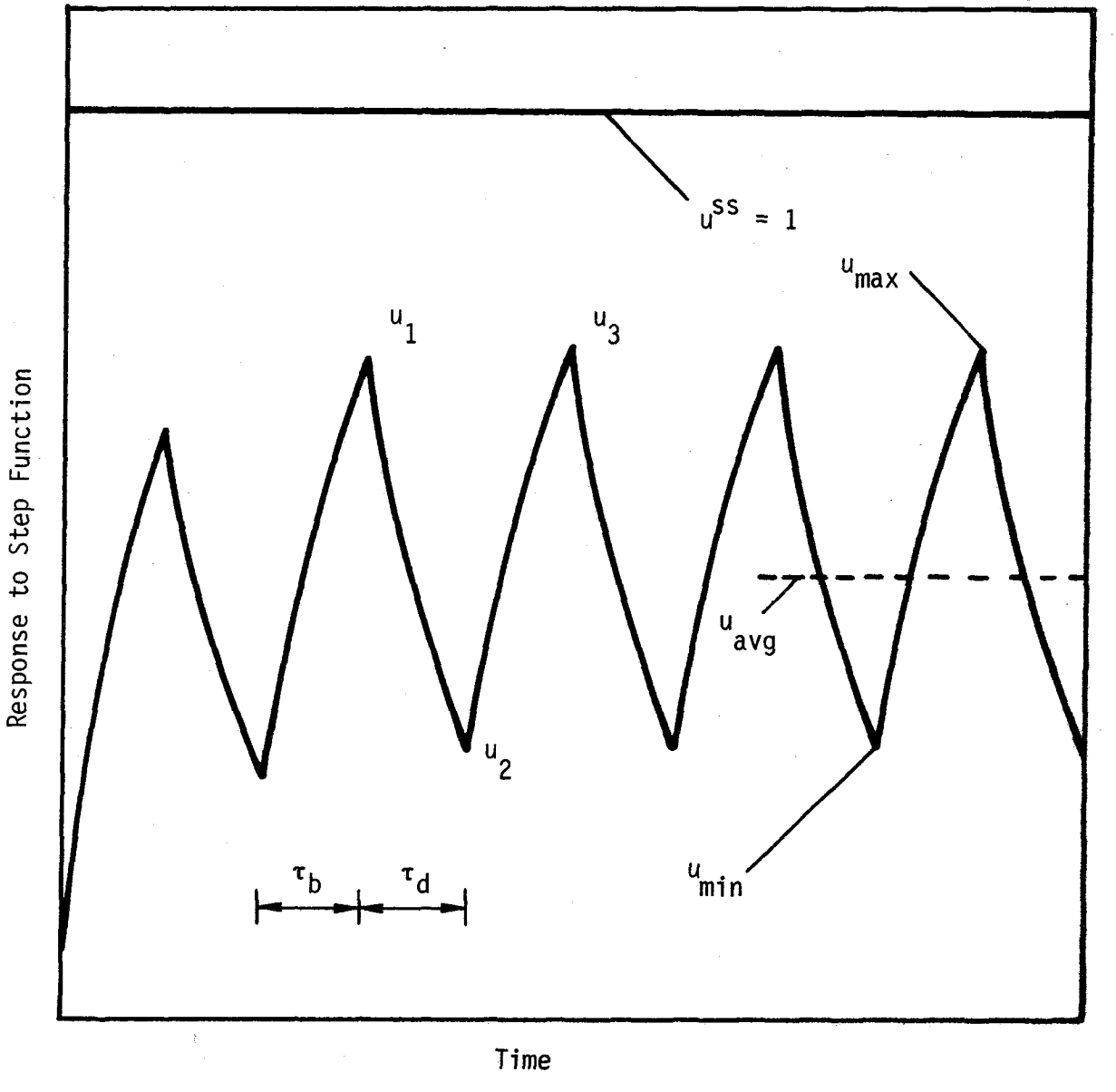

Figure 5.2.2-16 Thermal response to a pulsed source.

$$u_2 = u_1 e^{-\tau_d} \qquad (5.2.2\text{-}77)$$

Between points 2 and 3, the source is on for some time $\tau_b = t_b/t_c$ where t_b is the burn time. Then u_2 and u_3 are related as

$$u_3 = 1 + (u_2 - 1)e^{-\tau_b} \qquad (5.2.2\text{-}78)$$

Parameter u_2 may be eliminated between Eqs. (5.2.2-77 and -78). Also at quasi-equilibrium, $u_1 = u_3 = u_{max}$, so

$$u_{max} = \frac{1 - e^{-\tau_b}}{1 - e^{-(\tau_b + \tau_d)}} \qquad (5.2.2\text{-}79)$$

The minimum response u_{min} is calculated from Eqs. (5.2.2-77 and -79) as:

$$u_{min} = \frac{1 - e^{-\tau_b}}{1 - e^{-(\tau_b + \tau_d)}} e^{-\tau_d} \qquad (5.2.2\text{-}80)$$

The average response of a cycle after achieving quasi-equilibrium, u_{avg}, is calculated by integration. The result, surprisingly, is rather simple

$$u_{avg} = \tau_b/(\tau_b + \tau_d) = \text{duty cycle} \qquad (5.2.2\text{-}81)$$

It is interesting to know how many cycles it takes to achieve quasi-equilibrium, N_{qe}. Ideally, it is reached only at $\tau = \infty$. But in practice one could set a criterion such as when 95% or 99% of the saturation value has been reached. A closed form analytical result for number of cycles to quasi-equilibrium seems difficult, however, a simple rule based on observation and physical behavior may be written as

$$\frac{1}{\tau_b + \tau_d} < N_{qe} < \frac{1}{\tau_b} \qquad (5.2.2\text{-}82)$$

Thermal Characteristic Times

The thermal characteristic time was calculated in Eq. (5.2.2-71) in terms of the solid breeder volume, area and shape factor. Here, specific relations for the two solid breeder geometry under consideration (namely, planar and

Table 5.2.2-3. Basic Mechanism for Solid Breeder Thermal Instability

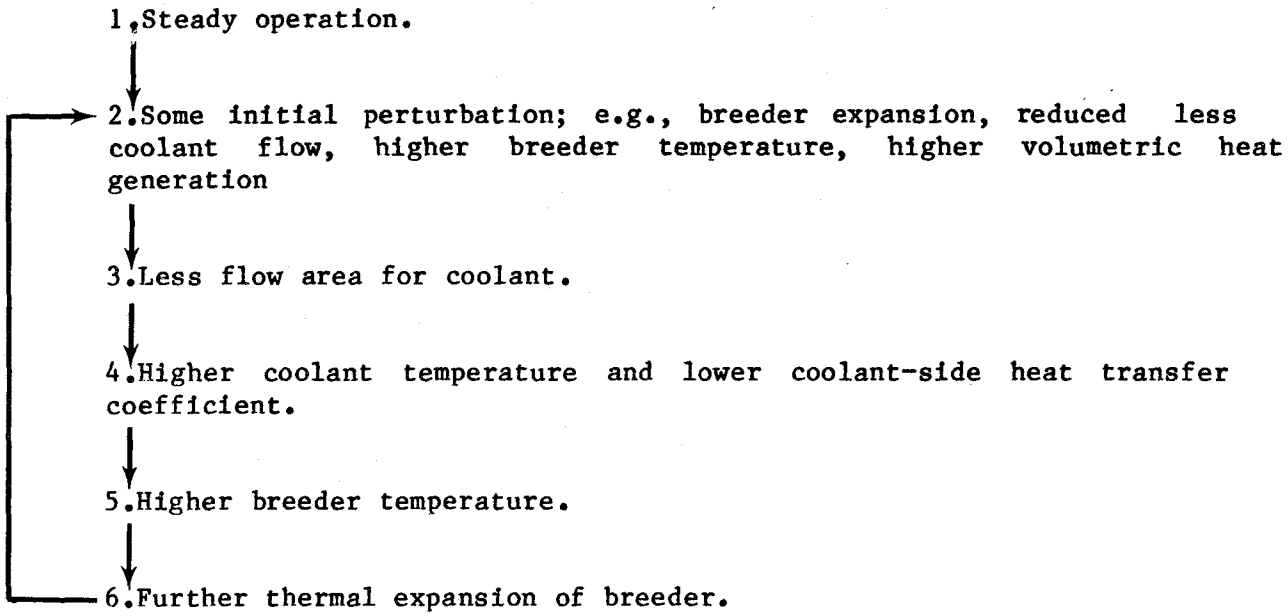

cylindrical) are given. Using temperature profiles obtained earlier, the characteristic time for the planar breeder is:

$$t_c = \frac{\rho_b c_{pb} d_b}{h_{eq}} (1 + 2h_{eq} d_b / 3k_b) \qquad (5.2.2\text{-}83)$$

and similarly, for the cylindrical breeder,

$$t_c = \frac{\rho_b c_{pb} r_i / 2}{h_{eq}} (\beta - 1) [1 + (h_{eq} r_i / 2k_b) f_\beta^2 \ln\beta] \qquad (5.2.2\text{-}84)$$

where

$$f_\beta = (\beta \ln\beta - \beta + 1)/(\beta - 1) \ln\beta \qquad (5.2.2\text{-}85)$$

and

$$\beta = r_o^2 / r_i^2. \qquad (5.2.2\text{-}86)$$

The most important result of this transient study is these characteristic times since they set the tone for transient thermal behavior. The thermal time scale is calculated to be about 37s and 50s for the layered and BOT front cell solid breeder reference blankets, respectively. These thermal characteristic times are very short compared to the operating life of the blanket in a reactor so should not create any problems. These characteristic times, however, may be comparable to the burn and dwell time of the test device and may limit the usefulness of the experimental results. Implications and solutions to this latter problem of a test module in a pulsed device will be discussed in detail in Section 5.3.2.

5.2.2.4 Flow Conditions

Off-normal conditions such as uneven flow distribution, flow induced vibrations, and thermal instability have a significant effect on design, operation, safety and lifetime of a fusion reactor. Table 5.2.2-1 summarizes some specific phenomena of concern. This section briefly reviews steady-state flow conditions and flow-induced vibrations. An analysis is then presented for a possible thermal coolant/breeder instability.

Steady-State Flow

The two primary quantities of interest to the thermal-hydraulics design of fusion blankets are the heat transfer coefficient and pressure drop. These are relatively well-understood for water and helium, and numerous correlations and graphs are available for many flow situations. Standard cases are those of fully developed laminar or turbulent flows in constant area channels. A rather extensive set of correlations is available in any heat transfer textbook (e.g., Reference 9). Special cases include, for example, flow in bends, entry length regions or flow around stagnation points. Information on these type of flow is also available in the literature (e.g., Reference 10). The important point here is that, unlike liquid metal blankets, the basic thermal-hydraulics under steady-state conditions is not a major concern.

Nonetheless, it will still be useful to measure the flow rate and heat transfer in the full blanket geometry. Confirming the pressure drop for helium cooled blankets, for example, may be important due to the high pumping power requirements. Thermal and hydrodynamic entrance regions exist in all of the flow geometries. For water and helium at the Reynold's numbers in these blankets, the entrance length is on the order of 10 hydraulic diameters[10] or typically less than 10% of the channel lengths, although it may be more significant in some helium cooled breeder designs.

Flow Vibrations

Any flow system can be considered as a network of forces (e.g., fluid pressure), springs (e.g., structural elasticity), and damping mechanisms (e.g., friction). Since there are a range of oscillations present due to turbulence and other phenomena, natural system frequencies may be excited.

Flow-induced vibrations are an important factor in the design of reactor components,[1,2] contributing to mechanical failure by fretting or wear as the vibrating structures rub against eachother. They can lead to large-scale failure such as the steam generator rupture in the Swedish Ringhals PWR after only 3000 hours of operation.[3] Such vibrations are possible in solid breeder blankets with multiple channels of high velocity coolant. However, neither the flow oscillations, the structural response, nor their interaction are easily modelled. The primary factors to be considered are:[4] the geometric aspect ratios; the reduced velocity (or inverse Strouhal number),

U/fd (where U is the free-stream flow velocity, f the vibration frequency and d the diameter; the mass ratio (structure inertia to fluid inertia), $m/\rho d^2$, where m is the mass per unit length of structure plus entrained fluid; and the damping factor or damping ratio ζ, a measure of the energy dissipation rate. Natural frequencies for flow oscillations occur around U/fd ~ 5 for vortex shedding; and U/fd ~ 1-100 for various aerodynamic instabilities. Fluid turbulence typically contains a range of frequencies. Structural vibration frequencies are roughly given by $f \sim (EI/m)^{0.5}/L^2$ (simple beams), where I is the moment of inertia and L is the beam length. Damping includes contributions from the flow, from the structure, and from the structural material itself.

Thermal Instability in Solid Breeders: Layered Design

In the solid breeders with layered breeder design (plate geometry), there is a direct relationship between the coolant flow and the temperature levels throughout the breeder. Higher breeder temperatures cause thermal expansion which results in less space for coolant flow. Reduced coolant flow then causes higher temperatures in the breeder and so on. It is clear that a problem of thermal instability might exist especially in situations where the coolant passage is very narrow as is the case for the reference Li_2O/He/HT-9 blanket. In this section, the instability is studied.

Analysis The physical model used for analyzing a plate solid breeder is shown in Fig. 5.2.2-17. A similar model could apply to the cylindrical geometry, but was not considered here. The basic positive feedback mechanism for the thermal instability is described in Table 5.2.2-3. The main question here is whether the resultant increase in the breeder thickness is larger than the original perturbation or not.

In performing the analysis, the following assumptions are made:

1. There is a fixed amount of space available for one breeder plate and one coolant flow channel. That is, an increase in one results in a decrease in the other;

2. The pressure drop available for coolant is constant. That is, any

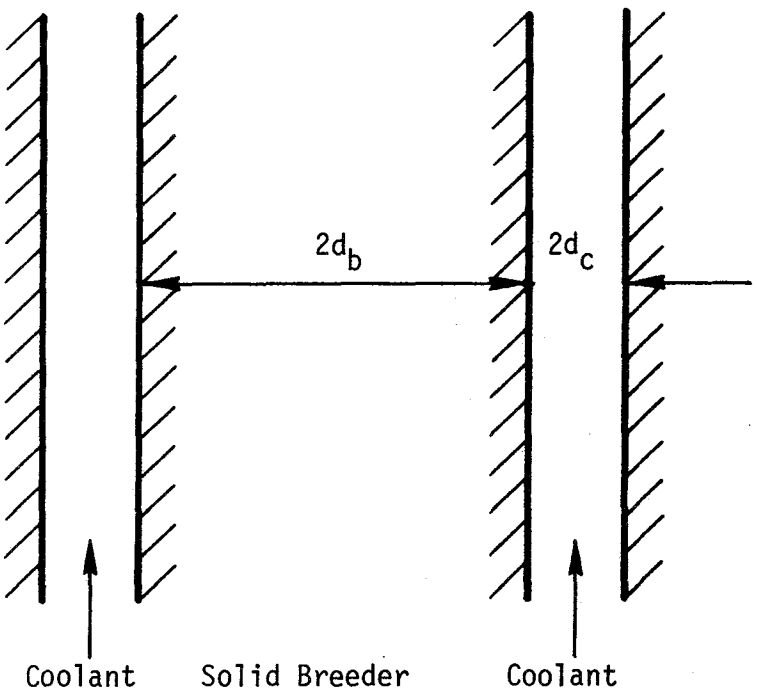

Figure 5.2.2-17 Schematic for the solid breeder thermal instability model.

decrease in coolant channel width, results in reduced coolant flow rate;

3. Unconstrained thermal expansion of breeder.

Consider some initial perturbation of the breeder thickness (perturbed parameters are denoted by superscript *)

$$d_b^* = d_b(1 + \varepsilon_b) \tag{5.2.2-87}$$

As a result, the following parameters are also perturbed:

$$d_c^* = d_c(1 - \varepsilon_c) \quad \text{coolant channel thickness} \tag{5.2.2-88}$$

$$(\dot{m}_c')^* = \dot{m}_c'(1 - \varepsilon_m) \quad \text{coolant mass flow rate} \tag{5.2.2-89}$$

$$(\dot{Q}_{v,a})^* = \dot{Q}_{v,a}(1 - \varepsilon_Q) \quad \text{volumetric heating rate} \tag{5.2.2-90}$$

$$h_{eq}^* = h_c(1 - \varepsilon_h) \quad \text{heat transfer coefficient} \tag{5.2.2-91}$$

The perturbations described in Eqs. (5.2.2-87) through (5.2.2-91) yield a further increase in breeder thickness according to Table 5.2.2-3 as

$$d_b^{calc} = d_b(1 + \varepsilon_{calc}) \tag{5.2.2-92}$$

The design is unstable if $d_b^{calc} > d_b^*$. To determine this relation, the following equations are used:

$$d_b + d_c = \text{constant} \quad \text{space constraint} \tag{5.2.2-93}$$

$$\Delta p = f \frac{L}{d_h} \frac{1}{2} \rho U_c^2 \quad \text{pressure drop} \tag{5.2.2-94}$$

$$f = 0.00316/Re^{1/4} \quad \text{friction factor} \tag{5.2.2-95}$$

$$d_h = 4 \text{ Area/Perimeter} = 4d_c \quad \text{hydraulic diameter} \tag{5.2.2-96}$$

$$Nu = 0.023\ Re^{0.8} Pr^{0.33} \qquad \text{Nusselt number relation} \qquad (5.2.2\text{-}97)$$

and the solid breeder temperature profile (from Section 5.2.2.3) is

$$T_{avg} - T_{in} = \frac{\dot{Q}_{v,a} d_b^2}{2k_b} q(\zeta) \left(\frac{2}{3} + \frac{2k_b}{h_c d_b} + \frac{4k_b L_b}{\dot{m}'_c c_{pc} d_b q(\zeta)} \int_0^{\zeta} d\zeta q(\zeta)\right) \qquad (5.2.4\text{-}98)$$

The particular goal is to determine ε_{calc} in terms of ε_b. This requires calculating all ε's.

ε_c: ε_c is calculated by using Eqs. (5.2.2-87 and -88) in Eq. (5.2.2-93)

$$\varepsilon_c = (d_c/d_b)\ \varepsilon_b \qquad (5.2.2\text{-}99)$$

ε_m : Equations (5.2.2-94, -95 and -96) are combined to obtain

$$\Delta p \propto \frac{\mu^{1/4} L \dot{m}_c'^{\,7/4}}{\rho_c d_c^3} \qquad (5.2.2\text{-}100)$$

Since pressure drop is assumed to remain constant,

$$\frac{\mu^{1/4} L\ \dot{m}_c'^{7/4}}{\rho_c d_c^3} = \frac{\mu^{1/4} L (\dot{m}_c'^{*})^{7/4}}{\rho_c d_c^{*3}} \qquad (5.2.2\text{-}101)$$

Substituting for $\dot{m}'_c$ and d_c in Eq. (5.2.2-101) from Eqs. (5.2.2-88 and -89),

$$\varepsilon_m = \frac{12}{7} \varepsilon_c \qquad (5.2.2\text{-}102)$$

and in terms of ε_b by using Eq. (5.2.2-99)

$$\varepsilon_m = \frac{12}{7} \frac{d_c}{d_b} \varepsilon_b \qquad (5.2.2\text{-}103)$$

ε_Q: This perturbation is due to the fact that the heat generation is constant per unit mass rather than per unit volume. Therefore, any breeder expansion results in reduction in volumetric heat generation.

$$\dot{Q}_{v,a}\, d_b = \dot{Q}^{*}_{v,a}\, d^{*}_b \qquad (5.2.2\text{-}104)$$

Usage of Eqs. (5.2.2-87) and (5.2.2-90) in Eq. (5.2.2-104) yields

$$\varepsilon_Q = \varepsilon_b \qquad (5.2.2\text{-}105)$$

ε_h: Upon substituting the definitions for Nu, Re and Pr, Eq. (5.2.2-97) reduces to

$$\frac{h_c d_c}{\dot{m}_c'^{0.8}} = \text{constant} \qquad (5.2.2\text{-}106)$$

Similarly, after using appropriate relations for h_c, d_c and $\dot{m}_c'$,

$$\varepsilon_h = 0.8\varepsilon_m - \varepsilon_c \qquad (5.2.2\text{-}107)$$

ε_m and ε_c in Eq. (5.2.2-107) may be replaced from Eq. (5.2.2-103 and -99) to arrive at

$$\varepsilon_h = 0.371\, \frac{d_c}{d_b}\, \varepsilon_b \qquad (5.2.2\text{-}108)$$

ε_{calc}: The resultant ε_{calc} is related to the perturbed T^{*}_{avg} as

$$\varepsilon_{calc} = \alpha_{th}(T^{*}_{avg} - T_{avg}) \qquad (5.2.2\text{-}109)$$

where α_{th} is the coefficient of thermal expansion. The perturbed T^{*}_{avg} is calculated from Eq. (5.2.2-98) by replacing the appropriate parameters by their perturbed values. If only first order ε terms are retained, many quantities will cancel from the right hand side of the Eq. (5.2.2-109), leading to

$$\varepsilon_{calc} = \frac{\dot{Q}_{v,a} d_b^2}{2k_b}\, \alpha_{th} q(\zeta)\, \left[\frac{2}{3}\,(2\varepsilon_b - \varepsilon_Q) + \frac{2k_b}{h_c d_b}\,(\varepsilon_b + \varepsilon_h - \varepsilon_Q)\right.$$

$$\left. + \frac{4k_b L_b}{\dot{m}_c' c_{pc} d_b q(\zeta)} \int_0^{\zeta} d\zeta q(\zeta)\,(\varepsilon_m + \varepsilon_b - \varepsilon_Q)\right] \qquad (5.2.2\text{-}110)$$

Upon substituting for ε_m, ε_Q and ε_h from Eqs. (5.2.2-103), (5.2.2-105) and (5.2.2-108), Eq. (5.2.2-110) reduces to:

$$\frac{\varepsilon_{calc}}{\varepsilon_b} = \frac{\dot{Q}_{v,a} d_b^2}{2k_b} \alpha_{th} q(\zeta) \left[\frac{2}{3} + 0.743 \frac{d_b}{d_c} \frac{k_b}{h_c d_b} \right.$$

$$\left. + 6.86 \frac{d_b}{d_c} \frac{k_b L_b}{\dot{m}'_c c_{pc} d_b} q(\zeta) \int_0^\zeta d\zeta q(\zeta) \right] \qquad (5.2.2\text{-}111)$$

Stability Criteria With respect to the magnitude of $\varepsilon_{calc}/\varepsilon_b$, there are three possible situations:

$$\text{Stable:} \quad \varepsilon_{calc}/\varepsilon_b < 1 \qquad (5.2.2\text{-}112)$$

$$\text{Neutral:} \quad \varepsilon_{calc}/\varepsilon_b = 1 \qquad (5.2.2\text{-}113)$$

$$\text{Unstable:} \quad \varepsilon_{calc}/\varepsilon_b > 1 \ . \qquad (5.2.2\text{-}114)$$

The most stringent stability criteria should come from the location with the highest value of $\varepsilon_{calc}/\varepsilon_b$. An argument similar to that used earlier for the minimum temperature of the planar solid breeder may be repeated here. The location of the most stringent stability criteria is

$$\zeta = 0 \qquad \text{if} \quad L_b h_c / \dot{m}'_c c_{pc} > 0.108 \ln [q(0)/q(1)] \qquad (5.2.2\text{-}115)$$

$$\text{any } \zeta = (0,1) \qquad \text{if} \quad L_b h_c / \dot{m}'_c c_{pc} = 0.108 \ln [q(0)/q(1)] \qquad (5.2.2\text{-}116)$$

$$\zeta = 1 \qquad \text{if} \quad L_b h_c / \dot{m}'_c c_{pc} < 0.108 \ln [q(0)/q(1)] \qquad (5.2.2\text{-}117)$$

In either case, the stability criteria, Eq. (5.2.2-112), when combined with Eq. (5.2.2-111) yields:

$$d_c > \frac{\dot{Q}_{v,a} d_b^2}{2k_b} q(\zeta) \frac{0.743 \frac{k_b}{h_c} + 6.86 \frac{k_b L_b}{\dot{m}'_c c_{pc} q(\zeta)} \int_0^\zeta d\zeta q(\zeta)}{\frac{2k_b}{\alpha_{th} \dot{Q}_{v,a} d_b^2 q(\zeta)} - \frac{2}{3}} \qquad (5.2.2\text{-}118)$$

if

$$\frac{2k_b}{\alpha_{th}\dot{Q}_{v,a}d_b^2 q(\zeta)} - \frac{2}{3} > 0 \qquad (5.2.2\text{-}118a)$$

That is any coolant channel width smaller than that in Eq. (5.2.2-118) is thermally unstable. An interesting observation is that for the cases that the denominator of Eq. (5.2.2-118) is negative, the breeder is unconditionally unstable,

$$\frac{3k_b}{\dot{Q}_{v,a}d_b^2 q(\zeta)} < \alpha_{th} \quad \text{unconditionally unstable} \qquad (5.2.2\text{-}119)$$

It is important to note that the relation in Eq. (5.2.2-119) is rather general and does not depend on the coolant or the coolant channel. It introduces an absolute maximum for the thickness of the solid breeder d_b (or for the heat generation). The physical reason for such a limit is that the temperature profiles are parabolic and hence proportional to the square of the breeder thickness. From Eq. (5.2.2-98),

$$\Delta T \propto \dot{Q}_{v,a} \quad d_b^2 \qquad (5.2.2\text{-}120)$$

But $\dot{Q}_{v,a}d_b$ is the total energy input and is constant. And since the swelling is directly related to thermal expansion, $d_b^{calc} \propto \Delta T$. Therefore,

$$d_b^{calc} \propto d_b \qquad (5.2.2\text{-}121)$$

Equation (5.2.2-121) indicates direct and possibly unstable feedback, and includes only the contribution from the breeder temperature profile, not from the coolant. It should be noted that the absolute limit in Eq. (5.2.2-119) does not depend on the two assumptions earlier made, i.e., limited space for breeder and coolant and constant pressure drop.

Two stability criteria were obtained, that is, Eqs. (5.2.2-118) and (5.2.2-119). One sets a minimum value for the coolant channel width while the other sets a maximum for the breeder thickness. Numerical calculations for the Li_2O/He/HT-9 reference blanket indicate that the following should hold in order to have a thermally stable solid breeder:

$$d_c > 0.4\text{mm} \qquad (5.2.2\text{-}122)$$

$$d_b < 74\text{mm} \qquad (5.2.2\text{-}123)$$

The limiting value for d_c in Eq. (5.2.2-122), although very small, is close to the design value ($d_{c,design} = 0.5$ mm). The second limit, set by Eq. (5.2.2-123), is actually very far from design value ($d_{b,design} = 5.25$ mm) and should not create any problems.

5.2.2.5 Corrosion

Corrosion can weaken structures (wall thinning, chemical embrittlement); change surface characteristics (reduced heat transfer, increased tritium permeation); remove breeder (LiOT mass transfer); and plug narrow purge, coolant or heat exchanger channels. While there is extensive experience with high temperature, high pressure water and helium coolant in reactor environments, the mechanisms for formation, transport and deposition of corrosion products are very complex and poorly understood. Reference (11) provides a recent review of corrosion chemistry with helium in High Temperature Gas Reactors.

Generally, the corrosion rate is very low in clean, high purity coolant conditions. The concern is for the effects of realistic impurities. For water and austenitic steels, typical corrosion rates are about 1 μm/yr under degassed, high temperature conditions.[12,13] Estimates for helium/steel system are around 0.1 μm/yr, including neutron sputtering.[18] This may not be enough to cause serious wall thinning or tube plugging where (> 10 μm/yr erosion rates would be of concern[1]) but can lead to appreciable activation product formation and transport around the loop.

Very high velocity flow may enhance surface erosion through cavitation (if boiling is present) or abrasion from suspended solids. However, typical blanket velocities should be well below these regimes.

The presence of a strong magnetic field is a poorly known factor. Possible effects include transport inhibition (bulk or ion diffusion), source or suppression of crud bursts, and effects on local corrosion rate (induced currents affecting electrochemistry, corrosion layer microstructure or orientation).[15]

For example, some iron oxides are ferromagnetic. In the presence of a varying magnetic field, the drag force on the particles will be balanced by a magnetic force,

$$F_{drag} \simeq \frac{\pi r_p^2}{2} C_D \rho_c (U_c - U_p)^2 \simeq \begin{cases} \frac{\pi r_p^2}{2} \rho_c U_c^2 & \text{for } U_c \gg U_p \\ 6\pi r_p \mu_c (U_c - U_p) & \text{for } U_c \simeq U_p \end{cases} \quad (5.2.2\text{-}124)$$

$$F_{mag} \simeq \frac{4}{3} \pi r_p^3 M \nabla B \quad (5.2.2\text{-}125)$$

where r_p is particle size; C_D is drag coefficient; μ_c and ρ_c are coolant viscosity and density; U_c and U_p are coolant and particle velocity; M is the particle magnetization and ∇B is the magnetic field gradient.

Although the drag force is very large on a particle at rest, it rapidly decreases as the particle is pulled up to the bulk flow speed. At some point, the magnetic force would inhibit further acceleration. The final velocity may be estimated as

$$\frac{U_c - U_p}{U_c} \simeq \frac{2 r_p^2 M \nabla B}{9 U_c \mu_c} \quad (5.2.2\text{-}126)$$

For nominal values of $r_p \simeq 10\text{-}100$ μm;[16] $\nabla B \simeq 1$ T/m; $M \simeq 10^5$ A/m; U_c, μ_c of about 5 m/s and 10^{-4} kg/m-s for water, and about 30 m/s and 3×10^{-5} kg/m-s for helium, then $(U_c-U_p)/U_c \simeq 0.002\text{-}0.4$. Thus it is possible that the magnetic field may inhibit corrosion particle transport.

Corrosion and mass transfer within the breeder are also of concern. Li_2O forms corrosive LiOT under certain conditions.[17] The transport of this compound from the breeder interior to the purge channel may lead to loss of breeder material and rapid erosion of the purge piping. Ternary ceramics like $LiAlO_2$ are not as corrosive or volatile, but there are concerns over reactions with the metal oxides that accumulate rapidly in the high burnup regions.

5.2.2.6 Summary

This section considered the thermal-hydraulic behavior of solid breeder

blankets. The analysis concentrated primarily on the first wall and breeder temperature profiles.

The two reference solid breeder blankets retain the high pressure first wall coolant in semi-cylindrical modules with azimuthally flowing coolant. The temperature profiles along the coolant channels vary sharply due to the variation in heat source. Tokamak first walls are dominated by surface heating, while mirror first walls are dominated by the nuclear bulk heating. Analyses indicated that the temperature variation was strong across the composite first wall away from the plasma, and azimuthally along the front surface. Axial variations within the cross-section such as around the first wall support fins were small.

The breeder temperature profiles, which are important for the breeder mechanical behavior and tritium recovery, were obtained analytically. The analysis includes the steady-state 1.5-D solution for two breeder geometries: planar and cylindrical. It was found that the planar design yields a mass-weighted temperature distribution, the "temperature density", that is peaked at colder temperatures, while the cylindrical breeder temperature density peaks near its maximum temperature. This indicates that one geometry has most of its breeder near the minimum temperature limit, while the other has most of the breeder near the upper limit.

To obtain more accurate temperature profiles and determine the significance of 2-D effects, axial conduction (planar breeder) and heat generation asymmetry (cylindrical breeder) were also considered. Axial conduction was found to slightly influence the breeder temperatures but is not a large effect, particularly since the slab breeders will be broken into small blocks (to minimize thermal stress cracking) which will inhibit heat transfer. However, the cylindrical asymmetry could strongly affect the maximum temperature. The latter considerations lead to a prescription for the cooling tube spacing in order to achieve a uniform maximum temperature.

The effect of a pulsed nuclear heat source was also analyzed. The basic model was based on the lumped capacitance principle, including corrections for the effect of volumetric heat generation on the breeder temperature profile. The thermal time constant for the two breeder geometries were obtained. In order to evaluate the breeder response, the principle of superposition was used. As expected, the general effect of pulsing is to lower the temperatures

and to cause cyclic variation. Analytic equations are provided for the breeder temperature response and the time to quasi-equilibrium.

Several aspects of flow conditions applicable to the breeder were considered, including flow-induced vibrations, entry lengths and a possible thermal instability for the plate breeder configuration.

Finally, corrosion was briefly considered. It is generally a complex subject that is certainly important in any power system, but is not expected to be a feasibility issue for the water/steel or helium/steel systems of interest here. While there is a fair amount of experience with these systems in a fission reactor environment, a fusion reactor will introduce some new effects. For example, although not believed to be significant, the effect of strong magnetic fields or field gradients on corrosion have apparently not been tested.

References for Section 5.2.2

1. M. A. Abdou et al., "Blanket Comparison and Selection Study (Interim Report)," Argonne National Laboratory, ANL/FPP-83-1 (October 1983).

2. W. E. Mason, Jr., "TACO - A Finite Element Heat Transfer Code," Lawrence Livermore National Laboratory, UCID-17980 (1978).

3. G. D. Morgan, personal communication, July 1984.

4. G. A. Deis, "Thermal Cycling Effects in Tokamak Reactor Blanket Components," Proc. of the 9th Symp. on Eng. Prob. of Fusion Research, Chicago, 1783 (1981).

5. K. Amano and K Inoue, "Analysis of coolant pressure fluctuation and induced vibration of liquid-metal fast breeder reactor fuel pins," Nucl. Tech., 65(3), 409 (June 1984).

6. K. Kikuchi et al., "Impurity Gas Effects on Friction and Wear of High-Temperature Materials for VHTRs", Nucl. Tech., 66(3), 491 (Sept. 1984).

7. S. Chen, "Flow-induced vibration and instability of some nuclear reactor components," paper B511, SMiRT 7, Vol. B, Chicago, August 22-26 (1983).

8. R. Blevins, "Flow-Induced Vibrations," Van Nostrand Reinhold, New York, (1977).

9. D. K. Edwards, A.F. Mills and V.E. Denny, "Transfer Processes," Second Edition, McGraw-Hill, New York (1979).

10. W. M. Rohsenow and J. P. Hartnett, "Handbook of Heat Transfer," McGraw-Hill Company, New York, 1973.

11. Several papers in Nucl. Tech., 66(2), 383-478 (August 1984).

12. M. Abdou et al., "A Demonstration Tokamak Power Plant Study (DEMO)", Argonne National Laboratory, ANL/FPP/82-1 (September 1982).

13. E. Rabald, "Corrosion Guide", 2nd ed., Elsevier, New York (1968).

14. W.E. Bickford, "Transport and Deposition of Activaton Products in a Helium Cooled Fusion Power Plant," Battelle Pacific Northwest Laboratory, PNL-3487 (Sept. 1980).

15. M. Abdou et al., "STARFIRE-A Commercial Tokamak Fusion Power Plant Study," Argonne National Laboratory, ANL/FPP-80-1, (1980).

16. G. Schultheiss, "Investigations of Local Blockage Formation and Dependence on Fuel Element Spacing," 7th SMiRT, Vol. C., Chicago, August 22-26, 273 (1983).

17. D. L. Porter, et al., "Neutron Irradiation and Compatibility Tessting of Li_2O", Jrnl. Nucl. Mat., 122 & 123, 929 (1984).

5.2.3 Tritium Recovery

Models, properties, and experimental data are presented in this subsection for the purpose of describing the behavior of tritium in fusion solid breeders. The emphasis is on tritium inventory, short- and long-term tritium recovery, and tritium permeation from the solid breeder to the primary coolant loop. Tritium inventory is an important design consideration because of the safety issue involved if a large tritium inventory is allowed to build up in the blanket. Short-term tritium recovery (or the time to achieve tritium self-sufficiency) is directly related to the economic issue of initial fuel investment while long-term tritium recovery helps to set the minimum tritium breeding ratio. Tritium permeation (or leakage) is both an economic and an environmental issue. High leakage rates will result in costly cleanup and processing systems in order to minimize the leakage from the primary to the secondary coolant and to recover the tritium for use as fuel.

By summarizing what is known about tritium behavior in solid breeders, two purposes are accomplished. The analytical models presented will show the sensitivity of tritium behavior to material properties and operating conditions and help guide the establishment of a systematic test plan. At the same time, these models form the basis for pre- and post-test analysis for these experiments.

5.2.3.1. Steady-State Tritium Behavior

Under steady-state operating conditions (e.g., tritium generation rate and temperature) and tritium response, the tritium release rate ($\dot{R}$) from the blanket is equal to the generation rate ($\dot{G}$). The primary concern under these conditions is the tritium retained (i.e., inventory) in the blanket ceramic, porosity and purge stream, metal structure, and coolant. The tritium released from the blanket is simply the difference between the total amount generated and the inventory. In addition, the generation rate and the tritium partial pressure in the gas phase are used to determine the tritium leakage rate.

Conceptually, the steady-state inventory (I) is divided into components in the ceramic breeder (I_b) - including the interconnected porosity and purge stream, the metal structure (I_m), and the coolant (I_c):

$$I = I_b + I_m + I_c \quad . \tag{5.2.3-1}$$

The breeder contains the largest component of inventory, and is further subdivided into retained tritium due to bulk diffusion (I_d), solubility (I_s), surface adsorption (I_a), and porosity-percolation/purge-stream-convection (I_p):

$$I_b = I_d + I_s + I_a + I_p \quad . \tag{5.2.3-2}$$

Diffusive Inventory (I_d)

After tritium is bred in the breeder, the initial process in tritium transport is bulk diffusion from the interior of the solid-breeder grains to the grain boundaries. Tritium is generated within the grain matrix at a rate per unit volume $\dot{g}$. Assuming a spherical, isothermal grain of radius r_g and temperature T, the intragranular diffusive inventory (assuming the grain boundary is a perfect sink for tritium) is given by[1]

$$I_g = \tau_r \dot{g} V_g \quad . \tag{5.2.3-3}$$

where

τ_r = $(r_g^2 / 15\ D)$, the mean residence time in s

r_g = the grain radius in cm

D = the diffusion coefficient in cm^2/s

= $D_o \exp(-Q/RT)$

D_o = a pre-exponential factor for the diffusion coefficient

Q = the apparent activation energy for diffusion in kcal/mol

R = 1.986×10^{-3} kcal/mol·K

T = temperature in K

$\dot{g}$ = tritium generation rate in $g/s \cdot cm^3$

and

V_g = $(4/3)\ \pi r_g^3$ = grain volume in cm^3.

In applying Eq. (5.2.3-3) to the whole blanket, care must be taken to properly account for the large variations in temperature and generation rate across the blanket. To simpify the analysis, the blanket is divided into unit cells. The two types of unit cells of practical interest in this study are the hollow cylinder and the plate (see Fig. 5.2.3-1). Integrating Eq. (5.2.3--3) over one unit cell gives

$$I_{cell} = \int_{V_{cell}} \tau_r \dot{g}(1 - \varepsilon)\, dV \ . \qquad (5.2.3\text{-}4)$$

where

V_{cell} = the breeder volume in a unit cell

ε = the breeder porosity fraction

and

$$dV = \begin{cases} r\,dr\,d\theta\,dz & \text{for the cylinder} \\ dx\,dy\,dz & \text{for the plate.} \end{cases}$$

The total tritium diffusive inventory in the blanket can then be found by summing over the unit cells, each employing the local temperature and tritium generation rate as appropriate:

$$I_d = \sum_{i=1}^{N} (I_{cell})_i \ . \qquad (5.2.3\text{-}5)$$

The application of Eqs. (5.2.3-4) and (5.2.3-5) to the blankets of interest is cumbersome. A number of simplifying assumptions have been employed to generate models which allow calculations to be performed for scoping studies and blanket comparisons. The first assumption is that variations in temperature and generation rate in the axial (z) direction for both cylindrical and plate unit cells are negligible. The second assumption is that the generation rate is constant in the x-direction for the plate and in the r and θ directions for each cylindrical unit cell. The assumptions with regard to temperature are less stringent than those concerning generation rate because

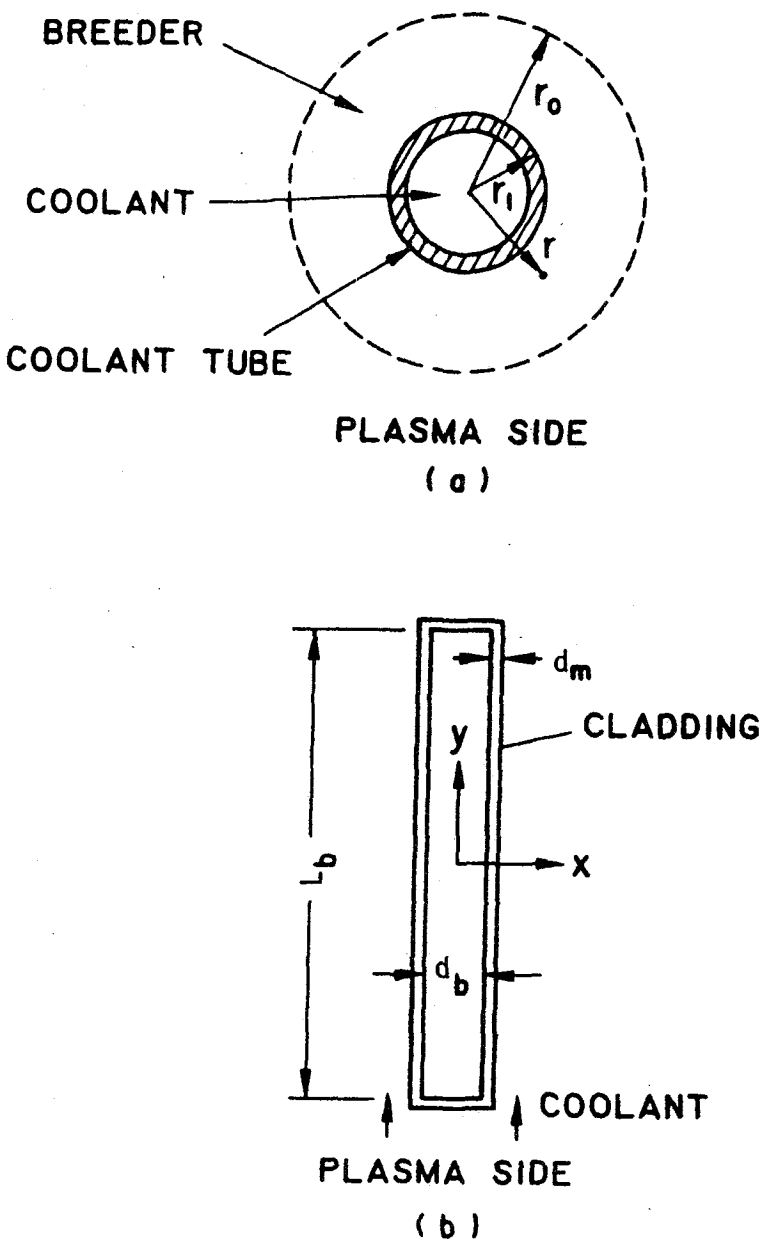

Figure 5.2.3-1. Representative cross-sections of unit cells for cylindrical (e.g. $LiAlO_2/H_2O$) and plate (e.g. Li_2O/He and $LiAlO_2$/He) geometries. Purge channels which are not shown are located at the breeder-cladding interface.

the tritium inventory varies in a highly nonlinear fashion with temperature, whereas variation with generation rate is linear.

Using these assumptions, Eq. (5.2.3-4) can be rewritten for the plate as:

$$(I_d)_{plate} = \dot{G}_p \int_{-1/2}^{1/2} h(\zeta) \left(\int_0^1 \tau_r(\xi,\zeta) d\xi \right) d\zeta \qquad (5.2.3\text{-}6)$$

where

$\dot{G}_p$ = the generation rate in g/s for the plate

ζ = the normalized position (y/L_b) along the coolant path

$h(\zeta) = \dot{g}(\zeta)/\bar{\dot{g}}$ = the normalized tritium production rate along the coolant path direction

ξ = the normalized position $(2x/d_b)$ in the plate thickness direction

$\tau_r(\xi,\zeta) = (r_g^2/15\ D_o)\exp(Q/RT)$

and

$T = T(\xi,\zeta)$.

If an exponential function is used to characterize the variation of generation rate with ζ, then

$$h(\zeta) = \dot{g}(\zeta)/\bar{\dot{g}} = \frac{\alpha \exp[-\alpha(\zeta + 1/2)]}{1 - \exp(-\alpha)}, \qquad (5.2.3\text{-}7)$$

where

$\dot{g}(\zeta)$ = the local tritium generation rate per unit volume

$\bar{\dot{g}}$ = the average tritium generation rate per unit volume

and

α = a nondimensional parameter in the exponential fit to the generation rate variation in the ζ direction.

A detailed discussion of the temperature distribution in the breeder plate is contained in Section 5.2.2. For the purposes of this section, the

steady-state profile is represented by:

$$T(\zeta,\xi) = T_s(\zeta) + \frac{\bar{\dot{Q}}_v d_b^2 \, \alpha \exp[-\alpha(\zeta + 1/2)]}{8k_b[1 - \exp(-\alpha)]} (1 - \xi^2) , \qquad (5.2.2\text{-}8)$$

where

$T_s(\zeta)$ = the breeder surface temperature

$\bar{\dot{Q}}_v$ = the average volumetric heat generation rate for the breeder

d_b = the breeder thickness

and

k_b = the average breeder thermal conductivity.

From a computational viewpoint the only explicit integration performed in Eq. (5.2.2-6) is in the ξ-direction. The integration in the ζ-direction is approximated by subdividing the plate into a number of axial sections, each with assumed constant heat and tritium generation rates. The inventories from these sections are then summed to approximate the inventory in a single plate.

It is desirable for scoping calculations to replace Eq. (5.2.3-6) with a simpler analytical expression which explicitly includes important design variables. If it is assumed that all of the plates have the same temperature and tritium-generation distributions, then the $\dot{G}_p$ in the equation can be replaced by the total generation rate ($\dot{G}$) for the ceramic blanket. Also, by assuming that the breeder surface temperature is constant (at T_{min}) along the coolant path - an assumption which leads to a slight overprediction of inventory, then Eq. 5.2.3-6 can be expressed in summation form as:

$$I_d = \frac{r_g^2 \dot{G}}{15 D_o} \sum_{i=1}^{N} (h_i/N) f_i \exp(Q/R\bar{T}_i) , \qquad (5.2.3\text{-}9)$$

where

$$h_i = N[\exp(\alpha/N) - 1][1 - \exp(-\alpha)]^{-1} \exp(-\alpha i/N)$$

$$h_o = \alpha[1 - \exp(-\alpha)]^{-1}$$

$$\bar{T}_i = T_{min} + (2/3)(h_i/h_o)\Delta T$$

$$f_i = \int_0^1 \exp[(Q/R\bar{T}_i)(\bar{T}_i/T_i - 1)]\, d\xi$$

$$T_i = T_{min} + (h_i/h_o)\Delta T(1 - \xi^2)$$

$$\Delta T = T_{max} - T_{min} = \bar{\dot{Q}}_v h_o d_b^2/(8\, k_b)$$

and

N = the number of axial sections used for the analysis.

Figure 5.2.3-2a shows the distribution of inventory in weight parts per million for the GA Li_2O/He/FS plate design ($\dot{G}$ = 1.85 × 10^{-5} wppm/s, r_g = 10 μm, T_{min} = 510°C, and T_{max} = 795 °C) as a function of α. The case α = 0 is the highly idealized situation of a uniform generation of heat and tritium within the plate. The more representative case of α = 2.3 corresponds to a 10:1 ratio of generation rates from the front to the back of the blanket, while α = 3.0 corresponds to a ratio of ~20:1. The assumed values of D_o and Q are 2.66 × 10^{-3} cm^2/s and 19.72 kcal/mol, respectively, for Li_2O. Notice that by neglecting the summation over axial sections [α = 0 in Eq. (5.2.3-9)], the total diffusive inventory is 2.09 × 10^{-5} wppm (1.08 × 10^{-2} g), whereas by including the sum I_d = 4.46 × 10^{-5} wppm (2.31 × 10^{-2} g) for α = 2.3 and I_d = 4.75 × 10^{-5} wppm (2.49 × 10^{-2} g) for α = 3.0. However, for all of these cases, the diffusive inventory for the Li_2O plates is exceedngly small.

The calculations are repeated (Fig. 5.2.3-2b) for the GA $LiAlO_2$/He/FS/Be plate design with $\dot{G}$ = 2.41 × 10^{-5} wppm/s, r_g = 0.1 μm, T_{min} = 520°C, T_{max} = 1000°C, D_o = 1.1 × 10^{-6} cm^2/s, and Q = 35.8 kcal/mol. The results are: I_d = 4.60 × 10^{-2} wppm (18.3 g) for the idealized case of α = 0; I_d = 0.130 wppm (52.0 g) for α = 2.3; and I_d = 0.155 wppm (61.8 g) for the more realistic case of α = 3.0.

In the case of the cylinder, more convenient approximations to Eqs. (5.2.3-4) and (5.2.3-5) can be obtained because the cylindrical unit cell extends only a small fraction across the blanket thickness, whereas the plate extends across the whole thickness. Equation (5.2.3-4) can be rewritten as

$$(I_d)_{cyl} = (r_g^2/15\, D(\bar{T}))\, f\, \dot{G}_{cyl}\,, \qquad (5.2.3\text{-}10)$$

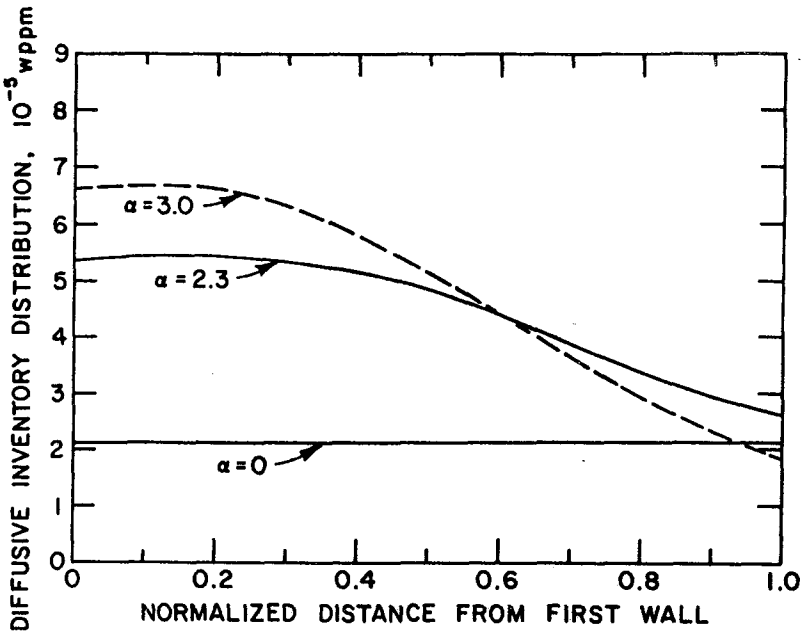

Figure 5.2.3-2a. Predicted distribution of diffusive tritium inventory in the Li_2O/He design as a function of normalized distance from the first wall. The parameter α determines the steepness of the generation rate profile (e.g. α = 2.3 implies a maximum-to-minimum ratio of 10).

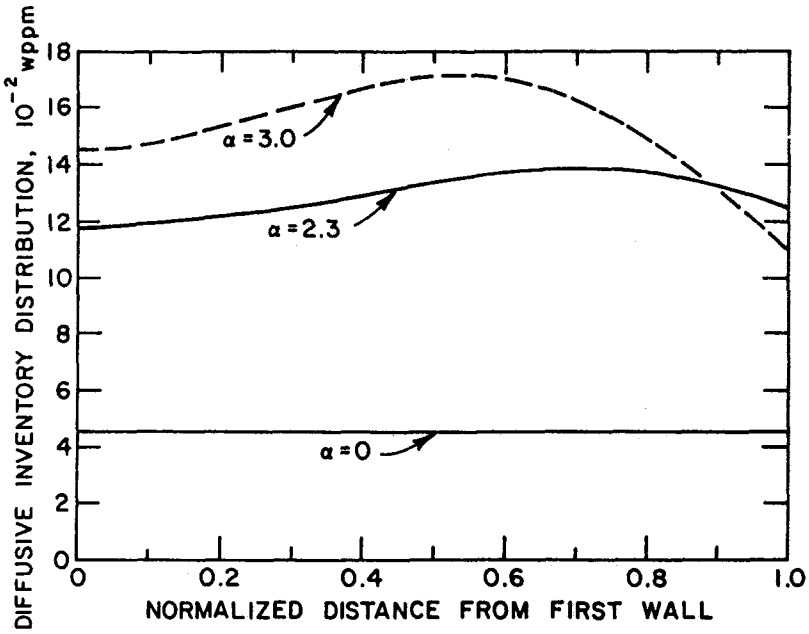

Figure 5.2.3-2b. Predicted distribution of diffusive tritium inventory in the $LiAlO_2$/He design as a function of normalized distance from the first wall. The parameter α determines the steepness of the generation rate profile (e.g. α = 2.3 implies a maximum-to-minimum ratio of 10).

where

$D(\bar{T})$ = the diffusion coefficient evaluated at the volume-averaged cell temperature

$\dot{G}_{cyl}$ = the tritium generation rate of the cell

$$f = (\beta - 1)^{-1} \int_1^{\beta} \exp\left[(Q/R\bar{T})\,(\bar{T}/T - 1)\right] d\xi \qquad (5.2.3\text{-}11)$$

$\xi = r^2/r_i^2$

$\beta = r_o^2/r_i^2$

r_o = the cell outer radius

r_i = the cell inner radius

r = an arbitrary radial position within the cell

$\bar{T}$ = the cell averaged temperature

T = a local temperature within the cell.

For the assumed case of radial heat flow from r_o to r_i, the average and local temperatures are given by

$$\bar{T} = T_{min} + \Delta T \left\{ \frac{\beta}{\beta - 1} - \frac{\beta - 1}{2(\beta \ln \beta - \beta + 1)} \right\}, \qquad (5.2.3\text{-}12)$$

$$T = T_{min} + \Delta T \left\{ \frac{\beta \ln \xi - \xi + 1}{\beta \ln \beta - \beta + 1} \right\}, \qquad (5.2.3\text{-}13)$$

where

T_{min} = the minimum cell temperature (at r_i)

and

$\Delta T = T_{max} - T_{min}$ = the radial temperature drop across the cell.

Summing Eq. (5.2.3-10) over the unit cells in the blanket gives

$$I_d = \dot{G} \left(r_g^2/15\right) \sum_{i=1}^{N} \left[D(\bar{T}_i)\right]^{-1} f_i \left(\dot{G}_{cyl}\right)_i / \dot{G} \ , \qquad (5.2.3\text{-}14)$$

where

$\dot{G}$ = the total tritium generation rate within the blanket in g/s or wppm/s.

A further simplication of Eq. (5.2.3-14) is possible by considering an "average" unit cell to characterize the whole blanket. If it is assumed that the whole blanket is operating at the volume-averaged heat generation $(\bar{\dot{Q}}_v)$ and tritium generation $(\bar{\dot{g}})$ rates, then the cell size is defined implicitly by:

$$\beta \ln \beta - \beta + 1 = \frac{4 \ k_b \Delta T}{\bar{\dot{Q}}_v r_1^2} \ , \qquad (5.2.3\text{-}15)$$

and Eq. (5.2.3-14) simplifies to

$$I_d = \left[r_g^2/15 \ D(\bar{T})\right] f \ \dot{G} \ . \qquad (5.2.3\text{-}16)$$

Equation (5.2.3-16) has been compared to Eq. (5.2.3-14) for an extreme case of an $LiAlO_2/H_2O/HT9/Be$ blanket with very steep gradients in $\dot{Q}_v$ and $\dot{g}$. The inventory from Eq. (5.2.3-16) was only 14% lower than that obtained by using the more detailed formula of Eq. (5.2.3-14). Figure 5.2.3-3 shows the results of the detailed calculation which yielded an inventory of 9.1 kg. Equation (5.2.3-16) gave 7.8 kg. Thus, Eq. (5.2.3-16) is recommended for the blanket-outside-of-tube designs.

A critical parameter in the equations for diffusive inventory is the diffusion coefficient. A review of the literature reveals a wide range of values for the diffusion coefficients for Li_2O and γ-$LiAlO_2$ depending on impurity levels within the sample, concentrations of water vapor in the sample and the atmosphere surrounding the sample, the rate limiting phenomena (e.g., bulk diffusion, grain boundary diffusion, dissolution surface desorption), and the experimentor's method for correlating and interpreting the data. A comprehensive review of the data (prior to 1982) for Li_2O is contained in Ref. 2 and summarized in Fig. 5.2.3-4 along with the latest single-crystal results of Guggi et al.[3] The use of single crystals eliminated the uncertainties associated with polycrystalline materials regarding the grain boundary ef-

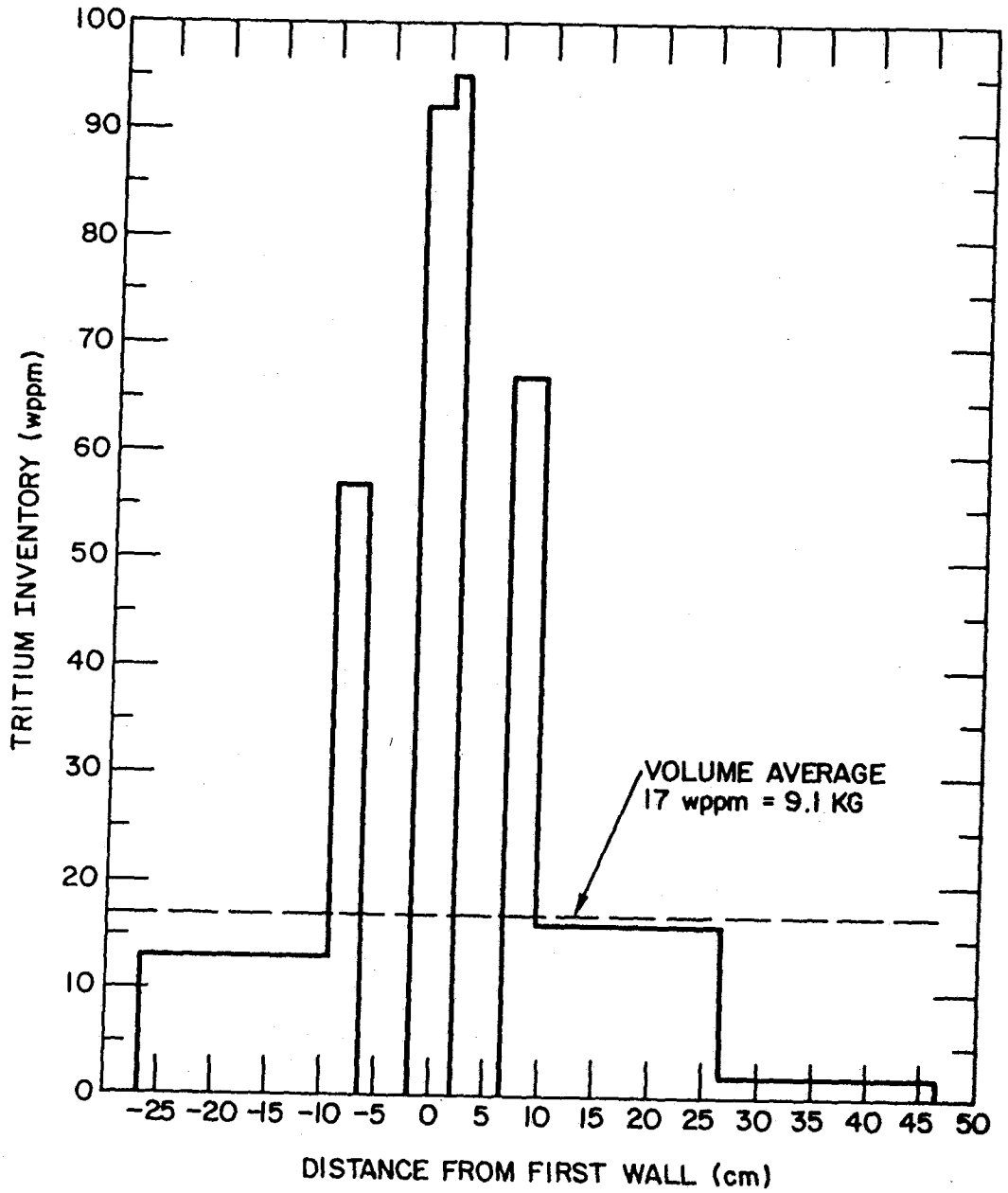

Figure 5.2.3-3. Distribution of the diffusive tritium inventory in an inboard and outboard $LiAlO_2/H_2O/HT9/Be$ blanket for T_{max} = 950°C, T_{min} = 360°C, $\dot{G}$ = 866 g/day, and r_g = 0.1 μm.

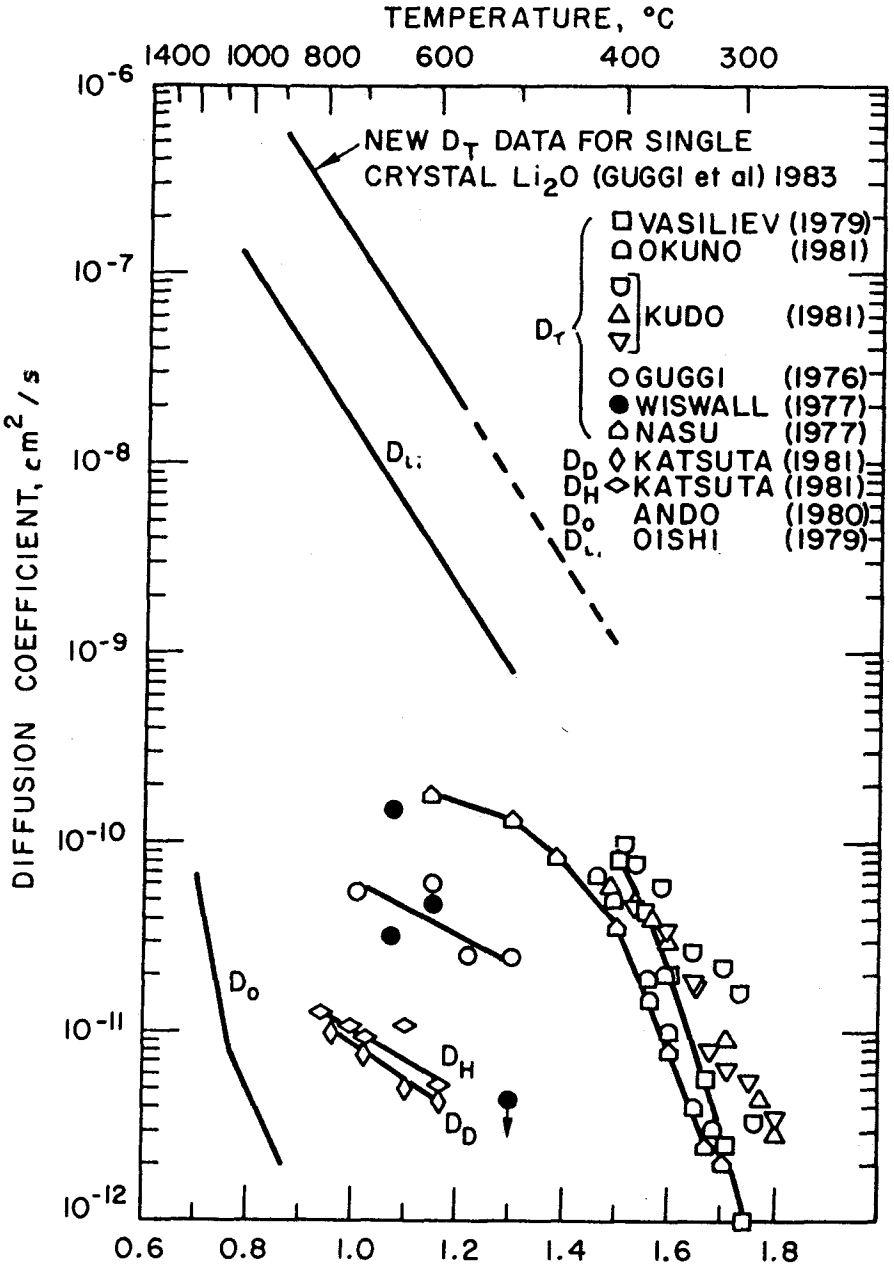

Figure 5.2.3-4. Temperature dependence of diffusion coefficients for tritium, oxygen, lithium, hydrogen, and deuterium in Li_2O .

fects. Guggi et al's results for the diffusion coefficient of tritium in Li_2O in the temperature range of 575 to 925°C are summarized by[3]

$$\ln(D/cm^2\ s^{-1}) = -(5.93 \pm 0.48) - (19.52 \pm 1.01\ kcal/mol)/RT\ , \quad (5.2.3\text{-}17)$$

where the ± numbers refer to three standard deviations.

As no comparable experiment has been performed on single crystal γ-$LiAlO_2$, a number of different experiments were reviewed and compared with the apparent diffusivities calculated from the TRIO-1 data (Fig. 5.2.3-5). Elleman et al[4,5] measured tritium diffusion in a related material (α-Al_2O_3) by recoiling tritium into the samples and recording the transient tritium released during post-irradiation heating. The measured activation energy for the single-crystal samples was 57.1 ± 2.4 kcal/mol. For sintered samples consisting of 4-μm grain size, the apparent activation energy was 43.8 ± 2.5 kcal/mol, which suggests the possible influence of grain boundary diffusion in lowering the effective activation energy for the sintered sample.

Wiswall and Wirsing[6,7] measured the response of pre-irradiated γ-$LiAlO_2$ powders and sintered pellets to post-irradiation annealing. They found very little difference in tritium release rates in loose powders and pelletized samples tested at 650°C. Their results are shown in Fig. 5.2.3-6 for the powdered samples (70-100 mesh) at temperatures of 500, 600, and 650°C. While the grain size was not specified, a grain radius of 0.1 μm (authors report submicron fine particle sizes) was assumed. Also, an error of a factor of ~2 was corrected in their data analysis by using a more accurate approximation to the transient release fraction (f) equation, where t is time and $\tau = r_g^2/D$:

$$f = 6\sqrt{t/\pi\tau)} - 3\ t/\tau\ . \quad (5.2.3\text{-}18)$$

Yunker[8] reports results for tritium diffusivity in $LiAlO_2$ in the temperature range of 400-650°C. Although no details are presented in the reference, the results are included in Fig. 5.2.3-6. Yunker's values of diffusivity per particle radius squared were converted to the points plotted in the figure by arbitrarily assuming a grain radius of 0.3 μm. Combining Yunker's data with the limited data of Wiswall and Wirsing suggests a range of activation energies of 35 to 50 kcal/mol.

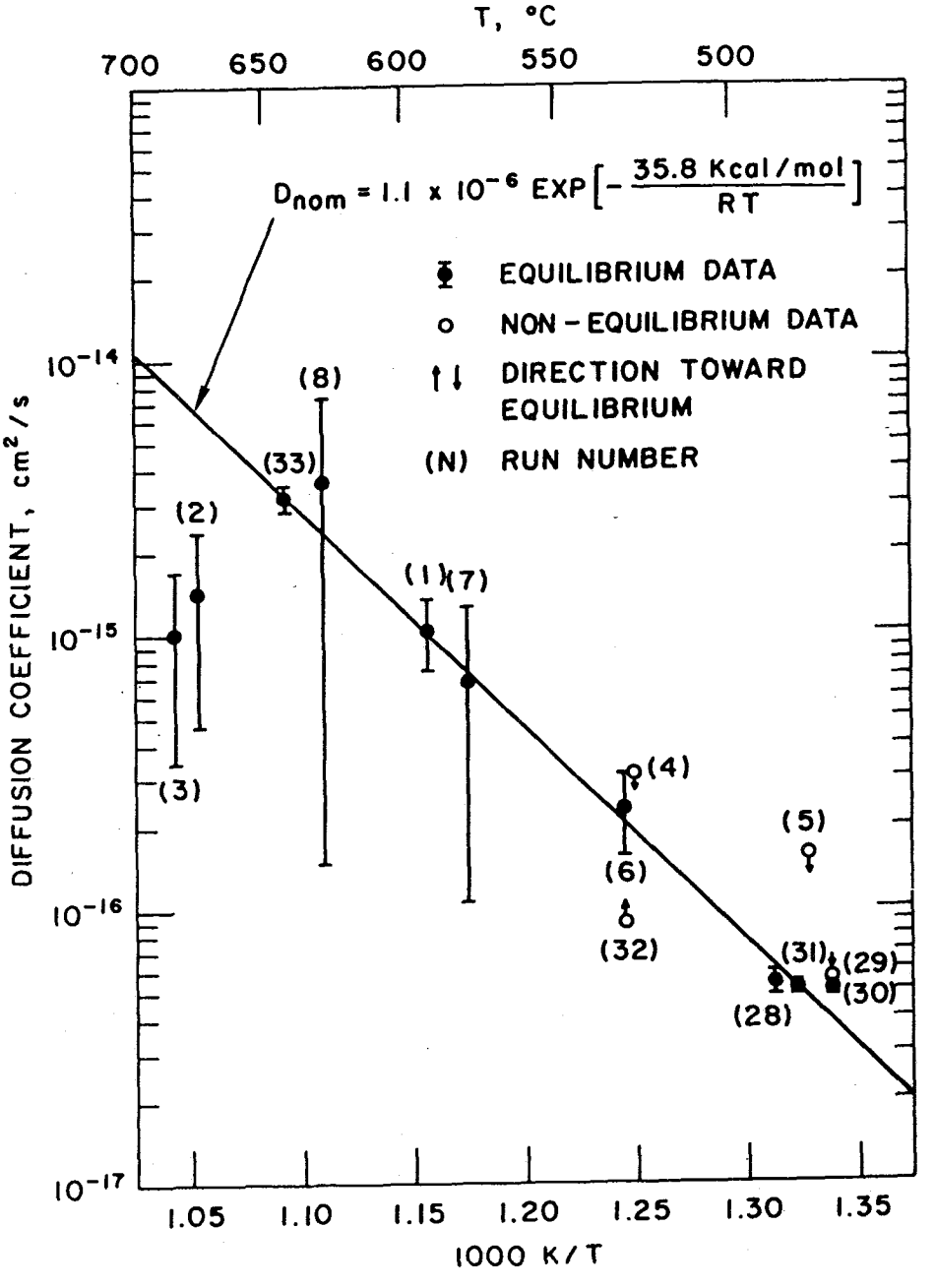

Figure 5.2.3-5. Diffusion coefficient for tritium in γ-$LiAlO_2$ determined from selected TRIO runs in which intragranular diffusion appeared to be the rate limiting phenomenon in tritium transport. The one-sigma bands are based on uncertainties in the generation rate ($\dot{G}$) and the inventory (I).

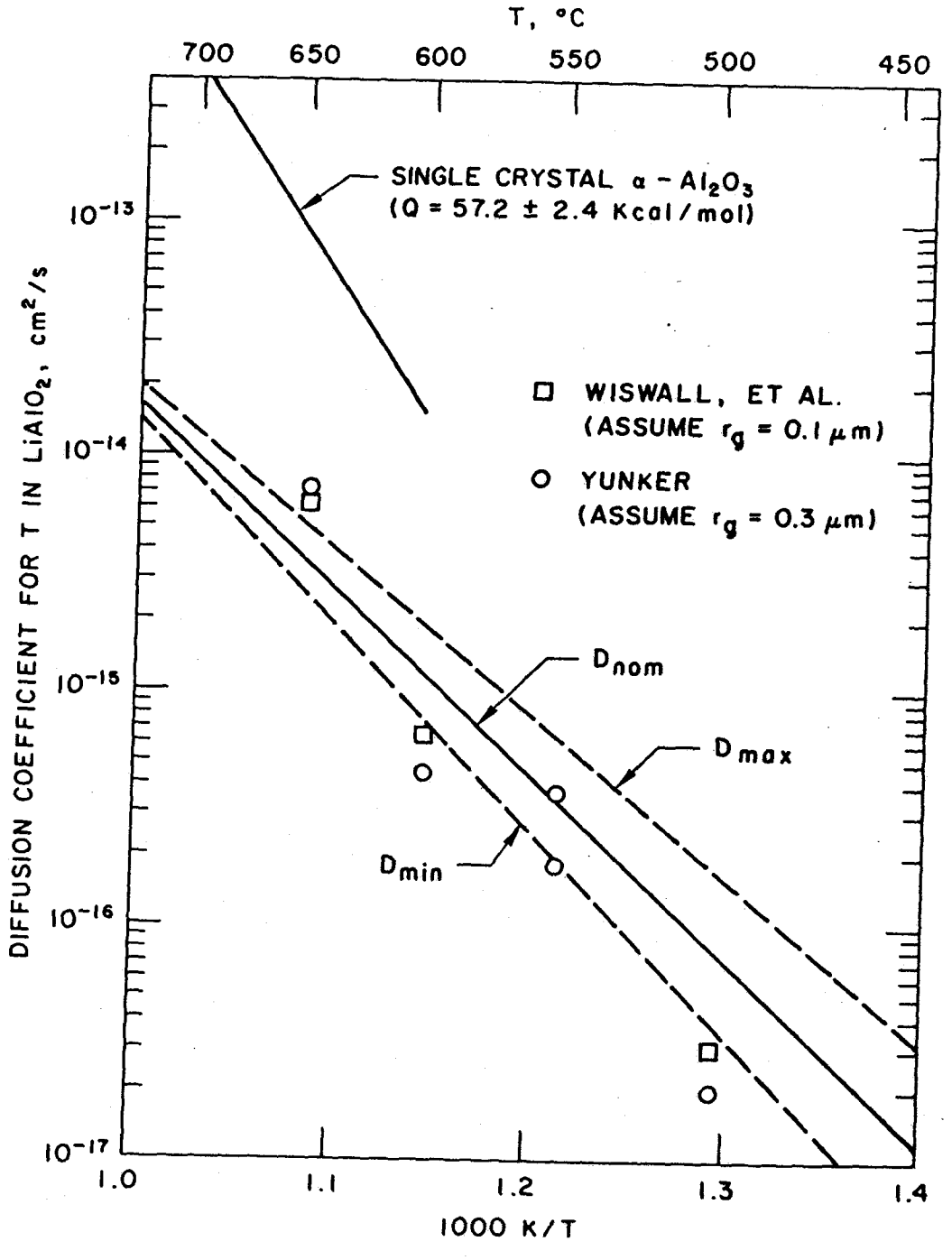

Figure 5.2.3-6. Comparison of selective data for tritium diffusion in γ-$LiAlO_2$ with TRIO-1 correlation (including uncertainties in grain size, inventory, and generation rate).

The TRIO data for runs 1-8 and 28-33 were analyzed to determine a bulk diffusion coefficient for tritium diffusion in γ-$LiAlO_2$. These runs were chosen because they exhibited characteristics of a bulk-diffusion-dominated transport mechanism. The sweep gas for all of these runs contained at least 0.1% H_2 which would tend to minimize the inventory associated with surface desorption. Equation (5.2.3-16) was inverted to solve for $D(\bar{T})$ as a function of the measured temperatures, the pre-irradiation grain size, the calculated generation rates, and the inventory measured directly for run 33 and deduced from release measurements for the other runs. Figure 5.2.3-5 shows the results for diffusion coefficient as a function of volume-averaged temperature. The results (which include a one-standard-deviation uncertainty estimate in I_d and $\dot{G}$) are summarized by:

$$\ln(D/cm^2 \cdot s^{-1}) = (-13.7 \pm 2.3) - (35.8 \pm 3.9 \text{ kcal/mol})/RT \quad (5.2.3\text{-}19)$$

For the purposes of comparison to other investigators, a ±30% uncertainty is associated with grain size because of the variability of grain size in the sample. Statistically including this in Eq. (5.2.3-19) gives:

$$\ln(D/cm^2 \cdot s^{-1}) = (-13.7 \pm 1.8) - (35.8 \pm 3.9 \text{ kcal/mol})/RT \quad (5.2.3\text{-}20)$$

Equation (5.2.3-20) is plotted in Fig. 5.2.3-6 and compared to the results of Yunker and Wiswall and Wirsing. Given that no uncertainty is included in the data of these authors, the agreement among the experimental results appears adequate.

Considerably lower activation energies have been obtained by other experimenters in less controlled experiments. Guggi et al[9] performed post-irradiation annealing experiments on γ-$LiAlO_2$ powders which were sonically sifted to a mean particle radius of 35 μm. They report an activation energy in the temperature range of 450-700°C of Q = 13.15 ± 0.27 kcal/mol. In addition, they report[10] a diffusivity of 7.2×10^{-8} cm^2/s at 900°C for a fused sample with a mean grain diameter of 1300 μm. One complicating feature of their experiment was that both the samples and the argon sweep gas contained substantial amounts of water vapor resulting primarily in the release of T_2O and HTO. Similarly, Vasiliev et al.[11] give an activation energy of Q ~ 13.8 kcal/mol for tritium diffusion in $LiAlO_2$ in the range of 400-800°C.

Sample calculations have been performed for the $LiAlO_2/H_2O$/FS/Be design using Eqs. (5.2.3-15, -16, and -19). The input parameters for this study are: $\dot{G}$ = 866 g/day, T_{max} = 1000°C, r_g = 0.1 μm, $\dot{Q}_v$ = 18 W/cm^3, r_i = 0.650 cm, and k_b = 1.1 W/m•K. Figure 5.2.3-7 shows the predicted diffusive inventory as a function of the minimum blanket temperature (T_{min}). The sensitivity of I_d to T_{min} is clearly demonstrated in this figure. At a minimum blanket temperature of 335°C, the diffusive inventory is estimated to be ~2 to ~10 kg with a nominal value of 4.5 kg. An increase of only 15°C in T_{min} results in a 50% decrease in inventory.

Solubility

The solubility of hydrogen isotopes and water vapor in Li_2O has been studied by several investigators. The results for the solubility of water vapor in Li_2O were summarized in the 1983 BSCC study.[12] In order to avoid precipitation of LiOH (LiOT) as a separate phase, the porosity/purge partial pressure of H_2O is limited by

$$p_{H_2O} \leq \begin{cases} (3.47 \times 10^6 \text{ atm}) \exp(-30.8 \text{ kcal/mol/RT}) & \text{for } T \leq 744 \text{ K} \\ (1.86 \times 10^3 \text{ atm}) \exp(-20.1 \text{ kcal/mol/RT}) & \text{for } T > 744 \text{ K} . \end{cases} \quad (5.2.3\text{-}21)$$

Assuming partial pressures of H_2O (T_2O) below these limiting values, the mole fraction of dissolved LiOH (LiOT) in Li_2O is given by

$$\log(X_{LiOH}) = (0.427 + 1.700 \times 10^{-4} T) \log (p_{H_2O}) + (-17.677 + 2.502 \times 10^{-2} T - 9.62 \times 10^{-6} T^2) , \quad (5.2.3\text{-}22)$$

where p_{H_2O} = H_2O partial pressure above Li_2O in atm.

Ihle and Wu[13] studied the solubility of deuterium in solid Li_2O under isothermal (515°C) conditions. Li_2O samples in open platinum boats were exposed to a deuterium atmosphere for a period of time. Based on the decrease in pressure due to absorption of D_2, they calculated the atom fraction in the solid. For deuterium pressures less than 1 torr (133 Pa), the relationship between dissolved fraction and deuterium pressure p_{D_2} was approximately linear suggesting that D_2 molecules are the dissolved species:

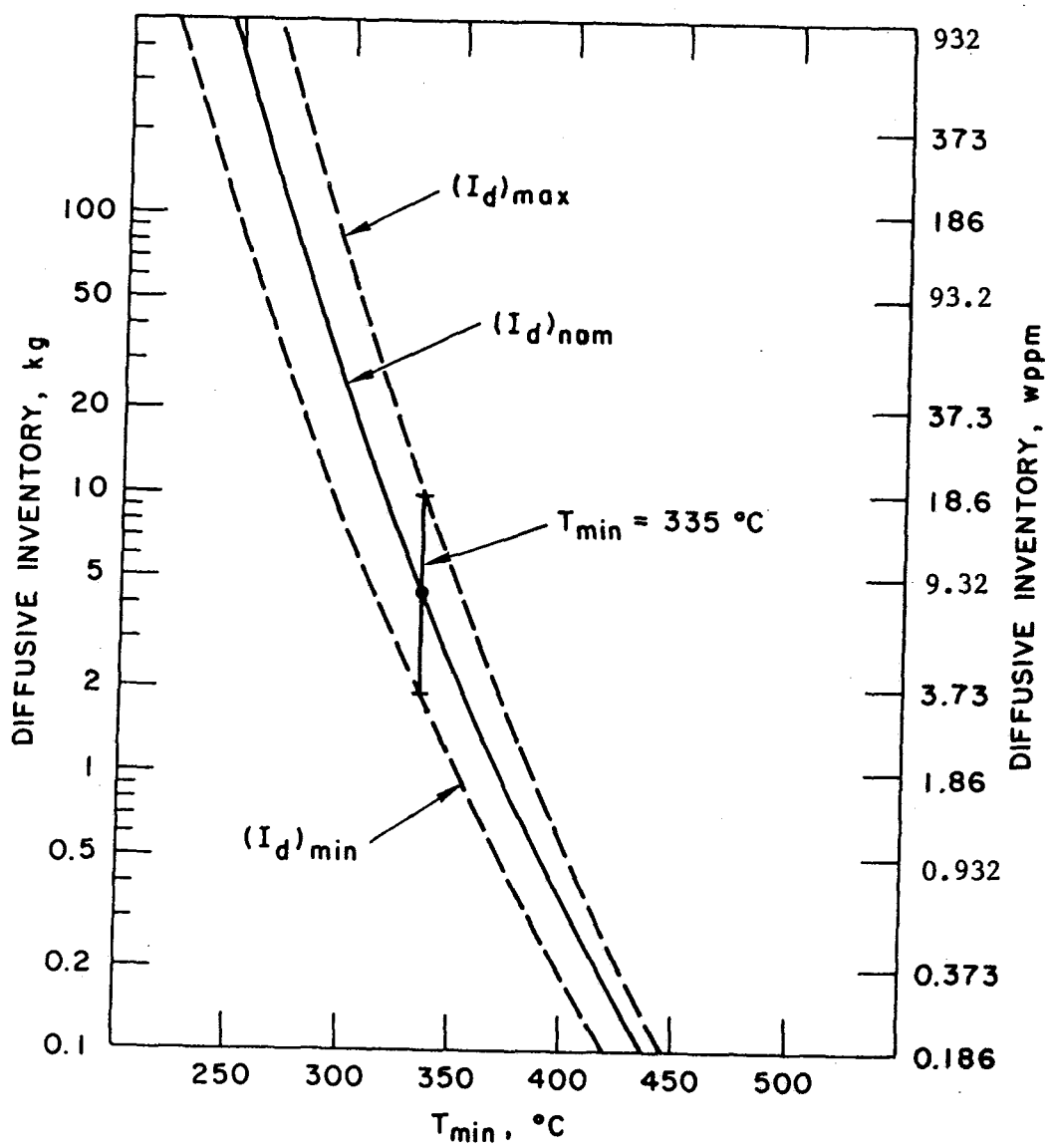

Figure 5.2.3-7. Predicted diffusive inventory for the $LiAlO_2/H_2O/HT9/Be$ design as a function of T_{min} for T_{max} = 1000°C, $\dot{G}$ = 866 g/day, and r_g = 0.1 μm.

$$X_D = 6 \text{ appm } (p_{D_2}/\text{Pa}) . \qquad (5.2.3\text{-}23)$$

Generalizing their results to the case of a T_2, H_2, HT environment and assuming no isotopic effects lead to the following equation for X_T in appm and wppm:

$$X_T = 6 \text{ appm } (1.8 \text{ wppm}) \cdot (p_{T_2} + p_{HT}/2) , \qquad (5.2.3\text{-}24)$$

where the partial pressures of T_2 and HT are in Pa. Equation (5.2.3-24) is valid for $p_{H_2} + p_{HT} + p_{T_2} < 100$ Pa. For excess H_2 leading to pressures above ~100 Pa, the absorption saturates at ~650 appm of hydrogen isotope.

The implications of Eq. (5.2.3-24) can be evaluated for two extreme cases. Assume that the purge stream in a reference blanket contains 1 Pa of T_2 and no HT. Then Eq. (5.2.3-24) predicts 1.8 wppm or ~1 kg of tritium dissolved in the reference Li_2O blanket. For the second case, assume that the purge contains HT and H_2 with $p_{HT} + p_{H_2} < 100$ Pa and $p_{HT} = 2$ Pa. Then, Eq. (5.2.3-24) predicts the same results as with pure T_2. However, if $p_{HT} + p_{H_2} >> 100$ Pa due to swamping the system with H_2, the dissolved tritium could decrease. As an extreme case, assume $p_{HT} = 2$ Pa and $p_{H_2} = 1000$ Pa. Using a limit of 660 appm results in 0.2 wppm of tritium in the solid or 0.1 kg in a reference blanket.

Kurasawa and Maroni[14] highlight a possible problem with adding hydrogen to the sweep or purge gas for an Li_2O blanket. Under the nonisothermal conditions of the blanket, the volatile hydrides LiH and LiT could form. While very little LiH (LiT) is expected to form under isothermal conditions, if the hydride were continuously transported out of the solid in a temperature gradient, the reaction could cause a problem with regard to mass transport of lithium out of the system.

More work needs to be done to determine the solubility of hydrogen isotopes in Li_2O as well as $LiAlO_2$. For example, Ihle and Wu performed a separate experiment in which the Li_2O was in a closed iron capsule. Their results at 515 and 600°C indicated approximately one-tenth the solubility of D_2 in Li_2O under these conditions. The authors argue that these samples probably did not come to equilibrium. Also, based on their experiment, it is not clear whether they were measuring surface adsorption or matrix solubility.

Surface Adsorption

In addition to the mechanisms associated with solubility within the matrix of a ceramic, the surface (e.g., pore/solid surface area) could act as a trap for the tritium species evolved. As the mechanisms associated with the surface effects are very complicated and as it is difficult to sort out solubility from surface adsorption in many experiments, the approach taken in this subsection is to examine experimental results for $LiAlO_2$ for which the solubility is assumed negligible. The tritium inventories deduced from the TRIO-01 test are used for this purpose.

TRIO runs 1-8 and 28-33 were used to determine the in-reactor diffusivity of tritium in $LiAlO_2$ (Fig. 5.2.3-5). These runs were selected because they exhibited the degree of temperature sensitivity one might expect from a process controlled by bulk diffusion. Also, for these runs, 0.1-1% hydrogen was added to the helium sweep gas, thereby minimizing the effects of surface trapping of tritium. However, after run 8, the hydrogen was removed from the sweep gas causing an instantaneous depression in the tritium release rate and an increase in tritium inventory. Figure 5.2.3-8 shows the difference between inventory remaining after each of these runs and the calculated diffusive inventory. This difference, $I - I_d$, is attributed to surface adsorption in this discussion although other interpretations are certainly possible.

While purge chemistry effects on tritium release clearly need more experimental work and modeling, a surface adsorption inventory of $I_a = 3 \pm 2$ wppm is used for γ-$LiAlO_2$ blankets with pure helium for a purge gas. Based on TRIO runs 1-8 and 28-33, $I_a = 0$ if 0.1% H_2 is added to the purge gas.

The Japanese in-situ experiment (VOM-15H) demonstrated that Li_2O is also sensitive to purge chemistry similar to that observed in TRIO-1. Figure 5.2.3-9 shows the release rate to generation rate fraction as a function of time for two sweep gas conditions. With the temperature held constant, the release rate decreases by a factor of ~10 when hydrogen is removed from the sweep gas. Addition of the hydrogen after 13 h causes a burst release. However, without further experimental controls, it is very difficult to determine whether the excess tritium is associated with solubility effects, surface effects, or artifacts of the metal piping in the system.

To further explore the degree to which γ-$LiAlO_2$ and Li_2O behave similarly

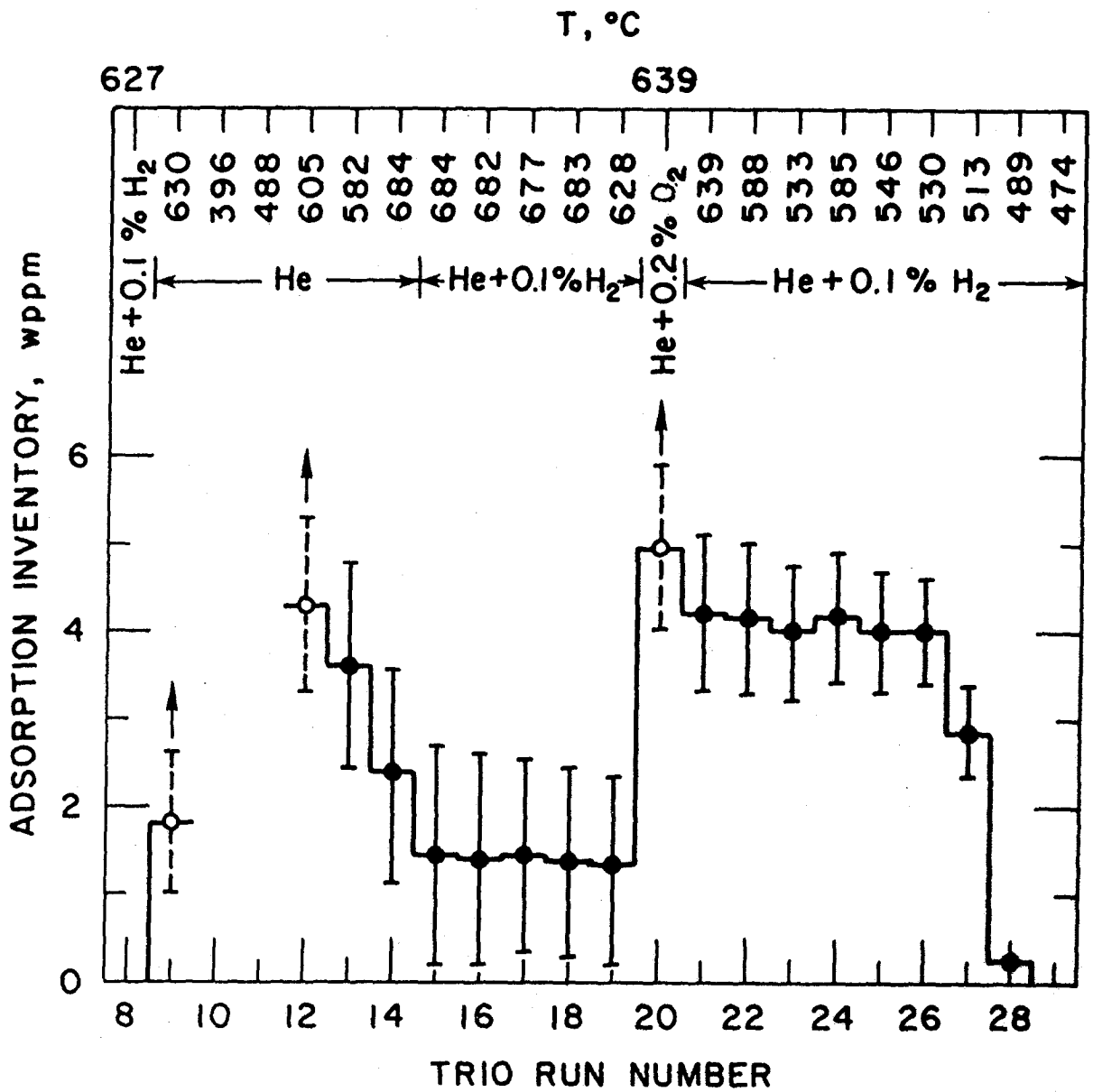

Figure 5.2.3-8. Estimation of "surface-adsorption" inventory for TRIO-1 runs 9-27 as a function of purge chemistry and average $LiAlO_2$ temperature.

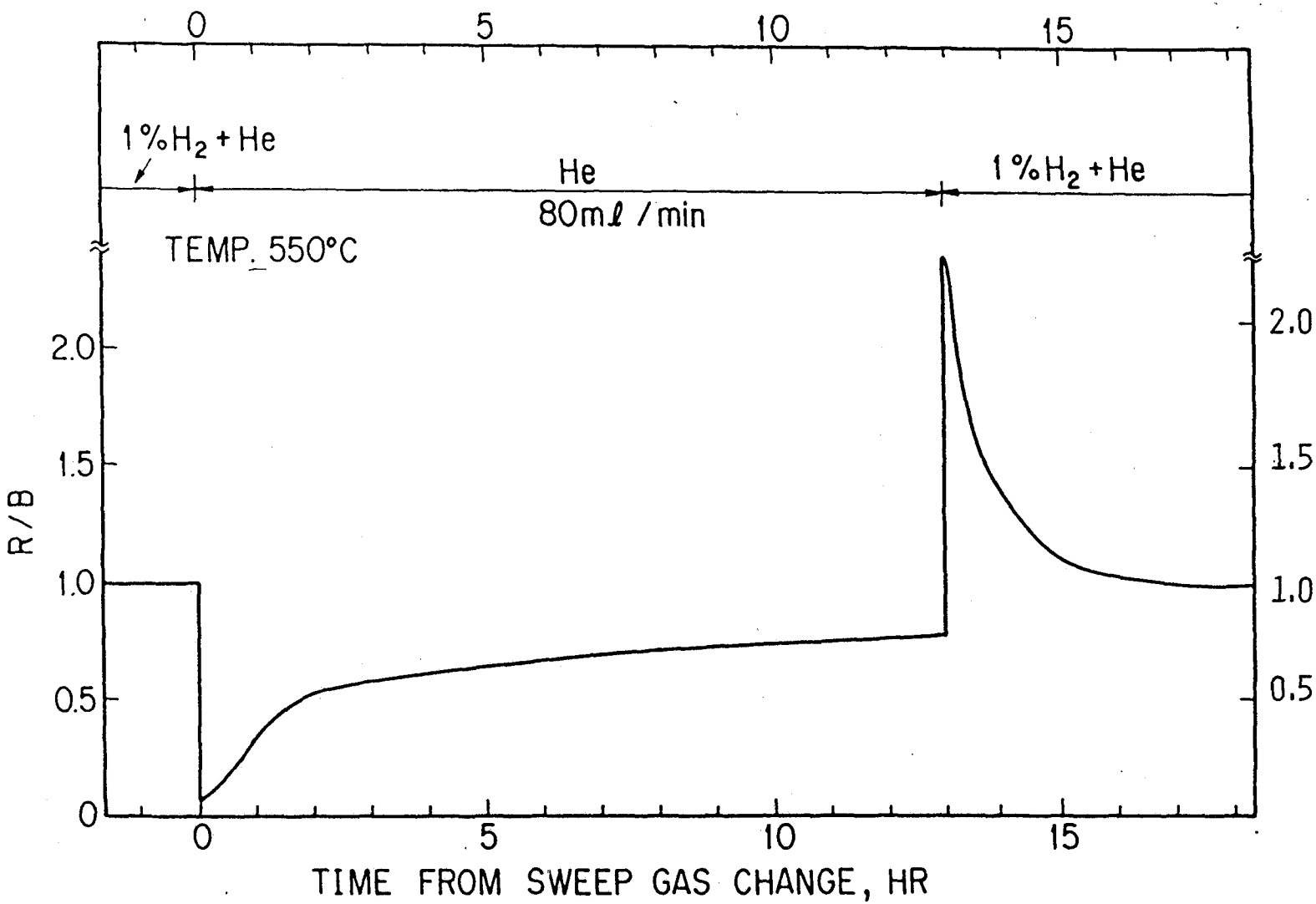

Figure 5.2.3-9. Effect of purge stream chemistry on the tritium release rate (R) to generation rate (B) ratio for Li_2O from the JAERI/VOM-15H experiment.

with respect to environment, the results of the FUBR-1A 100-day (~1 at% ^6Li burnup) irradiations are examined. Both the γ-$LiAlO_2$ and the Li_2O capsules are analyzed with the equation:

$$I_a + I_s = I - I_d \ , \qquad (5.2.3\text{-}25)$$

where

I is measured inventory

I_d is the calculated diffusive inventory

and

$I_a + I_s$ is the excess inventory.

Figure 5.2.3-10 shows the excess tritium inventory for the two solid breeders. Except for γ-$LiAlO_2$ at low temperature, the calculated diffusive inventory was negligible compared to the measured inventory. Even for the low-temperature γ-$LiAlO_2$ case, the calculated inventory was only ~10% of the measured inventory. Curve fitting of the temperature dependence of $(I - I_d)$ showed that the apparent activation energies for both Li_2O and γ-$LiAlO_2$ are in the range of 8-9 kcal/mole, which is consistent with a surface desorption phenomenon. While the results shown in Fig. 5.2.3-10 may raise more questions than they answer (especially when compared to the TRIO-1 results in Fig. 5.2.3-8), it appears that Li_2O and $LiAlO_2$ behave in a comparable manner with regard to excess inventory due to a surface adsorption mechanism. For design calculations, the same surface adsorption inventory (3 ± 2 wppm) for γ-$LiAlO_2$ is also used for Li_2O with a pure helium purge gas.

Porosity/Purge Stream Transport

The buildup of tritium partial pressure in the interconnected porosity and the purge stream has received a great deal of attention in the past[15,16] because of concerns about solubility and permeation into the primary coolant. The results of earlier modeling efforts are summarized in the following.

If it is assumed that the partial pressures of the released tritium and helium are small compared to the ambient pressure of the purge stream, then the transport of tritium through the interconnected porosity is dominated by

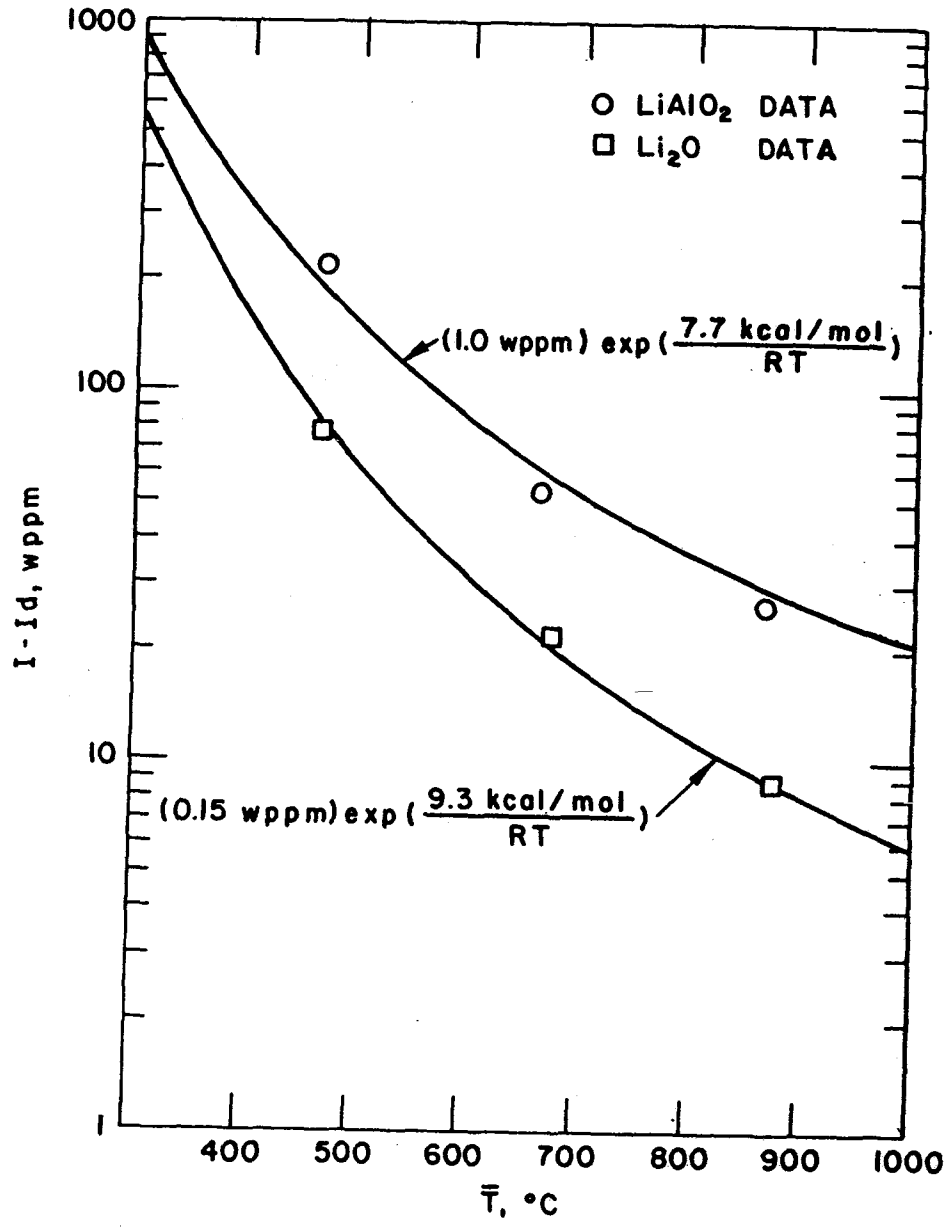

Figure 5.2.3-10. Measured tritium inventory in the FUBR-1A experiment (105 FPD) minus the calculated diffusive inventory.

gas diffusion. For a cylindrical unit cell with the purge tube located next to the coolant tube, an expression can be derived for the maximum and average tritium partial pressure in the interconnected porosity

$$p_A = (p_A)_i + \frac{(1/\varepsilon - 1)\, R\, \bar{T}\, \dot{g}_A r_i^2\, f(\beta)}{4\, W_A D_e(\bar{T})}, \qquad (5.2.3\text{-}26)$$

where

A = the tritium species (e.g., HT, T_2, HTO, T_2O desorbed from the pore/solid surface)

$(p_A)_i$ = the partial pressure of A in the purge stream

ε = interconnected porosity fraction

R = the universal gas constant

$\bar{T}$ = the average temperature in the porosity

$\dot{g}_A$ = the generation rate of species A per unit of 100% dense solid volume

r_i = the inner radius of the unit cell

W_A = the molecular weight of species A

$f(\beta)$ = $\beta \ln \beta - \beta + 1$ for maximum p_A

= $(\beta \ln \beta - \beta + 1)/(\beta - 1)$ average p_A

β = r_o^2/r_i^2

r_o = the unit cell outer radius

$D_e(\bar{T})$ = the effective diffusion coefficient for tritium species A in helium evaluated at the average cell temperature.

The expression for D_e depends on the ratio of mean free path for molecular collisions (λ) and the average pore radius (r_p). For $\lambda/r_p > 10$, Knudsen diffusion dominates and the diffusion of A is independent of the presence of the helium[17]

$$D_e = D_{KA}/T, \quad \text{for } \lambda/r_p > 10, \qquad (5.2.3\text{-}27)$$

where

T = tortuousity $(1/\varepsilon < T < 2/\varepsilon)$

$D_{KA} = (2\ r_p/3)[8\ RT/\pi W_A]^{1/2}$.

At the other extreme, i.e., $\lambda/r_p < 0.1$, ordinary molecular diffusion dominates the transport process and D_e is independent of the pore radius[18]

$$D_e = D_{AB}/T, \quad \text{for } \lambda/r_p < 0.1 , \tag{5.2.3-28}$$

where

$D_{AB} = (C/p)\ T^n$

p = total pressure in atmosphere

T = temperature in K

$C = 4.6 \times 10^{-5}$ cm^2/s•atm for HT
$= 4.2 \times 10^{-5}$ cm^2/s•atm for T_2
$= 3.6 \times 10^{-6}$ cm^2/s•atm for HTO
$= 3.5 \times 10^{-6}$ cm^2/s•atm for T_2O

$n = 1.823$ for HT and T_2
$= 2.334$ for HTO and T_2O.

In the transition region between Knudsen diffusion and ordinary diffusion, the following effective diffusion coefficient is recommended[17]

$$D_e = \left[T\left(1/D_{KA} + 1/D_{AB}\right)\right]^{-1} , \quad \text{for } 0.1 \leq \lambda/r_p \leq 10 . \tag{5.2.3-29}$$

Equation (5.2.3-26) with auxilliary Eqs. (5.2.3-27) through (5.2.3-29) is recommended for scoping calculations. While a number of simplifying assumptions were invoked in deriving these equations (e.g., isothermal unit cell), the estimated error associated with these assumptions is less than ±20%. This error is acceptable in light of the factor of 2 uncertainty in the tortuousity factor T. A relationship similar in form to Eq. (5.2.3-26) can be derived for the plate geometry. For a variety of tailored microstructures (e.g., sphere-pac, bimodal pore structure, monolithic structure with average pore radii >5

μm), the rise in tritium partial pressure across a unit cell is <1 Pa.

The average partial pressure in the purge stream can be derived from mass balance considerations under steady operating conditions. The partial pressure of tritium species A is simply

$$(p_A)_i = \dot{n}_A R \bar{T}_p / \dot{V}_p \ , \qquad (5.2.3\text{-}30)$$

where

$\dot{n}_A$ = the production (or arrival) rate of tritium species A in the purge channel

$\bar{T}_p$ = the average purge stream temperature

and

$\dot{V}_p$ = the volumetric flow rate of the purge.

Equation (5.2.3-30) can be used on a unit cell basis to find the distribution of $(p_A)_i$ across the blanket thickness or on a whole-blanket basis.

Permeation and Leakage

Permeation of gaseous species through a structural membrane can often be represented by the Richardson equation[19] (assuming one-dimensional flow):

$$J = -D \frac{dc}{dx} = -\frac{DS}{d_m} \left(\sqrt{p_1} - \sqrt{p_2}\right) \ , \qquad (5.2.3\text{-}31)$$

where

D = diffusivity of tritium species in the membrane,

S = Sievert's constant (solubility of tritium species in the membrane),

d_m = membrane thickness,

p_1, p_2 = upstream (breeder side) and downstream (coolant side) pressures of tritium species, respectively.

Permeability is defined as $P_m = DS$. For a negligible downstream pressure (p_2) in the coolant (i.e., $p_2 \ll p_1$), the mass flow rate of tritium species into the coolant loop is then

$$\dot{m} = JA \simeq -\frac{P_m A}{d_m}\sqrt{p_1}\ , \qquad (5.2.3\text{-}32)$$

where A is the surface area of the structural material exposed to the purge stream.

Few data exist for tritium permeation through structural materials. However, hydrogen permeation data through materials are quite extensive. In a recent literature review, Hassanein and Sze[20] surveyed the permeation data of hydrogen and its isotopes through iron and three other steel alloys (chromium ferritic steels, austenitic steels, and high-temperature steel alloys). Assuming applicability of the Richardson equation (Eq. (5.2.3-31), Hassanein and Sze recommended the following correlation for tritium permeability in HT9 (based on data of chromium ferritic steels):

$$P_m = 2.69 \times 10^{-3} \exp(-11100/RT)\ , \qquad (5.2.3\text{-}33)$$

where P_m is in units of cm^3 (STP)/cm·s·$atm^{1/2}$, and the HT9 surface is assumed to be relatively clean (i.e., no oxide layers). Inspection of the scattered data shows that they deviate from Eq. (5.2.3-33) by ~±50%. P_m can be converted to grams or Curies and used in Eq. (5.2.3-32).

More significant to the hydrogen (tritium) permeation through bare metal alloys is the effect of oxide layers, either preformed or formed in-situ on the metal surface. One group of data on high-temperature steel alloys showed permeation impeding factors as high as 500 at 650°C for Incoloy 802. Impeding factors for other alloys varied over a wide range to as low as 5 for In586 at 650°C. Oxide layer effects on hydrogen permeation through HT9 have <u>not</u> been experimentally investigated. For conservatism, a range of impeding factors (1-100) are assumed. In later calculations, these impeding factors are simply used to reduce P_m in Eq. (5.2.3-33) before it is substituted into Eq. (5.2.3-35). Also, since the assumed range of the oxide impeding factors more than embodies the correlation uncertainties (±50%) of the bare-alloy permeability, no separate consideration of the latter uncertainties is judged necessary.

For tritium leakage calculations, several different conditions may exist depending on the purge stream chemistry. In the case of no hydrogen addition to the purge stream, the probable tritium species are T_2 and T_2O. If the

predominant species is T_2 (e.g., 99%), then Eq. (5.2.3-32) may be used directly. If the predominant species is T_2O (e.g., 99%) which is assumed not to permeate through the coolant tube, then p_1 in Eq. (5.2.3-32) is interpreted as the T_2 partial pressure only. However, as solid breeder designers have elected to add 100 wppm hydrogen to the helium purge stream, some modification of the equation is required to reflect the isotope swamping effect. Based on TRIO-1 results, this situation produces tritium primarily in the form of HT. Equation (5.2.3-32) is modified to separate out the permeation of the two hydrogen isotopes:

$$\dot{m}_{H_2} + \dot{m}_{HT} = \left(P_m A/d_m\right) \sqrt{p_{HT} + p_{H_2}} \; . \qquad (5.2.3\text{-}34)$$

Equation (5.2.3-34) is indeterminate. However, the 100 wppm of H_2 in the purge corresponds to p_{H_2} = 20 Pa for a 1 atm (1.01×10^5 Pa) helium purge stream. Under these conditions, it is reasonable to assume that $p_{HT}/p_{H_2} \ll 1$. Equation (5.2.3-34) is thus rewritten in the following form to allow simplification under these conditions:

$$\left(1 + \dot{m}_{HT}/\dot{m}_{H_2}\right)\left(\dot{m}_{H_2} d_m/P_m A\right) = \sqrt{p_{H_2}}\,\sqrt{1 + p_{HT}/p_{H_2}} \; . \qquad (5.2.3\text{-}35)$$

Using the assumptions $p_{HT}/p_{H_2} \ll 1$ and $\dot{m}_{HT}/\dot{m}_{H_2} \ll 1$, we have

$$\dot{m}_{H_2} = \left(P_m A/d_m\right) \sqrt{p_{H_2}} \qquad (5.2.3\text{-}36)$$

$$\dot{m}_{HT} = \left(P_m A/2d_m\right) p_{HT}/\sqrt{p_{H_2}} \; . \qquad (5.2.3\text{-}37)$$

Using the relationship $\dot{m}_T = 3\,\dot{m}_{HT}/4$, we have an expression for the leakage rate of tritium from the breeder to the primary coolant

$$\dot{m}_T = \left(3\,P_m A/8\,d_m\right) p_{HT}/\sqrt{p_{H_2}} \; . \qquad (5.2.3\text{-}38)$$

The effects of isotope swamping can be seen clearly from Eq. (5.2.3-38) As the partial pressure of H_2 is increased, the allowable partial pressure of HT is increased for a fixed $\dot{m}_T$.

For the case of a pure helium purge stream, Eq. (5.2.3-32) (with the input in Table 5.2.3-1 and a tritium generation rate of 890 g/day) becomes

$$\dot{m}_T = (2.31 \times 10^5 \text{ Ci/day} \cdot \text{Pa}^{1/2}) \sqrt{p_{T_2}}/B_f , \qquad (5.2.3\text{-}39)$$

where B_f is the total barrier factor for the coolant tube (e.g., B_f = the number of oxidized surfaces times the impedance factor (IF) for one surface). For a leakage rate of 100 Ci/day, the range of limiting T_2 partial pressures in the purge is from 1.9×10^{-7} Pa for B_f = 1 (clean walls) to 0.017 Pa for B_f = 300 (three oxide surfaces and IF = 100). It is doubtful that any realistic designs could achieve such limits for reasonable purge flow conditions. The corresponding purge volumetric flow rate is obtained by combining Eqs. (5.2.3-39) with Eq. (5.2.3-30) to give

$$\dot{V}_p = (4.74 \times 10^{14} \text{ L/s}) \left(\frac{\text{Ci/day}}{B_f \dot{m}_T}\right)^2 \left(\frac{1}{1 + p_{T_2O}/p_{T_2}}\right) . \qquad (5.2.3\text{-}40)$$

Table 5.3.1. Solid Breeder Blanket Parameters Used in Tritium Permeation and Purge Flow Design Calculations for the $LiAlO_2/H_2O$/FS/Be Design

Parameters	Values
Structural material	HT9/DWT
Structure thickness (mm)	2 (0.75)
Total structural surface area exposed to purge (m^2)	1.74×10^4
Average structure temperature (°C)	335
Purge channel cross-sectional area (cm^2)	0.283
Average purge channel length (m)	6
Average purge temperature (°C)	350
Number of unit cells	1.202×10^5

For B_f = 300, $\dot{m}_T$ = 100 Ci/day, and p_{T_2O}/p_{T_2} = 0.01, $\dot{V}_p$ = 5.2 × 10^5 L/s which corresponds to 150 m/s linear velocity. However, for B_f = 300 and either $\dot{m}_T$ = 1000 Ci/day or p_{T_2O}/p_{T_2} = 0.99, $\dot{V}_p$ = 5.2 × 10^3 L/s and U = 1.5 m/s.

The above calculations assume that the helium purge stream contained no added hydrogen. The effect of isotope swamping will now be examined. For the design case of 100 wppm protium in the helium purge stream pressure of 1 atm at 350°C, the hydrogen partial pressure entering the blanket is 2 × 10^{-4} atm (20.3 Pa). Substituting this partial pressure into Eq. (5.2.3-38) gives

$$\dot{m}_T = (1.92 \times 10^4 \text{ Ci/day·Pa})(p_{HT}/B_f) . \qquad (5.2.3\text{-}41)$$

For a limit of 100 Ci/day and a barrier factor of 1 - 300, the range of limiting HT partial pressures is from 5.2 × 10^{-3} Pa to 1.6 Pa. Figure 5.2.3-11 shows the relationship between the limiting HT partial pressure in the purge and the leakage rate with the barrier factor as a parameter. In the figure, IF refers to the oxide impedance factor for a single surface. The total barrier factor for the double-walled tube (DWT) is assumed to be B_f = 3 IF.

The limiting purge flow rate corresponding to Eq. (5.2.3-40) is

$$\dot{V}_p \geq (3.5 \times 10^8 \text{ L/s}) \left(\frac{\text{Ci/day}}{B_f \dot{m}_T}\right) , \qquad (5.2.3\text{-}42)$$

if it is assumed (conservatively) that no HTO is formed. $\dot{V}_p$ is plotted as a function of $\dot{m}_T$ with IF as a parameter in Fig. 5.2.3-12. For the reference case of $\dot{m}_T$ = 100 Ci/day and IF = 100 (B_f = 300), the minimum volumetric flow rate is 1.2 × 10^4 L/s which corresponds to 3.5 m/s linear velocity.

5.2.3.2 Transient Tritium Behavior

The purpose of describing the transient behavior of tritium in the solid-breeder blankets is to understand the response time of the system to the initial reactor startup and to pulsing operation that may be used in a test reactor. The thermal and tritium transport response times are important factors in establishing limits on the minimum burn-dwell times of a test reactor such that the testing results are qualitatively representative and quantitatively extrapolatable to full-scale commercial-reactor operating conditions.

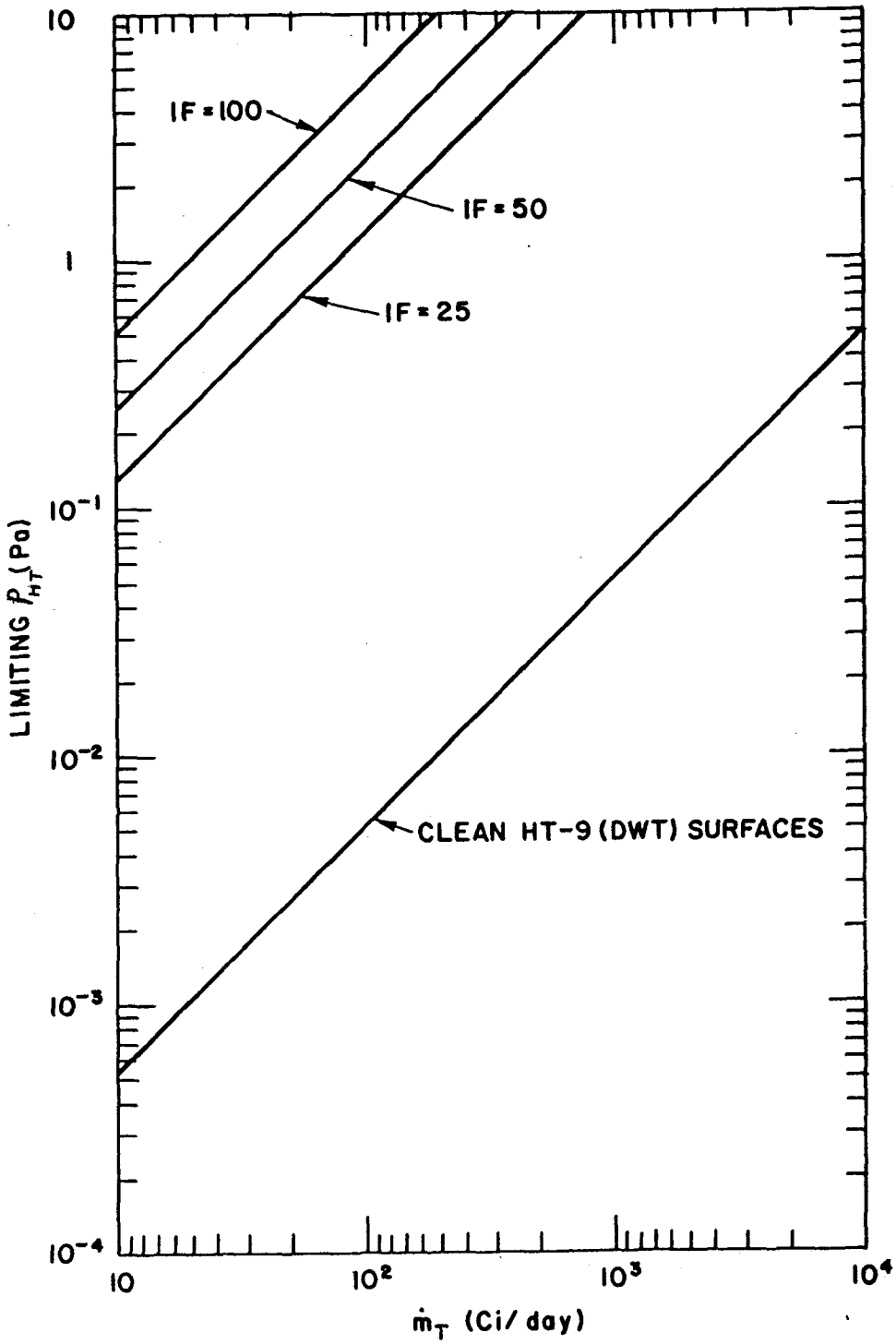

Figure 5.2.3-11. Limiting tritium partial pressure in the purge channel plotted as a function of the maximum tritium leakage rate ($\dot{m}_T$) into the primary H_2O coolant loop from the $LiAlO_2$ breeder through the HT-9 cladding. The parameter IF refers to the assumed oxide impedance factor.

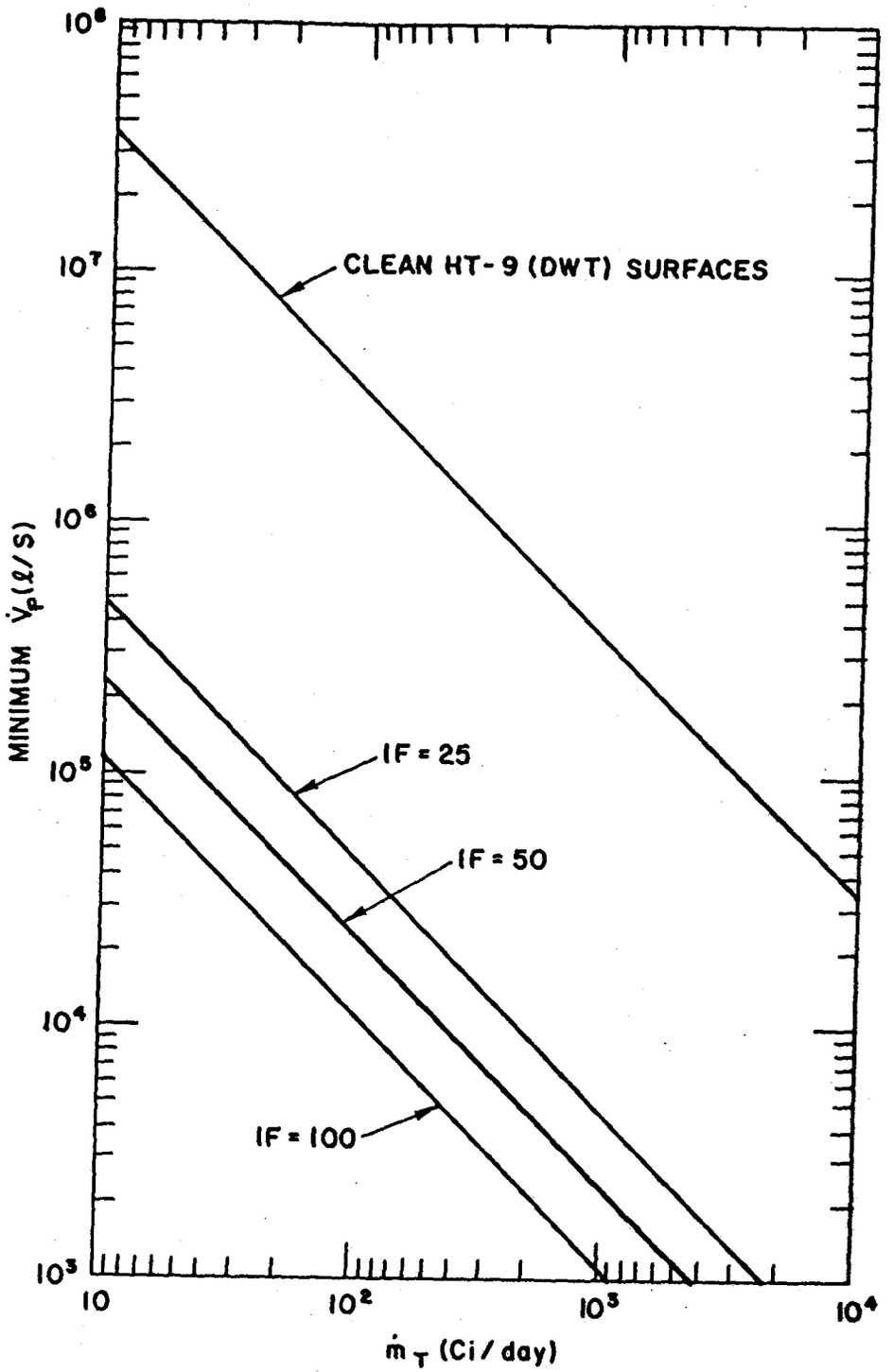

Figure 5.2.3-12. Minimum purge-channel volumetric flow plotted as a function of the maximum tritium leakage rate (see Fig. 5.2.3-11).

Bulk Diffusion

Classical solutions exist in heat and mass transfer literature[21] to describe the transient diffusion of tritium from an isothermal, spherical grain with the grain boundaries acting as a perfect sink for tritium. The fundamental equation for the inventory (I_g) within the grain is:

$$\dot{I}_g + \dot{R}_g = \dot{G}_g \,, \qquad (5.2.3\text{-}43)$$

where

$\dot{R}_g$ = release rate from the grain

and

$\dot{G}_g$ = generation rate within the grain.

The release rate is related to the gradient in tritium concentration (c) at the grain surface by:

$$\dot{R}_g = -4\pi r_g^2 D(\partial c/\partial r)_{r_g} \,, \qquad (5.2.3\text{-}43a)$$

where $(\partial c/\partial r)_{r_g}$ must be found by solving the diffusion equation. Solutions can be found in the literature for several idealized, but useful, cases. For a step change in generation rate and temperature (i.e., instantaneous startup) and zero initial tritium concentration, we have

$$\dot{R}_g/\dot{G}_g = 1 - (6/\pi^2) \sum_{n=1}^{\infty} (1/n^2) \exp(-n^2\pi^2 t/\tau) \qquad (5.2.3\text{-}44a)$$

$$I_g/(I_g)_{SS} = 1 - (90/\pi^4) \sum_{n=1}^{\infty} (1/n^4) \exp(-n^2\pi^2 t/\tau) \,, \qquad (5.2.3\text{-}44b)$$

where $\tau = r_g^2/D$.

Plots of the fractional release rate and inventory are shown in Fig. 5.2.3-13 as a function of dimensionless time for the case of instantaneous reactor startup. Note that the inventory fraction lags the release rate fraction.

A useful approximation to Eq. (5.2.3-43) can be obtained by assuming that

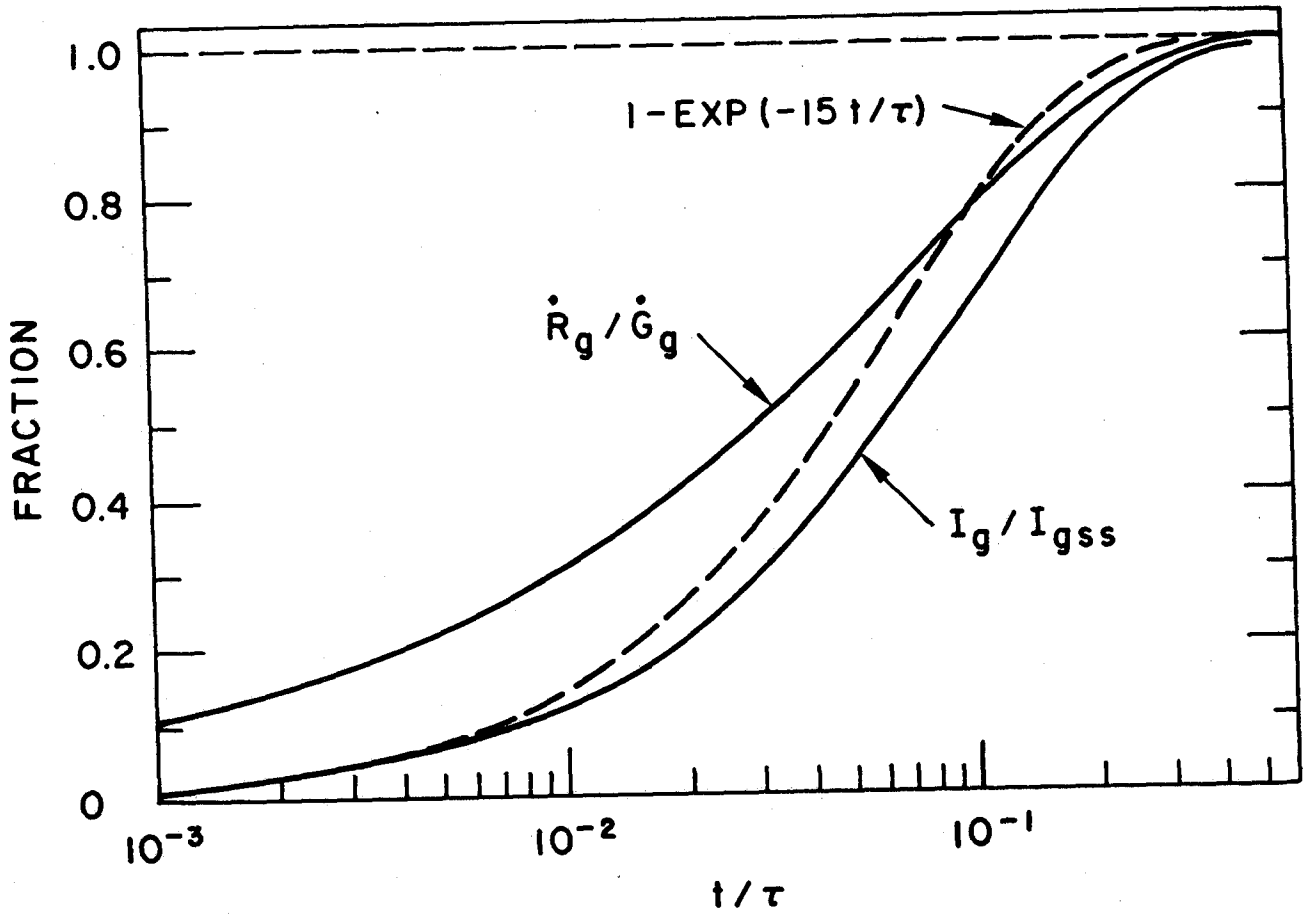

Figure 5.2.3-13. Comparison between exact and approximate analytical solutions for intragranular diffusion in a spherical grain in response to a step increase in generation rate.

the tritium concentration maintains a parabolic profile during the transient. The appropriate differential equation is:

$$\dot{I}_g + 15\, I_g/\tau = \dot{G}_g , \qquad (5.2.3\text{-}45)$$

Solutions to this equation for the instantaneous startup problem are:

$$\dot{R}_g/\dot{G}_g = I_g/(I_g)_{SS} = 1 - \exp(-15\, t/\tau) . \qquad (5.2.3\text{-}46)$$

The approximate and exact solutions are shown in Fig. 5.2.3-13.

Another useful solution to the diffusion equation is for the case of step changes in temperature for constant generation rate. If it is assumed that equilibrium has been achieved before the step change in temperature ($T_1 \rightarrow T_2$ at $t = 0$), then the exact solutions are:

$$\dot{R}_g/\dot{G}_g = 1 + (\tau_1/\tau_2 - 1)(6/\pi^2) \sum_{n=1}^{\infty} (1/n^2) \exp(-n^2\pi^2 t/\tau_2) \qquad (5.2.3\text{-}47a)$$

and

$$I_g/(I_g)_{SS2} = 1 + (\tau_1/\tau_2 - 1)(90/\pi^4) \sum_{n=1}^{\infty} (1/n^4) \exp(-n^2\pi^2 t/\tau_2) \qquad (5.2.3\text{-}47b)$$

where

$$\tau_1 = r_g^2/D(T_1)$$

$$\tau_2 = r_g^2/D(T_2)$$

and

$$(I_g)_{SS2} = (\tau_2/15)\dot{G}_g .$$

The extension of the single-grain model to the unit cells shown in Fig. 5.2.3-1 can be done formally by integrating over the generation rates and temperatures within the unit cells. For the case of the cylindrical unit cell we have

$$\left(\dot{R}/\dot{G}\right)_{cyl} = (\beta - 1)^{-1} \int_1^{\beta} \left(\dot{R}_g/\dot{G}_g\right) d\xi \qquad (5.2.3\text{-}48a)$$

and

$$\left(I/I_{SS}\right)_{cyl} = (\beta - 1)^{-1} \int_1^{\beta} \left(\dot{I}_g/\dot{G}_{SS}\right) d\xi \qquad (5.2.3\text{-}48b)$$

where $\xi = r^2/r_o^2$ and $\beta = r_o^2/r_i^2$ as before.

Calculations are performed with the idealized analytical solutions to verify the model with its $LiAlO_2$ diffusion coefficient and to investigate the system response time. Three TRIO-1 temperature transients are analyzed with Eqs. (5.2.3-47) and (5.2.3-48). The runs were selected based on: (1) 0.1% H_2 addition to the purge gas so that bulk diffusion is the rate-limiting mechanism; (2) relatively rapid temperature rise to match the analytical assumption; (3) steady-state inventory achieved prior to the temperature transient; and (4) clarity of the experimental response signal. Figures 5.2.3-14 through 5.2.3-16 show the measured temperature (T_e), generation rate $(\dot{G})$, and release rate $(\dot{R}_e)$ for TRIO runs 8, 28, and 31. Also shown are the assumed temperature transient (T_a) and the analytical predictions for the tritium release rate $(\dot{R}_{nom}, \dot{R}_{min}$, and $\dot{R}_{max})$ based on the nominal, minimum, and maximum values of the diffusion coefficient determined from the steady-state data in Fig. 5.2.3-5. Qualitatively, the agreement is excellent. Increases in temperature (runs 8 and 31) cause burst releases followed by a return to equilibrium. Decreases in temperature (run 28) cause a depression in the release rate followed by a return to equilibrium. The quantitative comparison between data and predictions is satisfactory considering the data uncertainties (±10%) and the idealized assumptions used in the analytical solutions.

Calculations have also been performed to characterize the tritium response (due to bulk diffusion) of a full-scale $LiAlO_2$ blanket to an instantaneous reactor startup. Figure 5.2.3-17 shows the release rate and inventory fractions for the reference $LiAlO_2/H_2O$/FS/Be blanket as a function of time and fluence (assuming 5 MW/m^2 neutron wall load). Equations (5.2.3-44) and (5.2.3-48) were used for these calculations under the assumption that an average unit cell can be used to characterize the blanket response. The release rate reaches 67.4% of equilibrium in ~1 min and asymptotically ap-

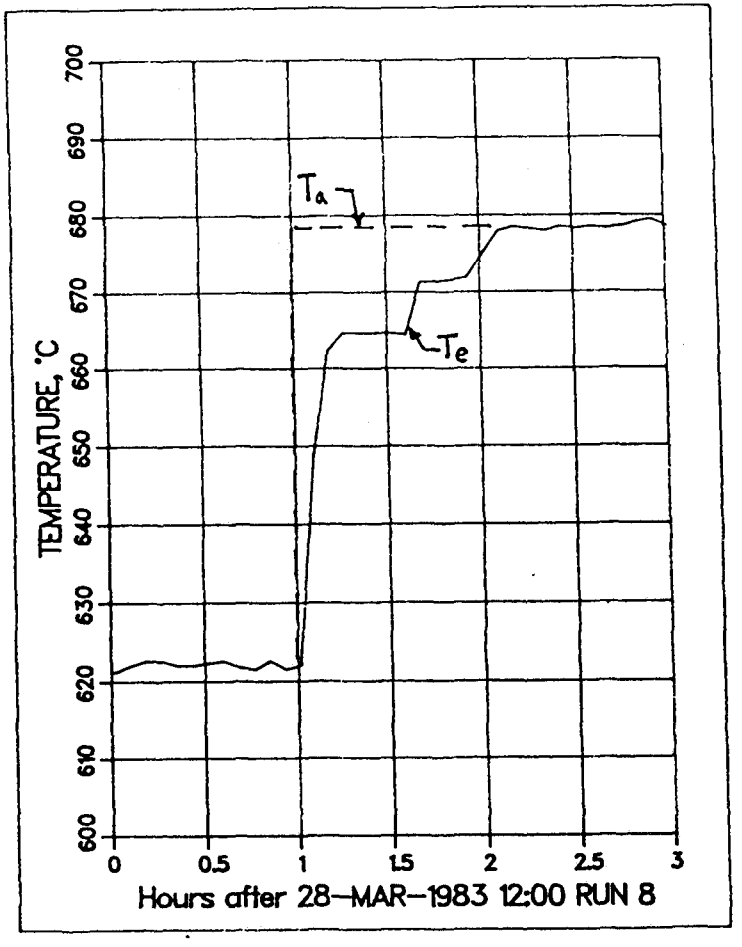

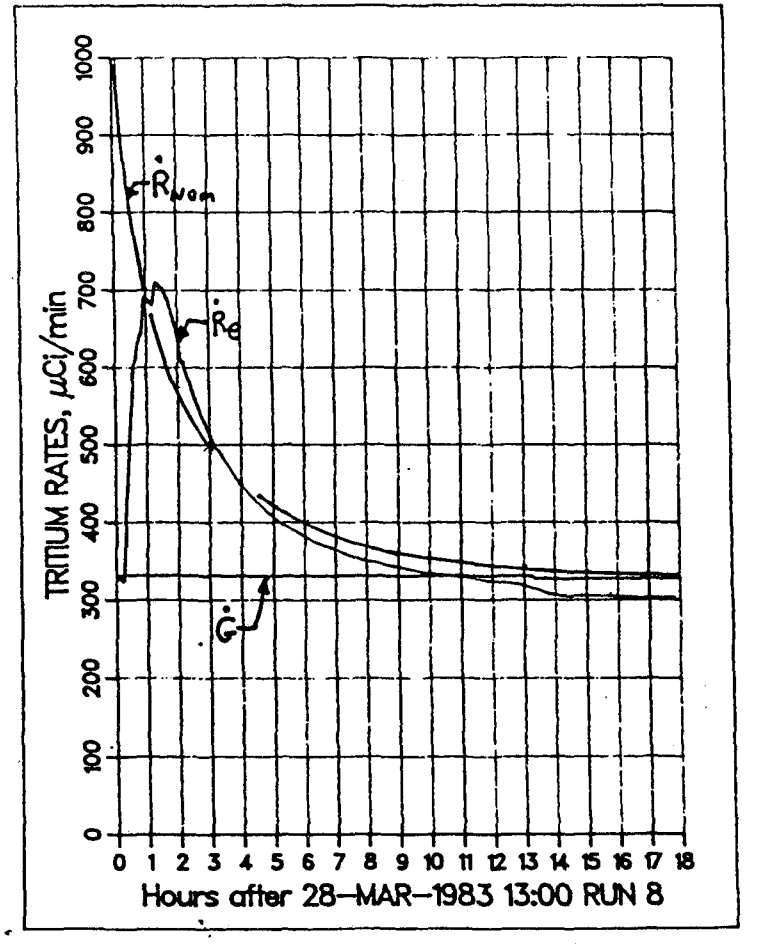

Figure 5.2.3-14. Analytical predictions for the nominal transient tritium release rate $(\dot{R}_{nom})$ for an idealized temperature variation with time (T_a). Experimental values for temperature (T_e), release rate $(\dot{R}_e)$, and generation rate $(\dot{G})$ for Run 8 are also shown.

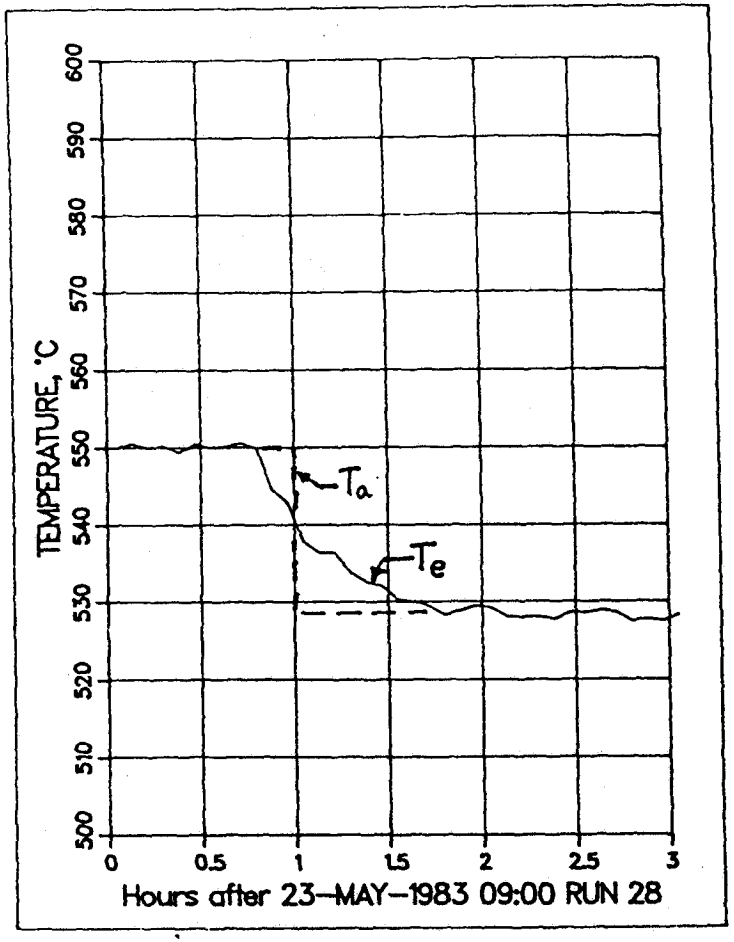

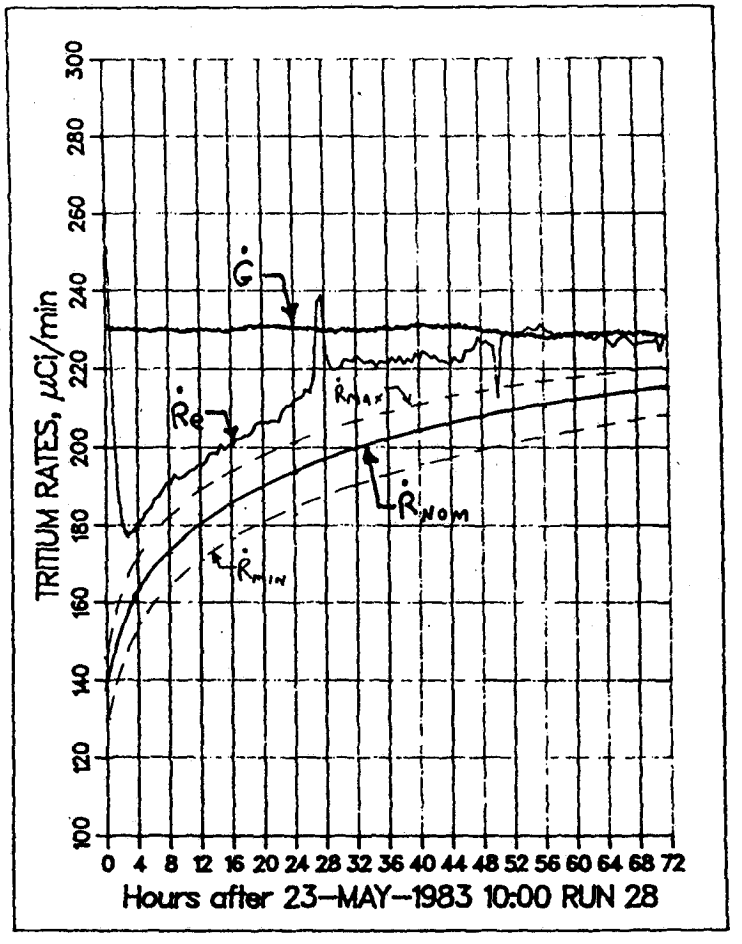

Figure 5.2.3-15. Comparison of analytical predictions and experimental results for TRIO Run 28. (See caption to Fig. 5.2.3-14.)

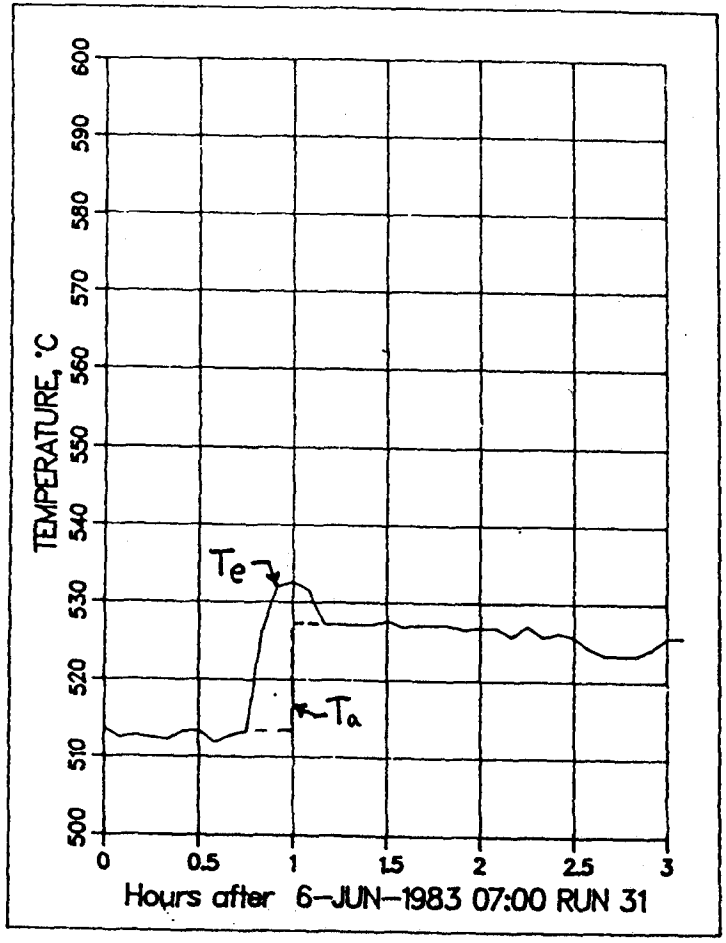

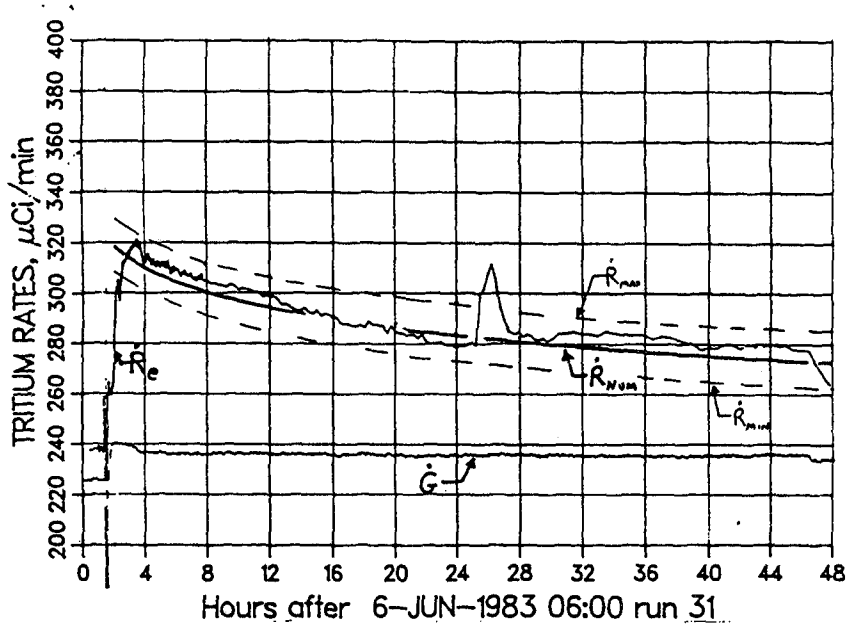

Figure 5.2.3-16. Comparison of analytical predictions and experimental results for TRIO Run 31. (See caption to Fig. 5.2.3-14.)

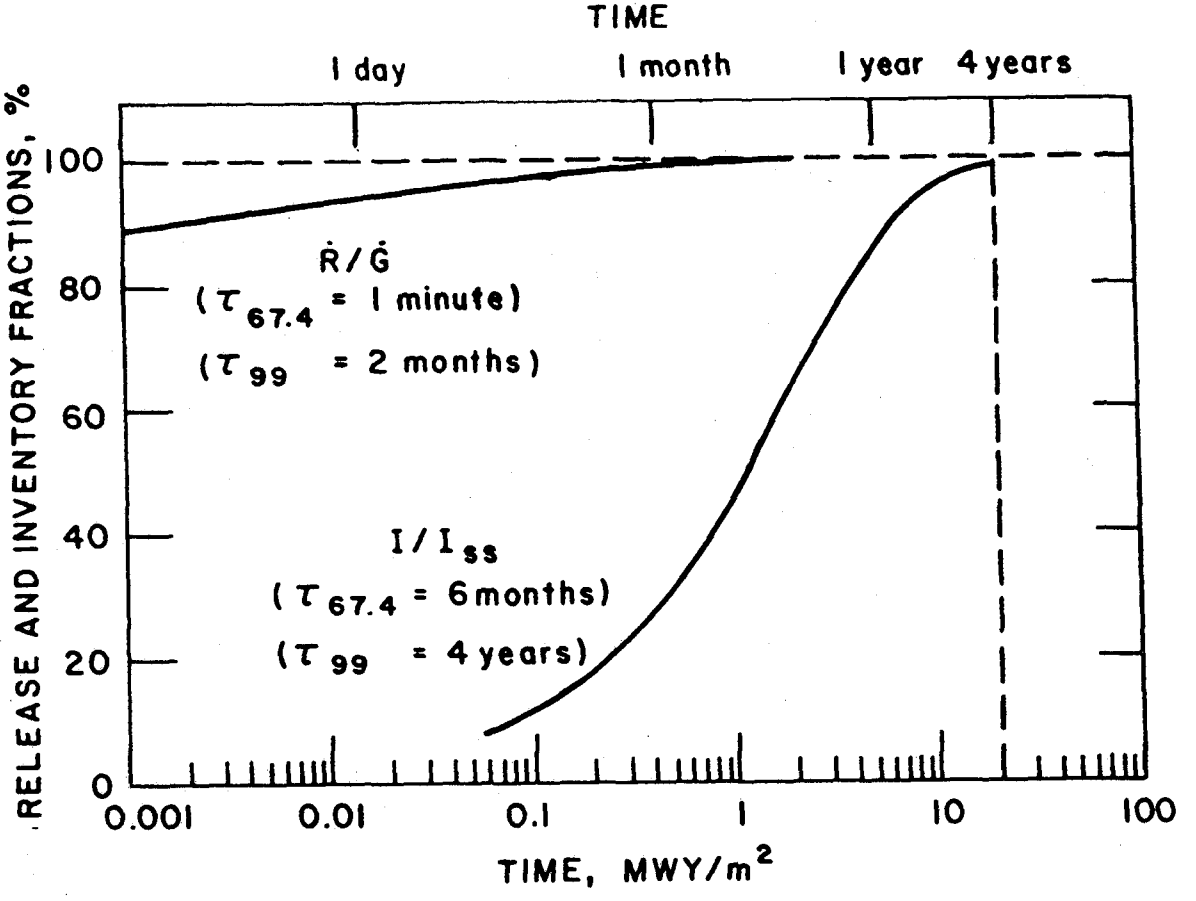

Figure 5.2.3-17. Tritium response to an idealized (i.e. instantaneous) reactor startup for the $LiAlO_2/H_2O/HT9/Be$ design with T_{min} = 350°C, T_{min} = 1000°C, and r_g = 0.1 μm.

proaches 99% of equilibrium at ~2 mo of blanket operation. The times to reach thermal equilibrium have been estimated at ~1 min for a unit cell near the first wall, ~8 min for an average unit cell, and ~45 min for a unit cell near the reflector at the back of the blanket. Therefore, the model assumption of instantaneous startup is reasonable for estimating the time to reach 99% of equilibrium tritium release rate.

The inventory is much more sluggish than the release rate. It takes ~6 mo for the inventory to build up to 67.4% of its equilibrium value and ~4 y to each 99% of equilibrium. The reason for this is that most of the inventory is building up in the lower temperature $LiAlO_2$ grains near the coolant tube wall. The response time for these cooler grains is quite slow.

The sensitivity of the time constants to reach 67.4% and 99% of equilibrium release rate to the minimum operating temperature is shown in Table 5.2.3-2 for a constant maximum temperature of 1000°C. Clearly, the time to reach 67.4% of equilibrium is relatively insensitive to T_{min}, whereas the time to reach 99% of equilibrium is highly sensitive to T_{min}.

Table 5.2.3-2. Time to Reach 67.4% and 99% of the Equilibrium Release Rate as a Function of Minimum Blanket Temperature for a Water-Cooled $LiAlO_2$ Blanket with a Maximum Temperature of 1000°C

T_{min}	$\tau_{67.4}$ (s)			τ_{99} (s)		
(°C)	Min.	Nom.	Max.	Min.	Nom.	Max.
600	15.5	29.2	55.4	4.50×10^3	5.22×10^3	6.05×10^3
550	17.9	33.7	62.8	1.43×10^4	1.45×10^4	1.50×10^4
500	21.2	38.9	71.3	4.16×10^4	4.67×10^4	5.27×10^4
450	24.6	44.6	81.0	1.35×10^5	1.77×10^5	2.35×10^5
400	29.0	51.5	91.8	5.22×10^5	8.53×10^5	1.34×10^6
375	31.7	55.4	97.8	1.11×10^6	1.98×10^6	3.41×10^6
350	34.8	59.4	104	2.57×10^6	4.87×10^6	9.67×10^6
325	37.8	64.4	112	6.16×10^6	1.33×10^7	2.74×10^7
300	41.0	69.5	119	1.53×10^7	3.71×10^7	9.30×10^7

Similar studies can be done for the plate design in Fig. 5.2.3-1. However, the equations are more complicated because of the variation of generation rate and temperature with position within the plate. Using an approach analogous to that used in deriving the steady-state Eq. (5.2.3-9), the response to an instantaneous startup can be formally written as

$$\dot{R}/\dot{G} = 1 - \sum_{i=1}^{N} (h_i/N)(6/\pi^2) \sum_{n=1}^{\infty} (1/n^2) \times \int_0^1 \exp(-n^2\pi^2 t/\tau_i)\, d\xi \qquad (5.2.3\text{-}49a)$$

and

$$I/I_{SS} = 1 - \sum_{i=1}^{N} (h_i/N)(90/\pi^4) \sum_{n=1}^{\infty} (1/n^4) \times \frac{\int_0^1 \tau_i \exp(-n^2\pi^2 t/\tau_i)\, d\xi}{\int_0^1 \tau_i\, d\xi}, \qquad (5.2.3\text{-}49b)$$

where $\tau_i = \tau(T_i)$ and I_{SS} is given by Eq. (5.2.3-9).

Because of the complexity of the plate equations, an upper bound is calculated for the equilibrium times for tritium diffusion. By assuming that all of the breeder is at the minimum operating temperature, T_{min}, the time for the release rate fraction to reach 99% of equilibrium is bounded by

$$(\tau_{99})_{\dot{R}} < 0.42(r_g^2/D_o) \exp(Q/RT_{min}) \qquad (5.2.3\text{-}50a)$$

and the time for the inventory fraction to reach 99% of steady-state is bounded by

$$(\tau_{99})_I < 0.46(r_g^2/D_o) \exp(Q/RT_{min}) . \qquad (5.2.3\text{-}50b)$$

For the $LiAlO_2$ plate design, r_g = 0.1 μm, $D_o = 1.1 \times 10^{-6}$ cm^2/s, Q = 35.8 kcal/mol, and T_{min} = 793 K (520°C) which result in $(\tau_{99})_{\dot{R}} < 3.3$ days and $(\tau_{99})_I < 3.6$ days. For the Li_2O plate design, r_g = 10 μm, $D_o = 2.66 \times 10^{-3}$

cm^2/s, Q = 19.72 kcal/mol, and T_{min} = 783 K (510°C) which result in $(\tau_{99})_R$ < 51 s and $(\tau_{99})_I$ < 56 s. Therefore, the tritium response time for the Li_2O plate design is of the same order of magnitude as the thermal response time.

The preceding analyses for the $LiAlO_2$ designs are significant in that bulk diffusion has been identified as the rate-limiting phenomenon in tritium transport for the case of isotopic swamping of the purge with protium. However, for Li_2O designs, the calculated tritium diffusive inventory is low and the response time for this component is relatively fast (on the order of the thermal response time). Thus, it is important in the case of Li_2O to examine other mechanisms whose time cosntants may determine the overall transient transport of tritium in the Li_2O design.

Solubility

Depending on the partial pressure of T_2O (or HTO) in the purge and interconnected porosity, a certain amount of tritium will be retained in the Li_2O as LiOT. For a range of temperatures and partial pressures, LiOT will precipitate out as a separate phase. Describing the transient response of such a process is complicated by the uncertainty in the diffusing species of tritium. One possible sequence of reactions is:

$$n + Li_2O \rightarrow LiOT + He \qquad (5.2.3\text{-}51a)$$

and

$$2LiOT \underset{\leftarrow}{\overset{\rightarrow}{}} Li_2O + T_2O \ . \qquad (5.2.3\text{-}51b)$$

These reactions are probable for relatively high concentrations of LiO, T, and LiOT. However, in fusion applications, concentrations of retained tritium are often <10 wppm. Such chemical reactions for the dilute system will depend on the diffusion rates of the species involved (see Fig. 5.2.3-5).

For the case of relatively pure Li_2O and helium purge, it is assumed that tritium and oxygen must diffuse to the grain boundaries and the pore/solid surfaces before T_2O is formed. As the tritium and oxygen on these surfaces achieve an equilibrium concentration, T_2O is desorbing from the sur-

face and percolating through the interconnected porosity to the purge. The establishment of an equilibrium concentration of tritium in the Li_2O then depends on the bulk diffusion, surface desorption, percolation, and convection time constants.

The time constant associated with percolation based on T_2O diffusion through the helium gas is on the order of

$$t_p \sim L_p^2/D_e \ , \qquad (5.2.3\text{-}52)$$

where L_p is the effective diffusion path length and D_e is the effective diffusion coefficient for T_2O in helium. For the case of the cylindrical geometry in Fig. 5.2.3-1 with the purge stream located near the coolant tube, L_p has values of 0.35 cm, 0.77 cm, and 1.62 cm, respectively, at the front, "middle", and back of the blanket. The effective diffusion coefficient depends on the microstructure of the blanket. For the sphere-pac design with 100% dense particles of 1200 μm, 300 μm, and 40 μm, the average pore size is large enough to justify the use of ordinary diffusion theory. Therefore, from Eq. (5.2.3-28),

$$D_e \geq (\varepsilon/2)(3.5 \times 10^{-6} \text{ cm}^2/\text{s}\cdot\text{atm})(T^{2.334}/p) \ . \qquad (5.2.3\text{-}53)$$

For $\varepsilon = 0.15$, $T = \bar{T} = 1100$ K, and $p = 1$ atm, $t_p < 1$ s. Therefore, for the purposes of this study, diffusion through interconnected porosity can be considered to be instantaneous for the cylindrical unit cell in Fig. 5.2.3-1. Similarly, the convective time for the purge gas is on the order of

$$t_c \sim L_c/U < 6 \text{ s} \ , \qquad (5.2.3\text{-}54)$$

where L_c (~6 m) is the length of the purge flow channel and U (~1 m/s) is the velocity of the purge gas.

Comparable percolation and convection calculations for the Li_2O plate design give small-time constants relative to tritium diffusion in the solid and relative to the thermal time constant for the system. Therefore, the time to reach a steady-state solubility inventory appears to depend primarily on the diffusion and surface desorption time constants.

Surface Adsorption

The problem of performing transient surface adsorption/desorption calculations is similar to that of performing solubility calculations. The relatively low surface concentrations and high pore/solid surface areas complicate the issue. It is assumed in this discussion that tritium and oxygen arrive at the pore/solid surface in elemental form. In order to desorb from the surface a molecular species of tritium (e.g., T_2, HT, T_2O, or HTO) must first form. An estimate is made here of the time it would take to cover these surfaces with enough tritium amd oxygen to make the formation of T_2O probable.

The specific surface area of commercially available Li_2O powder is ~0.2 m^2/g. Through fabrication into pellets or plates the resulting pore/solid surface area will be less. Assuming that it is ~0.02 m^2/g, then the time it takes to generate enough tritium and oxygen to saturate the surface can be calculated. Assuming a molecular diameter of ~1 Å and two-thirds of the surface area covered by tritium gives a time of 30 h to achieve this coverage at a generation rate of 1.85×10^{-11} $g(T)/g(Li_2O)s$. This number is clearly an upperbound in that T_2O will begin forming long before complete area coverage is achieved. There is also some question as to how long it would take the oxygen to diffuse to the surface under these conditions.

The above calculations are high idealized and approximate. More modeling and experimental work is clearly needed in this area. However, the issue can be skirted in the present designs because of the addition of hydrogen to the purge gas. The 100-wppm hydrogen flowing through the system at ~1 m/s is sufficient to enable the tritium to desorb from the surfaces in the form of HT. The time it takes the hydrogen to diffuse through the helium in the porosity and the HT to diffuse out to the purge stream is on the order of 1 s.

Other Effects

Time-dependent phenomena not included in the previous discussions relate to burnup and fast fluence effects. Irradiation damage to the ceramic (particularly at low temperatures) could cause a slow degradation of the diffusion coefficient with time. Thermal and irradiation-induced sintering and grain growth (particularly for Li_2O) will affect the percolation and diffusion

calculations. Finally, the helium-induced swelling in Li_2O could directly affect the tritium inventory by acting as a trap for tritium or indirectly affect tritium recovery by sealing off the purge flow channels. Each of these phenomena has a characteristic time which is longer than those previously calculated for Li_2O.

References for Section 5.2.3

1. K. Okula and D. K. Sze, "Tritium Recovery from Solid Breeders: Implications of Existing Data," University of Wisconsin, UWFDM-351 (1980).

2. J. A. Shearer, S. W. Tam, and C. E. Johnson, "Tritium Diffusion in Lithium Oxide Solid-Breeder Materials," J. Nucl. Mater. (in process). Abstract published in Trans. Am. Nucl. Soc. 44, 139 (1983).

3. D. Guggi et al., "Diffusion of Tritium in Single Crystal Li_2O," J. Nucl. Mater. 118, 100 (1983).

4. T. S. Elleman, L. R. Zumwalt, and K. Verghese, "Hydrogen Transport in Non-metallic Solids," Proc. 3rd. Top. Mtg. Technology of Controlled Nuclear Fusion, Sante Fe, NM, May 9-11, 1978, p. 763.

5. J. D. Fowler et al., "Tritium Diffusion in Al_2O_3 and BeO," J. Am. Ceramics Soc. 60, 155 (1977).

6. R. Wiswall and E. Wirsing," The Removal of Tritium from Fusion Reactor Blankets," Brookhaven National Laboratory, BNL-S0748 (1977).

7. R. Wiswall, E. Wirsing, and K. C. Hong, "The Removal of Bred Tritium from Solid Lithium Compounds in Fusion Reactor Systems," Proc. 14th IECEC Mtg., Boston, MA, August 5-10, 1979.

8. W. Yunker, "Continuous Extraction of Tritium from Irradiated Lithium Aluminate," Hanford Engineering Development Laboratory, TC-1745 (1980).

9. D. Guggi et al., "Tritium Release from $LiAlO_2$, Its Thermal Decomposition and Phase Relationship," Proc. Radiation Effects and Tritium Technology for Fusion Reactors, CONF-750989, Oak Ridge National Laboratory (1976), pp. III-416 to III-432.

10. D. Guggi, H. R. Ihle, and V. Kurz, "Tritium Release from Neutron Irradiated Lithium-Aluminum Oxides," Proc. 9th Symp. Fusion Technology, Garmisch-Partinkirchen (FRG), June 14-18, 1981, pp. 337-344.

11. V. G. Vasiliev et al., "Investigation of the Physical-Chemical Properties of Irradiated Inorganic Compounds of Lithium Oxides, Aluminate, and Silicates," US/USSR Workshop on Engineering and Economic Problems of ETF, Moscow and Leningrad (USSR), September 10-21, 1979.

12. M. A. Abdou et al., "Blanket Comparison and Selection Study," Argonne National Laboratory, ANL/FPP/83-1 (1983), pp. VIII-1 to VIII-21.

13. H. R. Ihle and C. H. Wu, "The Solubility of Deuterium in Solid Li_2O," J. Nucl. Mater. 123, 901 (1984).

14. T. Kurasawa and V. A. Maroni, "Infrared Spectroscopic Analysis of OH^- and OD^- in Crystalline Li_2O as a Function of Chemical Treatment,' J. Nucl. Mater. 119, 95 (1983).

15. D. L. Smith et al., "Analysis of In-Situ Tritium Recovery from Solid Fusion-Reactor Blankets," Proc. 4th Top. Mtg. Technology of Controlled Nuclear Fusion, King of Prussia, PA, CONF-801011 (1980).

16. M. A. Abdou et al., "A Demonstration Tokamak Power Plant Sutdy," Argonne National Laboratory, ANL/FPP-82-1 (1982), pp. 6-83 to 6-95.

17. N. Wakao, S. Otani, and J. M. Smith, "Diffusion and Flow in Porous Catalysts," AiChE J. 11, 439 (1964).

18. R. B. Bird, W. E. Steward, and E. N. Lightfoot, Transport Phenomena (J. Wiley & Sons, Inc., NY, 1960), p. 505.

19. O. W. Richardson, "Phil. Mag., Ser. VI.7, 166 (1904)

20. A. Hassenein and D. K. Sze, "Blanket Comparison and Selection Study," ANL/FPP Report (in process) (1984).

21. H. S. Carlslaw and J. C. Jaeger, Conduction of Heat in Solids (Oxford University Press, NY, 1978).

5.2.4 Structural Mechanics

Structural performance poses demanding requirements on the blanket design since failure is likely to have major consequences on operation and safety. The design process generally begins with consideration of basic elastic behavior under thermal and pressure loads, including complex geometries as necessary. Difficulties in analysis appear when other factors must be added.

Table 5.2.4-1 lists many important issues with respect to structural behavior. Welds and discontinuities are weak points because material property changes and stress concentrations due to the basic thermal and pressure stresses may exist. High temperatures and high stresses activate plastic behavior and creep, and require time-dependent calculations to track the evolution of the basic stresses. Although creep tends to relax thermal stresses, it can cause large displacements. Creep buckling and ratchetting are possible. Neutron irradiation can provide time-dependent properties (e.g., embrittlement), enhanced creep, and additional strains from swelling. Fatigue and crack growth limit the component lifetime under cycling conditions from startup, shutdown and pulsed operation. Corrosion and erosion enhance these factors (initiates cracks, weakens welds, remove material).

A complete blanket design must consider all these factors. Those that are not subject to analysis must be accounted for with design conservatism and testing. In this section, important structural phenomena are identified and basic models developed for later analysis of test requirements. The primary emphasis is on elastic behavior with thermal and pressure stresses since this sets the basic stress field that is then adjusted by these other factors.

5.2.4.1 First Wall Structural Behavior

The first wall must support dynamic and static mechanical loads, and at the same time sustain the thermal gradients and erosion resulting from the plasma heat and particle fluxes. Dynamic and static loads require high flexural rigidity. Since the first wall temperature rise is proportional to its thickness, thermal stresses require a thin first wall. Reasonable lifetime against erosion and corrosion requires a thick wall. Thus, a feasible design must satisfy many conflicting needs.

The first wall structures of the reference solid breeder blankets (Fig.

Table 5.2.4-1 Important Issues for Structural Behavior

First Wall

- Thermal and pressure stresses along coolant channel
- Swelling and irradiation creep, including differential effects
- Effects of residual stresses at shutdown
- Pulsing effects
- Crack growth, including grooved first walls
- Stress concentrations at joints and discontinuities
- Weld and joint behavior
- Interaction of first wall structure with module back supports
- Interaction of first wall structure with module end supports
- Fluence effects on structural properties
- Module-module interactions
- Plastic behavior, including ratchetting, deformation and buckling
- Effects of transient magnetic forces
- Effects of steady magnetic forces in ferritic steels
- Stress variation due to wall erosion and plasma-related property changes
- Effects of hydrogen embrittlement

Breeder Region

- Breeder thermal stresses
- Breeder/clad thermal stresses and interaction
- Clad and breeder creep and swelling, accommodation and interaction
- Effect of property changes with fluence and time-at-temperature
- Formation and effects of cracks on breeder behavior
- Stress concentrations
- Reliability of coolant tubes and effects of leaks
- Environmentally-assisted cracking
- Breeder relocation and lock-up
- Ballooning or plastic deformation of clad
- Mechanical fatigue and wear from flow-induced vibrations
- Effects of end-plates and supports on stresses in breeder region
- Pulsing effects

5.2.4-1) have an array of rectangular channels in a lobed or semi-cylindrical first wall. Coolant flow is azimuthally around the lobe perimeter. The first wall structure can be viewed as an assembly of curved I-beams. Assuming symmetry and ignoring axial end effects, the structural behavior can be analyzed based on a single curved I-beam.

Modelling

To address some of these issues and gain insight into scaling, a displacement-type finite element model based on Euler-Bernoulli beam theory was developed. The first wall structure is modeled as an assembly of curved I-beams, where each beam is discretized into linear 2-D frame elements. Forces and displacements along the elements are defined, and related to the total potential energy. By minimizing this total energy, a relationship between the forces and the displacements may be obtained of the form

$$\underline{\underline{K}}\ \underline{u} = \underline{F} \qquad (5.2.4\text{-}1)$$

where $\underline{\underline{K}}$ is the stiffness matrix, $\underline{u}$ is the displacement vector, and $\underline{F}$ is the applied force vector. Given the forces, this can be solved for the displacements. The primary assumptions are:

- homogenous isotropic, linearly elastic material;
- linear thermal expansion;
- material properties do not change in space or time;
- cross-sectional dimensions are small compared to the radius of curvature.

The model produces axial stresses due to bending and extension effects. Stress components acting within the plane of the cross-section are not determined due to the one-dimensional nature of the theory applied.

Stiffness Relation for a 2-D Frame Element Consider a 2-D frame element as given in Fig. 5.2.4-2. Its behavior for small displacements is a superposition of that of a bar and a beam. Let $u(x)$, $v(x)$ and $\beta(x)$ denote axial and transversal displacements and rotation along the element. In a displacement-type finite element description, each element is connected to adjacent elements through a set of displacements at each connecting node. The displacement field between the ends of an element are estimated by some interpolation scheme. This interpolated displacement field must:

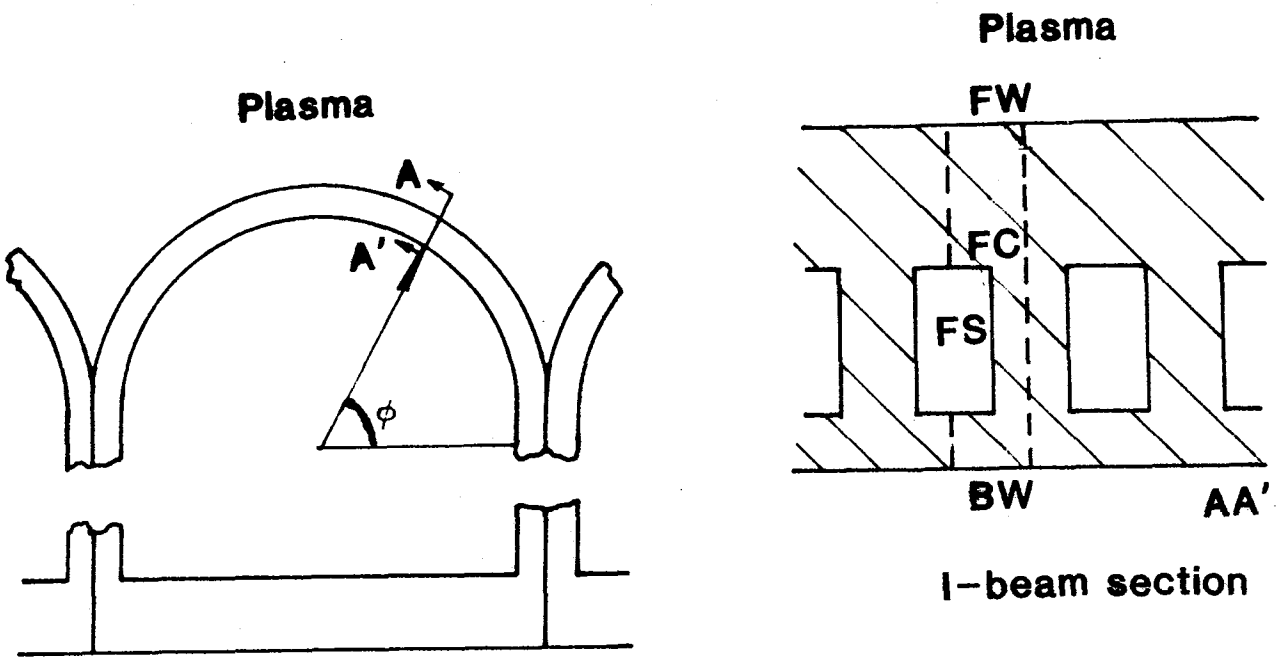

Figure 5.2.4-1 Lobe first wall showing representative I-beam section.

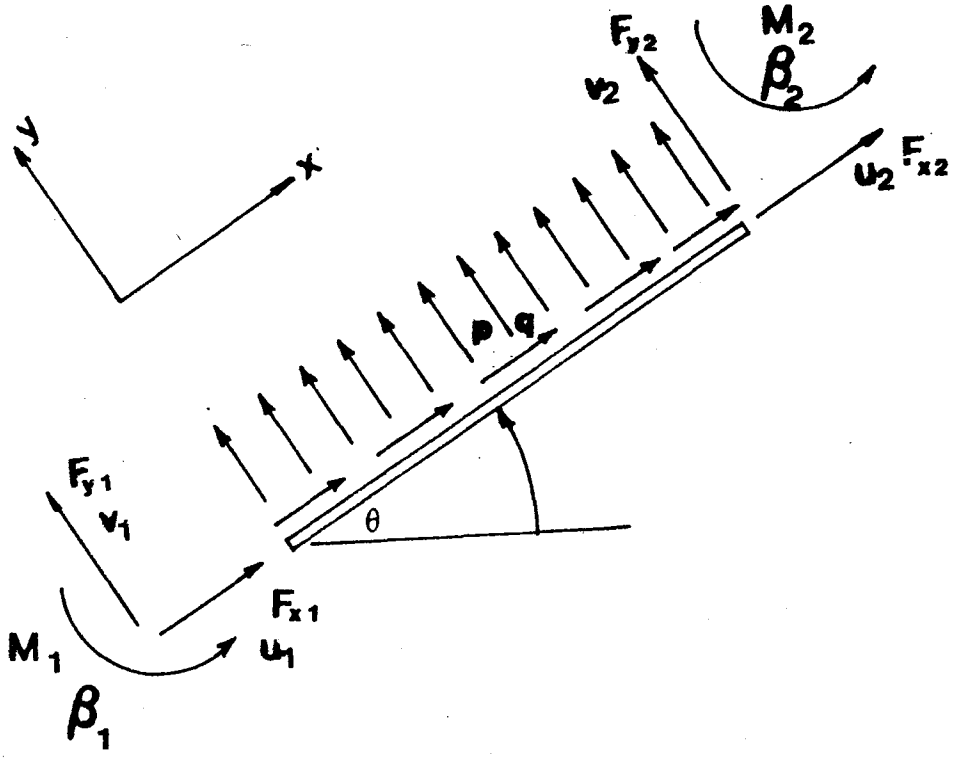

Figure 5.2.4-2 Local coordinate system and forces for analyzing the mechanical behavior of a 2-D frame element.

- describe the rigid body motions of a particular element;
- have sufficient freedom to allow kinematic continuity between elements;
- produce a displacement pattern corresponding to the constant strain state of the elements.

The last requirement is necessary in order to be able to converge to the true strain state upon refining the partition of a body in a general strain state.

Consider a linear interpolation for u(x) and a cubic interpolation for v(x). The rigid body motion of a bar is a translation which is clearly included in a linear displacement field. Since the nodal degrees of freedom are u_1 and u_2 in the axial direction, interelement continuity is granted. For a bar, the extensional strain is equal to the first derivative of the axial displacement field. Consequently, a linear interpolation function permits a constant strain state. The rigid body motions of a beam are uniform transversal translation and a rotation, both of which are included in a cubic interpolation field. Four nodal degrees of freedom, v_1 and v_2 in the transverse direction and β_1 and β_2 in the rotational direction, are necessary because classical beam theory requires displacement and slope to be continuous between the elements. This makes it necessary to choose at least a cubic interpolation function. The constant strain mode for thin beams is a constant curvature which requires at least a quadratic displacement field. Thus, the displacements and rotations are given in terms of the nodal values by:

$$u(x) = [1-\xi \quad \xi] \begin{bmatrix} u_1 \\ u_2 \end{bmatrix} \tag{5.2.4-2a}$$

$$v(x) = [1-3\xi^2+2\xi^3 \quad L(\xi-2\xi^2+\xi^3) \quad 3\xi^2-2\xi^3 \quad L(-\xi^2+\xi^3)] \begin{bmatrix} v_1 \\ \beta_1 \\ v_2 \\ \beta_2 \end{bmatrix} \tag{5.2.4-2b}$$

where $\xi = x/L$ and L is the length of the element.

The axial strain is expressed in terms of the displacement field from Euler-Bernoulli beam theory[1] as:

$$\varepsilon_{xx} = \frac{\partial u}{\partial x} - y \frac{\partial^2 u}{\partial x^2} \tag{5.2.4-3}$$

The axial stress is given by linear stress-strain relations:

$$\sigma_{xx} = E(\varepsilon_{xx} - \alpha\Delta T) \qquad (5.2.4\text{-}4)$$

and the strain energy is:

$$Q_{strain} = \frac{1}{2}(\varepsilon_{xx} - \alpha\Delta T)\,\sigma_{xx} = \frac{E}{2}(\varepsilon_{xx} - \alpha\Delta T)^2 \qquad (5.2.4\text{-}5)$$

The total potential energy of the element $Q_{total} = Q_{strain} + Q_{external}$ also includes the potential energy of the external forces:

$$Q_{external} = -F_{x1}u_1 - F_{x2}u_2 - \int_0^L p(x)\,v(x)\,dx - F_{y1}v_1 - F_{y2}v_2$$
$$- M_1\beta_1 - M_2\beta_2 - \int_0^L q(x)\,u(x)\,dx \qquad (5.2.4\text{-}6)$$

Applying the theorem of minimum potential energy[2], $\delta Q_{total} = 0$, leads to the complete stiffness relation for a single element:

$$\begin{bmatrix} F_{x1} \\ F_{y1} \\ M_1 \\ F_{x2} \\ F_{y2} \\ M_2 \end{bmatrix} = \underline{\underline{K}} \begin{bmatrix} u_1 \\ v_1 \\ \beta_1 \\ u_2 \\ v_2 \\ \beta_2 \end{bmatrix} - \begin{bmatrix} qL/2 \\ pL/2 \\ pL^2/12 \\ -qL/2 \\ pL/2 \\ -pL^2/12 \end{bmatrix} - \begin{bmatrix} -F_{th} \\ 0 \\ M_{th} \\ -F_{th} \\ 0 \\ -M_{th} \end{bmatrix} \qquad (5.2.4\text{-}7)$$

where

$$\underline{\underline{K}} = \frac{E}{L} \begin{bmatrix} A & 0 & 0 & -A & 0 & 0 \\ & 12/L^2 & 6I/L & 0 & -12I/L^2 & 6I/L \\ & & 4I & 0 & -6I/L & 2I \\ & & & A & 0 & 0 \\ & & \text{symmetric} & & 12I/L^2 & -6I/L \\ & & & & & 4I \end{bmatrix}$$

$$F_{th} = \int_A \alpha\,\overline{\Delta T}(y,z)\,dA \qquad M_{th} = \int_A y\,\alpha\,\overline{\Delta T}(y,z)\,dA$$

where A denotes the area of the cross section and I is the moment of inertia. The temperature field T(x,y,z) has been replaced by

$$\overline{T}(y,z) = \frac{1}{L}\int_0^L T(x,y,z)dx \qquad (5.2.4\text{-}8)$$

which does not affect convergence if one uses fine enough elements to capture the change of the thermal field in the x direction. It can be observed that thermal effects appear as a consistent load vector. It can also be shown that the stiffness matrix, $\underline{\underline{K}}$, exhibits all the necessary rigid body motions and constant strain modes as can be anticipated from the order of interpolations used to describe the displacement field.

For practical applications it is convenient to express all the nodal displacements and forces in terms of global coordinates. This involves changing the displacements, forces and stiffness matrix for each element over to the global coordiate system through standard transformation matrices.

Solution procedure The solution begins with defining a discretization of the given structure. Then assume the elements to be interconnected at nodal points and establish a system stiffness relation. It will take a form similar to that of an element stiffness relation, $\underline{\underline{K}}\,\underline{u} = \underline{F}$, where $\underline{\underline{K}}$ is a banded matrix. The bandwidth is determined by the numbering of the nodes.

Boundary conditions are included as modifications to the global stiffness relation. For example:

(a) Built-in or fixed conditions: $u = 0$, $v = 0$, $\beta = 0$;

(b) Symmetry conditions: $v = 0$, $\beta = 0$;

(c) Simple support or pinned conditions: $u = 0$, $v = 0$.

The i^{th} degree of freedom is deleted by zeroing out the i^{th} row and i^{th} column of $\underline{\underline{K}}$ and setting $K_{ii} = 1$. This guarantees that, upon solving the equation, the i^{th} displacement component will be zero.

Finally, the global stiffness relation may be solved based on the applied forces and boundary conditions to yield the nodal displacements. These displacements may be used through the element stiffness relations to solve for nodal forces, and these nodal forces in turn used to recover the stresses within the elements.[3]

Analysis

This modeling process was applied to the first wall analysis. Taking advantage of symmetry, one half of the lobed first wall structure was considered. The corresponding boundary conditions are shown in Fig. 5.2.4-3a. To discretize the structure, it was divided into five elements. Calculations to check accuracy using ten elements were also performed. The results were so close that five elements were used afterwards. Integrals appearing in the expressions for the thermal forces and moments were calculated by Simpson's rule using 12 partitions of the cross-sections.

Figure 5.2.4-3a shows the pure pressure stresses for the Li_2O/He/HT-9 reference tokamak design. It can be observed that the stress distribution is fairly uniform and the second wall is in a slight compression as a result of the built-in end. In Fig. 5.2.4-3b, the pure thermal stresses can be seen for the same design. At $\theta = 90^0$, one can see a stress distribution similar to that of a straight beam with built-in ends. This is plausible since the geometry locally is similar. At $\theta = 0^0$, the small thermal gradient across the wall and the built-in conditions produce local bending which result in a different stress distribution. Fig. 5.2.4-4a is a plot of the thermal and pressure stresses acting simultaneously, which corresponds to the superposition of the previous two figures. Note that the stress distribution is not axisymmetric, the curved structure, axial thermal variations and end constraints produce a complex stress pattern.

The combined beginning-of-life stresses lead to a peak tensile stress of about 300 MPa. Although within the estimated $3S_{mt}$[4] limits for primary plus secondary stresses in HT-9 at 550°C, the first wall temperature is over 650°C in some regions of high stress, and the stress locally exceeds the $3S_{mt}$ guidelines. Disruption loads will further aggravate this problem. The addition of grooves to the first wall will shift the peak stress location inward to colder and stronger material, but raises questions regarding stress concentrations and crack initiation. In this analysis, only the ungrooved first wall is considered.

Figure 5.2.4-4b shows a simulated end-of-life condition with thinner first wall assuming, for lack of data, uniform erosion. The major difference is an increase of the pressure stresses in the first wall coupled with the decrease of the thermal stresses, which resulted in a net elevation of the

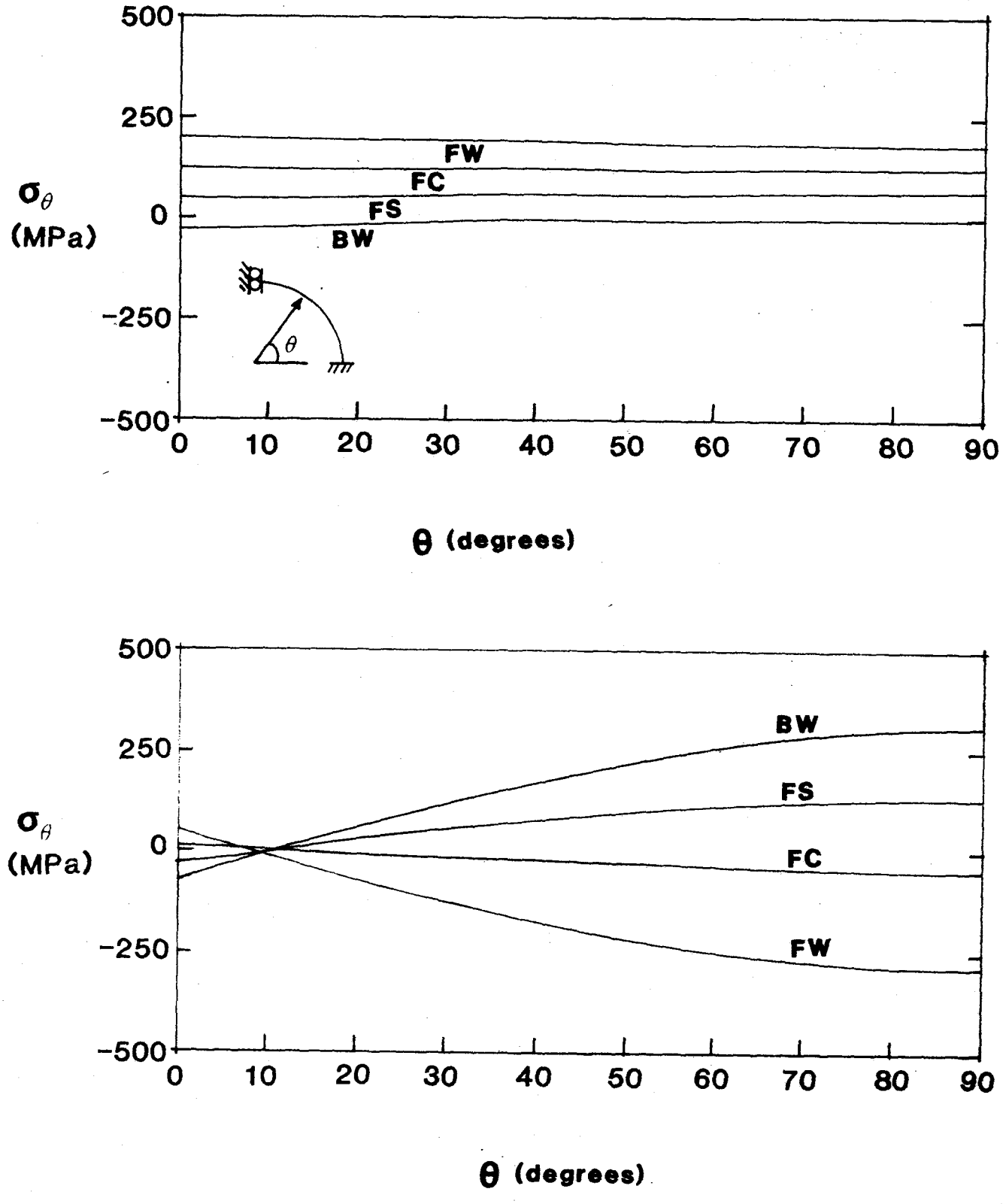

Figure 5.2.4-3 Pressure and thermal stress profiles in Li_2O/He/HT-9 tokamak first wall: (a) pressure stresses; and (b) thermal stresses. The stress profiles are given at the four points indicated on Figure 5.2.4-1, where FW is first wall plasma surface, FC is first wall coolant surface, FS is midway through the fin support, and BW is the back wall breeder side surface.

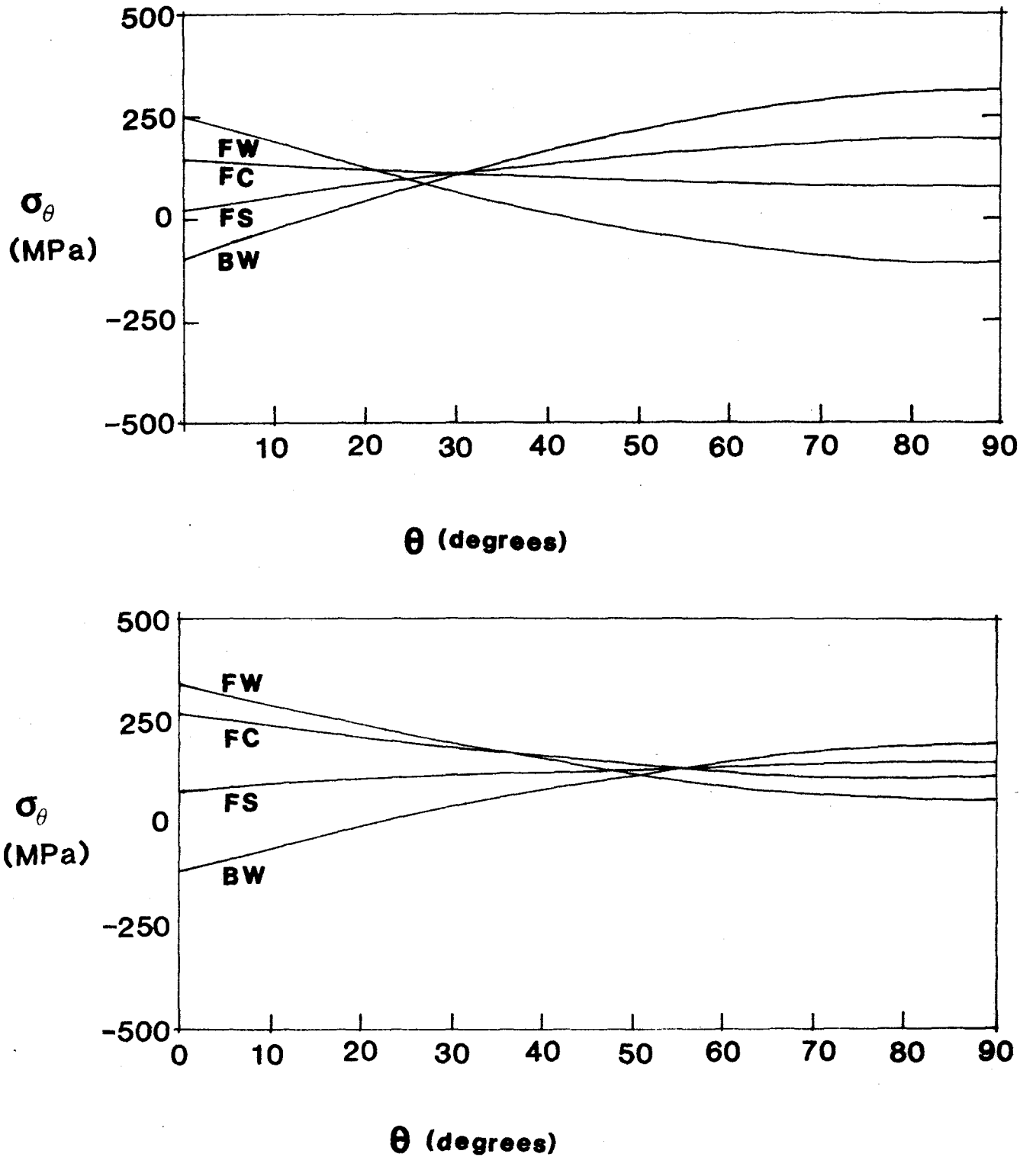

Figure 5.2.4-4 Pressure plus thermal stress profiles in Li_2O/He/HT-9 tokamak first wall: (a) beginning-of-life; and (b) at end-of-life thickness assuming uniform erosion.

first wall stresses.

These particular results were obtained with built-in or fixed boundary conditions at the inlet ($\theta=0^0$) based on contact with adjacent blanket modules at that point, and with no axial displacement or rotation at the module tip ($\theta=90^0$) based on the module symmetry. Other boundary conditions were also analyzed to model different mechanical arrangements. For example, the Li_2O/-He/HT-9 module has an opening in the back wall at the module tip in order for the first wall coolant to enter the breeder region. This reduced structural configuration was modelled by using a hinged boundary condition at the tip, and the calculated stress distribution is shown in Fig. 5.2.4-5a. Alternately, the blanket might be designed such that the modules just touch at power, allowing space for thermal expansion. This was modelled by allowing full motion in the transverse direction at $\theta=0^0$ as shown in Fig. 5.2.4-5b.

There are two factors contributing to a particular stress pattern. Constrained ends tend to decrease the pressure stresses due to their load carrying capacity. On the other hand, they increase the thermal stresses since thermal expansion is limited. For the hinged top case, one can see a drop in the stress level due to the released end constraint. For the freed edge, however, the stress level is higher than the hinged top case due to the increased pressure stresses.

Both these cases have substantially lower pressure and thermal stresses than the reference calculation, raising the question as to whether they are more appropriate boundary conditions or indicate design changes that would improve the mechanical behavior.

In fact, the built-in end conditions at the joints with the side walls are valid since there is no rotation or translation in the radial direction due to symmetry. Furthermore, while the modules may be designed to just come into contact at power in order to limit the force they exert on each other, this point cannot be considered completely free to expand because of the influence of the side walls and axial module supports which firmly anchor the first wall to the cold support structure of the blanket.

Secondly, the application of symmetry conditions in a continuous curved beam at the module tip may not be entirely realistic, depending upon the presence of the channel. However, simply removing the thin 0.3 mm back wall

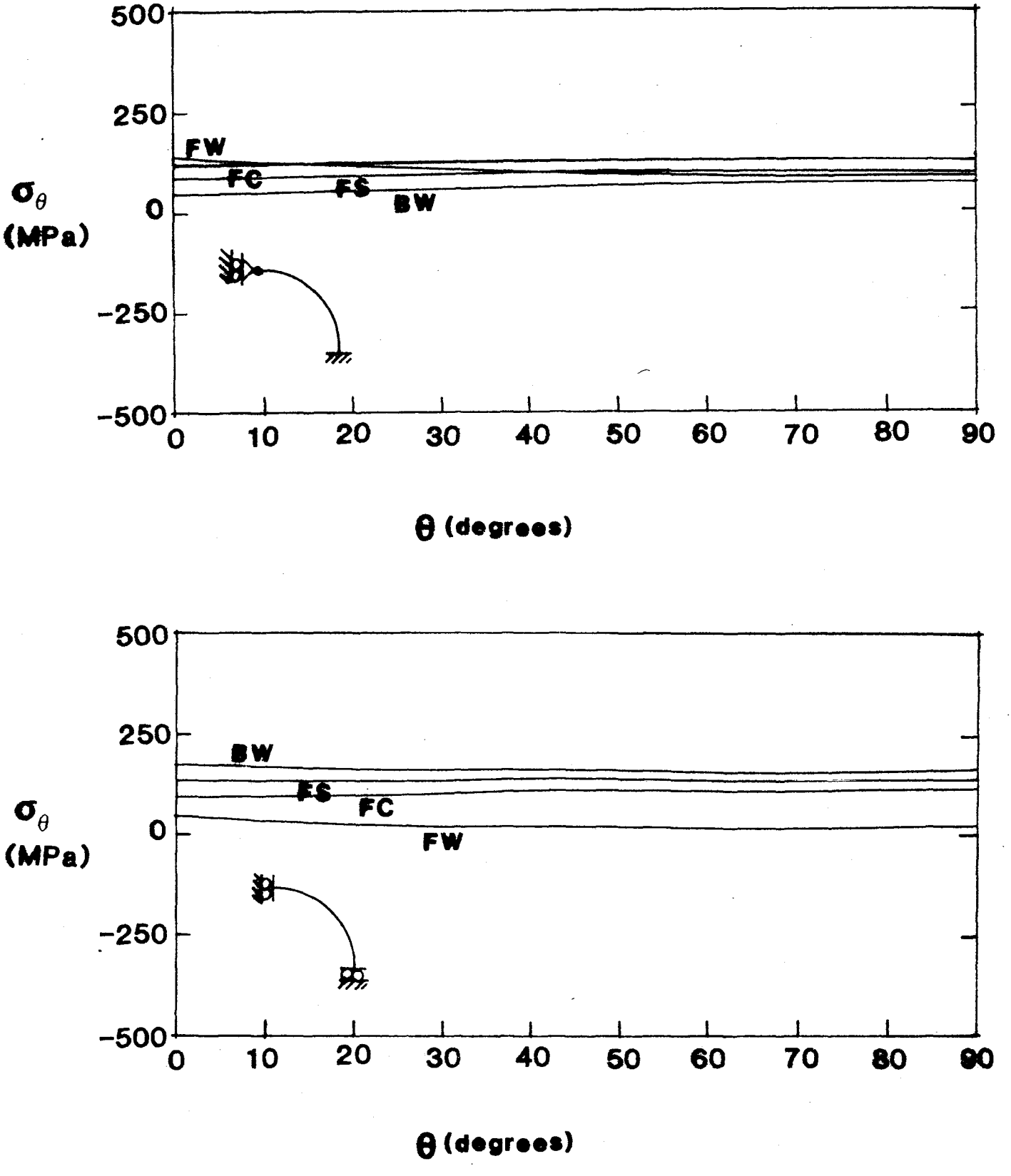

Figure 5.2.4-5 Pressure plus thermal stress profiles in Li_2O/He/HT-9 tokamak first wall: (a) hinged-fixed boundary conditions; and (b) symmetry-symmetry boundary conditions.

as needed to let the coolant flow through will not have much effect on the stresses as compared to the 3.5 mm first wall. For the effect to be as marked as shown in Fig. 5.2.4-5a, at least the supporting fins would also need to be removed. If such a design is used to alleviate the global stresses, it will result in stress concentrations at the tip itself. A detailed analysis would be necessary to quantify these stress concentrations at the tip where the present model would not be applicable.

Figure 5.2.4-6a is a stress plot for a possible mirror reactor first wall. It is substantially different from the previous pictures due to the different geometry (6 mm first wall plasma side surface) and temperature distribution. Figure 5.2.4-6b shows the stresses for the reference $LiAlO_2$/-H_2O/PCA/Be blanket. Basically it has the same features as the He-cooled blanket except for a slight asymmetry resulting from the thermal field.

Limitations

The primary limitation of this analysis is that it is strictly elastic. Elastic-plastic analysis is necessary since the stresses exceed the elastic limit. At high temperatures, an elastic/perfectly plastic constitutive law could be assumed. Furthermore, time-dependent plastic behavior due to thermal and irradiation creep should be included.

Swelling is also a significant phenomenon for an axially restrained structure, such as a curved member. The effect of misalignments and imperfect geometry was not considered here, but play important roles in structures prone to buckling. Finally, a large range of potential failure modes and contributors such as fatigue, crack growth, thermal ratchetting and radiation damage were not analyzed.

5.2.4.2 Breeder Region Structural Behavior

Effects that can influence the solid breeder mechanical behavior include thermal stresses, hydrostatic pressure loads from coolant and purge, radiation induced swelling and creep, and various mass redistribution phenomena such as sintering, grain growth or LiOT condensation (at least affecting local material properties). The consequences may be quite serious - breach of breeder containment, distortion of structure leading to coolant flow blockage, closing of purge gas channels, reduction of internal porosity, or changes in tempera-

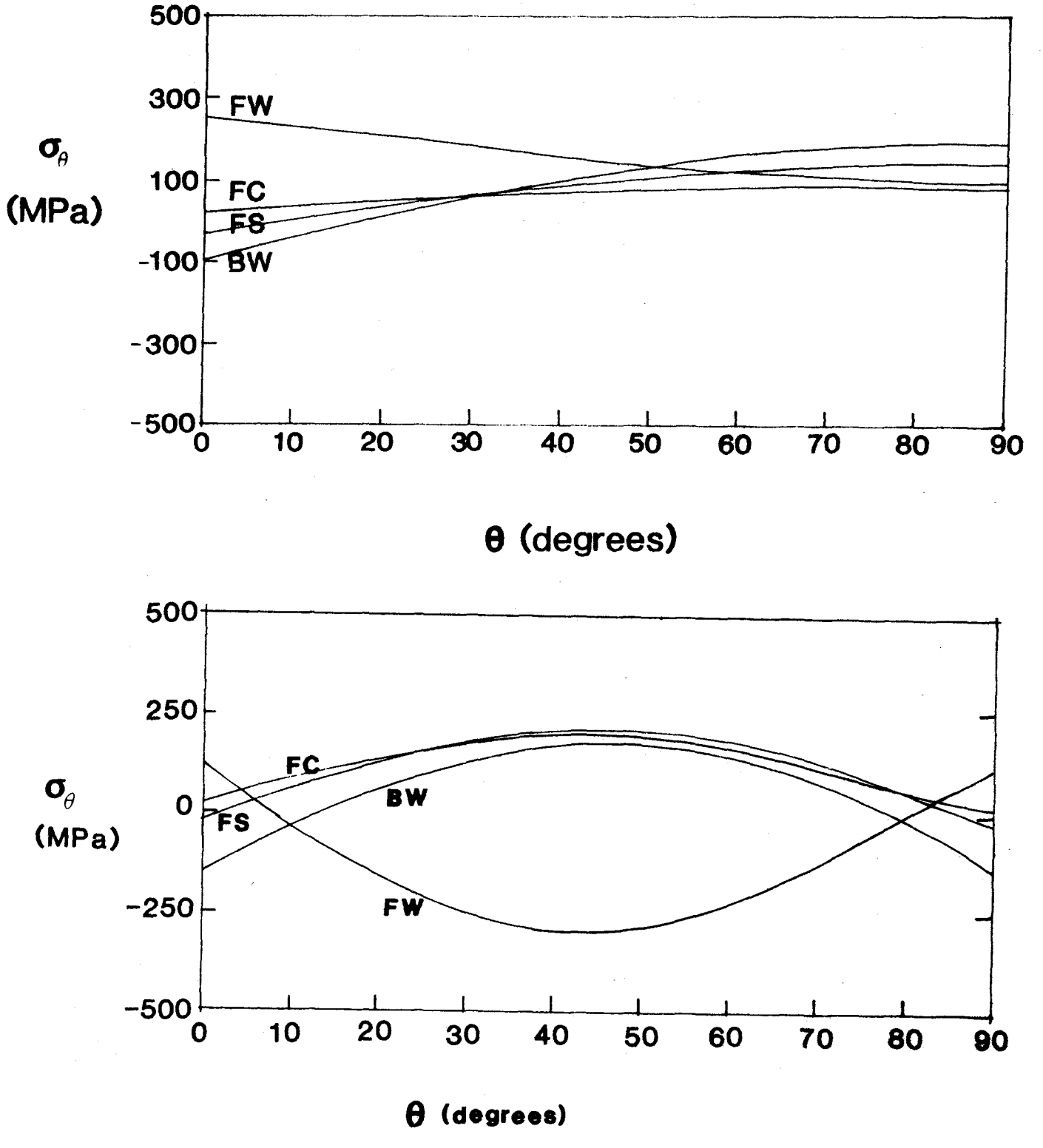

Figure 5.2.4-6 Pressure plus thermal stress profiles in: (a) Li_2O/He/HT-9 mirror first wall; and (b) $LiAlO_2$/H_2O/PCA/Be tokamak first wall.

ture that reduce tritium recovery.

First consider solid breeder behavior under the key driving influences of thermal expansion, swelling and creep, and neglecting any interaction with the clad or surrounding structure. The analysis will then be extended to a more detailed model, including thermal stress and the clad interaction, and lead to specific modifications that define the two reference solid breeder blankets.

The basic model assumes:

- slab geometry;
- linear elastic material behavior;
- plane stress behavior in the axial direction;
- no stress in the slab thickness direction;
- plate is constrained from bending;
- no applied loads;
- time and position independent properties.

For example, these apply to a thin, unconstrained slab of solid breeder with symmetric heating and radiation damage through the slab thickness.

The total strain ε_{tot} is the sum of contributions from thermal expansion, swelling, creep, and elastic strains,

$$\varepsilon_{tot} = \alpha(T-T_{ref}) + \varepsilon_{sw} + \varepsilon_{cr} + \frac{\sigma}{E} \qquad (5.2.4\text{-}9)$$

Averaging over the slab thickness,

$$\bar{\varepsilon}_{tot} = \alpha(\bar{T} - T_{ref}) + \bar{\varepsilon}_{sw} + \bar{\varepsilon}_{cr} \qquad (5.2.4\text{-}10)$$

where $\bar{\sigma} = 0$ since there are no applied loads. Furthermore, assuming ε_{tot} is independent of position, which is plausible for thin plates[5], then $\varepsilon_{tot} = \bar{\varepsilon}_{tot}$ and the local stress (directed parallel to the plate edges) is:

$$\sigma = E\,[\alpha(\bar{T} - T) + (\bar{\varepsilon}_{sw} - \varepsilon_{sw}) + (\bar{\varepsilon}_{cr} - \varepsilon_{cr})] \qquad (5.2.4\text{-}11)$$

Assume simple but standard models for swelling and steady-state creep:

$$\frac{d\varepsilon_{cr}}{dt} = A_{cr} e^{-Q/\kappa T}\, \sigma^{n} \qquad (5.2.4\text{-}12a)$$

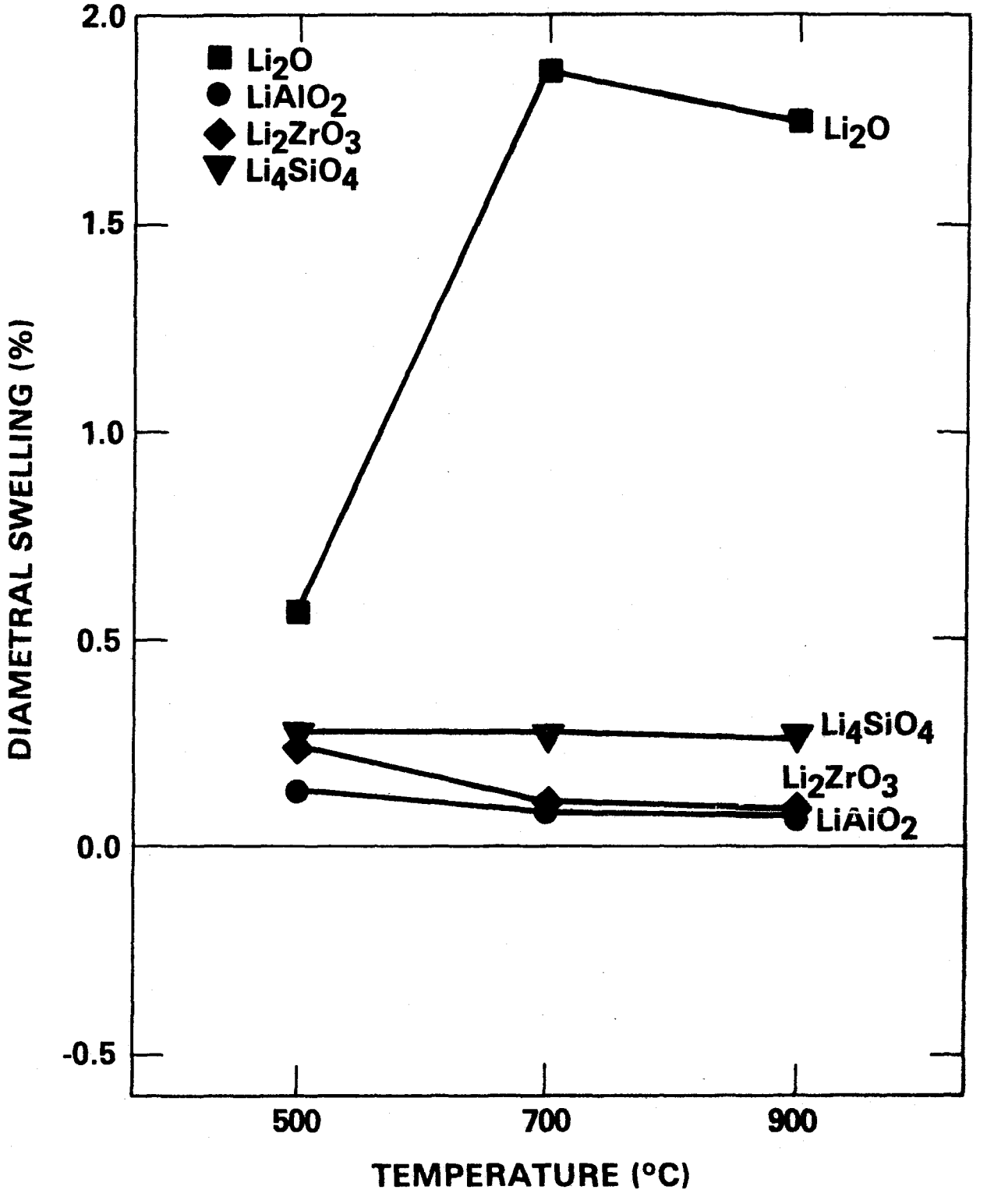

Figure 5.2.4-7 Swelling behaviour of some breeder ceramics after fast irradiation to 10^{27} captures/m^3.(6)

$$\frac{d\varepsilon_{sw}}{dt} = B_{sw} \qquad (5.2.4\text{-}12b)$$

where t is time; and A_{cr}, Q_{cr}, B_{sw} and n are property constants. Data on swelling in some solid breeders[6] is shown in Fig. 5.2.4-7. In general, the swelling strain rate is expected to be proportional to the He production rate (or local flux), with the exact rate dependent on temperature due to the subsequent movement of helium in the solid. There is apparently no published data on the creep behavior of Li_2O or $LiAlO_2$. Metals typically show creep also proportional to the flux, with $n \sim 1$ under irradiation and $n \sim 3$-4 for thermal creep.[7]

In the presence of radiation with $n \sim 1$, then $\bar{\varepsilon}_{cr} \sim 0$ and Eq. (5.2.4-11) becomes:

$$\frac{d\sigma}{dt} + EA_{cr}\sigma = E[\bar{B}_{sw} - B_{sw}(T)]; \qquad \sigma(0) = E\alpha(\bar{T} - T) \qquad (5.2.4\text{-}13)$$

leading to:

$$\sigma(t) \simeq E\alpha(\bar{T}-T)\, e^{-EA_{cr}t} + \frac{\bar{B}_{sw}-B_{sw}}{A_{cr}}\,[1-e^{-EA_{cr}t}] \qquad (5.2.4\text{-}14)$$

and during the dwell time, with $n \sim 3$ and $B_{sw} \sim 0$, then:

$$\sigma(t) \simeq \frac{\sigma_0}{[2EA_{cr}t + 1]^{0.5}} \qquad (5.2.4\text{-}15)$$

These can be used to obtain rough estimates of the contribution of the different effects to solid breeder behavior. Representative numbers are given in Table 5.2.4-2, where it can be seen that all effects are potentially significant. It is worth noting that part of the solid breeder design problem is in handling the initial thermal expansion.

To extend this analysis to 2-D, the finite element code SAP5[8] was employed. Specifically, a 2-D plate element from the Li_2O/He/HT-9 reference blanket was analyzed for thermal stresses at startup. Figure 5.2.4-8a shows the breeder dimensions and temperature field assumed, while Fig. 5.2.4-8b and -8c shows the corresponding thermal stresses through the unconstrained breeder. Except for end effects near the top, $\sigma_{th} = E\alpha(\bar{T}-T)$ correctly gives the

Table 5.2.4-2 Contributors to Solid Breeder Mechanical Behavior

	Li_2O[a]	γ-$LiAlO_2$[b]	UO_2[c]
Temperatures:			
$\bar{T}$ (K)	1100	1200	1300[d]
ΔT (K)	400	600	1500
T_{melt} (K)	1700	1900	3100
Properties:			
%Theoretical density	85	60	92
E (MPa)	5.5×10^4	-	1.5×10^5
α (1/K)	3.3×10^{-5}	1.2×10^{-5}	1.1×10^{-5}
$\sigma_{fracture}$ (MPa)	20	-	120
A_{cr} (1/MPa-yr)	-	-	0.001
B_{sw} (%/MW-yr/m^2)	0.7	< 0.1	-
Equivalent strains:[e]			
Thermal strain, ε_{th}	0.007	0.004	0.008
Swelling strain, ε_{sw}	0.03	< 0.005	-
Creep strain, ε_{cr}	-	-	0.1
Tensile fracture strength, σ_f/E	0.0004	-	0.0008
Coolant hydrostatic pressure, p/E	0.0001	-	0.00004

[a] Li_2O data from Reference (4) for fusion reactor conditions.

[b] $LiAlO_2$ data from References (4,9,10).

[c] UO_2 data, for comparison, from Reference (7) for LWR conditions.

[d] Typical average fuel pin temperature is much higher (~ 1800 K). However, UO_2 is very soft over 1700 K so values given here apply to the cold outer region.

[e] One year at 5 MW/m^2 for breeder, at 10^{19} fissions/m^3-s for UO_2; 100 MPa stress for creep strain estimate; 5 MPa coolant pressure.

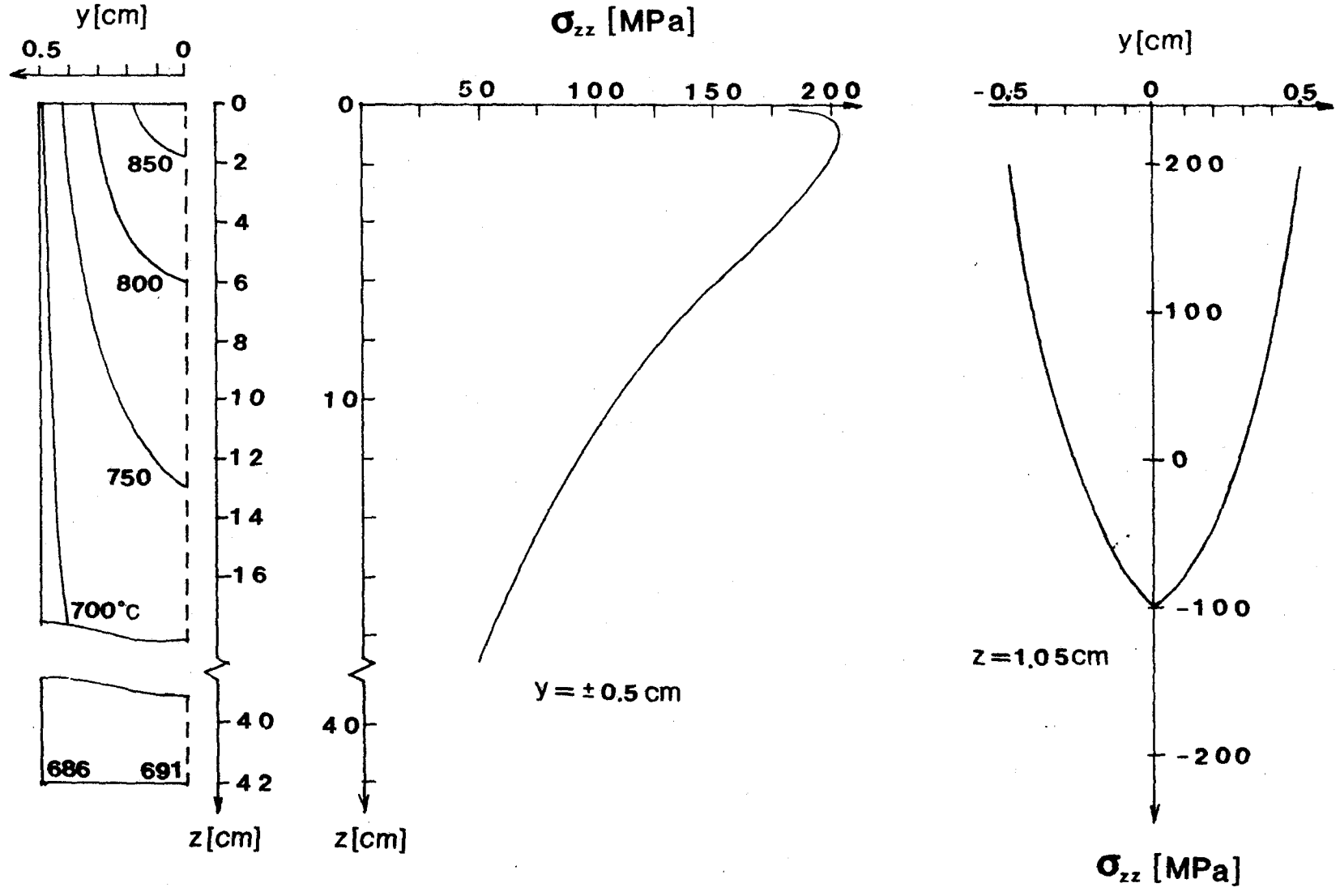

Figure 5.2.4-8 Temperature and thermal stress profiles in Li_2O slab under reactor heat load conditions (α = 3.3 x 10^{-5}/K, ν = 0.25, E = 5.5 x 10^4 MPa assumed).

thermal stresses. The peak stresses are about 200 MPa tensile. Comparing this with the fracture strength of 20 MPa[4] at 800 °C, it is expected that this ceramic would crack on startup.

The significance of the breeder/clad interaction is illustrated when a truss element is placed along the top of the breeder, simulating cladding around the breeder. Using nominal clad properties for the reference blanket (0.25 mm thick HT-9) and assuming the same average temperature as the breeder, the difference in thermal expansion coefficients leads to very large elastic tensile stresses on the clad - over 1000 MPa. If the end clad is a semi-cylindrical cap, then the differential force should be reduced by about the ratio of clad stiffnesses (curved to straight, assuming the breeder is much stiffer than either), but the maximum stress is not reduced as much due to bending stresses in the cylindrical cap,

$$\frac{[\sigma_{clad}^{curved}]_{max}}{[\sigma_{clad}^{straight}]_{max}} = \frac{K_{clad}^{curved}[1 + 3\, d_{br}/d_{clad}]}{K_{clad}^{straight}} = \frac{4}{\pi}\frac{d_{clad}}{d_{br}} \simeq 0.03$$

Although these calculations were for a Li_2O slab, they are more generally applicable to other solid breeders which are similarly expected to have appreciable thermal expansion and be fairly brittle. Significant differences in swelling rates have been measured and so, for example, swelling is not believed to be a contributor to $LiAlO_2$ behavior. Differences in creep rates may also exist, but there is presently no hard data, although some preliminary data[9] suggests that Li_2O is very soft and creeps readily at expected breeder temperatures.

From these 2-D calculations, it is clear that two practical modifications are needed to a basic slab of solid breeder. First, cracking due to thermal stresses at startup is likely unless the breeder is "pre-cracked" to limit the maximum stresses or made thin to limit the ΔT (although this leads to more structure and so reduces breeding). Pre-cracking is the design choice in the reference Li_2O/He/HT-9 blanket, where 1 x 1 x 3 cm^3 blocks of Li_2O are used. This has the advantage of placing the "cracks" perpendicular to the surface so they do not interfere with heat conduction to the coolant, and of providing direct pathways for tritium transport from the interior to the purge

channels. However, it may complicate assembly and add stress concentrations at the breeder/clad boundary. The equivalent design choice in the reference $LiAlO_2/H_2O$/PCA/Be design is to use a sphere-pac breeder, with 1.2 mm and smaller pellets. This also resolves the thermal stress cracking problem, but complicates fabrication and introduces a new fuel form which is not as well understood as solid ceramic nuclear elements.

The second design modification to the basic "solid" breeder is to design the structure and breeder so as to handle differential stresses - 1% thermal strains at startup, and potentially 4% strains due to swelling under irradiation. In the Li_2O design, the cladding top and bottom are designed to be flexible and expand with the breeder. However, this more complicated bellows-like design requires high ductility in a high fluence environment, and may be subject to buckling or rupture if there is a large coolant/purge stream pressure difference. The $LiAlO_2$ structure with double-walled water piping is much more rigid. The thermal expansion (swelling is not anticipated) would be accommodated through rearrangement of the sphere-pack into porosity or free space. Concerns here are that the spheres may not be as free to move as desired due to sintering, lockup or other effects.

5.2.4.3 Magnetic Forces

The dominant magnetic field effect in solid breeder blankets is believed to be mechanical loads due to transient magnetic fields, typically caused by plasma disruptions. These forces have been estimated to be equivalent to a pressure force of ≤ 1 MPa for tokamaks and mirrors.[10,11]

There is also some contribution to the steady-state stress fields due to the interaction of the magnetic field with ferritic steel structural materials such as HT-9. Various estimates have placed this contribution as being on the same order as the weight of the blanket, and have concluded that it can be handled through proper design of the supporting structure.

References for Section 5.2.4

1. S. Timoshenko, "Strengths of Materials", Van Nostrand, New York (1956).

2. K. Washizu, "Variational Methods in Elasticity and Plasticity", Pergamon Press, New York (1975).

3. O. C. Zienkiewicz, "The Finite Element Method", McGraw-Hill, New York (1967).

4. M. Abdou et al., "Blanket Comparison and Selection Study, Interim Report", Argonne National Laboratory, ANL/FPP-83-1 (October 1983).

5. S. Timoshenko, "Theory of Plates and Shells", McGraw-Hill, New York (1959).

6. G. Hollenberg, "Fast neutron irradiation results on Li_2O, Li_4SiO_4, Li_2ZrO_3 and $LiAlO_2$", Jrnl. Nucl. Mat., 122 & 123, 896 (1984).

7. D. R. Olander, "Fundamental Aspects of Nuclear Reactor Fuel Elements", Energy Research and Development Administration, TID-26711-P1 (1976).

8. K. Bathe, E. Wilson and F. Peterson, "SAPIV, A Structural Analysis Program for Static and Dynamic Response of Linear Systems", Earthquake Engineering Research Center, EERC 73-11 (April 1974).

9. G. Hollenberg, personal communication, August 1984.

10. M. Abdou et al., "STARFIRE - A Commercial Tokamak Fusion Power Plant Study", Argonne National Laboratory, ANL/FPP-80-1 (September 1980).

11. G. D. Morgan, personal communication, February 1984.

5.3 Requirements for Scaled Testing

5.3.1 Neutronics

5.3.1.1 Introduction

The basic neutronic environment of the reference solid breeder blankets under reactor conditions was characterized in Section 5.2.1. A fusion facility for the engineering testing of fusion blankets is likely to be smaller in both dimensions and power as compared to a commercial fusion power reactor. For the same geometry, changes in neutron power affect neutronics parameters proportionally. The effects of configuration on neutronics, however, are more complex. For example, it may be possible to enhance the effective neutron wall load by adding neutron multiplier or fissile material to the breeder.

A summary of neutronics issues which may affect or be affected by the scaled test is given in Table 5.3.1-1. It is important to consider these effects since neutrons are the basic driver for the blanket behavior, including heat deposition, tritium generation and radiation damage. The issues can be divided into two categories: issues related to the test device and to the test module. Device-oriented issues include the effect of device size, plasma distribution, and test port geometry. Module-oriented issues include the effects of the module size, which is important because it affects the required test volume. In this section, the specific effects considered are:

- device size (plasma/first wall radius);
- test module size, including thickness and width;
- test port reflector conditions;
- test module composition.

The analysis concentrates on profiles of nuclear heating rate, tritium production rate and radiation damage parameters (displacement per atom or dpa, helium and hydrogen production rates) which are important to many aspects of blanket behavior. Neutronics testing to verify tritium breeding ratio is discussed separately (Chapter 7) since the required accuracy is very high and demands an accurate simulation of the commercial reactor neutronic environment.

Table 5.3.1-1 Neutronics Issues for Engineering Scaling

Category	Technical Issues
1. Test Device	a. device size (plasma/first wall radius) effect b. plasma distribution (neutron source) effects
2. Test Port	a. effects of test environment, especially reflector and plug b. effects due to change in neutron spectrum.
3. Test Module	a. test module size: i. thickness effect and required minimum thickness ii. width and height effect and required minimum dimensions iii. parameter profiles around curved first wall b. effects due to changes in design of test module c. effects arising from geometrical complexity; e.g., streaming through coolant channels and local hot spots d. burnup of breeding material and required test time e. effectiveness of neutron multiplier, fissile material and enrichment f. activation of module components: i. afterheat ii. biological dose and handling of test module

5.3.1.2. Method of Analysis

The same Li_2O/He/FS blanket module as was used in the reference calculation is considered here. For calculational purposes, the test facility is assumed to be a mirror with a 15 cm plasma radius, 25 cm first wall radius, and a 2 MW/m^2 first wall neutron load. Figure 5.3.1-1 shows a conceptual drawing of the assumed blanket module test. The module is irradiated in a test ports, where the module would be inserted into the space between the module reflectors. The remaining space may be filled with a plug if necessary. The reflector material is assumed to be stainless steel.

Calculations were carried out under three different models: 1-D cylindrical model which represented a full coverage blanket and enabled analysis of both the device dimension and the module thickness effects; a 2-D r-θ geometry model and a 3-D model, both of which expressed the geometrical heterogeneity of the test conditions and were used to analyze geometry (reflector) effects. The 1-D calculation was done with the ANISN code,[1] as in the reference blanket calculations. The 2-D r-θ calculation was performed with DOT 4.3,[2] with 23 group constants (n 13 and γ 10), based on the VITAMIN-C/MACLIB-IV library,[3] with the P_3S_4 (16 directions) approximation. The 3-D calculation was carried out with the pointwise Monte Carlo code MCNP,[4] based on its RMCCS/MCPLIB nuclear data library.

The analysis for the effect of module design (material composition) changes was based on the direct sensitivity analysis method with the ANISN code using the material configuration in Fig. 5.3.1-2. This was taken from the BCSS reference design[5] for the Li_2O/He/FS concept. The volume fraction of the HT-9 structure and the plasma radius are slightly different from that assumed in the other analyses. The blanket region was divided into two zones, Blanket 1 and Blanket 2, and different material compositions were assigned to each part. The Li_2O density was 80% theoretical density, a little less than the reference blanket (Appendix D). The sensitivity analysis was done by varying one of the design parameters such as structure volume fraction and the direct forward calculation results compared with those of the reference case.

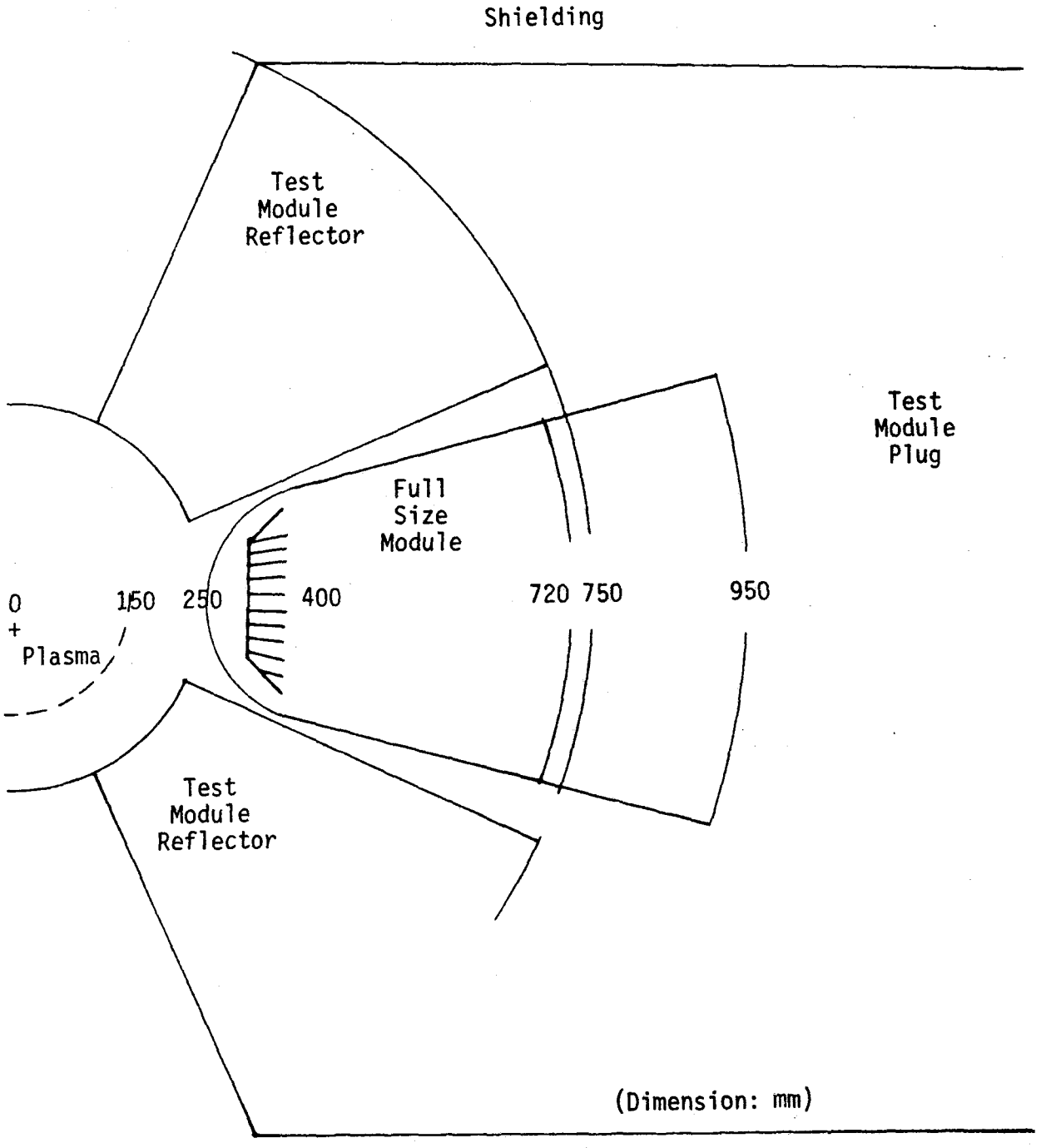

Fig. 5.3.1-1 Conceptual drawing of a blanket module test.

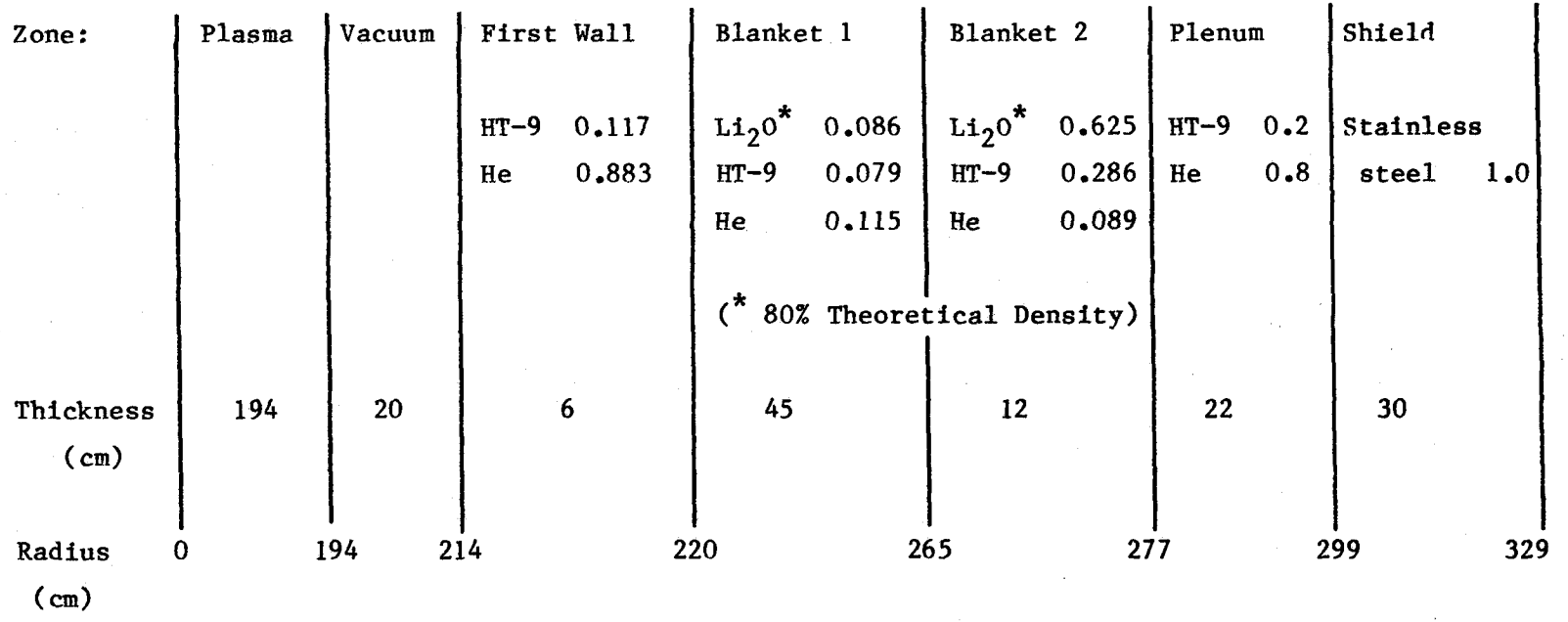

Figure 5.3.1-2 Reference blanket for the material composition sensitivity analysis

5.3.1.3. First Wall Neutronics Parameters

The impact of the test device and the test module on the peak neutronics parameters in the first wall, their profile or attenuation within the first wall, and their variation around the first wall perimeter are discussed.

Device Size Effect on Neutronic Parameters

It is clear that for fixed plasma power density, the neutron wall load and associated neutronics parameters (bulk heating, dpa, etc.) decrease with the plasma radius due to the drop in neutron flux. It is not as clear that the neutronics parameters should decrease with the device size for fixed neutron wall load. However, this is illustrated in Fig. 5.3.1-3 for the heating rate in different devices (described in Table 5.3.1-2). If the heating rates are normalized to the same peak value (Fig. 5.3.1-4), there is seen to be little difference in the actual profile. Similarly, Figs. 5.3.1-5 and -6 for the atomic displacement and He production rates show the dependence of the absolute value, but not the profiles, on the device size. This effect may be explained as follows.

Table 5.3.1-2 Device Dimensions

	Plasma Radius	First Wall Radius
Tokamak reactor	253 cm	273 cm
Mirror reactor	50 cm	60 cm
Mirror test device	15 cm	25 cm

The neutron wall wall load is proportional to the uncollided neutron current, J^{uncol}, while the neutronics parameters are related to the neutron flux, which can be written as

$$\phi^{tot} = \phi^{uncol} + \phi^{scat} \qquad (5.3.1\text{-}1)$$

where ϕ^{scat} is the scattered neutron flux component. Using the albedo concept

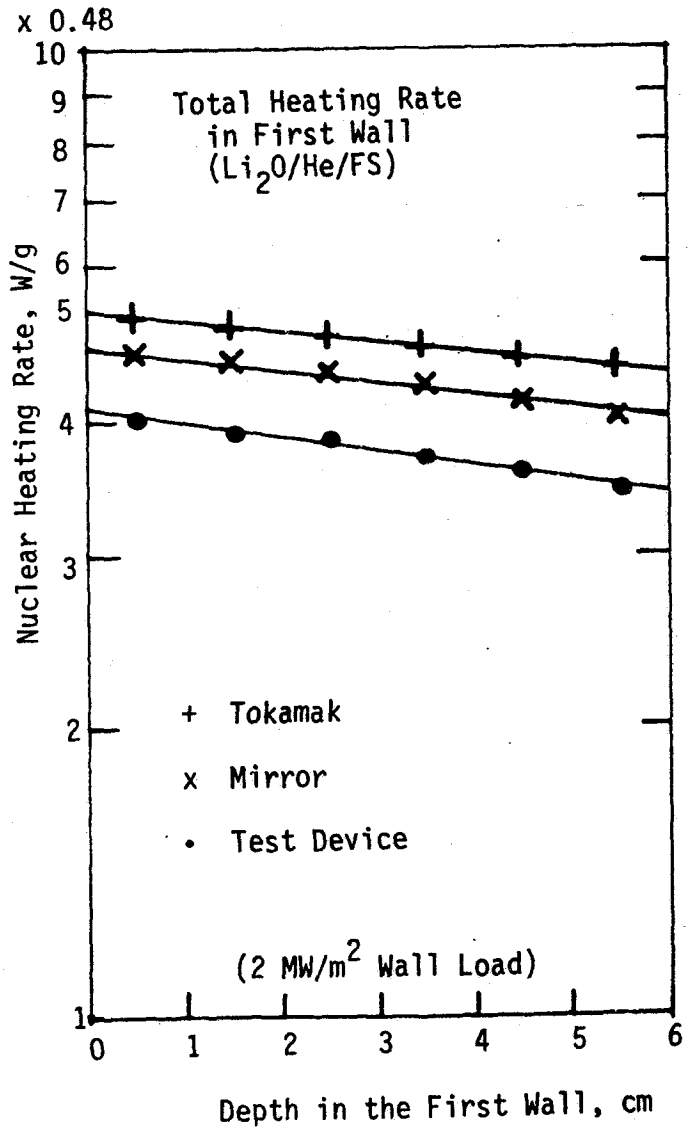

Fig. 5.3.1-3 Device size effect on the nuclear heating rate profile in the first wall.

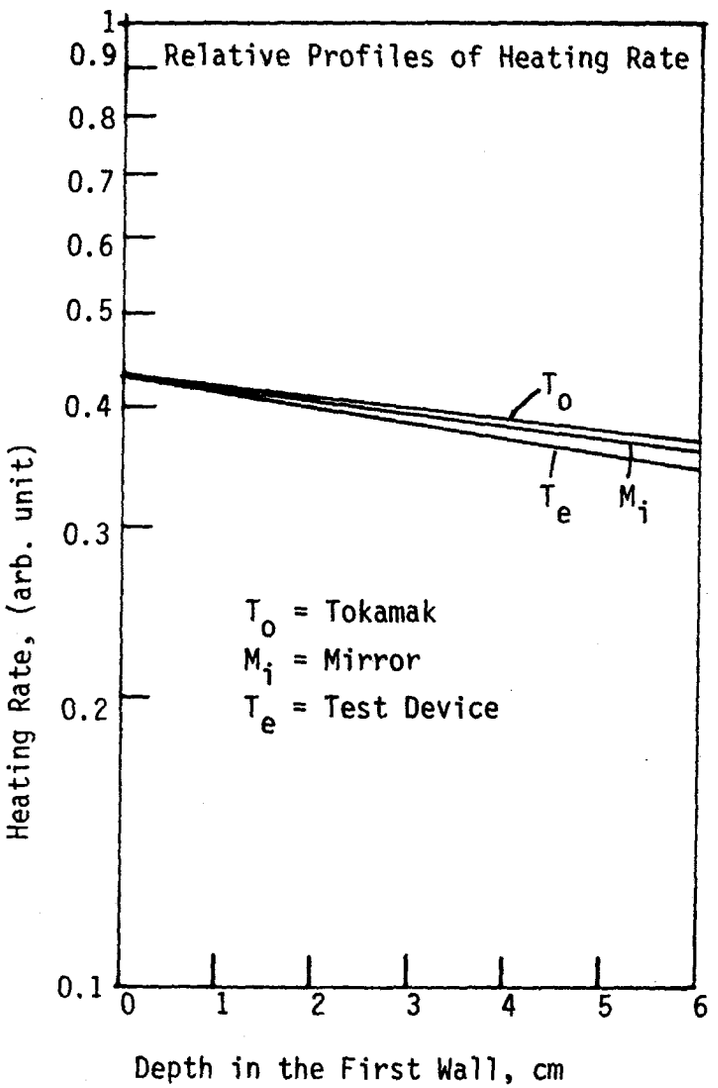

Fig. 5.3.1-4 Device size effect on the gradient of the profile.

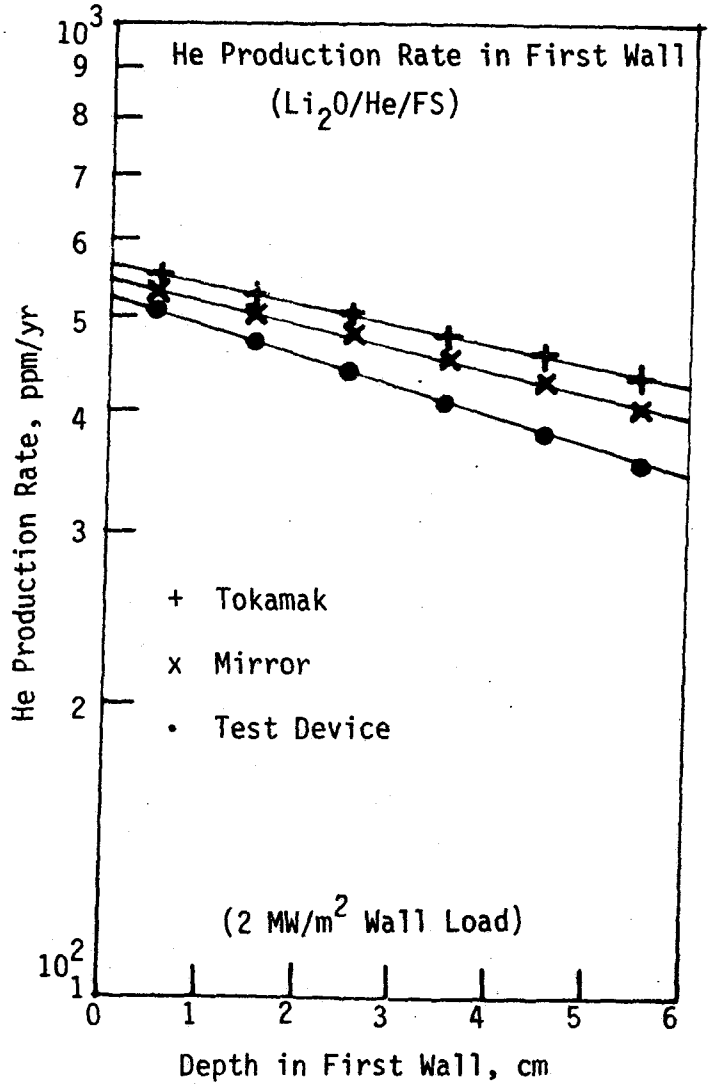

Fig. 5.3.1-5 Device size effect on the profile for the He production rate in the first wall.

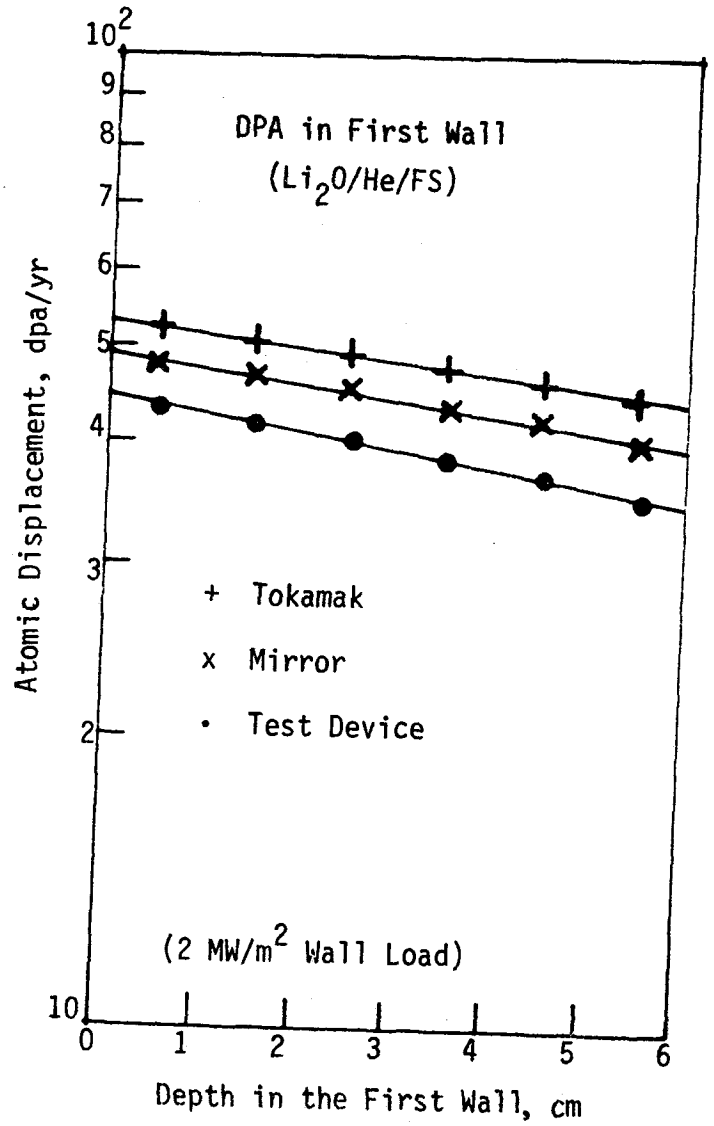

Fig. 5.3.1-6 Device size effect on the profile for the atomic displacement rate in the first wall.

which states that some fraction of the incident flux at a boundary is reflected, the total reflected neutron current coming out from the first wall after multiple reflection, is

$$J^{refl} = (a + a^2 + \ldots)J^{uncol} = \frac{a}{1-a} J^{uncol} \qquad (5.3.1\text{-}2)$$

where *a is the albedo* value and a << 1 assumed. The angular distribution of the reflected neutrons tends to have a cosine distribution, so the neutron flux corresponding to the current J^{refl} will be

$$\phi^{refl} = \frac{2a}{1-a} J^{uncol} \qquad (5.3.1\text{-}3)$$

As the wall is closed, all the reflected neutrons from the first wall to the vacuum chamber will strike the wall again, so the total scattered neutron flux, should be

$$\phi^{scat} = 2\phi^{refl} = \frac{4a}{1-a} J^{uncol} \qquad (5.3.1\text{-}4)$$

Neutronic parameters such as dpa (displacements per atom) are obtained by multiplying the flux by the cross-sections as

$$DPA = \Sigma_{dpa}\, \phi^{tot} = \Sigma_{dpa} J^{uncol} \left(\frac{\phi^{uncol}}{J^{uncol}} + \frac{4a}{1-a}\right) \qquad (5.3.1\text{-}5)$$

Normalizing by the wall load, then $\Sigma_{dpa} J^{uncol}$ is the same value for every device so the size scaling factor C_s for each parameter is

$$C_s = \frac{\phi^{uncol}}{J^{uncol}} + \frac{4a}{1-a} \,. \qquad (5.3.1\text{-}6)$$

The He production is caused only by high energy neutrons, for which the albedo is generally small and the second term negligible, so

$$C_s^{He} \sim \frac{\phi^{uncol}}{J^{uncol}} \qquad (5.3.1\text{-}7)$$

Figure 5.3.1-7 shows albedo data for cylindrical walls.[6] Using this data and a calculated value from the tokamak blanket analysis of a ~ 0.52, the size scaling factor, C_s, was estimated. The results are compared in Fig.

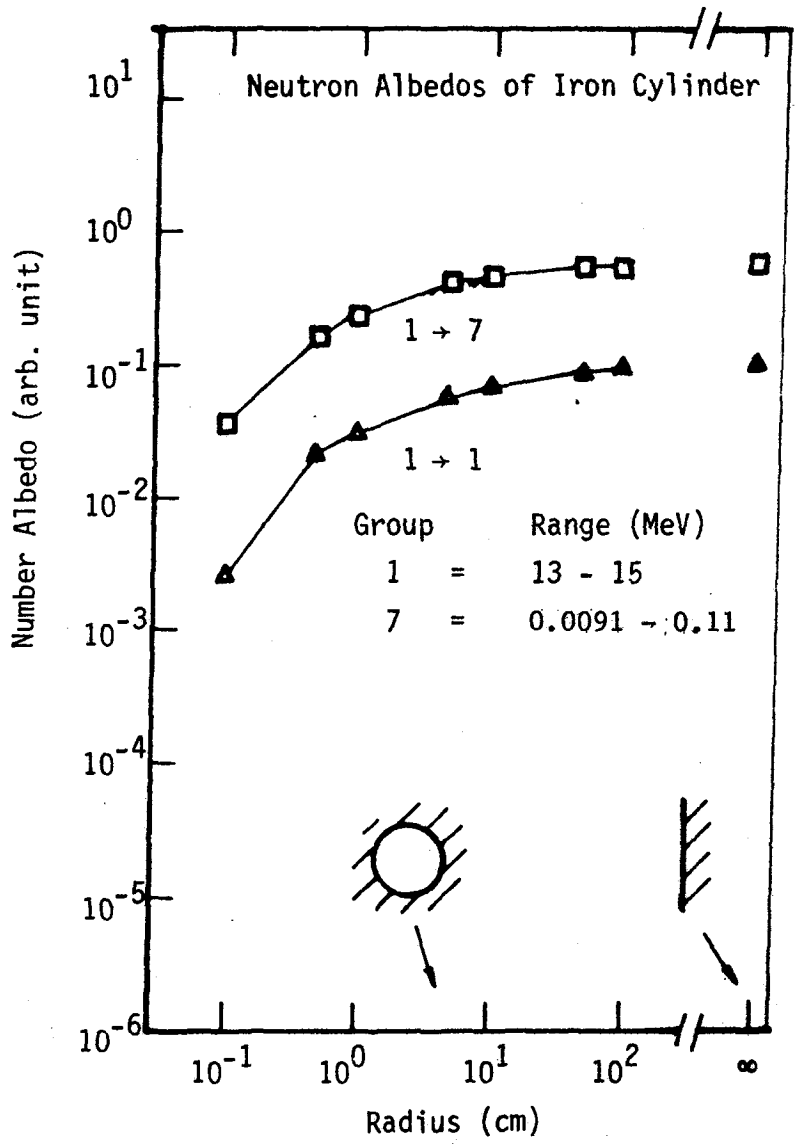

Fig. 5.3.1-7 Dependence of neutron albedo value on the wall radius. The symbol "1→7" means that incident neutrons are in group 1 and reflected ones in group 7.

5.3.1-8 with the peak neutronics parameters obtained from Figs. 5.3.1-3, -5 and -6. All results are normalized to unity at the reference tokamak condition, and plotted as a function of the ratio of plasma to first wall radius, r_p/r_f. Equation (5.3.1-6) gives a good estimation of the heating and dpa variation with size, and Eq.(5.3.1-7) describes the He production rate.

This scaling factor C_s depends on both the plasma and the first wall radii. When the first wall radius is fixed at 273 cm (tokamak reactor), and the plasma size decreased, C_s varies as the solid line in Fig. 5.3.1-8. The decrease of C_s from the tokamak reactor to a line source condition (r_p=0 cm) is only 6%. On the other hand, when the first wall radius is varied while r_p/r_f=0.933 (tokamak reactor) is fixed, then the variation in the C_s value is shown in Fig. 5.3.1-9. The neutronics parameters decreases sharply when the device radius is decreased below 20 cm.

The conclusion is that the radius of the test device should be larger than 20 cm. Otherwise, the neutronics parameters - other than He production which depends only on r_p/r_f - will be much smaller than are expected at the same wall load in a large device. This geometrical effect is due to the lower amount of backscattering or reflection back into the plasma in the more curved geometry. However, the device size is not expected to make an appreciable difference in the actual first wall profiles of these parameters.

Neutron Attenuation in the First Wall

The actual first wall profiles as illustrated in Fig. 5.3.1-3 reflect the neutron attenuation, and may be described by

$$g(x) = g(0)e^{-\gamma\varepsilon x} \qquad (5.3.1\text{-}8)$$

where x is the depth in the wall, ε is the volume fraction of the first wall structure, γ is the attenuation coefficient, and g(0) is the value at the front of the wall. The calculated γ values for the mirror reactor, which is representative of all the devices, are summarized in Table 5.3.1-3.

Corresponding values for the $LiAlO_2/H_2O/Be/FS$ blanket are also listed. These were obtained from the calculations described in Section 5.2.1. As the first wall material is the same, the attenuation rates are similar. However, note that there is some dependence on the first wall neutron spectrum.

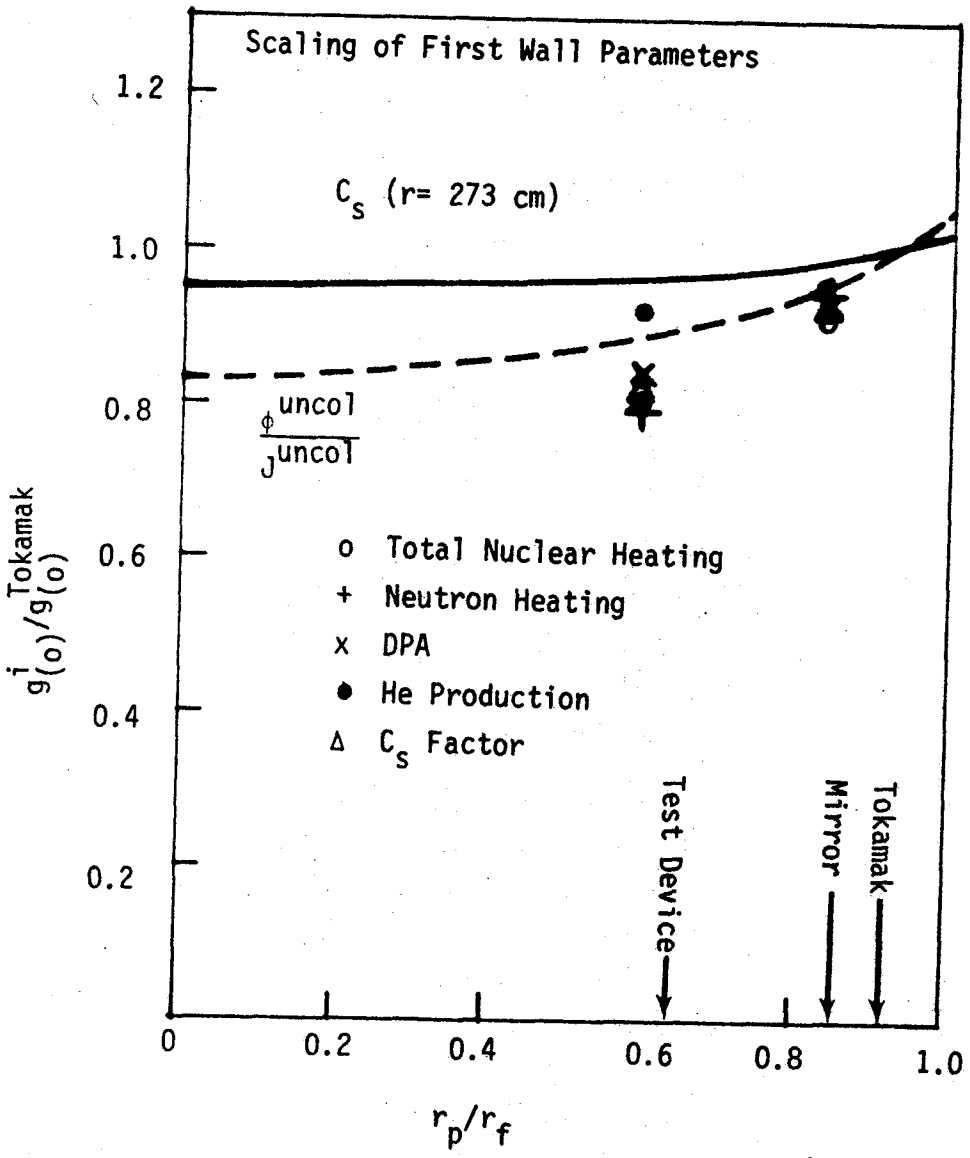

Fig. 5.3.1-8 Scaling of the first wall neutronics parameters with device size.

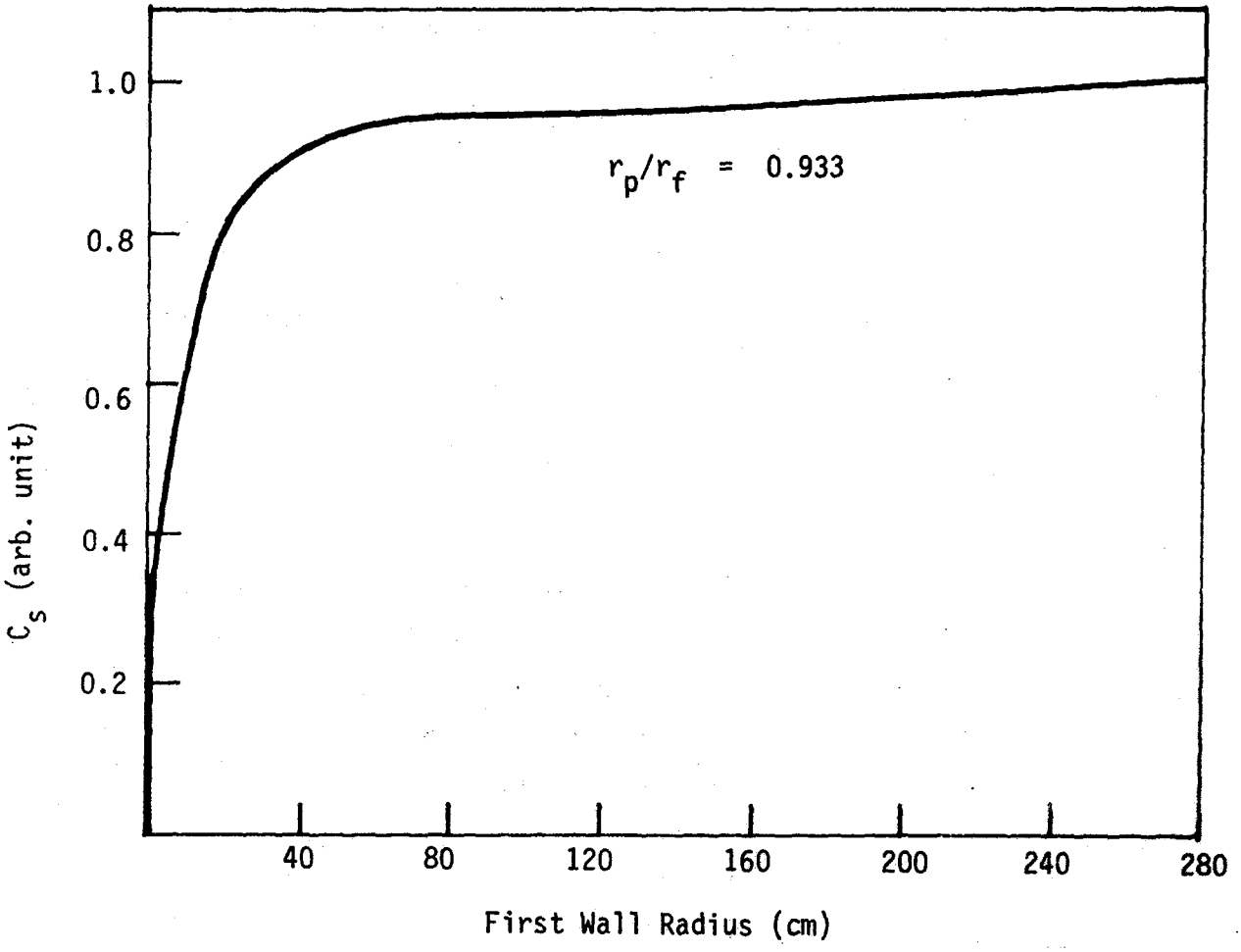

Fig. 5.3.1-9 Scaling factor C_s as a function of first wall radius with the condition $r_p/r_f = 0.933$.

Table 5.3.1-3 Attenuation Coefficient of Neutronics Parameters in the First Wall*

Blanket	Nuclear Heating (1/cm)	DPA (1/cm)	He production rate (1/cm)
Li_2O/He/HT-9	0.133	0.171	0.264
$LiAlO_2$/H_2O/HT-9/Be	0.143	0.192	0.263

*$g(x) = g(o)e^{-\gamma\varepsilon x}$ where x is depth in first wall, ε is structural volume fraction, γ is attenuation coefficient, and g refers to heating, DPA or He production.

Since there are circumstances under which the first wall dimensions may be increased in a scaled test (for example, to preserve the temperature drop under reduced surface heating), the flux attenuation may become significant. In particular, Figure 5.3.1-10 shows the attenuation of the heating rate through the first wall as a function of the wall thickness scaling factor (the ratio of the first wall thickness of the test module to that of the reference module). As given in Table 5.3.1-3, the heating rate behaves exponentially with a scale length of about 7 cm. The DPA rate and He production rate in HT-9 have attenuation scale lengths of about 5 and 4 cm, respectively, so will decrease even faster than the heating rate.

Azimuthal Profile of Neutronic Parameters in First Wall

The first wall of the reference solid breeder blanket modules has a cylindrical or lobe shape with a 15 cm radius. Little variation in neutronics parameters (e.g., nuclear heating) around the azimuthal perimeter of the curved first wall is expected in tokamak reactors since the device size - the first wall radius - is much larger than the lobe radius. However, the profile may be changed when the module is placed in small test devices. Three-dimensional Monte Carlo calculations were performed for the analysis of this effect. Figure 5.3.1-11 shows the calculational model for the assumed test

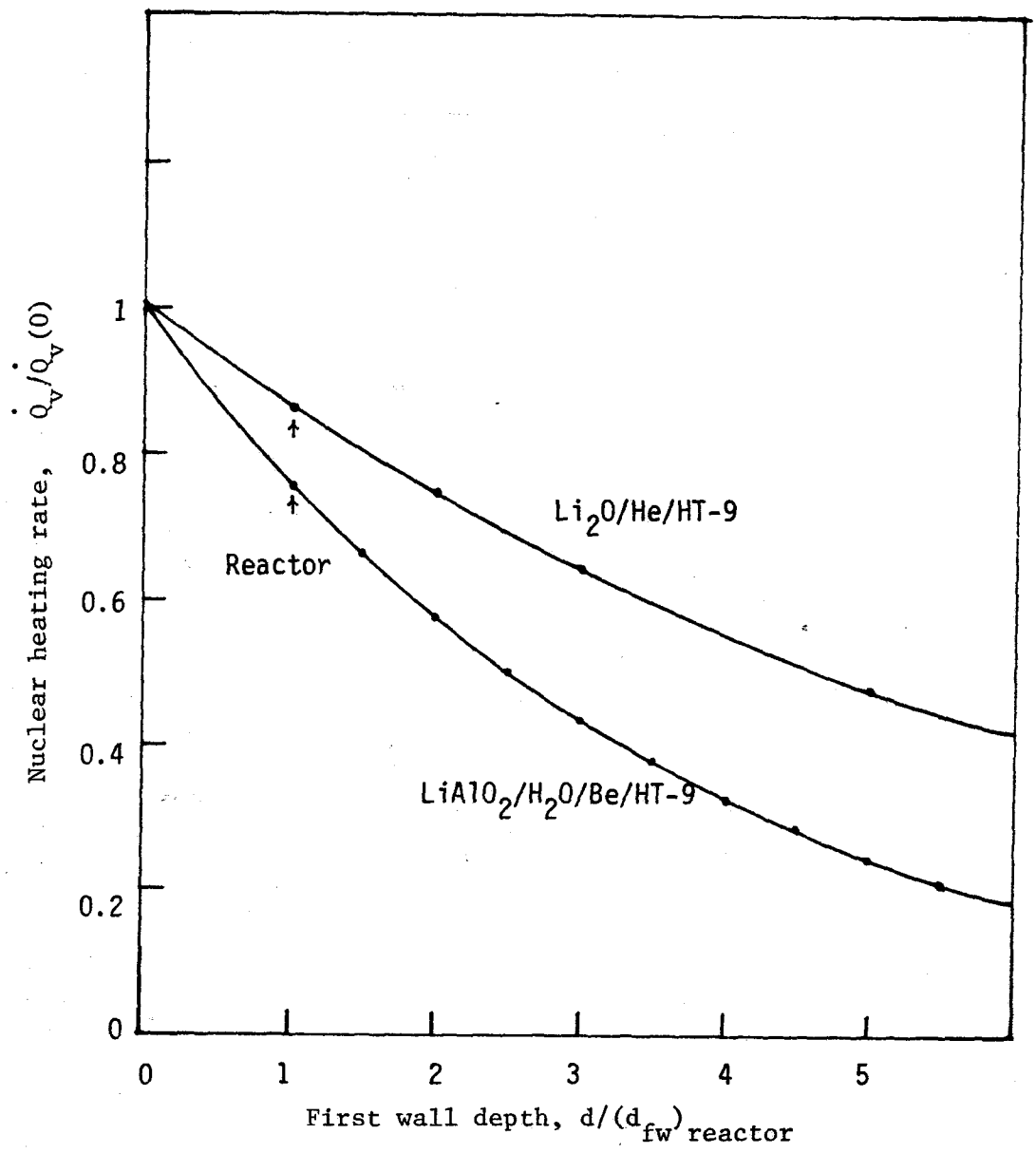

Figure 5.3.1-10 Attenuation of nuclear heating rate through the first wall. The reference reactor thickness is 10.8 mm and 11.9 mm for the Li_2O/He/HT-9 and $LiAlO_2/H_2O$/PCA/Be blankets, respecively.

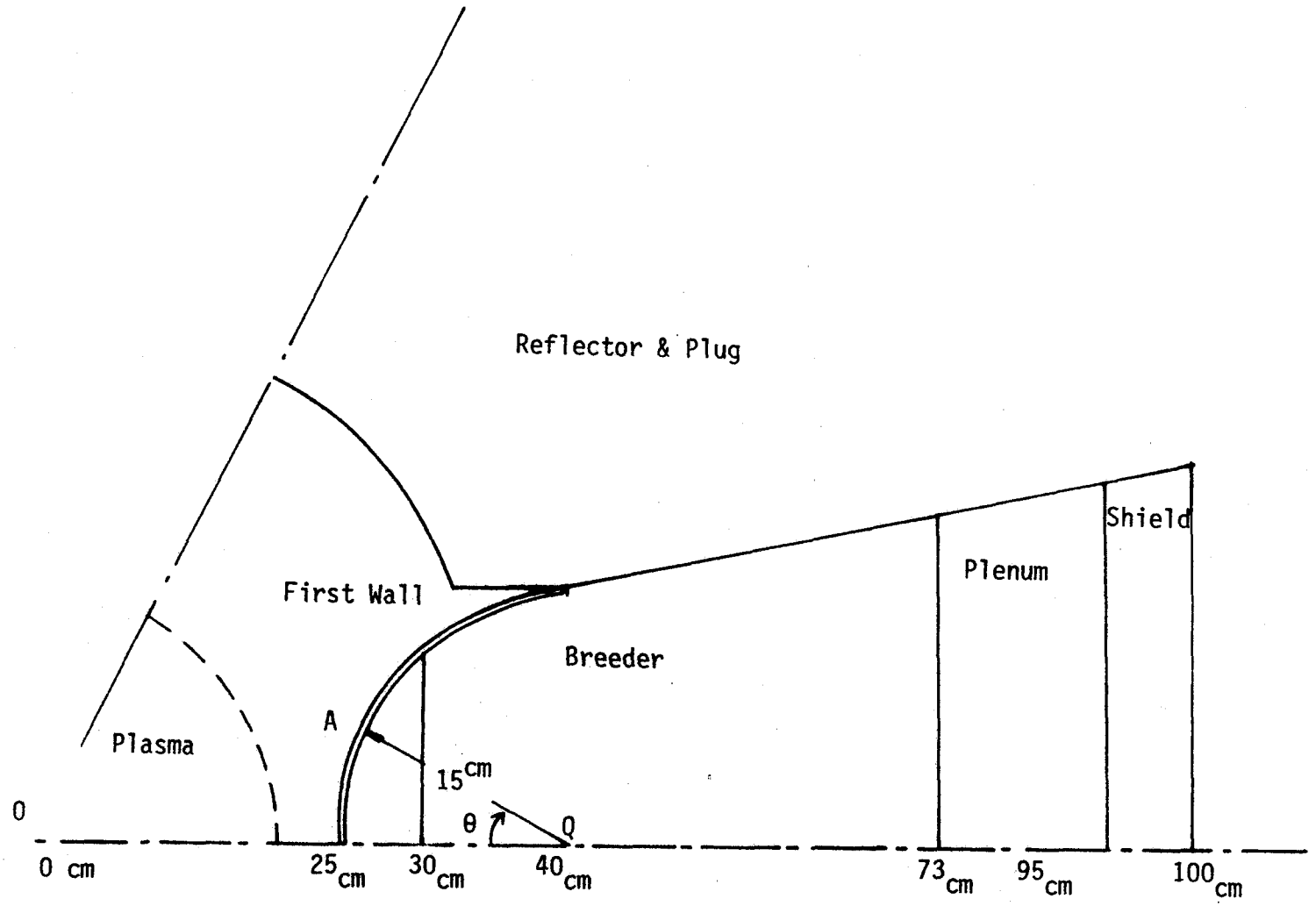

Fig. 5.3.1-11 Calculational model of the module testing for the Monte Carlo calculations.

geometry. A uniformly distributed plasma was assumed, with a radius of 1 cm, 15 cm, and 24.95 cm to check the effect of source size.

Figure 5.3.1-12 shows the distribution of uncollided neutron flux as a function of position in the first wall, where the position was measured in the azimuthal direction by the angle θ between the module center line OQ, shown in Fig. 5.3.1-11, and the radial direction QA (from the surface origin Q to the position A). As is shown in Fig. 5.3.1-12, the uncollided fluxes vary approximately as 1/r with increasing angle, where r is the distance from the plasma center line to the position. And the device size effect causes a higher flux for the larger plasma. The He production rate, which was not calculated, will be similar to the uncollided neutron distributions in Fig. 5.3.1-12, considering the high threshold energy for He producing reactions.

Figure 5.3.1-13 shows the total nuclear heating rate and its contributions from neutrons and gamma rays. In both Fig. 5.3.1-12 and -13, the curve are scarcely dependent on the plasma size except for a small effect near the front (center region) of the wall. However, the azimuthal variation in heating and He production is significant. The 1/r approximation is better for the He production rate, but is clearly an oversimplification for nuclear heating, which scales faster. The dpa rate was not analyzed, but will behave similar to the neutron heating rate because dpa production is closely related to the neutron energy deposition.

Assuming the 1/r approximation also holds for the mirror and tokamak reactors, the azimuthal heating rates are as in Fig. 5.3.1-14. The curves are normalized at $\theta=0^{o}$. It is seen that as the device dimensions decrease, the variation gets larger. This may lead to difficulties in preserving temperature profiles and structural behaviour in scaled first wall tests.

5.3.1.4 Breeder Region Neutronics Parameters

The effect of device size and power level on the neutronics parameters in the breeder region are considered. Then the test module and reflector geometry is analyzed to determine useful test volume and test port configurations. Finally, the effect of varying the material volume fraction is considered.

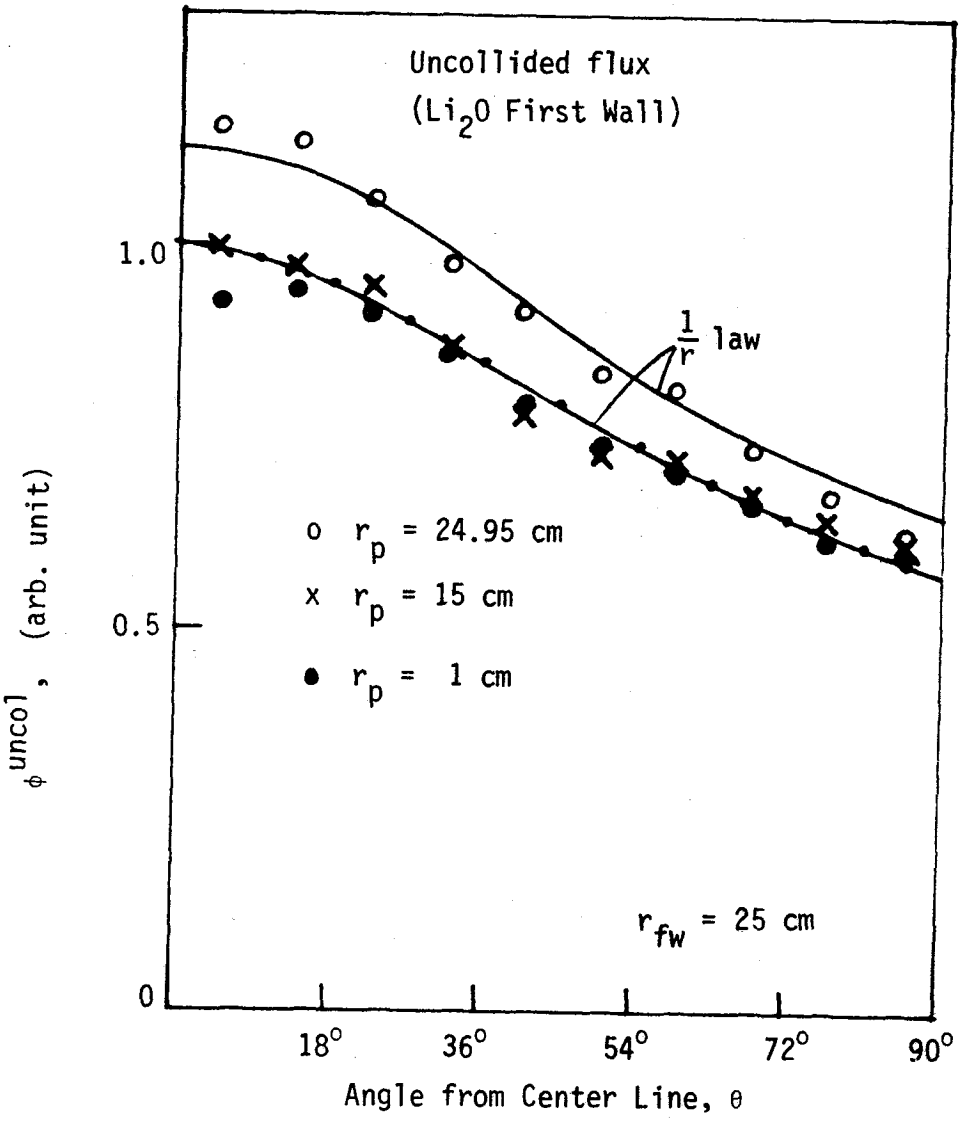

Fig. 5.3.1-12 Azimuthal variation of uncollided neutron flux for three different sources.

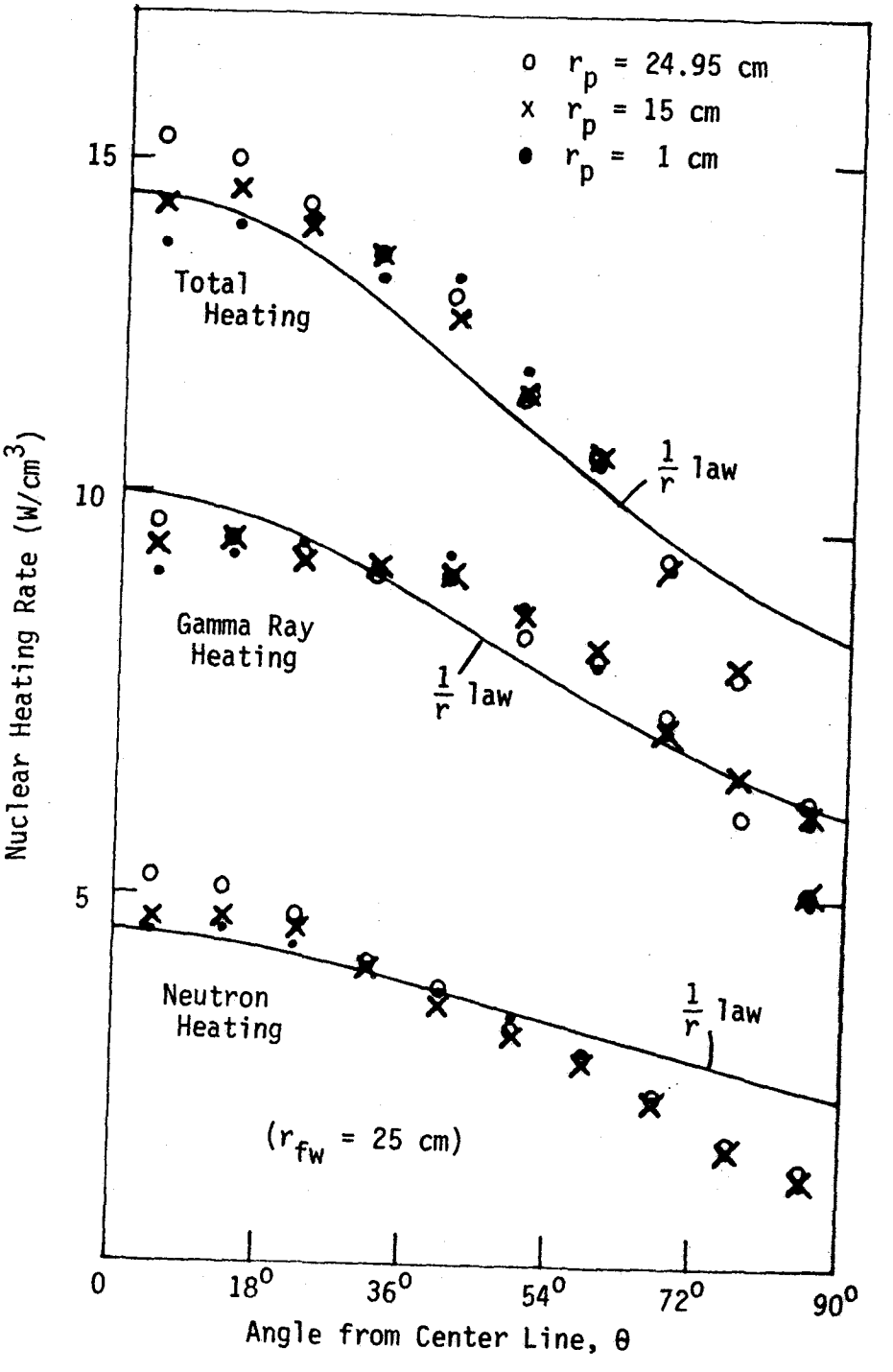

Fig. 5.3.1-13 Azimuthal profiles of total heating rate and contributions from neutrons and gamma rays in the first wall with different neutron sources.

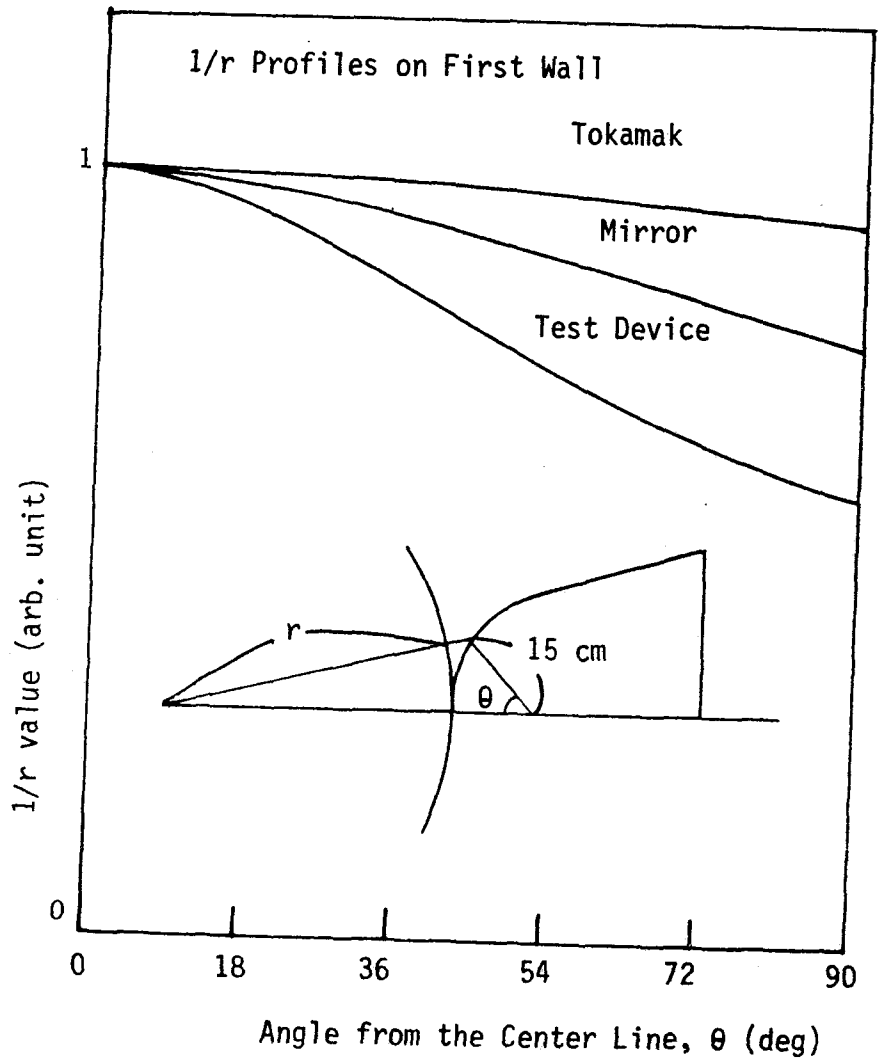

Fig. 5.3.1-14 Dissimilarity of the profiles for the neutronics parameters due to the device size effect.

Device Size Effect on Neutronic Parameters

Figure 5.3.1-15 shows the profiles of the nuclear heating and tritium production rates in the breeding zone for three devices, i.e., the reference tokamak and mirror reactors, and a small mirror test facility. The profiles are very similar, the difference is mainly in the absolute value. This is due to the same device size effect as was discussed in the first wall section. The values at the front edge of the breeder were obtained from Fig. 5.3.1-15 and plotted in Fig. 5.3.1-16 in a similar manner as Fig. 5.3.1-8. The horizontal axis, however, was changed to $r_p/(r_f + 6\ \text{cm})$ in order to be applicable at the front of the breeding zone. The solid line shows the ratio ϕ^{uncol}/J^{uncol} as in Fig. 5.3.1-8. The same scaling equation, Eq. (5.3.1-6), may be used although "a" is now a general scaling variable and not the albedo. (The broken line in Fig. 5.3.1-16 was drawn by hand to smoothly connect the points.)

The profiles for tritium production and nuclear heating from Fig. 5.3.1-15 were renormalized to the values of the test device at the front edge of the breeder, and are shown in Fig. 5.3.1-17. The relative profiles are seen to scarcely depend on the device size, excluding the back region where ~ 20-30% discrepancies are noticeable. These discrepancies are probably not important because the neutronics parameters are very small in the back as compared to other region. Thus, the relative depth profiles of the heating and tritium production rates in the breeder are not affected by the device size effect.

Effect of Lithium Burnup Rate on Test Time Requirements

Lithium burnup is of concern since it will lead to a change in tritium generation over time, to a shift in peak generation location further into the breeder, and since there are potential chemistry changes associated with both the burnup rate (e.g., excess oxygen concentration in Li_2O) and the total burnup (e.g., cumulative concentration of metal oxides in $LiAlO_2$).

Table 5.3.1-4 shows typical burnup rates of Li nuclei in the Li_2O and $LiAlO_2$ blankets at 2 MW/m^2 neutron wall loading. The atomic density of ^6Li or ^7Li at time t is

$$n(t) = n_0 e^{-\frac{t}{\tau}} \qquad (5.3.1\text{-}9)$$

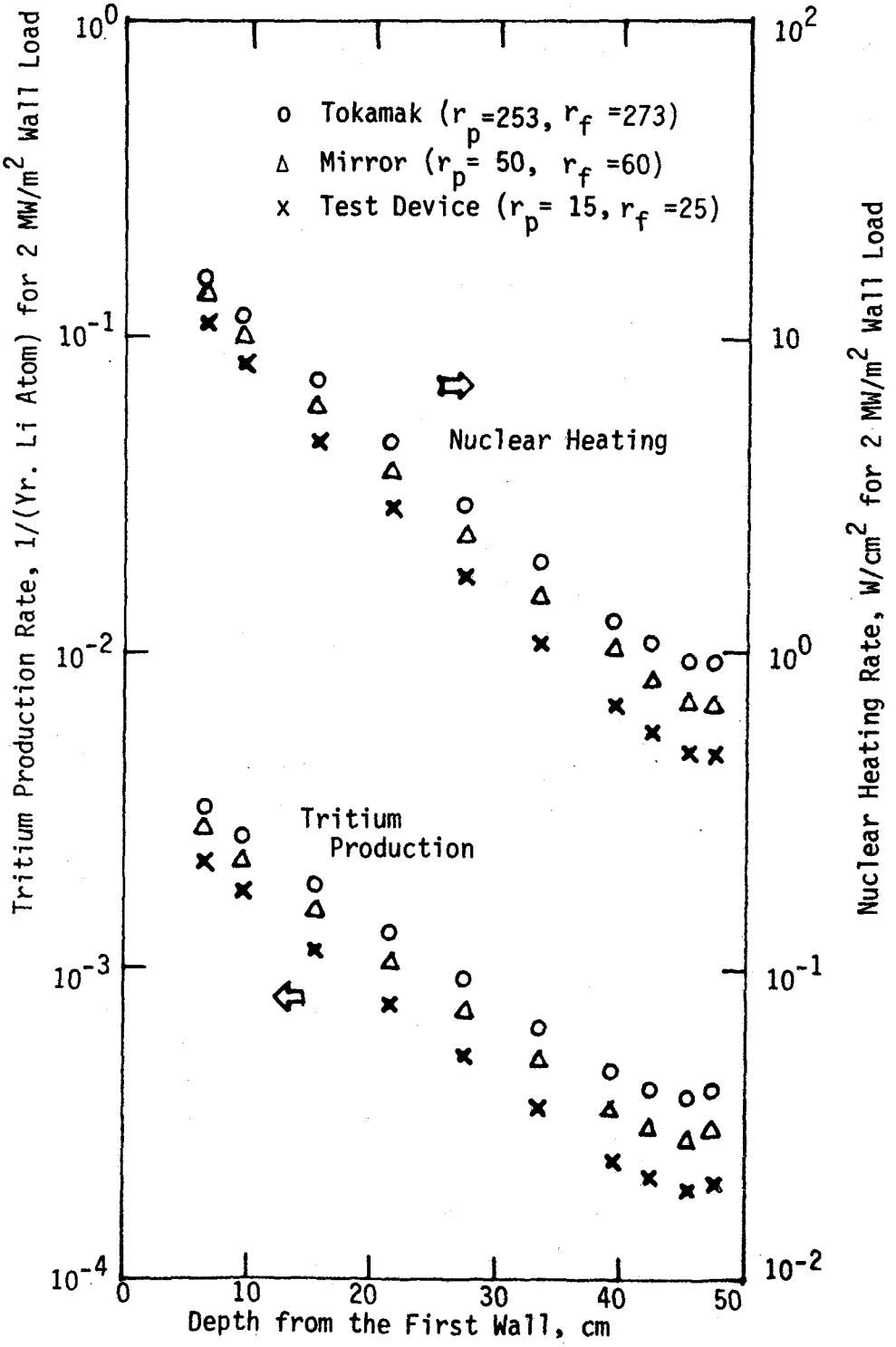

Fig. 5.3.1-15 Device size effect on the profiles of the nuclear heating rate and the tritium production rate in the breeding zone.

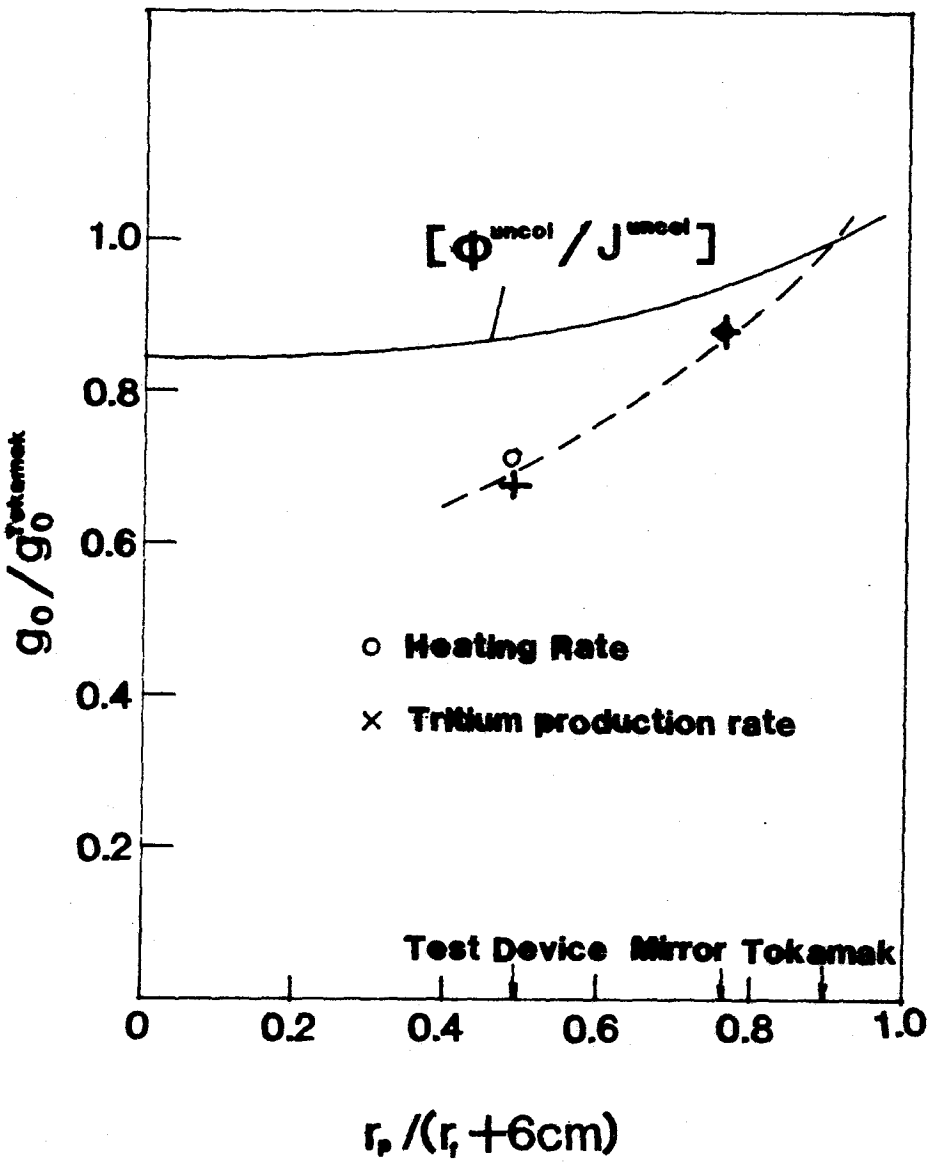

Figure 5.3.1-16 Scaling of neutronics parameters at the front edge of the breeding zone with the device size.

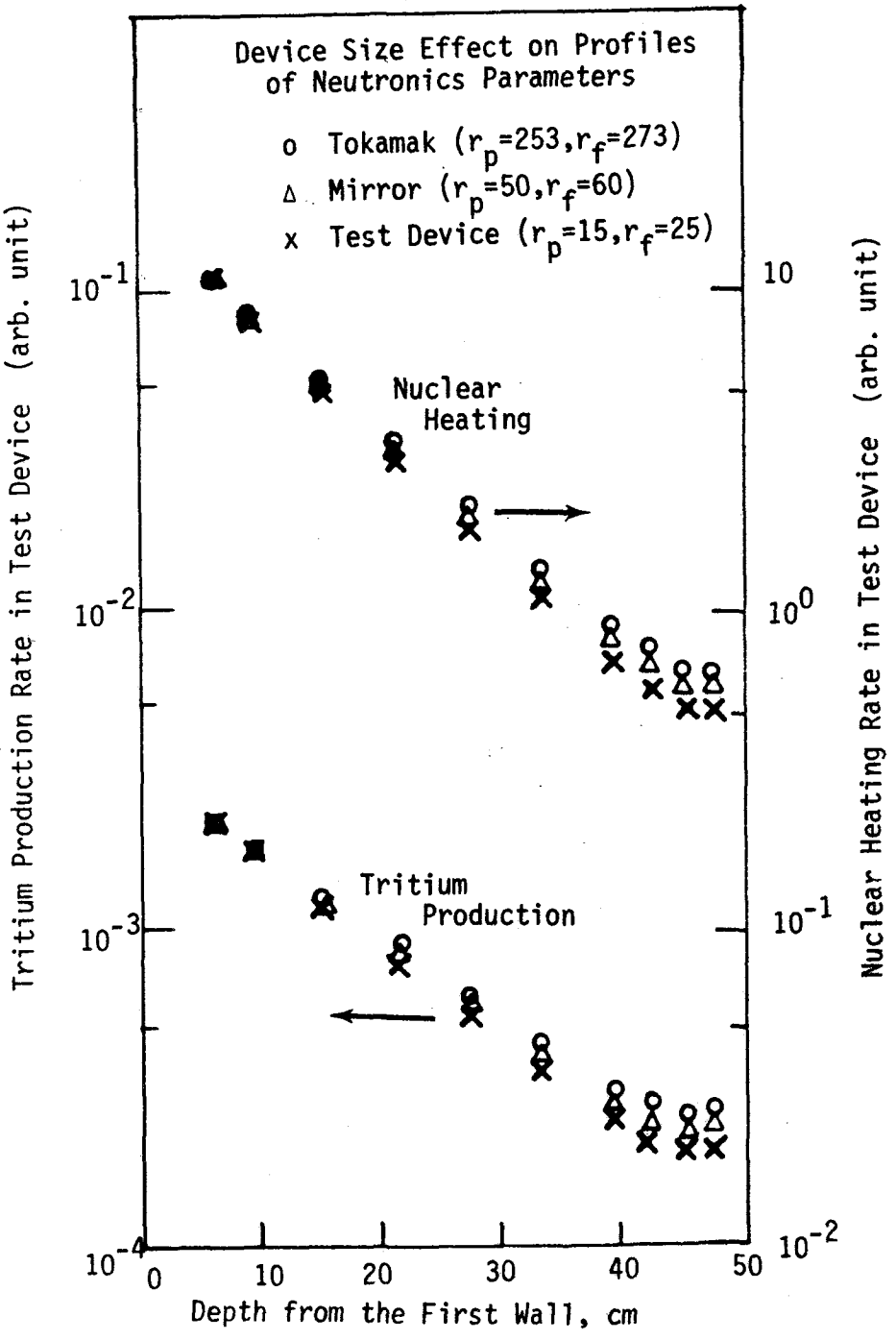

Fig. 5.3.1-17 Device size effect on the relative profiles of neutronics parameters in the breeding zone.

Table 5.3.1-4 Lithium Burnup Time at 2 MW/m^2 Neutron Wall Load

Blanket	Nuclide	Front of Breeding Zone (yr)	Center of Breeding Zone (yr)
Li_2O/He/FS	^6Li	43	82
	^7Li	443	3300
$LiAlO_2$/H_2O/FS/Be	^6Li	4	294
	^7Li	714	6250

where n_0 is the initial atomic density ($1/m^3$) at startup, t is the time from startup in years, and $1/\tau$ is the burnup rate (1/year).

Preserving the burnup rate requires maintaining the neutron flux at reactor values. Preserving total burnup requires operating the device for extended periods if the neutron flux is reduced. The largest burnup concern is with the $LiAlO_2$ front blanket, where 50% burnup is achieved within a year under reactor conditions. At 2 MW/m^2, 2.5 years of continuous operation would be needed for an equivalent burnup. Consequently, unless scaled tests under reduced wall load are allowed to run for years, there will be little variation in tritium breeding or nuclear heating due to lithium burnup, and probably also limited information gained on other burnup-related effects.

Effect of Breeder Thickness on Neutronics Parameters

A small test module with a thin breeding zone may be necessary due to test volume constraints. However, while this may not strongly affect the first wall, parameters like breeder heating rate are sensitive to variations of the breeding zone thickness. Direct neutron transport calculations were repeated for various sized test modules to quantify this concern.

Figure 5.3.1-18 shows the calculational models used in the analysis. Two types of test modules were assumed. One of them (Type A, or reflected module) had the same first wall, plenum and shield as in the full sized module, while the other (Type B, or unreflected module) had neither plenum nor shield, and a free surface boundary conditions was imposed at the outer surface.

Figure 5.3.1-19 shows results of reflected module (Type A) calculations. The profile of nuclear heating rate is locally enhanced (within about 4 cm) by neutron reflection from the back plenum. Elsewhere, the heating rate profile is very close (about 10% deviation) to the results for the full size module. The tritium production rate profile is similar, although the reflector effect is more pronounced because low energy neutrons are more important for tritium production than for nuclear heating, and because reflected neutrons are more likely to have low energies. Excluding the region where the reflection effect is pronounced, the profile is also very close (about 20% deviation) to that of the full size module.

Figure 5.3.1-20 shows the total tritium production, obtained by integrating the tritium production rate over the breeder volume, as a function of the breeder thickness. About 80% of the tritium production of the full breeder is obtained with a 20 cm thick breeder zone, which is about half the full breeder thickness.

Figures 5.3.1-21 and -22 show the profile of the tritium production rate in the unreflected Type B module. The profile of the tritium production from ^{7}Li (T_7) is not affected by the breeder thickness. However, the tritium production from ^{6}Li (T_6) is lower because the thinner breeder with no reflector allowed more neutrons to leak from the system. The magnitude of the leakage effect on the total tritium production (T_6+T_7) is larger than that of the reflector effect in the geometry with shield (Type A). Moreover, the leakage effect lowers the total tritium production. Thus the unreflected thin breeder module has several disadvantages and no advantages relative to the thin test module with shield and reflector.

For the $LiAlO_2/H_2O/Be/HT-9$ blanket, enriched lithium is assumed so the blanket is more sensitive to the low energy reflected neutrons. It is expected that there will be larger effects from thinning the breeder zones, and that it will be more important to add a reflector to minimize leakage.

Zone:	Plasma	Vacuum	First Wall	Breeder	Plenum	Shield	30% albedo
Thickness: (cm)	15	10	6	variable	22	30	

Type A configuration (with reflector)

Zone:	Plasma	Vacuum	First Wall	Breeder	0% albedo
Thickness: (cm)	50	10	6	variable	

Type B configuration (without reflector)

Figure 5.3.1-18 One-dimensional models of test module for the analysis of the module thickness effect

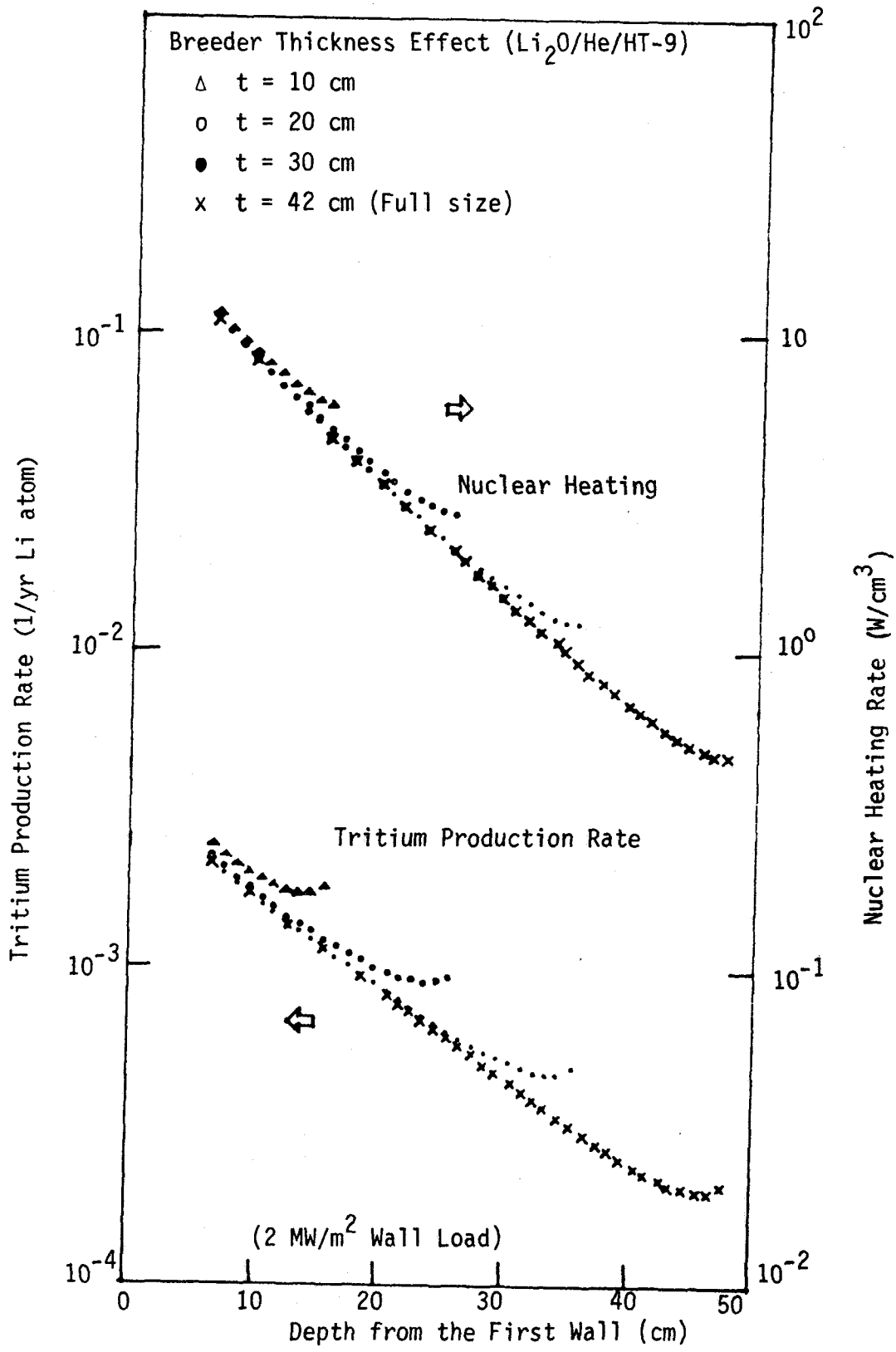

Fig. 5.3.1-19 Module thickness effect on the profiles for the neutronics parameters.

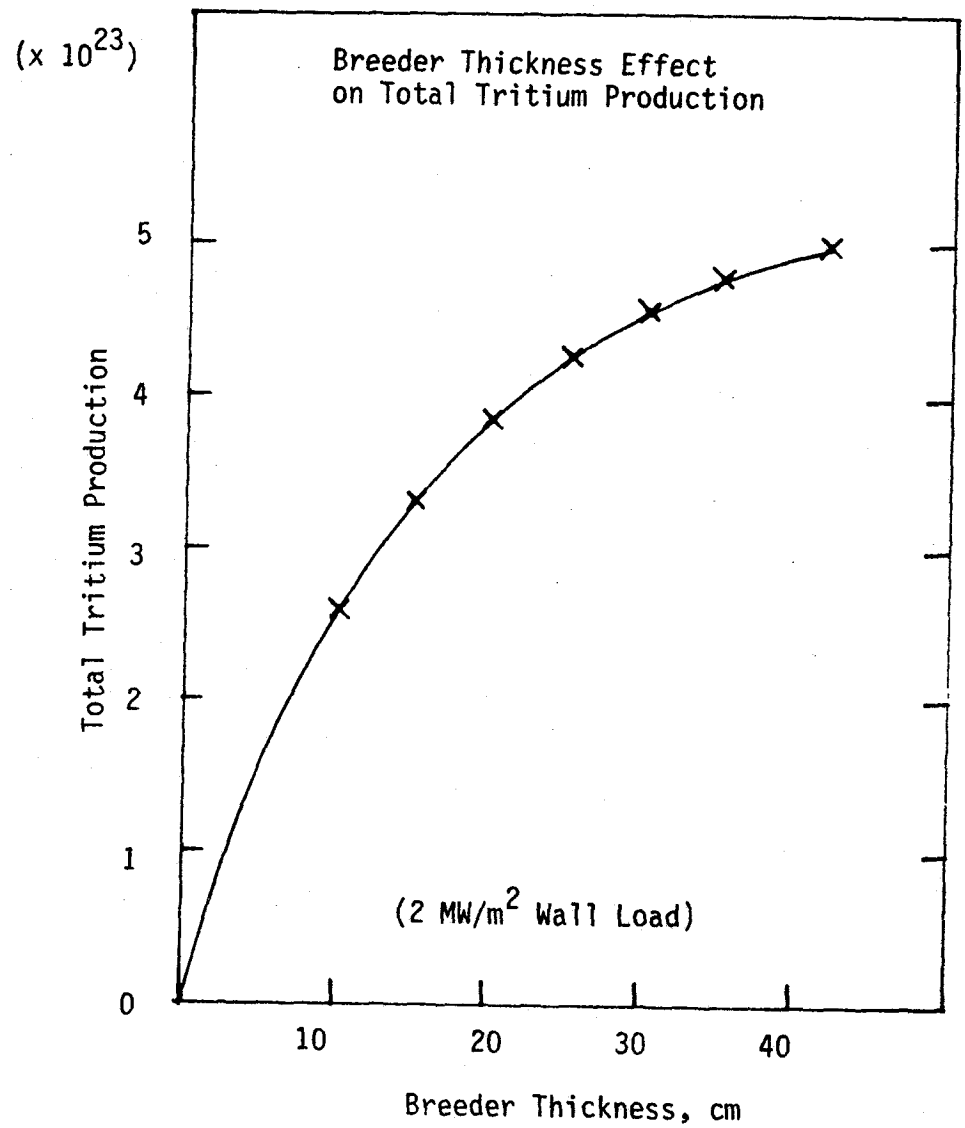

Fig. 5.3.1-20 Total tritium production in the test module as a function of the module thickness.

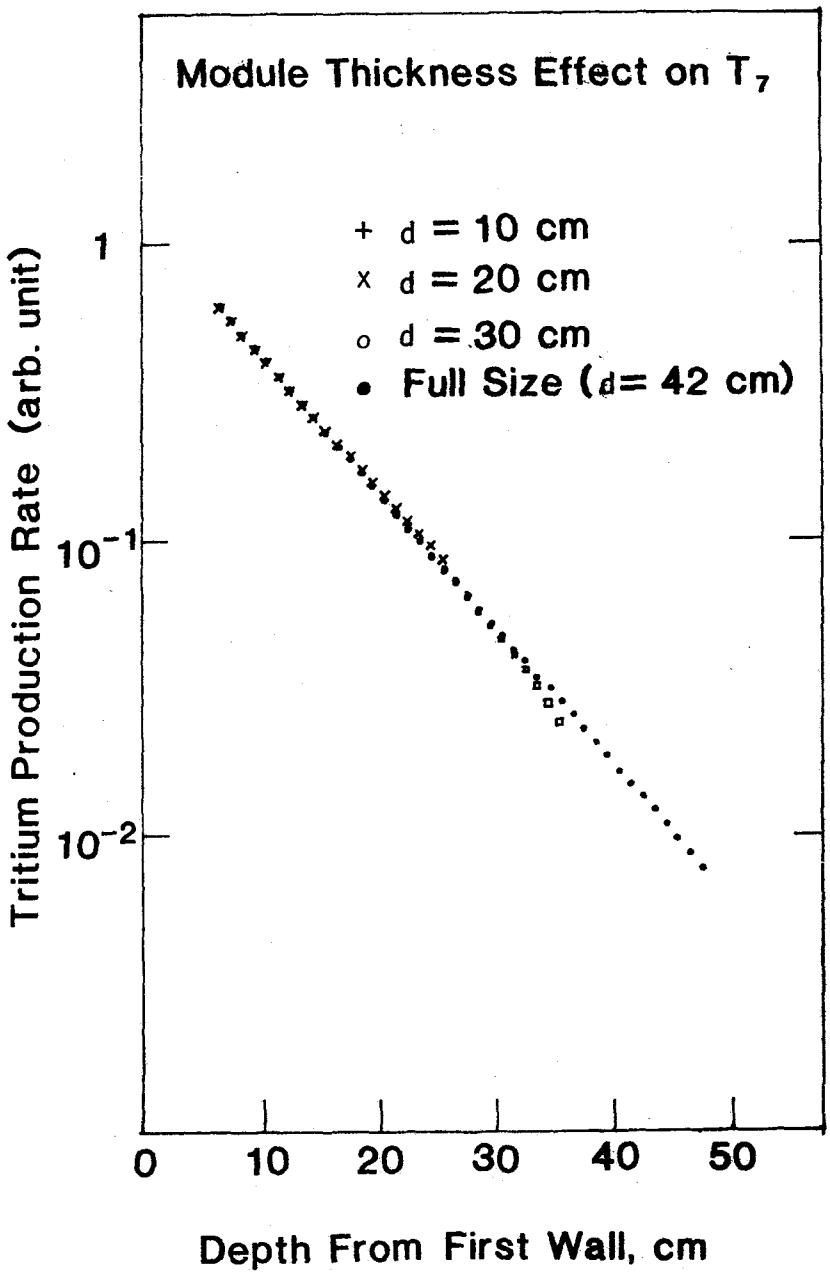

Figure 5.3.1-21 Tritium production rate through ^{7}Li(n,n')αT reactions as a function of the module thickness.

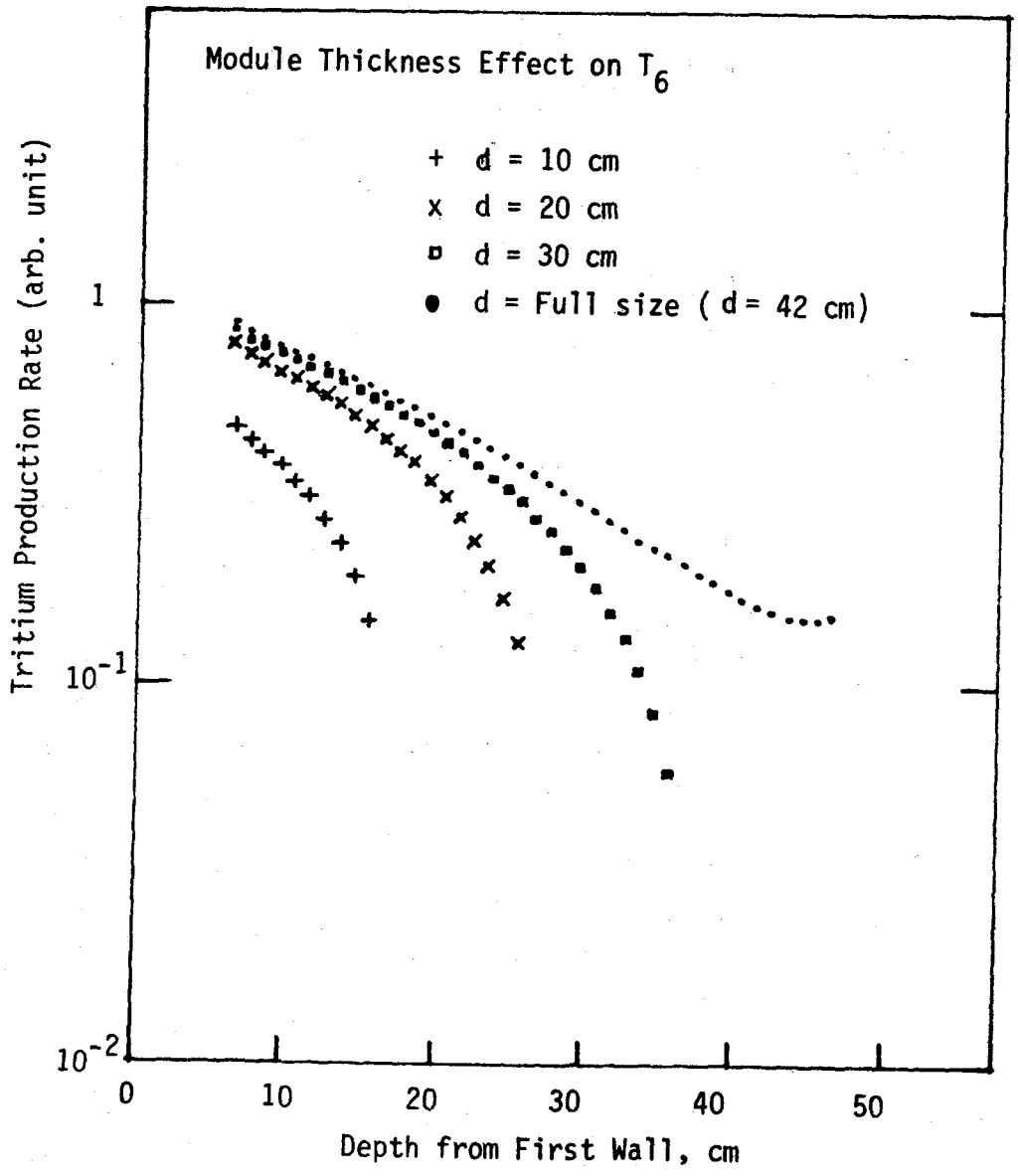

Fig. 5.3.1-22 Tritium production rate through ^{6}Li (n,α)T reactions as a function of the module thickness.

To summarize this particular analysis, thin breeder regions of at least 20 cm will retain the neutronics profiles, generate at least 80% of the full breeder tritium production rate, and allow an appreciable variation (factor of 2-3) in flux and fluence across the breeder. It is important to retain the shield or other reflector to minimize neutron leakage. $LiAlO_2$ is probably more sensitive to thinned breeder than Li_2O. For first wall testing, as little as 10 cm would be sufficient to establish the heating rates with reflected neutrons and gammas.

Effect of Test Module Environment

If the module is placed in a test port which can only accommodate a single test module, then the module will be surrounded by reflectors and plug rather than other blanket modules. This may disturb the neutronics parameter profiles in the test module and decrease the usefulness of the test port. This is particularly important for a tritium breeding ratio test where close simulation and high accuracies are needed, as discussed in Chapter 7. On the other hand, neutron multiplication and enhanced reflection may give rise to a higher volumetric heating or tritium production, partially compensating for a decrease in test device neutron wall load. The question is how strong is the effect and how far the neutron field perturbation extends inside the module. The analysis of this problem will be shown here.

Figure 5.3.1-23 shows 2-D models of the test environment. The geometries were defined in r-θ coordinates and the analysis performed with the DOT-4.3 code. Two types of the reflector and plug were considered. Type A is the regular arrangement with a reflector and plug, while Type B has no reflector and is specially designed to enhance the breeder neutron flux.

Figure 5.3.1-24 shows depth profiles of the nuclear heating and tritium production rates in the breeder zone for the Type A geometry. The data denoted as 1-D calculation in the figure are those for full coverage geometry. Results of the two-dimensional calculation for the single module test condition were averaged over the θ direction to get the data at each radius.

The nuclear heating rate was less influenced by the reflector as compared to the tritium production rate; the tritium production rate was enhanced by a factor of two at the top of the breeder, while the heating rate was only increased 20%. The reason is that tritium production is more sensitive to low

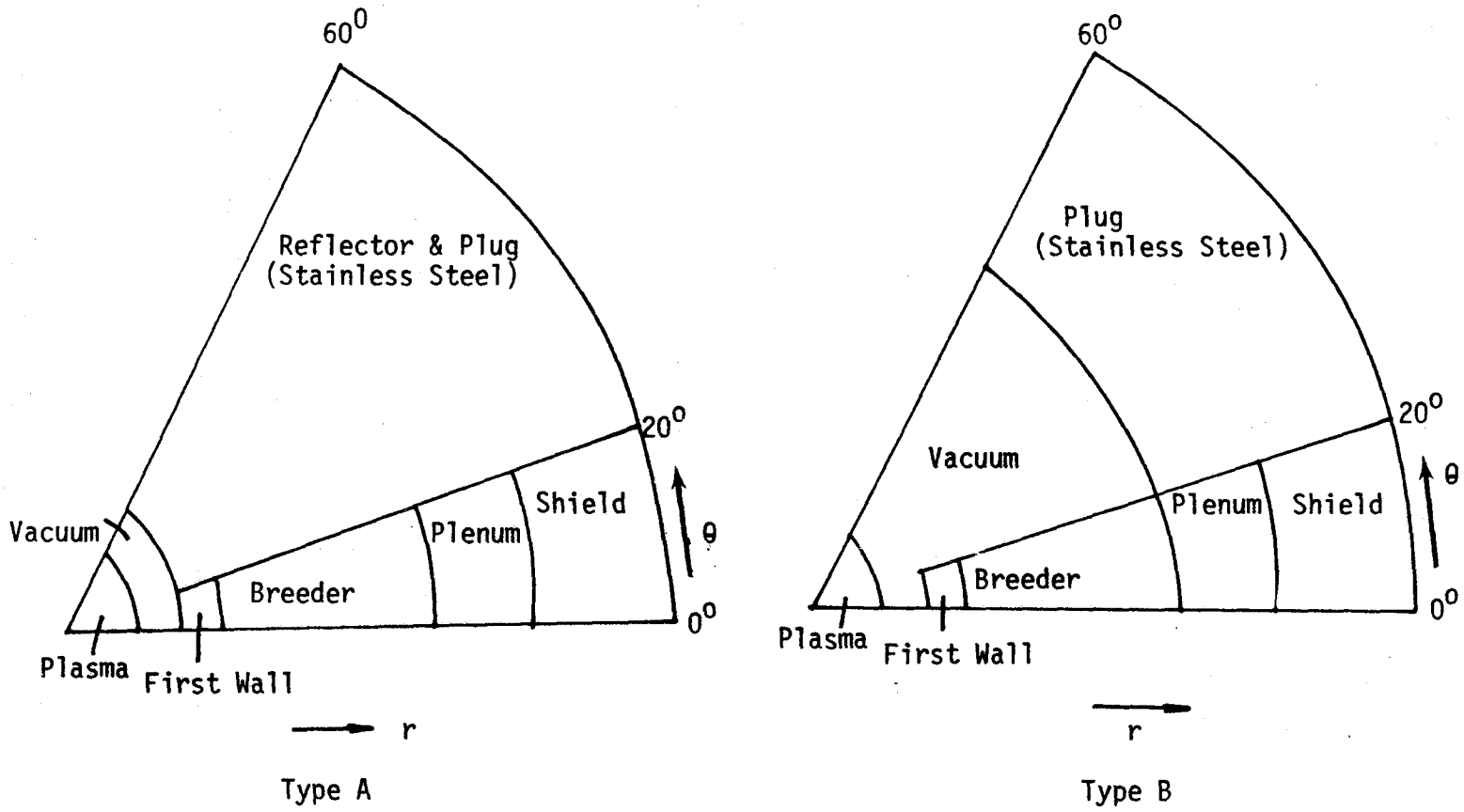

Fig. 5.3.1-23 Two dimensional calculation models.

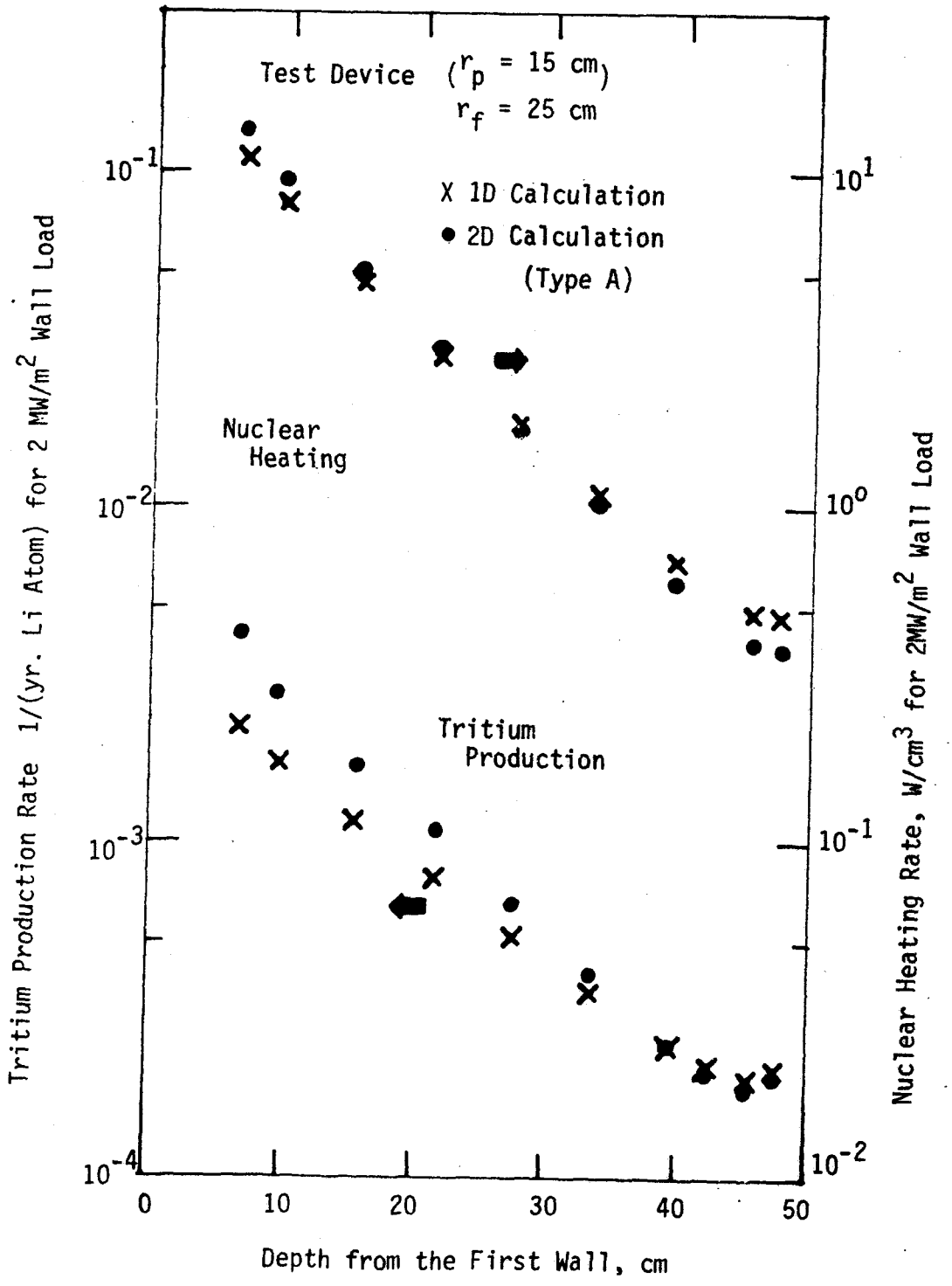

Fig. 5.3.1-24 Depth profiles for the nuclear heating rate and the tritium production rate in the test module calculated in the full coverage and the regular-reflector partial coverage geometries.

energy neutrons, which were produced in the reflector by (n,2n) reactions. Neutron multiplication is pronounced in the front region, where the neutron spectrum is harder, so the enhancement ocurred mainly in the front region. High energy neutrons leaked away from the module more quickly in the single module test geometry as compared to the full coverage geometry, so the values became a little lower at the back of the breeder. Overall, the reflector influence on heating rate is very small, while tritium production is affected quite deep into the breeder.

Figure 5.3.1-25 shows the profile of the nuclear heating rate along the θ direction at the front, middle and back of the breeder, where the module half-width is 11 cm, 20 cm and 26 cm, respectively. At the breeder front, the nuclear heating rate was increased not only near the edge, where the value increased sharply, but also in the center region by about 20% as compared to the full coverage case. At the back, the heating rate near the center is ~ 25% less than the full coverage, although the values were enhanced more strongly near the edge than they were at the front of the breeder. The influence of the reflector extended to about 7 cm at the back.

Figure 5.3.1-26 shows similar results for the tritium production rate. This was dominated by $^{6}Li(n,\alpha)T$ reactions, so the reflector influence was more pronounced than in the heating rate. In fact, the influence is noticeable up to 10 cm from each side at any depth.

Figure 5.3.1-27 shows depth profile of the nonreflector geometry Type B. The profile is also the result of averaging over the θ direction. As the module side wall was exposed to fast neutrons, the profile became much more uniform than in the regular reflector geometry. The nonreflector geometry enhanced the parameter at deep positions drastically, so it will be useful to enhance rear blanket fluence, heating or tritium production rates. Figures 5.3.1-28 and 29 show the azimuthal profiles of the parameters. As direct neutrons hit the side wall of the module, the edge effect is more pronounced than in the regular reflector geometry. It extends about 13 cm in from each side at the midpoint and the back, but influences the entire region at the breeder front.

If the azimuthal variation in neutronics profiles near the module edge is undesirable, then the test requires a reflector with similar neutronic properties to those of the module itself. Very good behavior could be obtained with

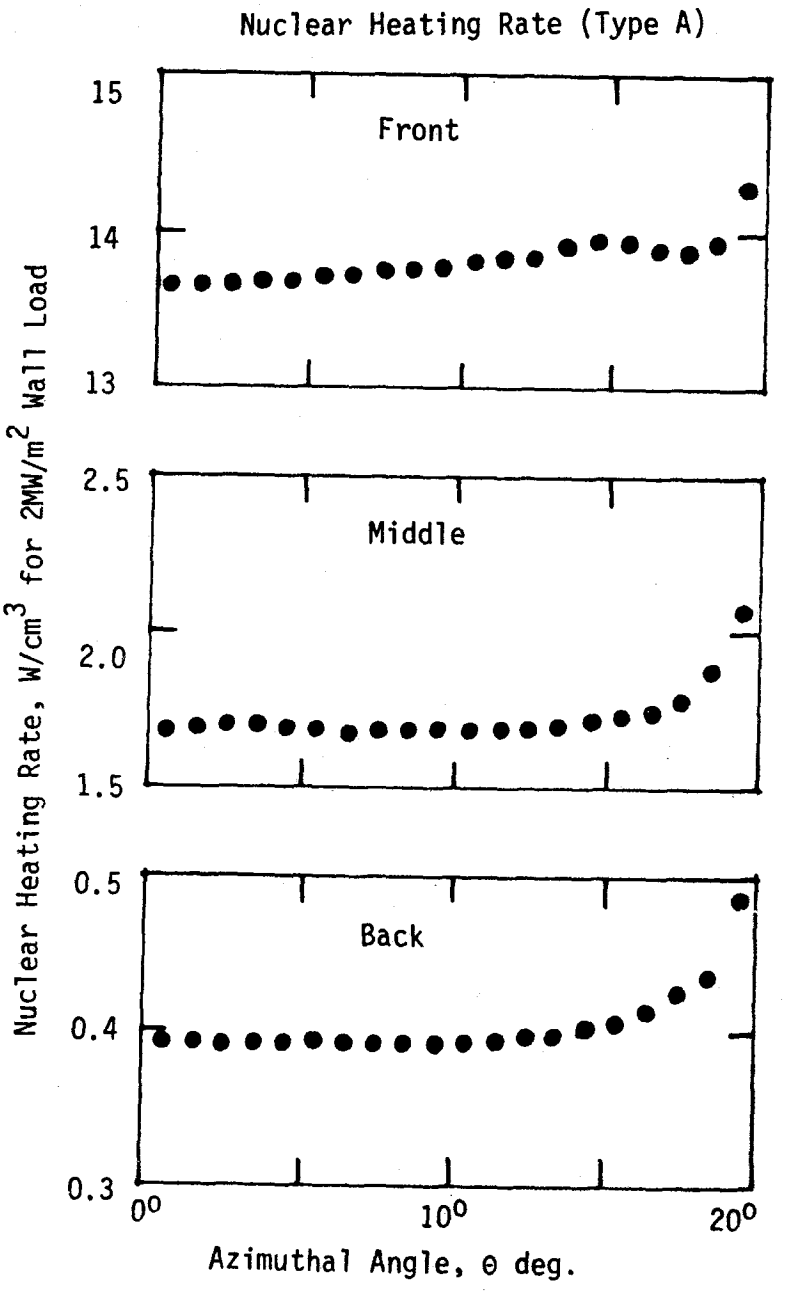

Fig. 5.3.1-25 Azimuthal profiles for the nuclear heating rate at the front edge, midpoint and the back of the breeder in the regular test condtion with the reflector and plug.

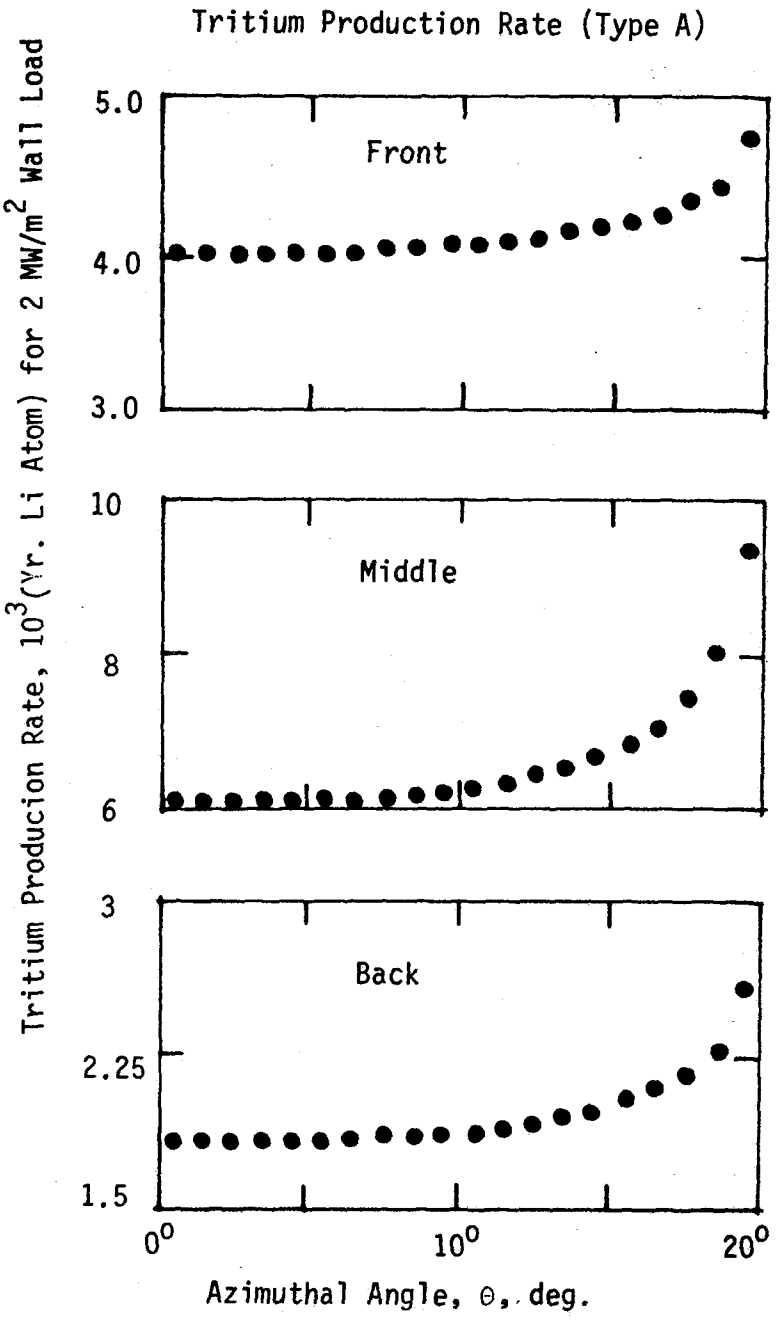

Fig. 5.3.1-26 Azimuthal profiles for the tritium production rate at the front edge, midpoint and the bottom of the breeder in the regular test condition with the reflector and plug.

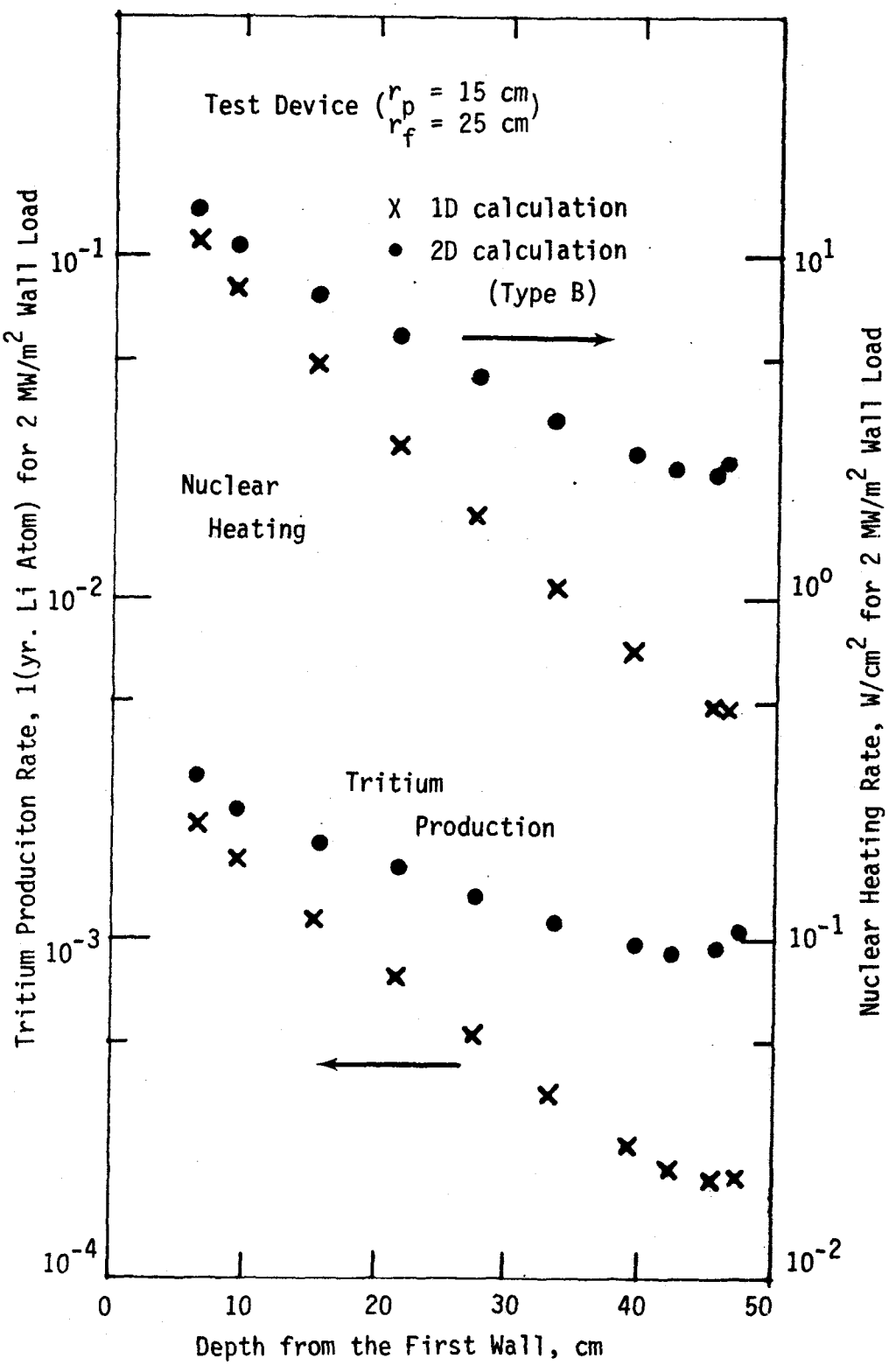

Fig. 5.3.1-27 Depth profiles for the nuclear heating rate and the tritium production rate calculated in the full coverage and the non-reflector partial coverage geometries.

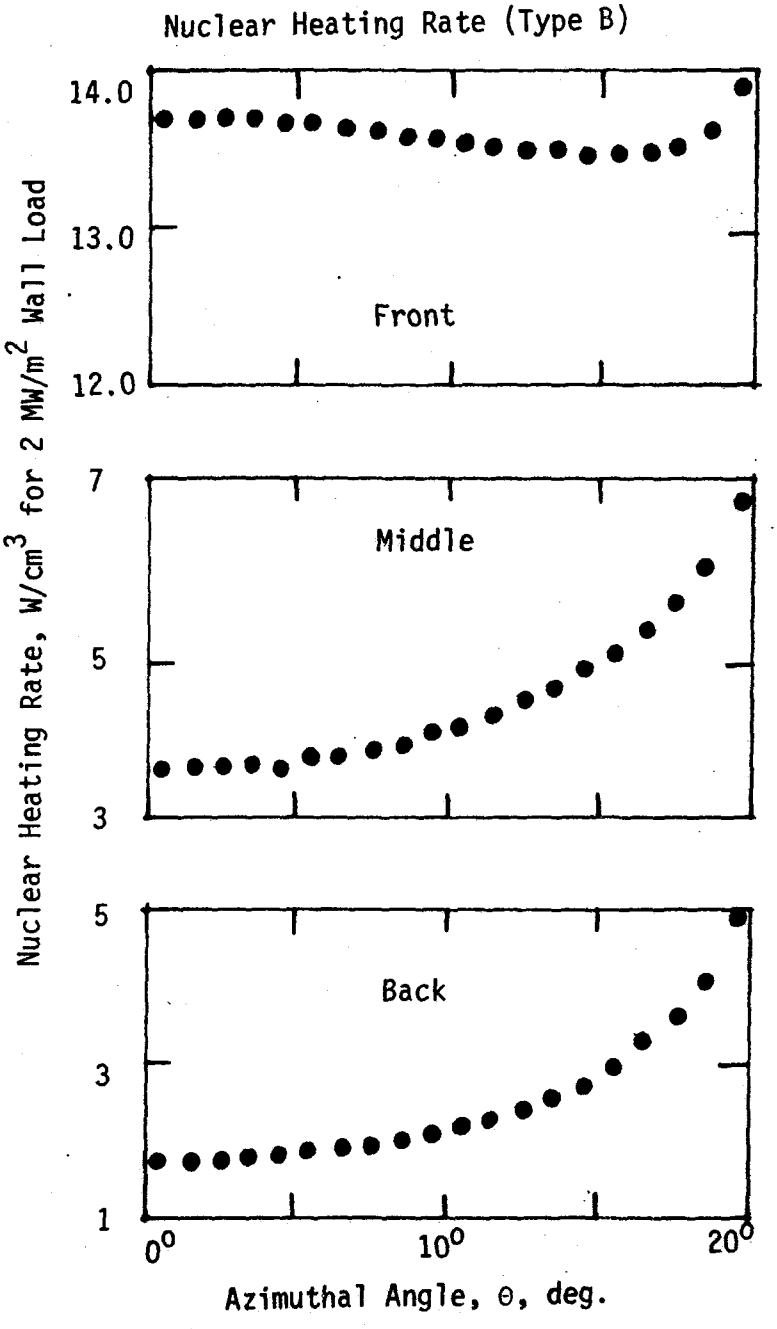

Fig. 5.3.1-28 Azimuthal profiles for the nuclear heating rate at the front edge, midpoint and bottom of the breeder obtained in the nonreflector test geometry.

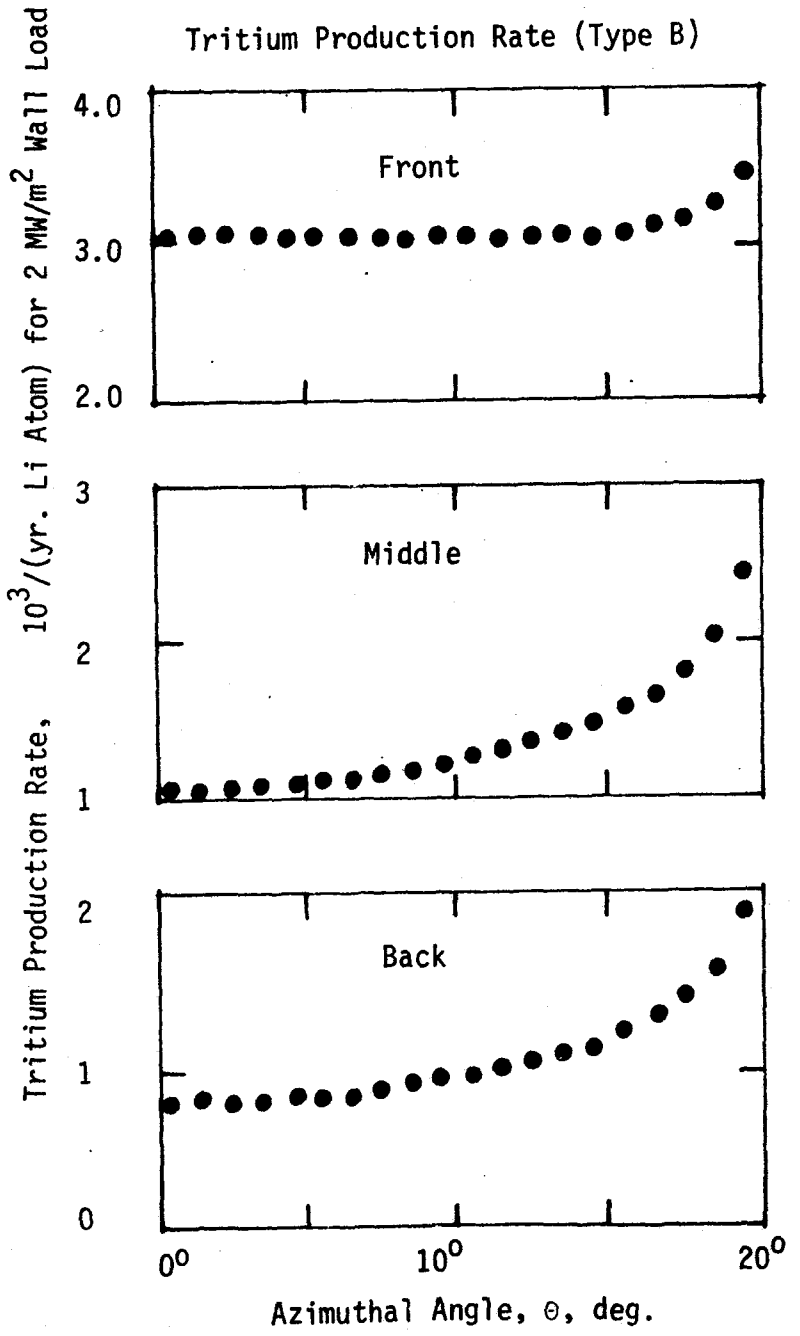

Fig. 5.3.1-29 Azimuthal profiles for the tritium production rate at the front edge, midpoint and bottom of the breeder obtained in the nonreflector test geometry.

a buffer blanket which has the same material composition as that of the test module, although possibly different internal structure. Lithium can also be replaced with boron because both materials show a similar energy dependence of the neutron absorption cross sections.

In summary, the reflector test port geometry may appreciably enhance the tritium production and heating rates in the breeder. A solid steel type of reflector will lead to enhancements of 100% in tritium production and 20% in heating in the front 20 cm of the Li_2O breeder since neutrons may be reflected into the breeder module rather than being absorbed by lithium under reactor full-coverage conditions. Moving the reflector further back will expose the sides of the test module to direct neutrons, and can significantly increase the tritium production and heating at the rear of the breeder (a factor of five), although this will occur primarily within 13 cm of the module edge. The reflector effect will be more pronounced in the $LiAlO_2$ blanket module because the 90% enriched ^6Li makes the blanket parameters more sensitive to low energy neutrons, and hence to the geometrical configuration.

Material Composition Effects on Neutronics Parameters

In a scaled test module, the internal structure of the breeder may be modified by changing thicknesses, densities, or even material constituents. For example, the breeder thickness might be increased under reduced bulk heating conditions in order to keep the solid breeder within the operating temperature for tritium recovery. Or the breeder density or lithium enrichment increased to enhance the tritium production. It is possible that fissile material would be added to increase both heating and tritium production. While these changes would affect several aspects of the blanket behavior, they may also alter the basic neutronics profiles. Here, the effect of varying the basic structural or breeder volume fractions is considered.

The material configurations in Fig. 5.3.1-2 was used as the reference case. Note that the breeder is divided into two zones, Blanket 1 and Blanket 2. The analysis was performed with the ANISN code in one-dimensional cylindrical geometry, and is based on the direct sensitivity method.

In the first case considered, the volume fraction of the structure (HT-9) in Blanket 1 was increased by 100% or 300%, and the volume of the Li_2O decreased by the same amount so the He coolant volume was kept fixed. The

results of the calculation are shown in Fig. 5.3.1-30 in comparison with the reference case results. The 300% increase in structure volume fraction made the nuclear heating rate profile a little steeper (+10% at the front and -40% at the back of the Blanket 1 zone), but the overall deviation is relatively small. Similar comments apply to the tritium production rate, although these decreased even at the front of the breeder. The reason for the decrease is the higher rate of neutron capture in the structure.

In the second case, the Li_2O density was decreased from 80% to 70% or 60%. The Li_2O grains were assumed to be packed more loosely in the breeder plates, and the vacuum volume was correspondingly increased. Figure 5.3.1-31 shows the calculated results. Both nuclear heating and tritium production rates decreased near the front of the breeder, but increased at deeper position. This was because it was easier for neutrons to penetrate through the lower density breeder to deep regions.

These results indicate that the neutronics parameters are not strongly sensitive to the material volume fractions. Thus, it is reasonable to consider varying dimensions or densities if needed to preserve non-neutronic blanket behavior. However, the usefulness of changes in composition specifically to modify or enhance the neutronics paramaters was not analyzed.

5.3.1.5. Summary

A fusion test facility is likely to be different in both neutron power and configuration from a reactor. The test module itself may even be changed. Some neutronics consequences of these differences were explored here. Changes in neutron wall load directly affect the absolute values of neutronics parameters such as nuclear heating rate, tritium production and radiation damage. The effects of the configuration are more complex. They may be divided into effects due to changes in the test facility and to changes in the test module.

The device size affects the absolute values of the neutronics parameters, even for fixed neutron wall load due to geometric effects related to the surface curvature. In particular, the first wall radius should be larger than 20 cm or the neutronics parameters will be more than 20% smaller than expected in a larger device at the same wall load. The azimuthal profiles of neutronics parameters around the module first wall perimeter are also affected by the

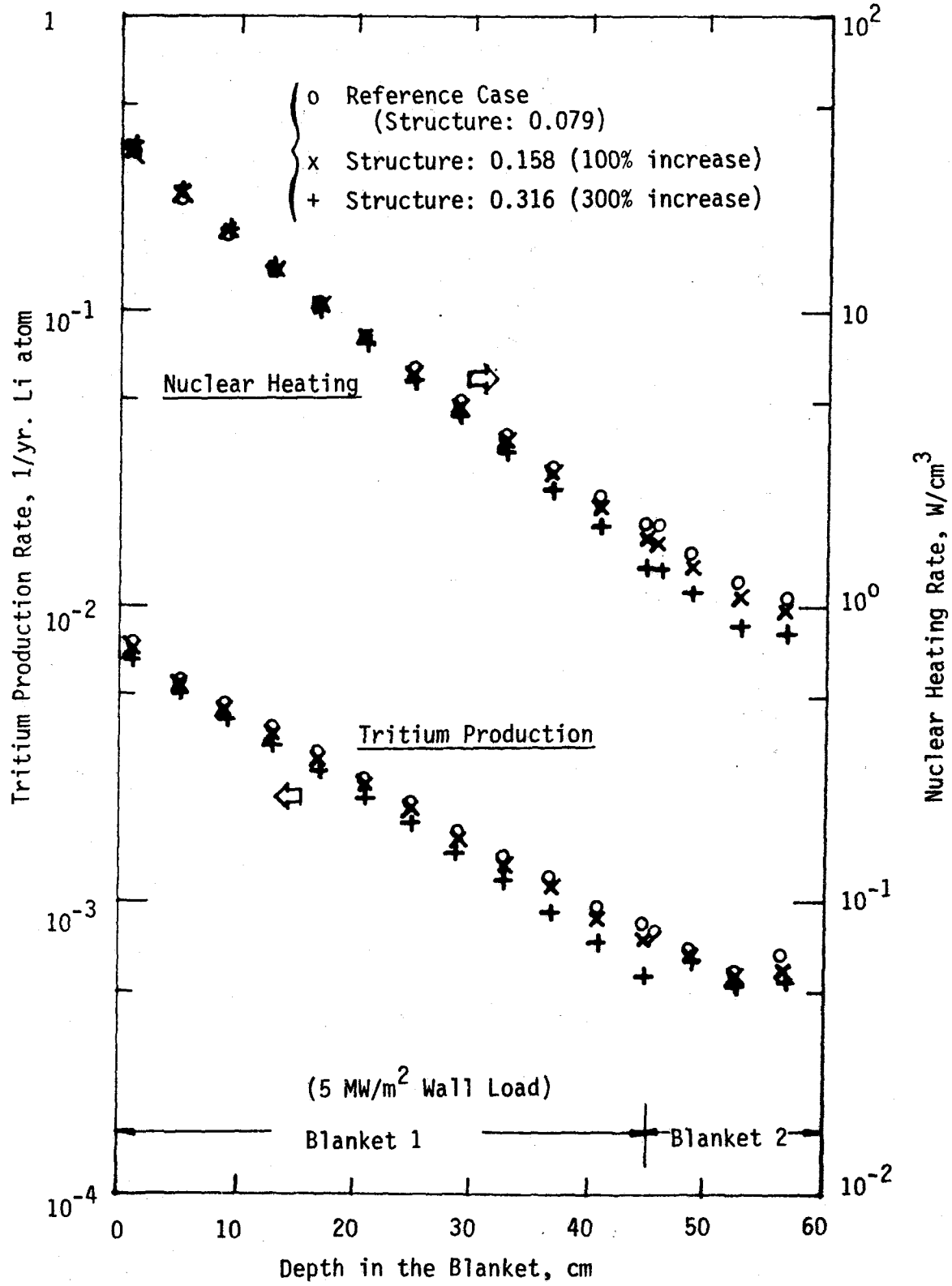

Fig. 5.3.1-30 Effect of the structure volume fraction on the profiles for the neutronics parameters in the breeding zone.

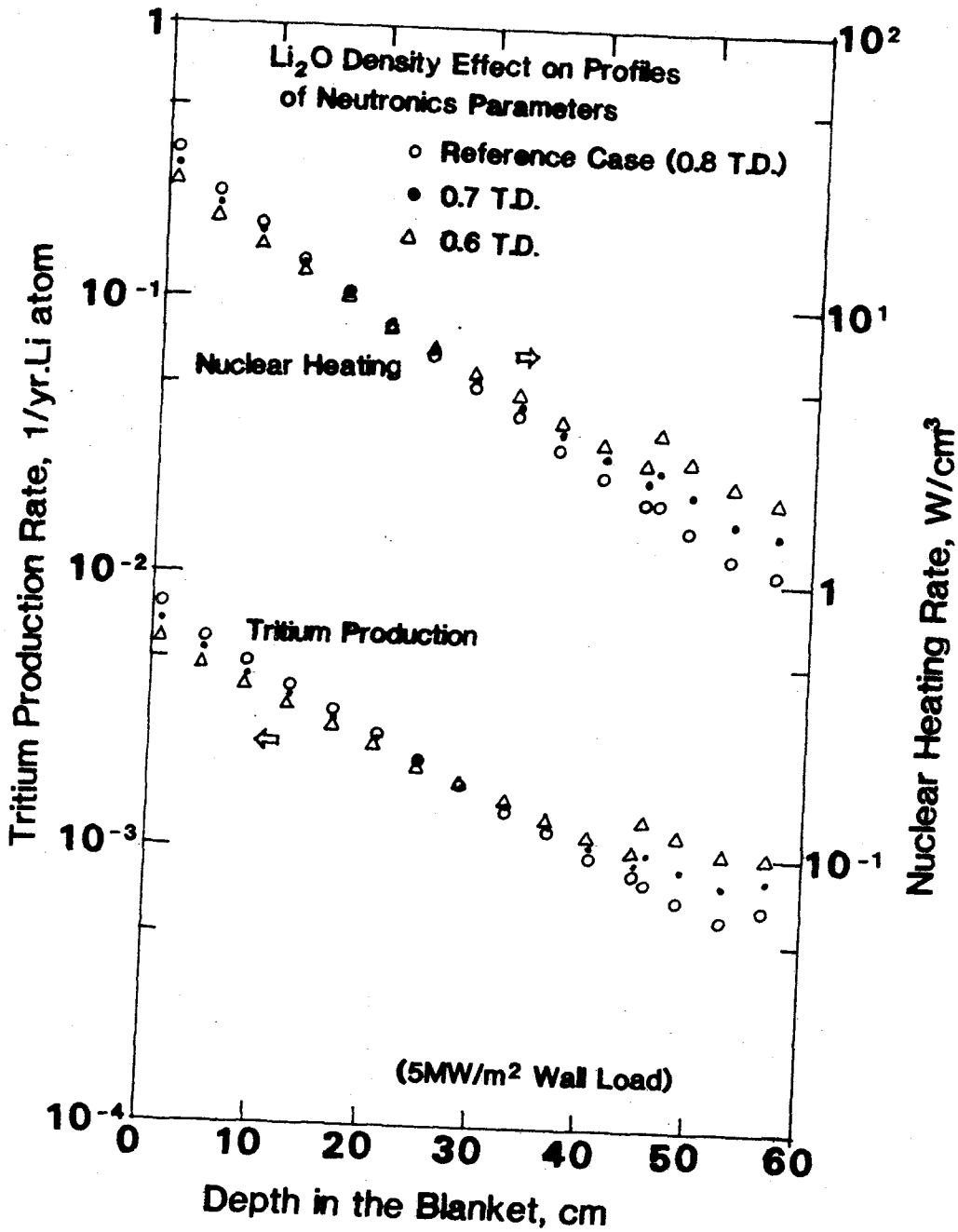

Figure 5.3.1-31 Impact of the Li_2O density factor on the profiles for the neutronics parameters in the breeding zone.

device size. For the nuclear heating rate, a 1/r profile is expected, where r is the distance from the plasma centerline. This profile effect is larger in smaller test devices. The corresponding test requirement is to keep the first wall radius large compared to the module dimensions. Conversely, changes in the device size have little effect on the depth profiles of the neutronics parameters which are governed primarily by the neutron mean free path in the materials.

The test environment in the test facility may also influence the module neutronics behavior. A single module placed in a test port where it is surrounded by reflector and structure - not other breeder modules - will give rise to higher tritium production and heating rates at the front of the breeder by ~ 100% and ~ 20%, respectively, for the Li_2O/He/HT-9 blanket and stainless steel reflector. If the reflector is moved back to expose the module side directly to neutrons, then the neutronic parameters at the breeder back are enhanced by a factor of five. This latter enhancement holds within about 13 cm of the edges due to the attenuation of the neutrons.

The test module itself may also be modified to suit the scaled test conditions. Normally, the first wall is thin compared to the neutron mean free path so there is little variation in neutron flux and related parameters across the first wall. For example, the effective attenuation length for the nuclear heating rate is ~ 70 mm for both the Li_2O and $LiAlO_2$ tokamak blanket first walls, while the reactor wall thickness is 10.8 mm and 11.9 mm, respectively. If the first wall thickness is increased in the test module, however, then there eventually is appreciable attenuation in neutron flux and fluence across the first wall. This degrades the neutronics performance of the breeder, but may also give rise to undesirable effects in the first wall. This suggests limiting the first wall dimensions to less than the neutron mean free paths, or about 5 cm based on the rapid attenuation of the high energy neutrons needed for He production (swelling) and transmutation.

The thickness of the test module may be decreased to conserve test volume. The breeder thickness does not strongly affect the neutronics parameters in either absolute value or profile if a rear shield or reflector is used to minimize neutron leakage. A minimum thickness of 20 cm is suggested in order to achieve over 80% of the full tritium production and to allow for interactions between radial breeder regions with substantially

different neutron exposure.

The peak burnup of lithium atoms is about 7% in Li_2O and 50% in $LiAlO_2$ under reference conditions, and less under reduced neutron wall load conditions. The change in tritium production and heating under scaled test conditions (reduced wall load and limited test time) is not likely to be large, but the need to explore burnup-related effects may set test requirements.

The neutronics parameters are not strongly sensitive to the material composition in the breeder zone. For example, a 300% increase in the structural volume fraction caused a +10% deviation at the front and a -40% deviation at the back. And a decrease in the Li_2O density results in more moderate profiles, the attenuation coefficient of which is roughly proportional to the total atom density in the breeder.

These conclusions are largely based on analysis of the Li_2O/He/HT-9 blanket, but are expected to be applicable to other solid breeder blankets. The major difference is that many other solid breeders require a neutron multiplier and ^6Li enrichment in order to achieve sufficient tritium breeding. This leads to a greater contribution of low energy neutrons to their neutronics behavior than in the Li_2O breeder considered. In particular, the breeder thickness effect and the influence of the test port configuration will be more pronounced. Suppressing these effects requires that the reflector and plug material use materials with similar neutronics properties to those in the test module - i.e., lithium or boron.

References for Section 5.3.1

1. W. W. Engle, Jr., "A User's Manual for ANISN", Oak Ridge National Laboratory, RSIC-CCC-82 (July 1973).

2. "DOT-IV, Version 4.3, One- and Two-Dimensional Transport Code System", Oak Ridge National Laboratory, RSIC-CCC-429 (April 1982).

3. "VITAMIN C: 171 Neutron, 36 Gamma Group Cross-section Library in AMPX Interface Format for Fusion Neutronics Studies", Oak Ridge National Laboratory, Pkg DLC-41 (1978).

4. Los Alamos Monte Carlo Group, "MCNP - Monte Carlo Neutron and Photon Transport Code", Oak Ridge National Laboratory, RSIC/CCC-200 (1983).

5. M. A. Abdou et al., "Blanket Comparison and Selection Study, Interim Report", Vol. I and II, Argonne National Laboratory, ANL/FPP-83-1 (October 1983).

6. K. Shin and T. Hyodo, "Analysis of Applicability of Albedo Concept to Neutron Streaming Through Ducts and Slits", Proc. 6th Inter. Conf. on Rad. Shielding, Tokyo (May 1983).

5.3.2 Thermal Analysis

5.3.2.1 Introduction

In Section 5.2.2, several phenomena related to the thermal behavior of solid breeder blankets were considered. The goal was to understand the thermal-hydraulic conditions and phenomena under reactor conditions, and to develop models for describing these phenomena. Here, these models are applied to determining the module thermal behavior under scaled test conditions, evaluating methods to preserve temperature profiles and flow conditions, and to determine test requirements based on these analyses. In particular, the effects of a test facility that has a reduced heat source, operating time (i.e., pulsed operation) and small test volume are considered with respect to the first wall temperature distribution, breeder temperature distribution, flow conditions and (briefly) corrosion.

5.3.2.2 First Wall Temperature Distribution

The first wall temperature profile is important for structural behavior and tritium permeation. But if the first wall heat source (surface or volumetric) in the test facility is reduced relative to the reactor values, then the temperature distribution will not be preserved. This is illustrated in Fig. 5.3.2-1 for the reference Li_2O/He/HT-9 tokamak blanket. As the heat source decreases, so does the temperature rise across the structure.

In order to maintain the temperature distribution in any test facility, consider the dependence of the temperature profile on controllable variables. Specifically, the overall profile may be roughly described by an inlet temperature, T_{inlet}; a bulk coolant rise, ΔT_{bulk}; a film rise, ΔT_{film}; and a first wall surface rise, ΔT_{fw}. From Section 5.2.2.1, these are:

$$\Delta T_{bulk} \simeq c\,(q_s d_{fw} + 1.6\,\dot{Q}_v d_{fw}^2 + \ldots)\,\frac{R_{fw}}{U_{fw} d_{fc} d_{fw}} \qquad (5.3.2\text{-}1a)$$

$$\Delta T_{film} \simeq c\,(q_s d_{fw} + \dot{Q}_v d_{fw}^2)\,\frac{d_{fc}^{0.2}}{U_{fw}^{0.8} d_{fw}} \qquad (5.3.2\text{-}1b)$$

$$\Delta T_{fw} \simeq c\,(q_s d_{fw} + 0.5\,\dot{Q}_v d_{fw}^2) \qquad (5.3.2\text{-}1c)$$

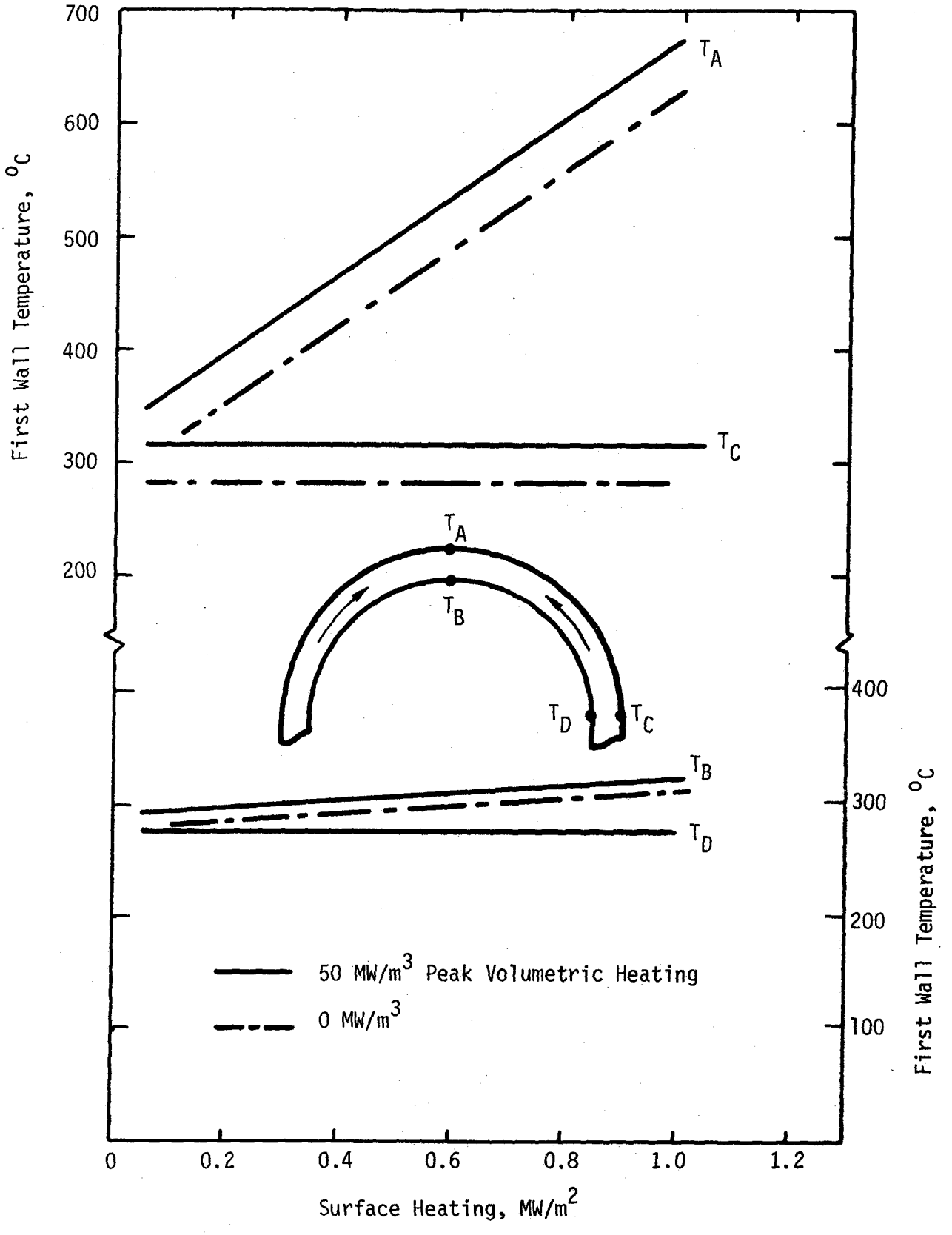

Figure 5.3.2-1 Effect of reducing the heat source on the Li_2O/He/HT-9 tokamak first wall temperature distribution.

where R_{fw} is the first wall lobe radius of curvature, d_{fc} is the equivalent diameter of the first wall cooling channels, U_{fw} is the first wall coolant velocity, d_{fw} is the first wall thickness, q_s is the surface heat flux, $\dot{Q}_v$ is the volumetric heating and c contains leading constants and materials properties.

In addition, the temperature profile is still important within the first wall, and it might be useful to preserve the average temperature, $\overline{\Delta T}_{fw}$, or the temperature gradient, $\overline{\nabla T}_{fw}$.

$$\overline{\Delta T}_{fw} \simeq c\,(q_s d_{fw} + 0.7\,\dot{Q}_v d_{fw}^2) \qquad (5.3.2\text{-}2a)$$

$$\overline{\nabla T}_{fw} \simeq c\,(q_s d_{fw} + 0.5\,\dot{Q}_v d_{fw}^2)\,\frac{1}{d_{fw}} \qquad (5.3.2\text{-}2b)$$

For example, thermal stresses in a simple structure are zero at the average temperature position, and increase (in tension or compression) away from this point. Thus it would be desirable to maintain $\overline{\Delta T}_{fw}$ and its location to preserve thermal stresses.

There will also be local variations in temperature, such as in the vicinity of the channel supporting walls,

$$\Delta T_{fs} \lesssim c\,(q_s d_{fw} + \dot{Q}_v d_{fw}^2)\,\frac{d_{fs}}{d_{fw}} \qquad (5.3.2\text{-}3)$$

where d_{fs} is the supporting wall thickness. As these equations alone show, it is difficult to exactly preserve the temperature profile as the heat source changes. In particular, the term $(q_s d_{fw} + b\,\dot{Q}_v d_{fw}^2)$ is common, but $b \simeq 0.5$-1.6, depending on the particular ΔT. Thus the relative contribution from surface and volumetric heating cannot be retained.

However, it is desirable to see how close the temperature can be simulated, and derive test requirements based on where the deviation becomes "large." A plausible approach is to maintain ΔT_{fw} (for the thermal stress range) and T_{inlet}, ΔT_{film} and ΔT_{bulk} (for overall average temperatures). It should be noted that there is no unique method, and this particular one may not be optimum. However, it has the advantage of simplicity and illustrates the features that are likely to be observed for any reasonable approach.

Preserving ΔT_{fw} involves varying d_{fw} with q_s and $\dot{Q}_v$ as given by Eq. 5.3.2-2c. The results are shown in Fig. 5.3.2-2a for the reference Li_2O/He-/HT-9 tokamak, and in Fig. 5.3.2-2b for the reference Li_2O/He/HT-9 mirror first wall. In general, surface heating dominates tokamak first walls at reference conditions, while volumetric heating dominates mirror first walls (see also Fig. 5.2.2-2 and -3). Surface heating contributes 85% of the peak ΔT_{fw} in the reference tokamak blankets, and only 25% in the mirror blankets. As the overall heat source is reduced (q_s and $\dot{Q}_v$) and the structure thickened to preserve ΔT_{fw}, the volumetric heating becomes more important. The effect on the first wall temperature profile is shown in Fig. 5.3.2-3. Here, changes in the heat source, whilte preserving ΔT_{fw}, can be seen to affect the temperature profile, and the location and magnitude of the average temperature within the first wall. The tokamak first wall is more strongly affected.

Maintaining ΔT_{bulk} and ΔT_{film} presents a few more choices including changing other dimensions and the flow velocity. As discussed in Section 5.3.4, structural mechanics considerations prefer maintaining geometric aspect ratios. Thus all dimensions are scaled once d_{fw} is chosen. This leaves the first wall velocity, U_{fw}, as a controllable variable. Preserving ΔT_{bulk} and ΔT_{film} corresponds to maintaining Re_{fw}.

If these changes are made, then the effects of varying the heat source on the first wall temperature profile may be calculated. Using the 2-D model described in Section 5.2.2.1, the resulting temperature distribution is shown in Fig. 5.3.2-4.

It can be seen that, for the reference tokamak reactor conditions, surface heating is critical to preserving the temperature distribution. Tokamak first walls are generally dominated by the surface heating contribution and reducing the overall heat source leads to substantial difficulties in preserving temperatures unless surface heating remains dominant. In fact, for some test purposes, it would be preferable to do without volumetric heating if only a limited amount of surface heating is available. Of course, neutron effects are important for integrated testing with radiation damage and tritium production so substantial volumetric heating should be present. Thus, for a given reduction in overall heat source, a tokamak device or any high surface heating test facility would be the most useful. There is no incentive to add additional volumetric heating to the first wall region.

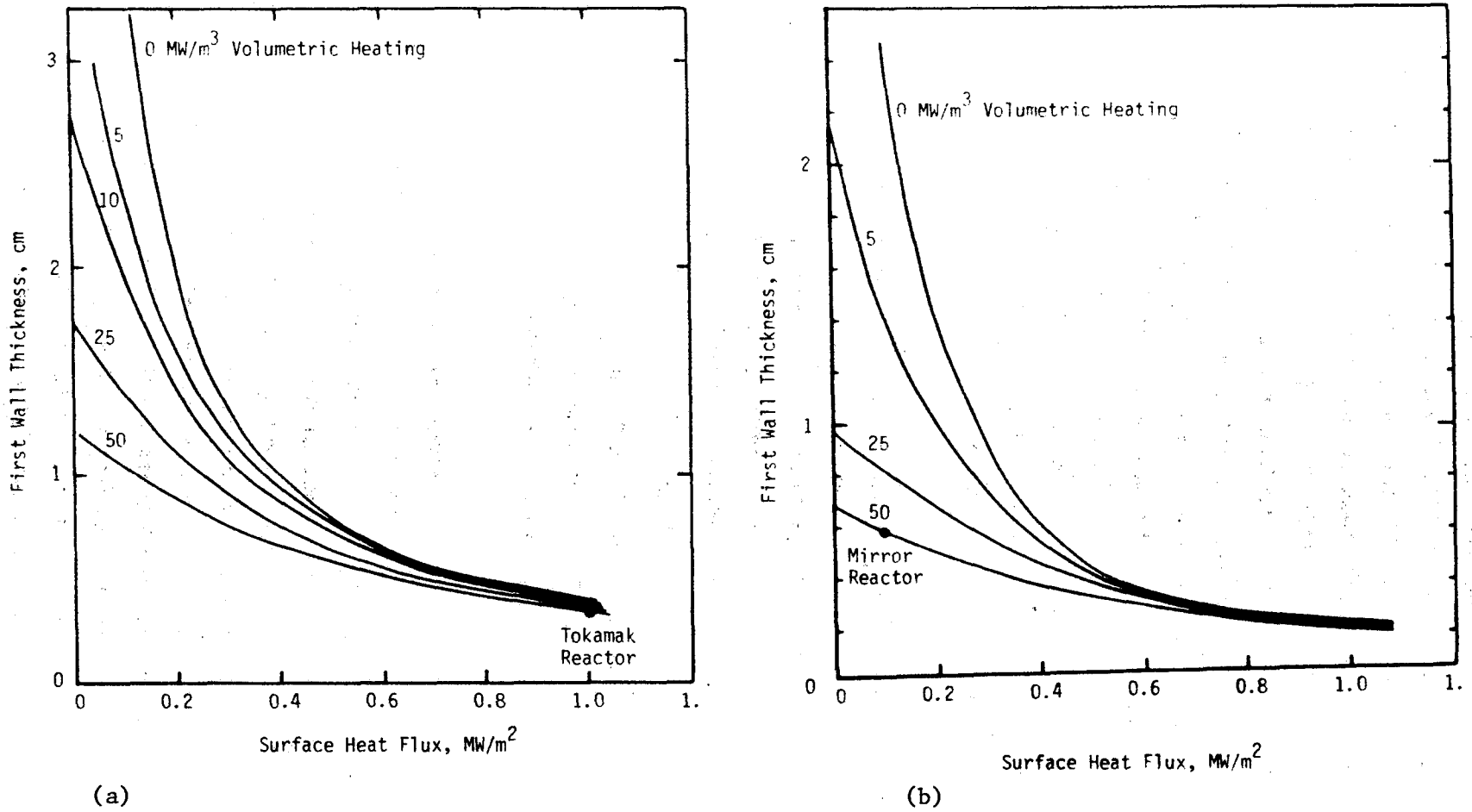

Figure 5.3.2 First wall thickness needed to maintain the first wall ΔT under changed heat load conditions for the Li_2O/He/HT-9 tokamak (a) and mirror (b) blankets.

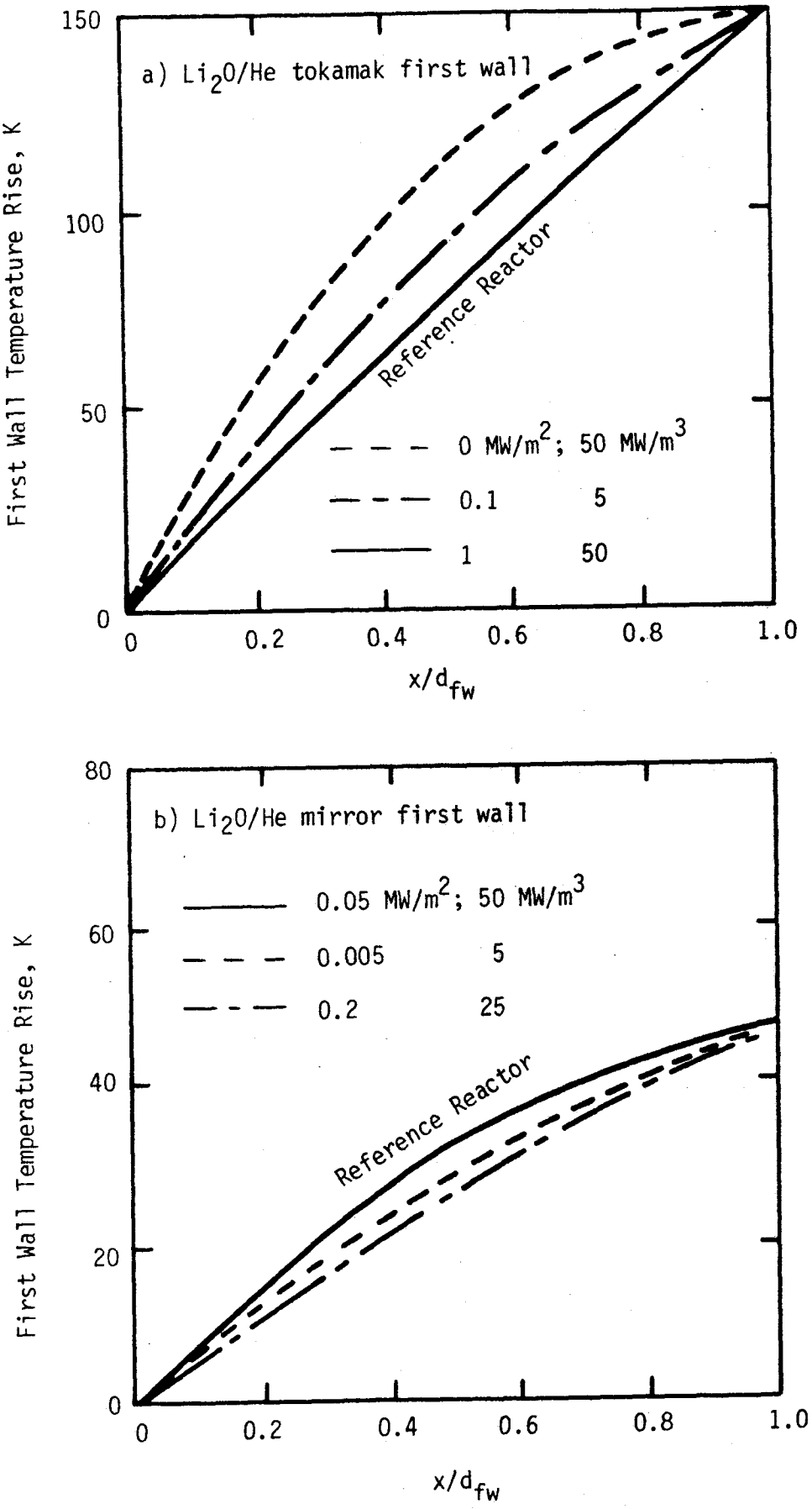

Figure 5.3.2-3 First wall temperature profile under various heat source conditions, with first wall thickness scaled to preserve the overall ΔT.

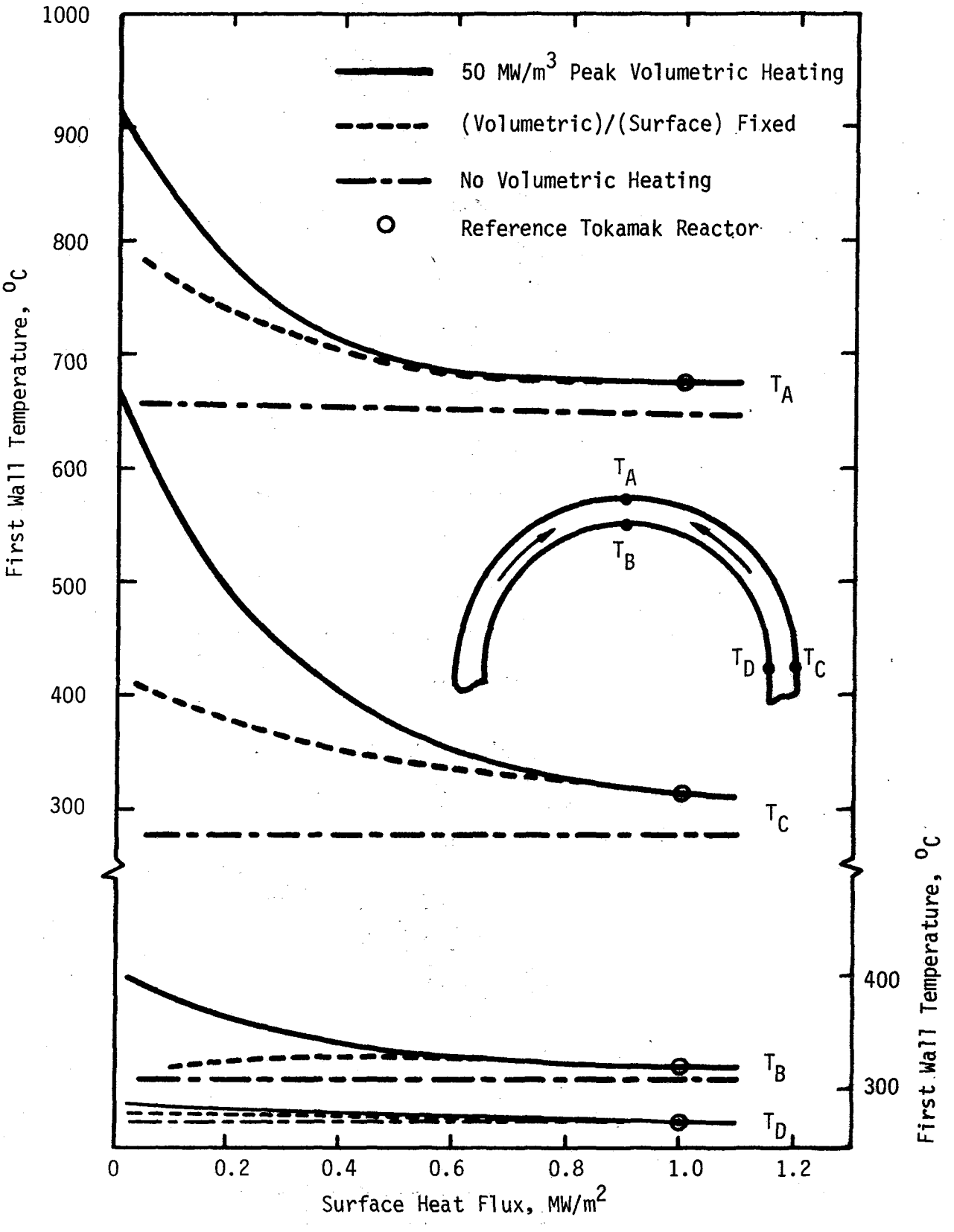

Figure 5.3.2-4 Effects of changing heat source on Li_2O/He/HT-9 tokamak first wall temperature distribution under scaled first wall conditions.

Alternately, a mirror first wall is largely determined by volumetric heating under reference conditions. Under reduced heat source conditions, the first wall would be thickened and volumetric heating enhanced. Thus a mirror first wall scales better under reduced heat source conditions. However, many mirror test facility designs have small central cells (for cost savings) and substantial central cell neutral beam power (to maintain the plasma) leading to potentially larger surface heat fluxes than may be present in a mirror reactor. For example, TDF[1] estimated an average central cell surface heat flux of 0.1-0.3 MW/m^2, with up to 10 MW/m^2 in the vicinity of the neutral beams. If this surface heating is not reducable, it becomes the dominant contributor to the first wall, and the same problems occur as with tokamaks.

The important point is to that first wall temperatures that are dominated by surface or by volumetric heating will not be preserved if this dominant form of heating is not preserved. As a rough measure of this point, consider $\Delta T_s/\Delta T_v$, where ΔT_s is the first wall temperature rise due to surface heating and ΔT_v is the temperature rise due to bulk heating:

$$\frac{\Delta T_s}{\Delta T_v} \simeq \frac{2q_s}{\dot{Q}_v d_{fw}} \qquad (5.3.2\text{-}4)$$

For a volumetric-heating dominated mirror blanket, $\Delta T_{fw} \simeq \dot{Q}_v d_{fw}^2/2k$ and $\Delta T_s/\Delta T_v \ll 1$, leading to the test requirement

$$q_s \ll \left(\frac{\dot{Q}_v k \Delta T_{fw}}{2}\right)^{0.5} \qquad (5.3.2\text{-}5)$$

For a surface-heating dominated tokamak blanket, $\Delta T_{fw} \simeq q_s d_{fw}/k$ and $\Delta T_s/\Delta T_v \gg 1$, leading to

$$q_s \gg \left(\frac{\dot{Q}_v k \Delta T_{fw}}{2}\right)^{0.5} . \qquad (5.3.2\text{-}6)$$

These are shown in Fig. 5.3.2-5 for the Li_2O/He/HT-9 and $LiAlO_2/H_2O$/PCA/Be reference designs.

5.3.2.3 Solid Breeder Temperature Distribution

Almost all of the phenomena which are essential to solid breeder mechanical behavior and tritium recovery are strongly temperature dependent. Figure

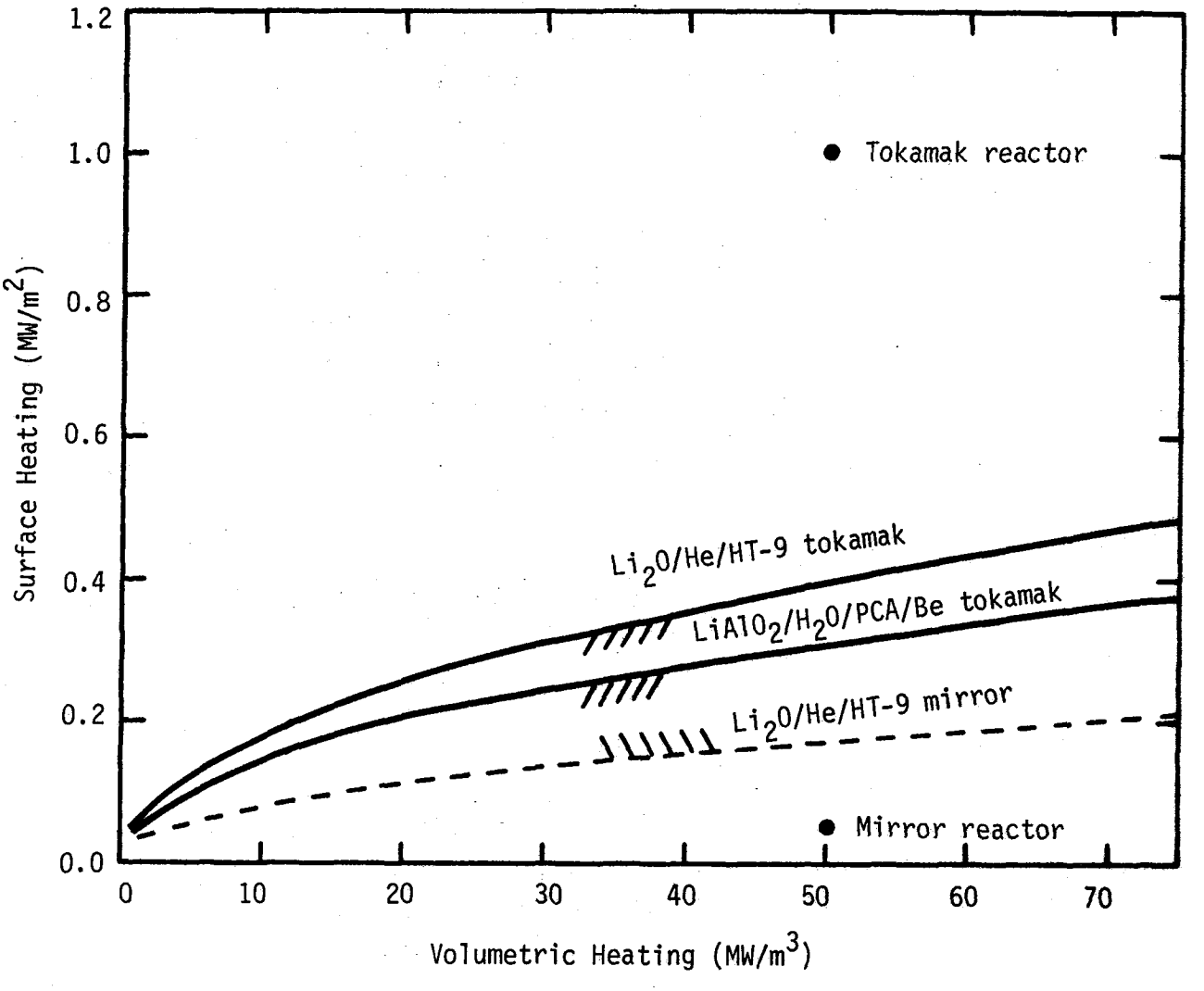

Figure 5.3.2-5 Boundary between surface heating and volumetric heating dominated first wall temperature profiles.

5.2.2-6 depicts this graphically. Therefore, it is important that an "act-alike" test module have the same temperature distribution as the reference blanket solid breeder.

Effects of Reduced Volumetric Heating

Under reduced heating conditions, the temperature profile in the breeder and coolant retain the same basic shape but with reduced range, gradient and average values. It is desirable to modify the blanket design to compensate for these changes and restore the breeder temperatures. To address this problem, the temperature profile may be characterized by a limited set of bounding parameters and these examined to determine the conditions necessary to preserve them as the heat source changes.

Neglecting changes in the heat generation profile, there are six basic contributors to the breeder temperature profile: coolant bulk temperature rise, ΔT_c; film temperature rise, ΔT_{film}, clad temperature rise; gap temperature rise, ΔT_{gap}; breeder temperature rise, ΔT_b, and the breeder temperature gradient, ∇T_b The first two are generally small, well understood and can be controlled by altering the coolant inlet conditions, coolant channel dimensions and coolant flow rate. The gap conductance may be very important, but its scaling is uncertain and not treated in this analysis. The breeder temperature rise is particularly important since the breeder must operate within a specific temperature window. The breeder temperature gradient is not presently considered significant under reference conditions, but may cause unexpected effects. As a minimum goal for preserving the temperature "distribution", the coolant conditions could be altered so as to maintain the breeder minimum temperature, and the breeder temperature rise itself controlled by other means.

Breeder Temperature Rise The breeder temperature profile in radial slab and axial cylinder geometry has been calculated in Section 5.2.2. The basic profile in the breeder is essentially unchanged under reduced volumetric heating conditions, although the range and average values will decrease. In particular, under uniform heat generation conditions, the temperature variation from the breeder centerline to the nearest coolant channel is given by

$$\Delta T_b = \frac{\dot{Q}_v \, d_b^2}{2\,k} \; f(d_b/d_c) \qquad (5.3.2\text{-}7)$$

where

$$f(x) = \begin{cases} 1 & \text{slab} \\ \left(1 + \frac{1}{x}\right)^2 \ln(1+x) - \frac{1}{x} - \frac{1}{2} & \text{cylinder} \end{cases} \qquad (5.3.2\text{-}7a)$$

where d_b is the coolant-to-breeder centerline distance and d_c is the coolant channel half-width. In order to preserve ΔT_b under reduced heating, it is necessary to alter the thermal conductivity or change the dimensions. Since the effective breeder thermal conductivity is uncertain, the only practical approach is to adjust the dimensions according to Eq. (5.3.2-7). Note that for the cylindrical case, over the range $d_b/d_c \sim 0.1\text{-}5$ of interest, $f(d_b/d_c)$ varies from 1 - 2. This variation may be neglected as a first approximation (with the understanding that it could be included in more detailed analyses), leading to the fundamental scaling approach

$$d_b \propto \dot{Q}_v^{-0.5} \qquad (5.3.2\text{-}8)$$

As a numerical example, consider a test facility with a neutron wall load of 1 MW/m^2. Table 5.3.2-1 lists the reference blanket breeder parameters as well as those of a Li_2O/He/HT-9 test module assuming the above scaling relation (and similar approximations for the film, gap and coolant temperature rise). Since the test module volumetric heating is smaller, the breeder thickness has been increased such that the same breeder temperature rise is achieved. Figure 5.3.2-6 shows the test module solid breeder with contours of constant temperatures, obtained with a 2-D finite element conduction code. The numerical results of the reference blanket are also shown for several breeder locations, and it can be seen that the temperatures of the reference breeder and test module are fairly close.

However, there are several phenomena that were not considered in this analysis, including axial conduction, temperature gradients, variation in heat generation profile, coolant entry length and breeder end effects.

Axial Conduction It was shown in Section 5.2.2 that axial conduction affects the breeder by decreasing the front breeder temperature while increasing the

Table 5.3.2-1. Solid Breeder Blanket Parameters

	Li_2O/He tokamak	$LiAlO_2$/H_2O/Be tokamak	Li_2O/He test module
Neutron wall load, MW/m^2	5	5	1
Peak nuclear heating, MW/m^3	50	60	10
Nuclear heating attenuation length, m	0.1	0.1	0.1
Unit cell dimensions:			
Along coolant channel, m	0.42	2	0.42
Cross-section, m^2	0.011 x 2	0.02 x 0.02	0.025 x 2
Coolant inlet velocity, m/s	20	5	6.3
Inlet heat transfer coefficient, W/m^2-K	2550	20000	972
Gap conductance, W/m^2-K	3000	—	3000
Coolant pressure, MPa	5.1	15.2	5.1
Purge stream pressure, MPa	0.1	0.1	--
Coolant inlet/outlet Temperatures, °C	320/510	280/320	320/510

Plain Numbers Test Module Numerical Result

( ) Reference Blanket Numerical Result

All numbers in ^{o}C

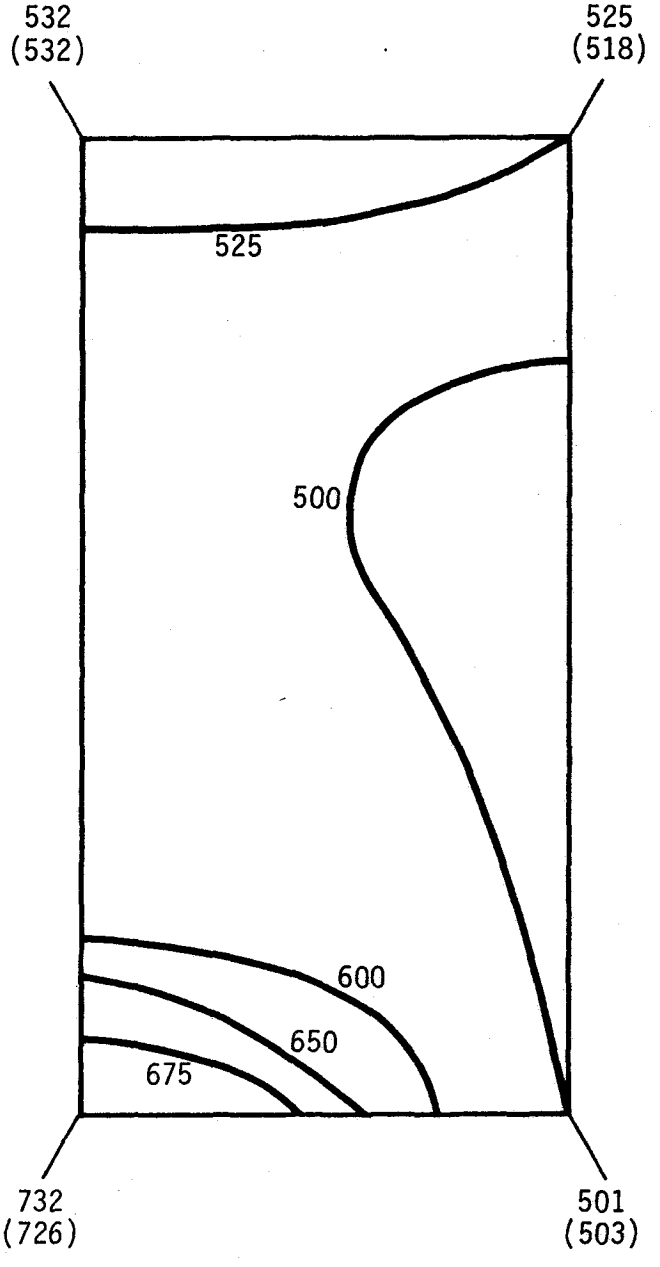

Figure 5.3.2-6 Temperature contours for layered solid breeder test module ($q_{nw,T}$ = 1 MW/m^2) and its comparison with Li_2O/He/HT-9 reference blanket.

back temperature. This is not a major effect under reactor conditions due to the thinner breeder and lower temperature gradients in this axial direction. However, under reduced heating with the thicknesses modified as described by Eq. (5.3.2-8), axial conduction may become more significant in reducing the important peak temperatures.

One way to handle axial conduction cooling of the front breeder in the test module, if necessary, is to thicken the breeder so as to add further heating and increase the breeder temperature rise,

$$d_b \propto \left(\dot{Q}_v\, g(0)\right)^{-0.5} \qquad (5.3.2\text{-}9)$$

The back temperature, however, will be doubly higher now due to the increased thickness to compensate for the front conduction cooling as well as the axial conduction. Overall, however, axial conduction is not expected to be a major influence on the temperature profile for either the plate or axial cylinder breeder designs.

Temperature Gradients In fission fuel pins, the temperature gradient is about 5×10^5 K/m and a variety of processes are activated. For example, closed pores migrate up the temperature gradient; and fuel constituents such as oxygen, plutonium and fission products are redistributed.[2] The speed of these diffusional processes is generally of the form[2,3]

$$U \sim \frac{Ce^{-Q/\kappa T}}{T^n} \nabla T \qquad (5.3.2.10)$$

where the exact dependence varies with the rate controlling phenomena - solid matrix diffusion, surface diffusion or vapor diffusion, for example. Typical speeds are $0.1\text{-}10 \times 10^{-10}$ m/s for pore and fission gas movement in fission fuel pins.[2,3]

In solid breeders, the diffusion of pores, helium bubbles, LiOT and tritium will also be affected by the temperature gradient. However, typical gradients are around 5×10^4 K/m, or an order of magnitude less than in fission fuel. Furthermore, the temperature is generally colder. Thus it is not presently believed that the temperature gradient is significant in solid breeders. But since there is very little data to confirm this, and assuming

that the effects scale directly with $\overline{\nabla T}_b$, it would be desirable to preserve the gradient in the test module.

The average temperature gradient across the solid breeder is

$$\overline{\nabla T}_b \propto \frac{\Delta T_b}{d_b} \propto \frac{\dot{Q}_v d_b^2}{d_b} \qquad (5.3.2\text{-}11)$$

Consequently, it is not possible to preserve both the breeder ∇T and ΔT simultaneously ($\Delta T \propto \dot{Q}_v d_b^2$), and if the latter is considered more important, then

$$\overline{\nabla T}_b \propto \dot{Q}_v^{1/2} \qquad (5.3.2\text{-}12)$$

In other words, the temperature gradient decreases as the volumetric heating (i.e., neutron wall load) decreases.

Effects of Pulsed Operation

So far, the test module thermal behavior has been considered under steady-state conditions. But it is likely that near-term test devices will be pulsed. In this section, the consequences and test requirements due to pulsing effects on solid breeder temperatures are considered.

Figure 5.3.2-7 shows the temperature-time history of the reference breeder (designed for steady-state operation) under particular pulsed conditions. The figure shows the values for breeder maximum and minimum temperatures, as well as those for steady-state operation. It is observed that it takes about two full cycles (under these pulsed conditions) for the breeder temperature to approach quasi-equilibrium conditions. However, the peak quasi-equilibrium temperatures are considerably lower than those for steady state.

Furthermore, Figure 5.3.2-7 does not reveal the entire extent of the breeder deviation from steady-state conditions. This may be better visualized by a plot of the temperature density, which shows the mass distribution of temperature averaged over the breeder and one pulse. Figure 5.3.2-8 shows the breeder temperature density for steady operation and for pulses where the burn and dwell time are equal to the breeder thermal characteristic time. It is seen that the temperature density under pulses is drastically different than

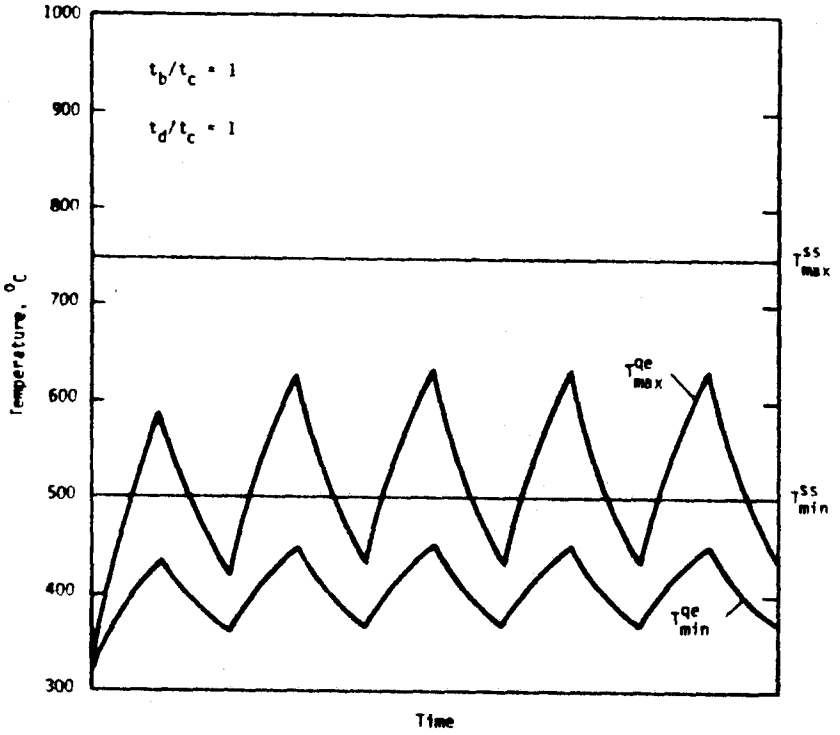

Figure 5.3.2-7 Temperature-time history of solid breeder under pulsed conditions.

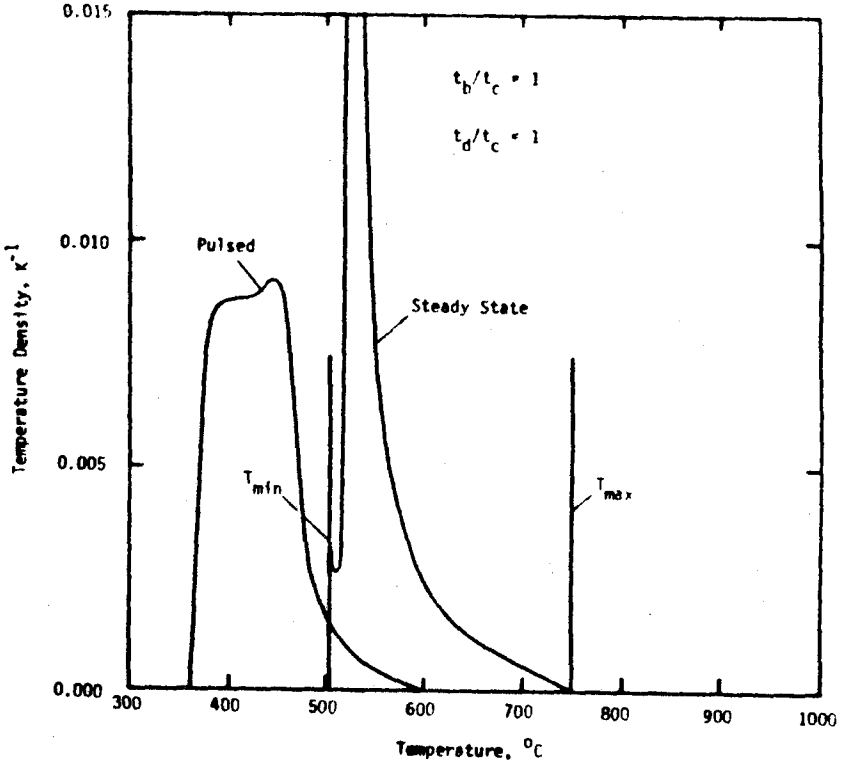

Figure 5.3.2-8 Comparison of temperature density at steady-state and pulsed conditions in the Li_2O blanket.

that for steady operation. Two distinctive pulsing effects may be observed: (1) the whole temperature distribution has shifted to lower temperatures; and (2) the temperature density is more spread out.

Modified Breeder under Pulses Since the temperature variations due to pulsing may cause unacceptable changes in tritium recovery and structural behavior, consider possible approaches to recovering the steady-state conditions. At least two obvious degrees of freedom exist for achieving this goal:

1. Increasing coolant inlet temperature;

2. Increasing breeder thickness.

The effect of each of these modifications may be estimated from the breeder temperature solution in Section 5.2.2 (slab geometry),

$$T^i_{max} = T_{in} + (c_1 d_b + c_2 d_b^2)\, u^i \qquad (5.3.2\text{-}13)$$

$$T^i_{min} = T_{in} + c_1 d_b u^i \qquad (5.3.2\text{-}14)$$

where c_1 and c_3 are constants depending on breeder geometry and properties and u^i (i = min, avg or max) is the thermal response of the breeder to a unit step function in heat generation. It may be observed that combinations of these two modifications might be more useful in controlling the temperature under pulsed operation than either alone. The temperatures in Eqs. (5.3.2-13) and (5.3.2-14) are read as, for example, T^{avg}_{max} is the time-averaged value of the breeder maximum temperature. It is seen that for any desired values of T_{min} and T_{max}, Eqs. (5.3.2-13) and (5.3.2-14), can be solved for the coolant inlet temperature, T_{in}, and breeder thickness, d_b.

To illustrate possible test module design options, four types of modifications are considered. The first two are based on modifying coolant temperature and breeder thickness, the third is based on modifying only breeder thickness, and the fourth is based on modifying only coolant flow conditions. These modifications are best described illustratively in Fig. 5.3.2-9, and are defined by:

Type 1 (Figure 5.3.2-9a)

$$\text{average } (T^{qe}_{min}) = T^{ss}_{min} \qquad (5.3.2\text{-}15)$$

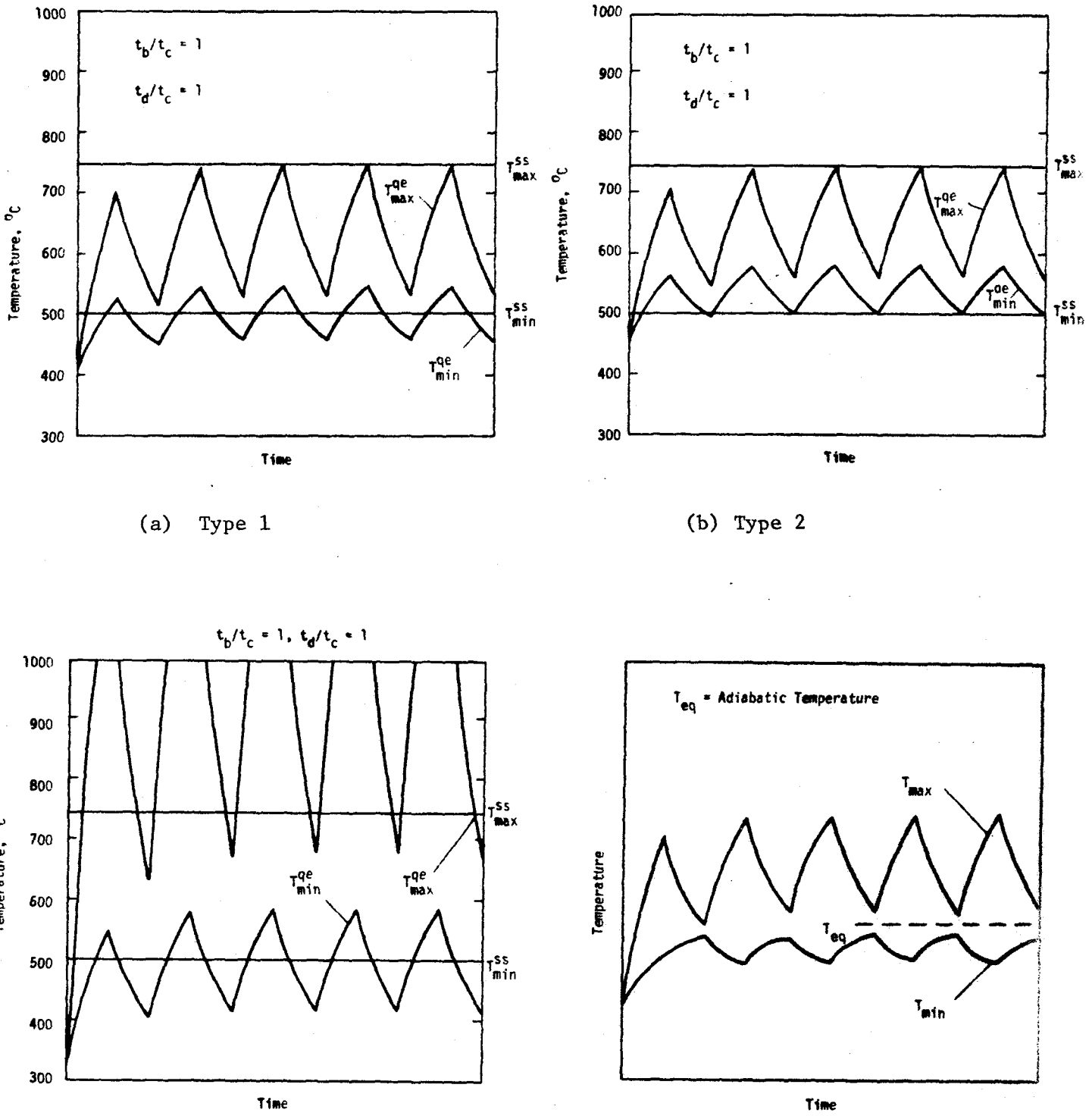

Figure 5.3.2-9 Temperature-time history of solid breeder under pulsed condition for various breeder modification types.

$$\text{maximum } (T^{qe}_{max}) = T^{ss}_{max} \qquad (5.3.2\text{-}16)$$

Type 2 (Figure 5.3.2-9b)

$$\text{minimum } (T^{qe}_{min}) = T^{ss}_{min} \qquad (5.3.2\text{-}17)$$

$$\text{maximum } (T^{qe}_{max}) = T^{ss}_{max} \qquad (5.3.2\text{-}18)$$

Type 3 (Figure 5.3.2-9c)

$$\text{average } (T^{qe}_{min}) = T^{ss}_{min} \qquad (5.3.2\text{-}19)$$

$$\Delta T = 0 \qquad (5.3.2\text{-}20)$$

Type 4 (Figure 5.3.2-9d)

coolant flow turned off during dwell time

The consequences of the modifications can also be seen through the breeder temperature density profiles. Figure 5.3.2-10 show the temperature density under steady-state and pulsed conditions for breeder modified types 1-3. Again, a plausible burn and dwell time equal to the breeder thermal characteristic time has been chosen in these numerical examples. It can be seen that the temperature densities under pulsed conditions are now closer to those for steady state than in the case of unmodified breeder (Fig. 5.3.2-8).

Type 1 has the advantage of having an averaged low temperature equal to minimum steady state temperature, which is derived in cconsideration of those phenomena dependent on temperature. Type 2, meanwhile, has the advantage of having a distribution shape slightly closer to that for steady state. Also, its minimum temperature does not fall below the minimum steady-state temperature. Depending on the importance of the lower temperature limit, either modification may be preferred. Type 3 does not reproduce the temperature density as well, but does avoid modifying the clad temperature and possibly affecting tritium permeation or structural behavior. Type 4 was not analysed in detail here. The idea is to shut off the coolant flow rate during the dwell period, and so thermally isolate the breeder. It is expected that the fluctuations may be weaker and remain within the temperature window without

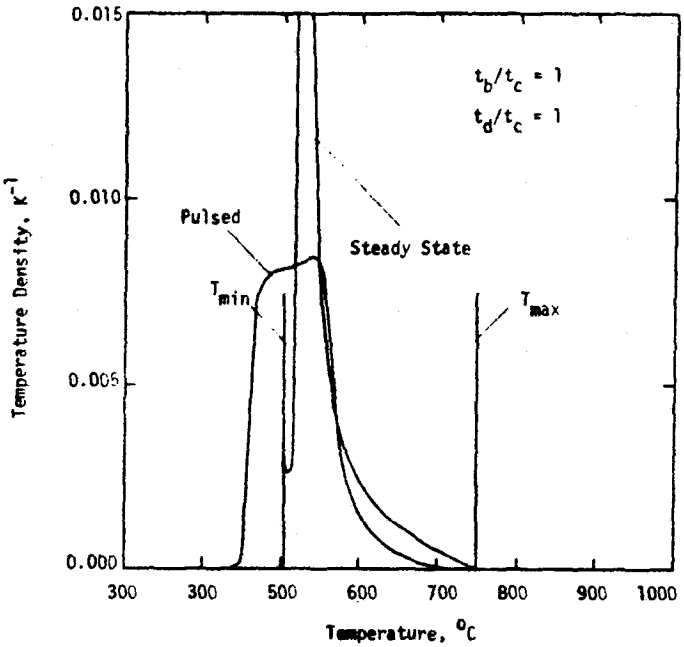

(a) Type 1

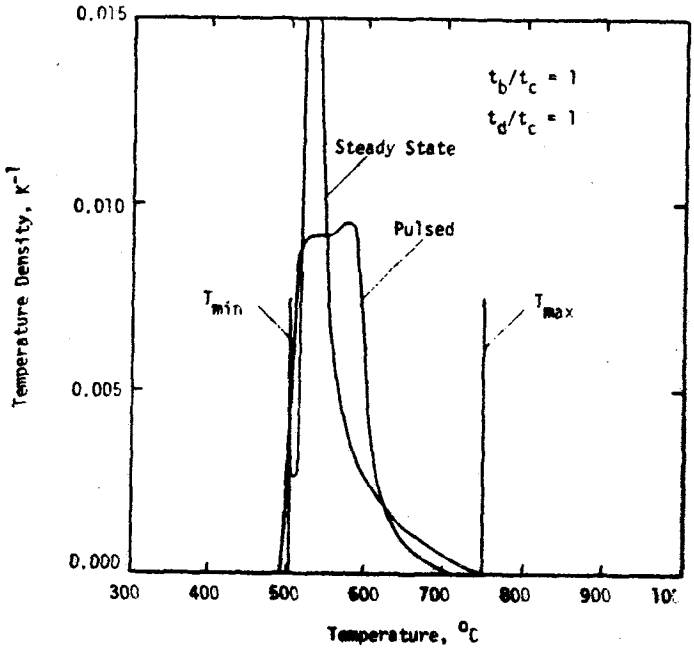

(b) Type 2

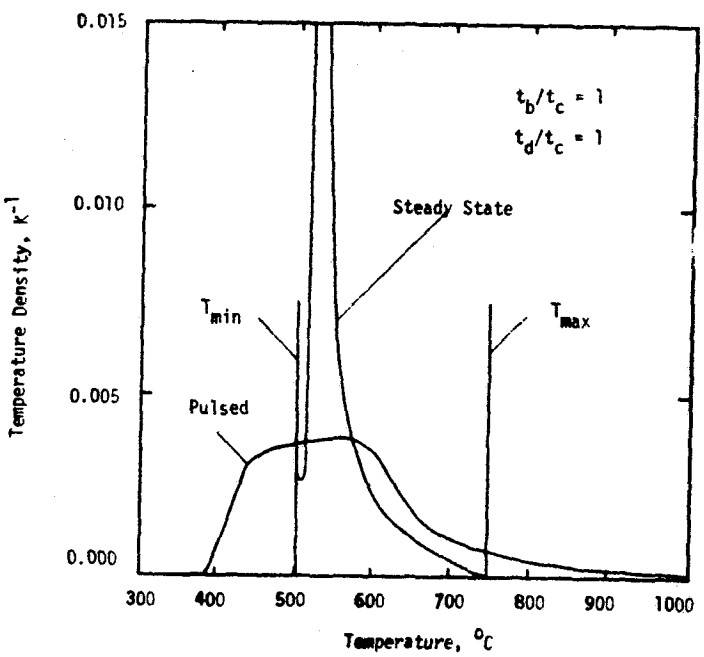

(c) Type 3

Figure 5.3.2-10 Comparison of temperature denisty at steady state and quasi equilibrium pulsed conditions for various breeder modifications.

ted. However, in no case has the true steady-state distribution been recovered.

Burn and Dwell Time Basically, these modifications can modify the breeder to compensate for the reduction in average input power as a result of the pulsing. However, the "rounding" of the time-averaged temperature density cannot be controlled. Given, then, that pulsing can affect the breeder temperature distribution in ways that may not be entirely compensated, one can consider what amount of pulsing is acceptable. For demonstration purposes, only breeder modification Type 1 is considered. The results are shown in Figs. 5.3.2-10 and 5.3.2-11, where burn and dwell times are varied over a wide range. Two classes of behavior are observed:

1. Longer burn and shorter dwell times tend to give a reasonable overall distribution. The distribution has a sharp peak and does not fall as much to lower temperatures.

2. Shorter burn and longer dwell times tend not to reproduce the desired time-averaged distribution. The temperature density is shifted to colder temperatures and has a relatively rounder peak. In extreme cases, the temperature density develops a second (and cold) peak due to the long time spent in the dwell period.

The corrections necessary for these modifications are calculated by solving Eqs. (5.3.2-13) and (5.3.2-14) with the desired maximum and minimum temperatures. Figure 5.3.2-12 show the results for the coolant inlet temperature and breeder thickness corrections for modified breeder Types 1 and 2. In these figures, the particular correction is plotted as a function of duty cycle for various values of the burn time. The coolant inlet temperature correction is seen to be generally less than 200 K in the range plotted. However, it increases with decreasing duty cycle and increasing burn time. It is also observed that the Type 2 modifications require more correction. The breeder thickness correction, d_b^{qe}/d_b^{ss}, is plotted in Fig. 5.3.2-12. The correction is usually in the range of 0.7-2 for the range of parameters considered. The corrections required for Type 3 modification are not shown but simply given by

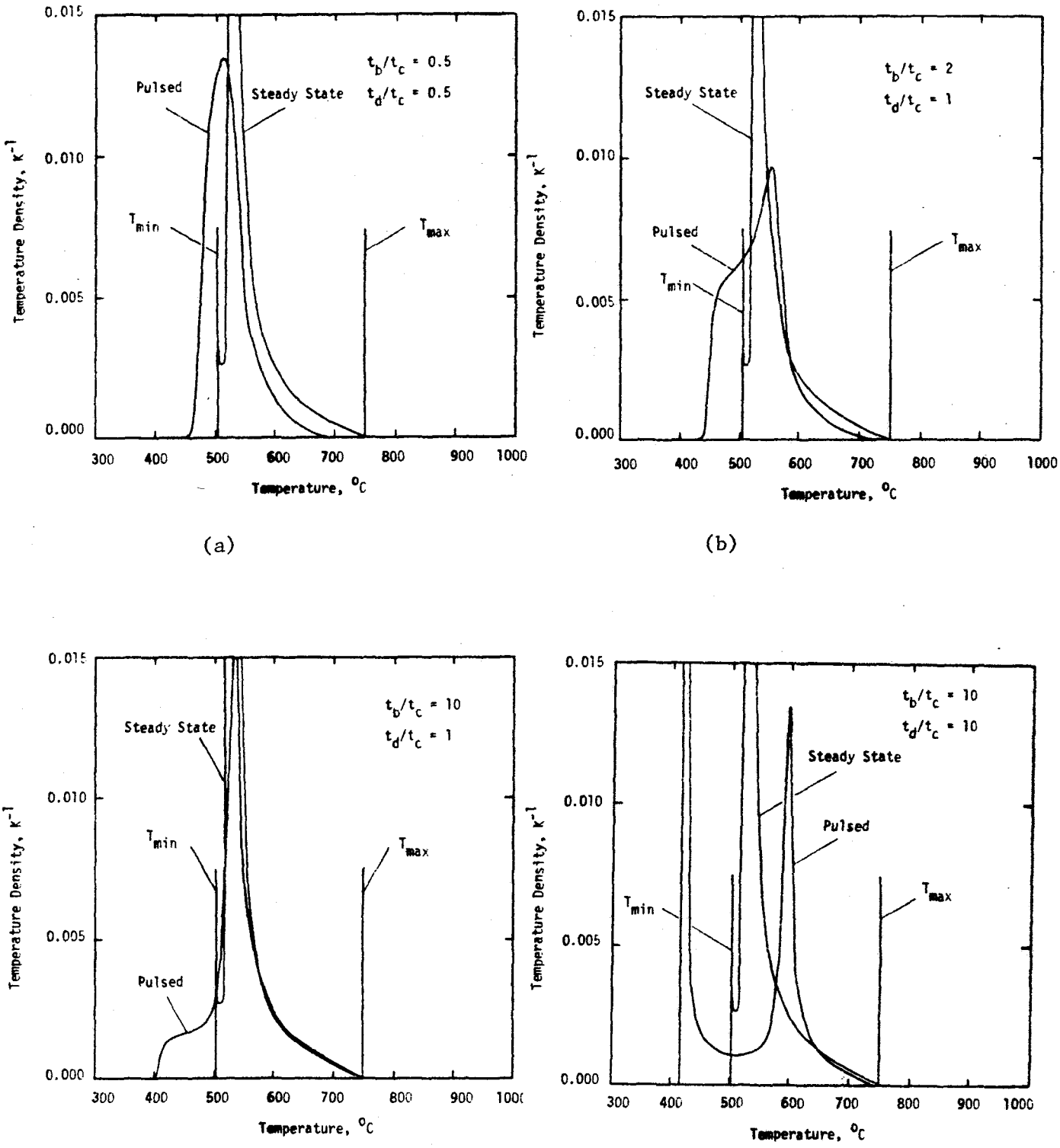

Figure 5.3.2-11 Comparison of temperature density at steady state and quasi equilibrium pulsed conditions for various burn and dwell times.

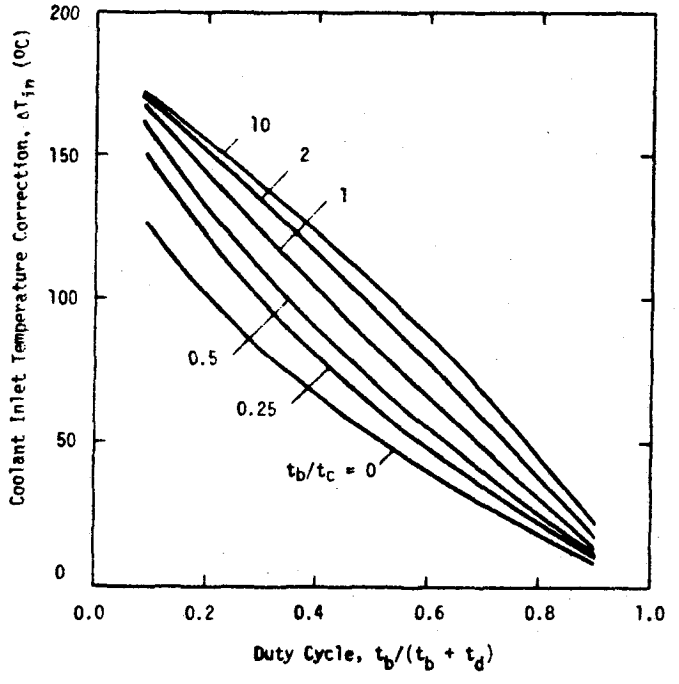

(a) Type 1

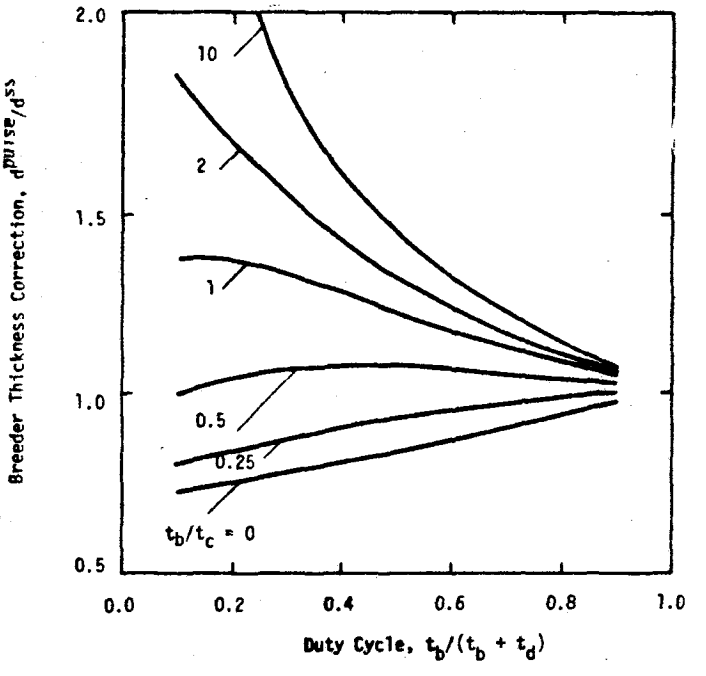

(b) Type 1

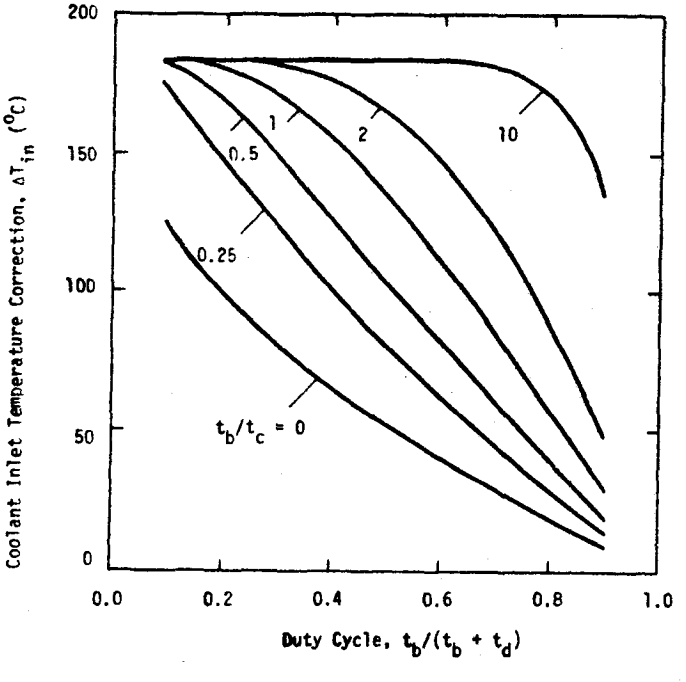

(c) Type 2

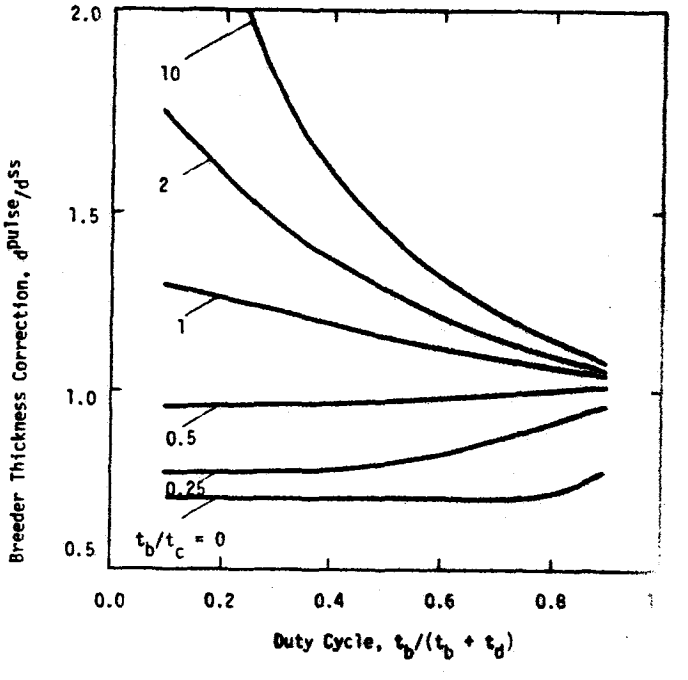

(d) Type 2

Figure 5.3.2-12 Coolant inlet temperature and breeder thickness corrections for breeder modified types 1 and 2.

$$\Delta T_{in} = 0 \tag{5.3.2-21}$$

$$\frac{d^{qe}}{d^{ss}} = \frac{1}{u^{avg}} = \frac{t_b + t_d}{t_b} = \frac{1}{\text{duty cycle}} \tag{5.3.2-22}$$

Although a systematic and quantitative way of measuring the closeness of the temperature distribution of the test module under pulsed conditions to the true steady-state reference temperature is lacking, it is possible to qualitatively define, based on the results of Figs. 5.3.2-10 and 5.3.2-11, limits on burn and dwell times. Figure 5.3.2-13 shows such a qualitative judgment. This figure has divided the range of burn and dwell times into three categories. First, the good distribution region, where $t_b/t_c > 3$ and $t_d/t_c < 3$. This region generally produces temperature distributions similar to those of steady state with a sharply peaked temperature density. Second, the fair distribution region, where $t_b/t_c < 3$ and $t_d/t_c < 3$. This region is characterized by temperature distributions that are slightly shifted and have round peaks. Finally, the poor distribution region, where $t_d/t_c > 3$. This region is associated with highly shifted temperature distributions and with having two peaks. It should be noted, however, that $t_d/t_c < 3$ may be too generous since it allows the breeder to almost fully cool off during the dwell time, leading to large temperature fluctuations, and $t_d/t_c < 1$ is preferred.

Characteristic Times So far, burn and dwell times have always been normalized by the characteristic time, and it has not been possible to set absolute test requirements. The characteristic time, however, does not remain constant when the breeder is redesigned for a reduced heat source and pulsed environment. Thermal characteristic times for Type 1 modified breeder is shown in Fig. 5.3.2-14 as a function of test device neutron wall load while duty cycle and burn times are varied. Figure 5.3.2-14a is for the case of unity duty cycle, or steady-state operation. As the neutron wall load decreases, the modified breeder becomes thicker and the characteristic time increases.

Longer characteristic times demand longer burn time if, for example, the condition of $t_b/t_c > 3$ is required (see Fig. 5.3.2-13). Alternately, if the burn time is given, say 300 s, then the characteristic time should be less than about 100 s. Now for a fixed duty cycle, say 0.5, it can be concluded from Fig. 5.3.2-14c that such a characteristic time requires that the neutron

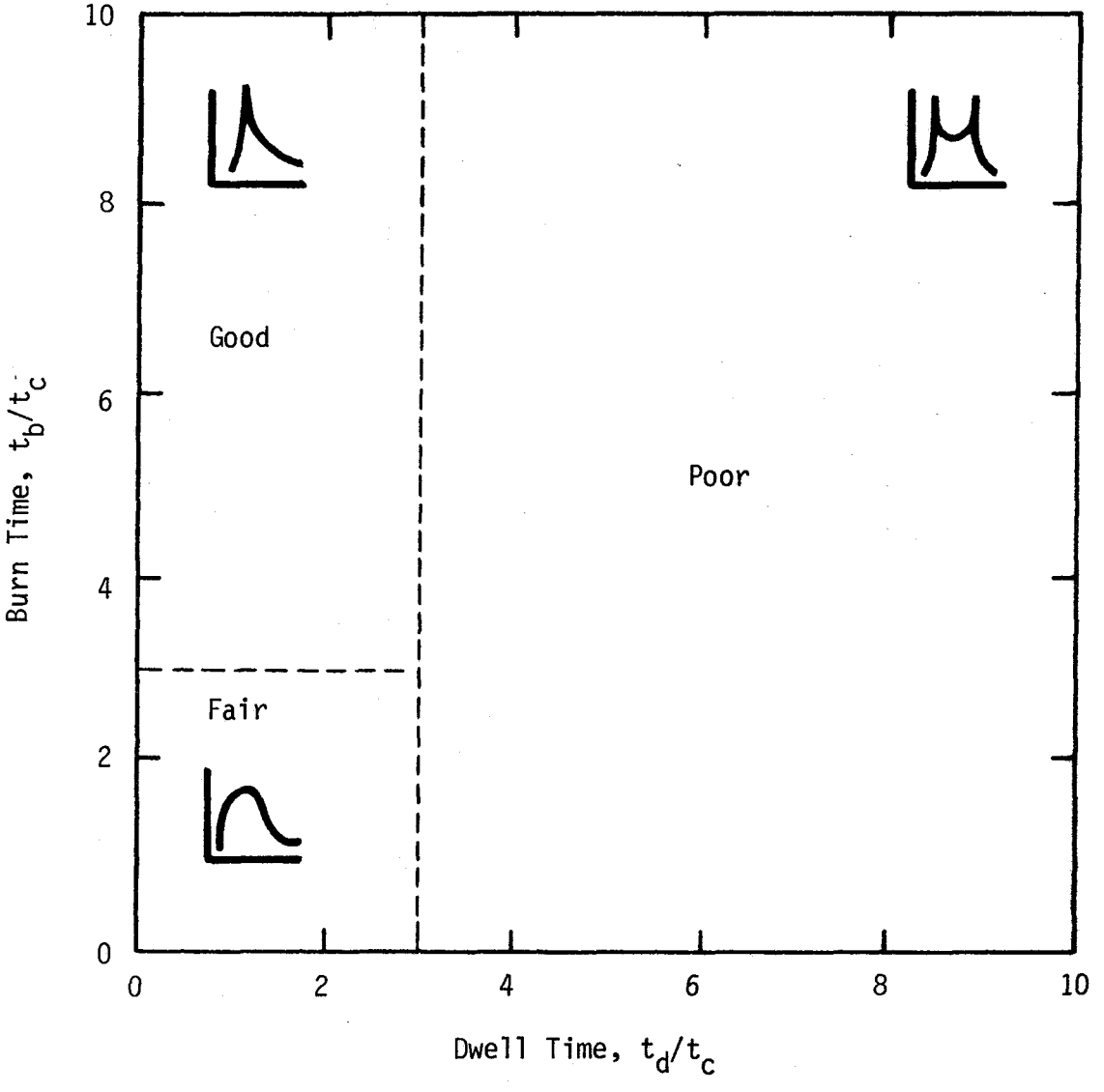

Figure 5.3.2-13 Act-alike temperature density regions vs. burn and dwell times.

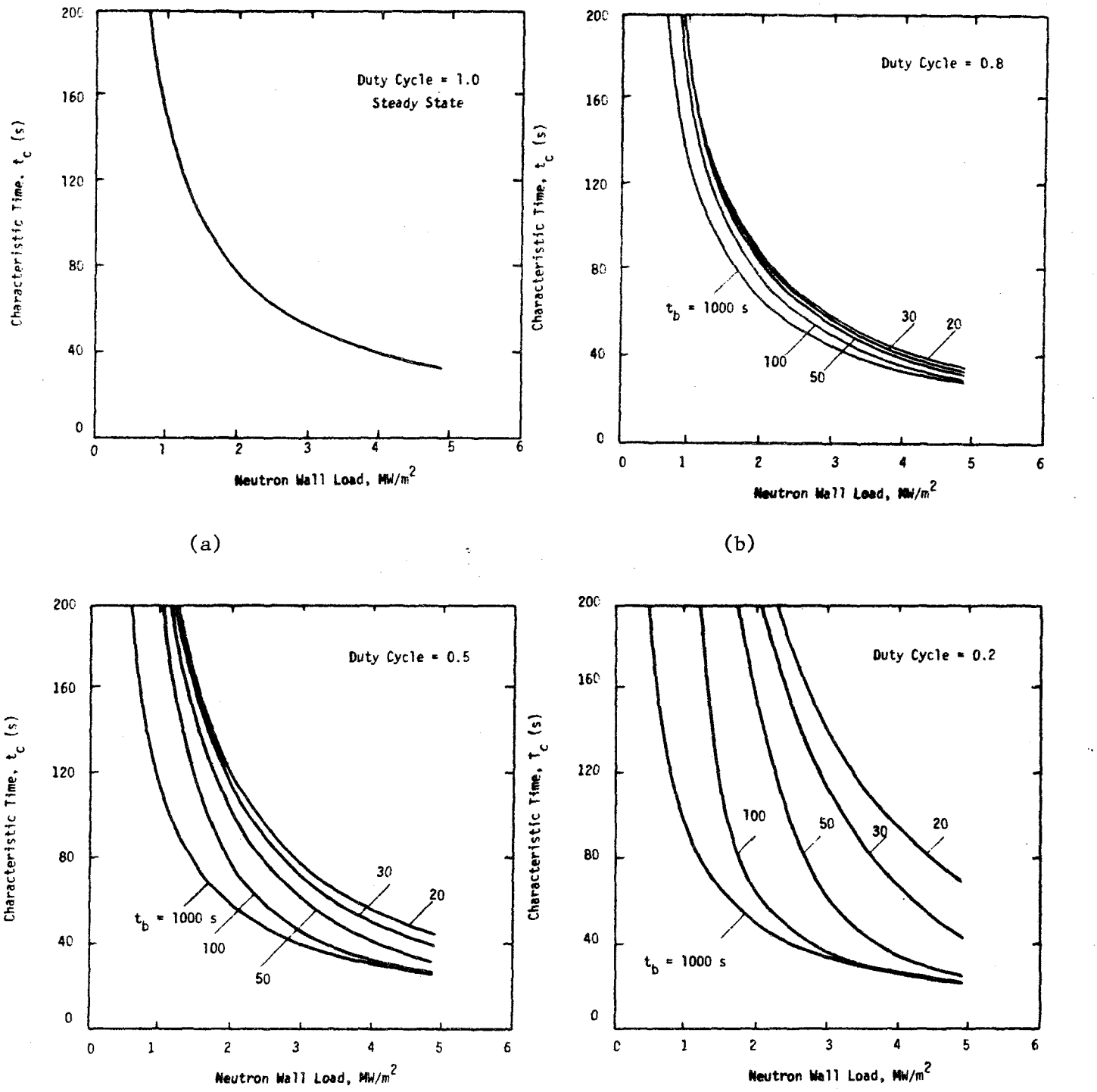

Figure 5.3.2-14 Solid breeder thermal characteristic time vs. neutron wall load for various burn time and duty cycle (modified breeder type 1).

wall load of the test device be greater than 1.8 MW/m^2. Similar calculations may be done for various burn time and duty cycle. Figure 5.3.2-15 shows the result of such calculations.

This figure plots the needed burn time versus the test device neutron wall load for various duty cycles. The results for duty cycle less than 0.5 is shown in dotted line signifying the fact any duty cycle less than 0.5 yields a poor test module (see Fig. 5.3.2-13). It is observed than the relation between burn time and neutron wall load (both major device parameters) is not a strong function of duty cycle. It is also seen that at around neutron wall load less than 1.5 MW/m^2, the required burn time sharply increases, suggesting that any test device wall load less than about 1.5 MW/m^2 will need very long burn times.

The dwell time limit is also available from Fig. 5.3.2-15, although not directly. Assume, for example, a burn time of t_b = 400s and a duty cycle of 0.8. Figure 5.3.2-15 indicates a minimum neutron wall load of about 1.3 MW/m^2. If this minimum wall load is chosen, the requirement on the dwell time is already met (duty cycle of 0.8 and burn time of 400 s yield a dwell time of 100 s) since $t_d < t_c$ which will correspond to a fair test module. But what if a neutron wall load larger than the minimum required is chosen? Larger wall load means a smaller characteristic time, which in turn means larger t_d/t_c for the same dwell time. This may result in poor test module thermal behavior. The correct limits on dwell time should be redetermined from Fig. 5.3.2-14.

Within a reasonable approximation, however, it is possible to construct a single figure showing limits on burn time, dwell time, and neutron wall load. This is possible due to the observation from Fig. 5.3.2-14 that these limiting parameters are not generally a strong function of duty cycle. Figure 5.3.2-16 shows this relation based on a duty cycle of 0.8, but approximately true for any duty cycle.

Again, an example will best describe this figure. Given a burn time of 400 s, the minimum neutron wall load consistent with $t_b/t_c > 3$ is 1.3 MW/m^2, and the corresponding maximum dwell time is 130 s. However, if a larger neutron wall load is chosen in order to have generally better test conditions, say q_{nw} = 3 MW/m^2, then a maximum dwell time of 50 s is obtained. It is interesting to note that while increasing the neutron wall load helps any

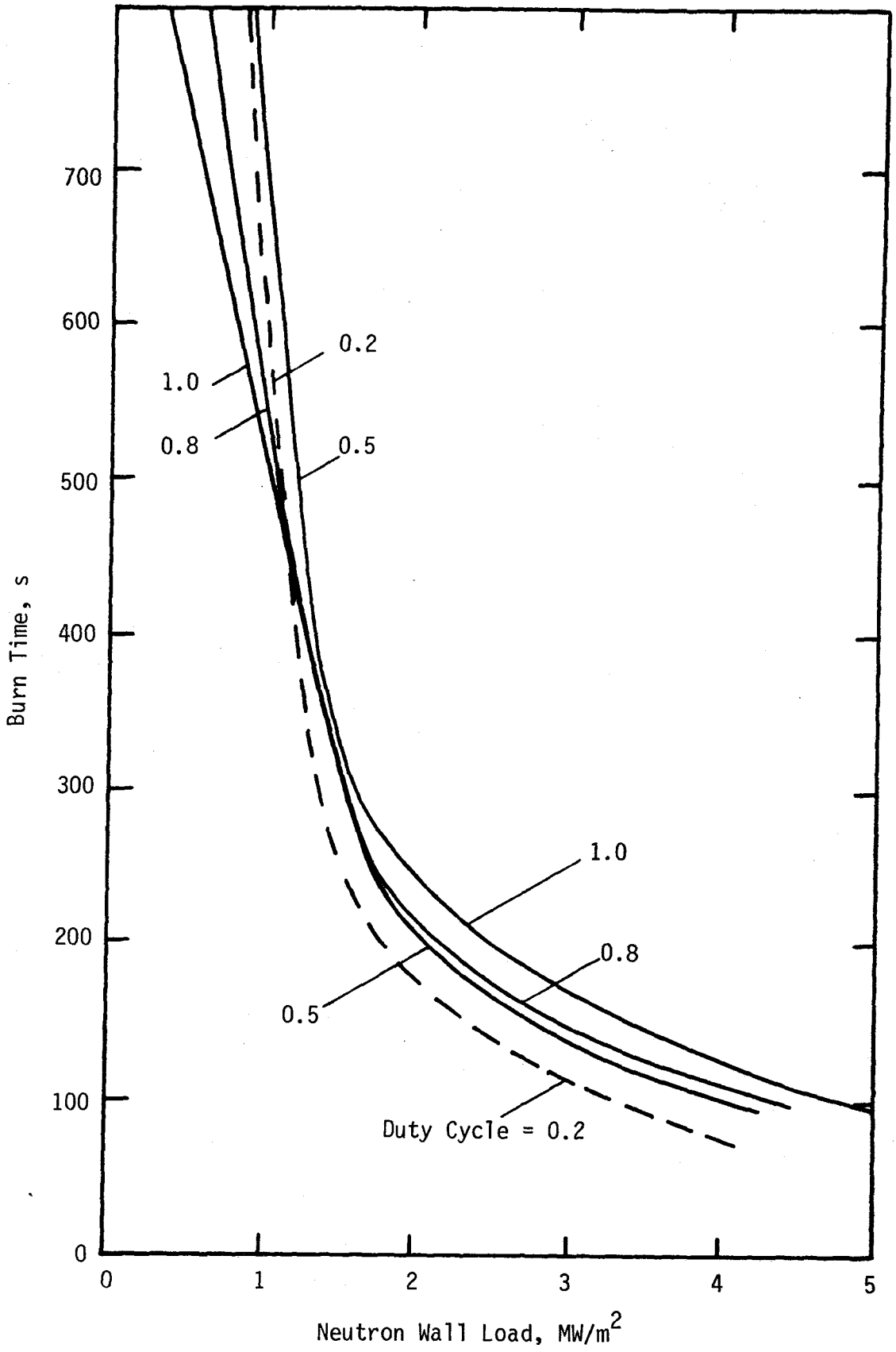

Figure 5.3.2-15 Minimum burn time vs. neutron wall load and duty cycle Li_2O/He/HT-9 test module.

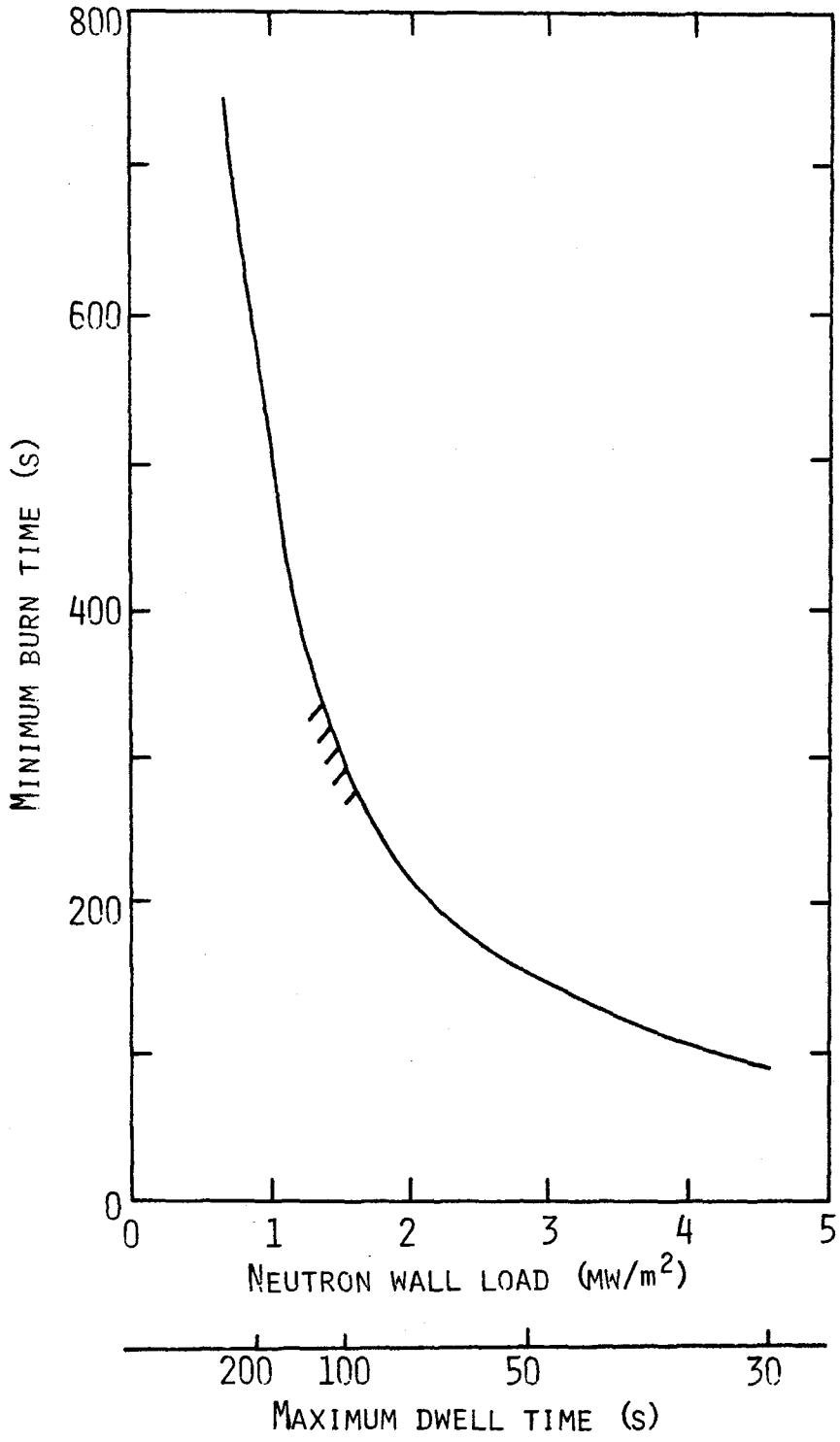

Figure 5.3.2-16 Relation between minimum burn time, maximum dwell time, and minimum neutron wall load for the Li_2O/He/HT-9 test module.

given burn time look more attractive with respect to the characteristic time, it correspondingly imposes tighter limits on the dwell time.

5.3.2.4 Flow Conditions

Flow Distribution

The reference blankets contain 20-50 first wall channels per meter of axial length, and 20-200 breeder coolant channels. It is normally assumed that the flow will be distributed equally under reactor conditions. In any event, it is desirable for the test module to retain these flow conditions. One question is how many channels are needed to maintain the multiple flow path characteristics of the reference blankets. This would be important for channel-to-channel flow oscillations, or flow redistribution around deformed channels or local hot-spots. Space constraints dictate that as few channels as necessary be retained.

There may not be a definitive answer, but one calculation is to assume that the total work done by an external pump on the system of multiple channels is fixed, that is $P_{pump} = \Delta p \dot{V} \simeq$ constant, where P_{pump} is the pump power, Δp is the pressure drop across the channels (uniform inlet and exit pressures), and $\dot{V} \sim UA$ is the volumetric flow rate. Typical pumps roughly exhibit this behavior although there is also a maximum Δp and a maximum $\dot{V}$. Assuming $\Delta p = f(L/d)\rho U^2/2$; $f = c_f/Re^{0.2}$ and $Re = \rho Ud/\mu$, , then

$$\Delta p = C\dot{V}^{1.8} \qquad (5.3.2\text{-}23a)$$

where

$$C = \frac{c_f \, L \, \rho^{1.8} \, \mu^{0.2} \, 2^{3.6}}{d^{4.8} \, \pi^{1.8}} \qquad (5.3.2\text{-}23b)$$

For N parallel channels,

$$\Delta P = C_i \dot{V}_i^{1.8} , \qquad i = 1, \ldots N \qquad (5.3.2\text{-}24a)$$

$$\Delta p \sum_{i=1}^{N} \dot{V}_i = P \qquad (5.3.2\text{-}24b)$$

Defining the ratio of channel "friction factors" by

$$\lambda_{ij} = (C_j/C_i)^{1/1.8} \qquad (5.3.2\text{-}25)$$

Then, if all channels are identical except for some channel j, $C_j \neq C_i$, Eqs. (5.3.2-24) gives

$$C_i \dot{V}_i^{2.8}(N - 1 + \lambda_{ij}) = P \ , \qquad i \neq j \qquad (5.3.2\text{-}26)$$

Furthermore, defining $\dot{V}_o = (P/CN)^{1/2.8}$ as the unperturbed flow rate, then

$$\frac{\dot{V}_i}{\dot{V}_o} = \left(\frac{N}{N - 1 + \lambda_{ij}}\right)^{1/2.8} \ , \qquad i \neq j \qquad (5.3.2\text{-}27)$$

$$\frac{\dot{V}_j}{\dot{V}_o} = \lambda_{ij} \ \frac{\dot{V}_i}{\dot{V}_o} \qquad (5.3.2\text{-}28)$$

and the Reynold's number scales similarly.

Assuming that changes in friction factor are due to changes in channel diameter (from deformation, manufacturing tolerances), then $\lambda_{ij} \simeq (d_i/d_j)^{2.67}$. Figure 5.3.2-17 shows the variation in flow rates, $\dot{V}_i/\dot{V}_o$, as a function of N and λ_{ij}. Under reference conditions, $N \gg 10$. The number of channels needed to maintain the same response to a channel perturbation depends on the size of the perturbation. Possible effects are 1% based on thermal expansion, 4% based on swelling, $\lesssim$ 1 mm for manufacturing tolerances. From the figure, it can be seen that for up to 50% reduction in channel diameter (i.e., factor of four times reduction in flow area), 10 channels preserves better than 85% of the infinite channel response.

Flow Vibrations

Flow vibrations are strong functions of the global geometry and coolant conditions since these affect the frequency range of the flow vibrations, the natural structural frequencies, and the magnitude of the damping. The presence of flow vibrations is probably best checked with a full component under

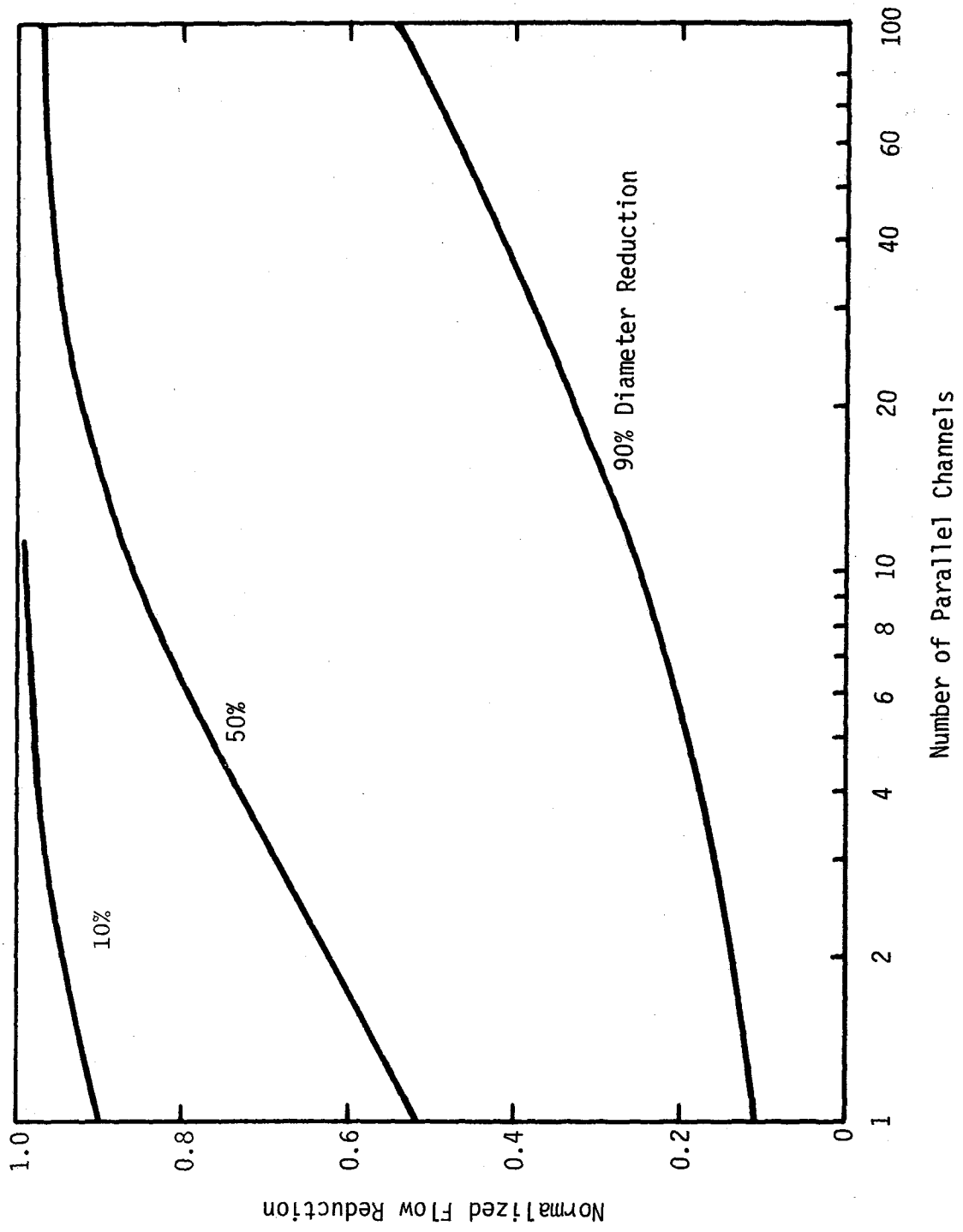

Figure 5.3.2-17 Flow reduction inparallel channels if one is partially blocked, normalized to flow reduction with infinite parallel channels, assuming fixed pumping power.

full flow conditions. This would miss any effects from heating (distortion of structure) or radiation damage, but these are probably secondary concerns.

In a scaled module, it is best to preserve geometric aspect ratios; the "reduced velocity", U/fd, where f is the vibration frequency of the structure; and the mass ratio, $m/\rho d^2$, the ratio of structural mass to fluid mass per unit length. Natural frequencies are complex, but simple beams behave with $f \sim (EI/mL^4)^{0.5}$ where I is the moment of inertia and L is the beam length.

If a very rough rule-of-thumb is acceptable for scaling purposes, then note that the onset, and strength, of many instabilities is related to U/fd and its value relative to the mass ratio $m/\rho d^2$. From simple dimensional considerations, these imply that the scaled test should preserve UL^2/d^2.

Thermal Instability

There is a region of thermal instability associated with layered solid breeder design of Li_2/He/HT-9 reference blanket (see Section 5.2.2). The present design is in the stable region. Therefore, the test module should at least be in the stable region too. However, due to many uncertainties including approximations and assumptions made in the analysis, hot spot factors, flow instabilities and so on, one prefers to have the test module and the reference blanket at the same relative position in the stable region. That is:

$$\left(\frac{d_c}{d_{c,cr}}\right)_{test} = \left(\frac{d_c}{d_{c,cr}}\right)_{reference} \qquad (5.3.2\text{-}29)$$

where $d_{c,cr}$ is the critical coolant half channel width.

5.3.2.5 Corrosion

Corrosion mechanisms in general are very complex and not completely understood. However, there is a reasonable amount of experience with water and helium coolant to provide some confidence in the blanket behavior. At a minimum, a scaled test that includes corrosion effects should preserve the coolant chemistry (type and concentration of impurities), coolant hydraulics (e.g., Reynolds number), and blanket temperatures.

5.3.2.6 Summary

It is very important that any test module reproduce the important characteristics of the blanket thermal behavior since these govern the design and operation of the blanket, and drive many known and probably many unknown processes. Concerns addressed here include the first wall and solid breeder temperature profiles, particularly breeder axial conduction (plate breeder geometry), cylindrical heat generation asymmetry (breeder-outside-tube geometry) and pulsing effects, as well as some aspects of flow behavior.

It is likely that the test facility will operate with a lower heat source than the reactor. In order to preserve temperatures throughout the blanket, some combination of adjusting dimensions and coolant inlet conditions seems necessary. However, these can only compensate some aspects of the temperature profile. For example, it is not generally possible to preserve both the breeder temperature rise ΔT and gradient ∇T simultaneously. A more complex and important issue is preserving the first wall temperature profile to retain thermal stresses, mechanical behavior and tritium permeation. First wall temperature profiles are dominated by volumetric heating in mirror reactors and by surface heating in tokamaks. This sense of heat source dominance should be retained under test conditions, leading to the balance in test requirements which shows that, for a given test facility neutron wall load, there is a minimum useful surface heating for testing tokamak blankets, and a maximum useful surface heating for testing mirror blankets.

Another important concern is the thermal behavior of the solid breeder under pulsed heat source. Almost all important phenomena within the breeder are highly temperature dependent, so it is important to preserve not just the temperature extremes, but also the breeder-averaged temperature distribution or "temperature density". It is evident that pulsing has two major effects: (1) the entire temperature is shifted to colder values due to the reduced average heat source; and (2) the temperature "density" is smeared out due to the time spent cooling down during the dwell period. While the former can be compensated by increasing the breeder thickness and adjusting coolant conditions, the latter is strongly related to the pulsing itself and leads to burn/dwell time limits.

References for Section 5.3.2

1. "A Tandem Mirror Technology Demonstration Facility", Lawrence Livermore National Laboratory, UCID-19328 (October 1983).

2. D. Olander, "Fundamental Aspects of Nuclear Reactor Fuel Elements", Energy Research and Development Administration, TID-26711-P1 (1976).

3. F. Nichols, "Transport Phenomena in Nuclear Fuels under Severe Temperature Gradients", Jrnl. of Nucl. Mat., 84, 1 (1979).

5.3.3 Tritium Recovery

The results presented in Section 5.2.3 can be used in a preliminary fashion to determine the requirements for scaled testing from a tritium recovery viewpoint. If the reference designs continue to use a helium purge gas with 100 wppm hydrogen (i.e., protium) added to the purge, then the diffusive inventory (I_d) should be the major component of the solid breeder inventory (I_b). For the plate designs the diffusion inventory is given by:

$$I_d = \frac{r_g^2 \dot{G}}{15 D_o} \sum_{i=1}^{N} (h_i/N) f_i \exp(O/R\bar{T}_i) , \qquad (5.2.3\text{-}1)$$

where the primary design variables are grain size (r_g), generation rate ($\dot{G}$), average temperature ($\bar{T}$), and the distributions of temperature and tritium generation (h_i and f_i). For scaling purposes, it is useful to express $\dot{G}$ in units of wppm/s.

The equation for the cylindrical geometry given in Section 5.2.3 is:

$$I_d = [r_g^2/15\ D(\bar{T})] f \dot{G} , \qquad (5.3.3\text{-}2)$$

where the variables are the same as those given for the plate. In both cases, the neutron wall load in the test facility will probably be considerably less than the design goal of 5 MW/m^2. Assuming that the temperatures are simulated correctly, the reduced neutron flux can be compensated for partly by increasing the ^6Li enrichment of the fuel (as was done in FUBR) or increasing the grain size. The problem with increasing the grain size is that this will also affect the helium behavior which scales in a much more complicated manner to grain size than does the tritium behavior. Also, the grain size is not a time-independent variable (particularly for Li_2O). If tritium recovery is the only goal of the experiment, then it is recommended that the enrichment be increased in order to simulate $\dot{G}$. However, if the experiment is also designed to investigate neutronics and tritium breeding, then the enrichment should be maintained at the design value and Eqs. (5.3.3-1) and (5.3.3-2) used to extrapolate the experimental results to design conditions.

Accepting the lower generation rate in the test module, the tritium permeation (or leakage) to the primary coolant can be simulated by reducing the purge flow velocity proportionately according to the equation:

$$(p_{HT})_i = n_{HT} R \bar{T}_p / V_p \quad , \qquad (5.3.3\text{-}3)$$

where $n_{HT} = 2\, n_{T_2}$ and n_{T_2} is the production rate of tritium in moles/s. By keeping n_{HT}/V_p the same for the module as the design, the correct partial pressure is maintained. The leakage rate is then preserved according to:

$$m_T = (3\, P_m A / 8\, d_m) p_{HT} / \sqrt{p_{H_2}} \quad , \qquad (5.3.3\text{-}4)$$

where A is the mean surface area for permeation and d_m is the thickness of the membrane.

In the preceding discussion the assumption of a steady-state test device was made. It is likely that the test device will be cycled with some specified burn time (t_b) and dwell time (t_d). The major problem with a pulsed test device is to determine the requirements for t_b and t_d such that the experimental results for tritium inventory are qualitatively representative and can be extrapolated in a quantitative manner to design blanket conditions. The primary requirement for tritium behavior is that the burn cycle be sufficiently long enough to allow the minimum, maximum, and average breeder temperatures to achieve the design values.

For the Li_2O plate design, a burn time of ~1 min greater than the time to reach thermal equlibrium appears to be sufficient to achieve steady-state release rate, providing that the minimum blanket temperature is not less than 510°C throughout the burn cycle. This calculation assumes: (1) surface adsorption and bulk solubility minimized by adding protium to the purge; (2) no grain growth or sintering; (3) no decrease in the bulk diffusion coefficient due to irradiation damage; and (4) no adverse affects of helium bubbles (e.g., trapping) or helium-induced swelling (e.g., hot pressing of purge channels and interconnected porosity.)

As all of the above are likely to have some effect on the inventory, the additional 1 min of burn time beyond thermal equilibrium will be sufficient to achieve a quasi-steady inventory and release rate for Li_2O early in the test period. The surface adsorption/solubility terms could take as long as a day to reach equilibrium. The last three items have time constants on the order

of months. The difficulty then with a burn time of ~1 min which maintains at least the minimum temperature of 510°C for the full cycle and achieves the maximum temperature for some fraction of the cycle, is converting the results to equivalent full-power hours and extrapolating to design conditions.

The tritium response of the $LiAlO_2$ plate is much slower than that of the Li_2O plate, but the analysis is somewhat simpler in that $LiAlO_2$ is more stable and bulk diffusion is more dominant. A burn time of $t_b \sim 4$ days appears to be sufficient to establish equilibrium inventory and release time. Even if surface adsorption is a factor, equilibrium surface concentrations should be achieved during this time period.

For the $LiAlO_2/H_2O$ design, the low breeder temperatures (T_{min} = 350°C) result in very long times to equilibrium. Table 5.2.3-1 shows the release rate time constants for 67.4% and 99% of steady-state values as a function of the minimum blanket temperatures. An upper bound on the burn time requirements can be found by assuming that the blanket must reach thermal equilibrium before tritium is released. The time for thermal equilibrium is estimated to be <50 min based on the slow response near the back of the blanket. The additional times for 67.4% and 99% of equilibrium for the release rate are $\tau_{67.4}$ < 2 min and τ_{99} < 4 mo. Therefore, it appears that in order to have results that are amenable to analysis, a burn time of at least 1 h is required. This should be sufficient to achieve a release rate fraction of greater than 67.4% for the first cycle. It would then take less than 3000 cycles to achieve an effective tritium release rate of 99%. The time to achieve a steady-state inventory, however, is considerably longer, as indicated in Fig. 5.2.3-16.

Additional calculations were performed to determine the effects of not achieving the maximum temperature for the $LiAlO_2/H_2O$ design during the burn cycle. Figure 5.3.3-1 shows the results of an idealized (i.e., instantaneous) startup with T_{min} fixed at 350°C and T_{max} instantly achieving values from 700-1000°C. The lower the value of T_{max}, the longer the time response and the higher the end-of-life inventory relative to the design case.

Given the high degree of uncertainty in the preceding discussion of transient tritium behavior, the recommendations with regard to burn-dwell requirements are, at best, preliminary and highlighted for further investigation. The assumption that bulk diffusion is rate limiting for Li_2O (even with pro-

tium swamping) is debatable in that it leads to predicted inventories of $\sim 10^{-4}$ wppm. Clearly, the presence of small amounts of impurities in the Li_2O and the helium coolant (particularly H_2O) could change this result dramatically. More confidence is associated with the $LiAlO_2$ plate design for which inventories of ~0.2 wppm were calculated. The most confidence is associated with the $LiAlO_2/H_2O$ design calculations for which tritium inventories of ~15 wppm were predicted.

The recommendations for burn-dwell times in Table 5.3.3-1 are the best estimate of tritium behavior at present. For burn times shorter than these values, a more sophisticated transient analysis must be performed, and it will be exceedingly difficult to sort out mechanistic interpretations of the data if the results differ considerably from the expected tritium behavior.

As the recommended burn times for the $LiAlO_2$ designs are relatively long, a practical interpretation of the numbers in Table 5.3.3-1 is that these represent desired times at steady-state design temperatures. If short burn times are used, these indicate the minimum number of cycles required to get useful information on tritium inventory, assuming no fluence or burnup degradation of the diffusivities.

Table 5.3.3-1. Preliminary Recommendations for Burn-Dwell Times for Scaled Tests to Simulate the Behavior of Tritium in Li_2O/He and $LiAlO_2$/He Plate Designs and $LiAlO_2/H_2O$ Designs

Design	Minimum Burn Time[a] (s)	Minimum Dwell Time (s)
Li_2O/He	2.0×10^2	b
$LiAlO_2$/He	3.5×10^5	b
$LiAlO_2/H_2O$	1.0×10^7	b

[a]Based on achieving thermal equilibrium and a tritium-release rate of 99% of steady-state during the first burn cycle.

[b]Determined more by thermal equilibrium requirements than tritium recovery considerations.

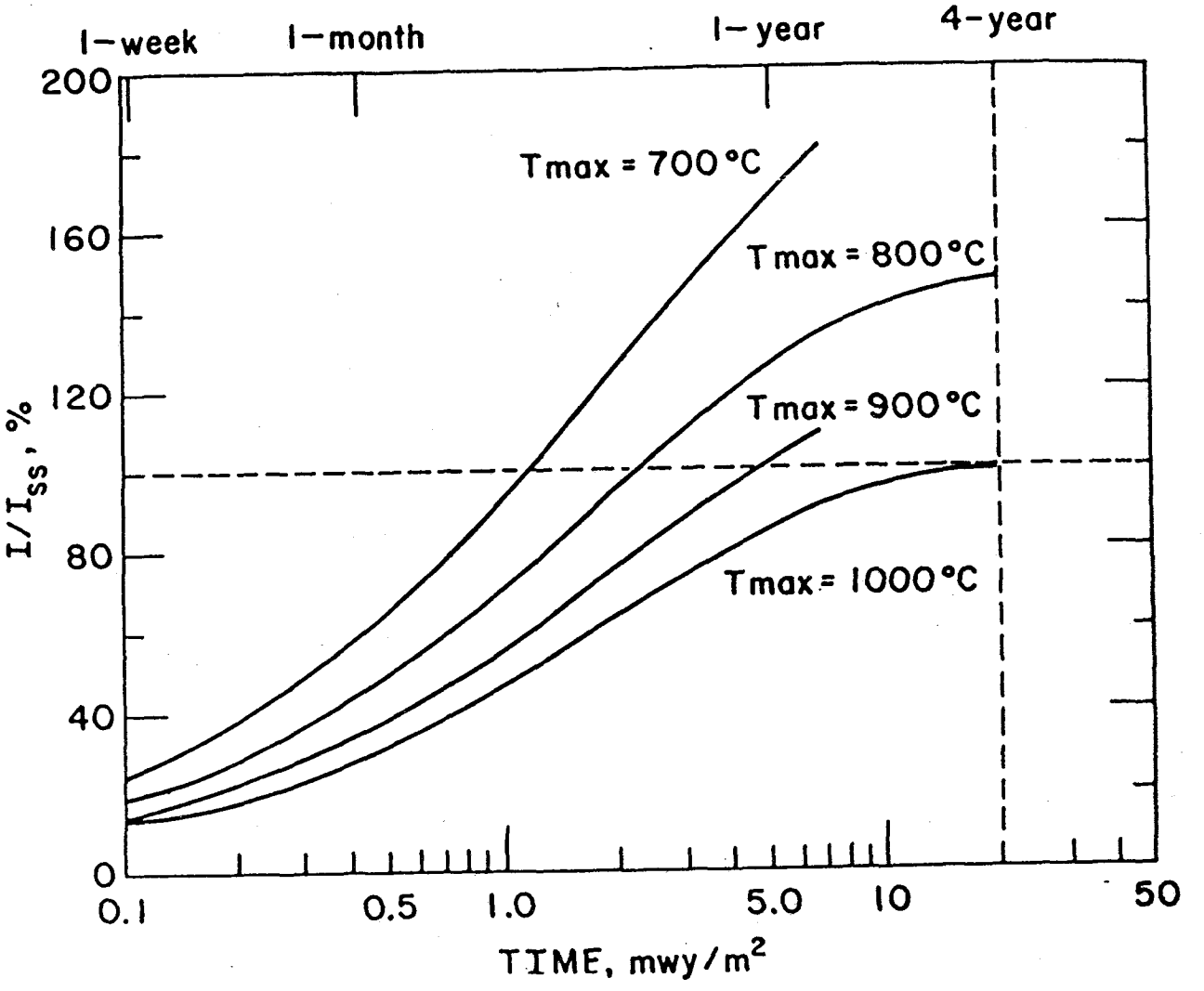

Figure 5.3.3-1. Influence of maximum temperature achieved during each burn cycle on the tritium inventory for a constant minimum temperature of 350°C. I_{SS} refers to the inventory for the reference case of the $LiAlO_2/H_2O$/Be/HT-9 blanket with T_{min} = 350°C and T_{max} = 1000°C.

5.3.4 Structural Mechanics

5.3.4.1 Introduction

In the structural analysis of the reference blankets in Section 5.2.4, the basic data and models was described and the important features identified. In this section, the significant factors in structural mechanics are considered, and the corresponding requirements for scaled testing determined where possible.

The scaled test conditions necessary to evaluate beginning-of-life (BOL) behavior are primarily constrained by changes in the heat source (surface or volumetric), leading to possible changes in the temperature distribution, and by test volume limitations. The ability to address end-of-life (EOL) concerns is additionally constrained by fluence and time (operating or pulsed) limitations. Each scaled test constraint is considered separately.

5.3.4.2 Scaling of Steady-State Thermo-Elastic Behavior

Consider the general structural field equations:[1]

$$\frac{\partial \sigma_{ij}}{\partial x_j} + \rho F_i = 0 \qquad \text{equilibrium} \qquad (5.3.4\text{-}1a)$$

$$\sigma_{ij} = \frac{E}{(1+\nu)}\,\varepsilon_{ij} + \frac{E\nu}{(1+\nu)(1-2\nu)}\,(\varepsilon_{11}+\varepsilon_{22}+\varepsilon_{33})\,\delta_{ij} - \frac{E}{(1-2\nu)}\,\alpha T \delta_{ij}$$

$$\text{stress-strain} \qquad (5.3.4\text{-}1b)$$

$$\varepsilon_{ij} = \frac{1}{2}\left(\frac{\partial u_i}{\partial x_j} + \frac{\partial u_j}{\partial x_i}\right) \qquad \text{strain-displacement} \qquad (5.3.4\text{-}1c)$$

where σ_{ij} is the stress tensor; ρ is density; F_i is a body force; E and ν are elastic constants; α is the thermal expansion coefficient; and u_i is the displacement vector.

The stress inside a given volume is dependent on the surface boundary conditions. Consider an arbitrary surface whose boundary condition at each point is one of three possibilities:

$$u_i = [u_i]_{bc} \qquad \text{prescribed displacement} \qquad (5.3.4\text{-}2a)$$

$$\frac{\partial u_i}{\partial x_j} = \left[\frac{\partial u_i}{\partial x_j}\right]_{bc} \qquad \text{prescribed strain} \qquad (5.3.4\text{-}2b)$$

$$\sigma_{ij} n_j = p_i \qquad \text{prescribed pressure or traction} \qquad (5.3.4\text{-}2c)$$

where $\underline{n}$ is the outward surface normal vector and $\underline{p}$ is the applied pressure or traction force.

Suppose that $u_i(x_j)$ is the unique solution[1] of Eq.(5.3.4-1) and its boundary conditions, Eq.(5.3.4-2), and consider the effects of a linear scaling in all dimensions: $\underline{x}' = c\,\underline{x}$ where c is some scaling factor, and ' denotes scaled conditions. Assume that the boundary conditions and body forces are scaled also as

$$\left[u_i'(x_j')\right]_{bc} = c\,\left[u_i(x_j)\right]_{bc} \qquad (5.3.4\text{-}3a)$$

$$\left[\frac{\partial u_i'(x_j')}{\partial x_j'}\right]_{bc} = \left[\frac{\partial u_i(x_j)}{\partial x_j}\right]_{bc} \qquad (5.3.4\text{-}3b)$$

$$p_i'(x_j') = p_i(x_j) \qquad (5.3.4\text{-}3c)$$

$$T_i'(x_j') = T_i(x_j) \qquad (5.3.4\text{-}3d)$$

$$F_i'(x_j') = c\,F_i(x_j) \qquad (5.3.4\text{-}3e)$$

Then the solution to the scaled problem is given by $\sigma_{ij}'(x_k') = \sigma_{ij}(x_k)$ and $u_i'(x_j') = c\,u_i(x_j)$ - i.e., same stress distribution and linearly scaled displacements. This can easily be verified by substitution into Eq.(5.3.4-1) and its boundary conditions.

In summary, linear thermoelastic stress distributions are exactly scaled if: 1) all dimensions are proportionally changed; 2) the temperature and pressure distributions are not changed; and 3) body forces and externally imposed displacements are scaled; and 4) strain boundary conditions are not changed.

5.3.4.3 First Wall Structural Behavior

The structural behavior of the first wall is determined by thermal and

pressure stresses at startup, by transient magnetic loads during operation, and by lifetime related effects including radiation damage, plastic behavior, cycling and corrosion.

Thermal effects Previous calculations in Section 5.2.4 have shown the nature of the first wall pressure and thermal stresses at the beginning-of-life. The peak combined stresses in the Li_2O/H_2O/PCA/Be tokamak design are about +300 MPa (Fig. 5.3.4-1a) and locally exceed the high temperature, high irradiation $3S_{mt}$ guidelines.[2] The addition of grooves to the first wall will shift the peak stress location inward to colder and stronger material, but raises questions regarding stress concentration and crack initiation. In this analysis, only the ungrooved first wall is considered. It is clear, however, that thermal plus pressure stresses are very significant in first wall design and should be preserved under scaled conditions.

Simple estimates of thermal stress imply that if the ΔT across the structure is preserved, then the magnitude or range of the thermal stresses, $\sigma_{th} \sim E\alpha\Delta T$, is also preserved. Corresponding simple estimates of tangential stresses in the first wall surface layer are $\sigma_{fw} \sim p_c(d_{fc}/d_{fw})^2$ due to pressure bending stresses in the first wall; or radial stresses in the supporting channels of $\sigma_{fs} \sim p_c(d_{fc}/d_{fs})$, where p_c is the coolant pressure, d_{fw} is the first wall thickness, d_{fc} is the coolant channel diameter and d_{fs} is the support channel thickness. These imply that gross pressure stresses are also preserved if the pressure and geometric aspect ratios are unchanged. More careful consideration based on the theoretical analysis presented in Section 5.3.4.1 confirm these conclusions if certain additional conditions are met.

If the heat source is reduced from reactor conditions, the temperature profile will change (see Fig. 5.3.2-1), leading to much reduced thermal stresses and a change in the overall first wall stress distribution. One method of preserving the temperature is to increase the first wall thickness as the heat source drops. The effectiveness of this approach is discussed in Section 5.3.2, but it appears possible to retain gross features of the temperature distribution (average and extreme values) over some range in heat source conditions.

It may be important to determine where appreciable deviations in stress distribution occur due to the inability to exactly preserve the temperature

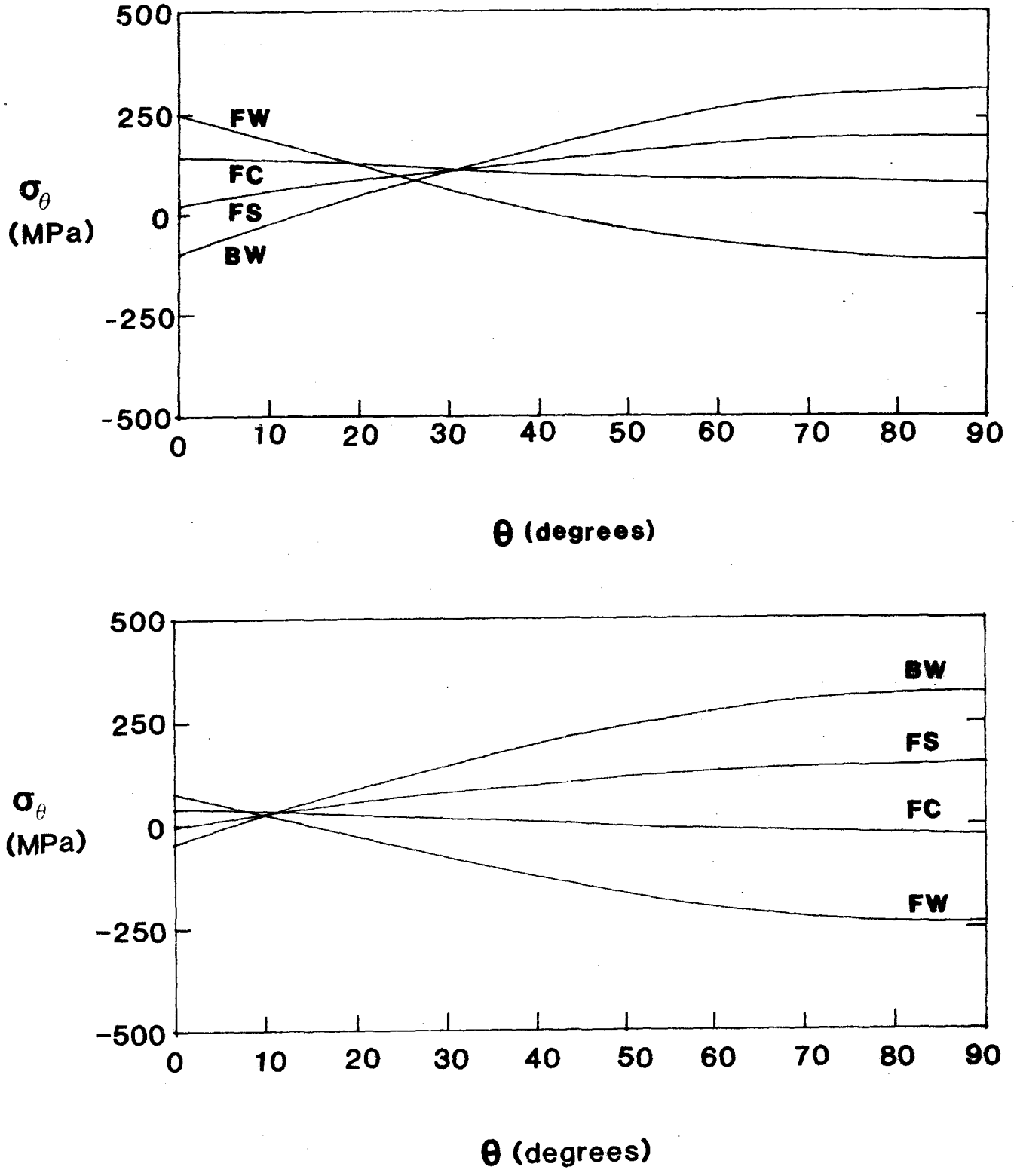

Figure 5.3.4-1 First wall thermal plus pressure stress profile in the Li_2O/He/HT-9 first wall: (a) reference reactor; and (b) scaled test conditions corresponding to x5 decrease in surface and volumetric heating.

profile in the lobed first wall under changed heat source conditions. In Fig. 5.3.4-1, the calculated thermal and stress profile is shown for the Li_2O/He-/HT-9 tokamak first wall under reference conditions and under scaled conditions corresponding to a drop in surface and volumetric heating by a factor of five (i.e., dimensions increased x3.8, coolant velocity decreased by x3.8, as discussed in Section 5.3.2). The corresponding deviations in temperature profile are given in Section 5.3.2.2. The stress profiles are similar in shape, as may be expected, but are appreciably different in magnitude. Since thermal stresses are sufficiently high as to be a major design concern, they must be closely preserved for a useful scaled structural test module, leading to limits on the tolerable deviation in first wall temperature distribution. Although there is no exact boundary, if the example just given is considered as "too different", then this implies a minimum neutron wall load of 1 MW/m^2.

First wall size effects As the heat source is reduced, it is possible to increase dimensions, maintain pressures and maintain geometric aspect ratios, and thus preserve the thermal and pressure stresses in the scaled test within certain bounds related to the temperature distribution. However, while this may mean that 2 x 2 mm^2 tokamak coolant channels become, say, 8 x 8 mm^2 as the total heat source is reduced a factor of five, it also implies that the module first wall width changes from 0.3 m to 1.2 m. This size scaling may be limited by the available space in the test facility.

Consequently, it is worth considering the significance of not increasing the first wall lobe radius (or module half-width) on the thermal and pressure stress distributions, even if all other dimensions and boundary conditions are correctly scaled and assuming that the temperature distribution is exactly preserved. In fact, the characteristic ΔT's considered in Section 5.3.2 imply that the first wall lobe radius might be independently changed and still essentially preserve the overall temperature distribution.

Based on the finite element model described in Section 5.2.4 and the Li_2O/He/HT-9 tokamak first wall, Figure 5.3.4-2a shows the effect of increasing all dimensions by a factor of three, except the first wall radius. Compared to the reference blanket, the general shape of the stress distribution is retained, but the peak stresses are substantially larger, particularly in compression.

Figure 5.3.4-2b also shows the effect on the overall stress profile if the back wall is thickened from 0.3 to 3 mm, under tokamak reactor heat source conditions. Since this places the mass-averaged first wall temperature closer to the colder back wall, the overall effect is to make the stress distribution more compressive. This again illustrates the importance of retaining geometric aspect ratios for preserving the overall stress distribution.

To translate this size constraint into test device requirements, it is necessary to estimate the amount of stress discrepancy between the reference stress distribution and that under the scaled test conditions. Assume that temperatures are exactly preserved by thickening the first wall dimensions (discussed in detail in Section 5.3.2), and that all other structural scaling conditions are met except that the first wall lobe radius will be independently varied. Figure 5.3.4-2a illustrates the resulting stresses for an increase in first wall thickness by three.

Comparing with the reference stresses, Fig. 5.3.4-1a, it is desirable to have some measure or margin factor, M, that quantifies the difference between the two distributions, and thus the "usefulness" of the scaled test for thermal and pressure stress behaviour. One estimate, for example, is the root-mean-squared deviation over the entire stress distribution. However, since "usefulness" cannot be rigorously defined, a simpler but more qualitative judgement of M is made here that is based on the average magnitude of the change in stresses at the extreme points, expressed as a multiplicative factor. Thus, the stress profile in Fig. 5.3.4-2a is estimated as $M \sim 2 \pm 1$.

Evaluating some other cases, the resulting estimate of the effect of varying the lobe radius relative to other first wall dimensions has the general shape shown in Fig. 5.3.4-3. For example, suppose test volume constraints limit the width of the test module to 1.2 m, or a factor of 4 increase in first wall lobe radius. Suppose also that a deviation of about 50% (i.e., $M \sim 1.5$) in thermal plus pressure stresses is the maximum acceptable for the scaled test. Then the maximum increase in general first wall dimensions is 6. This corresponds to a limit in overall heat source reduction by a factor of 8.4 from reference tokamak conditions, although the exact limit depends on the relative reduction in surface and volumetric contributions (see Fig. 5.3.2-2).

The first wall axial length also affects the required test volume. It

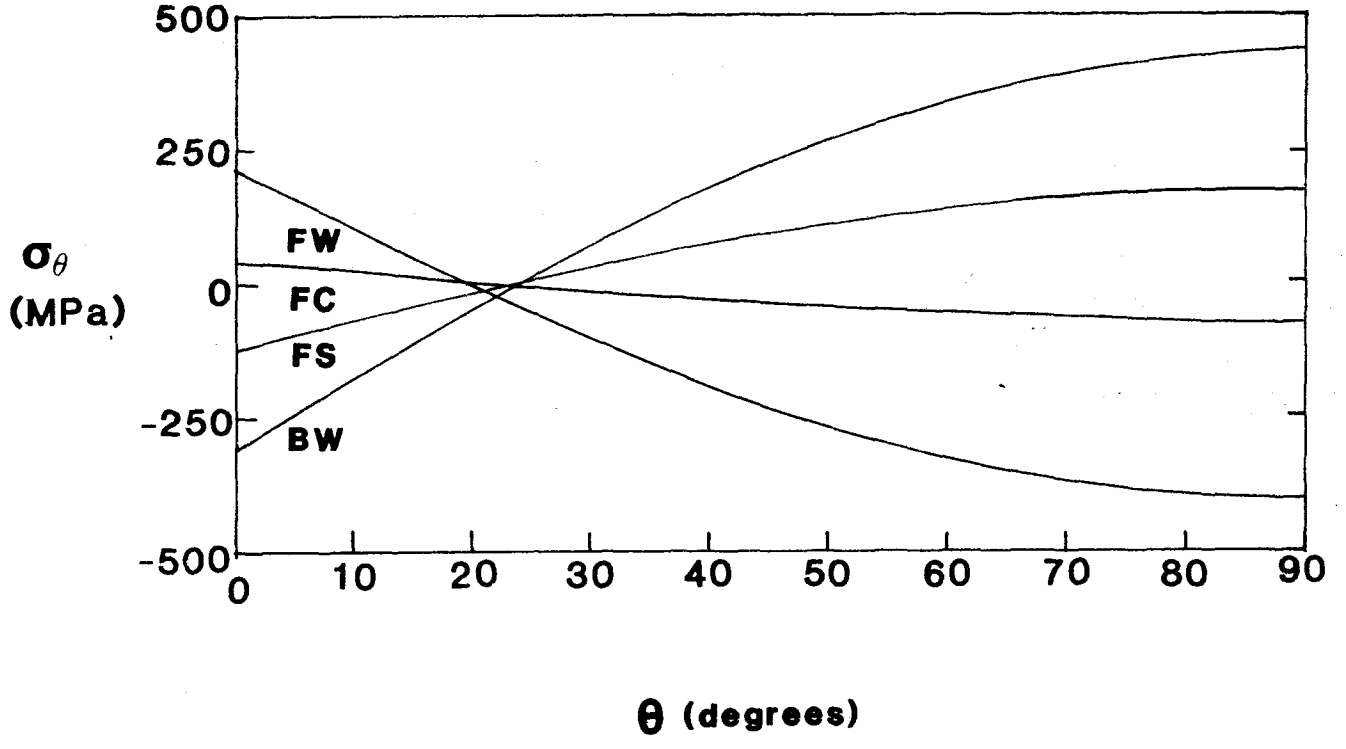

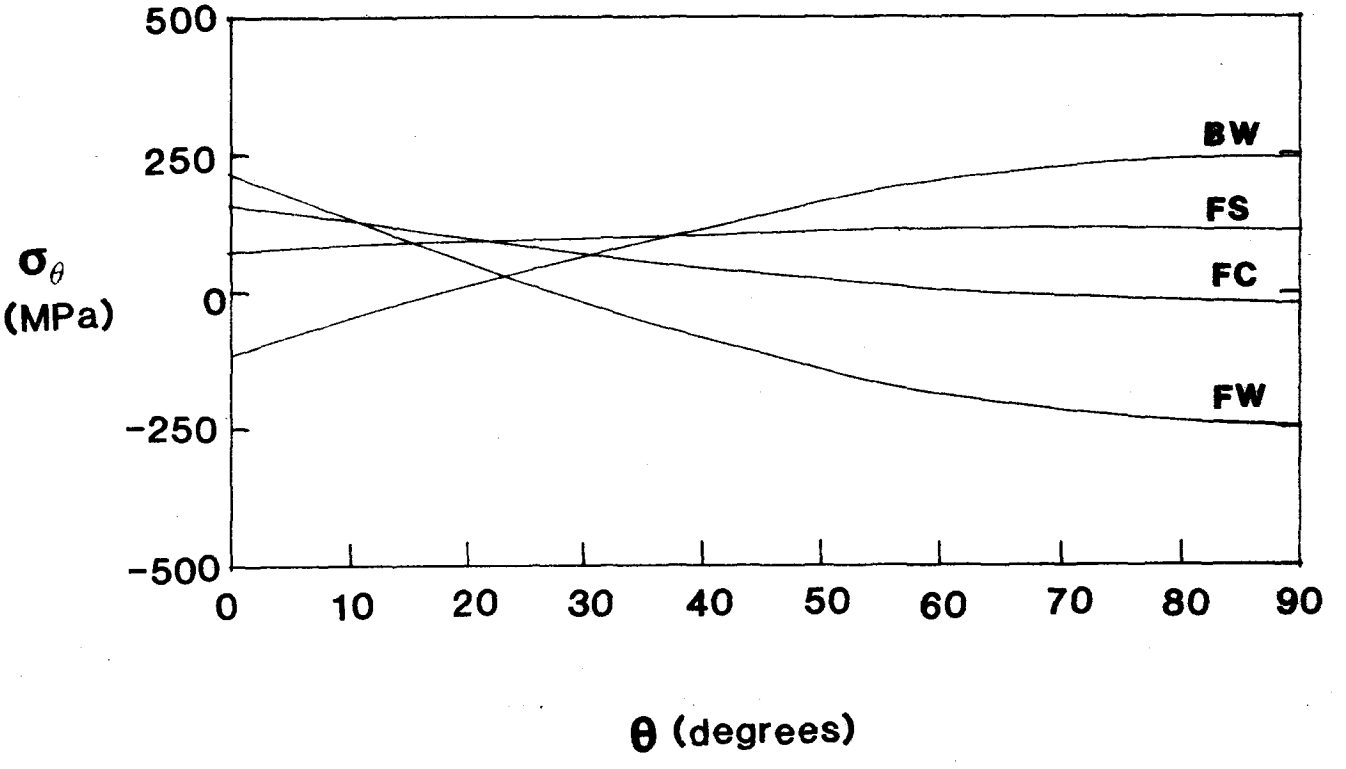

Figure 5.3.4-2 First wall thermal plus pressure stress profile in the Li_2O/He/HT-9 tokamak first wall: (a) under scaled test conditions with temperatures preserved and all dimensions scaled x3 except the first wall lobe radius which remains fixed at 0.15 m; and (b) under reference tokamak heat source conditions but the back wall is increased from 0.3 to 3 mm.

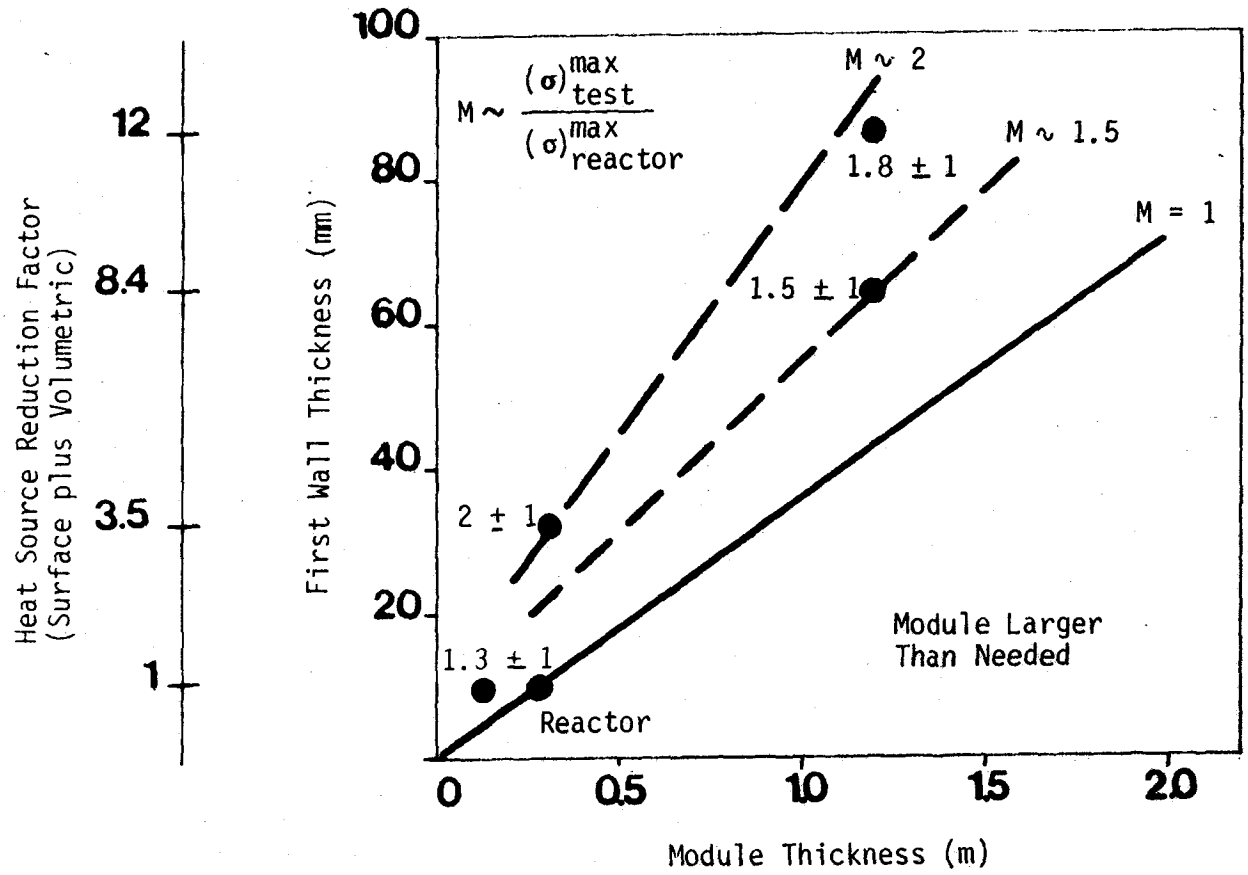

Figure 5.3.4-3 Size effects on the preservation of thermal and pressure stresses in the Li_2O/He/HT-9 first wall. The change in first wall channel dimensions may be related to changes in the heat source conditions by the need to preserve the first wall temperature distribution.

may be important to simulate the interaction between the curved first wall membrane and the supporting endplates. For example, the latter may be designed to be rigid and resist the first wall thermal expansion. This problem was not analyzed here, but it is anticipated that the thickness of the end plates may be modified to preserve the relative "stiffnesses" of the first wall and end plates.

Radiation effects Although no detailed calculations were performed, the impact of neutron irradiation over time is expected to be substantial, with irradiation creep, swelling and general property changes.

From simple models described in Section 5.2.4, the rate of creep relaxation of stresses is about $\tau_{cr} \sim 1/EA_{cr}$ or about 2 dpa for HT-9 and PCA. Since blanket modules are expected to operate for much longer periods (~ 1 yr or 60 dpa, allowing only for annual maintenance), the stresses should normally be completely relaxed to their steady-state values. Of course, during shutdown, these stresses will reappear with inverted signs. The ability to conduct tests into this regime would be desirable.

While creep is certainly important, the influence of swelling is not as clear since present data are consistent with very low swelling rates of HT-9 and PCA to over 100 dpa. If materials testing confirms this, and if component lifetime is expected to be limited by the onset of breakaway swelling, or before it by other concerns such as surface erosion, then swelling will not be important until test modules exceed the breakaway fluence.

A more immediate concern for scaled tests is with the variation in radiation effects (flux and fluence) across the component. With 5 cm attenuation lengths for dpa production, for example, there is little variation across the 1 cm tokamak composite first walls. However, in a scaled test with, say, a 5 cm thick first wall (to preserve the temperature distribution under a reduced heat source), the attenuation is very significant. Assuming creep and swelling are proportional to the fluence, then the back of the composite first wall would receive about 40% less fluence than the front surface, leading to nontypical stress distribution and relaxation.

Pulsing effects While commercial reactor blankets are expected to be virtually steady-state, scaled tests may be performed in pulsed test facilities.

The presence of pulsing raises structural concerns regarding crack initiation, crack growth and thermal ratchetting, for example. Such testing would bring out some aspects of reference blanket behavior since some cycling is expected anyway. However, there will be differences due to the different points in the component lifetime at which the cycling occurs (Fig. 5.3.4-4). For example, the actual component would likely cycle in the creep-relaxed stress state, recovering the high initial stresses but with reversed signs. The test module, however, might cycle even during the stress relaxation time. Thus, while the alternating stress magnitude would be preserved, the average stress and the sense of compression versus tension would not be, leading to potentially different failures.

There are additional concerns that long dwell times could also lead to stress redistribution. Since this would depend on the dwell temperatures, it might be desirable to cool the component enough to "freeze" the stress state, although not so much as to add additional stresses or approach embrittlement.

Furthermore, the general scaling of dimensions to preserve temperatures and overall stresses may not preserve local stress concentrations, crack growth, buckling or fatigue behavior. These are certainly significant, but have not been analyzed.

5.3.4.4 Breeder Region Structural Behavior

The two primary structural mechanics concerns in the breeder region are the breeder/structure interaction leading to breach or distortion of the structure, and internal breeder structural changes from internal or external forces. In both cases, a primary factor is the temperature profile since it generates the thermal expansion driving force at startup (no time for creep relaxation), and since it is a strong influence on many processes (including swelling, creep and sintering) that change microstructure or forces.

Thermal and size effects In Section 5.2.4.2, the dependence of thermal, swelling and creep stress on temperature and flux was shown for a simple geometry. If the temperature and flux profile is preserved, then these stresses are also preserved. In Section 5.3.4.2, it is also shown that linear thermo-elastic stresses (e.g., thermal and pressure) can also be preserved in arbitrary geometries if the temperature, body forces and boundary conditions

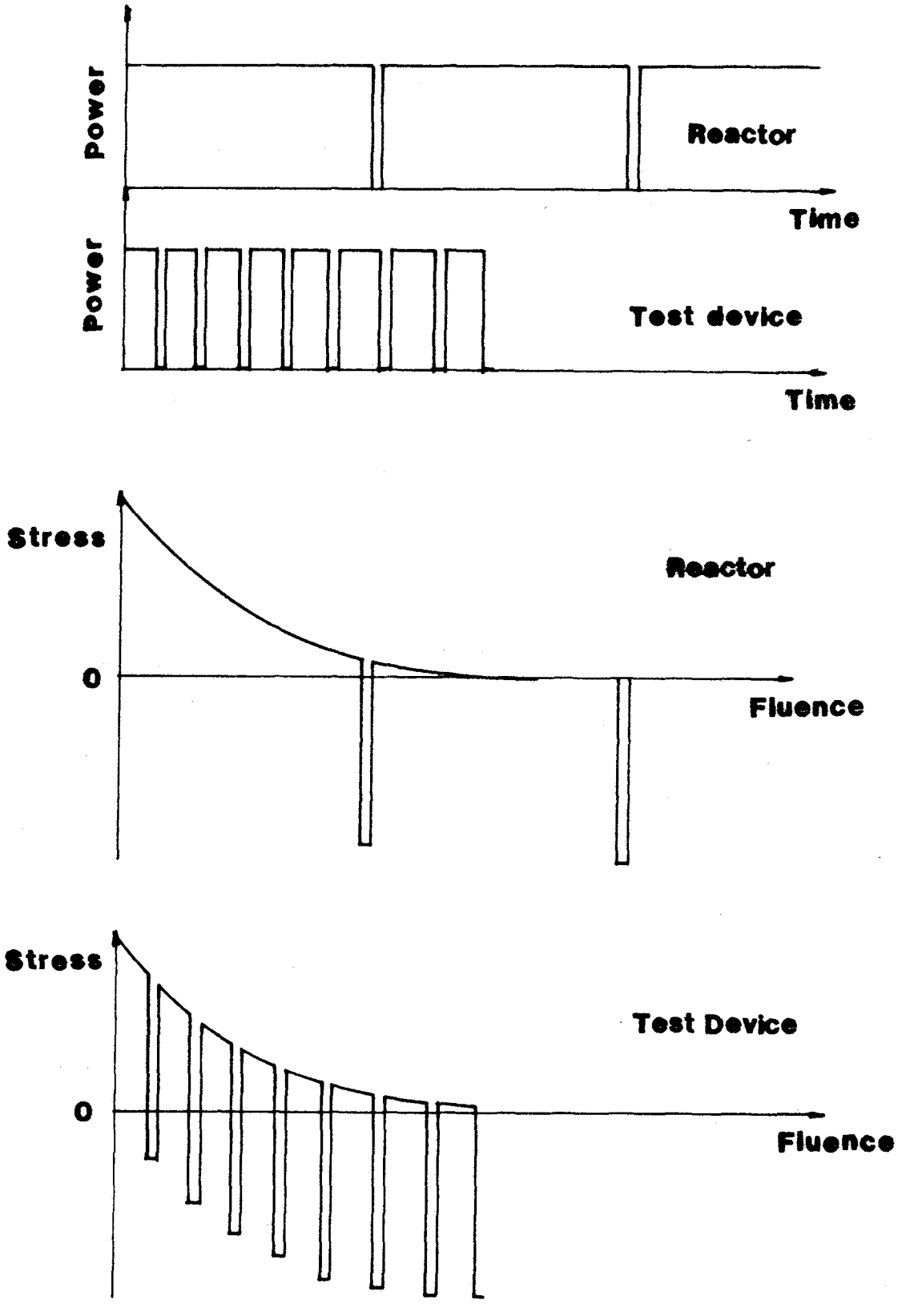

Figure 5.3.4-4 Effects of pulsing differences between a reactor and short burn test device on the time-dependent stresses, showing stress relaxation due to creep and the recovery of residual stresses during the dwell period.

are scaled appropriately with the geometry. Consequently, a primary breeder testing requirement is to maintain temperature profiles.

In Section 5.3.2, the ability to maintain the breeder temperature profile was discussed in some detail. The test requirements determined there are directly relevant to the solid breeder structural behavior. Specifically, if the heating rate profile is similar but the magnitude changed due to reduced neutron wall loading, then the steady-state temperature distribution can be preserved by reasonable increases in the breeder dimensions. If the device is pulsed, the need to preserve the temperature profile for the solid breeder structural behavior leads to requirements on the burn and dwell times.

Radiation effects Equation 5.2.4-14 indicates that the time scale for creep relaxation is $\tau_{cr} \sim 1/EA_{cr}$, where A_{cr} is a function of flux and temperature. Furthermore, the steady-state stress level B_{sw}/A_{cr} is also related to the flux. The creep rate is not known for solid breeder materials. As a very rough guide, τ_{cr} is about 2 dpa (~ 300 hrs under fusion reactor conditions) - for many nuclear structural alloys, and on the order of 10-100 hrs (under LWR conditions) for UO_2 below 1100 K.[3] It would be desirable to expose the breeder region to similar fluences in order to see the steady-state stress levels resulting from the interaction of creep relaxation, swelling (see also Fig. 5.2.4-7), and interaction between solid breeder and clad. There are many other fluence related effects will influence the breeder mechanical behavior. Some of these are further discussed in Chapter 8 with respect to fluence goals for the test module.

Pulsing effects Time-dependent and pulsing related effects on the breeder region structural behaviour have not been treated other than in the discussion on preserving temperatures under pulsing (Section 5.3.2.2). They will certainly be important. For example, transient thermal gradients during handling or startup may be a primary factor in the cracking of solid breeder pellets.

5.3.4.5 Summary

Preserving stress distributions in scaled tests of solid breeder blanket modules leads to several test requirements. For general thermoelasticity, maintaining temperature distribution and coolant pressure, and scaling all dimensions and body forces leads to preserved stresses and proportional displacements. If dimensions are increased, however, to compensate for a reduced heat source and preserve the temperatures, then several factors become limiting - the overall size of the blanket may become too large, or the variation in radiation effects through the blanket may be changed due to increased attenuation. Furthermore, it is not possible to exactly preserve the temperature distribution under scaled test conditions and the temperature deviations lead to corresponding deviations in the stresses. Radiation effects in general suggest a minimum fluence goal for the first wall of 5 dpa in order to achieve the creep-relaxed stress state.

A number of phenomena were not considered here in detail, but are probably significant. The primary concerns are fluence and pulsing effects in the solid breeder mechanical behaviour, the breeder/structure interaction, and crack growth in the first wall.

References for Section 5.3.4

1. R. J. Atkin and N. Fox, "An Introduction to the Theory of Elasticity", Longman, New York (1980).

2. M. Abdou et al., "Blanket Comparison and Selection Study, Interim Report", Argonne National Laboratory, ANL/FPP-83-1 (October 1983).

3. D. Olander, "Fundamental Aspects of Nuclear Reactor Fuel Elements", Energy Research and Development Administration, TID-26711-P1 (1976).

5.4 Test Module Design

5.4.1 Introduction

In the previous sections, solid breeder blankets were analyzed to determine the important phenomena under reactor conditions, and to identify scaled test methods and requirements in order to reproduce the reference component behavior. However, these considerations were based on particular analyses of blanket behavior, while an actual integrated test must combine all aspects of blanket performance. In this section, the basic design of a blanket test module is considered in order to bring out conflicts and identify the characteristics of a scaled test module.

5.4.2 Parametric Test Module Design

It is useful to consider these integrated aspects of scaled testing in the context of a test module design. Here, the basic features of an integrated test module are considered parametrically under arbitrary test facility conditions of surface heating, volumetric heating, tritium generation and test volume.

The basic blanket parameters - the independent variables - are given in Table 5.4-1, along with typical values in the reference blankets. These include device-related parameters such as surface heat flux or test module length that are presumed to be specified independently by the test facility design. They also include blanket-specific parameters such as first wall thickness or purge flow rate that could be changed if needed to preserve some desirable feature of an operating blanket. The list is certainly not complete, but does contain the most useful variables. For example, altering the grain size of the solid breeder is a possible way to help control tritium levels. However, it is not clear that this would be useful since grains will grow under typical breeder conditions, particularly in Li_2O, and the effects of grain size on tritium and helium transport are not entirely understood.

In Table 5.4-2, the blanket conditions of interest - the dependent variables - are given. Also shown are simplified equations relating these parameters to the independent variables of Table 5.4-1 that are approximately correct under reference steady-state conditions, at least. These relations are described in or inferred from the appropriate part of Section 5.2. These

blanket conditions are not a complete set. Many important phenomena related to radiation damage or breeder/clad mechanical interaction, for example, are not shown. However, the basic characteristics of the temperature, stress (pressure and thermal), flow and tritium distributions are present.

The process of developing a parametric test module design is to take these conditions, with their models, and vary the independent variables to preserve the blanket conditions as device parameters change. Specifically: (1) determine which conditions are more important in order to handle any conflicts; (2) starting with the most important blanket conditions, determine how to vary any independent variables with device parameter so as to preserve these conditions; (3) iterate as necessary when conflicts are identified, trying different independent variables where possible or balancing among the importance of the conditions. The results of two particular analyses are given in Table 5.4-2. The "look-alike" module does not change any dimensions - only flow inlet conditions are allowed to vary. The "act-alike" allows any independent variable from Table 5.4-1 to change in order to have the test module behave like the full component.

For example, the temperature profile in the first wall region is important for thermal stress, creep, tritium permeation, material properties, and radiation effects. This 3-D profile cannot be completely characterized by a few variables, but certainly key parts include the temperature rise across the first wall surface, ΔT_{fw}, the coolant film rise, ΔT_{film}, the coolant bulk temperature rise, $\Delta T_{coolant}$ and the coolant inlet temperature, T_{fin}. For most phenomena, it is important to maintain average temperatures at reactor conditions, but for stresses it is more important to maintain ΔT_{fw}. For some phenomena such as permeation, ∇T_{fw} might also be significant.

Consider the first wall temperature rise first. If surface heating is dominant, then $\Delta T_{fw} \sim q_s d_{fw}$. Since surface heating is an independent device parameter, it is allowed to vary freely. Thus, if the first wall thickness is fixed in the test module, ΔT_{fw} will decrease whenever the surface heat is decreased. In a test device with low surface heating, such a "look-alike" first wall would not preserve ΔT_{fw}, and thus not maintain thermal stresses, among other phenomena.

On the other hand, if the first wall thickness d_{fw} is varied to suit the available surface heating, then it is possible to preserve ΔT_{fw}. This has

been done in the "act-alike" scaling shown in Table 5.4-3. However, although this maintains ΔT_{fw}, note that d_{fw} is now a constrained variable and is not free to be used to preserve other phenomena.

In tokamaks, the assumption of surface heating dominance is true within 20%, although in mirrors or test devices, bulk heating may be equally or more important. If surface heating is not dominant, then a more exact expression must be used for ΔT_{fw} including the bulk heating contribution. This will lead to a more complex expression for the act-alike scaling of d_{fw} as a function of q_s and $\dot{Q}_v$, but will not change the approach or conclusions.

The film temperature rise is given by $\Delta T_{film} \sim q_s/(\dot{m}''_{fw})^{0.8}$ based on a Dittus-Boelter heat transfer coefficient, and $\dot{m}''_{fw} \sim \rho_c U_{fw}$ is the mass flux, ρ_c is the coolant density, and U_{fw} is the first wall coolant velocity. Preserving ΔT_{film} under varied q_s implies controlling the mass flux such that $\dot{m}''_{fw} \sim 1/q_s^{0.2}$ (only one significant digit is retained in this scaling). Finally, maintaining $\Delta T_{coolant}$ places a requirement on the ratio R_{fw}/d_{fc} since $\dot{m}''_{fw}$ is already constrained.

However, from flow conditions as characterized by the Reynold's number, and the thermal and pressure stresses in the first wall, there are additional requirements on d_{fc}, the coolant pressure p_c, the overall geometric ratios, and on the first wall lobe radius R_{fw}. A plausible approach to maintaining all these first wall conditions is to vary the first wall thickness and mass flow rate to maintain ΔT_{fw} and ΔT_{film}, to preserve geometric aspect ratios and to maintain the coolant pressure. Then, within the accuracy of the parametric relations used, these key conditions are maintained under test device conditions. Note that $\Delta T_{coolant}$ and Re_{fw} are not exactly preserved, but are at worst slowly varying functions of the surface heating.

Again, it is emphasized that the parameters considered here do not fully characterize the first wall temperature, stress and flow conditions, and furthermore the parametric relations used may be approximate. More exact analyses of the effects of scaling on first wall stresses and temperatures were given in Section 5.3. Nonetheless, the important point is that the first wall temperature distribution, thermal and pressure stress distribution, and flow regime can be approximately maintained in a test device under reduced heat source conditions with little conflict between the scaled variables.

This line of thinking is not yet complete since the breeder region still must be considered. The temperature distribution is very important for tritium transport, thermal stresses, tritium permeation, creep, material properties, sintering, mass transfer, radiation effects. As in the first wall, it is desirable to preserve $\overline{T}$ and ΔT in each region. The breeder temperature gradient ∇T_{br} might be important for some unknown processes, but apparently not on the basis of known phenomena. The clad ΔT was neglected as a small and well-understood contribution. The gap ΔT is, however, important but poorly understood. As shown here, the gap heat transfer coefficient is assumed dominated by the contact pressure between solid breeder and clad or structure. In the ductile clad Li_2O/He/HT-9 design, this pressure should be dominated by the coolant pressure, while in the stiffer $LiAlO_2$/Be/H_2O/PCA blanket, the pressure is probably more related to the thermal expansion of the solid breeder. Flow conditions are again represented by the Reynold's number, while structural behavior is dominated initially by thermal stresses. Radiation effects and the breeder/structure interaction are very important, but are difficult to model.

Under "look-alike" conditions where dimensions are not changed (although flow rate might be), the temperature distribution and thermal stresses are not maintained if the volumetric heating changes. Under the "act-alike" approach, the steady-state temperature distribution (average and temperature rise in each region) can be approximately preserved as shown. The key losses are the gap ΔT (an appreciable loss, but not really controllable since it is not well-modelled), the breeder ∇T, (not believed important for any known processes under breeder conditions, but potentially significant), and the bulk coolant ΔT (a small contributor to the overall temperature profile).

The scaled test should preserve the tritium inventory distribution, including its contributions from the various breeder regions and transport processes in order to preserve concentration-dependent processes. The leading variables to preserve tritium concentrations are the temperature profile, tritium generation rate, breeder structure (porosity, grain size) and purge conditions. The temperature can be approximately maintained as already discussed, tritium generation is considered a device parameter, and the breeder microstructure influence is too poorly understood to be a useful variable, so the only remaining controls are related to the purge flow. These

can be used as shown (Table 5.4-1) to maintain the tritium levels in the pores (and thus the soluble inventory) and in the purge stream itself, but there are no useful controls on the diffusive tritium concentration. This is a major contributor to overall inventory and, while the basic diffusive process is retained, any concentration effects would not be (e.g., local deviations from assumed Li_2O thermochemistry due to high concentrations of free oxygen). The influence of surface adsorption is also not well-understood and so difficult to maintain, although preserving temperatures, tritium vapor pressures, and surface microstructure (pore size, grain size) should help.

Since the test facility may be pulsed or have a shorter operating time than a reactor, it is useful to consider how the various process time constants were affected by the scaling. In general, thermal and flow related time constants are retained under "look-alike" scaling (they are dominated by dimensions), but not under "act-alike" scaling. Tritium time constants are functions of temperature and dimensions. Interestingly, the diffusive response time - usually the controlling time - is maintained, even though the diffusive inventory is not.

5.4.3 Summary

Within the range of independent variables available - primarily dimensions and flow parameters - the ability of a scaled test to preserve basic blanket features was considered. Two basic options were evaluated: (1) a "look-alike" test module where all dimensions are fixed at the reference design values, and (2) an "act-alike" test module that varied any plausible design parameter. The intent was to preserve the basic temperature, stress, tritium and flow distributions.

The analysis was based on simple parametric relations, and did not consider some important behavior in detail. These include creep (although temperature and initial stresses are considered), radiation or fluence effects (again, temperatures were considered), specific failure modes such as crack growth (geometry, temperature and overall stress levels were considered), mechanical interactions related to the solid breeder (external pressures, internal expansion, internal structure and temperature were considered), interactive effects on tritium recovery (temperature and geometry were considered), safety issues (tritium inventory, temperature and time constants were

considered), and magnetic field effects.

The results indicate that a number of important operational features related to temperature, thermal and pressure stresses, tritium inventory and flow conditions can be simultaneously maintained in a scaled blanket test module (within the accuracy of the parametric relations used). An approximate test module design may be obtained from Table 5.4-2 by evaluating the scaling factors for the particular device parameters of interest.

This analysis also does not indicate any fundamental conflicts between the first wall and the breeder scaling methods considered. There are, however, limits on the usefulness of scaled testing due to fundamental conflicts between, for example, preserving temperature distributions and reducing the test module time constants or size under reduced heat source conditions. It is also expected that not all features of the temperature profile can generally be maintained; some because of fundamental difficulties (e.g., ΔT versus ∇T), some because the basic models needed to derive scaling methods are not well-known (e.g., ΔT_{gap}), and some because there are other more important conditions that required the extra degree of freedom. It will also be difficult to adjust the diffusive tritium concentrations to maintain reactor levels unless the neutron flux or lithium enrichment can be altered.

Finally, transient behaviour of the test module will not be similar to the reference blanket in the scaled tests considered here (which emphasized steady-state similarity) since the various time constants do not in general scale proportionally to each other.

Table 5.4-1 Solid Breeder Blanket and Device Independent Variables

Parameter	$Li_2O/LiAlO_2$ Blankets	Test Module+ "Look-alike"	Test Module+ "Act-alike"
Surface heat flux, q_s	1/1 MW/m^2	q_s*	q_s*
Volumetric heating, $\dot{Q}_v$	50/50 MW/m^3	$\dot{Q}_v$*	$\dot{Q}_v$*
Tritium production rate, G	10^{19} T/s-m^3	G*	G
First wall lobe radius, R_{fw}	0.15 m	1	$1/q_s$
Blanket axial length, L_{bl}	2 m	L_{bl}*	L_{bl}*
Breeder radial depth, L_{br}	0.6/0.5 m	1	L_{br}*
Coolant inlet, T_{fin}	275/280 C	$f(q_s)$	1
Coolant pressure, p_c	5.2/15.2 MPa	1	1
First wall velocity, U_{fw} ($\dot{m}''_{fw} = \rho_c U_{fw}$)	60/3 m/s	1	$q_s^{1.2}$
First wall thickness, d_{fw}	3.5/5.5 mm	1	$1/q_s$
FW coolant diameter, d_{fc}	1.8/3.8 mm	1	$1/q_s$
FW rib thickness d_{fs}	1.0/1.3 mm	1	$1/q_s$
Breeder inlet, T_{bin}	334/280 C	$f(q_s)$	1
Breeder pressure, p_b	5.1/15.2 MPa	1	1
Breeder velocity, U_{br} ($\dot{m}''_{br} \sim \rho_c U_{br}$)	20/5 m/s	1	$Q_v^{0.6}$
Breeder thickness, d_{br}	1.1/0.5 cm	1	$1/Q_v^{0.5}$
Breeder channel diameter, d_{bc}	0.1/1 cm	1	$1/Q_v^{0.6}$
Purge pressure, p_p	0.1/0.1 MPa	$f(\dot{Q}_v)/G$	1
Purge channel spacing, L_p	0.8/2 cm	$1/L_{bl}$	1
Channel purge flow rate, V_p	10^{-4} m^3/s	G	$G\ L_{bl}/Q_v^{0.5}$
Purge channel diameter, d_p	1.5/6 mm	G	$(GL_{bl})^{0.5}\ Q_v^{0.25}$

* Independent variables

\+ If parameter X has scaling Y, then $X_{test}/X_{reactor} = Y_{test}/Y_{reactor}$
A scaling identified as f(Z) indicates a complex but strong dependence on Z.

Table 5.4-2 Solid Breeder Blanket Conditions and Phenomena

Parameter	Parametric Scaling	Test Module "Look-alike"	Test Module "Act-alike"
ΔT_{fw}	$q_s d_{fw}$	q_s	1
ΔT_{film}	$q_s/\dot{m}''^{0.8}_{fw}$	q_s	1
$\Delta T_{coolant}$	$R_{fw} q_s/\dot{m}''_{fw} d_{fc}$	q_s	$1/q_s^{0.2}$
Re_{fw}	$\dot{m}''_{fw} d_{fw}$	1	$q_s^{0.2}$
σ_{th}	$f(\Delta T_{fw}, d_{fw}/R_{fw})$	$f(q_s)$	1
σ_{fs}	$p_c(d_{fc}/d_{fs})$	1	1
σ_{fw}	$p_c(d_{fc}/d_{fw})^2$	1	1
$\Delta T_{breeder}$	$\dot{Q}_v d_{br}^2$	$\dot{Q}_v$	1
$\nabla T_{breeder}$	$\dot{Q}_v d_{br}$	$\dot{Q}_v$	$\dot{Q}_v^{0.5}$
ΔT_{gap}	$\dot{Q}_v d_{br}/p_{contact}$	$f(\dot{Q}_v)$	$\dot{Q}_v^{0.5}$
ΔT_{film}	$\dot{Q}_v d_{br}/\dot{m}''^{0.8}_{br}$	$\dot{Q}_v$	1
$\Delta T_{coolant}$	$\dot{Q}_v d_{br}/\dot{m}''_{br} d_c$	$\dot{Q}_v$	$\dot{Q}_v^{0.5}$
Re_{br}	$\dot{m}''_{br} d_{bc}$	1	1
ε_{th}	$\Delta T_{breeder}$	$\dot{Q}_v$	1
$n_{diffusion}$	$\dot{G}\ f(T)$	$\dot{G}\ f(\dot{Q}_v)$	$\dot{G}$
$n_{solubility}$	$f(n_{pore}, T)$	$f(\dot{Q}_v)$	1
n_{pore}	$d_{br}^2\ \dot{G} p_p/T^2 + n_{purge}$	1	$\dot{G}/\dot{Q}_v + 1$
n_{purge}	$\dot{G}\ L_{bl} d_{br} L_p/\dot{V}_p$	1	1
$t_{c,fw}$	R_{fw}/U_{fw}	1	$1/q_s^{2.2}$
$t_{th,fw}$	d_{fw}^2 or $d_{fw}/\dot{m}''^{0.8}_{fw}$	1	$1/q_s^2$
$t_{c,br}$	$(L_{bl}$ or $L_{br})/U_{br}$	$(L_{bl}$ or 1)	$(L_{bl}$ or $L_{br})/\dot{Q}_v^{0.6}$
$t_{th,br}$	d_{br}^2 or $d_{br}/\dot{m}''^{0.8}_{br}$	1	$1/\dot{Q}_v$
$t_{diffusion}$	$f(T)$	$f(\dot{Q}_v)$	1
$t_{solubility}$	$f(n_{pore}, T)$	$f(\dot{Q}_v)/\dot{G}$	$1/\dot{G}$
t_{pore}	$d_{br}^2 p_p/T^2$	$1/\dot{G}$	$1/\dot{Q}_v$
t_{purge}	$\dot{V}_p/d_p^2$	1	$1/\dot{Q}_v$

5.5 Engineering Scaling

5.5.1 Introduction

At the integrated testing stage in the development of blanket technology, enough prior testing should have been done to provide basic property data and to identify phenomena. The purpose of these tests is to quantify interactions, demonstrate the concept, and check for and determine the significance of "unknowns". This verification process is difficult under scaled test conditions. If the blanket is not changed, it will behave differently and so not verify the full operation. On the other hand, if the blanket is modified to preserve the operating features, then it is not the actual component that is truly verified, but the scaled test module. Engineering scaling is the process of determining how to do the test while minimizing these concerns.

As considered in the previous sections, solid breeder blankets were analyzed to determine the important blanket conditions and phenomena under reference reactor conditions, to identify blanket modifications that reproduced specific aspects of reference component behavior, and to determine the limits of usefulness of these modifications. In this section, the overall test requirements and limits of usefulness for interactive and integrated testing, based on the limited analyses described here, are summarized.

5.5.2 Test Requirements for the "Unknowns"

A prime function of the integrated stage of blanket development is to identify any remaining unknowns. It is thus desirable to determine the test requirements for the scaled test such that it will demonstrate all the unknowns that the full component would. However, it is inherent in the definition of the "unknowns" that they cannot be easily classified and tested. The only definitive resolution of unknowns is through cumulative experience operating the component in normal service.

A useful step, though, may be to consider the characteristics of unknowns brought out by integrated tests. Unknowns may be characterized by whether the effects are basically unexpected, or whether they represent phenomena that had been identified as of concern but as being essentially non-calculable. This is the "unknown unknown" and "known unknown" distinction. For example,

the pressure drop across the blanket is not precisely known because the complex geometry makes accurately solving the Navier-Stokes equations impracticable. There may be bounding estimates with small or large uncertainties, but actual measurements of the pressure drop will be required to determine this design parameter.

Within these categories, three further distinctions may be identified:

- synergistic effects from multiple environmental conditions;
- physical interactions between different regions;
- local phenomena.

The first type is brought out when all the environmental conditions are put together. While the environmental conditions themselves need not interact directly, their effects may be enhanced when other environmental conditions are present. For example, bulk heating of the breeder will raise its temperature and cause thermal creep, however until a test with both temperature and neutron irradiation is made, the much faster radiation-enhanced creep would not be observed.

The second type is identified when multiple physical regions are put together. For example, tests on the front part of the breeder would miss interactions between the hot, high fluence front breeder and the colder, low fluence back breeder. Or single channel tests will miss flow instabilities and redistribution that occur with multiple channels.

The third type consists of local, non-interactive phenomena. For example, at high pressures, tritium permeation appears to be controlled by dissociation and atomic diffusion. However, while high pressures may conveniently speed up permeation tests, permeation may actually be controlled by different processes (chemisorption, molecular diffusion?) at the very low tritium partial pressures relevant to fusion blankets (10^{-7} - 10^{0} Pa T_2).

The general nature of the test requirements can be estimated based on this structuring of the unknowns. First, any "known unknown" is at least partially tested by trying to reproduce or retain the phenomena under the relevant reactor-like conditions. The degree to which the phenomena is "known" allows an assessment of the important conditions that need to be reproduced. This leads to many of the test requirements identified in earlier sections. These unknowns often depend on the complexities of the blanket and its processes, which should consequently be retained in the test module.

Secondly, "unknown unknowns" suggest other general test requirements. The first requirement is to maintain as many environmental conditions as possible. Exactly which conditions is hard to say a priori, but at a minimum certain basic operational features that are potential energy sources, and thus able to "activate" phenomena, should be present. These should specifically include thermal (temperature, radiation), mechanical (stress, flow, radiation), chemical (tritium) and electromagnetic (magnetic field) energy sources. The second class of unknowns require the test module to include all blanket regions - multiple channels, first wall, breeder and inlet/exit manifolds. The final class of unknowns are based on individual regions or conditions, and should also be largely included if the various environmental conditions and physical regions are present.

5.5.3 Test Device Requirements

The device parameters with a strong influence on test module conditions and on the test device cost can be grouped into the six categories of heat source, neutron radiation, operating time, test volume, device geometry and magnetic field.

The behavior or response of the solid breeder blanket to these test device parameters can be grouped into roughly five categories also (as in the analyses in Section 5.2 and 5.3):

- neutronic behavior;
- thermal behavior;
- flow and corrosion behavior;
- tritium behavior;
- structural behavior.

Table 5.5-1 shows some blanket responses to the device parameters. Clearly, each device parameter has many effects. Furthermore, the direct blanket response to the device environment can in turn influence further blanket behavior. For example, the structural response due to neutron-induced swelling may lead to blocking of the tritium purge channels.

It has not been possible to analyze this full complexity of blanket behavior and determine whether the tests can reproduce all these interactions under scaled conditions. However, a wide range of important issues were considered, and it is unlikely that consideration of other effects will make

Table 5.5-1 Direct Relationships Between Test Device Parameters and Blanket Performance

Blanket Performance	Test Device Parameters: Heat source	Neutron Radiation	Operating Time	Device Geometry, Test Volume	Magnetic Field
Neutronics	Geometrical changes due to thermal expansion	Burnup	?	Neutronic boundary conditions	?
Thermal	Temperature profile	Thermal conductivity and breeder/gap conductance changes	Transient temperature distribution	Thermal boundary conditions	?
Structural	Material properties Thermal stresses Thermal creep Crack initiation and growth	Swelling Irradiation creep Property changes	Fatigue Crack growth Ratchetting	Breeder depth Module length Module width	Steady-state and transient forces
Flow and Corrosion	Coolant properties Corrosion rate Re and Nu regimes	Corrosion? Neutron sputtering	Corrosion equilibrium	Flow distribution Entry lengths Multiple channel phenomena	Corrosion?
Tritium	Diffusion and other transport processes Solubility Mass transfer Grain growth Porosity changes	H^3 generation Burnup-related thermochemistry changes	Permeation equilibrium Inventory and recovery equilibrium	Purge channel length Radial depth for front/back interaction Width for multiple element interactions	?

the test requirements any less stringent. Thus the present results may be interpretted as, if anything, optimistic regarding the scaled test usefulness.

The test requirements as identified here are summarized and discussed below. It is convenient to consider them in terms of the five classes of test device parameters: heat source, neutron radiation, operating time, test volume, device geometry and magnetic field.

5.5.3.1 Heat Source

The fusion heat source is directly related to the plasma size and power density, which in turn are direct cost drivers for the test device. Surface heating may be simulated with non-plasma sources such as charge-exchange from neutral beam injectors or electrically-heated radiative filaments. Volumetric heating may be supplemented with electric heaters or with the addition of fissile material into the breeder region. This analysis did not consider the usefulness of these supplemental heat sources. Rather, the intent was simply to derive the basic requirements on the heat sources, whatever their origin.

Surface heating and bulk heating Surface heating is related to the plasma radiation and charge particle flux, while bulk heating is related to the neutron wall load. These may be changed - particularly reduced - in a test facility. The primary effect is on the first wall and breeder temperatrue distribution, which in turn affect a number of phenomena.

To retain the first wall temperature distribution under reduced heat source conditions, a plausible approach is to increase dimensions. By also varying the coolant flow rate, it is possible to preserve the average and extreme temperatures in each region, within certain limits. The required increase in dimensions is shown in Fig. 5.5-1 for one blanket, similar increases are needed for the others. Ideally, all dimensions should be scaled by the same factor as the first wall thickness. If these changes are made, the temperature distribution will be approximately preserved.

Note that in a tokamak, the surface heating is most important. In fact, with no bulk heating - i.e., no neutrons - a very good simulation of the first wall temperature is possible down to very low surface heat fluxes. The presence of bulk heating substantially complicates the temperature scaling at reduced heat source conditions since increasing the thickness preferentially

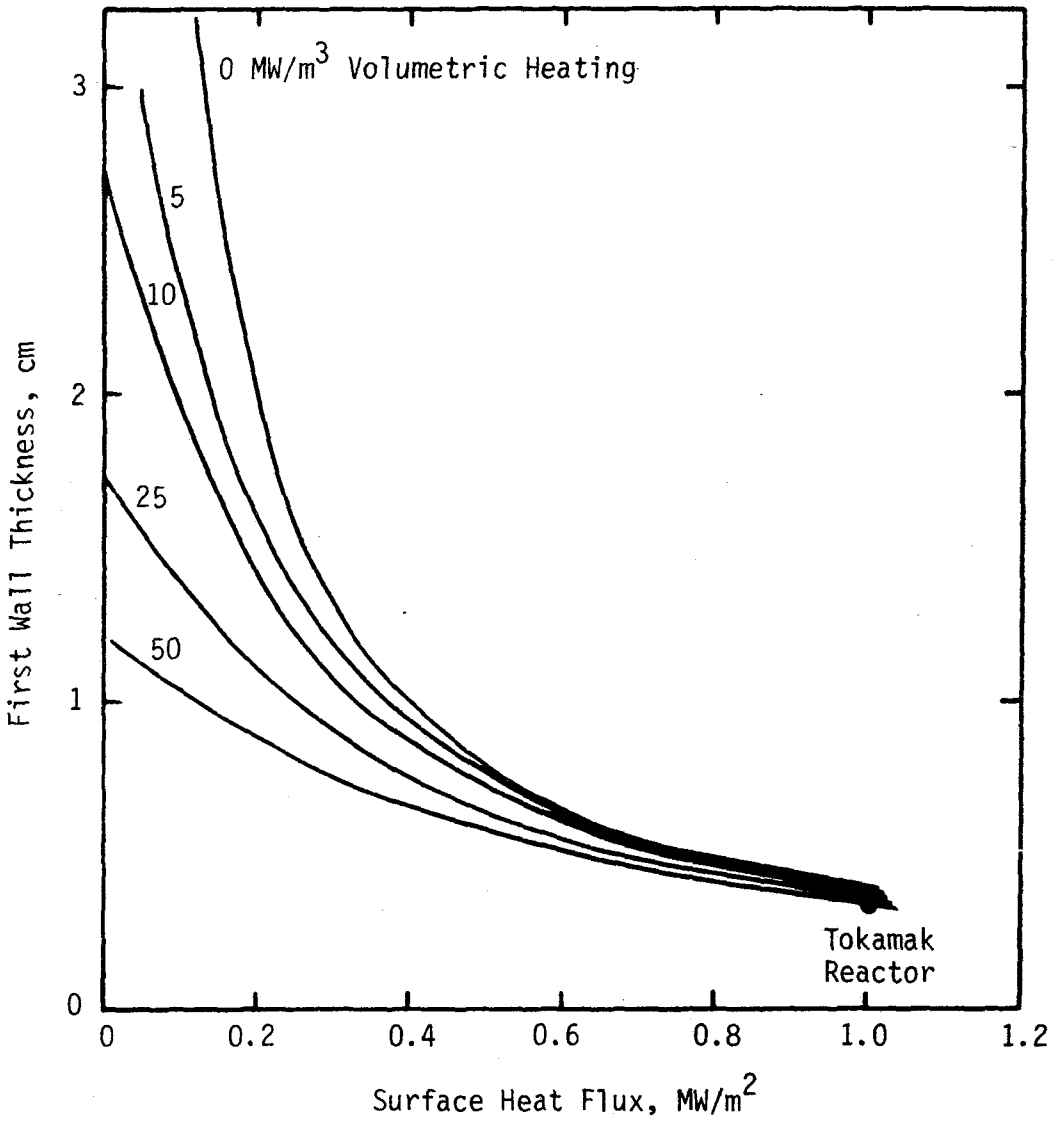

Figure 5.5-1 First wall thickness needed to maintain the first wall ΔT under changed heat source conditions for the Li_2O/He/HT-9 tokamak blanket.

increases the bulk heating contribution (it scales with thickness squared).

Alternately, in mirrors it is bulk heating that dominates. In the absence of any surface heating, bulk heating can be made to provide a reasonable temperature simulation over a wide range of heating rates. However, while the test facility is likely to be lower in bulk heating than in a reactor, the surface heating may well be larger than in the mirror reactor. A tokamak test facility will naturally have a large surface heat flux, but even a mirror test facility may have appreciable surface heating due to charge-exchange neutrons from the small, often beam-driven central cell plasma. If there is too much surface heating, it is similarly expected that the first wall temperature distribution will not be preserved.

This balance between surface and bulk heating is shown in Fig. 5.5-2, illustrating the desired heating regime for preserving the first wall temperature profile for both tokamak and mirror first walls. This boundary, shown for three representative first wall designs, is basically the point at which the first wall makes the transition between bulk heating and surface heating dominated temperatures. It is difficult to preserve the temperatures beyond this transition since surface and bulk heating contribute differently to the various parts of temperature profile (e.g., first wall, film and bulk coolant temperature rise).

The breeder region temperatures must also be controlled to reproduce the reactor conditions for tritium recovery and structural behavior. Under reduced neutron wall load, the bulk heating will decrease. The temperature may be maintained by increasing the breeder thickness. Some concerns related to changing the thicknesses in the breeder region are an increase in axial conduction, an increase in the variation in neutron heating across the unit cell, and enhanced neutron attenuation in the breeder due to increased structure or coolant volume fractions. However, these were not found to present problems for scaled testing. For example, the heating rate changed by less than 10% changes for a 300% increase in the structural volume fraction in the Li_2O/He/HT-9 tokamak blanket.

5.5.3.2 Neutron Radiation

A wide variety of effects occur in solid breeder or structural alloys under neutron irradiation. Some effects such as the creep and swelling rate

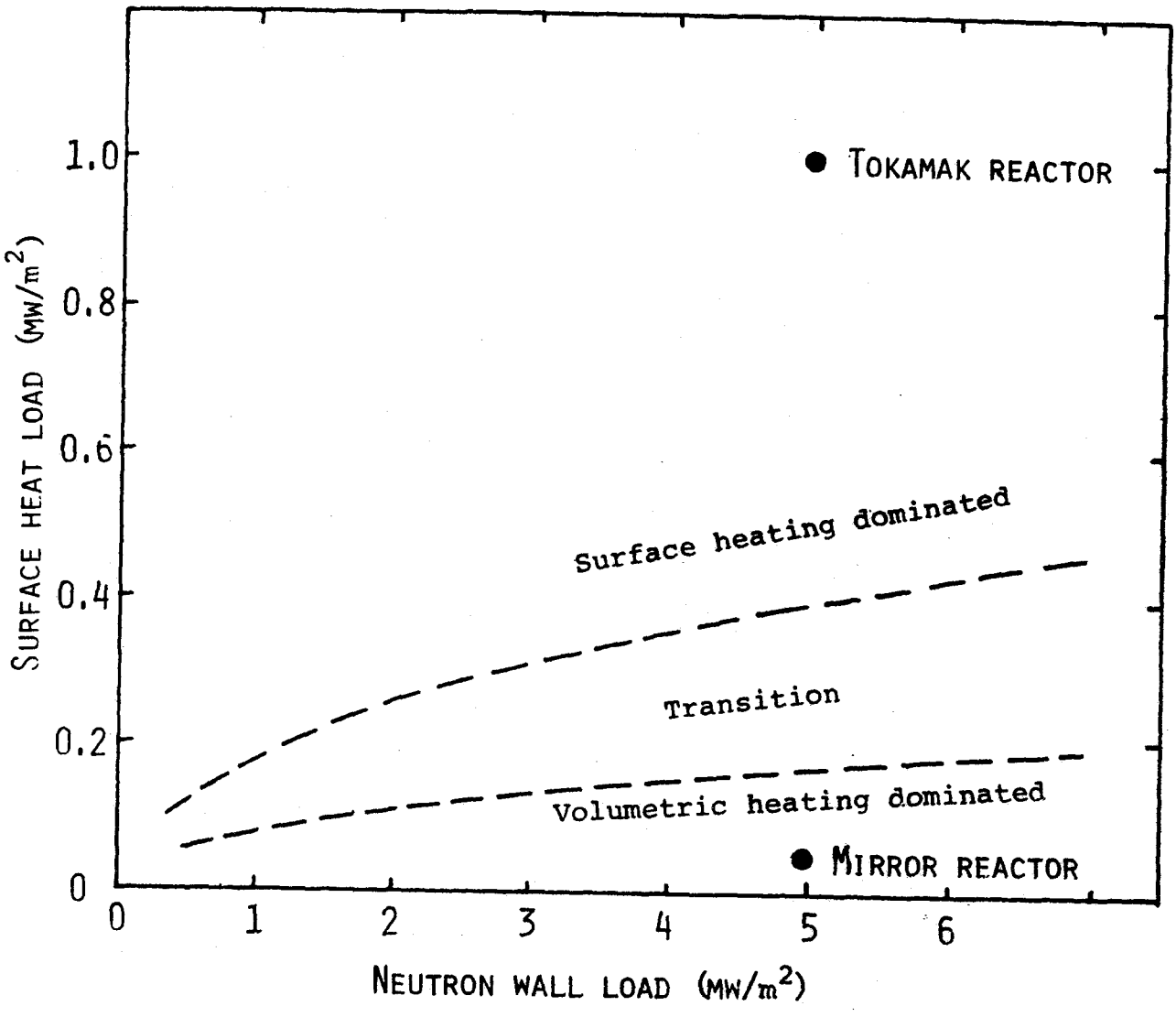

Figure 5.5-2 Boundary between surface heating and volumetric heating dominated first wall temperature profiles.

are directly related to the neutron flux, while others such as property changes are related to the cumulative fluence. Furthermore, many effects such as helium production are related to the neutron energy spectrum since the neutrons must be energetic enough to activate particular processes.

No detailed analyses of fluence effects has been considered here, although many fluence-related effects for structural behavior (creep relaxation, property changes), tritium recovery (temperature changes due to thermal conductivity or gap conductance, LiOT formation) and solid breeder mechanical interaction issues would be observable by 1 - 4 MW-yr/m^2.

However, fluence differences between blanket regions were considered to some extent. In particular, Fig. 5.5-3 shows the neutron heating rate (and faster for radiation damage) attenuation through the first wall as a function of first wall thickness. Under reactor conditions, there is little attenuation in the first wall and the heating and damage rates within the first wall are uniform. As the thickness increases, the radiation effects or fluence profile changes in the first wall, and is reduced in magnitude in the breeder. From the first wall viewpoint, the change in fluence from front to back of the first wall - and thus the change in swelling and creep - can become structurally significant. From the breeder viewpoint, the thickened first wall represents an additional effective reduction in the neutron wall load. The effect may be enhanced with breeders such as Li_2O where the contribution of higher energy neutrons through the ^7Li reaction is important.

5.5.3.3 Operating Time

Present experiments have pulses that typically last for a few seconds, with very low overall availability (less than 1%). Reactors, however, will run at essentially steady-state conditions, with operating times of several months and overall availabilities of 60% or so to be competitive with other centralized electric generating stations. Clearly, substantial improvements in device burn length and availability are necessary for commercialization. However, the need for long burn lengths and high availabilities when testing blankets may not be so clear. Ideally, the test should be operated beyond any significant startup transients and allowed to settle into its long-term operating mode. In practice, this might be achievable by single, long pulse burns. Or it might be reached by a series of sequential pulses lasting for

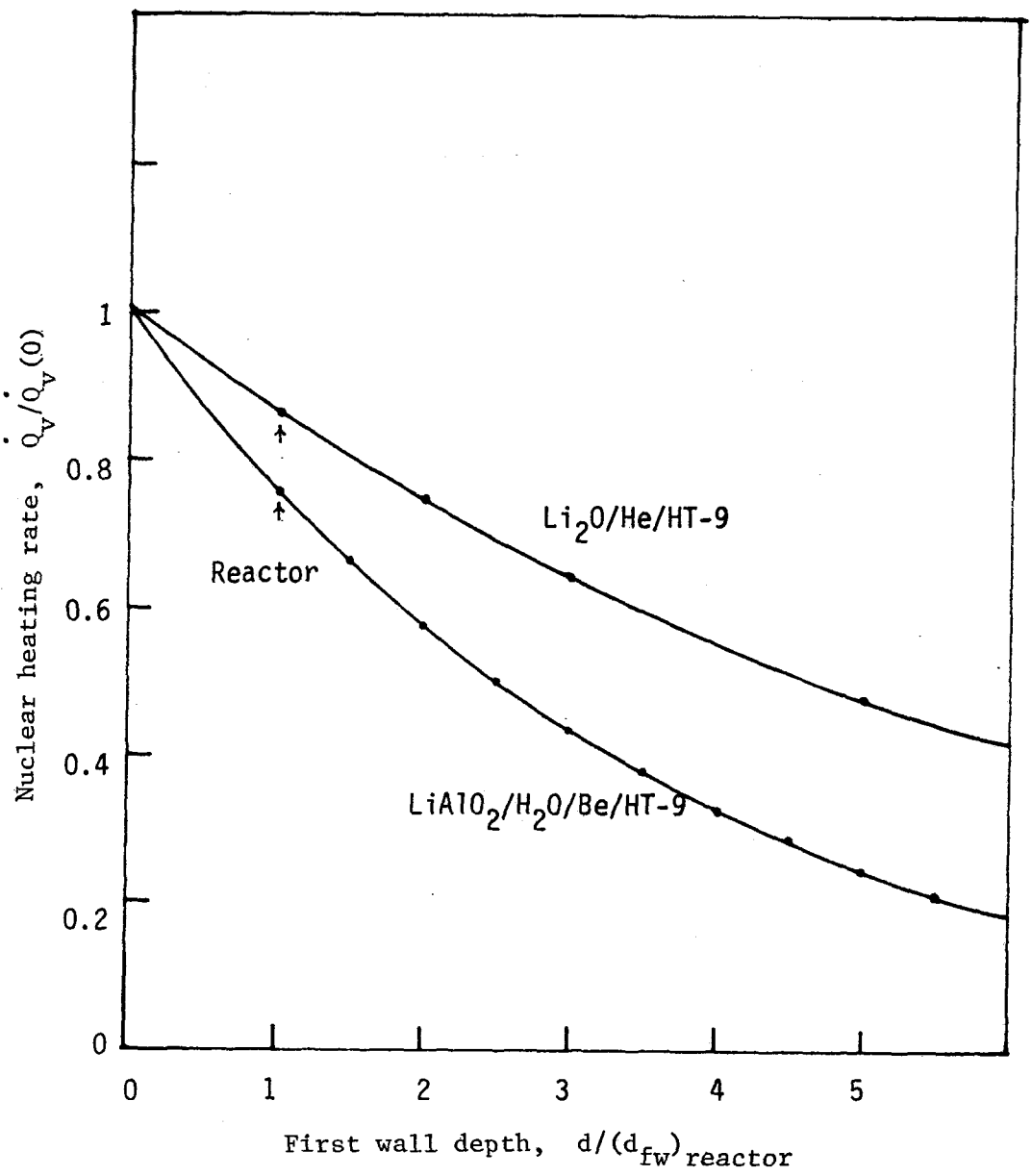

Figure 5.5-3 Attenuation of nuclear heating rate through the first wall. The reference reactor thickness is 10.8 and 11.9 mm for the Li_2O/He/HT-9 and $LiAlO_2/H_2O$/PCA/Be blankets, respectively.

some sufficiently long period to reach quasi-equilibrium conditions. This latter period is referred to as the Minimum Continuous Operating Time, MCOT.

Burn/Dwell time The various thermal and flow time constants for the reference solid breeder blankets are much less than about one minute. For example, the Li_2O/He/HT-9 breeder reaches 95% of equilibrium temperatures in about 45 s, while the time for the helium to flow through the entire module is only 0.3 s. The back cells of the $LiAlO_2/H_2O$ blanket, however, may take up to 45 min to achieve thermal equilibrium under reference conditions. These time constants are largely controlled by the dimensions of the structure and breeder. Tritium equilibrium times, however, are very long, up to almost four years to reach 99% of the final inventory in the $LiAlO_2/H_2O$/PCA/Be. Thus a blanket module in a full reactor will quickly reach thermal equilibrium, but will slowly approach its final tritium conditions well into its design life.

Under scaled test conditions, there are two immediate problems. First, the overall operating life of a test device is likely to be relatively short and limit the ability of a test module to reach tritium equilibrium. A more feasible goal is to reproduce the approach to equilibrium.

Secondly, while a test device might reasonably achieve 60 s burns suitable for thermal equilibrium under reactor conditions, this is not necessarily sufficient time under general scaled test conditions. Typically, the dimensions of the module are increased to retain temperatures under reduced test facility heat source conditions. However, this increases the thermal time constants. Furthermore, if the pulses are relatively short, then an additional scaling of dimensions will be necessary to account for the pulsing effect on the average temperature profiles. These can quickly accumulate to make the thermal time constants very long.

If the device is pulsed on times short compared to these characteristic thermal response times, the blanket temperatures will oscillate as shown in Fig. 5.5-4a for the Li_2O/He/HT-9 breeder region. This will affect the mass-weighted and time-averaged temperature distribution - the "temperature density" as shown in Fig. 5.5-4b. It may also add new effects related to fatigue and crack growth, thermal ratchetting, permeation barrier degradation or a large number of transient related phenomena that would not be significant for the reference blankets.

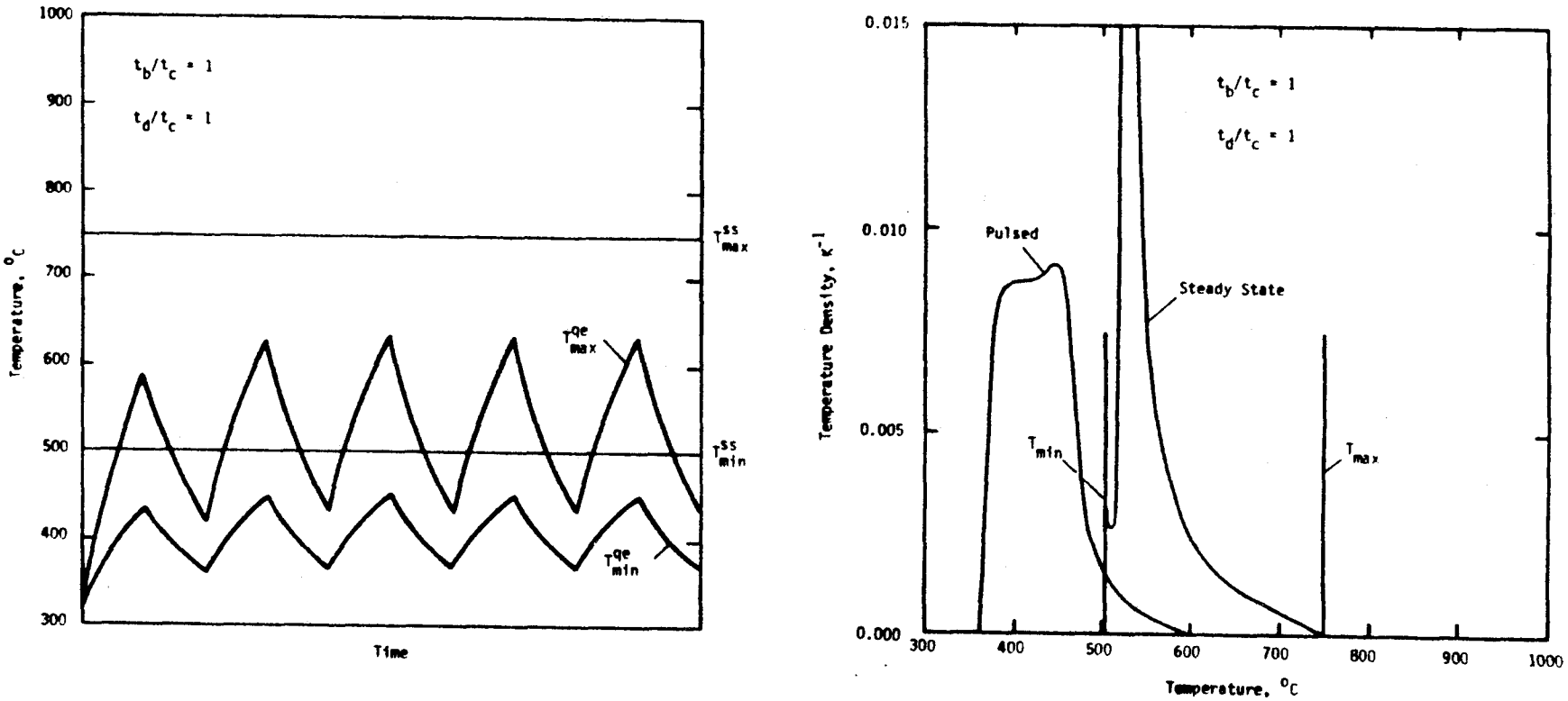

Figure 5.5-4 Effect of pulsing on the Li_2O/He/HT-9 breeder showing: (a) minimum and maximum temperatures; and (b) mass- and time-weighted temperature distribution.

Since the solid breeder (especially tritium recovery and structural behavior) is very sensitive to the operating temperature distribution (not just the average or extremes), as illustrated in Fig. 5.5-5, it provides a particularly strong constraint on device cycling. Pulsing generally leads to two temperature-related consequences: (1) a general shifting to colder temperatures; and (2) a spreading out of the temperature due to the time spent in the colder dwell part of the cycle. The former can be compensated, for example, by increasing the breeder thickness to boost the average power input into the breeder. The second can only be reduced by limiting the length of the dwell period. In particular, the breeder should not be allowed to fully cool down during the dwell period, requiring that the dwell time not exceed roughly three times the characteristic thermal time, preferably no more than one time constant to limit the extent of the cycling. The burn time, on the other hand, should be sufficient to approach thermal equilibrium in each pulse, or be at least three times this thermal time.

Note that there is a balancing between the burn and dwell time. Decreasing the neutron wall load and consequently increasing the thermal time constants through increased breeder dimensions will increase the required minimum burn time, but also increase the maximum dwell time. This is shown in Fig. 5.5-6, based on the Li_2O/He/HT-9 breeder design. For a neutron wall load of about 1 MW/m^2, the needed burn time is at least 500 s to approach thermal equilibrium on each pulse, while 1000 s would be desirable to actually operate at equilibrium in each burn. Correspondingly, a dwell time of 150 s or less is desirable.

Minimum Continuous Operating Time If the device operates with burn times sufficient to approach thermal equilibrium on each pulse, then a quasi-equilibrium state will be reached within a few cycles. This state may be maintained as long as necessary to reach some cumulative operating goal. This goal may be related to achieving some level of neutron damage, or accumulate enough time at high temperature for some structural rearrangement (creep relaxation, steady crack growth, breeder sintering) or to achieve tritium recovery equilibrium.

The verification of tritium behavior is accomplished by monitoring the tritium release rate and final inventory. Generally, attaining 67% of the

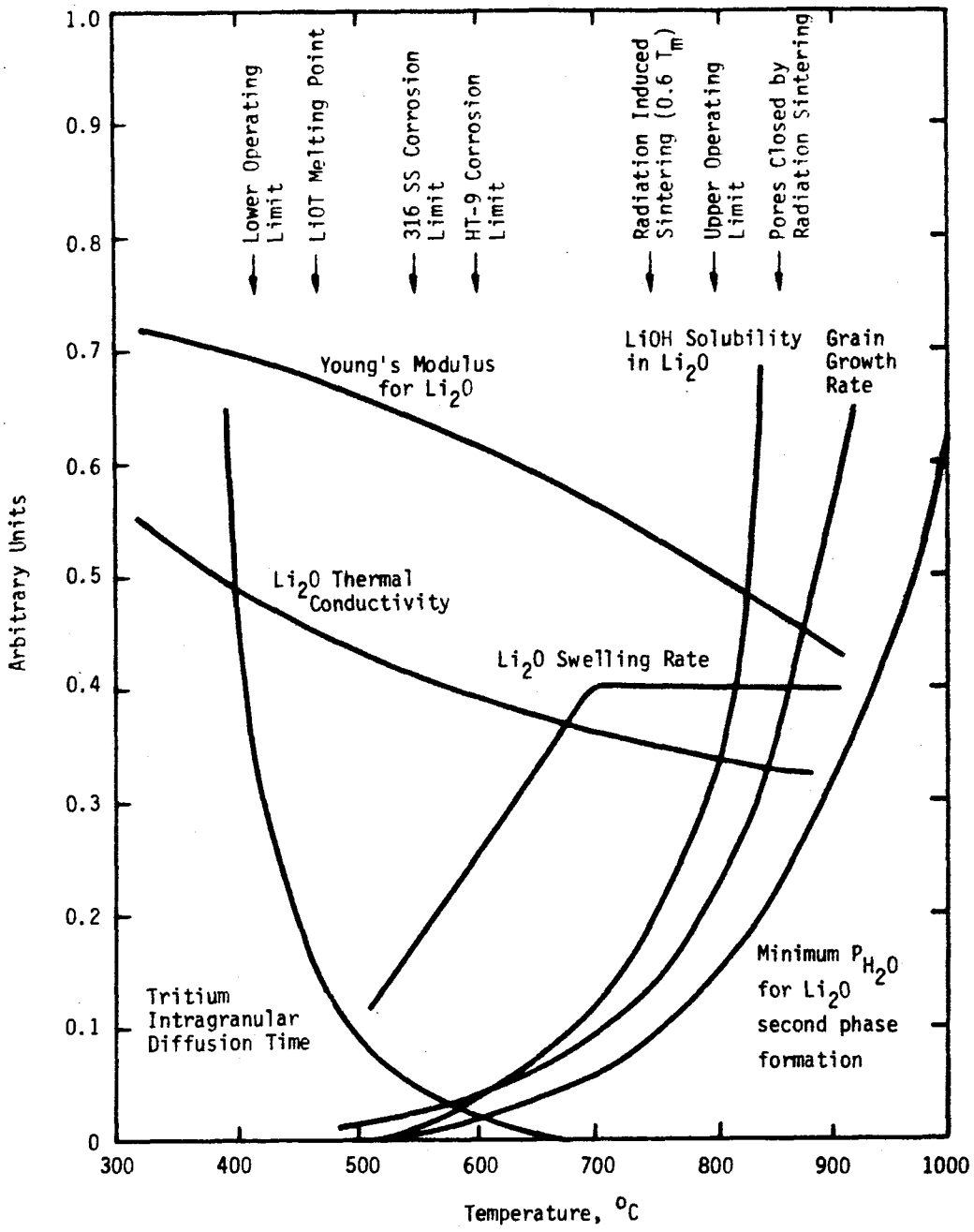

Figure 5.5-5 Temperature dependence of various phenomena occuring in Li_2O under irradiation

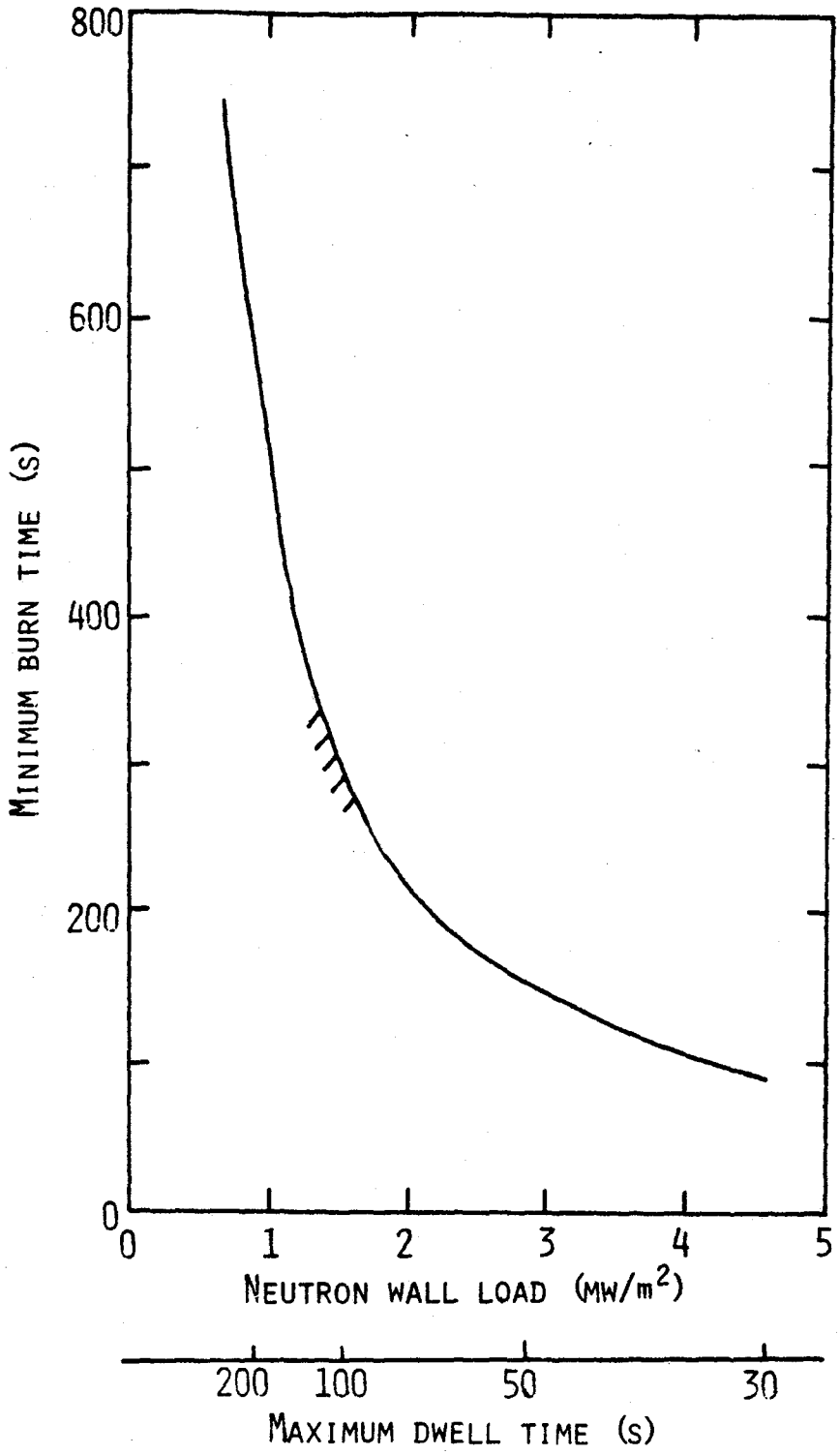

Figure 5.5-6 Relationship between maximum burn time, maximum dwell time and minimum neutron wall load based achieving thermal equilibrium in the Li_2O/He/HT-9 test module.

equilibrium release rate may be accomplished early in the test and accurately measured, but 99% recovery or inventory requires substantial operating times. Present calculations assuming the addition of hydrogen into the purge stream indicate that intragranular diffusion is the largest contributor to the total inventory. Consequently, Li_2O and $LiAlO_2$ will probably achieve 67% of the equilibrium release rate within about two minutes, independent of the neutron wall load. In order to reach 99% inventory equilibrium, however, total operating times of three minutes, four days and four years are needed for Li_2O, hot $LiAlO_2$ (over 510°C) and cold $LiAlO_2$ (over 350°C) respectively. Other processes have time scales on the order of a day (solubility, surface adsorption) or months (fluence effects), and will increase as the neutron wall load decreases. Thus a MCOT of one to eight weeks seems desirable. Other than fluence effects, though, this particular device parameter may be sensitive to the particular breeder design.

5.5.3.3 Test Volume

The amount of test volume available will limit the number of test modules or assemblies that can be fitted into the device simultaneously. It may even be so small that it directly limits even the size of a single module - width, length and/or depth.

Width A primary test requirement comes from the first wall structural behaviour, where it is necessary to treat the full curved arch of the first wall, requiring a width of 0.3 m for the reference blanket. However, under reduced heat source conditions, it is necessary to increase the dimensions of the first wall, including the radius of the arch and so the width of the test module. Figure 5.5-1 shows how the first wall dimensions must increase to preserve the temperature profile, while Fig. 5.5-7 shows the trade-off between the first wall width, the first wall dimensions, and the accuracy of simulation of first wall thermal plus pressure stresses.

The breeder width also increases as the bulk heating decreases, so as to preserve the overall temperature profile. This increase is generally as the square root of the change in bulk heating (i.e., neutron wall load), plus an additional factor for any pulsing effects. For example, a drop in neutron wall load from 5 to 1.2 MW/m^2, with a short burn/long dwell pulse leads to a

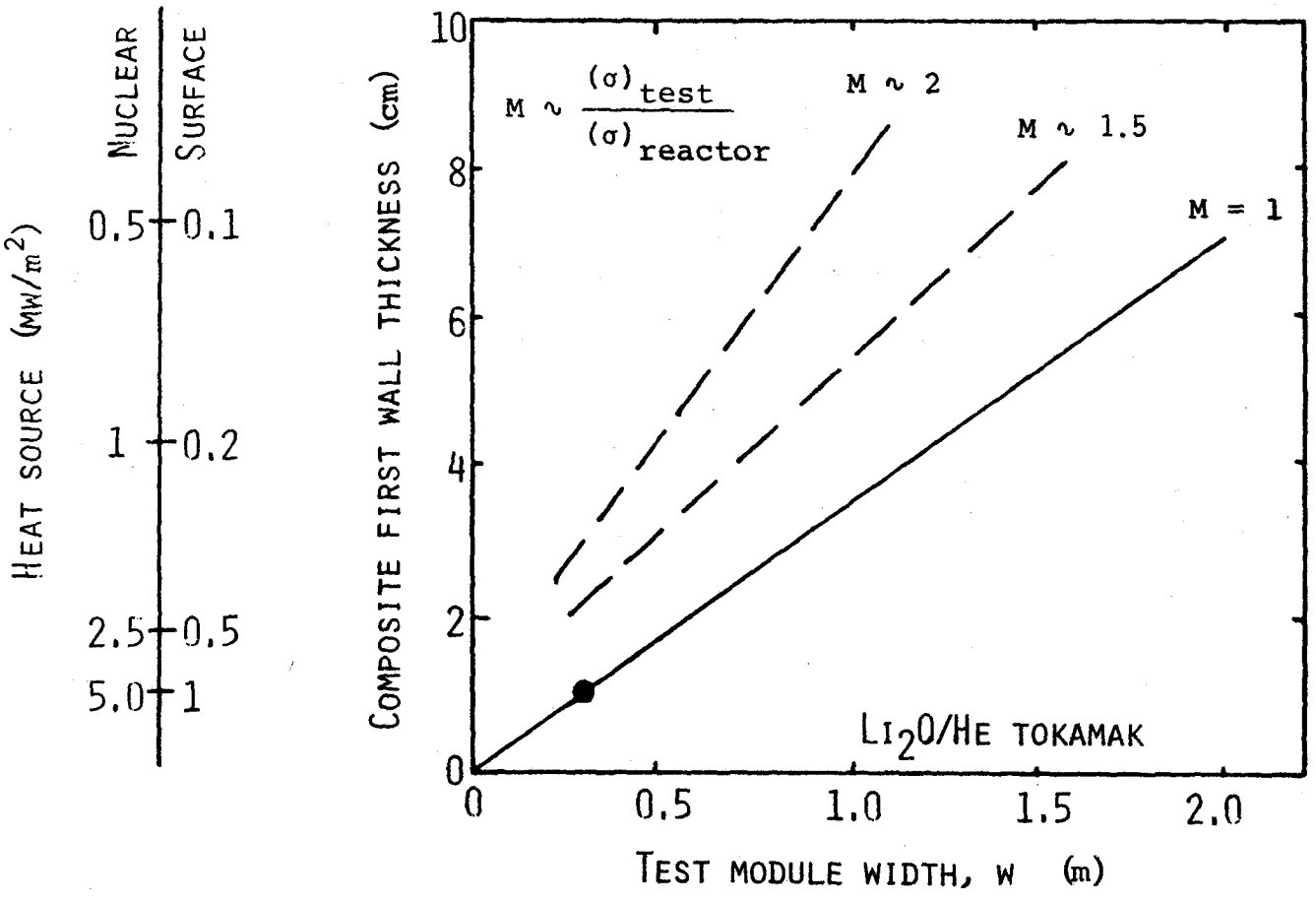

Figure 5.5-7 Test module width and device heat source trade-off for preserving Li_2O/He/HT-9 first wall thermal plus pressure stresses.

Li_2O breeder plate increase from 1 to 2 cm. Although large, the width of the test module was 30 cm to start, and would likely also have increased. Thus there is still room for several plates within the breeder to check for multiple channel or plate-plate interactions.

Length The axial blanket length is around 2-4 m. It would be desirable for this to be as small as possible in the test module. One concern in reducing the module length is the interaction between the hot expanding first wall and the module end plates. This interaction depends on the relative stiffness of the two pieces. It may be possible to adjust the thickness of the end plate so as to control this relative stiffness, regardless of the length of the test module, and so approximately simulate the axial interaction. However, this has not been analyzed. Furthermore, the design of the breeder region, such as the double-walled U-tubes in the $LiAlO_2/H_2O$ blanket, may also impose constraints based on reasonable bend radii in the tubes.

Another possible concern related to axial length is with respect to the number of first wall cooling channels needed to simulate flow distribution, vibration or instabilities. The reactor first wall has 40-200 channels of 2-5 mm length. A simple model of flow redistribution due to partial channel blockage suggests that 10 channels is sufficient to simulate 85% of the flow redistribution pattern of a much larger number of channels. Thus a minimum axial length of 5 cm would seem sufficient, increasing as the heat source decreased in parallel with the first wall thickness increase, so perhaps 20 cm at 0.2 MW/m^2 surface heating in a tokamak.

Depth The blanket depth is about 0.8 m, with 0.15 m arched first wall and 0.4-0.5 m breeder and 0.2 m manifold. The first wall depth must be retained since the curved arch is an important part of the first wall structural behaviour. This leads to a depth requirement of 15 cm under reference conditions, increasing as the heat source decreases as previously discussed.

The module depth direction also contains the exponential attenuation in fluence, radiation effects and tritium production in the breeder. In the Li_2O plate design, each breeder plate sees the full variation, while in the $LiAlO_2$ breeder-outside-tube configuration, each unit cells is uniformly irradiated and there is less potential for interaction between hot, high fluence regions

and cold, low fluence regions. The attenuation rate is essentially the same regardless of the breeder depth, but it is desirable to place a shield or other reflector behind the module so as to increase the general flux level in the module. About 20 cm of breeder are needed to achieve 80% of the full reactor tritium production, under reference conditions.

5.5.3.5 Device Geometry

The neutronics parameters (nuclear heating, tritium production and radiation damage) are affected by the test facility geometry since this determines the flux and spectrum of the neutron source to the test module.

Device size It is possible that the test device will be much smaller in size than the reference reactors, as in mirror test facilities where the plasma radius is about 0.15 m as compared to 2.5 m in a tokamak reactor. As the radius is decreased, total power and neutron wall load will also decrease for fixed plasma power density. However, as the device size is decreased, geometrical effects reduce the scattered component of neutron flux in the first wall and so reduce the corresponding radiation effects faster than would be expected, as shown in Figure 5.5-8. In order to retain the equivalent first wall heating or neutron damage due to some neutron wall load at reactor sized first walls, the test device neutron wall load must be correspondingly increased, particularly below a first wall radius of 20 cm. Furthermore, below this point there is also a deviation in the relative rates of heating, dpa and helium production.

A second effect of device size is on the distribution of heat source around the first wall. If distances from the plasma center to points on the first wall perimeter change disproportionately as the first wall radius is decreased, then the heat source distribution around the first wall will be altered. In general, this effect can be avoided by keeping the first wall radius large compared to the module first wall dimensions. For the reference blankets, the first wall lobe radius is 15 cm. However, under scaled test conditions, the first wall size generally increases as the first wall heat source decreases.

Other than these effects, however, the influence of the test device size on the magnitude and profile of the heat source, particularly in the breeder region, is small.

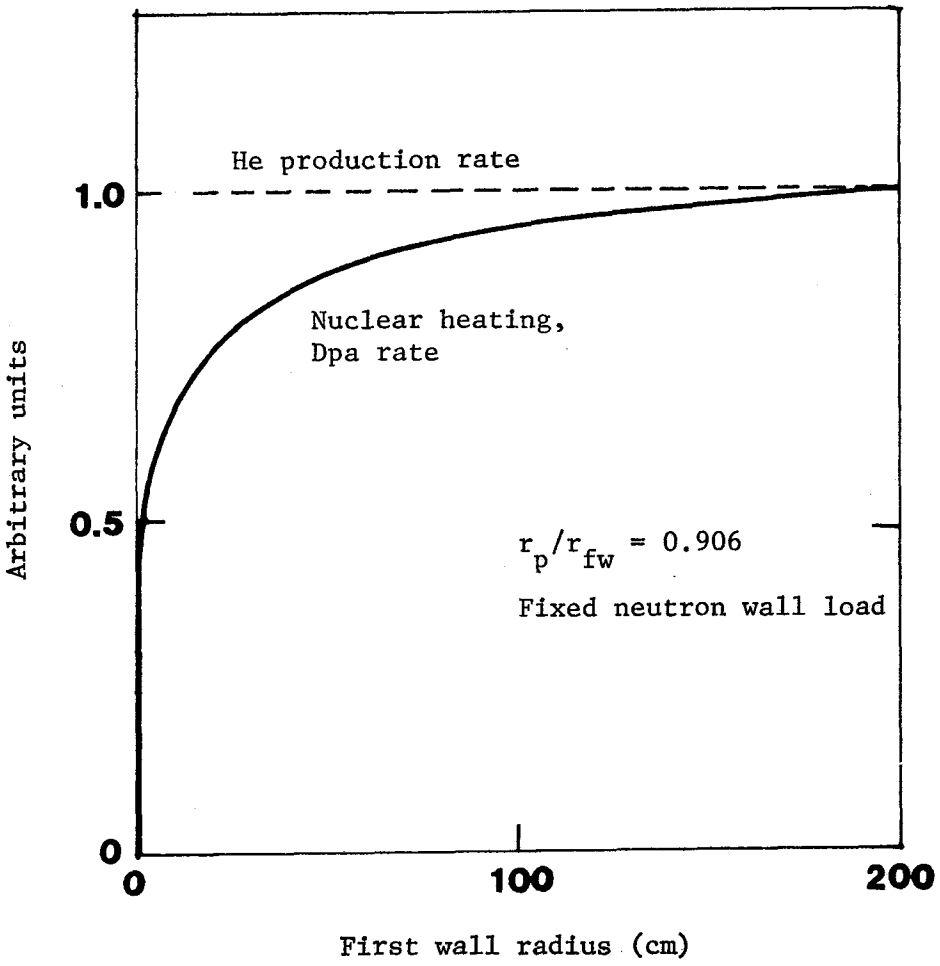

Figure 5.5-8 Loss of neutronics parameters in first wall due to geometrical effects in small-sized devices.

Test port The arrangement of the device environment in the immediate vicinity of the test module will influence the heating rate and radiation effects in the module since the test module will not in general be surrounded by similar blanket modules as in the reactor full-coverage geometry. Neutron reflectors can enhance the neutron flux. If the reflector is moved further back, then the sides of the module can be exposed to more direct neutrons. These are predominantly reflected or scattered neutrons from the test port, and consequently are typically lower energy. These may affect the heating rate, damage rates or tritium production rates by as much as factors of two in the front of the blanket. The back regions of the breeder may be increased a factor of five in tritium production or heating if the reflector is pulled away from the test module sides. However, the flux is still much less than at the breeder front. This effect extends a few neutron mean free paths into the test module sides, or about 10 cm. Thus, it is not entirely suitable for testing a full width module.

5.5.3.6 Magnetic Field

The dominant magnetic field effect in solid breeder blankets is believed to be mechanical loads due to transient magnetic fields, typically caused by plasma disruptions. There is also some contribution to the steady-state stress fields due to the interaction of the magnetic field with ferritic steel structural materials such as HT-9. Then there is a further range of speculations on the possible influence of magnetic field on corrosion - formation, transport and deposition.

No detailed evaluation of the test requirements for magnetic field were performed here since this is not presently believed to be a significant contributor to solid breeder blanket behavior. Nonetheless, the magnetic field represents a potential energy source of about 10 MJ/m^3 at 5 T and there are identifiable interactions, so the possibility of serious unexpected effects makes it desirable to not entirely neglect this environmental condition.

5.6 Summary and Recommendations

An important goal of this chapter is to provide some measure of the usefulness of integrated testing of solid breeder blankets as the test device parameters are changed from the reference reactor values. In particular, solid breeder blankets were analyzed to determine the important blanket conditions and phenomena under reference reactor conditions, and to identify test requirements based on scaled test behavior that reproduced the reference component behavior. The general features of a scaled test module were considered parametrically to bring out the trade-offs that occur when the individual scaling methods are integrated together.

The device parameters with a strong influence on test module behavior and on the test device cost can be grouped into the six categories of heat source, neutron radiation, operating time, test volume, device geometry and magnetic field. It has not been possible to analyze this full complexity of blanket behavior and determine whether the tests can reproduce all these interactions under scaled conditions. However, a wide range of important issues were considered. Furthermore, it is unlikely that consideration of other effects will make the test requirements any less stringent.

These results are based primarily on analyses of the first wall and breeder configurations for the reference Li_2O/He/HT-9 and $LiAlO_2$/H_2O/Be/PCA blankets. However, the analyses were often at such a general level that it is likely that the conclusions would not be appreciably different for most solid breeder blanket designs based on present concepts.

The basic "minimum" scaled test facility appears to require at least 1 MW/m^2 neutron wall load. The surface heat flux should be above 0.3 MW/m^2 for testing tokamak blankets, and below 0.1 MW/m^2 for testing mirror blankets. A burn time of at least 500 seconds is needed to reach thermal equilibrium under these scaled conditions, and preferably longer to allow some time at equilibrium. The dwell time should not exceed 150 s so as to avoid too much cycling of temperatures and other possible effects. Reaching 99% or so of the steady-state tritium inventory would require a continuous operating time (100% availability) of days to months, depending on the particular breeder design. An appreciable magnetic field would be desirable to confirm that there are not major surprises, although no specific limits can be suggested. However, it is

likely that any fusion test device will have appreciable magnetic fields in the few Tesla regime anyway. No detailed fluence goals were considered here, but the range 1-3 MW/m^2 is generally expected to establish a number of important effects and any consequent interactions. The test device itself should be at least 20 cm in first wall radius, and preferably on the same order or larger than the first wall dimensions of the test module. The test port should be made of some neutron reflector to enhance the neutron flux in the vicinity of the test module, with a plug or shield to minimize leakage out the module rear. The test volume must be about 1 m wide x 0.5 m long x 1 m deep, under these test facility conditions, for each module to be tested.

It is desirable, and apparently possible from the scaling considered here, to have a combined first wall and breeder region in the test module. Essentially one type of test module should be able to indicate most basic operational features of the full component under the conditions given above. (Other than neutronics verification, which is considered separately in Chapter 7.) Of course, multiple modules would be necessary to gather statistics, fluence-related information, and explore off-normal operation. Furthermore, these analyses only brushed the surface of the many phenomena that should be considered. It is possible that further work will indicate more restrictive test requirements or the need for different test modules to explore different aspects of blanket behavior.

Nomenclature for Chapter 5

a	Neutron albedo
A	Area, m^2
A_{cr}	Factor in creep rate formula
B	Magnetic field strength, Tesla
B_f	Barrier factor for tritium permeation
B_{sw}	Factor in swelling rate formula
c	Concentration, $1/m^3$
c_p	Specific heat, J/kg-K
C_D	Drag coefficient
d	Depth, distance, diameter, m
D	Diffusion coefficient, m^2/s
E	Young's modulus, N/m^2
E_n	Neutron energy, eV or J
f	Frequency, 1/s
f	Friction factor
$f(x)$	General function
F	General force, N or N/m^2 or N/m^3
$g(x)$	General function
$\dot{g}$	Volumetric tritium generation rate, $kg/s-m^3$
$\dot{G}$	Tritium generation rate, kg/s
h	Heat transfer coefficient, W/m^2-K
$h(x)$	Profile factor for tritium generation rate
I	Moment of inertia, m^4
I	Tritium inventory, kg
J	Neutron or particle current, $1/m^2-s$
k	Thermal conductivity, W/m-K
K	Stiffness, N/m
K	Permeability, m^2
L	Length, m
m	Mass, kg
$\dot{m}$	Mass flow rate, kg/s
$\dot{m}'$	Mass flow rate per unit length, kg/s-m
$\dot{m}''$	Mass flux, $kg/s-m^2$
M	Moment, N-m

M	Magnetization, A/m
M	Difference between parameter in test module and reactor blanket
n	Atomic density, $1/m^3$
$\dot{n}$	Tritium source or arrival rate, g/s
$\underline{n}$	Surface normal vector
n_t	Coolant tube density, tubes/m^2
N_{qe}	Number of burn/dwell cycles to quasi-equilibrium
Nu	Nusselt number, Nu = hd/k
p	Pressure, N/m^2
$\underline{p}$	General traction of pressure vector, N/m^2
p	Transverse force per unit length, N/m
P	Pumping power, W
P_m	Permeability, $P_m = DS$, $m^3/m\text{-}s\text{-}Pa^{0.5}$
Pr	Prandtl number, $Pr = \mu c_p/k$
q	Axial force per unit length, N/m
q_s	Surface heat flux, W/m^2
q_{nw}	Neutron wall load, W/m^2
$q(x)$	Profile factor for volumetric heating rate
Q	Energy, eV or J or J/m^3 or kcal/mol
$\dot{Q}_v$	Volumetric heating rate, W/m^3
r	Radial coordinate or dimension, m
R	Radial dimension, m
R	Ideal gas constant, 1.986×10^{-3} kcal/mol-K
Re	Reynold's number, $Re = \rho Ud/\mu$
S	Sievert's constant, $1/Pa^{0.5}$
t	Time, s
t_b	Plasma burn time, s
t_d	Plasma dwell time, s
t_c	Characteristic time, s
T	Temperature, K
u	Displacement in x-direction, m
u	Dimensionless temperature
U	Velocity, m/s
v	Displacement in y-direction, m
V	Volume, m^3
$\dot{V}$	Volumetric flow rate, m^3/s

x	Spatial coordinate, m
X	Concentration, ppm or $1/m^3$
y	Spatial coordinate, m
z	Spatial coordinate, m
w	Width, m
W	Molecular weight, kg/mol
α	Thermal expansion coefficient, 1/K
α	Coefficient for tritium generation profile
β	Angular rotation
β	r_o^2/r_i^2 in cylindrical geometry
γ	Effective attenuation coefficient, 1/m
δ_{ij}	Kronecker delta
ε	Strain
ε	Volume fraction
ζ	Damping ratio
θ	Angle
Θ	Temperature difference, K
κ	Boltzmann's constant, 1.3807×10^{-23} J/K or 8.6173×10^{-5} eV/K
λ	Mean free path, m
μ	Dynamic viscosity, kg/m-s
ν	Poisson's ratio
ξ	Dimensionless coordinate
ρ	Density, kg/m^3
σ	Stress, N/m^2
σ	Microscopic cross-section, m^2
Σ	Macroscopic cross-section, 1/m
τ	Dimensionless time
τ	Time constant, s
Υ	Pore tortuosity factor
ϕ	Neutron flux, n/m^2-s
ϕt	Neutron fluence, MW-yr/m^2 or n/m^2

CHAPTER 6

ANALYSIS AND ENGINEERING SCALING OF LIQUID METAL BLANKETS

TABLE OF CONTENTS

6. ANALYSIS AND ENGINEERING SCALING OF LIQUID METAL BLANKETS

6.1 Introduction

There are many uncertainties regarding the actual operation of blanket designs in the complex fusion environment. With our present limited level of understanding of blanket phenomena and in the absence of essential data, we cannot guarantee that existing designs are feasible or practical. For self-cooled liquid metal blankets, the largest sources of uncertainty are related to MHD effects, structural integrity, and materials compatibility. For example, MHD has a large impact on the issue of first wall cooling. This is particularly important in tokamak reactors, which typically have a high surface heat flux and neutron wall loading. Inadequate cooling impacts performance limits due to the maximum allowable temperatures and thermal stresses. MHD also causes a large pressure drop which leads to high pressure stresses that may exceed allowable stress limits. A more complete list of uncertainties in the operation of liquid metal blankets is contained in Chapter 3.

The high cost of a fusion reactor necessitates that risk associated with blanket performance be reduced as much as possible. Considering the large number of uncertainties, to achieve this will require a large amount of blanket analysis and testing. In Chapter 4, a complete set of needed tests was enumerated, including the entire range from specimen tests to full scale demonstration tests. In this chapter, more detail is presented regarding the requirements for the tests — that is, how to satisfy the testing needs. The most stringent requirements arise from the most integrated types of tests which appear to require a fusion test device. However, it is likely because of cost considerations that such a fusion test device will not provide the full scale parameters of a commercial reactor. Therefore, the adequacy and usefulness of integrated testing at reduced device parameters must be addressed.

There is a range of testing goals that must be met in a complete blanket testing and development program. These are identified explicitly because the test requirements depend strongly on the nature of the testing. They include: (1) fundamental experimentation to provide understanding of phenomena and data for verification of predictive capabilities, and (2) component verification

testing. The type of testing which one chooses depends on several factors, including the cost of the test and the risk involved if the test is not performed. Integrating these factors together into a rational test plan is a very complex job involving trade-offs among costs, benefits, and risks. One of the important goals of the work presented in this chapter is to define as clearly as possible the benefits of testing at scaled down conditions, which must include consideration of the nature of the information sought from the tests.

In fundamental experiments, the emphasis is on understanding basic blanket behavior and uncovering phenomena which are not well understood. It is often important in tests of this type to model details such as spatial profiles. Usually only one or a small number of effects are isolated, which alleviates the difficulty of simultaneously modeling many different environmental conditions. However, in some cases it is the interaction between several phenomena or environmental conditions which has the largest uncertainties. In this case, basic experiments provide the understanding necessary to plan and conduct the more complex, multiple interaction experiments.

For liquid metal blankets, many new basic phenomena in the fusion environment are complex and poorly understood. This places particular emphasis on studies of basic effects for these blankets. In addition, liquid metal blankets tend to be strongly interactive: MHD, thermal hydraulics, corrosion, and structure behavior are all related. This indicates that definitive basic information might be necessary from experiments with relatively high levels of integration.

Fundamental experiments also provide information necessary for verification of predictive capabilities. In some cases, modeling detailed phenomenological behavior is not possible, and special experiments are performed to provide direct experimental data for "lumped" or "global" parameters that can be used in simplified models.

Component verification tests are "black box" tests in the sense that details within the blanket are not as important as whether or not the blanket works as a whole. Failure modes and global performance parameters are emphasized. An effective component verification test requires either complete modeling of the blanket or sufficient understanding of the critical phenomena that incomplete modeling does not strongly affect the overall blanket behavior

and failure modes.

Engineering Scaling

One of the greatest difficulties in fusion testing stems from the very high cost of full scale testing in a fusion environment. It is most likely that the majority of integrated blanket testing will be performed in devices which have much lower power density than a commercial reactor. Other major device parameters may be altered in the test device as well, including the surface heat flux, magnetic field strength and geometry, and plasma burn scenario. The test device will also generally have a limited surface area and volume for performing the tests. This causes serious problems, because blanket behavior is strongly coupled to the device parameters.

Directly testing a module designed for full scale parameters in a reduced scale device results in a poor verification of the component. (In this context, the term "scale" refers to any device parameter, not only size.) For example, the structural integrity of the first wall is directly related to thermal stresses, which result from the surface heat flux and neutron wall load. Operating a blanket at a low fraction of full power conditions leads to lower first wall temperatures and stresses. If nothing was done to correct this problem, it would not provide a very useful test of the first wall. This type of "look-alike" test might still yield valuable information for verifying predictive capabilities and identifying synergistic effects.

In order to obtain maximum benefit from testing at reduced device parameters, principles of engineering scaling must be applied to the design of an "act-alike" test. Using engineering scaling, the test conditions and test elements themselves are controlled to reproduce the most critical behaviors which are expected to dominate the uncertainties in performance and failure modes in the real reactor blanket. For the example given above, an act-alike test of the effect of thermal stresses on the first wall structural behavior could be designed by increasing the thickness of the first wall. This would result in a larger temperature drop, and would therefore simulate the thermal stresses present in the real first wall under normal operating conditions. Act-alike testing is not only useful for verifying predictive capabilities, but also provides for component verification.

Complete act-alike behavior is difficult, if not impossible, to achieve

at reduced device parameters. This stems from the complex, integrated nature of the blanket. Scaling conflicts often occur when two different phenomena require different modifications to retain the essential features, or when more than one device parameter is changed simultaneously. For example, increasing the first wall thickness to maintain thermal stresses also causes a reduction in pressure stress. This problem could be fixed by modifying some other test parameter, but new problems invariably develop each time the test is altered from the reference conditions.

The process of engineering scaling requires a substantial amount of understanding of blanket behavior in order to assure that important phenomena are maintained under scaled conditions. Yet, the need for testing implies that there are substantial uncertainties involving the blanket behavior. This apparent contradiction epitomizes the difficulty of engineering scaling: the ability to exactly quantify the requirements for scaled testing would indicate the lack of need for testing at all. Scaling for liquid metal blankets is a particular problem because our understanding of the basic blanket behavior is so poor. This makes it very difficult to quantify uncertainties. It is assumed that before integrated tests are actually designed that extensive separate and multiple effects testing will be performed, allowing for a more informed and useful test design.

One can choose to emphasize one or several blanket behaviors at the expense of others, which results in a "scaled test option." By performing several different scaled test options, one might hope to reconstruct most of the important blanket phenomena. Interactive, or "synergistic", issues can be easily lost with this approach. Care must be exercised to identify and eliminate the omission of important interactive effects. Test module design and general principles of scaled testing are discussed in more detail in sections 6.4 and 6.5.

Another inherent weakness of scaled testing is the loss of information on unanticipated effects. One of the primary purposes for fundamental experiments and final component verification is to discover unexpected phenomena. Integrated testing can help identify these phenomena to some extent, because of the simultaneous presence of many environmental factors. But by scaling the test element or test conditions, unexpected phenomena may be changed in a way that cannot be predicted.

Overview

In this chapter, the principles of scaled engineering testing are developed for liquid metal blankets and applied to the design of an actual test module. The purpose is to provide as much quantitative input as possible to the cost/benefit tradeoffs involved in defining test devices. In order to understand how to design a useful scaled test, or how to create act-alike conditions, it is first necessary to understand how the liquid metal blanket behaves and just what is meant by "act-alike" behavior. The way in which liquid metal blankets behave is an evolving topic of research that needs to be nourished. Therefore, a large amount of effort was invested in studying basic blanket behavior. Five major technical disciplines were studied, including MHD fluid flow and pressure drop, thermal hydraulics, corrosion, structural behavior, and neutronics. The details of the analysis are presented in Section 6.2.

For each of the technical disciplines, parametric relations were developed to describe how the most important phenomena vary with the device parameters and operating conditions. These are presented as requirements for scaled testing in Section 6.3. In Section 6.4, a preliminary test module design is carried out in order to demonstrate the procedure and to uncover some of the problems which arise when all of the elements of engineering scaling are employed.

The test requirements and lessons learned from the test module design are then summarized in Section 6.5 and conclusions are stated in Section 6.6.

Detailed analysis requires that a specific design be treated. For the majority of the liquid metal blanket work, the lithium cooled BCSS Toroidal/-Polodidal Flow design was chosen as the reference design. (See Figure 6.1-1 and Appendix D.3 for details of the reference design.) One of the key features of this design is the existance of both poloidal and toroidal coolant channels. In order to improve first wall cooling, the first wall is constructed of small channels which are fed by the larger poloidal channels. The first wall structure and flow paths are therefore somewhat complex compared to many other self-cooled liquid metal blanket designs. A limited amount of analysis was also performed for the MARS LiPb blanket (Figure 6.1-2), which

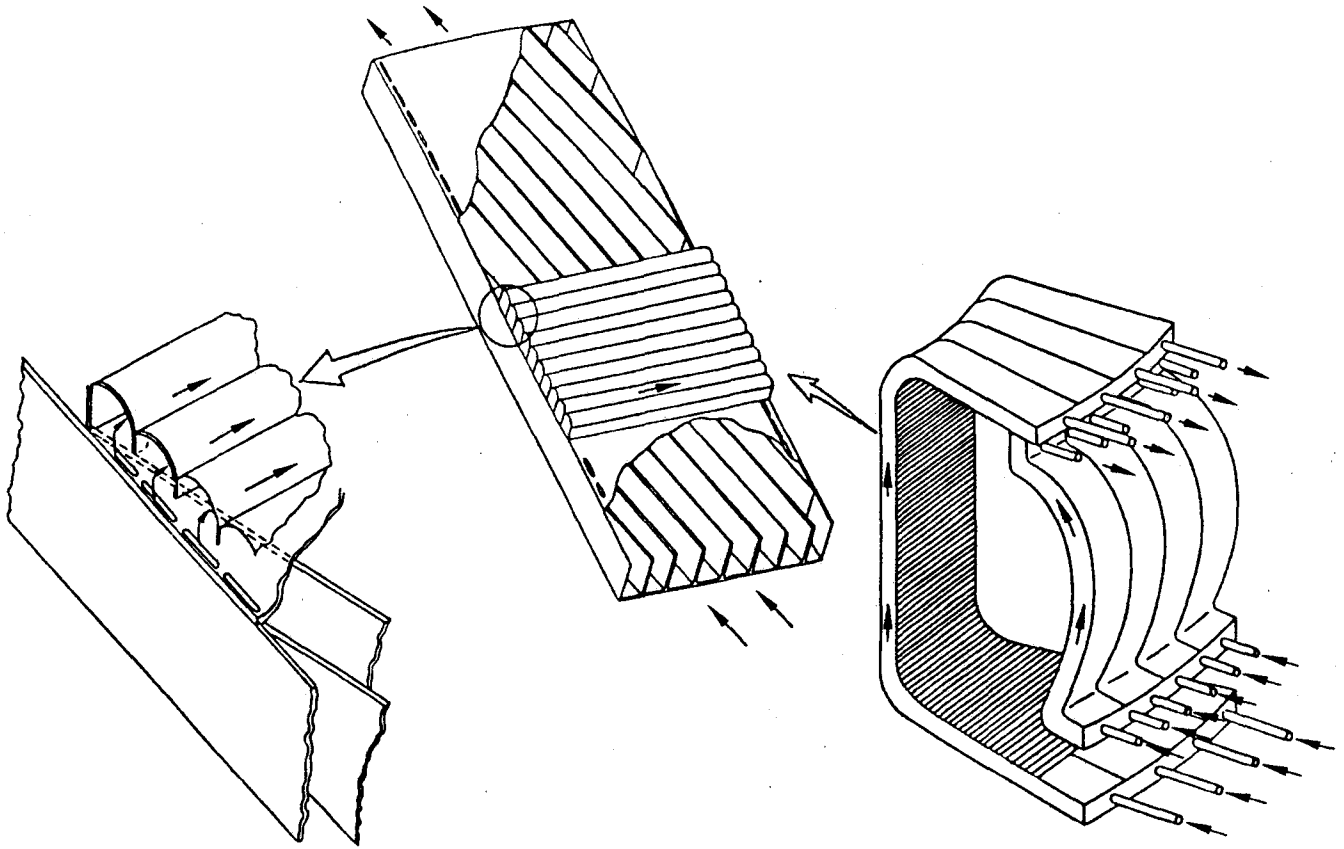

Figure 6.1-1 BCSS poloidal/toroidal flow blanket concept.

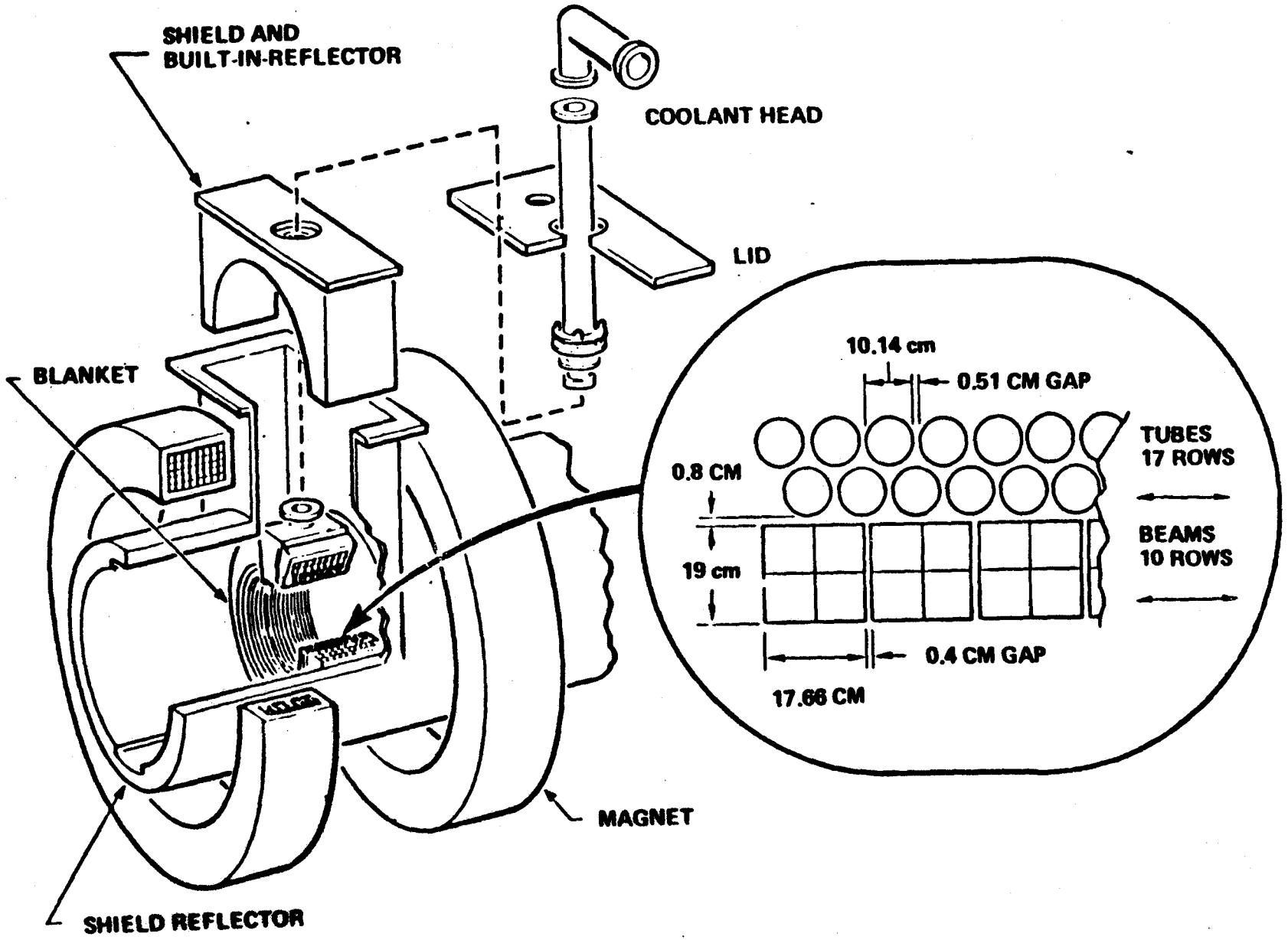

Figure 6.1-2 MARS lead-lithium electric power blanket.

consists of a simpler geometry. In this design, the coolant flows in curved tubes which run only perpendicular to the field.

In order to extend the applicability of the conclusions, general trends and generic design features are emphasized. The BCSS Toroidal/Poloidal Flow design has several basic features which are found in other blankets, including a composite flat plate first wall structure with first wall cooling channels, coolant flow in directions parallel and perpendicular to the field, bends, orifices, etc. In some ways, this design is a good choice of a reference design because its complexity leads to a complex set of test requirements.

The MARS design is an good complimentary example. It has very simple coolant flow paths, low first wall heat flux characteristic of the tandem mirror, and a type of support structure which leads to different kinds of design problems and test requirements. For the BCSS design, there is ample support of the first wall throughout the blanket, provided by the poloidal and toroidal channel walls. The local structural response is thought to be dominated by radial profiles of temperature, swelling, etc. The response in the toroidal and poloidal directions is somewhat decoupled due to the internal support structure. (This does not apply for the external support of the entire blanket module.) For the MARS design, coolant tubes travel all the way around the plasma with little support. This results in a complicated structural response which depends strongly on both the radial and axial directions.

6.2 Analysis of Blanket Behavior

6.2.1 MHD Fluid Flow and Pressure Drop

6.2.1.1 Overview

Importance of MHD Fluid Flow and Pressure Drop

MHD pressure drop is a critical issue in liquid metal blankets. The operating pressure of the coolant increases with increasing pressure drop, which induces severe stresses in the first wall. If the pressure drop is very high, then the combination of pressure stresses, thermal stresses, and other loading conditions in the fusion environment could rule out certain liquid metal designs. High MHD pressure drop is undesirable not only because it induces severe stresses in the wall, but also because the pumping power increases with the pressure drop. The pumping power must be low compared with the output power of a fusion reactor.

MHD effects on flow distribution are another important issue in liquid metal blankets. If flow distribution is not uniform, local hot spots may appear in a blanket. In particular, the velocity profile in a first wall cooling channel is important. It affects both the first wall temperature and the corrosion rate of the wall as will be discussed in Sections 6.2.2 and 6.2.3.

Current Status of Research

MHD fluid flow has been studied by many researchers both analytically and experimentally, but there still remain uncertainties such as those listed in Table 6.2.1-1. Most of these have been studied already to some extent, but important problems remain. Some of them are completely unsolved. The reason is that both analysis and experiment on these subjects are very difficult. In the analysis it is necessary to solve flow equations and eddy current equations simultaneously. As the eddy currents flow in a plane perpendicular to the fluid flow, the problem is essentially three dimensional with few exceptions. Computer codes are very useful tools in flow analysis, but there is no multi-purpose code now available which can solve MHD flow problems.

Experiments are also difficult in this field. Large magnets are needed. Liquid metal technology has been developed in LMFBR projects, but the use of liquid metal still poses some problems. Most of the experimental works

treated very simple flow such as flow in a straight pipe with uniform magnetic field.

Generality of Uncertainties

The MHD problem depends on blanket design. Some issues in Table 6.2.1-1 are not generic but specific to certain designs. For example, the effects of mixing vanes are a specific problem in a blanket which uses the vanes. But it is impossible to construct a blanket with straight ducts alone which are insulated from each other. It is necessary to reduce the uncertainties listed in Table 6.2.1-1 before construction of a fusion reactor.

Major Uncertainties

Every uncertainty in Table 6.2.1-1 is important and should be studied much more in the future, but the global current effects and the time dependent problems seem to be most important. They remain completely unsolved, though they may determine the viability of the liquid metal blanket design. Major uncertainties will change as studies on these problems progresses. Although at present they are major uncertainties, it is expected that they will be solved in the future. At that time there may arise other uncertainties which are not included in the list.

In the following sections, two problems which have previously been unsolved are discussed, including global current effects and the entry length for flow development with an angled magnetic field.

Table 6.2.1-1 List of Uncertainties

I. MHD pressure drop
   A. Channel shape effects
      1. Irregular cross section[5],*
      2. Nonuniform wall thickness[5]
   B. Two or three dimensional flow effects
      1. End effects (inlet/outlet)[1]
      2. Bends[4]
      3. Expansions and contractions[4]
      4. Branches (junctions)[4]
      5. Mixing vanes or helical flow paths[1],*
      6. Impinging jet[4],*
      7. Rough or grooved wall[2],*
      8. Flow nonuniformities due to obstructions, etc.[1],*
   C. Complex magnetic field and induced field effects
      1. Angled field effects[1]
      2. Effects of field gradients[4]
      3. Effects of field ripple[1]
      4. Effects of field changing with time, including constant B [1]
      5. Finite magnetic Reynolds number effects[5],***
      6. Thermoelectric effects[5],***
   D. Global current effects
      1. Adjacent channel effects[1]
      2. Effects of supporting structures[1]
   E. Effects of material properties (resistivity, etc.)
      1. Temperature dependence of material properties[1],**
      2. Changes in bulk properties with irradiation[1].**
      3. Changes in surface properties with corrosion[1],**

II. MHD effects on flow distribution
   A. Channel shape effects
      1. Effects on bulk flow profile[4]
      2. Effects on boundary layer thickness[4]
   B. Two or three dimensional flow effects
      1. Flow development entry lengths[3]

Table 6.2.1-1 List of Uncertainties (contd.)

2. Flow distribution in branches[1]
3. Flow distribution in bends/expansions and contractions[3]
4. Two dimensional flow structure (large eddy)[1]
5. Flow distribution in mixing vanes or helical flow paths[1],*
6. Flow distribution in impinging jet[2],*
7. Effects of rough or grooved wall on boundary layer thickness[2],*

C. Complex magnetic field effects
1. Angled field effects[1]
2. Effect of field gradients[4]
3. Effects of field ripple[1]

D. Global current effects
1. Parallel channel flow sharing[1]
2. Effects of eddy current in structures[1]

E. Turbulence
1. Source of turbulence and its effects[4],***
2. Decay of turbulence[4],***

F. Time dependent MHD phenomena
1. Instabilities[5],***
2. Pressure waves[5]
3. Effect of changing field, including constant B [1]
4. Distribution of increasing or decreasing flow[1]

---

[1]These problems remain completely unsolved.

[2]There is little work on these problems.

[3]There is some work, but more studies are needed on these problems.

[4]There is some good work, but uncertainties remain.

[5]These problems have been studied fairly well.

* These are design specific problems.

** These affect MHD behavior, but are not original MHD problems.

***These problems may be neglected in fusion blankets.

6.2.1.2 MHD Pressure Drop in Second Wall Orifice of Reference Liquid Metal Blanket

(1) Introduction

The reference liquid metal blanket is composed of toroidal first wall cooling channels and poloidal manifolds. At the toroidal ends of a blanket module, there are orifices in the second wall which connect the toroidal channel with the manifolds. The channels are partitioned by ribs which connect the first wall to the second wall. There is no insulation between the channels. In a straight duct, the eddy current induced in the coolant must flow back through the ribs as shown in Fig. 6.2.1-1. The current does not flow across the channels, therefore the neighboring channel effect can be ignored. However, the eddy current induced at the orifice flows across the channels as shown in Fig. 6.2.1-2. The eddy current induced in the orifice where the coolant crosses the magnetic field can flow back through the second wall or through the coolant in the area where it flows in parallel to the field. The current intensity in a multichannel assembly may be quite different from the intensity in a single channel, hence the MHD pressure drop may be different. The eddy current intensity and the MHD pressure drop are calculated in two extreme cases where slug flow and fully developed flow are assumed in the orifice.

(2) Slug Flow Model

The slug flow assumption is technically incorrect, since flow redistribution occurs; however, due to its simplicity, it is a useful tool to introduce this subject. The correct solution including flow redistribution will be considered in the following section. As will be discussed, the results of the slug flow solution neglect important features of the velocity profiles but predict the pressure drop with good accuracy.

Calculational Model and Assumptions

Figure 6.2.1-3 shows the coolant flow through the second wall orifices at both ends of the toroidal channel. The toroidal width of the blanket module is L and the poloidal width is W. There is an inlet opening between x=0 and x=a, and an outlet opening between x=L-a and x=a. Between x=a and x=L-a is

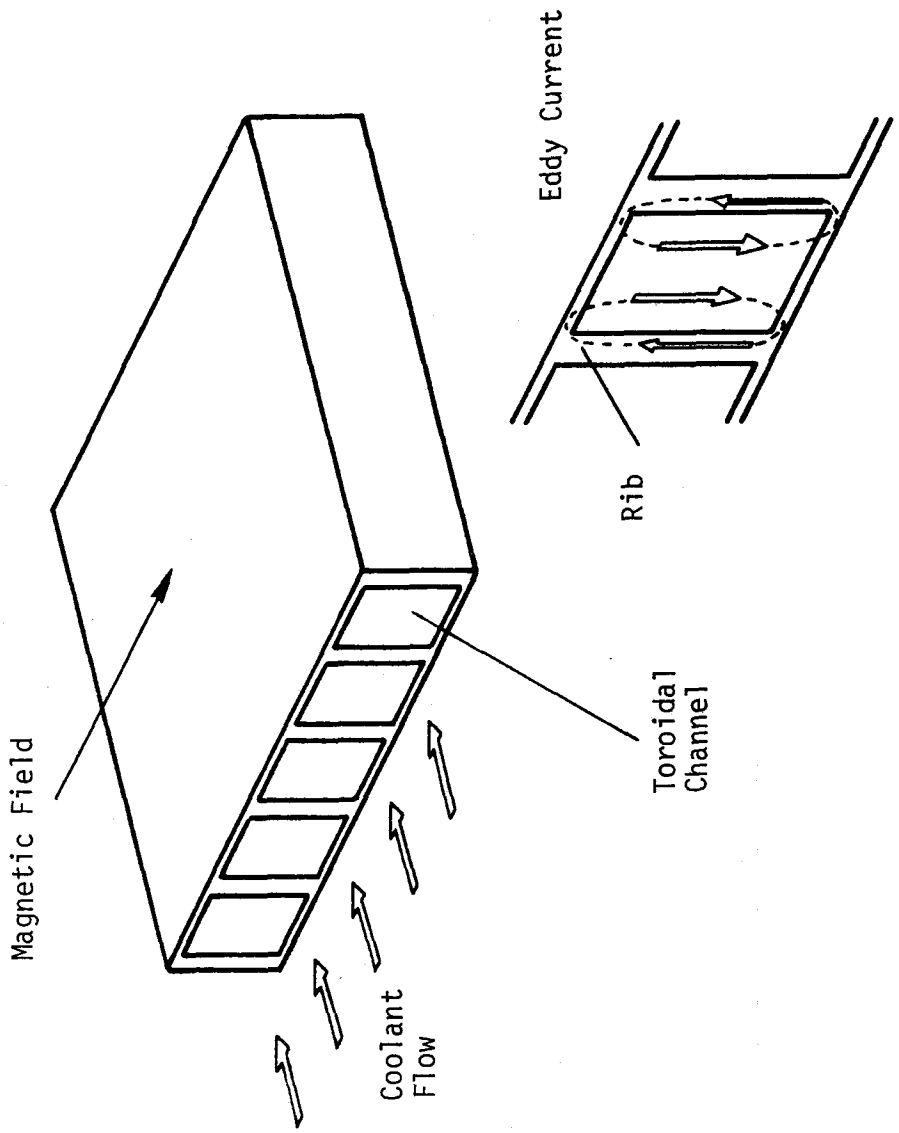

Figure 6.2.1-1 Eddy current in straight parallel duct.

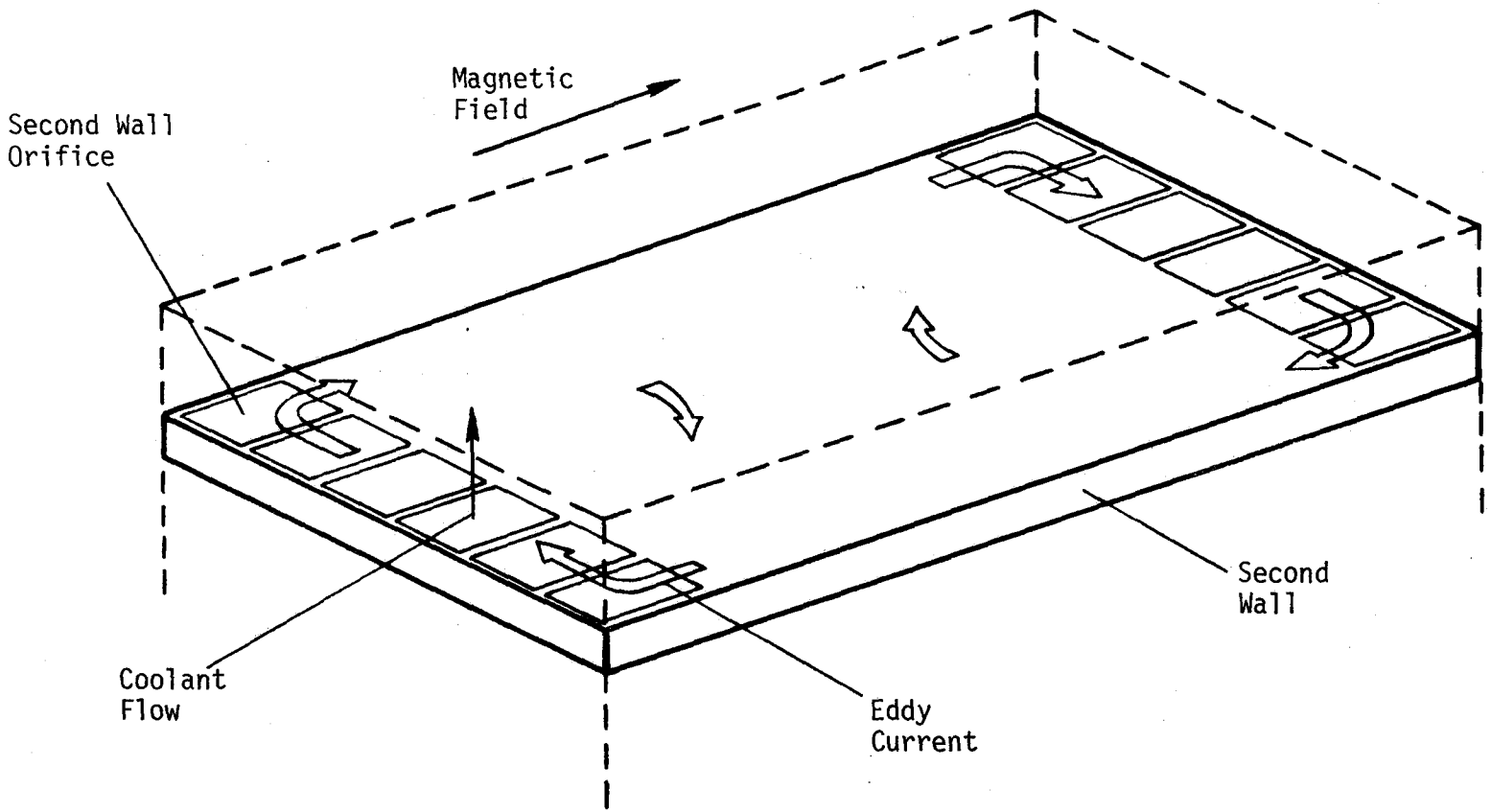

Figure 6.2.1-2 Eddy current induced in second wall orifice.

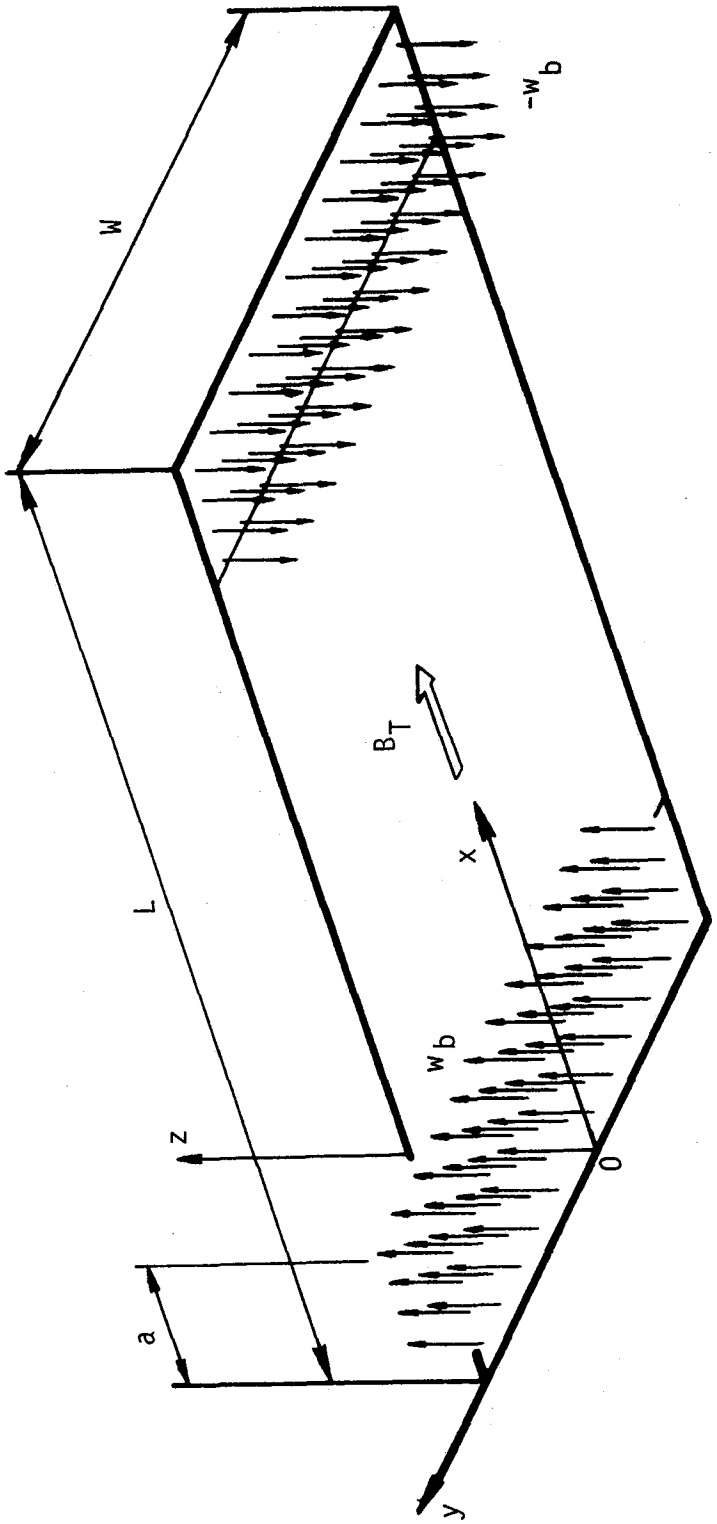

Figure 6.2.1-3 Slug flow model.

the second wall. Each toroidal channel has its own inlet and outlet orifices. The openings are partitioned by ribs into the orifices in the reference design, but in this analysis, the ribs and fluid are homogenized. There is a toroidal magnetic field, B_T, in the x direction. The radial and poloidal magnetic field intensities are assumed to be zero. The electrical conductivity of the wall is lower than that of the coolant, but for simplicity, the conductivities are assumed to be the same here. The induced magnetic field is assumed to be weak. The assumptions are summarized as follows:

(i) The coolant flows radially in the areas between x=0 and x=a and between x=L-a and x=L. The velocity is uniform. It is equal to w_b between x=0 and x=a and $-w_b$ between x=L-a and x=L (slug flow).

(ii) The eddy current flows only in the plane parallel to the wall. (two dimensional model)

(iii) The magnetic field is parallel to the x direction.

(iv) The detailed structure is homogenized in the model.

(v) The electrical conductivities of the coolant and the wall are assumed to be the same.

(vi) The magnetic Reynolds number is small.

The basic equations include:

Ohm's law

$$\underline{i} = \sigma_e(-\underline{\nabla}\phi_e + w_b B_T) \qquad (6.2.1\text{-}1)$$

and conservation of current

$$\underline{\nabla} \cdot \underline{i} = 0 \qquad (6.2.1\text{-}2)$$

where $\underline{i}(i_T, i_P)$ is the current intensity, σ_e is the conductivity of the coolant and the wall, ϕ_e is the electric potential and B_T is the toroidal magnetic field strength.

The current intensity is obtained numerically using a finite difference method. The plane shown in Fig. 6.2.1-3 is divided into rectangular elements and simulated by a network. The mesh size needs to be small enough not to affect the result.

Current Intensity Distribution

The generation of eddy currents, and hence MHD pressure drop, depends on two factors: the presence of an EMF "driving term" and the presence of a closed circuit for currents to flow.

The coolant flowing across the magnetic field in the area between x=0 and x=a creates a y-directional electromotive force. If a closed circuit exists, an eddy current will flow in the y direction. If the blanket surrounds the plasma as shown in Fig. 6.2.1-4, then the current can flow freely around the plasma. This corresponds to the case in which W/a is infinite. The current flows only parallel to the y axis in Fig. 6.2.1-3. The current intensity is the product of the electromotive force and the conductivity of the current path. As both the electromotive force and the conductivity of the path are uniform, the current intensity in the orifice is uniform and is expressed as follows:

$$i_P = \sigma_e B_T w_b \qquad (6.2.1\text{-}3)$$

When W/a is finite, the current must flow back through some return path. The current flows not only in the y direction, but also the x direction in order to return. The current path is distorted by the existence of boundaries perpendicular to the electromotive force. Fig. 6.2.1-5 shows the eddy current distribution in the case W/a=10 and L/a=10. (The current flow pattern is similar if the ratios W/a and L/a are maintained.) Part of the current flows back through the neighborhood of x=a. The current flows in an elliptic circuit around the point x=a and y=0 elongated in the y direction. The other part of the current reaches the orifices at the other end of the module. Since the direction of the electromotive force is opposite at the other end, the current flows in the opposite direction and returns. The circuit narrows near the edge of the blanket. The current intensity is not uniform; therefore the distribution of the current intensity must be considered.

The conductivity of the path depends on the current flow pattern. Therefore, the poloidal component of the current intensity in the orifices is modified by including a factor C in eq. (3):

$$i_P = C\ \sigma_e B_T w_b \qquad (6.2.1\text{-}4)$$

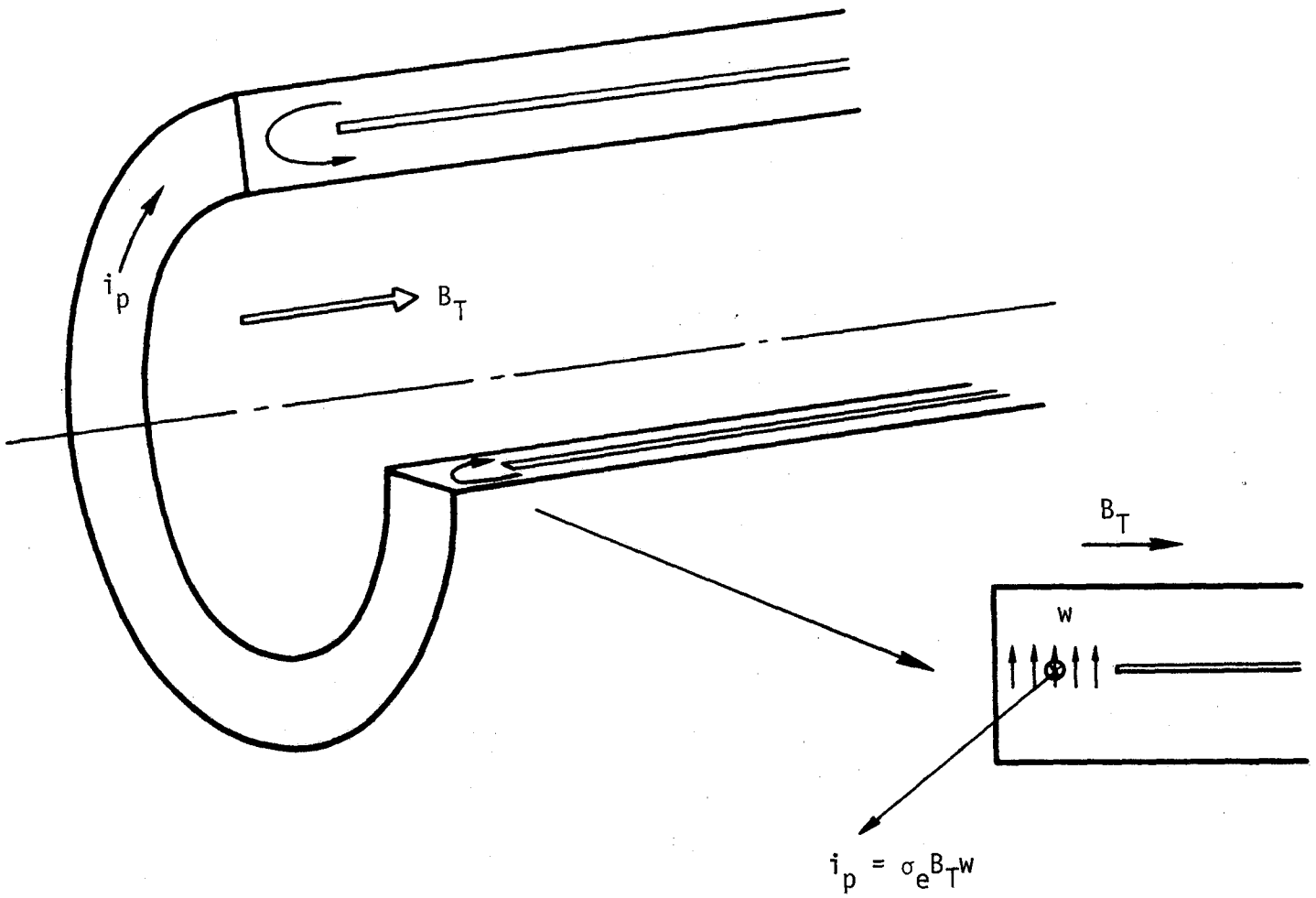

Figure 6.2.1-4 Cylindrical blanket.

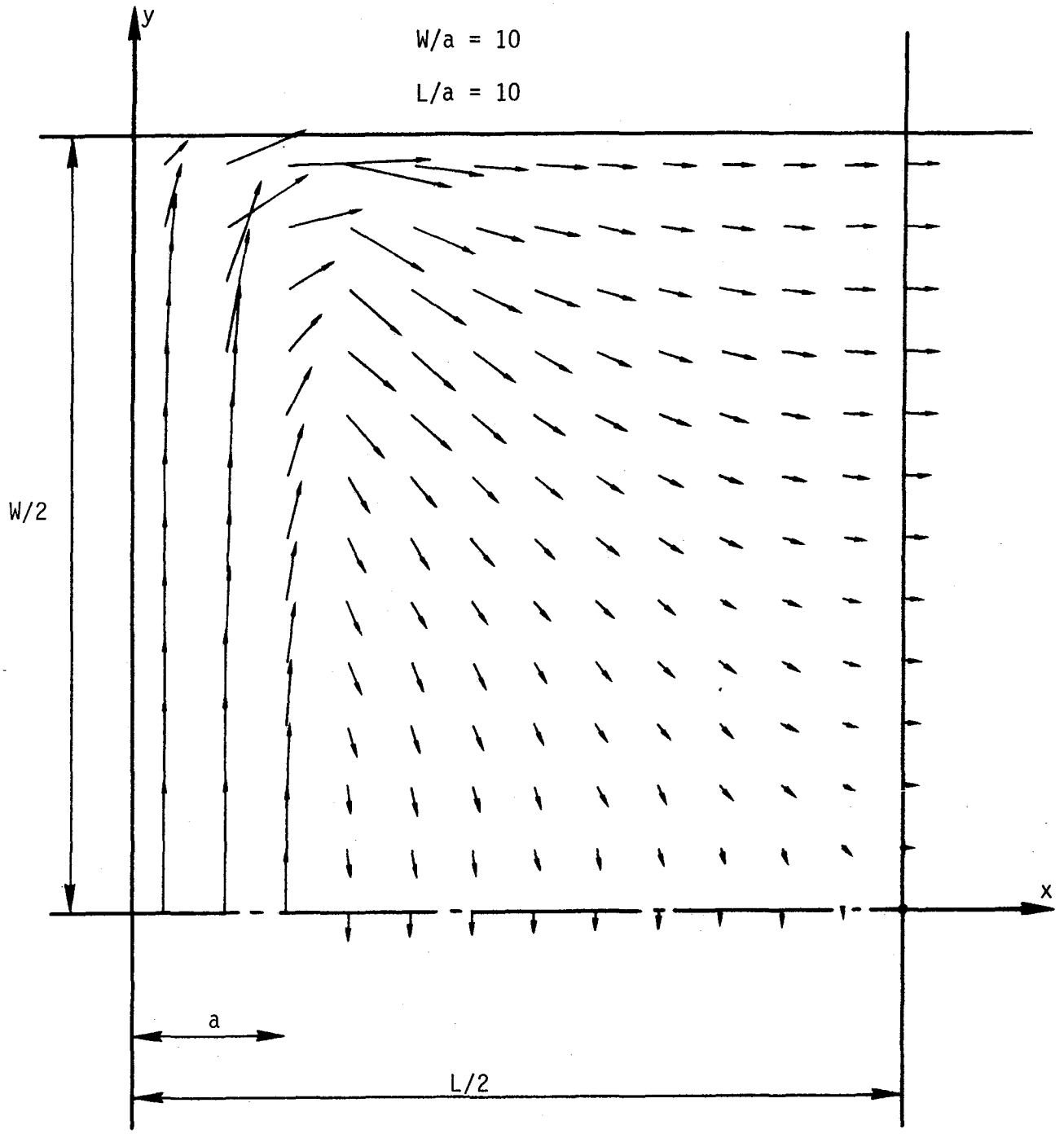

Figure 6.2.1-5 Eddy current distribution.

where C is a function of W/a, L/a, and the location in the opening (x/a,y/W). Figure 6.2.1-6 shows the distribution of C in the opening in the case of W/a=1 and L/a=10, as calculated by numerically solving Eqs. (1) and (2). The value of C is large near the second wall and changes exponentially in the x direction. C also changes in the y direction. It is largest at the point y=0 and is zero at both ends. In the single orifice case, W/a is usually around unity. Figure 6.2.1-6 represents the distribution of the y-directional current intensity in the single orifice. Figure 6.2.1-7 shows the result in the case of W/a=10 and L/a=10. C is nearly constant in the x direction, but it changes in the y direction in the same manner as in the case of W/a=1.

MHD Pressure Drop

Eddy currents in the magnetic field generate electromagnetic forces in the coolant. The force usually impedes the flow, thus an MHD pressure drop arises in the coolant. The pressure drop in the orifices is not uniform and is expressed as follows:

$$-\frac{dp}{dz} = C\,\sigma_e B_T^2\, w_b \qquad (6.2.1\text{-}5)$$

where C is a function of the location in the orifices and is the same as was used in eq. (4). Let us consider the average pressure drop in each orifice calculated by eq. (6)

$$-\overline{\frac{dp}{dz}} = \overline{C}\,\sigma_e B_T^2\, w_b$$

$$\overline{C} = \frac{1}{A}\left(\int_A C\,dA\right) \qquad (6.2.1\text{-}6)$$

A=ab is the area of one orifice, where b is the poloidal width. Figure 6.2.1-8 shows the value $\overline{C}$ in the case of a=b and L/a=10. The poloidal width of the blanket module W is k_{max} times the poloidal width of the orifice b, where k_{max} is the number of inlet or outlet orifices. The MHD pressure drop increases with increasing number of orifices, but $\overline{C}$ never exceeds unity. When there are several orifices, the pressure drop is high in the central orifices and is relatively low in orifices near the poloidal ends of the blanket module. Figure 6.2.1-9 shows the value of $\overline{C}$ in the middle orifice when there are many

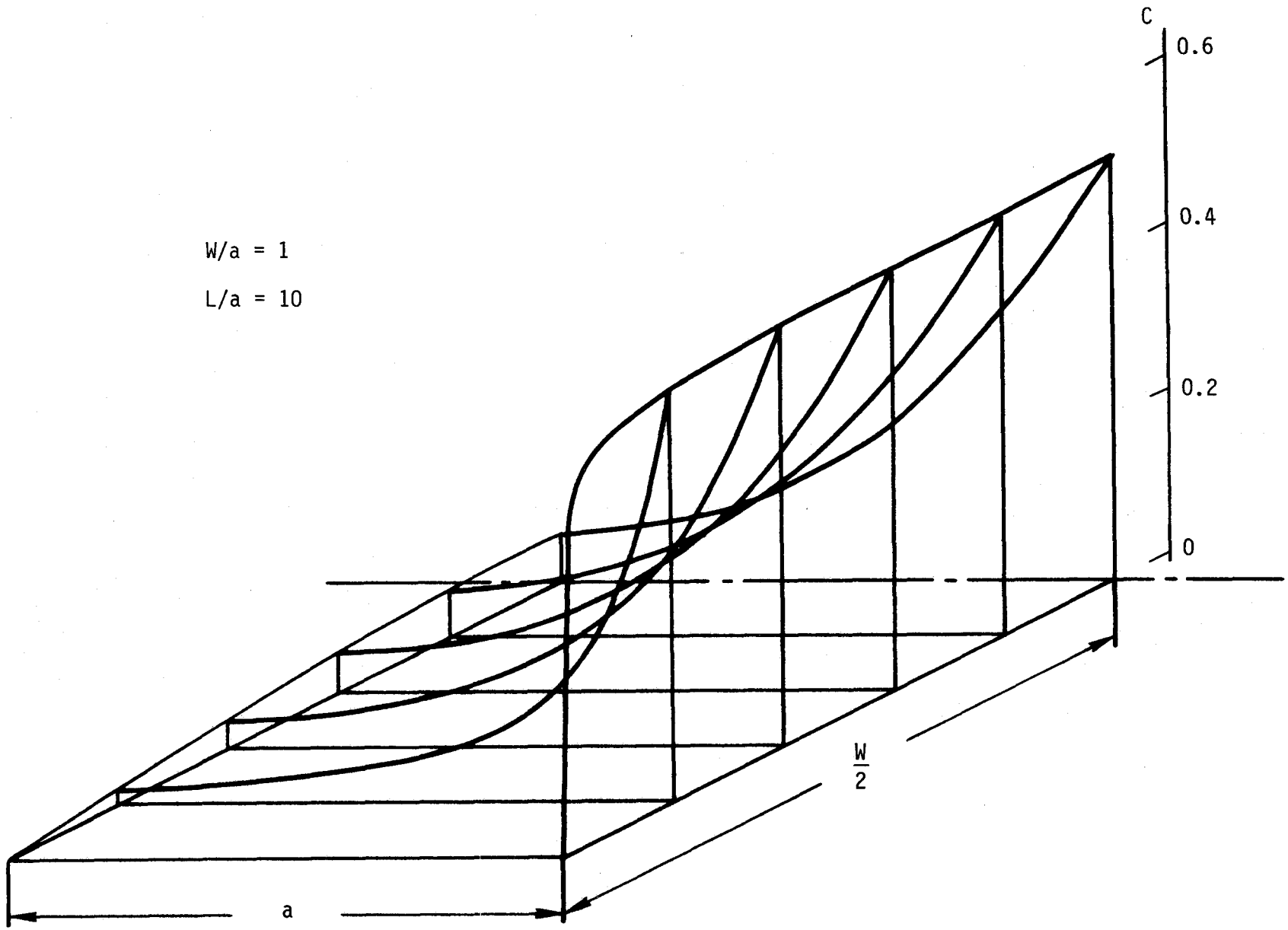

Figure 6.2.1-6 Poloidal current intensity (W/a = 1, L/a = 10).

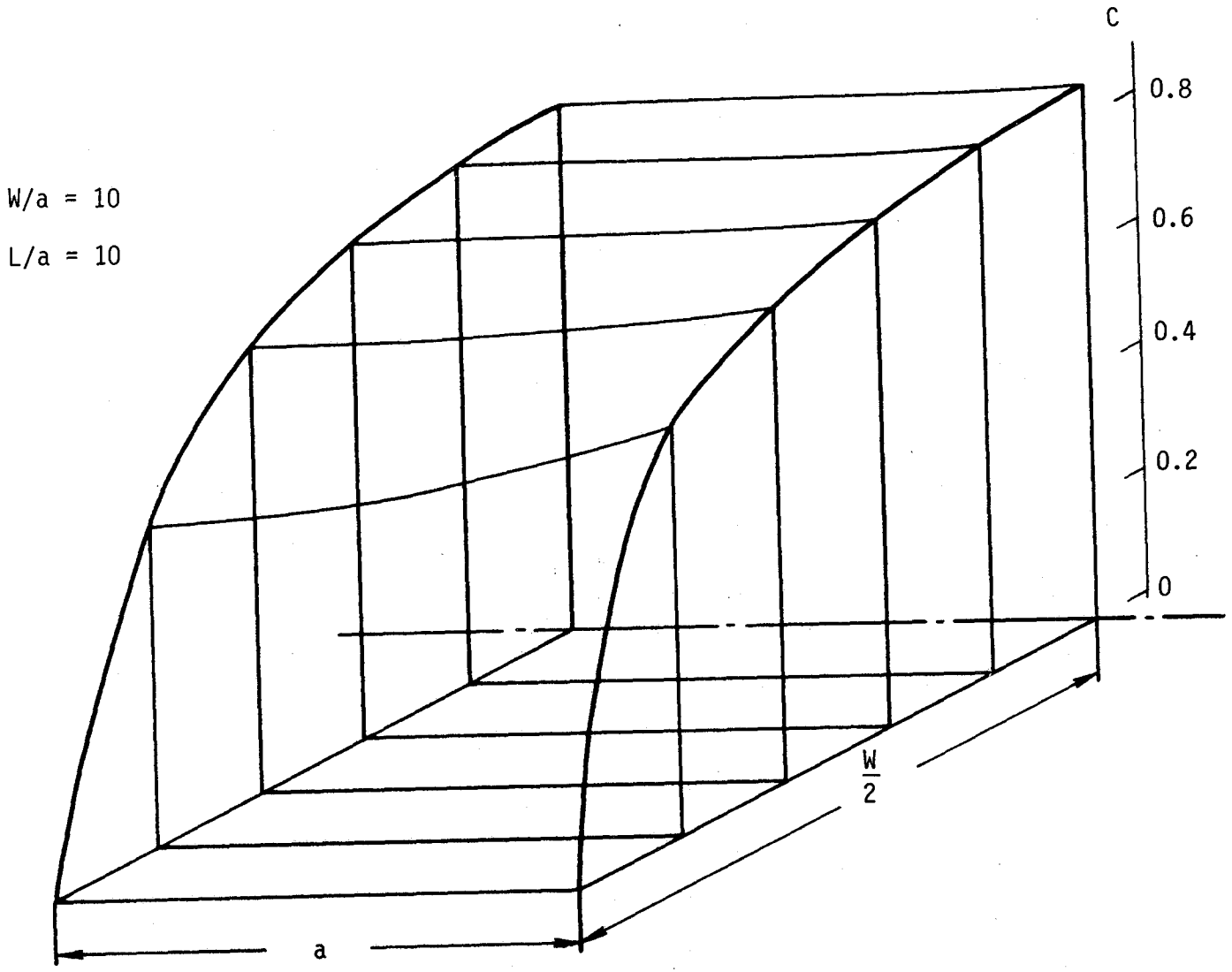

Figure 6.2.1-7 Poloidal current intensity (W/a = 10, L/a = 10).

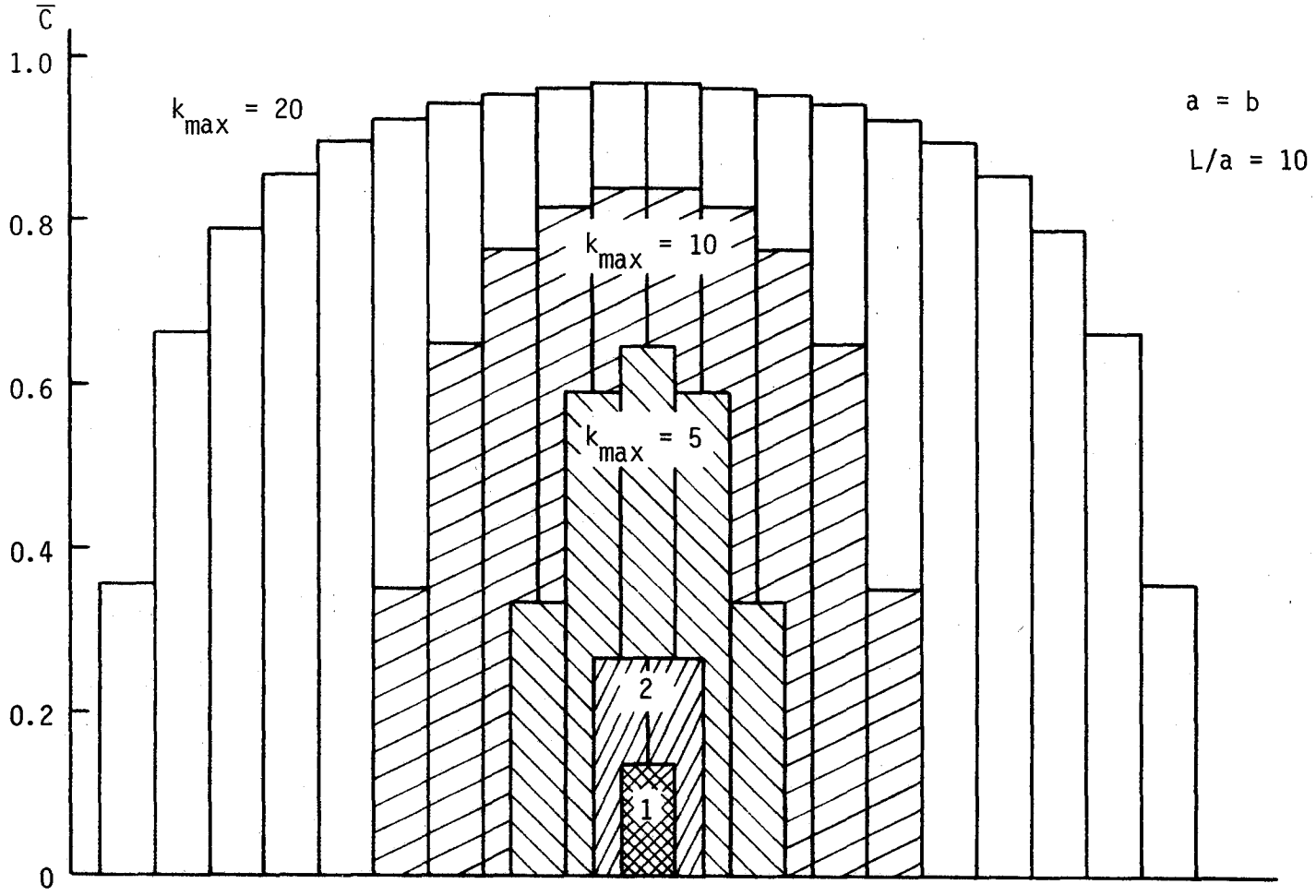

Figure 6.2.1-8 Average pressure drop coefficient in each orifice.

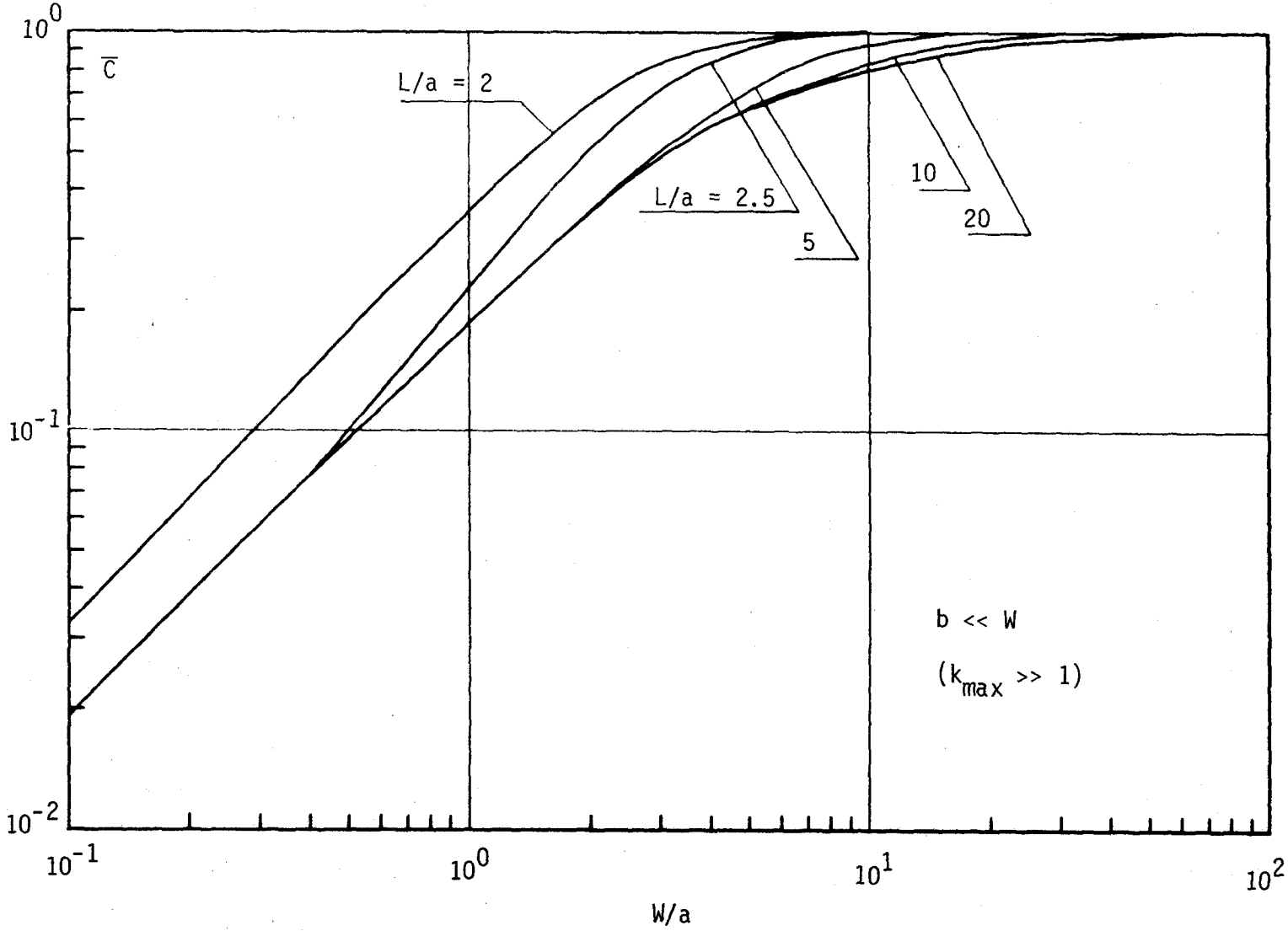

Figure 6.2.1-9 Average pressure drop coefficient in middle orifice.

orifices. It is a function of W/a and L/a. If W/a is larger than 100, $\overline{C}$ is unity regardless of the value of L/a.

Effect of Insulators

The current flow pattern changes greatly if there are any obstructions in the plane. An insulating partition parallel to the magnetic field in the opening of the second wall distorts the circuit and increases the resistance. Figure 6.2.1-10 shows the eddy current distribution in the case of W/a=10 and L/a=10. There are insulating partitions of length ℓ_p between each orifice of poloidal width b. Both ℓ_p and b are equal to a in the figure. Since there is no insulation between x=a and x=L-a, the multi-channel effect still remains. But the flow pattern in each orifice is similar to the pattern in the single orifice case. Figure 6.2.1-11 shows the effect of the insulating partitions between the orifices on the MHD pressure drop in the case of W/a=10, L/a=10 and b/a=1. Insulating partitions of length ℓ_p=a decrease the pressure drop greatly. There is little difference between the pressure drops in the cases of ℓ_p=a and ℓ_p=L. It is not necessary to extend the partition into the second wall. The insulator between adjacent orifices is quite effective.

Evaluation of the MHD Pressure Drop in the Reference Blanket

In the reference blanket, each toroidal channel has its own inlet and outlet orifices. The openings at both toroidal ends of the second wall are partitioned by ribs into orifices. For simplicity, the electrical conductivity of the wall is assumed to be the same as that of the coolant in the analysis, though the latter is twice as large.

When there are many orifices and the poloidal width of the blanket module W is far larger than the orifice width a, the pressure drop coefficient $\overline{C}$ in eq. (6) is unity in central orifices. $\overline{C}$=1 means that the resistivity in the return path is negligible; the second wall is wide enough to support the return current. Although the resistivity of the wall is higher in the reference blanket, it does not affect the result, but the ribs between the orifices have some effect. The electrical conductivity through the orifices in the poloidal direction is expressed as follows:

$$\sigma_e = \frac{b + t_w}{b/\sigma_f + t_w/\sigma_w} \qquad (6.2.1\text{-}7)$$

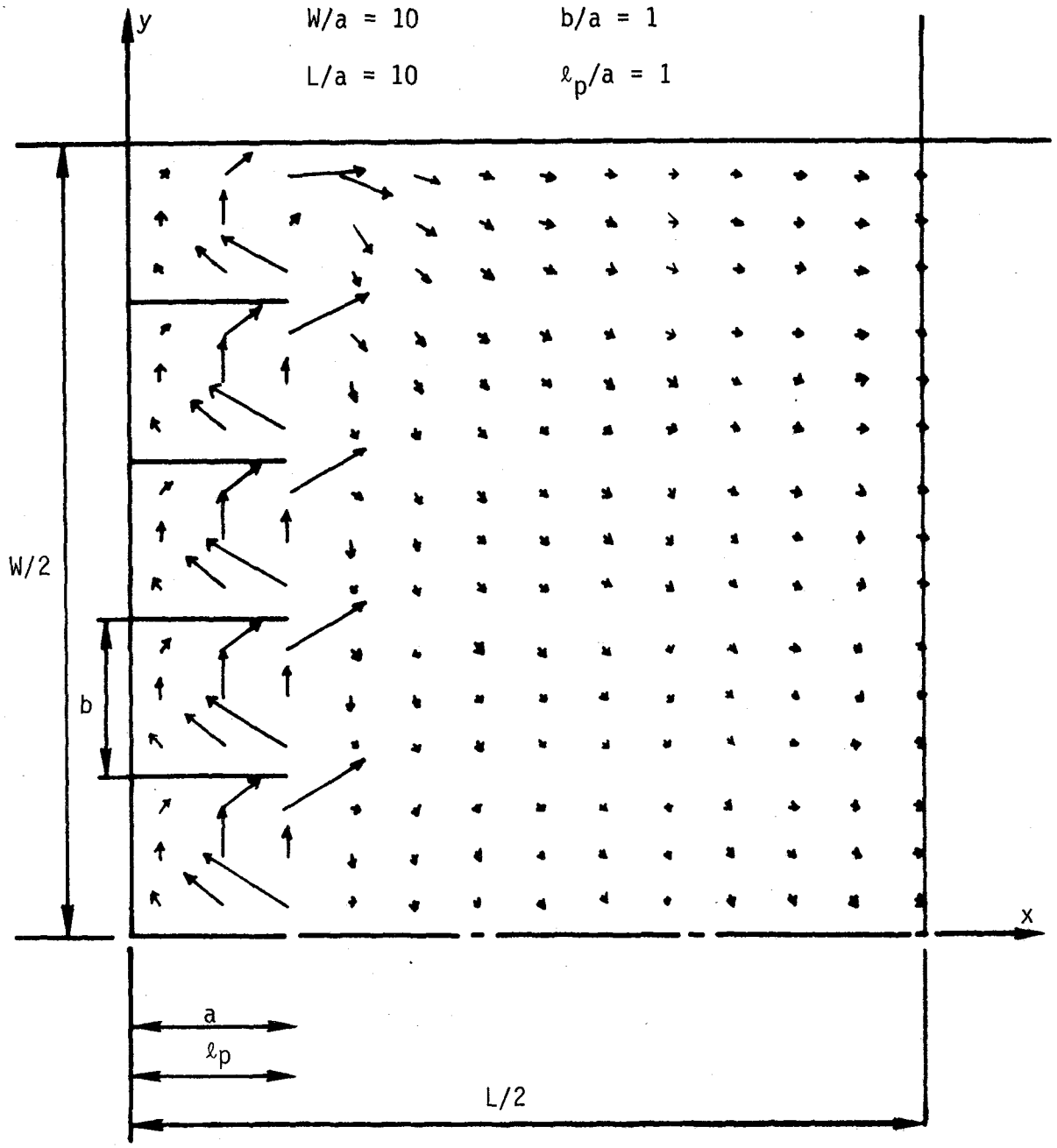

Figure 6.2.1-10 Eddy current distribution with insulator.

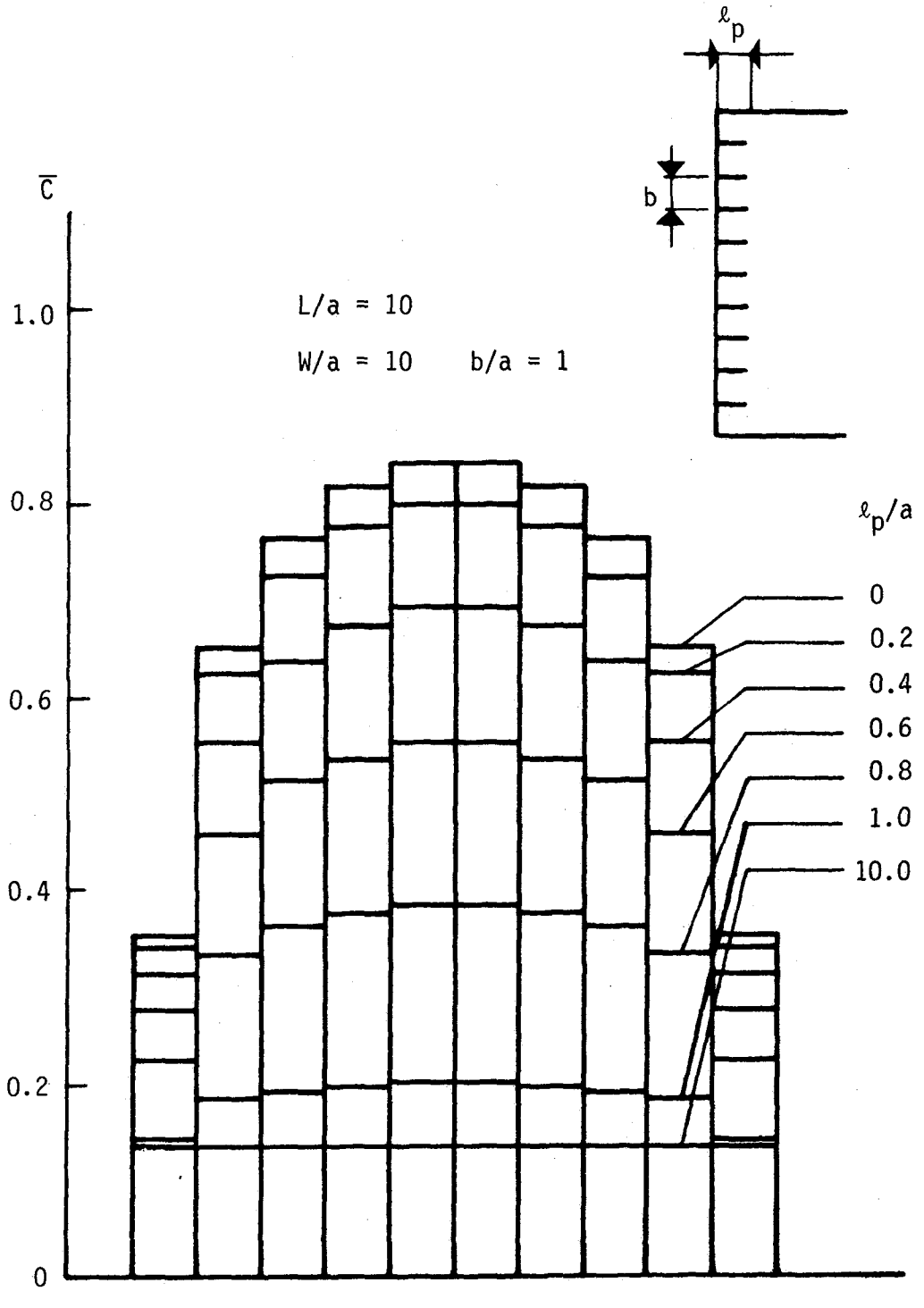

Figure 6.2.1-11 Effect of insulator length on pressure drop.

where σ_f and σ_w are the electrical conductivities of the coolant and the rib, and t_w is the thickness of the rib. Since the electromotive force is not induced in the ribs, the average electromotive force is not $B_T w_b$ but rather $B_T w_b b/(b+t_w)$. The MHD pressure drop per unit length can be calculated by the following equation:

$$-\frac{dp}{dz} = \overline{C}\ \sigma_e B_T^2\ w_b\ \frac{b}{b + t_w} \qquad (6.2.1\text{-}8)$$

The detailed dimensions of the second wall orifice are not given explicitly in the reference blanket design. Thus the following values are used:

toroidal width of orifice	a	45 mm
poloidal width of orifice	b	25 mm
rib thickness	t_w	3 mm
second wall thickness		15 mm
average velocity in orifice	w_b	1.56 m/s
magnetic field strength	B_T	7.5 T

The poloidal width of the blanket module is 9.3 m, which is far larger than the orifice width. The value of $\overline{C}$ is unity in this case. The electrical conductivity of the coolant is 3.0 MS/m and that of the rib is 1.5 MS/m. The MHD pressure drop per unit length is calculated to be 212 MPa/m. As the second wall thickness is 15 mm, the MHD pressure drop in the orifice is calculated to be 3.18 MPa.

In the above analysis, we assumed slug flow in the orifice, however, the pressure drop is not uniform in the orifice. Flow redistribution may occur, which would reduce the pressure drop. This will be discussed after the analysis using the fully developed flow model.

(3) Fully Developed Flow Model

The slug flow assumption is technically incorrect, since flow redistribution occurs. Thus, the fully developed velocity profile is used here, which appears if the second wall is thicker than the entry length. As the second wall is not so thick, the flow may not be fully developed in the orifice. But no one can predict the real profile. The pressure drop with fully developed

flow is calculated and is compared with the pressure drop with slug flow.

Calculational Model and Assumptions

Figure 6.2.1-12 shows the calculational model. The detailed structure is not smeared, but is included in the calculation. The toroidal width of the orifice is a and the poloidal width is b. There are thin ribs of thickness t_w between the orifices. On the right side of the orifice is a wall of thickness t_w' which is thicker than the ribs. On the left side is a non-conducting wall. The conductivity of the ribs and the thick wall is σ_w and the conductivity of the coolant is σ_f. The bulk velocity w_b through each orifice is assumed to be the same. The eddy current is assumed to flow only in the plane shown in Fig. 6.2.1-12. The magnetic field is parallel to the toroidal direction, and the radial and poloidal field intensities are assumed to be zero.

The coolant is incompressible and the flow is steady. The Stuart number or interaction parameter, $N = aB_T^2\sigma_f/w_b\rho$, denotes the ratio of the electromagnetic force to the inertial force, where ρ is the density of the coolant. A large Stuart number is assumed, which means inertia can be neglected and the velocity profile develops quickly. The Hartmann number, $Ha = aB_T\sqrt{\sigma_f/\mu}$, is also assumed to be large, which means the viscous force is negligible except in boundary layers. The magnetic Reynolds number Re_m, the ratio of the induced magnetic field strength to the applied magnetic field strength, is assumed to be small. Finally, thin boundary layers are assumed. MHD flow in ducts has thin boundary layers near walls perpendicular to the magnetic field, and relatively thick layers near walls parallel to the field. The latter thickness is proportional to $1/\sqrt{Ha}$ (1). The assumptions are summarized as follows:

(i) The coolant is incompressible.

(ii) The flow is steady.

(iii) The Stuart number is large, i.e., $N \gg 1$.

(iv) The Hartmann number is large, i.e., $Ha \gg 1$.

(v) The magnetic Reynolds number is small, i.e., $Re_m \ll 1$.

(vi) The boundary layers are thin, i.e., $Ha^{-1/2} \ll \phi_w (= \sigma_w t_w/\sigma_f a)$.

(vii) The ribs are so thin that the resistivity across them can be neglected.

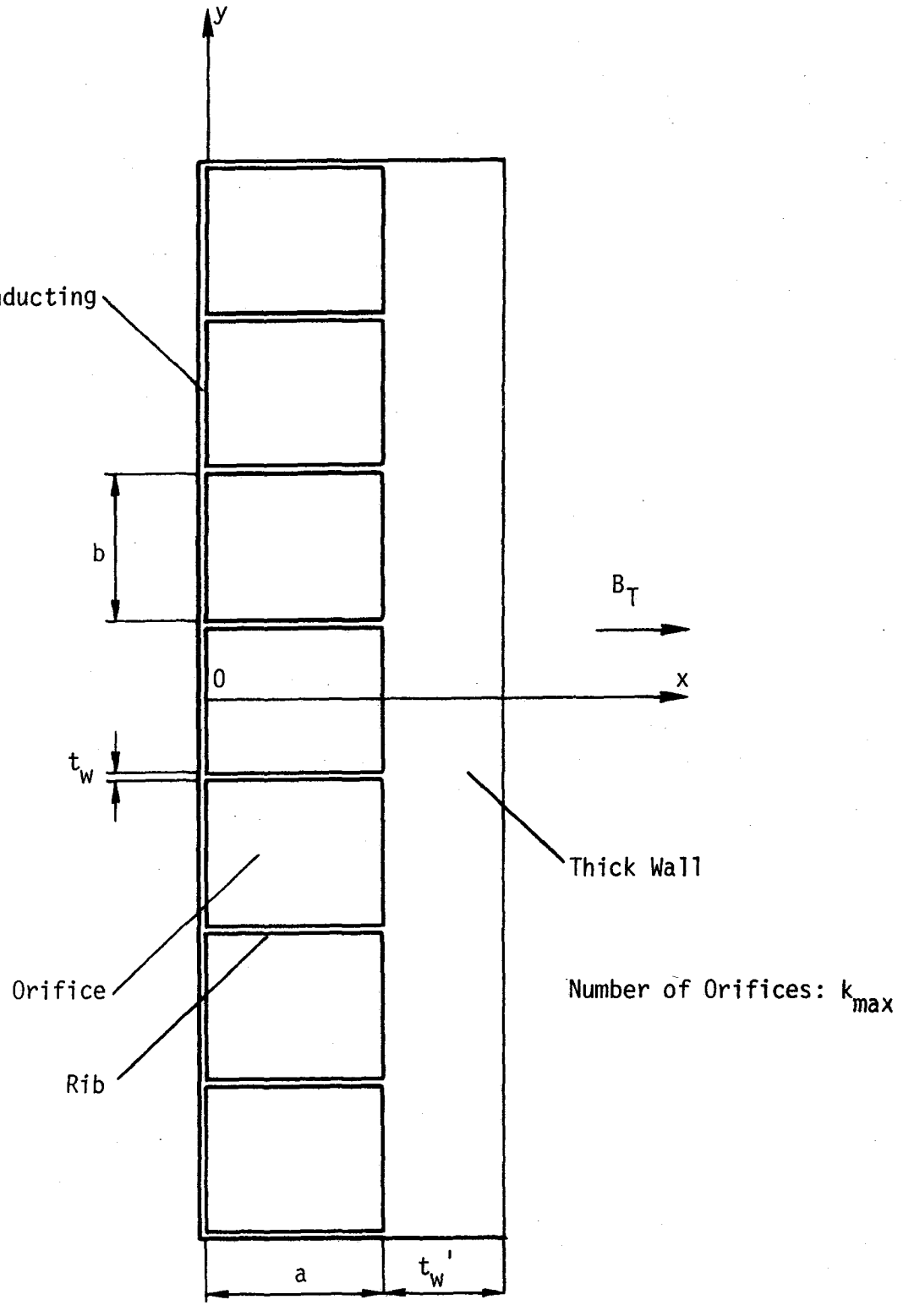

Figure 6.2.1-12 Fully developed flow model.

(viii) The eddy current flows only in the plane parallel to the wall.

(ix) The bulk velocity is the same in every orifice.

The basic equations are as follows:

Navier-Stokes equation

$$\rho (\underline{V} \cdot \underline{\nabla}) \underline{V} = - \underline{\nabla} p + \underline{i} \times \underline{B} + \mu \nabla^2 \underline{V} \qquad (6.2.1\text{-}9)$$

Ohm's law

$$\underline{i} = \sigma_f (- \underline{\nabla} \phi_e + \underline{V} \times \underline{B}) \qquad (6.2.1\text{-}10)$$

and conservation of current

$$\underline{\nabla} \cdot \underline{i} = 0 \qquad (6.2.1\text{-}11)$$

Current Intensity and Electric Potential in Each Channel

Equation (9) can be non-dimensionalized as follows:

$$N^{-1} (\underline{V}' \cdot \underline{\nabla}') \underline{V}' = - \underline{\nabla}' p' + \underline{i}' \times \underline{B}' + Ha^{-2} \nabla'^2 \underline{V}' \qquad (6.2.1\text{-}12)$$

where N is the interaction parameter and Ha is the Hartmann number. In the case when $N \gg 1$ and $Ha \gg 1$, the first and last terms are negligible, except in boundary layers or free shear layers, where large gradients and/or large velocities make these terms significant. Therefore, outside boundary and free shear layers,

$$\underline{\nabla}' p' = \underline{i}' \times \underline{B}' \qquad (6.2.1\text{-}13)$$

or

$$\underline{\nabla} p = \underline{i} \times \underline{B} \qquad (6.2.1\text{-}14)$$

The magnetic field is parallel to the x axis, hence poloidal and radial components of the field are zero. The current is assumed to flow in the plane shown in Fig. 6.2.1-12. Taking the curl of the above equation, we obtain:

$$\frac{\partial i_P}{\partial x} = 0 \qquad (6.2.1\text{-}15)$$

$$\frac{\partial i_P}{\partial y} = 0 \qquad (6.2.1\text{-}16)$$

where i_P is poloidal component of the current. The above equations mean that i_P is constant in each channel except at boundary layers where the assumptions of the model break down. Equation (11) can be rewritten as follows:

$$\frac{\partial i_T}{\partial x} + \frac{\partial i_P}{\partial y} = 0 \qquad (6.2.1\text{-}17)$$

Substituting eq. (16) into eq. (17), we obtain:

$$\frac{\partial i_T}{\partial x} = 0 \qquad (6.2.1\text{-}18)$$

The toroidal component of the current i_T is zero on the surface of the non-conducting wall at x=0, therefore i_T is identically zero:

$$i_T \equiv 0 \qquad (6.2.1\text{-}19)$$

which means that the eddy current flows only in the poloidal direction in the core region of the orifice.

Relation of Current Intensity Between Neighboring Channels

Fig. 6.2.1-13 shows the current paths in the plane. Because the poloidal current is constant, the current in the k-th rib $K_k(x)$ must satisfy the following equation:

$$K_k(x) = \int_0^x (i_{P,k} - i_{P,k+1})dx = (i_{P,k} - i_{P,k+1})x \qquad (6.2.1\text{-}20)$$

where $i_{P,k}$ is the poloidal current density in the k-th orifice. The current in the thick wall between the k-th and (k-1)th ribs, K'_k, is given as follows:

$$K'_k = a\, i_{P,k} \qquad (6.2.1\text{-}21)$$

The electric potential difference between the k-th and (k-1)th ribs at x=a is given as follows:

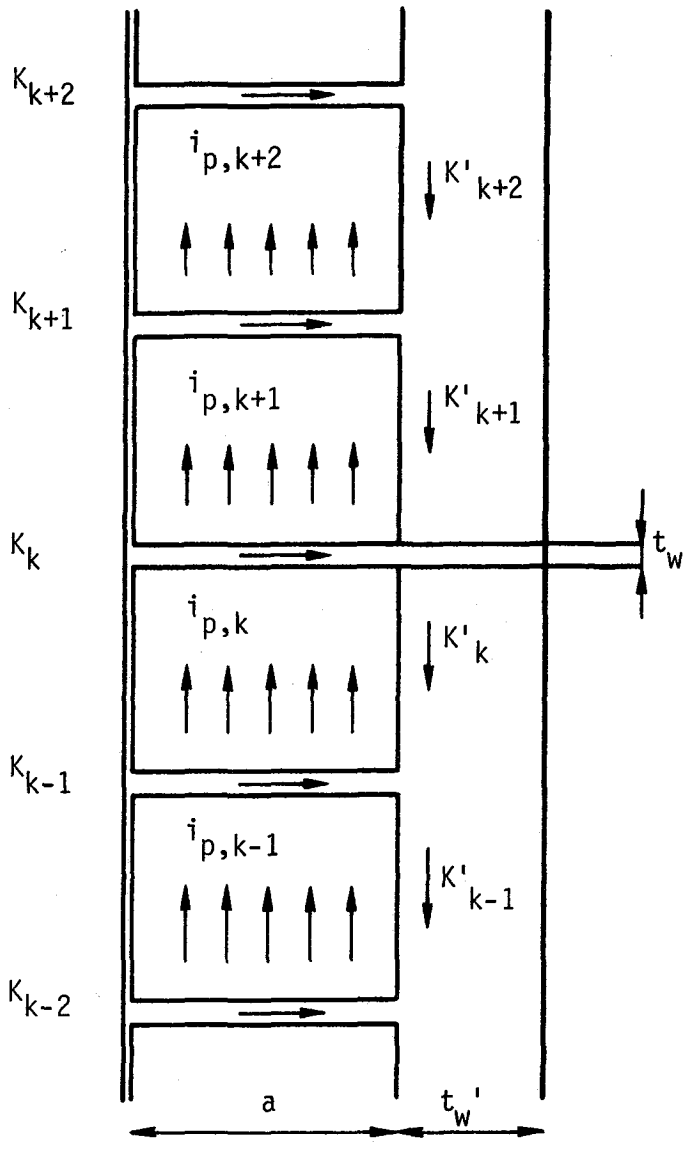

Figure 6.2.1-13 Current paths.

$$\Delta\phi_{e,k} = \frac{bK'_k}{\sigma_w t'_w} = \frac{ab}{\sigma_w t'_w} i_{P,k} \qquad (6.2.1\text{-}22)$$

where σ_w is the conductivity of the wall. The electric potential changes linearly along the thick wall between the k-th and (k-1)th ribs. As the magnetic field is parallel to the toroidal direction, there can be no electromotive force in this direction. Therefore, the electric potential in the fluid must be constant in the toroidal direction. If it was not constant, current would flow in the toroidal direction and Eq. (19) could not be satisfied. Therefore, the electric potential changes linearly along the poloidal direction in the core region between the k-th and (k-1)th ribs. The following uniform radial velocity is necessary to induce the above potential.

$$w_{core,k} = \frac{i_{P,k}}{\sigma_f B_T} + \frac{\Delta\phi_{e,k}}{b\, B_T} = \left(\frac{1}{\sigma_f} + \frac{a}{\sigma_w t'_w}\right) \frac{1}{B_T} i_{P,k} \qquad (6.2.1\text{-}23)$$

The electric potential along the rib is given as follows:

$$\phi_{e,k} = \int_x^a K_k(x) \frac{1}{\sigma_w t_w} dx + \phi_{eo,k}$$

$$= \frac{i_{P,k} - i_{P,k+1}}{2\sigma_w t_w} (a^2 - x^2) + \phi_{eo,k} \qquad (6.2.1\text{-}24)$$

where $\phi_{eo,k}$ is the potential at x=a. The difference in the electric potential between the rib and the coolant in the core region near the rib must be compensated by the electromotive force in the boundary layer. Therefore:

$$\int_0^{\delta} w_{BL,k} B_T dy' = -(\phi_{e,k-1} - \phi_{eo,k-1})$$
$$\int_{b-\delta}^{b} w_{BL,k}\, B_T\, dy' = \phi_{e,k} - \phi_{eo,k} \qquad (6.2.1\text{-}25)$$

where δ is the thickness of the boundary layer as shown in Fig. 6.2.1-14. We can obtain neither the boundary layer thickness nor the velocity distribution in it. But we can obtain the flow quantity in the boundary layer by Eq. (25). Figure 6.2.1-15 shows the distributions of the current and the electric potential in the rib. The schematic view of the velocity distribution in the orifice is shown in Fig. 6.2.1-16. In the core region, the velocity is

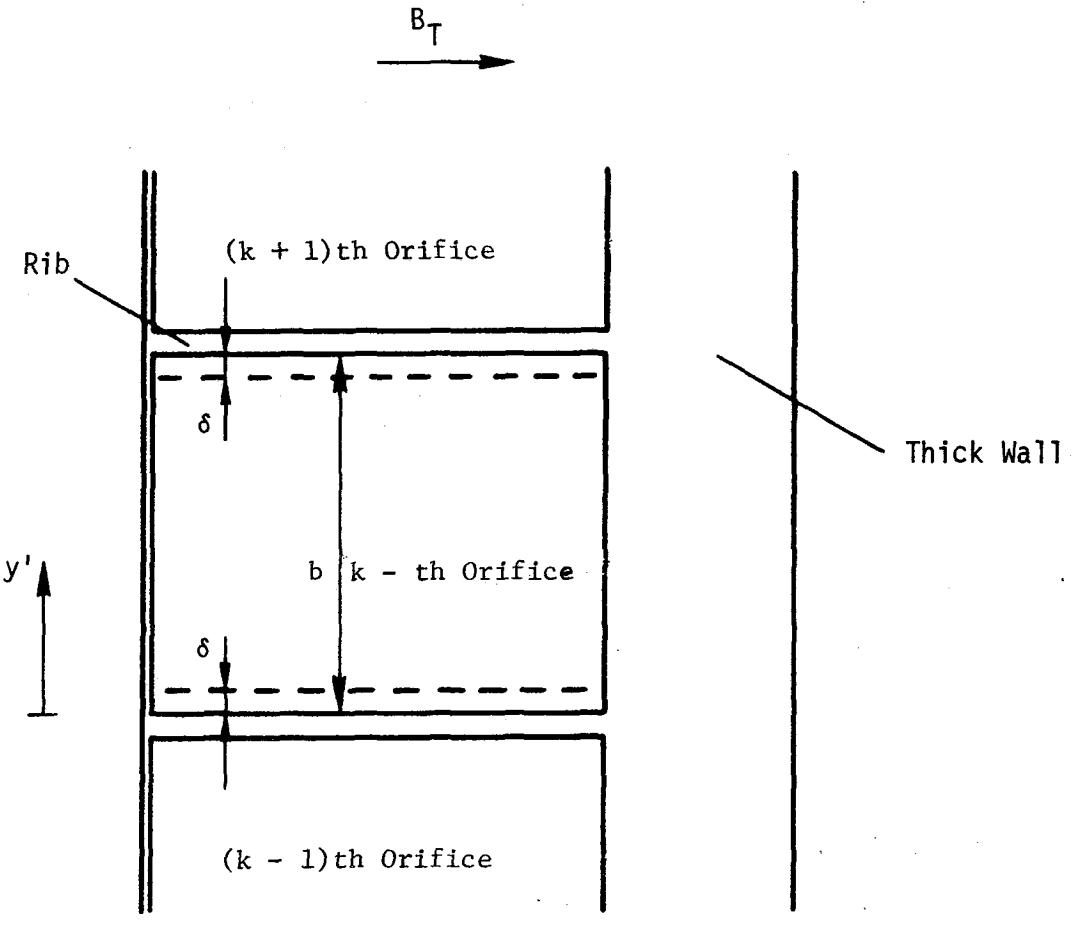

Figure 6.2.1-14 Boundary layer parallel to magnetic field.

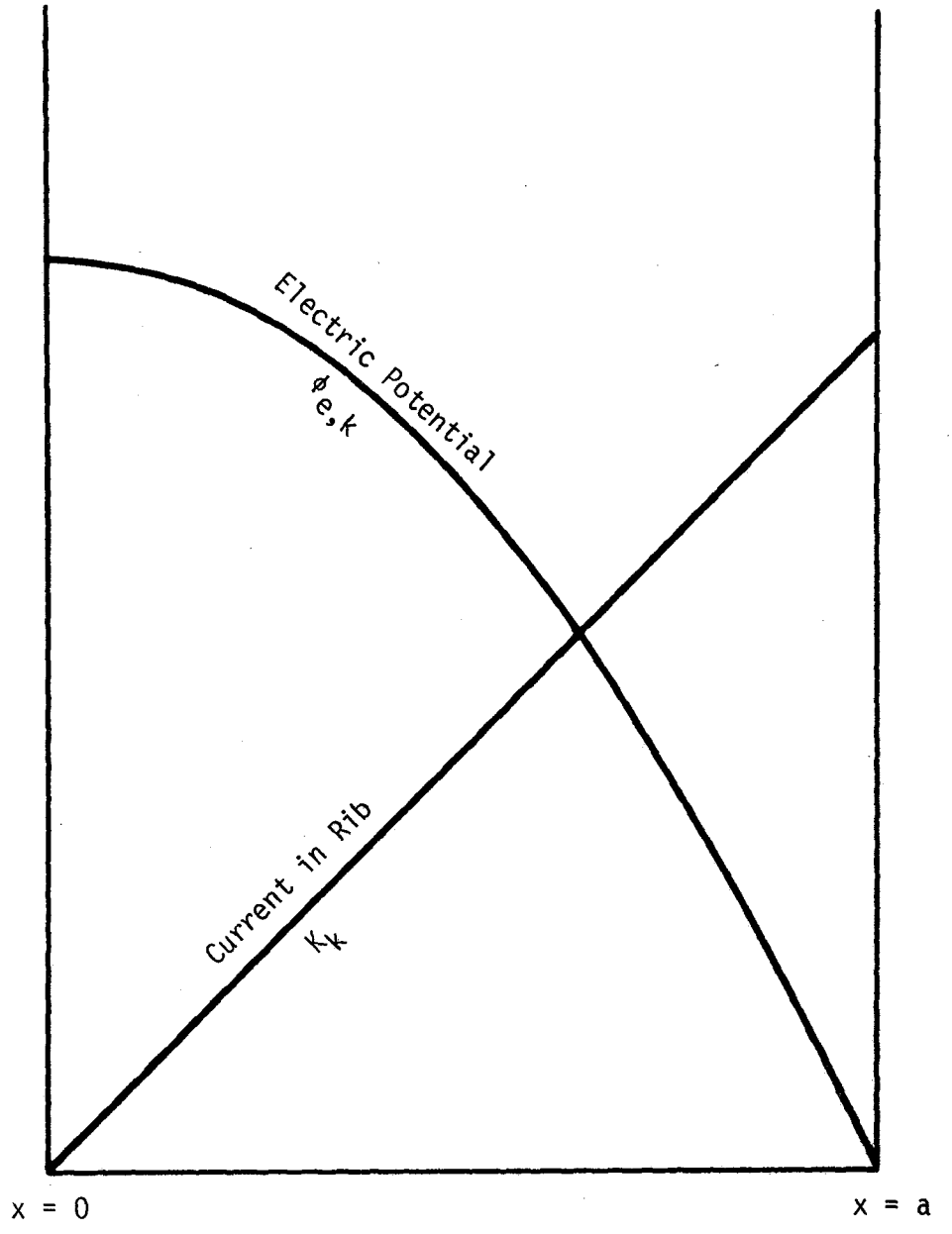

Figure 6.2.1-15 Distribution of current and electric potential in rib.

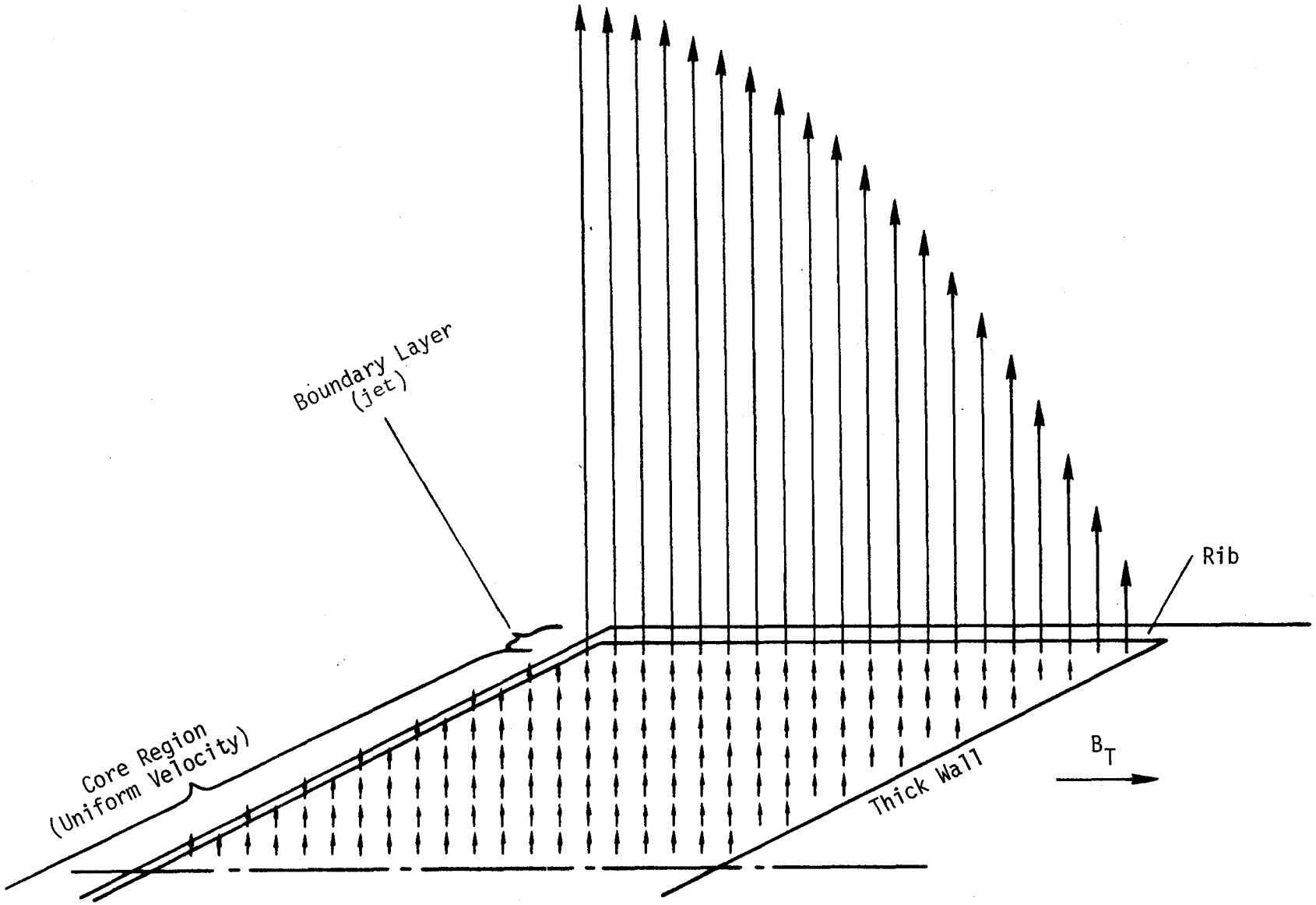

Figure 6.2.1-16 Velocity distribution in orifice.

uniform. In the boundary layer parallel to the rib, it has a parabolic distribution along the rib, though the distribution perpendicular to the rib is not obtained here. The total flow quantity in the boundary layer in the k-th orifice is given as follows:

$$Q_{BL,k} = \int_0^a \left(\int_0^{\delta} wdy' + \int_{b-\delta}^{b} wdy' \right) dx$$
$$= \frac{a^3}{3\sigma_w t_w B_T} (2i_{P,k} - i_{P,k+1} - i_{P,k-1}) \qquad (6.2.1\text{-}26)$$

The velocity in the core region of the k-th orifice is expressed as follows:

$$w_{core,k} = \frac{1}{ab} (Q_{total} - Q_{BL,k}) = w_b - \frac{1}{ab} Q_{BL,k} \qquad (6.2.1\text{-}27)$$

where w_b is the mean velocity in the orifice. Substituting Eqs. (23) and (26) into Eq. (27), we obtain:

$$\left(1 + \frac{\sigma_f a}{\sigma_w t_w'}\right) i_{P,k} = \sigma_f B_T w_b$$
$$- \frac{1}{3} \frac{\sigma_f a}{\sigma_w t_w} \frac{a}{b} (2i_{P,k} - i_{P,k+1} - i_{P,k-1}) \qquad (6.2.1\text{-}28)$$

The current intensity is zero on the outside of the blanket, hence:

$$i_{P,0} = 0 \qquad (6.2.1\text{-}29)$$

$$i_{P,k_{max}+1} = 0 \qquad (6.2.1\text{-}30)$$

where k_{max} is the number of orifices. Equation (28) expresses the relation of the current intensity between neighboring channels. Solving eqs. (28) through (30), we can obtain the current intensity in each channel.

Current Intensity Distribution

The current intensity in an orifice can be described as follows:

$$i_P = C \sigma_f B_T w_b \qquad (6.2.1\text{-}31)$$

where C is a function of the number of orifices k_{max}, the location of the

orifice k/k_{max}, $\phi_w(b/a)$ and ϕ_w' . Figure 6.2.1-17 shows the distribution of C in the case of $(1/\phi_w)(a/b) = (\sigma_f a/\sigma_w t_w)(a/b) = 54$ and $(1/\phi_w') = \sigma_f a/\sigma_w t_w' = 0$. If there is a single orifice, i.e., $k_{max}= 1$, C is calculated to be 0.027 by eq. (32).

$$C = \frac{1}{1 + \frac{2}{3}\frac{1}{\phi_w}\frac{a}{b} + \frac{1}{\phi_w'}} \qquad (6.2.1\text{-}32)$$

The value of C increases with increasing k_{max}. If there are more than 50 orifices, it reaches unity in the central orifices ($k/k_{max}\sim0.5$). It never exceeds unity even if there are more orifices. C is small in orifices near the poloidal ends of the blanket compared with that in central orifices. Figure 6.2.1-18 shows the result in the case of $(1/\phi_w)(a/b)=216$ and $1/\phi_w'=0$. The value of C is smaller in this case because the value of $(1/\phi_w)(a/b)$ is larger. If there are more than 100 orifices, it reaches unity. With a larger value of $(1/\phi_w)(a/b)$, the rate of increase of C is low, but C inevitably reaches unity with a sufficiently large number of orifices. Figure 6.2.1-19 shows the result in the case of $(1/\phi_w)(a/b)=54$ and $1/\phi_w'=1$. When $1/\phi_w'$ is not zero, C does not reach unity but reaches $\phi_w'/(1+\phi_w')$. In the case with a single orifice, the wall conductivity ratio of the thick wall perpendicular to the magnetic field affects the current intensity very little. In the case with many orifices, it is not ϕ_w but ϕ_w' that affects the current intensity.

Velocity Distribution in Orifice

The coolant velocity is very high near the wall parallel to the magnetic field as is shown in Fig. 6.2.1-16. The direction of the boundary layer jet is not always the same as the bulk flow. Figure 6.2.1-20 shows the directions of the jets in the case of $k_{max}=5$. The jet flows so that the induced electromotive force compensates the electric potential in the rib. The positive electric potential can be compensated by a jet in the positive direction on one side of the rib. On the other side of the rib, a positive jet cannot compensate the positive potential. Only a negative jet can compensate it. Thus the jets flow in opposite directions with nearly equal velocities on both sides of the rib.

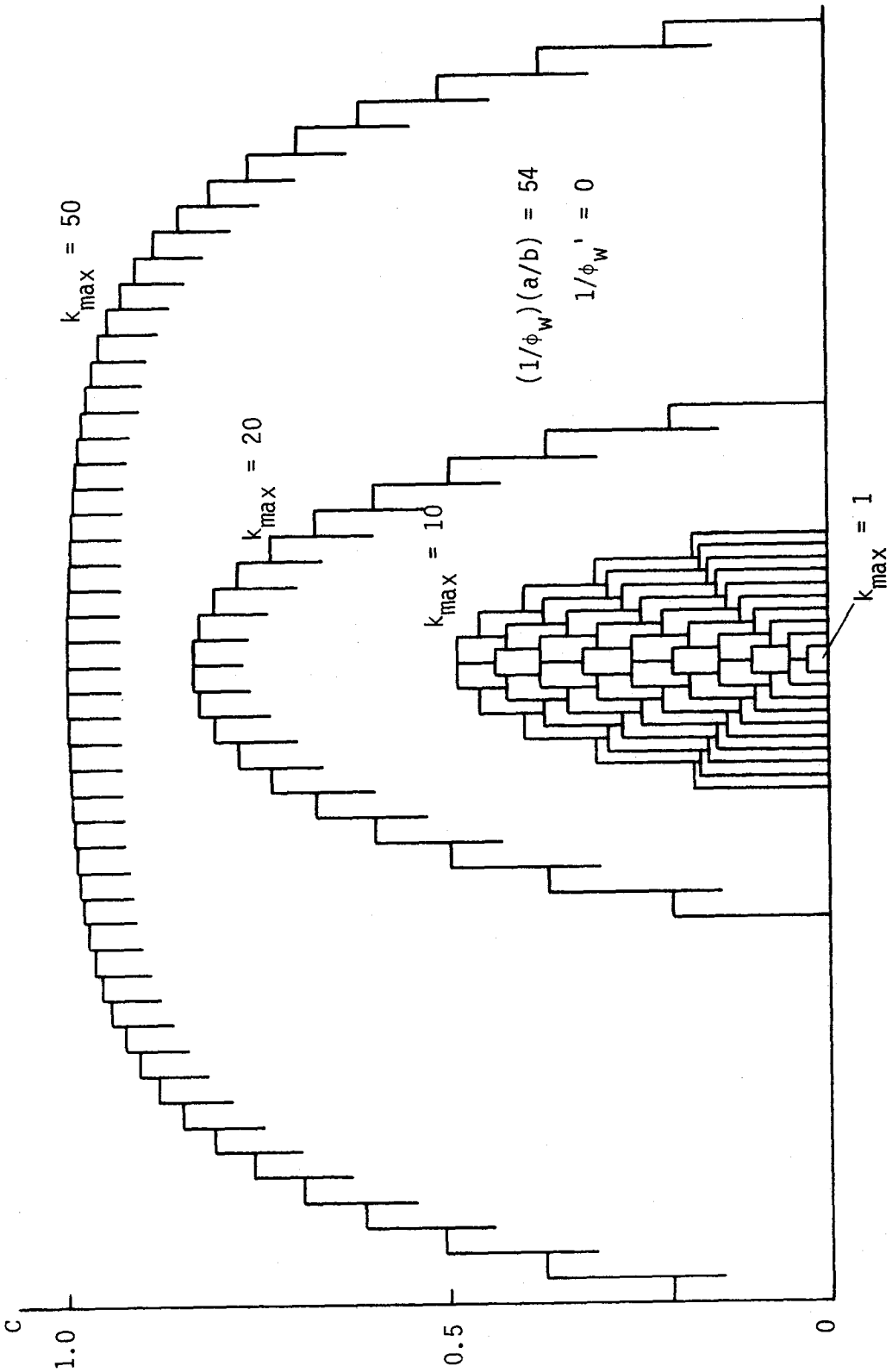

Figure 6.2.1-17 Pressure drop coefficient in each orifice.

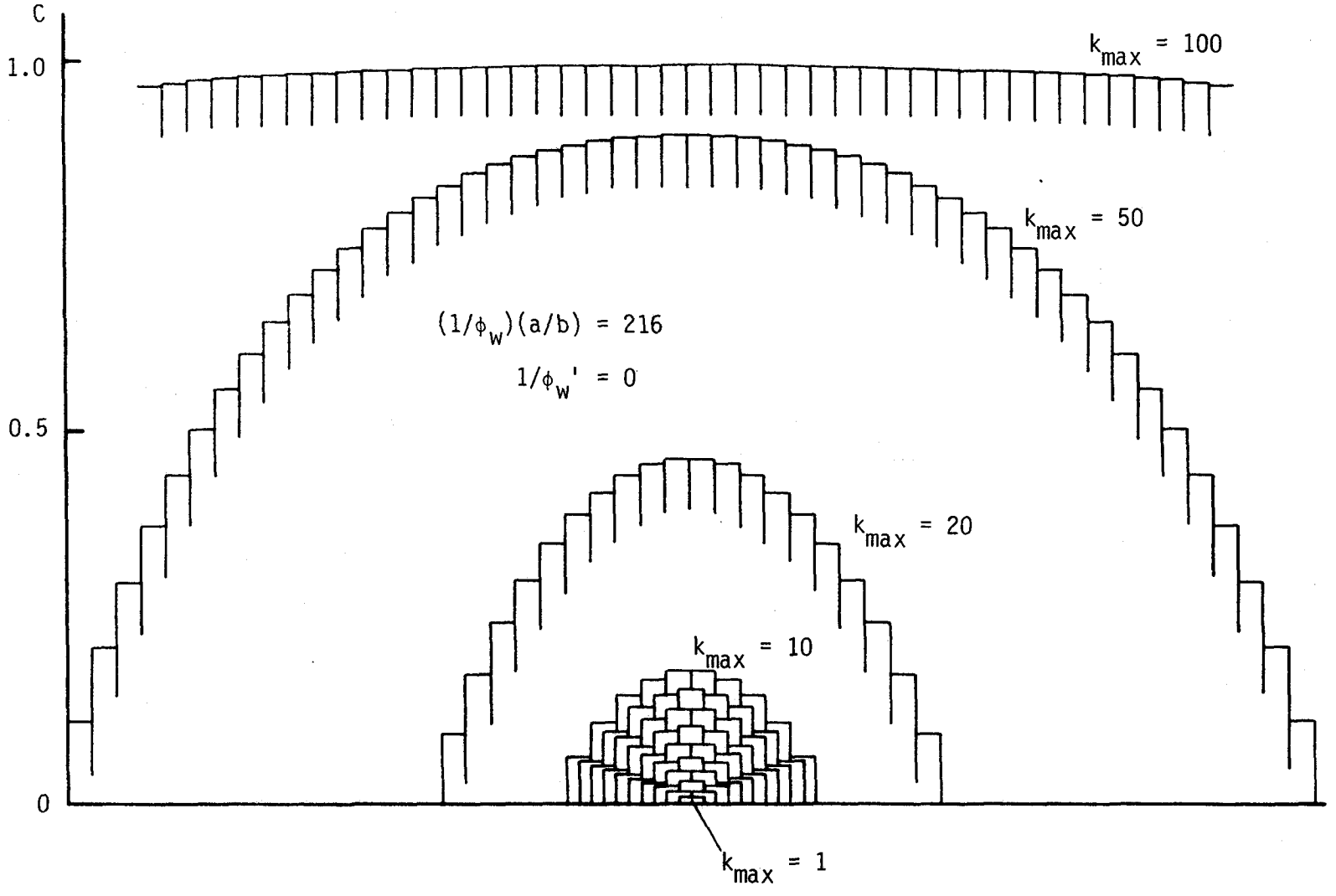

Figure 6.2.1-18 Pressure drop coefficient in each orifice.

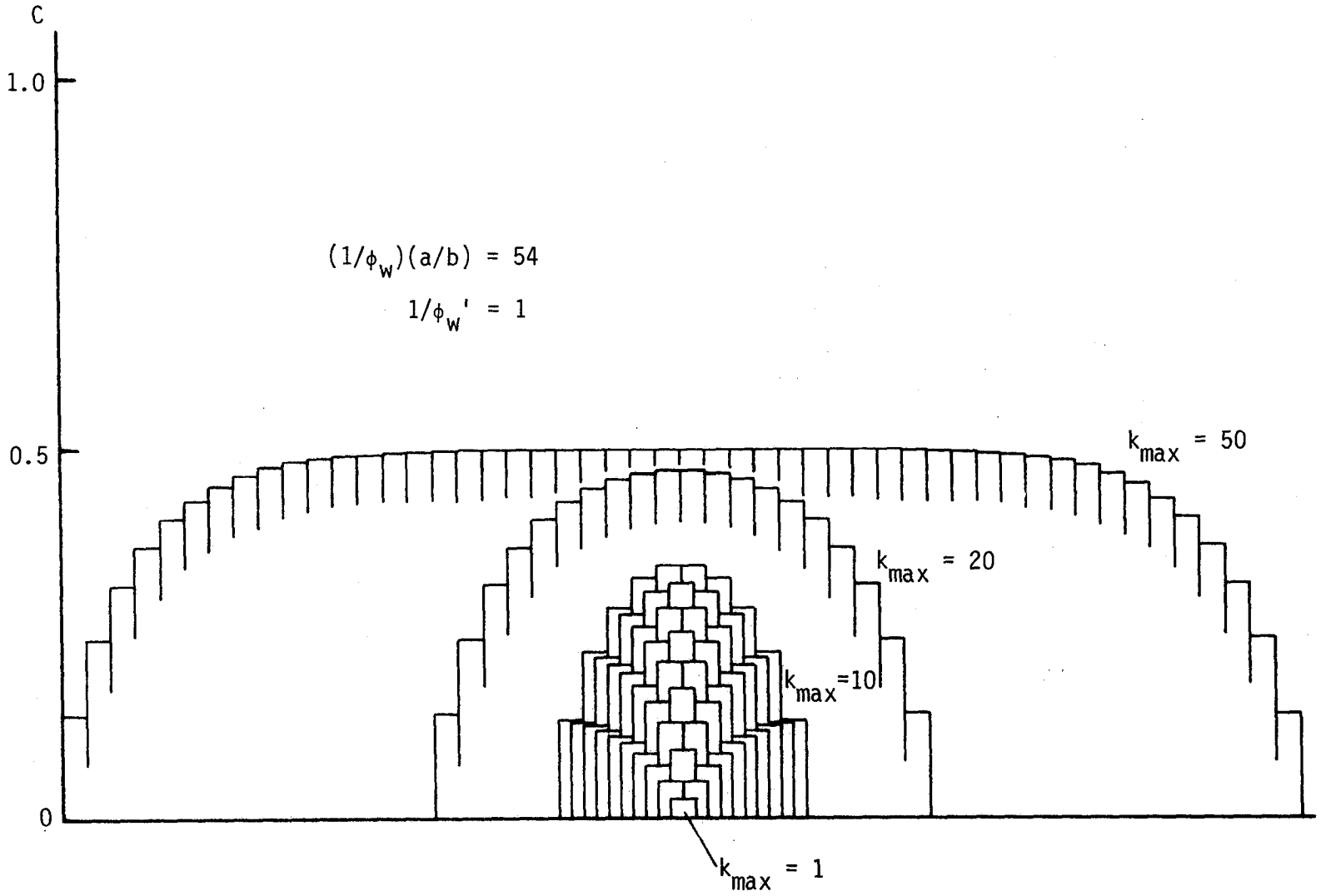

Figure 6.2.1-19 Pressure drop coefficient in each orifice.

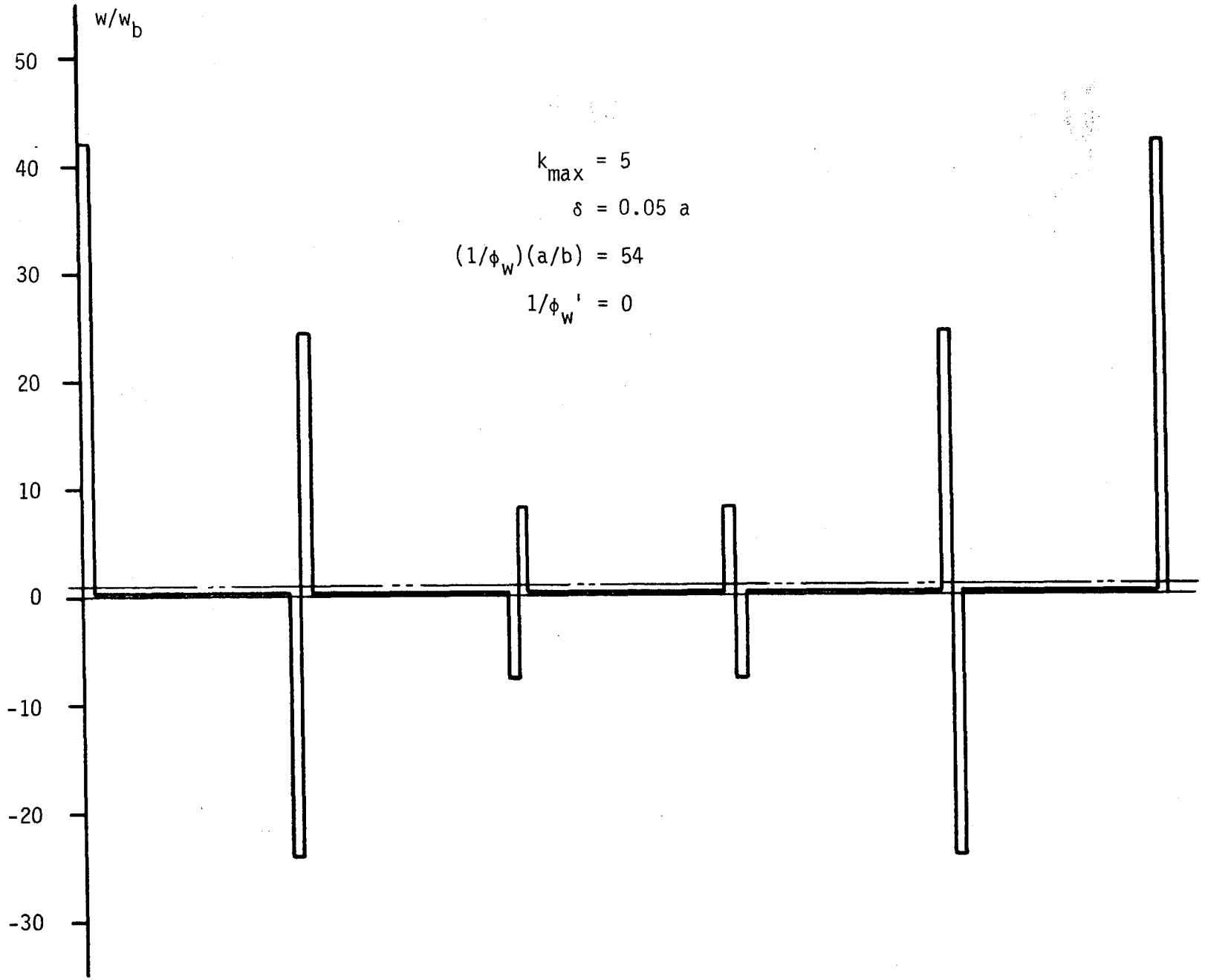

Figure 6.2.1-20 Velocity distribution in poloidal direction.

MHD Pressure Drop

The MHD pressure drop in an orifice can be described as follows:

$$-\frac{dp}{dz} = C\,\sigma_f B_T^2 w_b \qquad (6.2.1\text{-}33)$$

where C is the same constant used in eq. (31). C is nearly unity when there are many orifices, though it is very small when there is a single orifice.

Effect of Insulators

If there are insulating partitions between orifices, the MHD pressure drop can be reduced. Let us consider the case in which the current cannot cross the rib between x=0 and $x=\ell_p (0<\ell_p<a)$. There are two conducting walls of thickness t_w; one is insulated from the other. In this case, the pressure drop coefficient C with many orifices is calculated as follows:

$$C = \frac{1}{1 + \frac{2}{3}\frac{1}{\phi_w}\frac{\ell_p^3}{a^2 b} + \frac{1}{\phi_w'}} \qquad (6.2.1\text{-}34)$$

where C has the same meaning as in Eq. (5). If ℓ_p is equal to a, the above value is the same as that of the single orifice. Even if the insulating partition length ℓ_p is shorter than the toroidal width of the orifice a, it reduces the pressure drop fairly well. The insulator between adjacent orifices is quite effective.

Velocity Distribution with Equal Pressure Drop in Every Orifice

In the above analysis, we assumed that the bulk velocity is the same in every orifice. The bulk velocity should be the same in order to cool the first wall uniformly. However, in this case the MHD pressure drops in the orifices *are not the same*.

Let us suppose that the pressure drop is the same in every orifice and the velocities redistribute to comply with this condition. The MHD pressure drop is proportional to the poloidal current intensity. If the poloidal current intensity is the same in every orifice, the current in the ribs is zero except in the ribs at both ends of the blanket module. There is no electric potential difference along the ribs. The jets near the ribs do not

exist, except near the ribs at the poloidal ends of the blanket.

Since the velocity in the core region of the orifice is proportional to the MHD pressure drop, it is the same in every orifice. Hence the flow quantity in every orifice is the same except in the orifices at the poloidal ends of the blanket module where the wall jets exist. The flow quantity of the jet is given by the following equation:

$$Q_{BL} = \frac{a^3}{3\sigma_w t_w B_T} i_P = \frac{1}{3} \frac{\sigma_f a}{\sigma_w t_w} w_b a^2 \frac{1}{1+\sigma_f a/\sigma_w t_w'} \qquad (6.2.1\text{-}35)$$

where w_b is the average velocity in central orifices. The flow quantity in the end orifices is larger than that in other orifices by this amount. The flow quantity is the same in other orifices. In this case, the pressure drop coefficient C is exactly equal to $\phi_w'/(1 + \phi_w')$ if w_b is given by the average velocity in central orifices. Even if nonuniform distribution of the flow quantity among the orifices is allowed, the MHD pressure drop is not reduced.

Evaluation of the MHD Pressure Drop in the Reference Blanket

The MHD pressure drop in the second wall orifice of the reference blanket is calculated using the following values:

toroidal width of orifice	a	45 mm
poloidal width of orifice	b	25 mm
rib thickness	t_w	3 mm
toroidal length of second wall	t_w'	2910 mm
second wall thickness		15 mm
average velocity in orifice	w_b	1.56 m/s
magnetic field strength	B_T	7.5 T
number of orifices	k_{max}	332
conductivity of fluid	σ_f	3.0 MS/m
conductivity of wall	σ_w	1.5 MS/m
wall conductivity ratio (rib)	ϕ_w	1/30
wall conductivity ratio (thick wall)	ϕ_w'	32.3

As the toroidal length of the second wall is far larger than the orifice size, the current flows two dimensionally in the wall. This effect may increase the

resistivity in the thick wall of the model. The current induced by the flow in the inlet orifices is compensated by the current induced in the outlet orifices. The current can flow not only in the second wall but also through the coolant in the area where it flows parallel to the magnetic field. These effects may decrease the resistivity. In this calculation, we use the toroidal length of the second wall as the thick wall thickness t'_w. The pressure drop coefficient in the central orifices is calculated to be 0.97. Using eq. (33), the MHD pressure drop per unit length is calculated to be 255 MPa/m. The pressure drop across the second wall is calculated to be 3.83 MPa.

We assumed that the ribs are thin and the resistivity across them can be neglected, but in the reference blanket, the ribs are not so thin. If we take this effect into consideration, Eq. (36) should be used instead of Eq. (33).

$$-\frac{dp}{dz} = C \frac{b}{b/\sigma_f + t_w/\sigma_w} B_T^2 w_b \qquad (6.2.1\text{-}36)$$

Using this equation, the MHD pressure drop across the second wall is calculated to be 3.09 MPa, which is a little smaller than the above value, but still very large.

(4) Discussion

There is a small difference between the results with the slug flow model and the fully developed flow model. This is because the resistivity in the return current path was neglected in the former while it was given a finite value in the latter.

The thickness of the second wall is only 15 mm, which is so small that the flow may not be fully developed in the orifice. No one can predict the real velocity distribution in the orifices at present, because the flow equations and the eddy current equations must be solved simultaneously with a three dimensional model. However, the fact that the pressure drops with slug flow and fully developed flow are nearly the same suggests that the models are accurate. The pressure drop of more than 3 MPa in the orifice is so high that some modification of the design is needed.

The MHD pressure drop in the orifices can be greatly reduced by providing insulators as was discussed both in the slug flow and fully developed flow models. It is possible to insulate an orifice from the neighboring orifices

by making slits in the ribs or by using non-conducting materials. The modification of the design is small because the insulation is necessary only between the orifices. However, the use of insulators in a fusion environment is highly uncertain due to materials compatibility concerns and their low tolerance to neutron irradiation.

(5) Conclusions

The MHD pressure drop in the second wall orifice of the reference blanket was calculated with the slug flow model and the fully developed flow model. As there is no insulation between the orifices, the eddy current flows across neighboring orifices. The current flows back through the second wall, the cross sectional area of which is very large. Since the resistivity of the return path is low, the current intensity is high, which induces a very high pressure drop of more than 3 MPa.

With fully developed flow, there exist wall jets near the ribs which are parallel to the magnetic field. Calculations show the jets flow in opposite directions on each side of the rib, that is, on one side the jet flows in the direction opposite to the bulk flow.

The MHD pressure drop was shown to be greatly reduced if insulation is provided between the orifices.

The MHD pressure drop in a channel with adjacent channels in the direction perpendicular to the magnetic field is quite different from that in a single channel. Eddy currents may flow across the channels if there are many parallel channels. This global current greatly affects the MHD pressure drop. We cannot use formulas which are developed for a single channel in the presence of global currents.

6.2.1.3 MHD Flow in First Wall Cooling Channel of Reference Blanket

Introduction

In the reference design, the coolant in the toroidal channel flows across the poloidal magnetic field. The poloidal field of 0.5T is high enough to make the velocity profile uniform if the toroidal field is not too strong, but the toroidal field of 7.5T causes a strong resistive force against the radial

and poloidal components of the flow which are needed to develop the velocity profile. Therefore, the development of the velocity profile may be slow, and the profile may not be uniform for a considerable length of the toroidal channel. It is important to know the velocity profile in the channel, because it affects both the first wall temperature and the corrosion rate.

Basic Equations and Assumptions

The basic equations are as follows:

$$\text{div } \underline{V} = 0 \tag{6.2.1-37}$$

$$\rho \frac{D\underline{V}}{Dt} = - \text{grad } p + \mu \Delta \underline{V} + \underline{i} \times \underline{B} \tag{6.2.1-38}$$

where $\underline{V}$ is the velocity, ρ is the density, p is the pressure and μ is the viscosity. $\underline{i} \times \underline{B}$ is the electromagnetic force, where $\underline{i}$ denotes the eddy current density and $\underline{B}$ denotes the intensity of the magnetic field. The eddy current is induced by the liquid metal flow in the magnetic field. The current density can be obtained using Maxwell's equations and Ohm's law. As the electromotive force depends on the velocity, Eqs. (27) and (38) should be solved simultaneously with Maxwell's equations and Ohm's law. However, it is difficult to solve them simultaneously. For simplicity, the current density is obtained approximately in the following manner.

The poloidal magnetic field and the axial component of the velocity induce a radial electromotive force. If there are return current paths, the current will flow radially in the coolant. As the direction of the electromotive force is the same in every channel, the current can flow back only through ribs between the channels as shown in Fig. 6.2.1-21. The electrical conductivity of the rib is low compared with that of the fluid, hence the current density in the fluid depends strongly on the conductivity of the rib. If the velocity is uniform, the radial current density in the coolant is given as follows:

$$i_r = \sigma_f B_p u \frac{\phi_w}{1+\phi_w} \tag{6.2.1-39}$$

where σ_f is the conductivity of the coolant, u is the toroidal (axial) com-

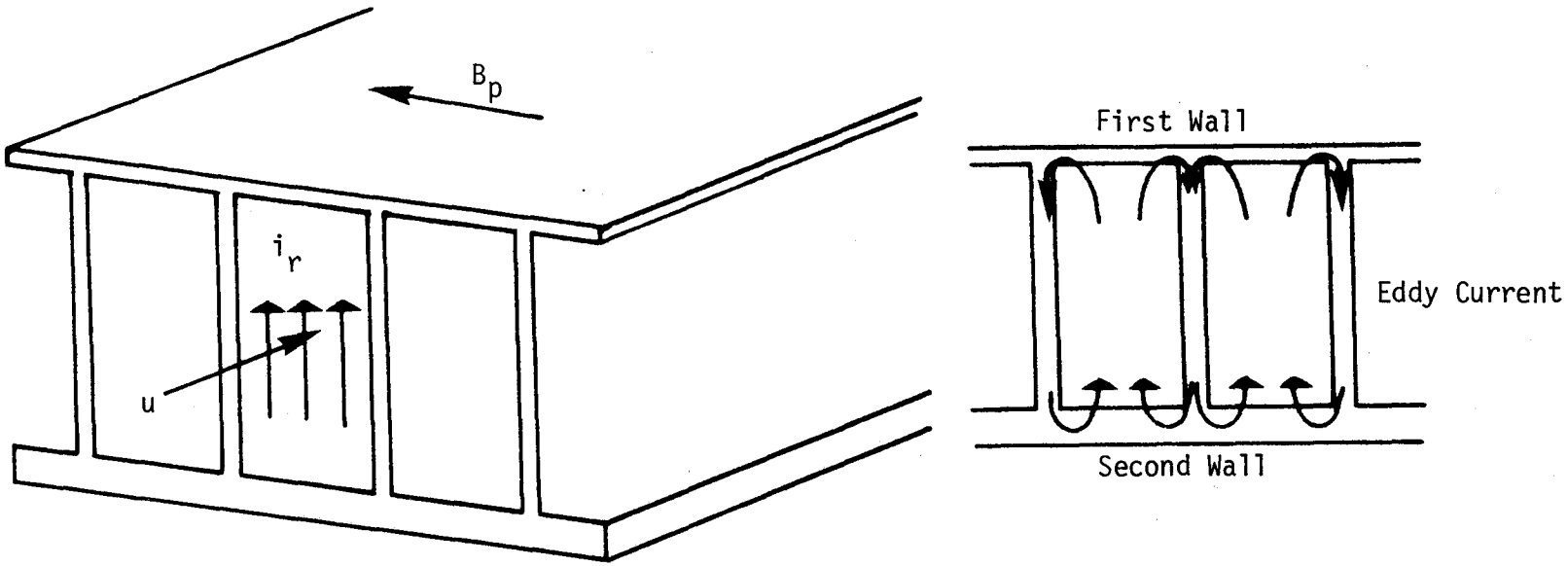

Figure 6.2.1-21 Eddy current in radial direction.

ponent of the velocity and B_p is the poloidal field intensity. ϕ_w is the conductivity ratio, given by:

$$\phi_w = \frac{\sigma_w t_w}{2\sigma_f a} \qquad (6.2.1\text{-}40)$$

where σ_w is the conductivity of the rib, t_w is the thickness of the rib and a is the half width of the channel.

Accounting for the nonuniform velocity profile, eddy currents will flow not only in the radial direction, but also in the poloidal direction as is shown in Fig. 6.2.1-22. The poloidal current intensity induced by the poloidal field is denoted as follows:

$$i_p' \text{ at rib surface} = \sigma_f B_p \frac{du}{dz} a \frac{\phi_w}{1+\phi_w} \qquad (6.2.1\text{-}41)$$

If the half width of the channel a is far narrower than the half width in the radial direction, i_p' is small and we can neglect the effect of the poloidal current induced by the poloidal field. In the following, we assume that a is infinitesimal in order to use a two dimensional model. Then the toroidal component of the electromagnetic force is given by:

$$- i_r B_p = - \sigma_f B_p^2 u \frac{\phi_w}{1 + \phi_w} \qquad (6.2.1\text{-}42)$$

In addition to the intra-channel current paths described above, there are two possible global current paths which intersect several channels. The poloidal electromotive force which drives these global currents comes from the interaction of the toroidal magnetic field and the radial component of the velocity. The coolant flows toward the first wall at the inlet of the toroidal channel, and flows away from the first wall at the outlet of the toroidal channel. Therefore, the radial component of the velocity is in opposite directions at each end of the channel, which means the electromotive force acts in opposite directions. As depicted in Fig. 6.2.1-23, the current induced at the inlet of the toroidal channel can flow back in the neighborhood of the outlet.

Because the toroidal channel is in contact with the polodial header where the coolant velocity is very low, eddy currents can flow back through the

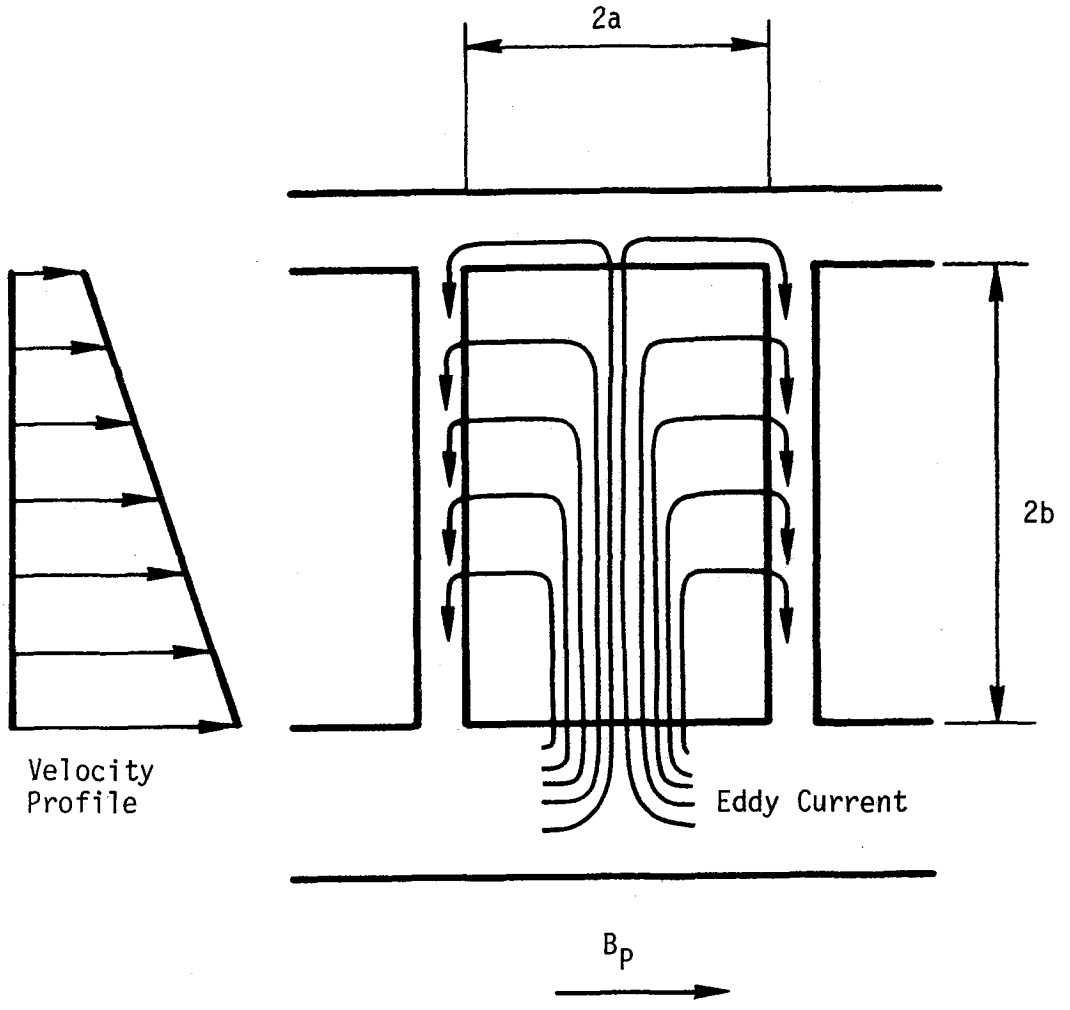

Figure 6.2.1-22 Eddy current with non-uniform velocity profile.

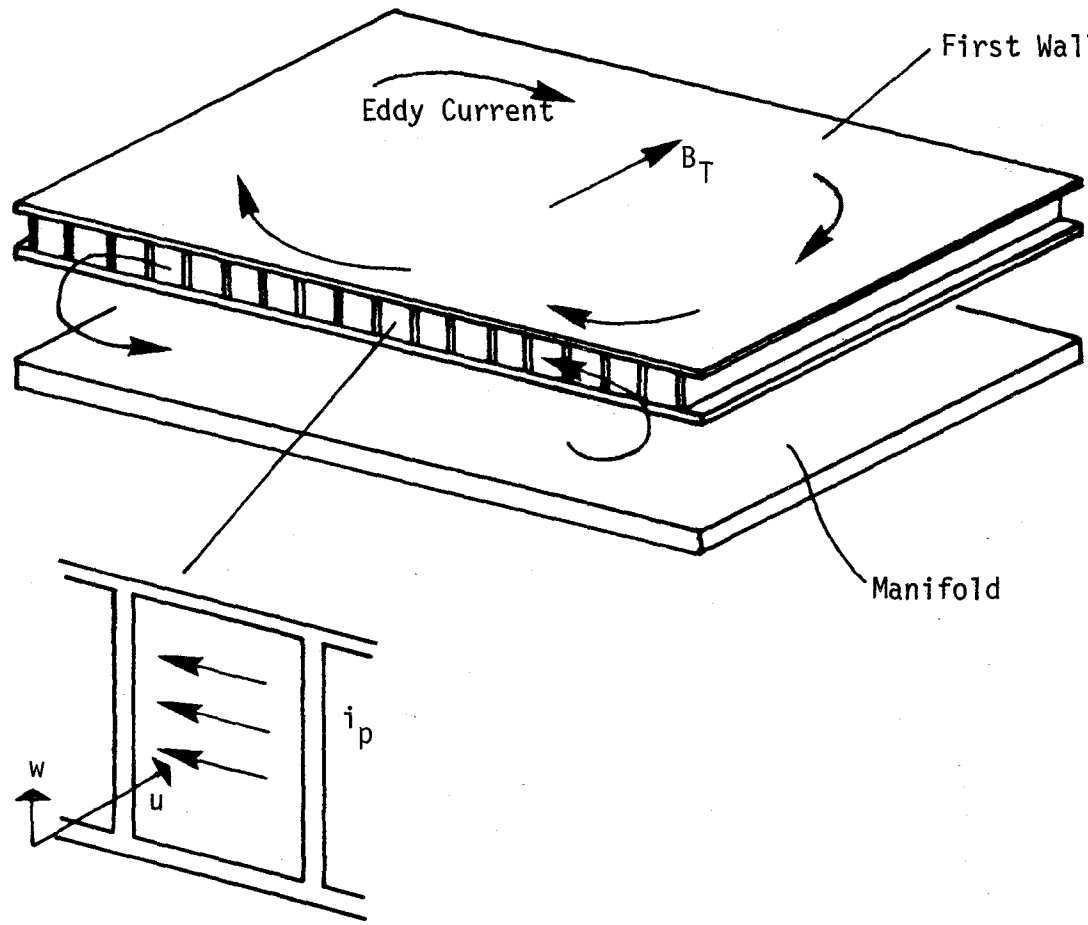

Figure 6.2.1-23 Eddy current in poloidal direction.

coolant in the header. These current paths are also shown in Fig. 6.2.1-23. As the electrical conductivity of both these return paths is high, the poloidal current density is given approximately as follows:

$$i_p = \sigma_f B_T w \tag{6.2.1-43}$$

where w is the radial component of the velocity and B_T is the toroidal field intensity. The radial component of the electromagnetic force is given by

$$- i_p B_T = - \sigma_f B_T^2 w \tag{6.2.1-44}$$

The Hartmann number is defined as follows:

$$Ha = Ba\sqrt{\sigma_f / \mu} \tag{6.2.1-45}$$

where B is the transverse field intensity and a is the channel half width parallel to B. In the toroidal channel of the reference blanket, the transverse field intensity, B_P, is 0.5T and the channel half width is 12.5 mm. The poloidal (or transverse) Hartmann number is calculated to be larger than 500. The square of the Hartmann number denotes the ratio of the electromagnetic force to the viscous force. It is very large, which means that even in the toroidal channel, the electromagnetic force is dominant and viscosity can be neglected. The basic equations (37) and (38) can be rewritten as follows:

$$\frac{\partial u}{\partial x} + \frac{\partial w}{\partial z} = 0 \tag{6.2.1-46}$$

$$u\frac{\partial u}{\partial x} + w\frac{\partial u}{\partial z} = - \frac{1}{\rho}\frac{\partial p}{\partial x} - \frac{C_x u}{\rho} \tag{6.2.1-47}$$

$$u\frac{\partial w}{\partial x} + w\frac{\partial w}{\partial z} = - \frac{1}{\rho}\frac{\partial p}{\partial z} - \frac{C_z w}{\rho} \tag{6.2.1-48}$$

where

$$C_x = \sigma_f B_P^2 \frac{\phi_w}{1+\phi_w} \tag{6.2.1-49}$$

$$C_z = \sigma_f B_T^2 \tag{6.2.1-50}$$

Calculational Models

Figures 6.2.1-24 and 25 show two different calculational models which are used to describe how the velocity profile develops. In Fig. 6.2.1-24, the coolant flows into the channel through an orifice at one end and out through the outlet at the other end of the channel. The direction of the inlet flow is parallel to the channel. The constricted flow at the inlet expands in the channel. In Figure 6.2.1-25, the coolant flows into the channel through a lateral opening at one end. The flow changes direction near the entrance.

Equations (10)-(12) are solved numerically using a finite difference method. The length of the channel is chosen so that the velocity near the first wall surface reaches more than 90% of the average velocity. The channel is divided into square meshes. The channel height d is divided into ten meshes except in a few cases.

Calculational Results

In both cases, the velocity profile at the point far away from the inlet is uniform due to the resistive force which is proportional to the velocity parallel to the channel. The rate of flow development is affected by the resistive force perpendicular to the channel. The flow must have a velocity component perpendicular to the channel when it is developing. The strong resistive force perpendicular to the channel delays the development.

Figure 6.2.1-26 shows how the flow develops in the case with the flow entering parallel to the channel. The entry length depends on the ratio of the lateral resistive force coefficient, C_z, to the axial coefficient C_x, and the constriction ratio at the inlet d_i/d. The resistive force is sufficiently strong for inertia to be neglected, hence the entry length does not depend on the individual values of the coefficients, but depends on their ratio. Figure 6.2.1-27 shows the effect of C_z/C_x on the velocity development near the wall on the opposite side of the inlet orifice in the case of $d_i/d=0.2$. The lengths which are necessary for the velocity near the wall to reach certain values are shown in Fig. 6.2.1-28. The entry length is proportional to the square root of the ratio C_z/C_x in the case with parallel inlet flow. Figure 6.2.1-29 shows the effect of d_i/d. The entry length is also proportional to d_i/d.

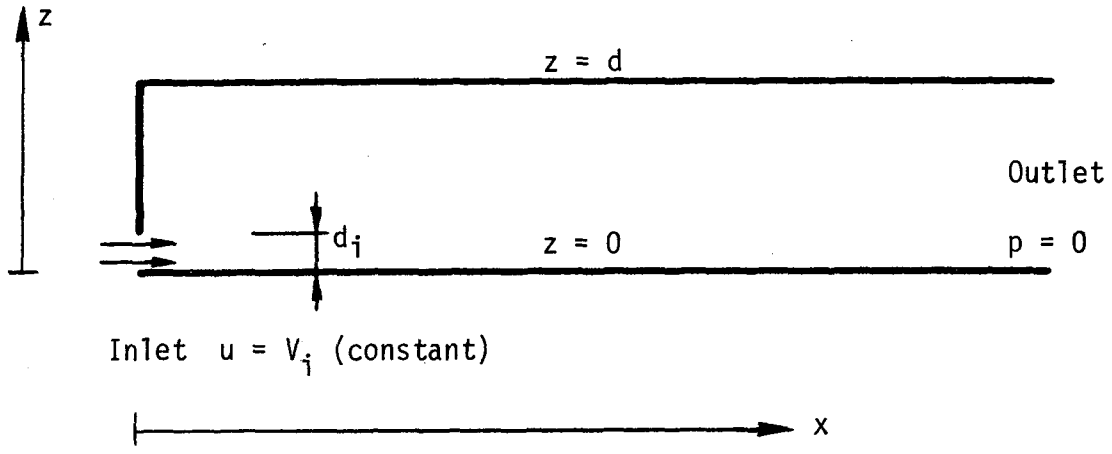

Figure 6.2.1-24 Straight channel with inlet orifice.

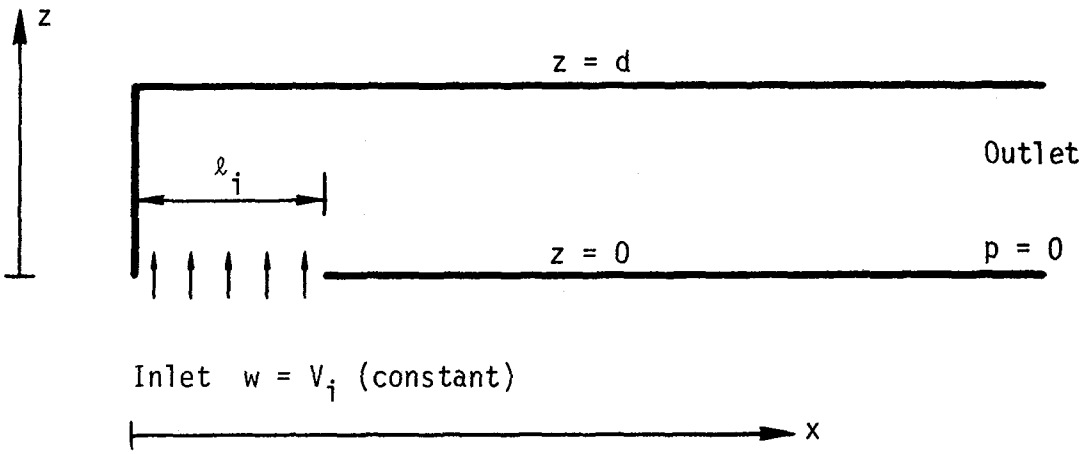

Figure 6.2.1-25 Straight channel with inlet bend.

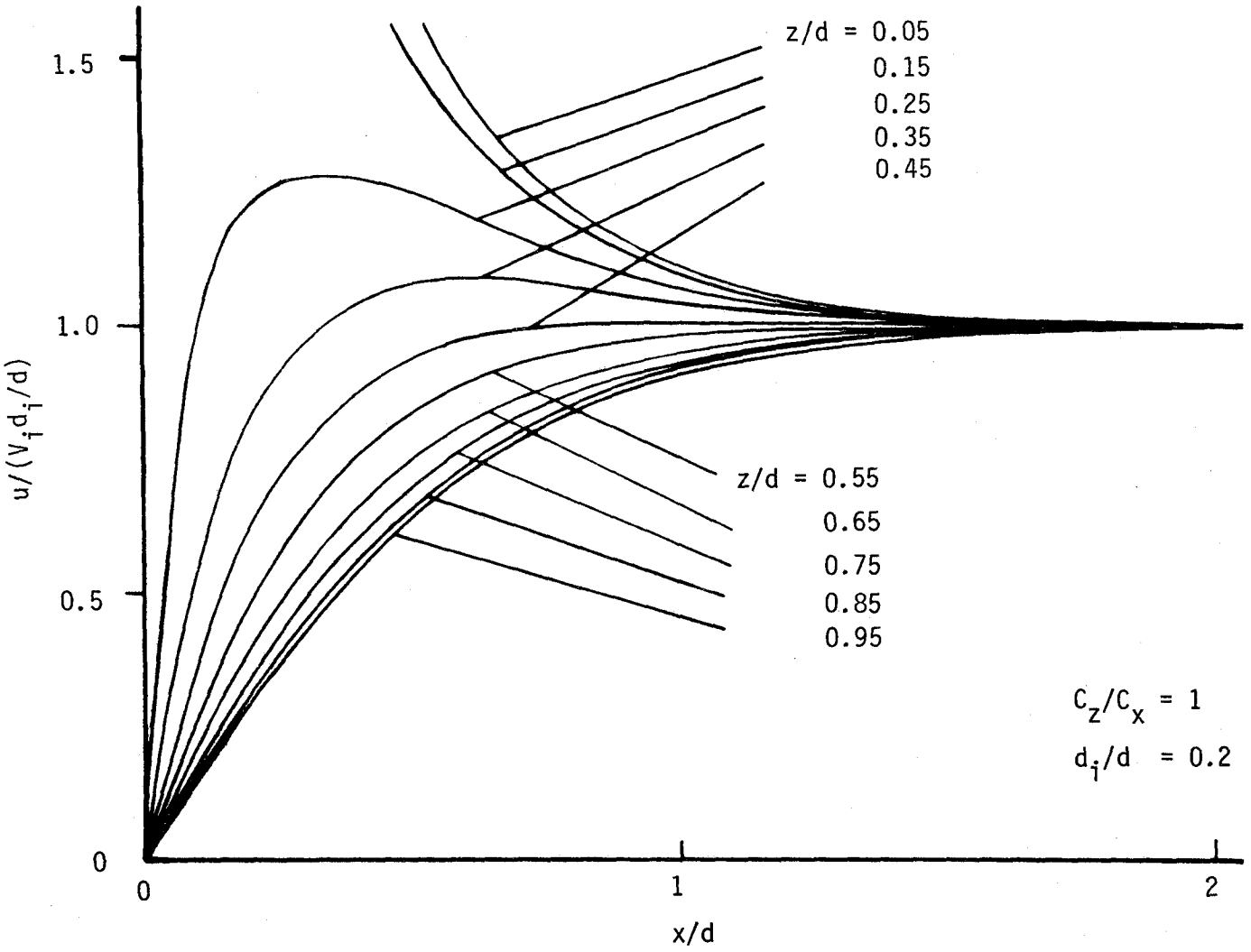

Figure 6.2.1-26 Flow development in channel with inlet orifice.

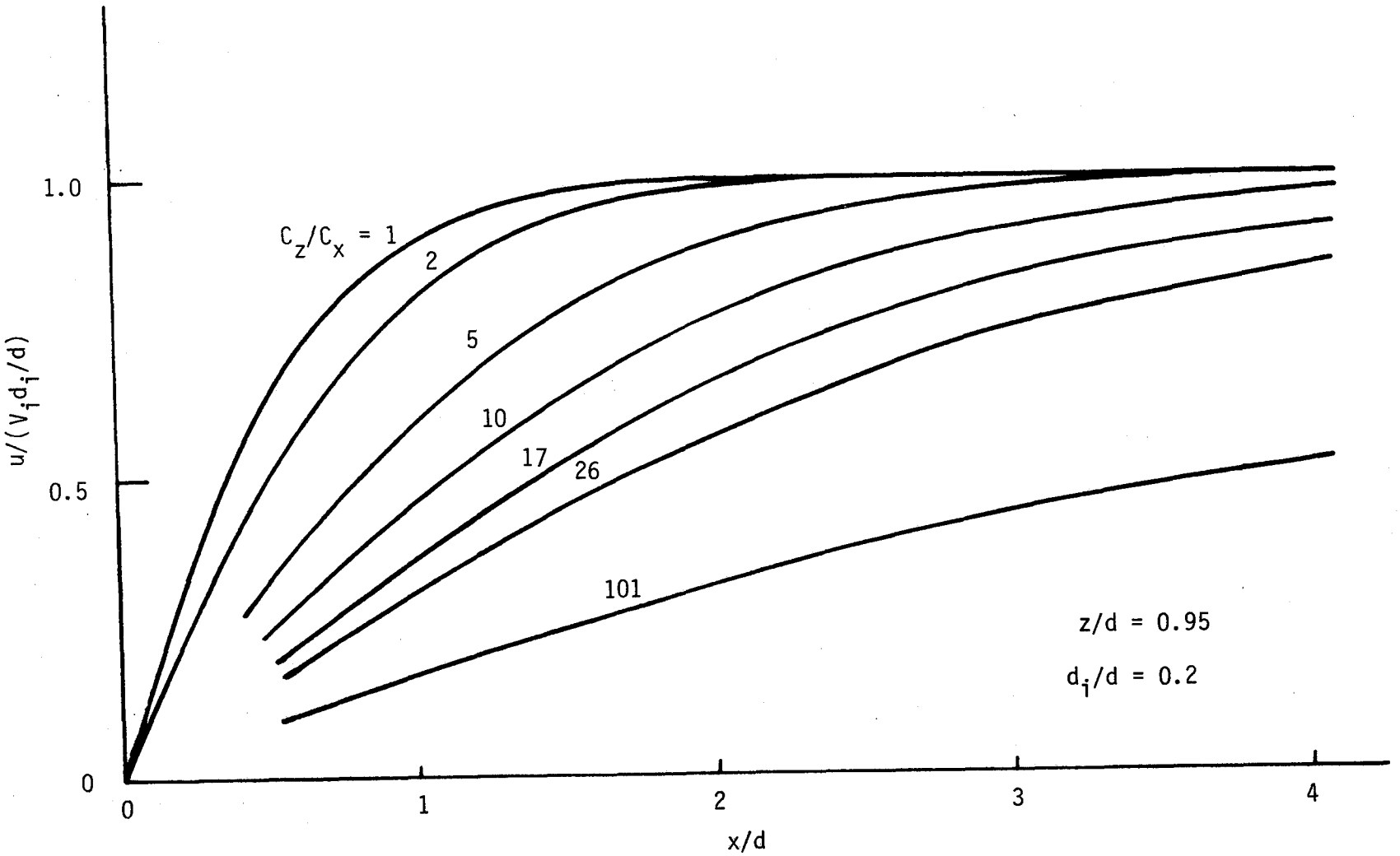

Figure 6.2.1-27 Effect of C_z/C_x on flow development.

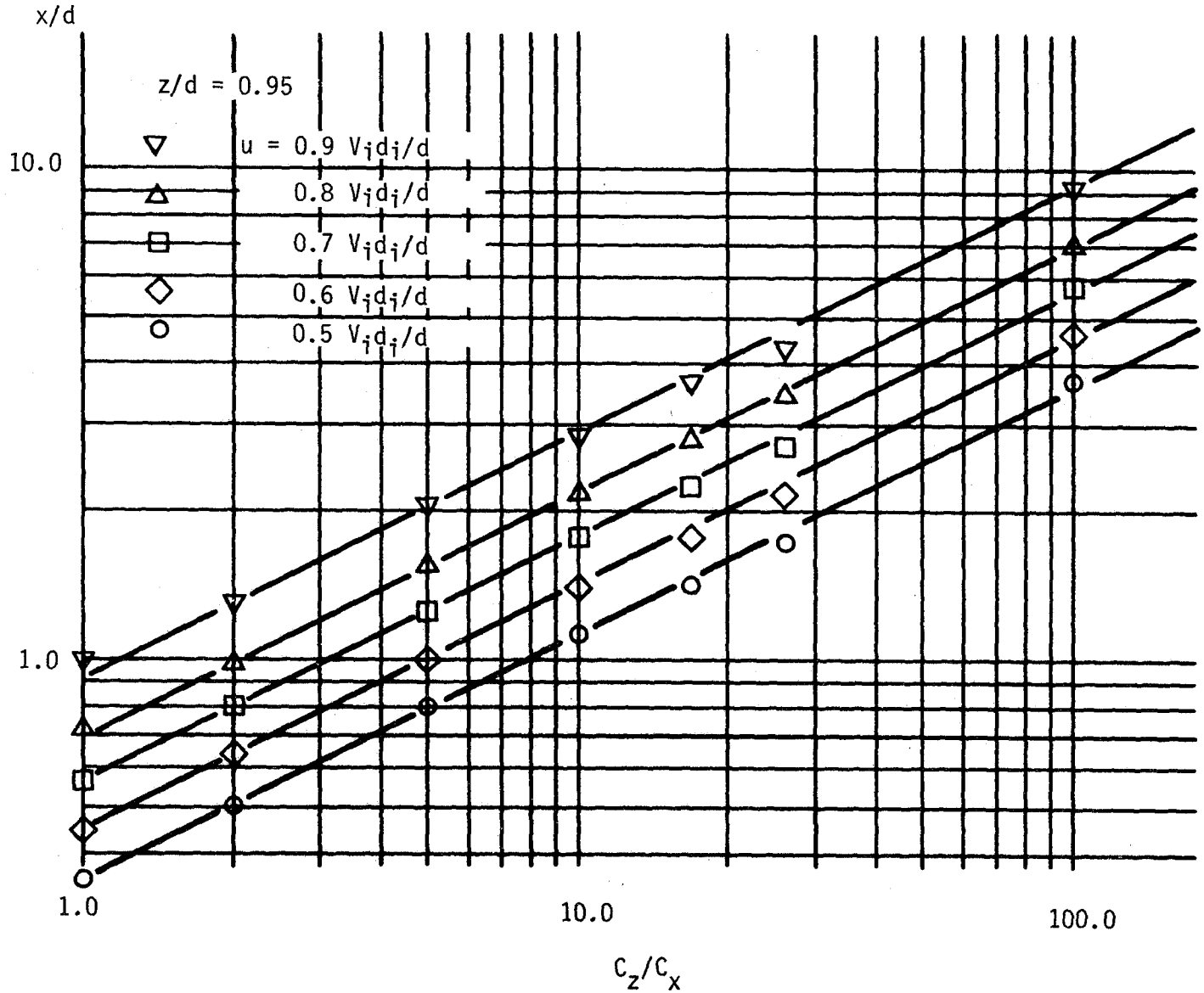

Figure 6.2.1-28 Effect of C_z/C_x on entry length.

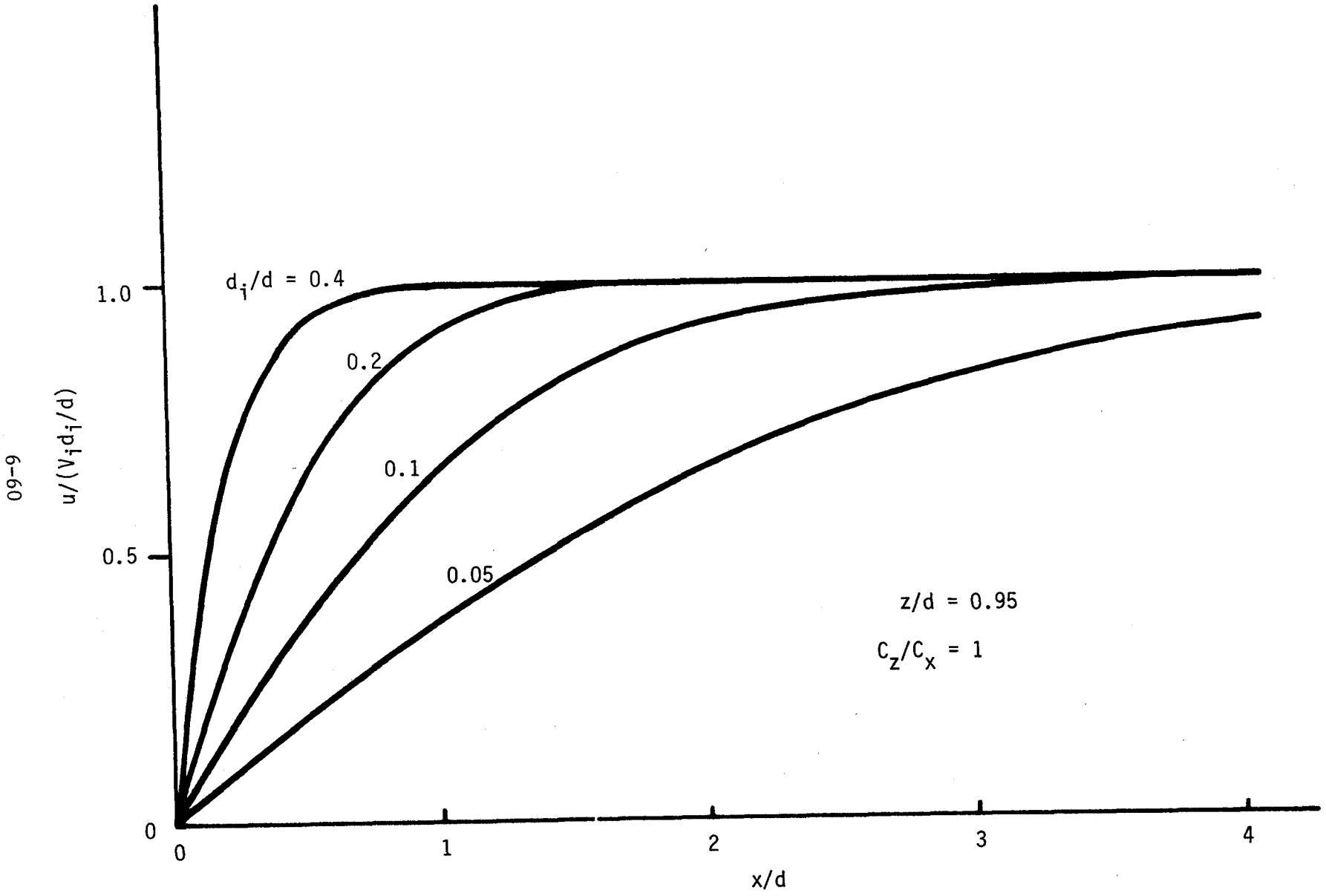

Figure 6.2.1-29 Effect of d_i/d on flow development.

Figure 6.2.1-30 shows how the flow develops in the channel with a lateral inlet, shown in Fig. 6.2.1-25. The entry length can also be expressed as a function of C_z/C_x and ℓ_i/d in this case. Figure 6.2.1-31 shows the effect of C_z/C_x on the velocity development near the wall on the opposite side of the inlet. The entry length is shown in Fig. 6.2.1-32. It is not proportional to the square root of the ratio C_z/C_x in this case, but is proportional to $(C_z/C_x)^{0.4}$ when C_z/C_x is between 5 and 100. In the case of $C_z/C_x<5$, the flow develops in the neighborhood of the entrance. In the region of $x<\ell_i$, there is an inlet opening on one side of the channel, hence the velocity on the other side is strongly affected by the inlet condition. The velocity on the other side increases not only because of the flow development, but also because of the increase in the flow quantity in the channel in this region. When C_z/C_x is larger than 5, the flow continues to develop downstream of the inlet region. The velocity near the wall increases because of the development. If the velocity profile at $x=\ell_i$ were not affected by C_z/C_x, the entry length might be proportional to $\sqrt{C_z/C_x}$ as it is in the case with the parallel inlet flow. Since the velocity profile at $x=\ell_i$ is affected by C_z/C_x, the entry length is proportional to $(C_z/C_x)^{0.4}$. Figure 6.2.1-33 shows the effect of ℓ_i/d if the flow continues to develop downstream of the inlet region. Figure 6.2.1-34 shows an example of the velocity profile in the channel. When x/ℓ_i is large, the velocity profile has a peak near the second wall which has the inlet opening.

Discussion

In the results using the model in Fig. 6.2.1-25, the velocity near the first wall does not increase continuously, but increases with fluctuations in the neighborhood of $x=\ell_i$. The convergence of the numerical solution was not good near this point. The fluctuations depended on the mesh size used in the calculation. However, the downstream velocity profile converges well and did not depend on the mesh size. Hence the fluctuations are thought to be ignorable in this study. They may, however, have some effect on the result. The channel length may also affect the result. Further study is needed on this problem.

We should stress the limitation of the applicability of the result. The result was derived on the assumption that the poloidal current induced by the

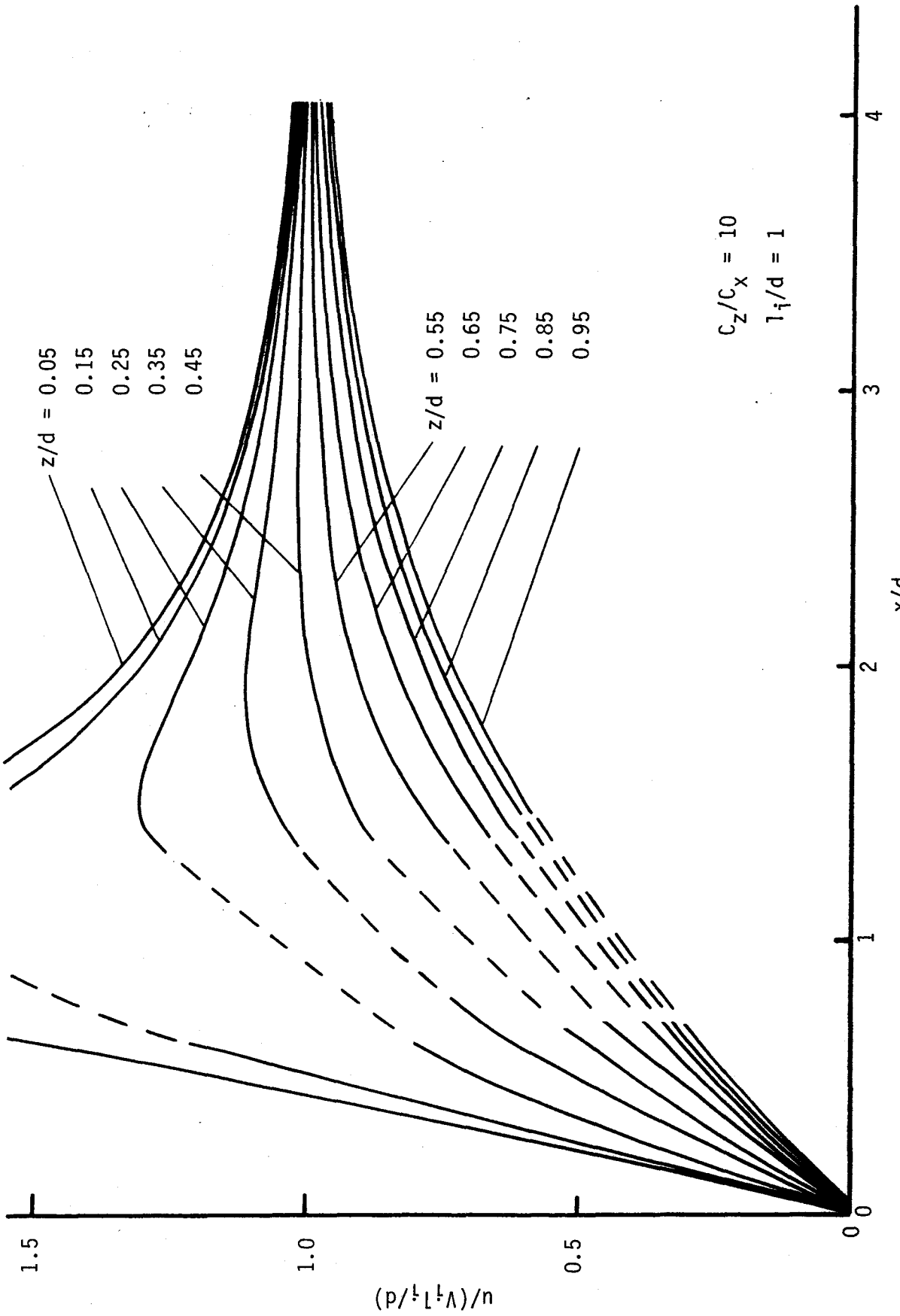

Figure 6.2.1-30 Flow development in channel with inlet bend.

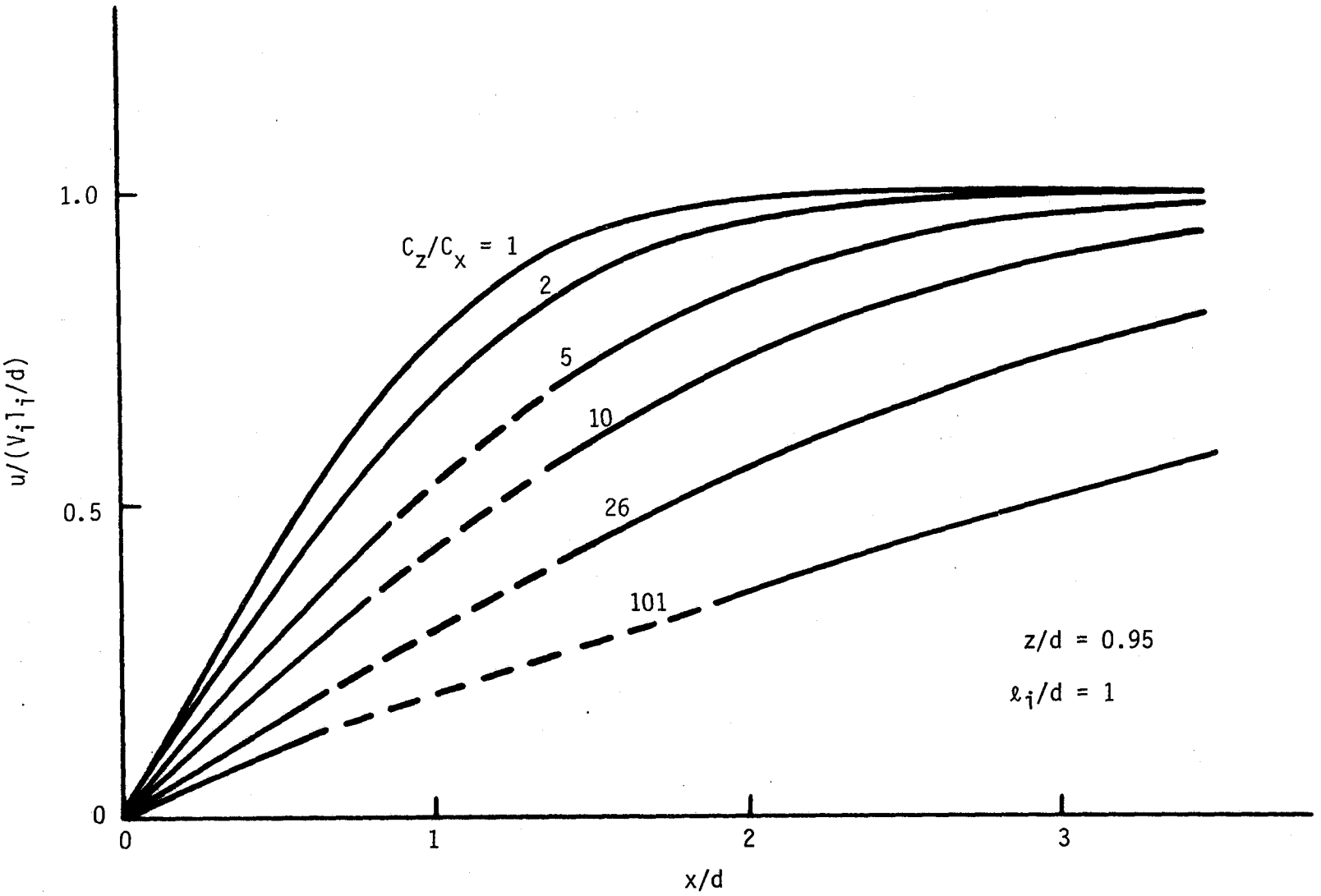

Figure 6.2.1-31 Effect of C_z/C_x on flow development.

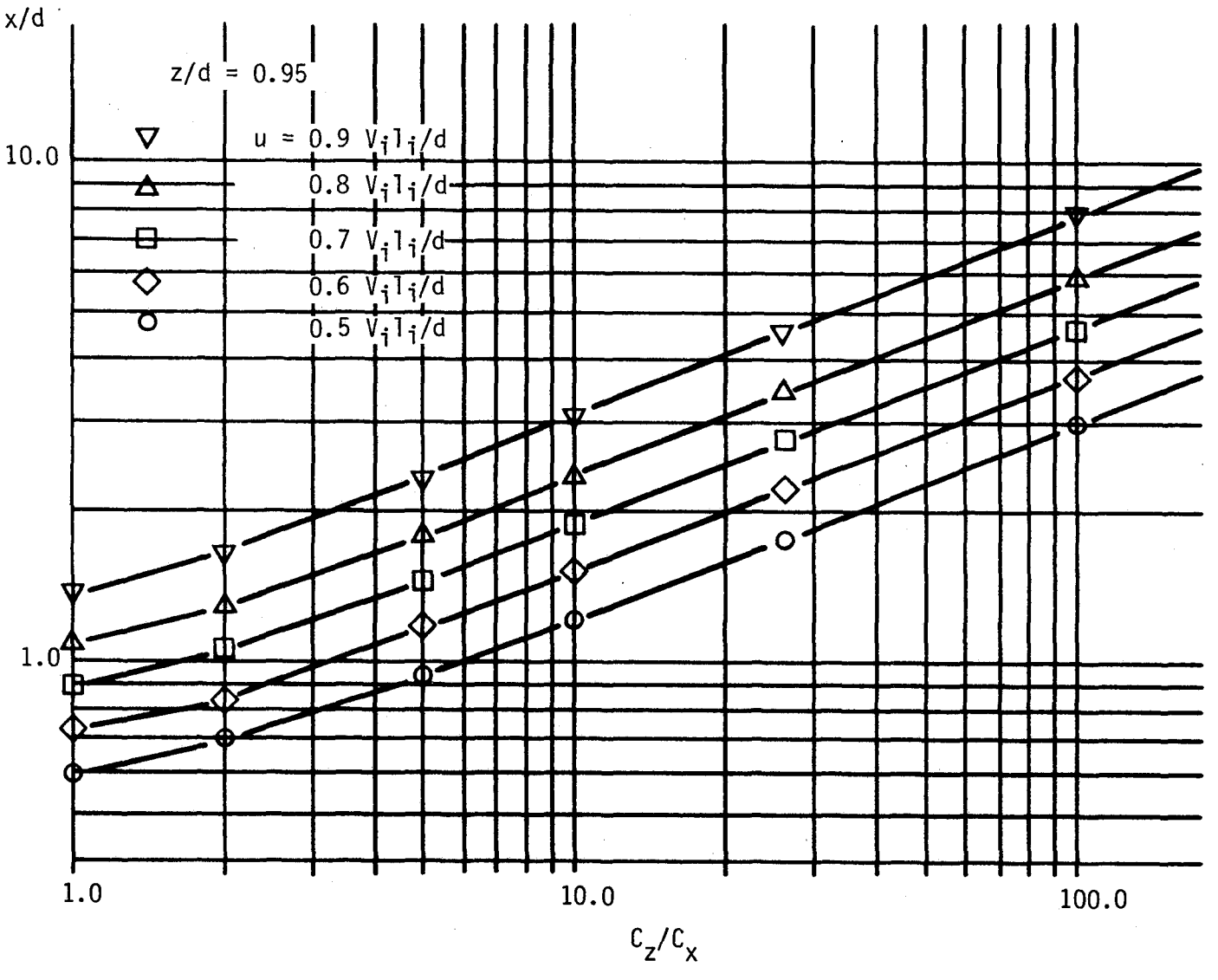

Figure 6.2.1-32 Effect of C_z/C_x on entry length.

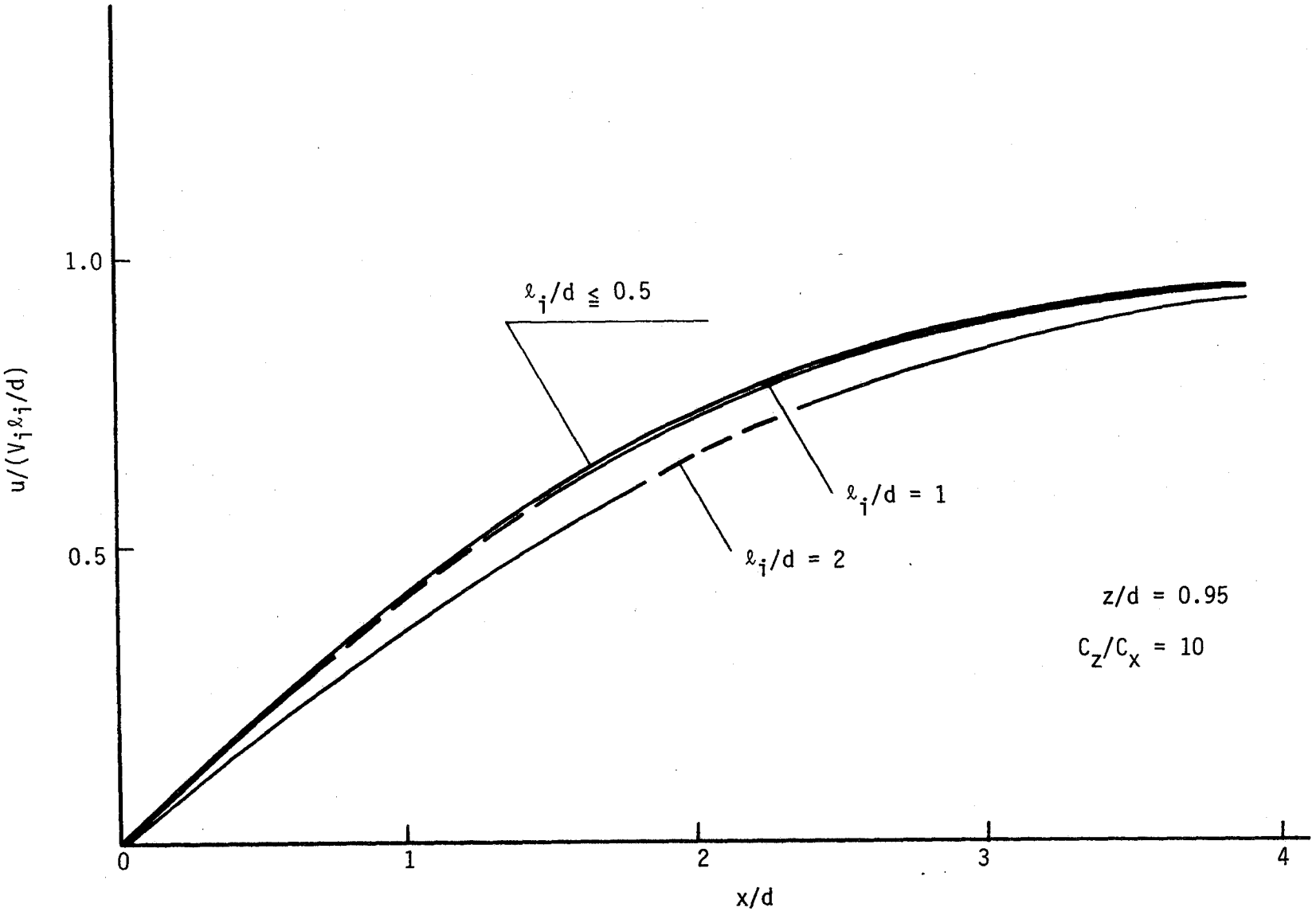

Figure 6.2.1-33 Effect of ℓ_i/d on flow development.

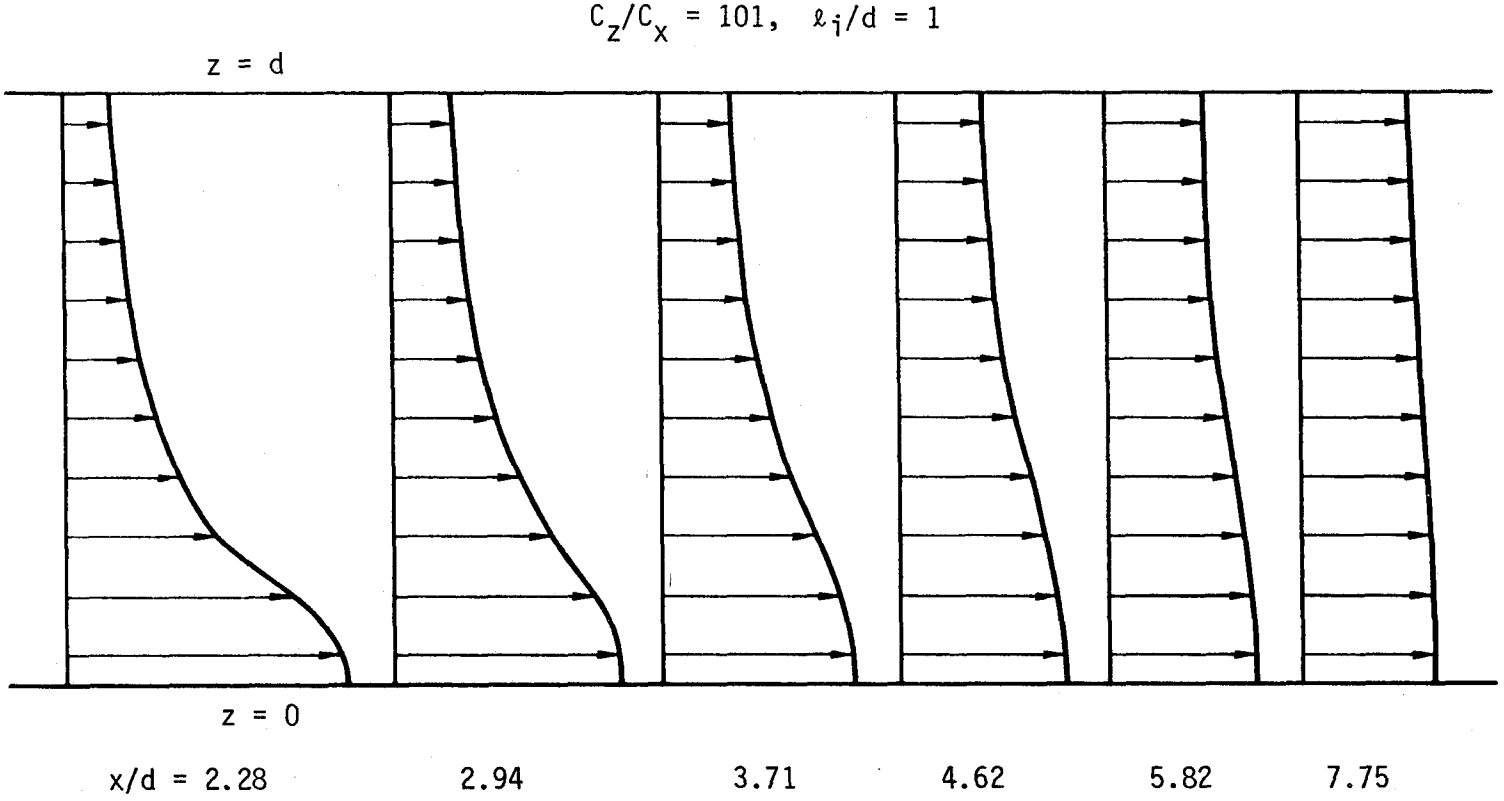

Figure 6.2.1-34 Velocity profile.

poloidal field and the gradient of the toroidal velocity component do not affect the flow development. If the channal has a finite width in the poloidal direction, we cannot neglect the effect. Let us examine the ratio of the poloidal current induced by the poloidal field i_p' to the poloidal current induced by the toroidal field i_p. The former can be denoted by eq. (41) and the latter by eq. (43) thus:

$$\frac{i_p'}{i_p} \sim \frac{B_P}{B_T} \frac{\phi_w}{1+\phi_w} \frac{du}{dz} \frac{a}{w} \qquad (6.2.1\text{-}51)$$

The velocity gradient du/dz is represented by u_b/d, where u_b is the average velocity. The radial velocity component w is represented by $u_b d/\ell_e$, where ℓ_e is the entry length and can be represented by $d\sqrt{C_z/C_x}$. Thus:

$$\frac{i_P'}{i_P} \sim \frac{B_P}{B_T} \frac{\phi_w}{1+\phi_w} \frac{\ell_e a}{d^2} \sim \frac{a}{d} \sqrt{\phi_w/(1+\phi_w)} \qquad (6.2.1\text{-}52)$$

Hence, if the above value is far smaller than unity, the result seems to be applicable. But the fully developed flow in a channel with a finite width has wall jets near the channel wall parallel to the magnetic field as was discussed in Sec. 6.2.1.2. Since we neglect the poloidal current induced by the polodial field, the fully developed flow is uniform and there is no wall jet in the result. The calculational model does not represent the flow in a channel with a finite width. In Fig. 6.2.1-24, we assumed that there is a free shear layer at x=0 and $z=d_1$. In the free shear layer, the velocity gradient is high and we can neglect neither the poloidal current induced by the poloidal field nor the viscosity. The viscosity may also affect the result. The current may flow not only in the plane perpendicular to the toroidal direction but also in the toroidal direction. The phenomenon is essentially three dimensional.

The analysis made here is preliminary; the results must be interpreted carefully.

Evaluation of the Entry Length in the Reference Blanket

The design values of the reference liquid metal blanket are as follows:

toroidal magnetic field intensity	B_T	7.5 T
poloidal magnetic field intensity	B_P	0.5 T
channel half width	a	12.5 mm
rib thickness	t_w	3 mm
channel length	L	3.0 m
channel depth	d	45 mm
entry length for $u/u_\infty = 0.05$		0.58 m
entry length for $u/u_\infty = 0.9$		1.52 m

The conductivity ratio ϕ_w is calculated to be 0.06. The ratio of the resistive force coefficients C_z/C_x is calculated to be 4×10^3. As the flow development in the case of $C_z/C_x=4\times10^3$ was not calculated, it is extrapolated using the results of lower C_z/C_x. Assuming that the entry length is proportional to $(C_z/C_x)^{0.4}$ when $10^2 \leq C_z/C_x \leq 4\times10^3$ the length which is necessary for the velocity on the first wall cooling surface to reach 50% of the full velocity is calculated to be 12.9d=0.58m. At 33.8 channel widths, or 1.52m downstream of the inlet, the velocity reaches 90% of the full value. The toroidal channel is 3m long. The above lengths cannot be neglected compared with the channel length.

The channels in the reference design have a finite half width of 12.5 mm. Equation (52) gives the value of the error current i_p'/i_p of 0.066, which is small compared with unity. In the fully developed flow, wall jets exist near the first and second wall. The flow quantities in jets are calculated to be 2.5% and 0.8% of the total flow quantity. This is small enough such that the calculational results should be applicable to the reference design. However, the peak velocity of the wall jet may be high because the boundary layer may be thin. The phenomenon is essentially three dimensional. Therefore there still remain large uncertainties on the applicability of the result.

The velocity profile in the toroidal channel is affected greatly by the inlet condition as is shown in Fig. 6.2.1-29. The entry length decreases with decreasing nonuniformity of the inlet velocity profile. The insulating partitions between the channels in the inlet bend reduces the MHD resistive force in the z direction greatly as was discussed in Section 6.2.1.2. In this case, the flow may be confined to a thin boundary layer near the insulating wall

between channels. This effect may cause another nonuniformity at the inlet. We cannot conclude that the nonuniformity in an insulated channel is less than that in a non-insulated channel until the phenomenon is calculated by a three-dimensional eddy current/flow development code. Further consideration is the subject for a future study.

Conclusions

Flow development under angled magnetic field was discussed. It was assumed that the radial component of the electromagnetic force is given by $-\sigma_f B_T^2 w$ while the toroidal component is $-\sigma_f B_P^2 u\phi_w/(1+\phi_w)$. The entry length was shown to be proportional to the square root of the resistive force coefficient ratio, $(B_T/B_P)\sqrt{(1+\phi_w)/\phi_w}$, if the inlet flow nonuniformity is not affected by the ratio. In the case with a 90° bend at the inlet, the entry length is proportional to the 0.4th power of the ratio. The ratio is very large in the reference liquid metal blanket, hence the entry length is very long. The coolant flows mainly in the neighborhood of the second wall for a considerable length of the channel.

The applicability of the above assumption was discussed. There still remain large uncertainties, hence further studies are needed on this problem.

6.2.2 Liquid Metal Thermal Hydraulics

6.2.2.1 Introduction

Thermal hydraulics considerations touch upon almost every aspect of blanket design, operation, safety, lifetime, etc. Temperatures in the blanket affect many phenomena, including (but not limited to) tritium inventory and permeation, corrosion, first wall stresses and blanket heat recovery. For the analysis in this section, the Li/Li/V reference blanket from the BCSS was chosen.[1] This is a self-cooled liquid metal blanket. Figure 6.2.2-1 shows the schematic of a sector of this blanket.

In spite of its simple geometry and appearance, this blanket has the most unusual temperature conditions of all BCSS reference blankets. Each toroidal flow channel, for example, is surrounded by two other toroidal channels at its sides and several poloidal channels on its back, all of them at different temperatures. Another peculiar thermal characteristic of this blanket can be observed in the poloidal channels. Moving along the toroidal direction, half of the poloidal channels are colder than the other half by 50-100°C (those containing coolant before and after passing through the toroidal channels, respectively).

Another special feature of this blanket is that it has both toroidal and poloidal coolant channels. As a result, at the bends, where poloidal channels connect to toroidal channels, the liquid metal must pass through the bend and cross lines of magnetic field. This yields unique behavior in pressure drop and velocity profiles which are dealt with in detail in Section 6.2.1.

Liquid Metal Generic Thermal Behavior

Blankets with liquid metals as coolants inherently possess their own generic thermal characteristics, some of which are described below.

1. The entire length of the toroidal channels is in the thermal entrance region. This will result in more efficient heat transfer at the first wall which in turn leads to lower first wall temperatures than those predicted for fully developed thermal conditions. This also yields larger temperature gradients over longer portions of the first wall and a spatially varying heat transfer coefficient.

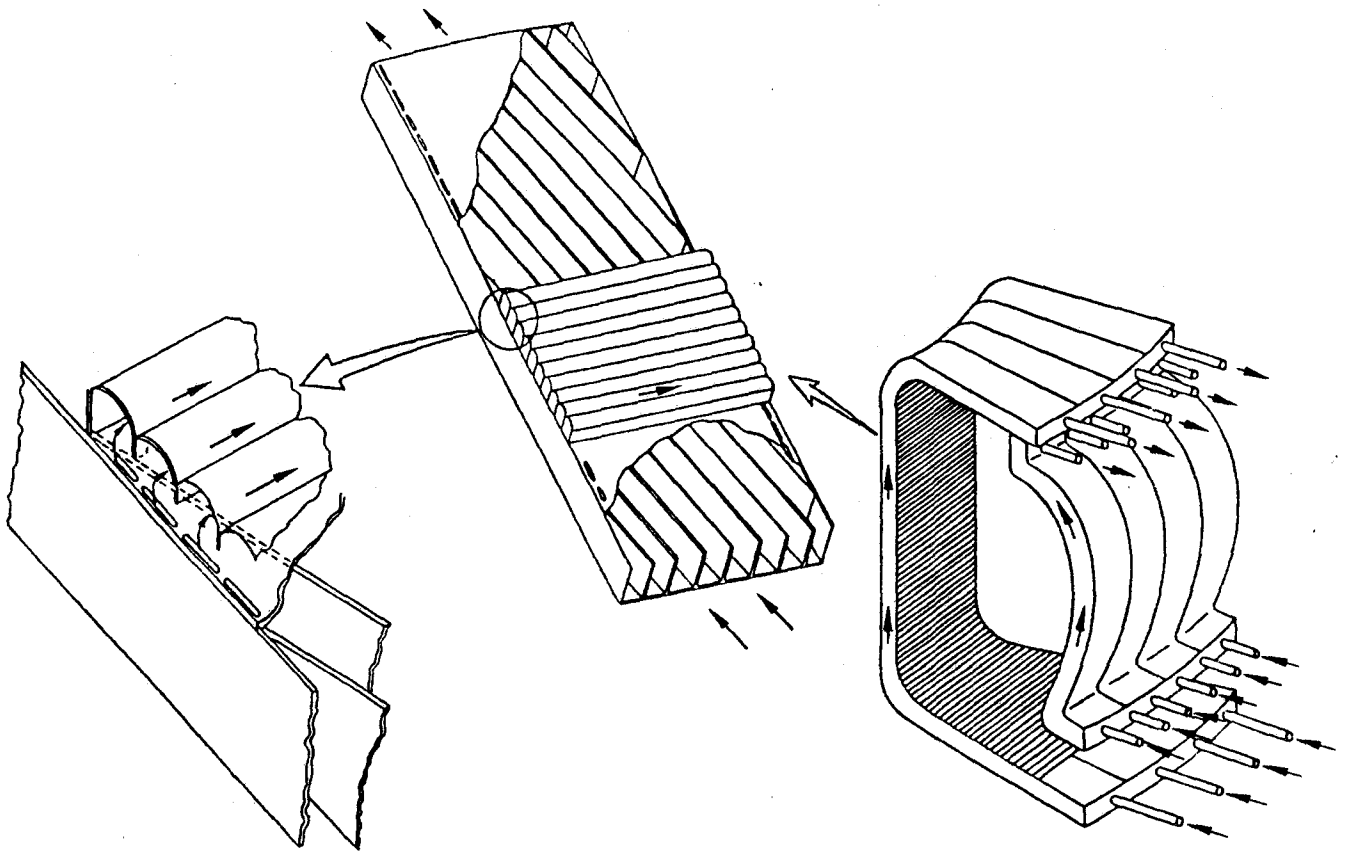

Figure 6.2.2-1 Schematic of poloidal/toroidal blanket (BCSS).

2. Flow of liquid metals under magnetic fields are often laminar, as turbulence is suppressed by the magnetic field. This distinguishes liquid metal thermal hydraulics from that in other systems where turbulent flows are unavoidable. Although laminar, one has to be careful not to assume a conventional laminar velocity profile.

3. It is believed that unusual velocity profiles may exist in liquid metal flows under magnetic field, especially in regions where the flow has to bend, cross the magnetic field lines or go through channels with varying flow areas. These unusual profiles could result in first wall temperatures much higher than expected, which in turn can cause poor blanket operation. Any uncertainty in velocity profiles could also reduce the usefulness of the experiments performed on "act-alike" test modules.

4. A substantial amount of heat is generated volumetrically in the liquid metal coolants. The obvious effect is that the coolant bulk temperature will be affected. The rather hidden effect of volumetric heat generation is in its altering the temperature profile and in turn the heat transfer coefficient. It is believed that the presence of heat generation generally reduces the heat transfer coefficient and results in higher structural temperatures.

It is essential for the proper understanding of liquid metal blankets that detailed thermal hydraulics studies be carried out.

In this section, we first study the effects of velocity profile and volumetric heat generation on the first wall heat transfer. Then, the thermal entrance region will be analyzed. Streamwise conduction and its effect on coolant temperatures is investigated next. Thereafter, residual turbulence in coolants under magnetic field is considered. Finally, the effect of a pulsed heat source on thermal behavior of liquid metal blankets is studied.

6.2.2.2 Velocity Profile and Volumetric Heat Generation

As mentioned in the previous section, the velocity profile and the volumetric heat generation are very important to the considerations of the

overall thermal hydraulics of liquid metal blankets. The fact that their effects are not additive and behave in a nonlinear manner makes these two parameters even more important. The following is a list of assumptions made which also indicates the phenomena that were not considered in this analysis.

1. The velocity profile is assumed to be fully developed. However, the effect due to development of velocity profile is not negligible. This assumption was made to simplify the analysis.

2. Analysis is performed for a 2-D flow, that is, flow between two infinite parallel plates.

3. Thermal boundary conditions are simplified to those of constant but different heat flux at each surface.

4. Axial (streamwise) conduction is ignored. The effect of axial conduction is investigated later in this section.

5. The blanket is operating under steady-state conditions.

6. Flow is perfectly laminar. The effects of residual turbulence is studied later in this section.

7. Fluid properties are assumed not to vary with temperature.

Analysis

Figure 6.2.2-2 shows the model used to analyze the first wall coolant channel. The surface heat flux at y = a, the plasma side, is a sum of the first wall heat flux and the heat generated in the first wall. The heat flux at the second wall, q_w^-, accounts for the heat generated in the second wall. The following assumptions are made.

1. The coolant flow is laminar. This assumption is reasonable for flow of liquid metals under magnetic flow.

2. The velocity profile is fully developed.

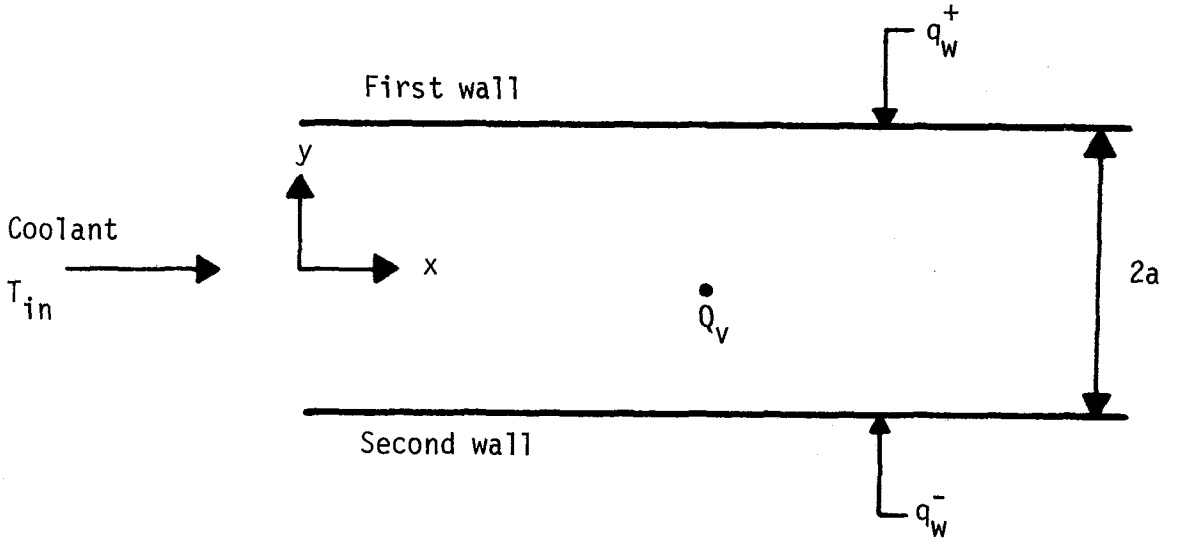

Figure 6.2.2-2 First wall channel hydraulics model.

3. The temperature profile is fully developed, that is

$$\frac{\partial T}{\partial y} \neq \text{fn}(x) \quad \text{and} \quad \frac{\partial T}{\partial x} \neq \text{fn}(y). \tag{6.2.2-1}$$

The thermal entry length problem is treated separately in Section 6.2.2.3.

The energy equation for the flow described above may be written as

$$\rho c_p u \frac{\partial T}{\partial x} = k \frac{\partial^2 T}{\partial y^2} + \dot{Q}_v \tag{6.2.2-2}$$

with boundary conditions as

$$k \left.\frac{\partial T}{\partial y}\right|_{y=a} = q_w^+ \tag{6.2.2-3}$$

and

$$k \left.\frac{\partial T}{\partial y}\right|_{y=-a} = q_w^- \tag{6.2.2-4}$$

A set of nondimensional parameters are defined as

$$\eta = y/a \tag{6.2.2-5}$$

$$f = u/u_b, \qquad \text{where} \qquad \int_{-1}^{1} d\eta f = 2 \tag{6.2.2-6}$$

$$\zeta = \alpha x/u_b a^2 \tag{6.2.2-7}$$

$$\lambda = \dot{Q}_v a^2/k \tag{6.2.2-8}$$

$$\gamma^{\pm} = q_w^{\pm} a/2k \tag{6.2.2-9}$$

Governing Eq. (6.2.2-2) with boundary conditions (3) and (4) are now written in terms of new dimensionless parameters as

$$f(\eta) \frac{\partial T}{\partial \zeta} = \frac{\partial^2 T}{\partial \eta^2} + \lambda \tag{6.2.2-10}$$

$$\left.\frac{\partial T}{\partial \eta}\right|_{\eta=\pm 1} = \pm 2\gamma^{\pm} \qquad (6.2.2\text{-}11)$$

Overall Energy Balance

An overall energy balance relates the rise in bulk temperatures to the total energy input in the coolant flow as

$$\frac{\partial T_b}{\partial x} = \frac{q_w^+ + q_w^- + 2\dot{Q}_v a}{\rho c_p u_b 2a} \qquad (6.2.2\text{-}12)$$

where

$$T_b = \frac{1}{2}\int_{-1}^{1} d\eta f T \qquad (6.2.2\text{-}13)$$

In terms of dimensionless variables and using the condition of fully developed temperature profile, Eq. (6.2.2-12) reduces to:

$$\frac{\partial T_b}{\partial \zeta} = \frac{\partial T}{\partial \zeta} = \gamma^+ + \gamma^- + \lambda \qquad (6.2.2\text{-}14)$$

Nusselt Number Definition

Two Nusselt numbers are defined based on the heat flux at the first and second walls,

$$Nu^{\pm} = \frac{q_w^{\pm}\, 4a}{k\,(T_w^{\pm} - T_b)} \qquad (6.2.2\text{-}15)$$

and in terms of dimensionless parameters

$$Nu^{\pm} = \frac{8\gamma^{\pm}}{T_w^{\pm} - T_b} . \qquad (6.2.2\text{-}16)$$

The Case of No Bulk Heating

This is the case where $\lambda = 0$ and is denoted by superscript o. Equations (6.2.2-10) and (6.2.2-14) are reduced and combined to obtain

$$\frac{\partial^2 T^o}{\partial \eta^2} = (\gamma^+ + \gamma^-)\, f(\eta). \qquad (6.2.2\text{-}17)$$

Equation (6.2.2-17) may be integrated twice while using boundary condition (6.2.2-11) to obtain

$$T^o - T_w^{o-} = (\gamma^+ + \gamma^-) \int_{-1}^{\eta} d\eta \int_{-1}^{\eta} f\, d\eta - 2\gamma^-(\eta + 1). \qquad (6.2.2\text{-}18)$$

At this point, Eq. (6.2.2-18) may be replaced in the bulk temperature definition, Eq. (6.2.2-13), to calculate T_b as

$$T_w^{o-} - T_b^o = 2\gamma^- + \gamma^- \int_{-1}^{1} f\eta\, d\eta - \frac{\gamma^+ + \gamma^-}{2} \int_{-1}^{1} d\eta\, f \int_{-1}^{\eta} d\eta \int_{-1}^{\eta} f\, d\eta. \qquad (6.2.2\text{-}19)$$

To calculate $T_w^{o+} - T_b^o$, Eq. (6.2.2-18) is evaluated at $\eta=1$ and then combined with Eq. (6.2.2-19) to eliminate T_w^{o-}.

$$T_w^{o+} - T_b^o = (\gamma^+ + \gamma^-) \int_{-1}^{1} d\eta \int_{-1}^{\eta} d\eta\, f - 2\gamma^- + \gamma^- \int_{-1}^{1} f\eta\, d\eta - \frac{\gamma^+ + \gamma^-}{2} \int_{-1}^{1} d\eta\, f \int_{-1}^{\eta} d\eta \int_{-1}^{\eta} f\, d\eta. \qquad (6.2.2\text{-}20)$$

Finally, Nusselt numbers at the first and second walls may be calculated by substituting Eqs. (6.2.2-19) and (20) into Eq. (6.2.2-16). We use a subscript o on the Nu to denote the case with no heat generation.

$$1/Nu_o^{\pm} = 1/4 - I_1/8 - I_1\,(q_w^{\mp}/q_w^{\pm} - 1)/16 \qquad (6.2.2\text{-}21)$$

where I_1 defined as:

$$I_1 = \int_{-1}^{1} d\eta\, f \int_{-1}^{\eta} d\eta \int_{-1}^{\eta} f\, d\eta. \qquad (6.2.2\text{-}22)$$

Equation (6.2.2-21) can be compared with results for limiting cases available in the literature. For slug flow in which $I_1=4/3$, the following two cases as calculated are consistent with the results of Hartnett and Irvine.[2]

$$Nu_o^{\pm} = 12 \qquad \text{if} \quad q_w^+ = q_w^- \tag{6.2.2-23}$$

and

$$Nu_o^+ = 6 \qquad \text{if} \quad q_w^- = 0 \tag{6.2.2-24}$$

For the case of parabolic velocity profile, where $I_1 = 1.0286$, the following results compare favorably with the results of Kays.[2]

$$Nu_o^{\pm} = 8.235 \qquad \text{if} \quad q_w^+ = q_w^- \tag{6.2.2-25}$$

and

$$Nu_o^+ = 5.385 \qquad \text{if} \quad q_w^- = 0 \tag{6.2.2-26}$$

The Case With Bulk Heating

For the case with heat generation, Eqs. (6.2.2-10) and (6.2.2-14) are combined to obtain

$$\partial^2 T/\partial\eta^2 = (\gamma^+ + \gamma^- + \lambda)f - \lambda. \tag{6.2.2-27}$$

A solution of the following form is adopted.

$$T(\zeta,\eta) = T^o(\zeta,\eta) + \Theta(\eta) + \lambda\zeta \tag{6.2.2-28}$$

In Eq. (6.2.2-28), $\lambda\zeta$ is added to account for temperature rise due to bulk heating and satisfy Eq. (6.2.2-14). $\Theta(\eta)$ is added to account for the effect of $\dot{Q}_v$ on the temperature profile. Equation (6.2.2-28) may be replaced in Eq. (6.2.2-27) while using Eq. (6.2.2-17) for T^o to obtain

$$d^2\Theta/d\eta^2 = \lambda(f - 1) \tag{6.2.2-29}$$

with the boundary conditions that

$$\partial T/\partial\eta = \partial T^o/\partial\eta \quad \text{at } \eta = -1 \text{ and } 1 \tag{6.2.2-30}$$

This leads to the relation

$$\partial\Theta/\partial\eta = 0 \quad \text{at } \eta = -1 \text{ and } 1. \tag{6.2.2-31}$$

Equation (6.2.2-30) represents the fact that the surface heat flux at the first and second walls are set by boundary conditions (3) and (4) and do not depend on the presence of heat generation. Equation (6.2.2-29) may be integrated twice from -1 to η while using Eq. (6.2.2-31) to obtain θ as:

$$\theta - \theta_w^- = \lambda \int_{-1}^{\eta} d\eta \int_{-1}^{\eta} (f-1)\, d\eta. \qquad (6.2.2\text{-}32)$$

The temperature profile, Eq. (6.2.2-28), may now be written as

$$T = T^o + \lambda\zeta + \theta_w^- - \lambda \int_{-1}^{\eta} d\eta \int_{-1}^{\eta} d\eta (f-1) \qquad (6.2.2\text{-}33)$$

Similarly, bulk temperature is calculated by substituting Eq. (6.2.2-33) in Eq. (6.2.2-13)

$$T_b = T_b^o + \lambda\zeta + \theta_w^- - \lambda I_2 \qquad (6.2.2\text{-}34)$$

where another multiple integral has been defined as

$$I_2 = \frac{1}{2} \int_1^1 d\eta\, f \int_{-1}^{\eta} d\eta \int_{-1}^{\eta} (1-f)\, d\eta. \qquad (6.2.2\text{-}35)$$

Finally, $T_w^+ - T_b$ and $T_w^- - T_b$ are calculated by using Eqs. (6.2.2-33) and (6.2.2-34) as

$$T_w^- - T_b = T_w^{o-} - T_b^o + \lambda I_2 \qquad (6.2.2\text{-}36)$$

$$T_w^+ - T_b = T_w^{o+} - T_b^o + \lambda I_2 + \lambda \int_{-1}^{1} d\eta \int_{-1}^{\eta} (f-1)\, d\eta. \qquad (6.2.2\text{-}37)$$

Nusselt numbers at both walls are calculated from their definition as

$$1/Nu^{\pm} = 1/Nu_o^{\pm} + (I_2 + I_3^{\pm})(\dot{Q}_v a/q_w^{\pm})/4 \qquad (6.2.2\text{-}38)$$

where $I_3^{\pm}$ is defined as

$$I_3^{\pm} = \int_{-1}^{\pm 1} d\eta \int_{-1}^{\eta} (f-1)\, d\eta \qquad (6.2.2\text{-}39)$$

Nu_o in Eq. (6.2.2-38) may be replaced from Eq. (6.2.2-21) to obtain a general

relation for Nusselt number as

$$1/Nu^{\pm} = 1/4 - I_1/8 - I_1(q_w^{\mp}/q_w^{\pm} - 1)/16$$

$$+ (I_2 + I_3^{\pm})(\dot{Q}_v a/q_w^{\pm})/4 \quad . \qquad (6.2.2\text{-}40)$$

A special case of Eq. (6.2.2-39) ($q_w^+ = q_w^-$) may be compared with the results in the literature. For a parabolic velocity profile (in which I_1 = 1.0286, I_2 = 0.0857, and $I_3^{\pm}$ = 0), Eq. (6.2.2-39) reduces to

$$1/Nu = 1/Nu_o + (3/140)(\dot{Q}_v a/q_w) \qquad (6.2.2\text{-}41)$$

which is identical to the results obtained by Sparrow.[4]

Results

To present the results, the first wall channels of the Li/Li/V reference blanket were analyzed. Table 6.2.2-1 lists the numerical values of the relevant parameters for this blanket.

Due to lack of detailed knowledge of velocity profiles in the toroidal first wall channels, and due to predictions that the velocity profiles might not be uniform at all or even symmetric, several different velocity profiles including slug, Couette, parabola, power and gaussian relations are examined. The power relation velocity profiles are shown in Fig. 6.2.2-3. The general formula is

$$\frac{u}{u_b} = f = \frac{n}{n+1}\,[1 - (y/a)^n] \qquad (6.2.2\text{-}42)$$

The parameter n is introduced where n = 2 is the parabola and $n \to \infty$ is the slug velocity profile. Gaussian velocity profiles which are shown in Fig. 6.2.2-4 have the general formula as

$$f = \frac{s\,(y/a + 1)\,\left(e^{-s^2(y/a+1)^2/4} - e^{-s^2}\right)}{1 - e^{-s^2} - s^2 e^{-s^2}} \quad . \qquad (6.2.2\text{-}43)$$

It should be stressed here that Eq. (6.2.2-43) is not the result of any analytical consideration. It simply is an algebraic fit (with certain condi-

Table 6.2.2-1 Specifications of the First Wall Channels of the Li/Li/V Reference Blanket

First wall thickness, mm	7.5
Second wall thickness, mm	15
Coolant channel width, 2a, mm	45
Heat generation in vanadium, $\dot{Q}_{v,V}$, MW/m^3	25
Heat generation in lithium, $\dot{Q}_{v,Li}$, MW/m^3	25
Surface heat flux, q_s, MW/m^2	0.5
γ^- dimensionless surface heat flux	45.76
γ^+ dimensionless surface heat flux	274.5
λ dimensionless volumetric heat generation	274.5

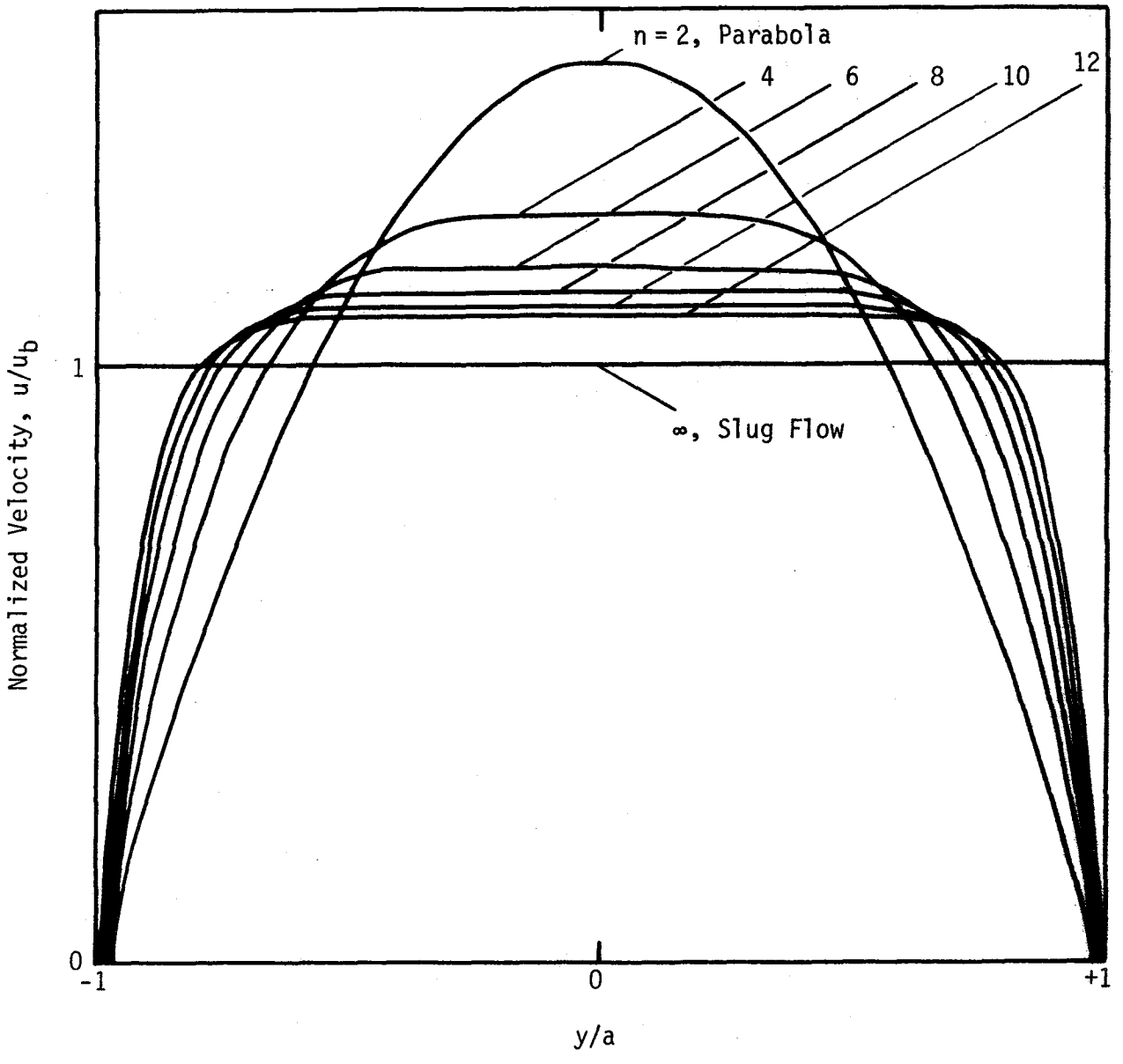

Figure 6.2.2-3 Power relation velocity profile.

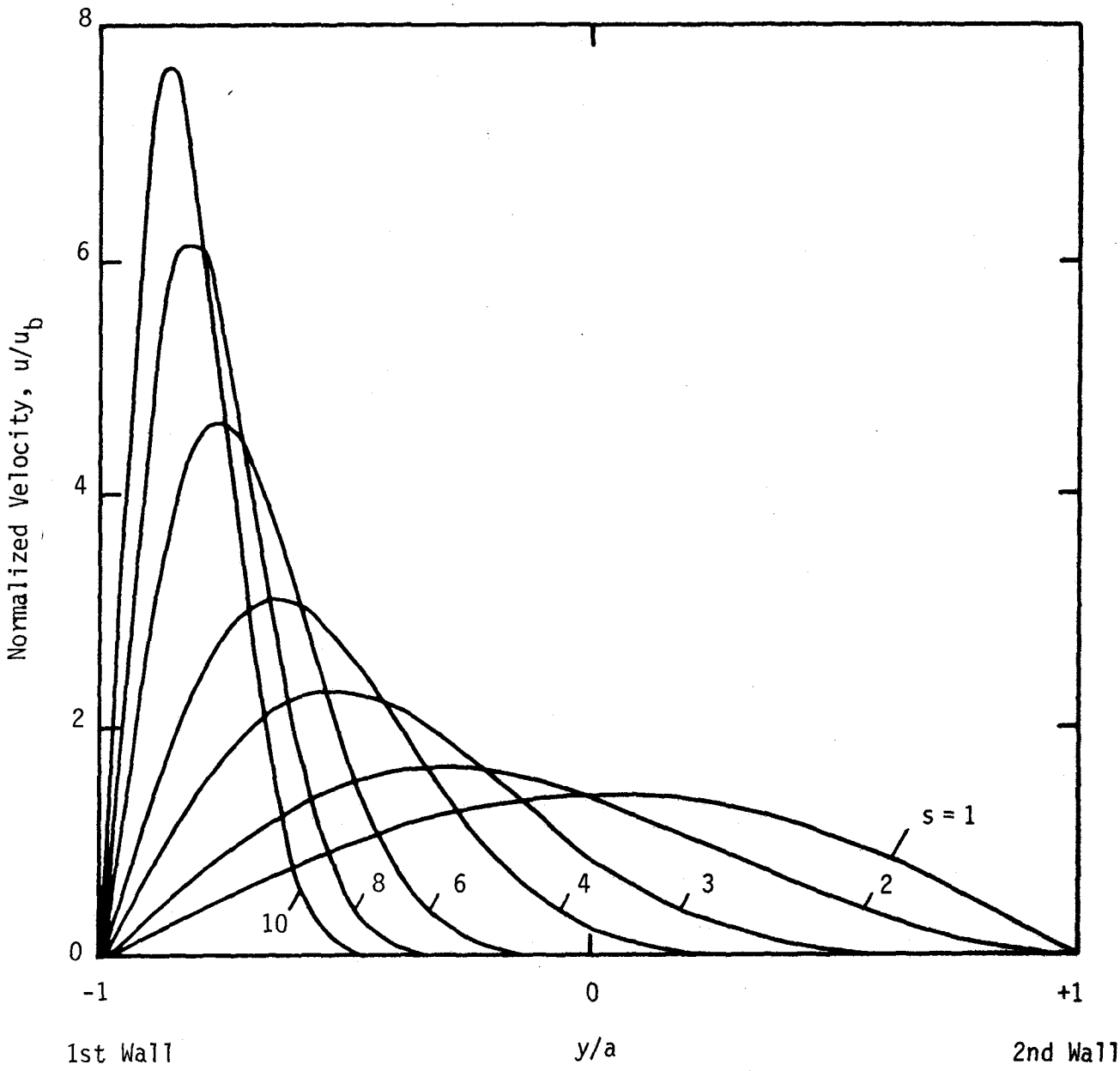

Figure 6.2.2-4 Gaussian velocity profiles with a skewing factor s.

tions on the values at the boundaries and on the integral of u) to help us investigate the effects on the first wall heat transfer of any peculiar velocity profiles.

Velocity Profile and Heat Generation

The results of investigations on the effect of velocity profiles and heat generation are condensed in Figs. 6.2.2-5 and 6.2.2-6. In these figures, the abscissa does not represent a quantitative parameter. Rather, it presents the velocity profiles from Figs. 6.2.2-3 and 4 in a progression of increasing nonuniformity. It starts with slug flow ($n \to \infty$). Thereafter, the parameter n in the power relation velocity profiles decreases down to $n = 2$ for parabolic profiles. At this point, the abscissa is switched to represent the Gaussian velocity profiles, starting with a skewing factor $s = 1$. Figure 6.2.2-4 demonstrates the fact that $s = 1$ is symmetric and very close to a parabolic profile. Thereafter, the skewing factor increases and with it the profile becomes more asymmetric. It should also be noted that there are two velocity profiles for each skewing parameter--one with the velocity peaked near the first wall and the other near the second wall (one being the mirror image of the other).

The ordinates in Figs. 6.2.2-5 and 6.2.2-6 are the inverse Nusselt number and the difference between the wall temperature and the coolant bulk temperature. It is very important to note that the values for temperature differences in these figures are those for fully developed flow. While the actual temperature differences for the toroidal channel may be up to two to three times smaller (since it is in the entrance region), the relative magnitude of the Nusselt numbers and temperature differences should remain more or less the same as the velocity profile and heat generation are varied.

Figures 6.2.2-5 and 6.2.2-6 show the heat transfer results for the first wall and second wall, respectively. It is noted from Fig. 6.2.2-5 that the first wall temperature increases only moderately as the velocity profile changes from slug flow all the way to parabolic. The first wall temperature increases drastically, however, as the velocity near the second wall increases with the skewed profiles. This kind of behavior (higher velocity near the second wall) is predicted to happen in the toroidal first wall channels. It can be seen that even a moderately skewed profile ($s = 3$) increases the first

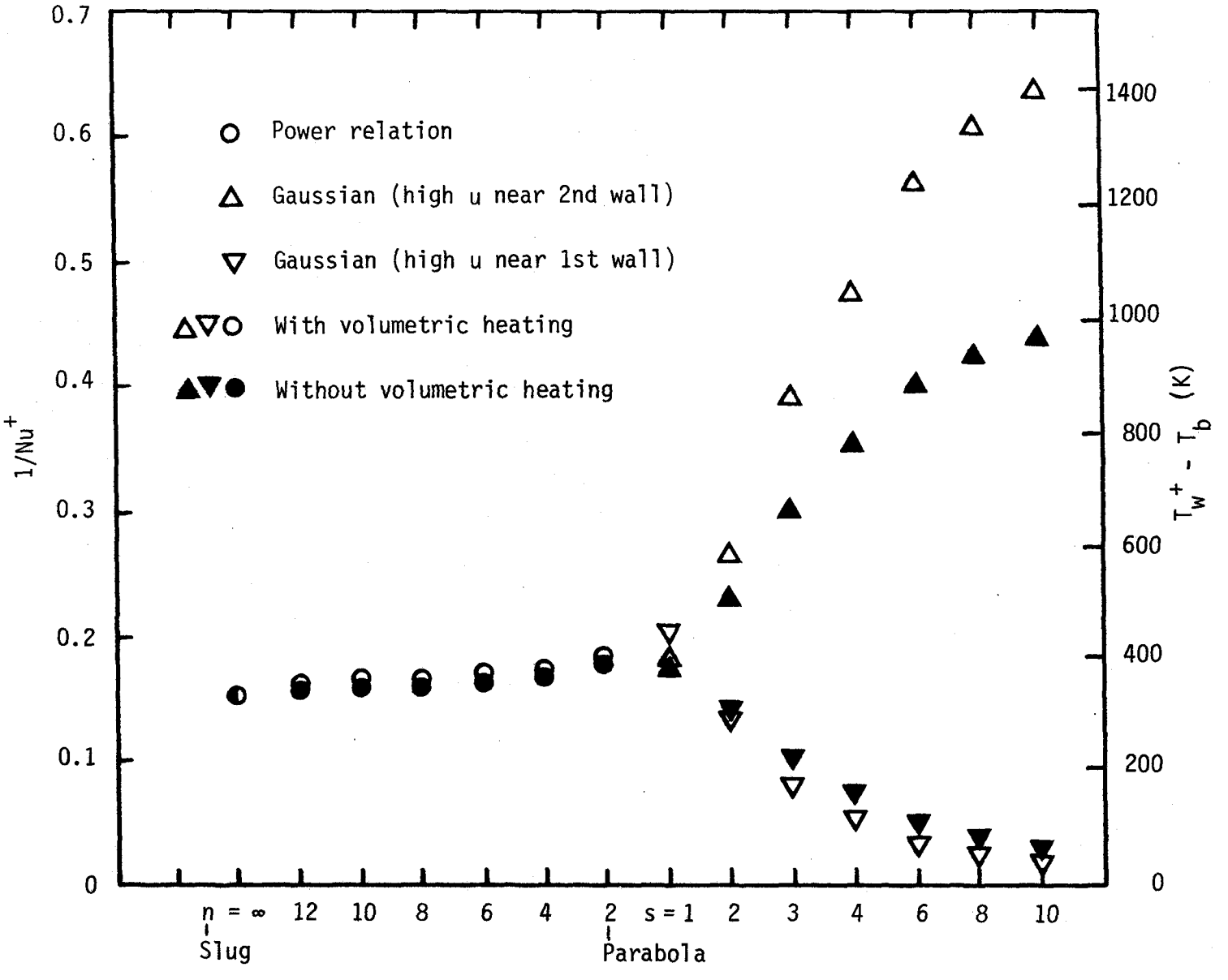

Figure 6.2.2-5 First wall Nusselt number and temperature for various coolant velocity profiles for Li/V reference blanket.

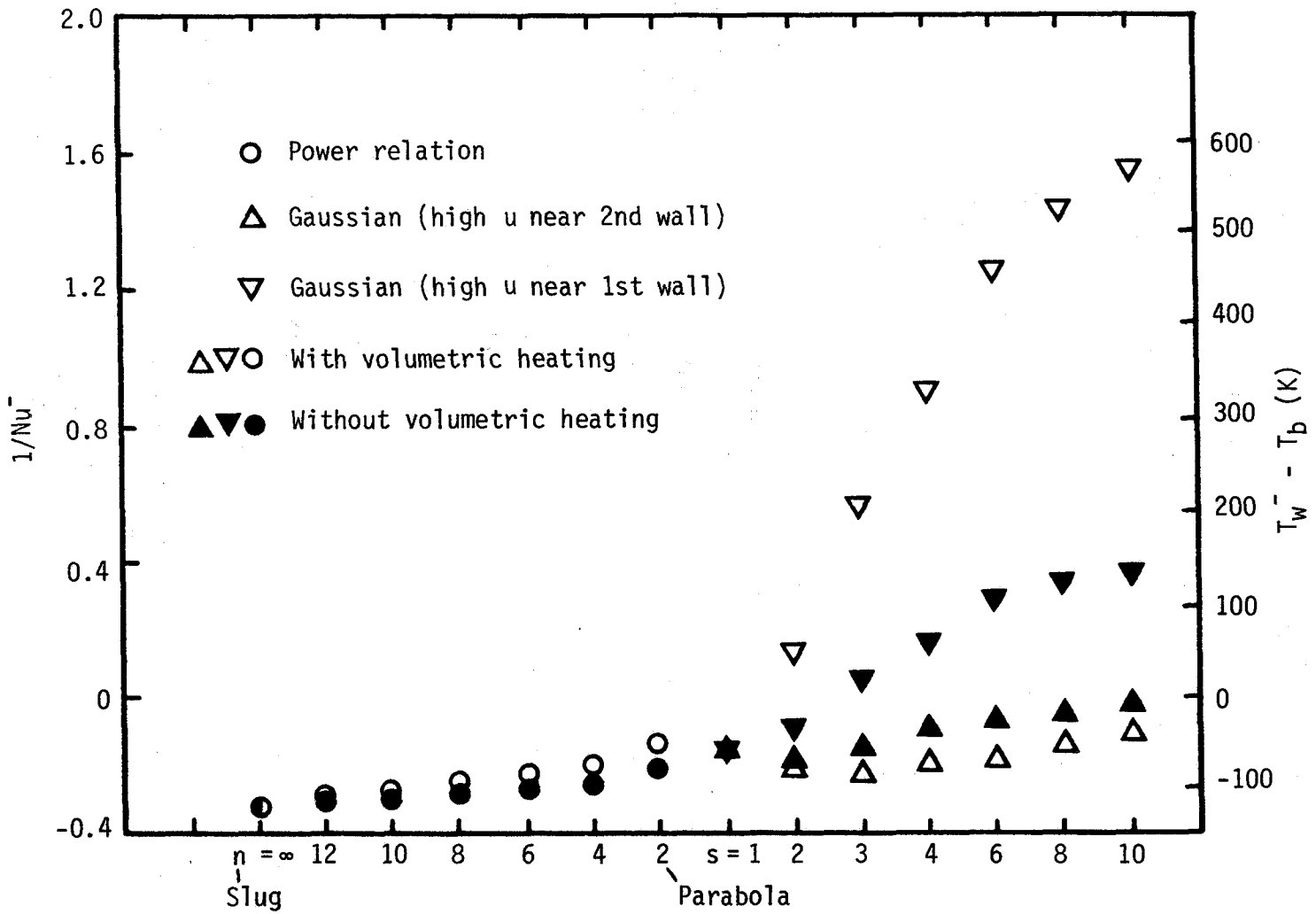

Figure 6.2.2-6 Second wall Nusselt number and temperature for various coolant velocity profiles for Li/V reference blanket.

wall temperature by a factor of two, which is more than enough to close the blanket design window. One potential solution that has often been suggested is to somehow direct more of the coolant near the first wall, e.g., by installing guide plates at the entrance of the toroidal channels. This is the case of Gaussian profile with higher velocity near the first wall. Figure 6.2.2-5 shows that this quickly reduces the first wall temperature as expected. Figure 6.2.2-6, however, shows a drastic increase to the extent that the blanket may fail due to large second wall temperatures. There is, however, a very small window of skewed velocity profiles (s = 1 or 2 with peak velocity near the first wall) that successfully reduces the first wall temperature while moderately increasing the second wall temperature.

The effect of heat generation on the first and second wall heat transfer are also included in Figs. 6.2.2-5 and 6.2.2-6. The heat generation effect is identically zero for slug flow. It starts to grow as the velocity profile approaches a parabola but is still small and about a few percent. The heat generation effect, however, quickly increases as the velocity profile is skewed. It can be seen from Fig. 6.2.2-5 that this effect can get as high as 30% for a moderate skewing factor of s = 4. This effect can be even higher for the second wall as can be observed from Fig. 6.2.2-6.

6.2.2.3 Entry Length Considerations

The entry length consideration is only for temperature profiles. The velocity profile is assumed to be fully developed although this is likely to be incorrect for some blanket geometries in which the hydrodynamic entry length is long. The energy equation governing the coolant temperature is:

$$\rho\, c_p u \frac{\partial T}{\partial x} = k \left(\frac{\partial^2 T}{\partial x^2} + \frac{\partial^2 T}{\partial y^2} + \frac{\partial^2 T}{\partial z^2}\right) + \dot{Q}_v \quad . \qquad (6.2.2\text{-}44)$$

Analytical treatment of Eq. (6.2.2-44) is straightforward, yet algebraically involved and cumbersome. First, a simple case of 2-D flow with no heat generation is treated analytically. Then the more general case of Eq. (6.2.2-44) is investigated numerically.

Analytical Treatment

There are two important differences in heat transfer mechanisms in non-

conducting coolants and in liquid metals. First, the very low Prandtl number of liquid metals implies that conduction makes an important contribution to the heat transfer from the wall to the bulk fluid. Second, eddy diffusivity due to velocity fluctuations is all but eliminated due to the suppression of turbulence by the strong magnetic field. The net result of these two factors is that thermal diffusion dominates the heat transfer. This leads to long thermal entry lengths.

The length scale for temperature profile development can be estimated from the ratio of the fluid residence time to the cross channel conduction time, i.e., the Fourier number:

$$Fo = \frac{x/u}{4a^2/\alpha} = \alpha x/4a^2 u \qquad (6.2.2\text{-}45)$$

where x is the coordinate along the channel length, a is the channel half width, u is the fluid velocity, and α is the thermal diffusivity. The criterion for fully developed temperature profiles is that the coolant resides in the channel long enough for conduction across the channel to take place, or Fo $>$ 1. For values of a, α, and u in the reference design, the entry length is of the order of 100 m. Since the typical channel length in a fusion blanket is the order of meters, the temperature profiles are always far from being fully developed (or Fo $\ll$ 1).

The fact that conduction dominates cross-channel heat transfer also allows a simple, analytic solution for the temperature profiles. Examination of the development of the temperature profiles provides insight into blanket behavior and important information for scaling. The Nusselt number is used as a simple composite indicator of the temperature profiles. The Nusselt number is defined by the expressions:

$$q_w = h\ (T_w - T_b) \qquad (6.2.2\text{-}46)$$

$$T_b = \frac{1}{2a} \int_0^{2a} T\ dy \qquad (6.2.2\text{-}47)$$

$$Nu = 4ha/k \qquad (6.2.2\text{-}48)$$

The temperature profiles and Nusselt numbers have been obtained in a

simplified geometry to demonstrate the entry length effects. The 2-D steady state convection equation for two infinite parallel plates (see Fig. 6.2.2-7) is easily converted into a 1-D transient conduction equation when the velocity profile is flat, or slug flow, and there is no internal heat generation. Using the transformation $dx = udt$,

$$\rho c_p u \frac{\partial T}{\partial x} = k \frac{\partial^2 T}{\partial y^2} \qquad (6.2.2.49)$$

becomes

$$\frac{\partial T}{\partial t} = \alpha \frac{\partial^2 T}{\partial y^2} \qquad (6.2.2-50)$$

The time coordinate now represents the distance which the slug of fluid has traveled along the channel. With the initial condition $T(0,y) = T_0$ and constant heat flux into one side of the channel, this equation is easily solved. The solution is:

$$T(t,y) = \frac{q_w}{4ak}(y^2 + 2\alpha t) + c_o + \sum_{n=1}^{\infty} c_n \cos\left(\frac{n\pi y}{2a}\right) e^{-n^2\pi^2\alpha t/4a^2} \qquad (6.2.2-51)$$

where the constants c_n are given by

$$c_0 = T_0 - \frac{q_w a}{3k} \quad , \quad c_n = (-1)^{n+1}\left(\frac{1}{n\pi}\right)^2 \frac{4q_w a}{k} \qquad (6.2.2-52)$$

Solutions are plotted in Fig. 6.2.2-8 for Fourier numbers of 0.05, 0.1, 0.15, and 0.2.

The Nusselt number is obtained from the definitions above as:

$$Nu = \left(\frac{1}{6} - \frac{1}{2\pi^2}\left\{2e^{-\pi^2 Fo} + \frac{1}{2}e^{-4\pi^2 Fo} + \frac{2}{9}e^{-9\pi^2 Fo} + \ldots\right\}\right)^{-1} \qquad (6.2.2-53)$$

The drop in Nusselt number as a function of distance into the channel is plotted in Fig. 6.2.2-9. As an example of the heat transfer regime of a real blanket, the exit of the toroidal channels of the BCSS reference design has a Fourier number of 0.02.

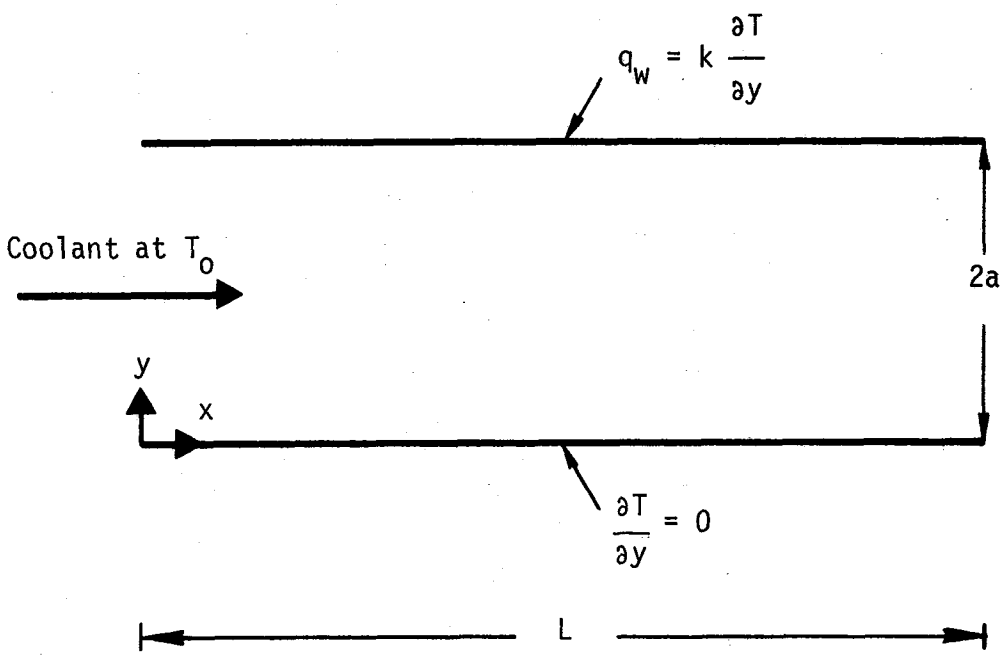

Figure 6.2.2-7 Entry length model.

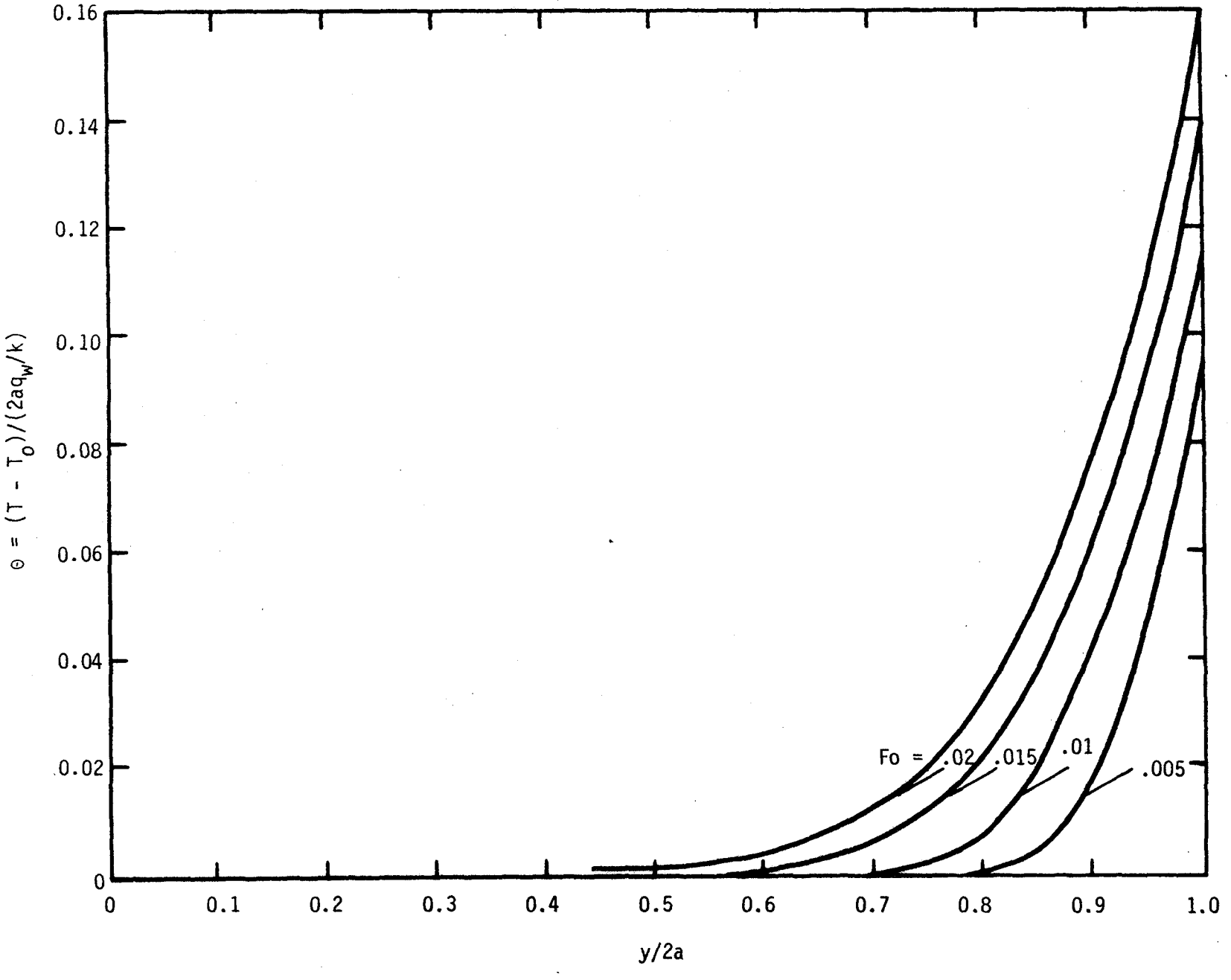

Figure 6.2.2-8 Dimensionless temperature profile in the entrance region.

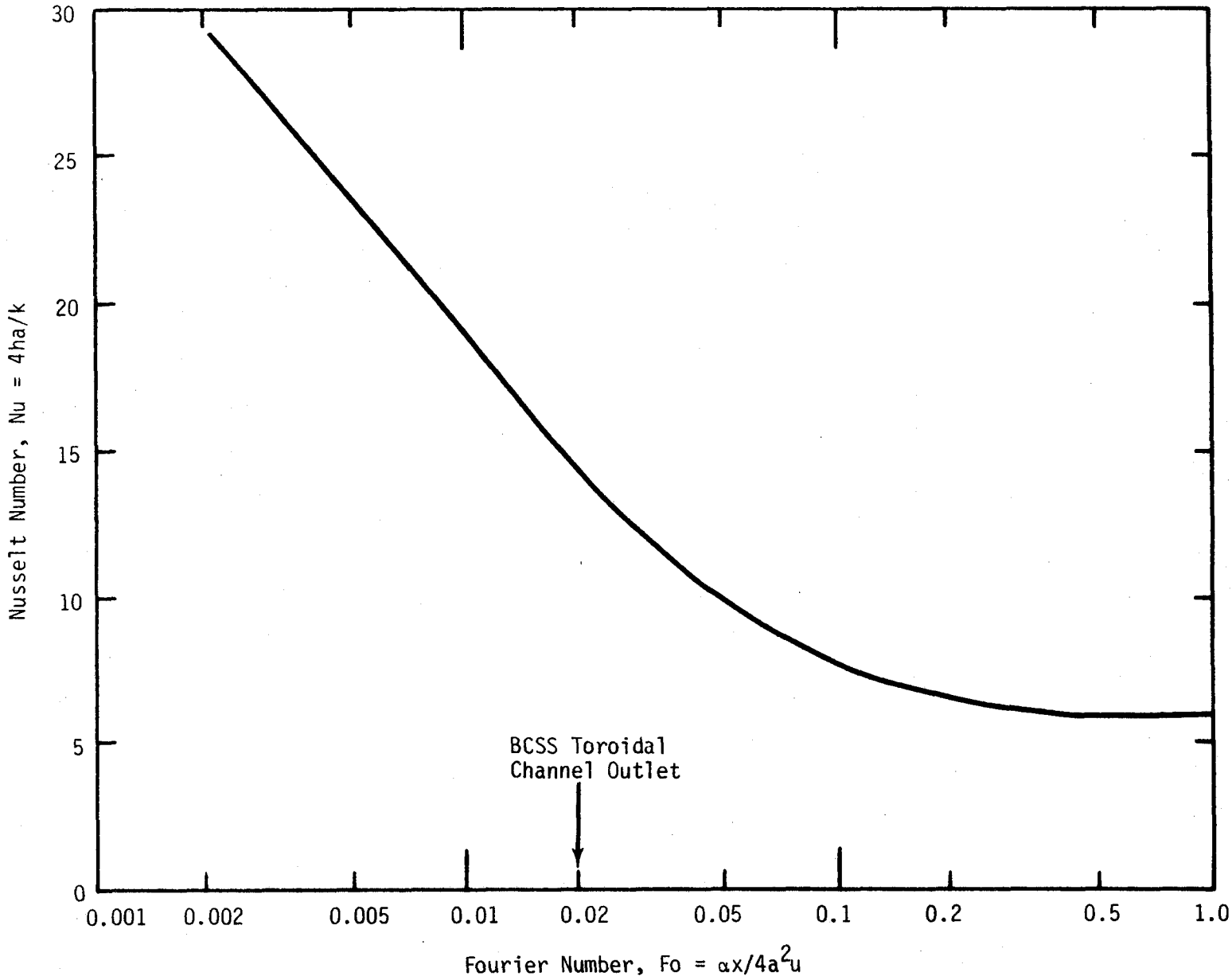

Figure 6.2.2-9 Entry length Nusselt number.

Numerical Treatment

Numerical techniques for 2-D or 3-D convective flows are not always unique or stable. In addition, there are not any numerical package codes for convection as opposed to several well known all purpose conduction numerical packages. Therefore, a conduction code was employed to solve the laminarized convective flow problem. This technique may be used in any situation with laminar flow.

One approximation is needed in order for this technique to be valid: streamwise conduction must be negligible. That is,

$$\frac{\partial^2 T}{\partial x^2} << \frac{\partial^2 T}{\partial y^2} + \frac{\partial^2 T}{\partial z^2} . \qquad (6.2.2\text{-}54)$$

Streamwise conduction and its effects on the thermal solution of this problem will be investigated later in Section 6.2.2.4. A normalized velocity distribution f may be defined as

$$f(y,z) = u(y,z)/u_b \qquad (6.2.2\text{-}55)$$

At this point, a pseudo time can be defined as

$$t_p = x/u_b . \qquad (6.2.2\text{-}56)$$

The distribution function f(y,z) may be added to the product of ρc_p as

$$\overline{\rho c_p}\ (y,z) = \rho c_p\ f(y,z) \qquad (6.2.2\text{-}57)$$

where a modified $\overline{\rho c_p}$ that varies throughout the medium has been introduced. After incorporating Eqs. (6.2.2-54) through (6.2.2-57), Eq. (6.2.2-44) may be rewritten as

$$\overline{\rho c_p}\ \frac{\partial T}{\partial t_p} = k\ \left(\frac{\partial^2 T}{\partial y^2} + \frac{\partial^2 T}{\partial z^2}\right) + \dot{Q}_v \qquad (6.2.2\text{-}58)$$

which is identical to a 2-D transient conduction equation. So, in summary, the steady-state convection problem (including entrance region effects) has been converted to a transient convection problem by introducing an artificial,

spatially dependent heat capacity function.

Boundary Conditions

The transformation of boundary conditions to the new coordinates is straightforward. Even boundary conditions that are varying in the direction of flow (x-direction) are treated easily. They simply become time dependent boundary conditions in the new system. In summary, the following are the features of conduction treatment of the convection problem:

1. Any geometry may be handled just as in the standard finite element conduction codes.

2. Boundary conditions varying with flow direction are treated easily.

3. Three-dimensional heat generation and fluid properties should pose no additional complications.

Results

As discussed earlier, temperature profiles throughout the entire toroidal first wall channel are in the entry length region. This results in heat transfer coefficients which vary considerably and are higher that predicted for fully developed flow. Figure 6.2.2-10 shows the entrance region Nusselt numbers for several different velocity profiles. In this figure, the Nusselt numbers are normalized by their fully developed values for two reasons. First, it is possible to estimate how fast the profiles are developing since all the curves go to unity. Second, being normalized to their fully developed values, any differences in the normalized Nusselt numbers are directly attributed to the nonlinear effects of the entrance region, heat generation, and velocity profiles. The results for fully developed Nusselt numbers will be presented and discussed later. It is seen from Fig. 6.2.2-10 that all of the Nusselt numbers start very high at the entrance point and drop more or less in a similar fashion. It is also observed that the normalized Nusselt number for all velocity profiles except slug flow are very close and that slug flow delivers the longest entry length. The exit location of the BCSS reference blanket is shown in the figure. It basically reaffirms the fact that the entire blanket is in the entrance region and that the average Nusselt number

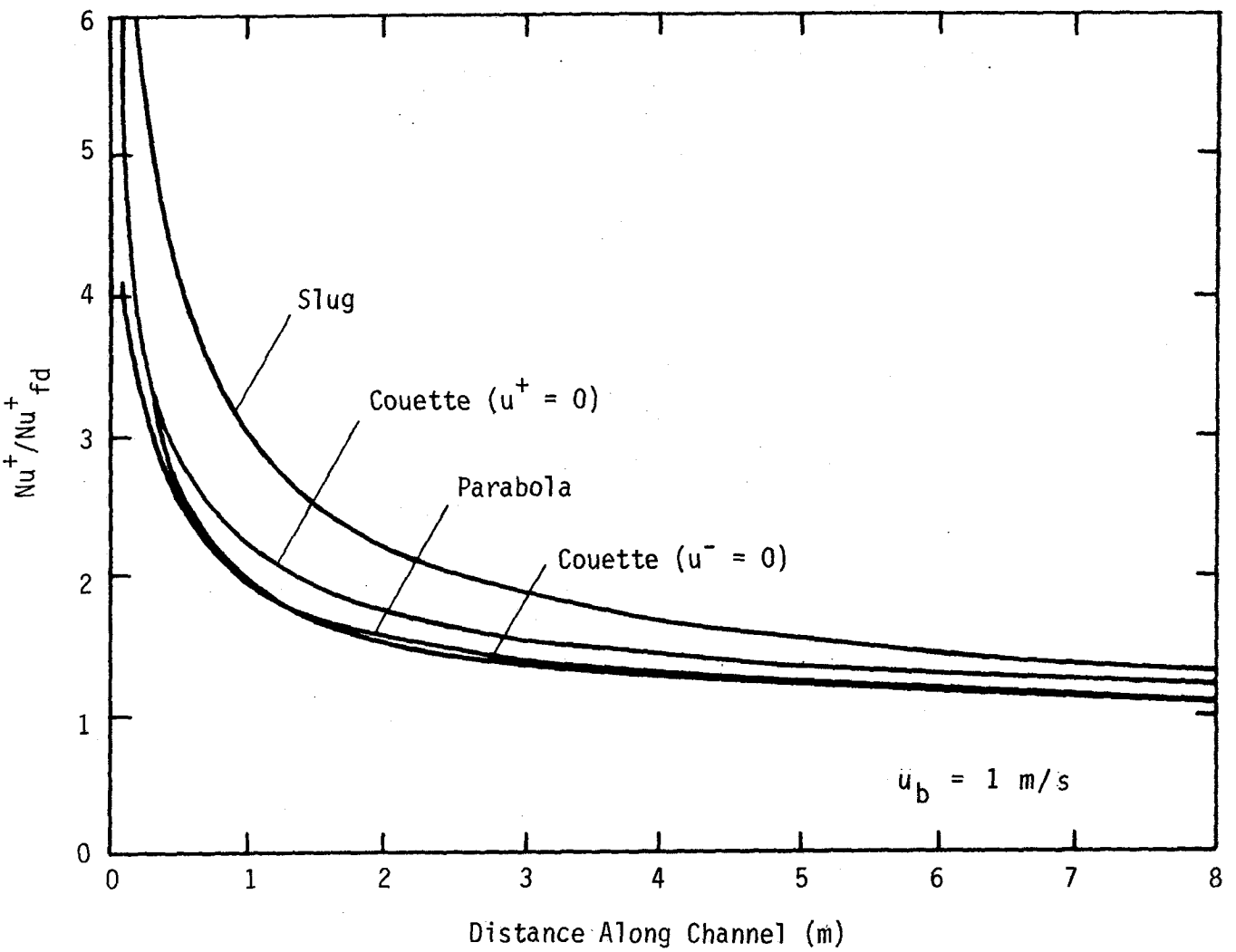

Figure 6.2.2-10 Entrance region Nusselt number in toroidal channel for various coolant velocity profiles.

in the toroidal channels can be as high as two to three times the fully developed Nusselt number, depending on the velocity profile.

6.2.2.4 Axial Conduction

Introduction

Axial (streamwise) conduction can alter the temperature profiles in the coolant channel. It is usually negligible in most ordinary convection problems, and thus neglected. However, axial conduction effects can be significant in low velocity, high thermal conductivity liquids. The situation in the toroidal and poloidal channels of the Li/Li/V reference blanket is with both low velocity (high MHD pressure drop) and high thermal conductivity (liquid metal). Since the axial conduction effect was neglected in the thermal analysis of first wall channels, its importance is examined in this section.

Another motivation for this investigation arises from the design of act-alike test modules. It is important to know the magnitude and functional dependency of axial conduction in order to successfully design an act-alike module.

Modelling

Axial conduction can be modelled in a simple fashion.[5] Figure 6.2.2-11 shows such a model. In the case where the surface heat flux is constant, all coolant temperatures including the bulk temperature increase linearly along the direction of flow. This results in a constant axial heat flux which in turn increases the bulk temperature. The effect of axial conduction can be seen through a simple energy balance

$$\frac{T_b - T_b'}{T_{out} - T_{in}} = \frac{k}{\rho c_p u_b L} \quad , \tag{6.2.2-59}$$

where T_b and T_b' are the coolant bulk temperatures with and without axial conduction respectively. Bulk temperature without axial conduction is simply related to inlet and outlet temperatures as

$$T_b' = (1 - x/L)\, T_{in} + (x/L)\, T_{out} \tag{6.2.2-60}$$

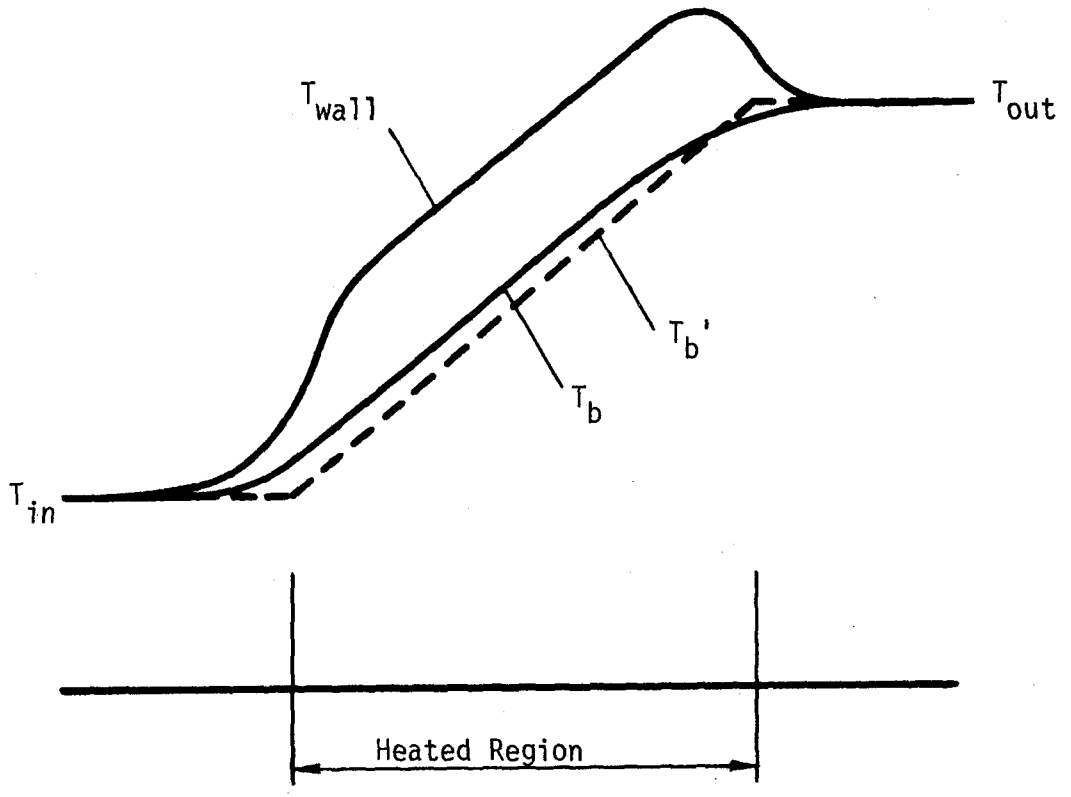

Figure 6.2.2-11 Axial conduction model.

Numerical Result

Equation (6.2.2-59) may be evaluated for the Li/Li/V reference blanket. For a typical toroidal channel, Eq. (6.2.2-59) yields

$$\frac{T_b - T'_b}{85K} = \frac{46.1\ W/mK}{(503\ kg/m^3)\ (4230\ J/kg)\ (1\ m/s)\ (2\ m)}$$

or

$$T_b - T'_b = 9.2 \times 10^{-4}\ K. \qquad (6.2.2\text{-}61)$$

The correction to the coolant bulk temperature is extremely small and will remain so even for substantially smaller coolant velocities.

6.2.2.5 Effects of Residual Turbulence

A simple analysis of the impact of residual turbulence was performed in order to ensure the validity of the many results of this and other sections which depend on the assumption of flow laminarization. It has been observed in experiments that after entering a region of magnetic field, a liquid metal retains a level of turbulent fluctuations which may be as high as $u'/u \simeq 1\%$, even in very high magnetic fields.[6,7] In addition, there may be sources of turbulence within the blanket which enhance this effect. The presence of turbulent fluctuations will enhance heat, mass, and momentum transport. The relative importance can be acertained by comparison with the laminar transport mechanisms.

The turbulent transport terms from the heat and momentum balance equations are usually expressed as

$$\overline{u'v'} = \varepsilon_m \frac{dv}{dy} \qquad (6.2.2\text{-}62)$$

$$\overline{u'T'} = \varepsilon_h \frac{dT}{dy} \qquad (6.2.2\text{-}63)$$

where u' and v' are the fluctuating values of velocity and ε_m and ε_h are the momentum and heat eddy diffusivities respectively. Eqs. (6.2.2-62) and (6.2.2-63) can be interpreted as definitions of the heat and momentum eddy diffusivities. The ratio of turbulent and laminar heat transfer, q_t/q_l, can

be written as:

$$\frac{q_t}{q_l} = \frac{\varepsilon_h}{\alpha} = \frac{E_e \varepsilon_m}{\alpha} \qquad (6.2.2\text{-}64)$$

where E_e is the ratio of eddy diffusivities - a quantity which has been studied semiempirically and is known as a function of Pr. E_e is less than unity in liquid metals because the high thermal conductivity results in equilibration of the temperature gradients within the eddy before the eddy exchanges the high and low temperature fluid elements.

Next the velocity fluctuations are assumed to be uncorrelated, so $\overline{u'v'}$ is approximated as u'^2.

$$\varepsilon_m = u'^2 \frac{1}{du/dy} \qquad (6.2.2\text{-}65)$$

Writing $f = u'/u$, we obtain

$$\frac{q_t}{q_l} = \frac{E_e}{\alpha} \frac{u'^2}{du/dy} = \frac{f^2 E_e}{\alpha} u^2 \frac{1}{du/dy} \qquad (6.2.2\text{-}66)$$

$$\frac{q_t}{q_l} = \text{Re Pr } f^2 \text{ E } [\frac{u/d}{du/dy}] \ . \qquad (6.2.2\text{-}67)$$

For $u/d \simeq du/dy$, Eq. (6.2.2-67) gives values of q_t/q_l of about 3×10^{-3}. This indicates that the contribution of eddy diffusivity to heat transfer is small. Near the wall, du/dy is likely to be very large, making the ratio even smaller.

6.2.2.6 Effects of Pulses

Pulsed neutron wall load directly affects the blanket temperatures. As discussed in Section 6.2.2.1, several phenomena are either driven by or dependent on blanket temperature, for example, first wall stresses, tritium permeation and inventory, corrosion and heat recovery. In this section, the effects of pulses on thermal behavior of the liquid metal blankets are investigated.

The investigation on pulsed operation may be useful to the full scale reference blankets as well as to the operation and design of the act-alike

test modules. It is useful for reference blanket to the extent that it would address some of the issues related to reactor startup and shutdown. The main motivation, however, comes from the fact that act-alike test modules may operate in devices with pulsed neutron wall loads.

A test module will act differently under pulsed conditions. The coolant and structure temperatures will generally be reduced and will always oscillate. This may severely reduce the usefulness of the results of the test for which the module has been designed. To avoid this, therefore, the effects of pulses are examined. This in turn means better interpretation of the results obtained from experiments performed on test modules. As a result of this investigation, it is expected that limits will be observed on major device parameters (in this case, pulsed conditions) beyond which the test modules are not close enough to true act-alike modules.

Analysis

The following assumptions are made in the analysis of the effects of pulses.

1. Steady hydrodynamics, i.e., no time-dependent velocity, pressure, etc.

2. Axial conduction in the coolant and blanket structure is negligible and ignored.

3. Pulses for neutron wall load and surface heating are square (no startup/shutdown periods).

Assumption 3 is made in order to simplify the analysis and the presentation of results and should not cause any significant error as long as startup and shutdown times are small compared to blanket characteristic times and to burn and dwell times.

The Li/Li/V reference blanket has been chosen for this investigation. Figure 6.2.2-12 shows a schematic of the toroidal and poloidal channels in the order that the coolant passes through them. Of course, the lengths of the poloidal channels before and after the toroidal channels can vary depending on

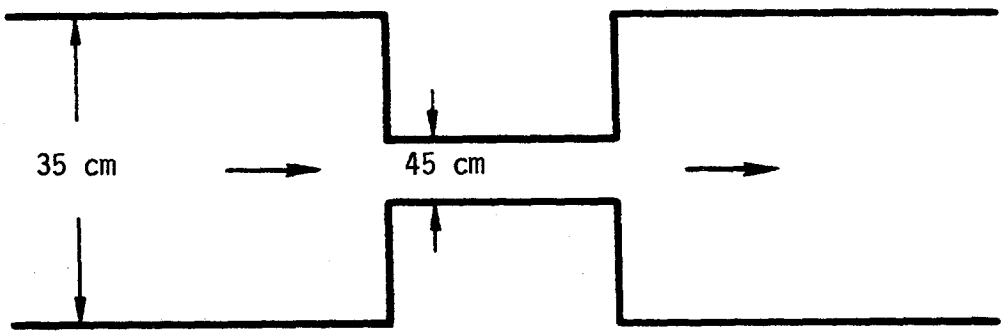

	Poloidal	Toroidal	Poloidal
Height, cm	35	4.5	35
Width, cm	25	82.1	25
Length, cm	490	302	490
Velocity, cm/s	41.9	103.3	41.9
Coolant Temp. Range, ^{o}C	300/382.5	382.5/467.5	467.5/550
Coolant Residence Time, s	11.7	2.9	11.7

Figure 6.2.2-12 Schematic of the toroidal and poloidal channels in the Li/Li/V reference blanket.

the location of the toroidal channels. The total length of the poloidal channels, however, does not depend on this location and is constant. In Fig. 6.2.2-12, the case of equal portions of poloidal channels is shown. This figure also includes some statistics on the poloidal/toroidal channels.

Solid Breeders vs. Liquid Metals

Solid breeders and self-cooled liquid metal breeders behave fundamentally differently under a pulsed environment. One major difference is in their heat removal mechanisms. In solid breeders, the heat which is generated in the solid must be conducted through the solid and convected away by the coolant. In self-cooled liquid breeders, the majority of the heat is deposited directly into the coolant and then carried away at the the coolant flow rate. It is clear that a pulsed environment affects the thermal condition of self-cooled liquid breeders much faster than that of solid breeders.

Blanket Characteristic Times

Before analyzing the effects of pulses, it is appropriate to identify all the blanket characteristic times. A list of such times is given below.

(1) Coolant Residence Time. This is the time it takes a fluid particle to travel through the blanket. This is a very important time constant since it is an indication of the thermal memory of the blanket. For example, if the fusion power is suddenly cut, after the residence time has elapsed, the blanket completely forgets that the power was ever on (only thermally, and neglecting after heat generation). The coolant residence time is given by:

$$t_R = \Sigma_i L_i/u_{bi} \qquad i = \text{channel segments} \qquad (6.2.2\text{-}68)$$

The residence time, as shown in the equation, is for the coolant exit location (x = L). It is different for each location in the blanket with its minimum value (zero) at the coolant entrance and maximum value at the coolant exit. It is noted that a short residence is in conflict with low blanket pressure drop since the latter requires higher velocities while the former needs lower velocities.

(2) Coolant Conduction Time. This is the time it takes the coolant temperature profile across the channel (perpendicular to the flow direction)

to become quasi-steady. This time constant is given by:

$$t_c = a^2_{channel}/\alpha_{coolant} \qquad (6.2.2\text{-}69)$$

where α is the thermal diffusivity.

(3) First Wall Conduction Time. This is the time it takes any thermal information to diffuse across the first wall (same as time necessary for the first wall temperature profile to become quasi-steady). This time is given by

$$t_{fw} = a^2_{fw}/\alpha_{fw}. \qquad (6.2.2\text{-}70)$$

(4) First Wall Temperature Rise Time. First wall temperature level is the product of a balance between heat generated in and transferred to the first wall and heat transferred from the first wall to the coolant. As soon as any element of this balance changes (such as pulsed heat generation), a new balance state (first wall temperature) is achieved. This is the characteristic time required to achieve the thermal balance. This time constant is given by

$$t_{tr} = (\rho c_p a)_{fw}/h_{coolant}. \qquad (6.2.2\text{-}71)$$

As expected, the first wall with higher thermal capacities will yield longer temperature rise time.

Evaluation of Time Constants

Table 6.2.2-2 lists the numerical values for various time constants identified above and calculated from Eqs. (6.2.2-68) through (6.2.2-71). The following observations can be made with respect to the numerical values in Table 6.2.2-2.

1. Coolant residence time, which is the most important time constant, is rather short, especially for the toroidal channels.

2. Coolant conduction time is not a determining factor. Its relatively high value compared to residence time, however, indicates that the coolant temperature profile never fully develops. This is in

Table 6.2.2-2 Numerical Results for Various Time Constants in Liquid Metal Blankets (in seconds)

Coolant residence time	
Total	26.3
Toroidal channel	2.9
Coolant conduction time (⊥ to flow)	23.4
First wall conduction time	3.1
First wall temperature rise	14.8

agreement with our statement in Section 6.2.2.1 that the entire coolant channel is in the thermal entrance region.

3. First wall conduction time is short, meaning that a quasi-steady first wall temperature profile is very easy to achieve.

Solution Methodology

The goal is to calculate the thermal response of a blanket under time-dependent loading. Fortunately, the basic energy equation, including conduction and convection, is linear with respect to volumetric heat generation. As a result, the system response to a step function heat generation may be appropriately integrated to obtain the response to any time-dependent neutron wall loading.

For the purpose of illustration, a single coolant channel with constant cross section is considered here. The extension to the actual geometry shown in Fig. 6.2.2-12 should be straightforward. Figure 6.2.2-13 shows the thermal history of a fixed location in the coolant for a step change in wall loading. It starts with the coolant inlet temperature and increases linearly with time. As expected, the temperature reaches its steady-state value after the residence time has elapsed and thereafter stays constant. Here only square pulses are considered. Figure 6.2.2-14 shows how one pulse may be broken into two step functions. It also shows the temperature response to one pulse. Naturally, in the real case where there are several pulses, the response toe ach is calculated and summed up to obtain the system's response to the pulses. Such a response to a typical set of pulses is shown in Fig. 6.2.2-15. The burn and dwell times here are normalized and given in terms of the residence time which, in fact, is the system's thermal characteristic time.

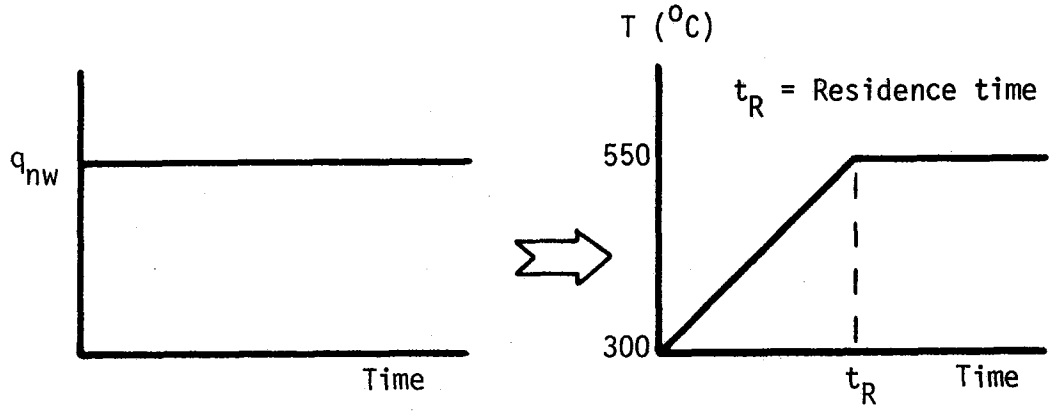

Figure 6.2.2-13 Blanket thermal response to a step change in neutron wall load.

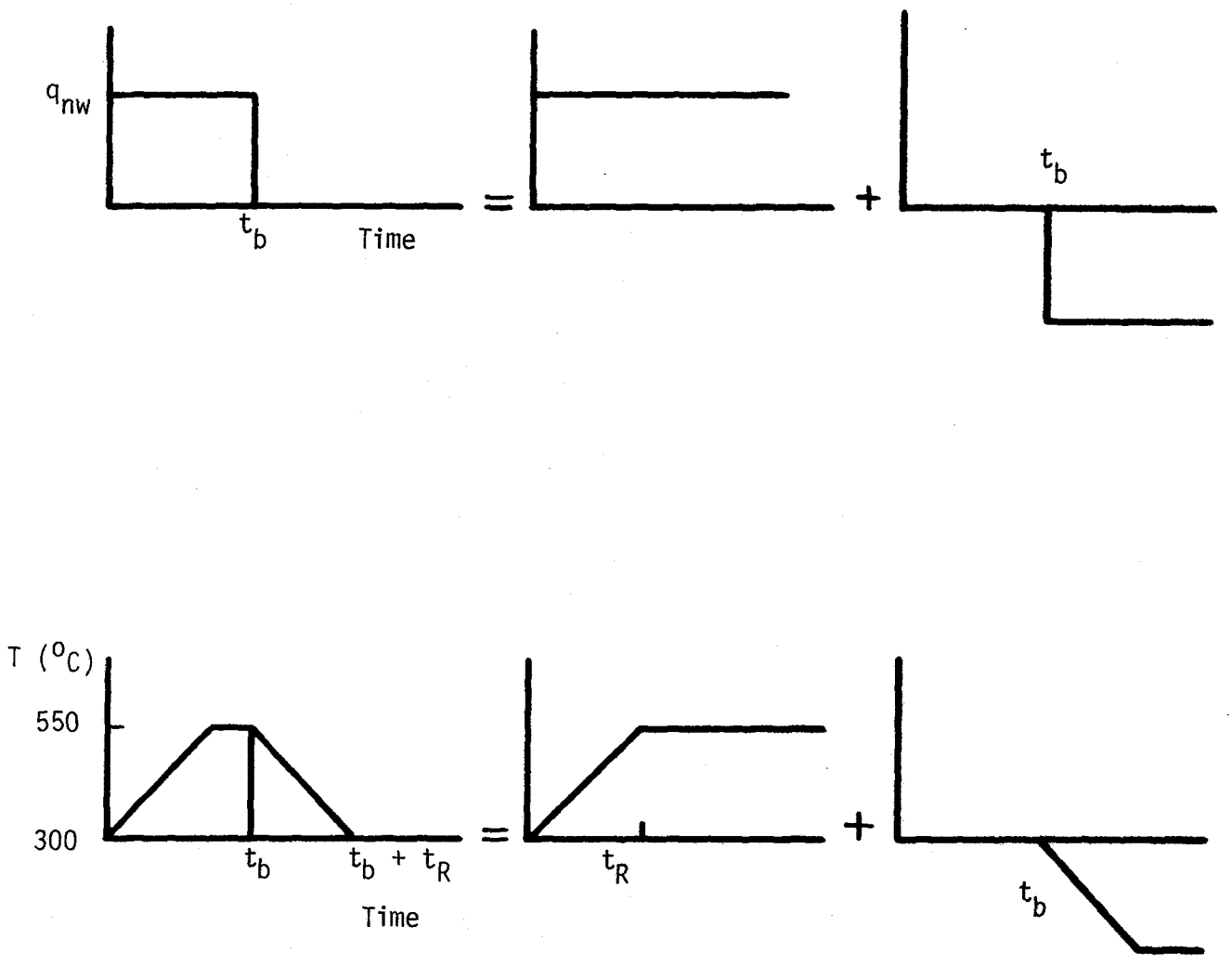

Figure 6.2.2-14 Principle of superposition and blanket thermal response to one pulse.

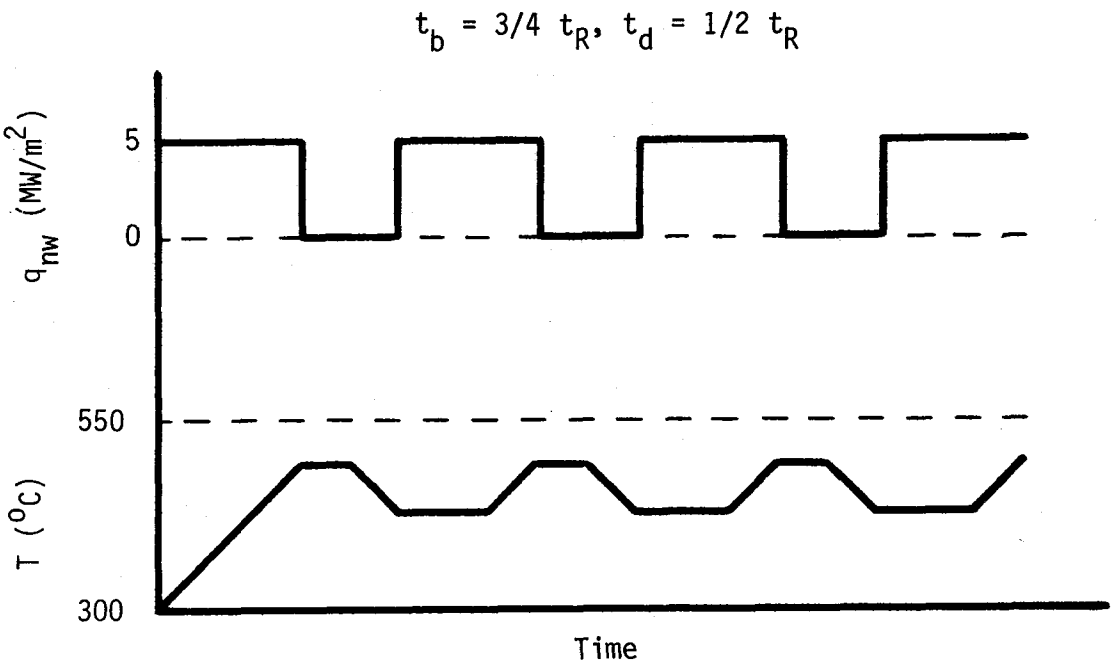

Figure 6.2.2-15 Coolant thermal response to a pulsed neutron wall load.

References for Section 6.2.2

1. "Blanket Comparison and Selection Study ," Argonne National Laboratory, ANL/FPP-83-1, 1983.

2. J.P. Hartnett and T.F. Irvine, AICHE Journal, 3, 313, 1957.

3. W.M. Kays, "Convective Heat and Mass Transfer," McGraw-Hill Company, New York, 1966.

4. W.M. Rohsenow and J.P. Hartnett, "Handbook of Heat Transfer," McGraw-Hill Book Company, New York, 7-147, 1973.

5. E.R.G. Eckert and R.M. Drake, Jr., "Analysis of Heat and Mass Transfer," McGraw Hill Book Company, New York, 1972.

6. R.A. Gardner and P.S. Lykoudis, "Magneto-fluid-mechanic Pipe Flow in a Transverse Magnetic Field. Part 1. Isothermal Flow," J. Fluid Mech., 47 (4), 737, 1971.

7. H. Branover and P. Gershon, "Experimental Investigation of the Origin of Residual Disturbances in Turbulent MHD Flows after Laminarization," J. Fluid Mech., 94 (4), 629, 1979.

6.2.3 Corrosion

6.2.3.1 Overview

Corrosion in liquid metal blankets has been identified as a critical technical issue in the development of liquid metal blanket technology.[1] The problems of corrosion include (1) transport and deposition of activated corrosion products to other subsystems (heat exchangers, piping, etc.), (2) redeposition of (activated) corrosion products in the heat exchanger and other cold parts of the primary cooling system, and (3) physical thinning and materials damage to load bearing structural material. For these reasons, corrosion is a critical phenomenon which must be considered for interactive testing of fusion blanket technology.

6.2.3.2 Corrosion Mechanisms and Processes

Liquid metal corrosion mechanisms are near-surface interactions by which the physical characteristics of a structural interface are altered by a chemical reaction with and/or through a liquid metal environment.

In general, corrosion is a stepwise process in which the reactants of chemical reactions are first transported to a solid/liquid interface. Next, the corrosion reactions occur at the interface, and then in the last step the products of the reactions are transported away from the interface. These steps are coupled in series and constitute a "resistance" to mass transfer, as shown in Figure 6.2.3-1. The rate of physical transport of the reactants to the interface is determined by a diffusive/convective process (resistance R_D). The rate of the chemical reaction is governed by a chemical kinetic process (resistance R_K).

Two basic types of corrosion reactions occur simultaneously in liquid metal systems: atomic dissolution and impurity reactions. In atomic dissolution, the structural constituents enter the liquid metal from the solid liquid interface without reacting with other atoms in the liquid metal. The reaction for atomic dissolution is given by

$$S_{(SOLID)} \rightleftarrows S_{(LM)} \qquad (6.2.3\text{-}1)$$

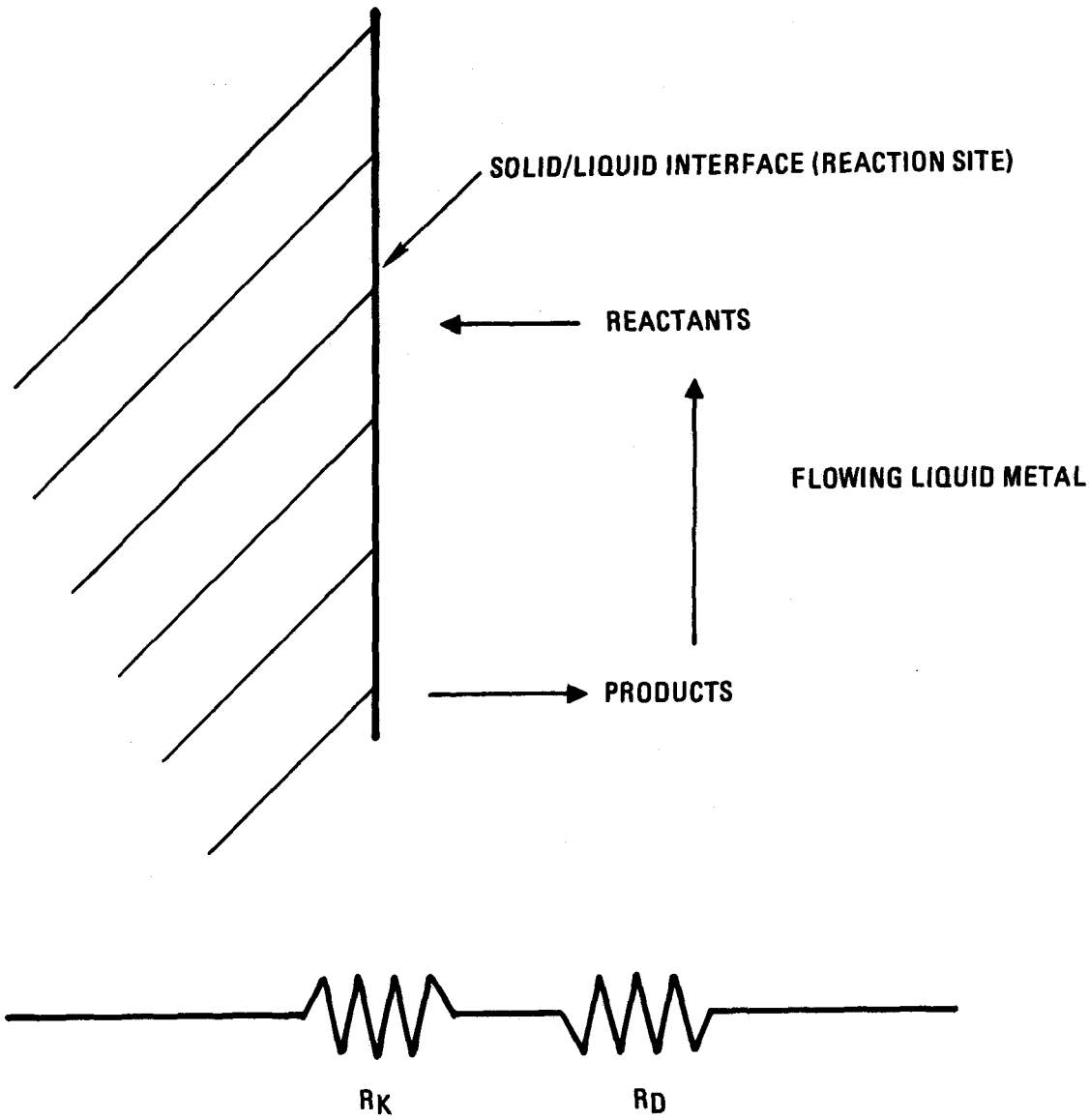

Figure 6.2.3-1 Schematic diagram of liquid metal corrosion.

where S is the structural element and subscript (LM) denotes elemental solution in a liquid metal. The mass transfer is driven by the difference in constituent solubility at the interface and the concentration in the liquid metal environment. In addition, the chemical solubility of the constituents depends on system temperatures; therefore, the presence of temperature gradients can enhance or hinder the mass transfer.

Interalloying is an interesting by-product of atomic dissolution. Structural species dissolved in one section of the system loop may be transported via the liquid metal coolant to another section where the local structure and foreign metal species combine or alloy. The degree of interalloying is highly dependent on the particular system temperature distribution and composition. Ammon[2] gives a fairly complete description of the interalloying process.

The interaction of interstitial impurities (impurity reactions) such as oxygen, nitrogen and carbon, from the coolant or structure with the structure has been found to be the major source of material degradation in some liquid metal systems.[2] Impurities can enter the system either from the liquid metal or from the structural alloys themselves. These so-called impurities can react at the interface to form complex intermetallic compounds. A sample reaction is given by

$$S_{(SOLID)} + I_{(LM)} \rightleftarrows SI_{(SOLID \text{ or } LM)} \qquad (6.2.3\text{-}2)$$

where S is the structural element and I is the impurity element. These product compounds are either highly soluble or adhere loosely to the surface and tend to easily dissolve or spall off into the coolant, thus enhancing the corrosion rate. The degree of the reaction and the importance of impurities are temperature dependent and become more important at elevated temperatures.

Unlike atomic dissolution, impurity reactions require the presence of "foreign" species other than coolant and structure in order to occur. The level of impurities will depend on the specific alloys used in and out of the blanket, the presence of a coolant purity control system, and the system temperature distribution in and out of the blanket.

The kinetics of the dissolutive reaction are simpler and better understood than those of the more complex impurity reactions. In some cases the actual complex corrosion products and reaction kinetics are not known. For

most dissolutive reactions, the products are known, but for some alloys, particularly vanadium, even dissolutive reaction kinetics data are scarce.

Once formed, corrosion products from either dissolution or impurity reactions must diffuse through the concentration boundary layer to the free stream. Uncertainty exists in the diffusive/convective transport of species between the bulk fluid and the interface. These uncertainties are due primarily to incomplete information and understanding of the local velocity profiles in and out of magnetic fields, and transport properties of the species and liquid metals.

Unknown interactions include the direct impact of magnetic field, induced electric currents and out of blanket constituents on the overall corrosion process.

The relative importance of each mechanism, dissolution or impurity interaction described is system specific. Austenitic stainless steels are dominated by dissolution mechanisms. Vanadium and its alloys are primarily limited by impurity interactions. Ferritic stainless steels seem to be somewhere between dissolution dominant and impurity dominant in nature.

6.2.3.3 Corrosion Modeling

Due to the lack of information regarding impurity reactions, corrosion modeling to date has centered around the dissolutive type of interfacial reaction. Further, modeling of the diffusive/convective step has concentrated on the understanding of the convective side resistance to mass transfer by assuming the interface is locally saturated (i.e. reaction (6.2.3-1) goes to completion) at the interface temperature. The assumption of local saturation is more valid for laminarized flow, such as that inside the magnetic field, than for fully turbulent flow, such as would be expected outside of the magnetic field in an intermediate heat exchanger, because the diffusive transport is controlling the mass transfer rate.

Corrosion data for most structural materials is available from out-of-field tests.[1] Little or no data exists for liquid metal structural corrosion in a magnetic field.

By assuming local saturation, the following calculations of dissolutive corrosion are admittedly pessimistic. However, the purpose of the modeling is

to determine scaling relationships which can be used to set test requirements for act-alike corrosion behavior and not to try to predict the absolute corrosion rate. By carefully exercizing simple models, it is possible to assess the impact of varying several test parameters on corrosion behavior.

6.2.3.4 Details of the Model

Figure 6.2.3-2 shows a sketch of the simple circular channel geometry used for modeling dissolution corrosion. In addition to the local interface saturation mentioned above, the following has been assumed: (1) Fully-developed laminarized velocity profiles, (2) Radially flat temperature profiles, (3) Linear axial temperature profile (constant heat flux), (4) Perfect cold trapping prior to inlet (zero inlet concentration), (5) Single species dissolution (iron in lithium coolant).

Assumption (1) is good for MARS and other designs that flow liquid metals across magnetic fields (excluding entrances regions), but may be poor for the BCSS toroidal/poloidal flow concept or for other designs that flow parallel to the magnetic field. The worst corrosion/deposition problems probably occur at the entrances and exits, where momentum, concentration and temperature boundary layers are thin or temperatures are high. Further work will be required to assess these complex effects. Assumptions (4) and (5) are probably the least valid of the list and will lead to errors in the prediction of corrosion rates. We anticipate that there will be some non-zero inlet concentration at the entrance to the hot region of the blanket. This inlet stream will contain species and impurities from the entire heat transport loop and these constituents will undergo diffusive/convective transport to and from the interface with possible interalloying or other reaction at the interface.

With these assumptions in mind, we can write the following set of governing equation, boundary and inlet conditions:

$$\frac{1}{r}\frac{\partial}{\partial r}\left(r\frac{\partial X}{\partial r}\right) = \frac{u(r)}{D_{12}}\frac{\partial X}{\partial z} \qquad (6.2.3\text{-}3)$$

Boundary Conditions:

$$r = a, \quad X = X_w(T_w) \qquad (6.2.3\text{-}4)$$

$$r = 0, \quad \frac{\partial X}{\partial r} = 0 \qquad (6.2.3\text{-}5)$$

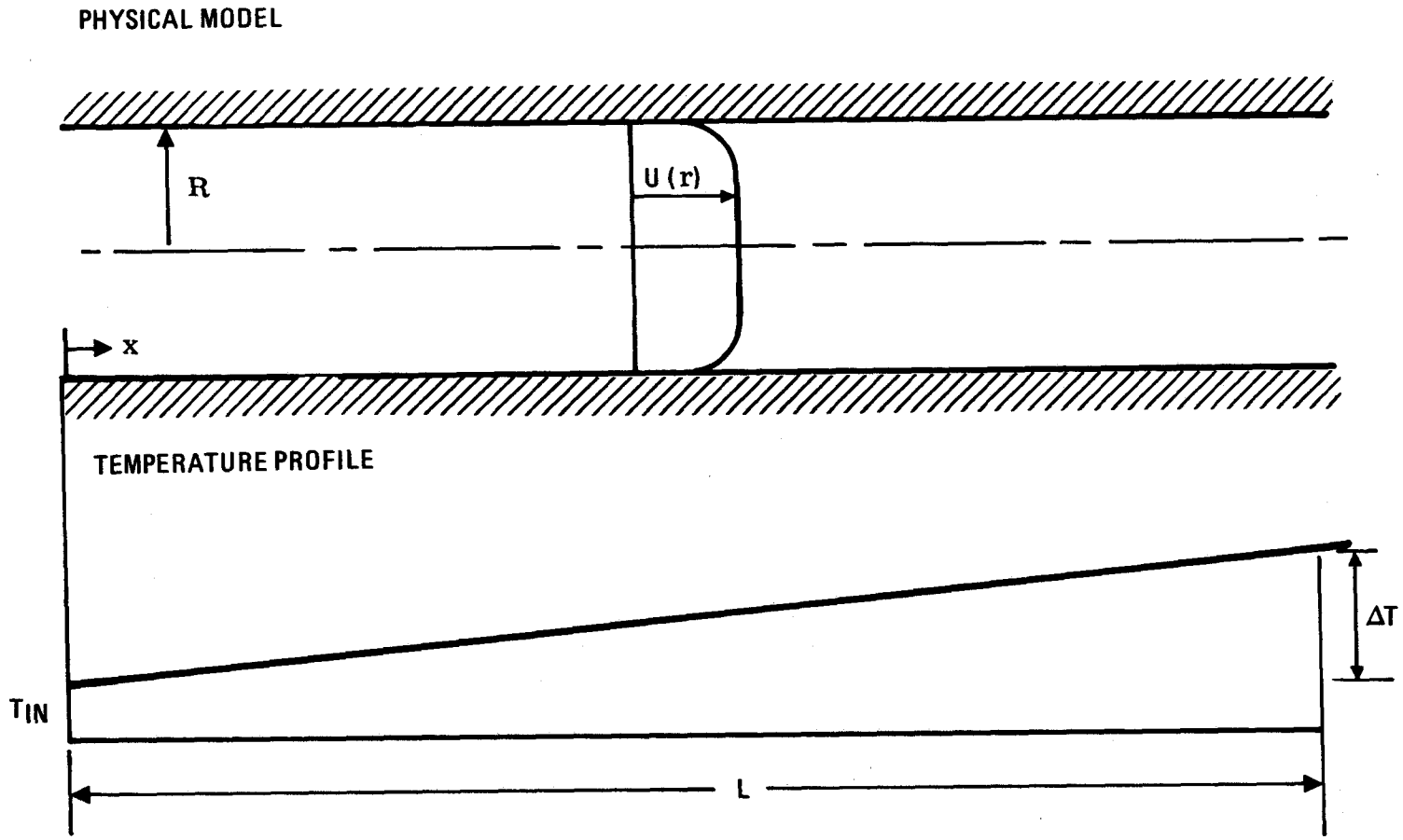

Figure 6.2.3-2 Sketch of channel geometry and temperature profile.

Initial

Condition: $z = 0, \quad X(r) = X_{inlet} = 0$ (6.2.3-6)

$$\frac{u(r)}{U_b} = f(r) \tag{6.2.3-7}$$

Where,

X = weight fraction of dissolved corrosion product (dimensionless)

z = axial coordinate (m)

L = channel length (m)

r = radial coordinate (m)

R = channel radius (m)

T_w = local temperature (K)

D_{12} = mass diffusion coefficient of species 1 in medium 2 (m^2/s)

$f(r)$ = velocity profile function (dimensionless)

U_b = bulk averaged velocity (m/s)

The species mass flux is proportional to the concentration gradient (corrosion rate) at the wall and is given by

$$j = -\rho D_{12} \left.\frac{\partial X}{\partial r}\right|_{r=a} \tag{6.2.3-8}$$

For arbitrary velocity profiles and wall temperatures, the mass transfer equation is most easily solved numerically. A finite difference code developed by Bjorndahl and Gordon[3] was used to solve for the axial and radial concentration and axial corrosion rate profiles.

Figure 6.2.3-3 shows examples of the computer-predicted concentration profiles 10 cm downstream from the inlet of a 400 °C isothermal duct using two different models for the diffusion coefficient and for various Hartmann numbers, as described below.

6.2.3.5 Results of Parametric Variations

Thus far, the effect of four system parameters, velocity profile, diffusion coefficient uncertainty, axial temperature increase and system fluid residence time, have been investigated using the model described above.

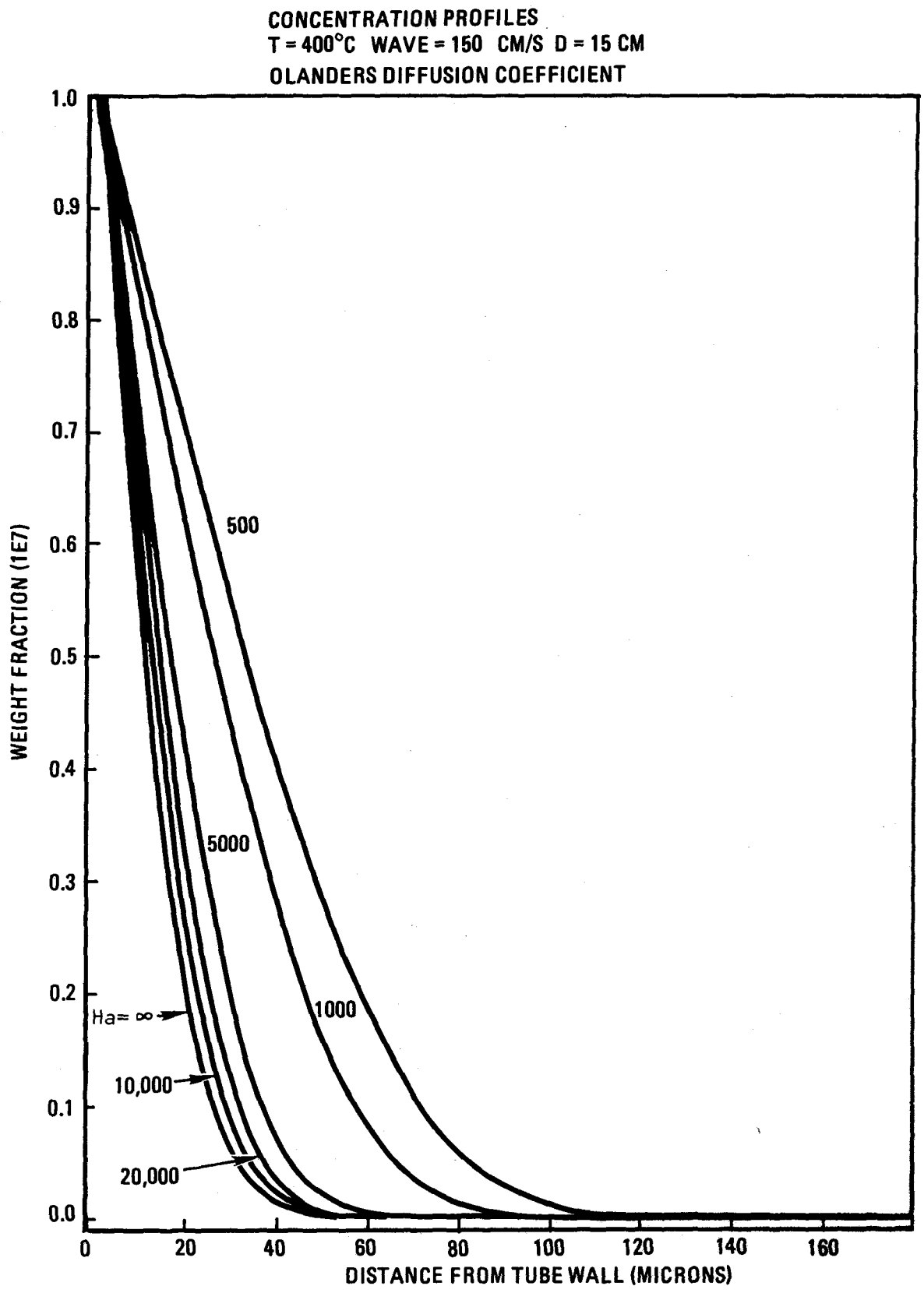

Figure 6.2.3-3 Sample output concentration profiles for isothermal channels.

Velocity Profile and Diffusion Coefficient Uncertainty

The species mass flux or corrosion rate is a strong function of the velocity profile, which can be seen via Reynolds' Analogy for momentum and mass transfer[4] or the governing equation 6.2.3-3.

The nature of the liquid metal velocity profiles that will be present in the blanket of a magnetically confinement fusion reactor are not fully understood. Flow laminarization is currently anticipated. The Hartmann velocity profile at high Hartmann number is given by

$$f(r) = \left(1 - e^{-H(\frac{r}{a} - 1)}\right) \qquad (6.2.3\text{-}9)$$

where

H = Hartmann number = $aB_o\sqrt{\sigma_e/\mu}$

B_o = magnetic field strength

σ_e = electrical conductivity of fluid

μ = viscosity of fluid

The Hartmann number is the dimensionless parameter relating the ratio of magnetic to viscous forces in the fluid. Typical reactor Hartmann numbers are on the order of 20,000. This solution for the velocity distribution is valid for flow of a conducting fluid in a uniform transverse magnetic field along a diameter of the tube parallel to the magnetic field.[5] The complete 2-dimensional velocity distribution in a circular channel is actually much more complicated than this.

Figure 6.2.3-4 shows typical radial Hartmann velocity profiles close to the wall for Hartmann numbers between 500 and ∞. An infinite Hartmann number corresponds to a flat velocity profile.

Diffusion coefficient data for lithium are scarce. It was necessary to estimate the mass diffusivity from available sodium data[6,7] and the Stokes Einstein theoretical model.[8]

The computer predictions indicate that there is a critical Hartmann number, H_c, which defines corrosion regimes in this model. The critical Hartmann number is defined by the ratio of velocity profile and mass diffusion length scales as,

$$\ell_H/\ell_D = \frac{a/H}{\sqrt{DL/U}} = 1 \qquad (6.2.3\text{-}10)$$

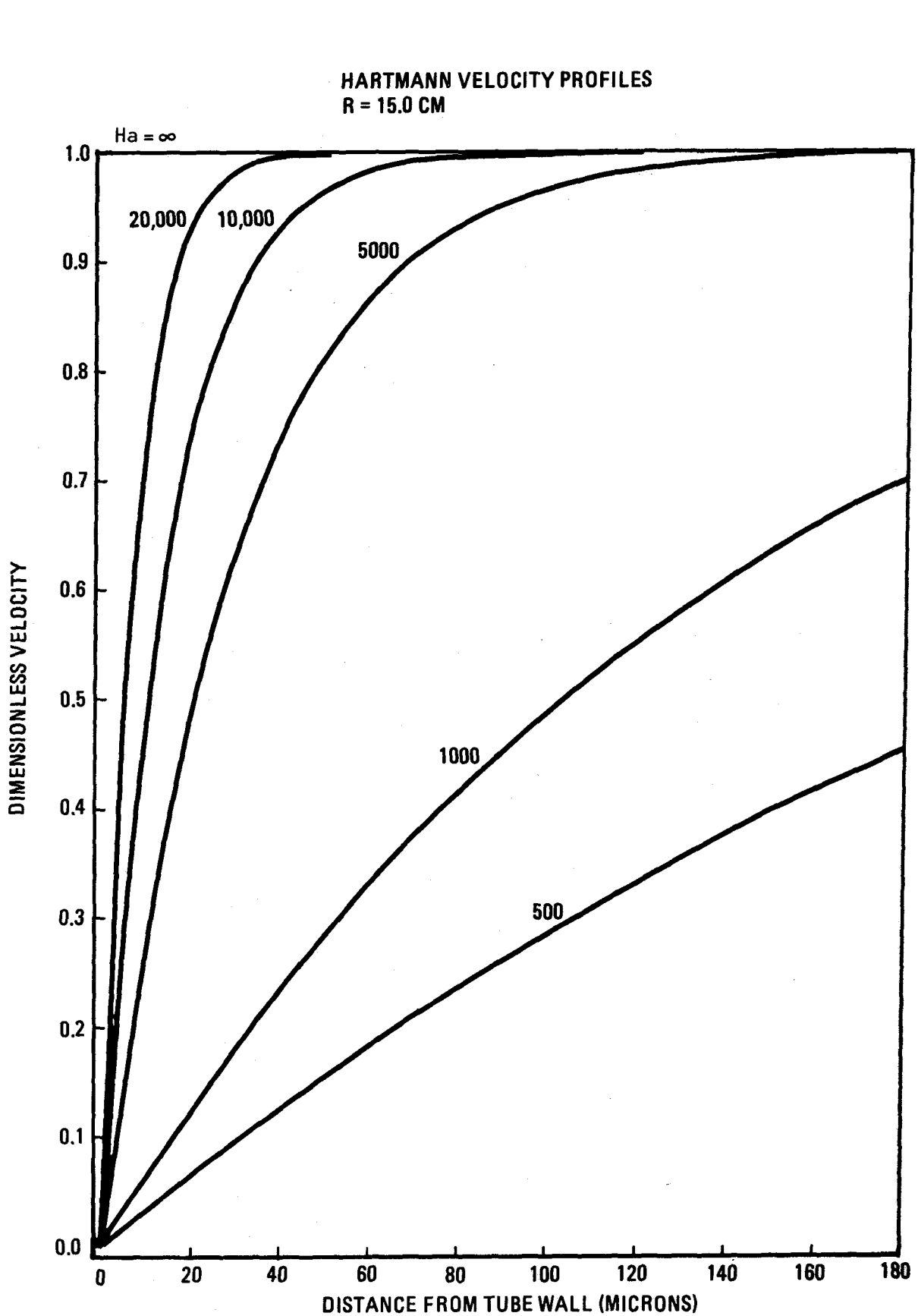

Figure 6.2.3-4 Sample Hartmann velocity profile near wall of channel.

where

ℓ_H = Characteristic length of velocity profile = a/H

ℓ_D = Characteristic length of concentration profile = $\sqrt{D_{12}L/U_b}$

a = Radius of channel

L = Channel length

U = Average velocity in channel.

Figure 6.2.3-5 shows a sample plot of equation 6.2.3-10 for both models of diffusion coefficient and the corresponding critical Hartmann numbers.

The corrosion rates, normalized to the corrosion rate for infinite Hartmann number, for both estimates of diffusivity are shown in Figure 6.3.3-1 (of the next section) as a function of Hartmann number. Three regimes appear to exist:

1. Low Hartmann Number ($H/H_c \ll 1$): In this regime, the concentration boundary layer is much thinner than the momentum boundary layer. The molecular diffusivity imposes a lower limit on the corrosion process.

2. Critical Hartmann Number ($H/H_c = 1$): The corrosion rate increases sharply to thinning of the momentum boundary layer with increasing Hartmann number while the concentration boundary layer remains essentially constant.

3. High Hartmann Number ($H/H_c \gg 1$): Further increases in Hartmann number do not increase the corrosion rate as the convective mechanism saturates. Saturation occurs when the velocity profile is constant throughout most of the concentration boundary layer.

Axial Temperature Increase

The increase of interfacial and free stream solubilities with increasing system temperature will alter the corrosion behavior of a heated channel from that of an isothermal one. For an isothermal channel, the mass transfer coefficient decreases monotonically with channel length as the concentration profile near the wall begins to build up (saturate). In a non-isothermal channel, the concentration at the wall increases as the temperature at the wall increases, and it is more difficult for the mechanism to saturate.

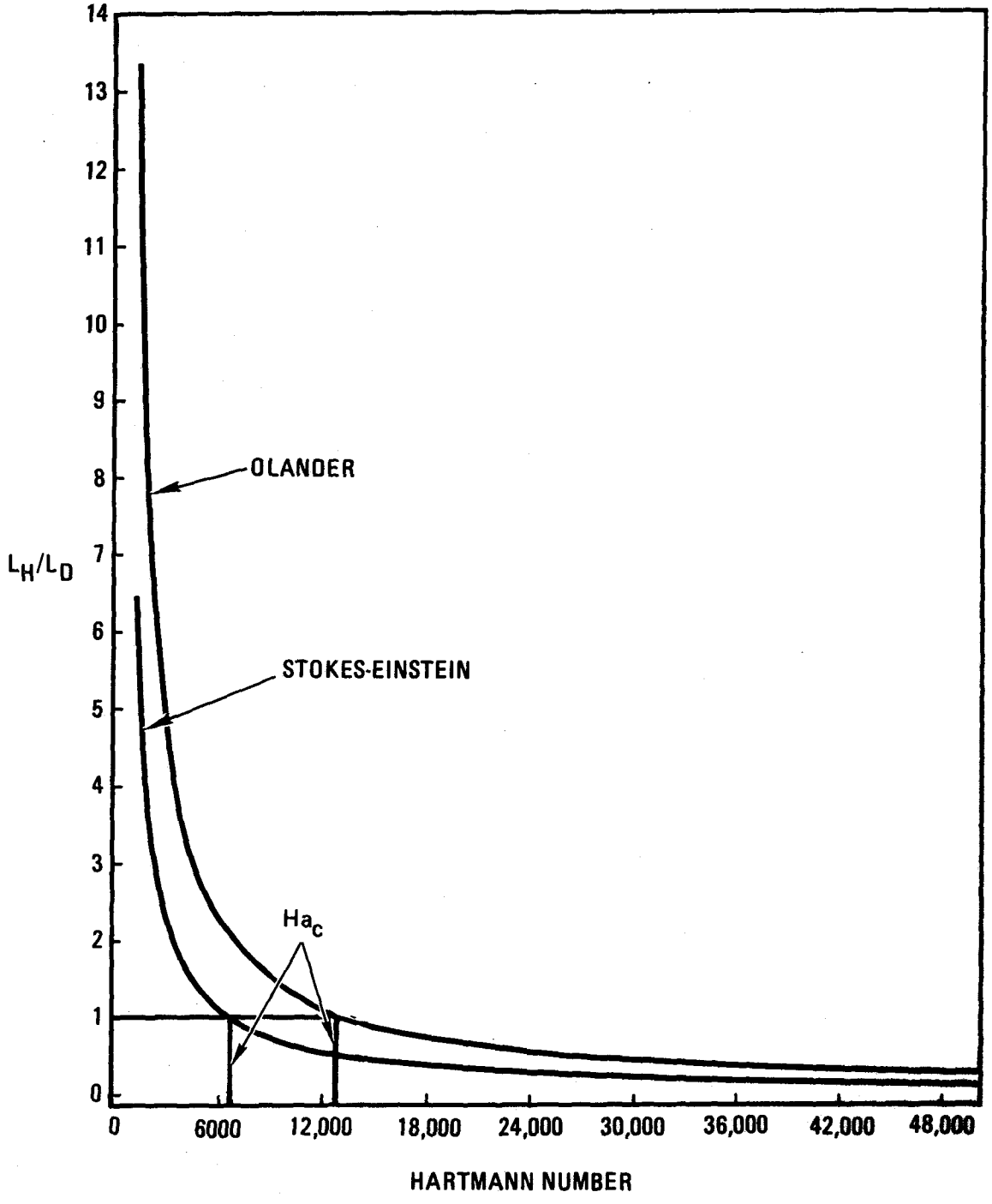

Figure 6.2.3-5 Ratio of Hartmann to diffusion length scales.

The effects of a linearly increasing axial channel temperature profile (constant heat addition along the channel) preserving either constant average or outlet temperature were studied. Sample results are shown in Figures 6.2.3-6 and 6.2.3-7.

The model indicates that an axial temperature gradient has a significant effect on the axial corrosion rate profile compared to an isothermal channel. Further, the behavior depends on whether the average or outlet temperature is maintained. The outlet temperature in most blanket designs is currently considered corrosion limited.[1] The allowable channel temperature rise will be restricted at the inlet by the melting point of the liquid metal coolant used and at the outlet by the material deposition rate in the secondary heat exchangers.

Fluid Residence Time

The channel residence time, as defined above, is the average time a "fluid packet" spends residing in the channel. Calculations indicate that similar corrosion behavior can be obtained by maintaining the channel residence time between two channels. If residence time scaling is valid, it would allow valid corrosion behavior testing in shorter test modules at reduced flow rates and capital expenditure. Figure 6.3.3-2 (of the next section) shows the predicted corrosion rate profile for two isothermal channels with the same residence time ($L_1/V_1 = L_z/V_z$). The two curves coincide if the abscissa is rescaled as z/L instead of z. This indicates that within the assumptions of the diffusive/convective model, residence time scaling is valid.

6.2.3.6 Conclusions

A liquid metal fusion reactor blanket will be a complicated, multi-dimensional mechanical/chemical/nuclear system. To claim complete knowledge of the corrosion and mass transport in such a system would be naive. However, trends and parameters can be identified that will be important. The analysis above has concentrated on a description of corrosion mechanisms and results from a dissolution model for liquid metal corrosion. Sample results have been presented for each of the parameters investigated to date--Hartmann velocity profiles, diffusion coefficient uncertainty, axial temperature increase and fluid residence time. The impact of these results on test requirements is given in Section 6.3.3.

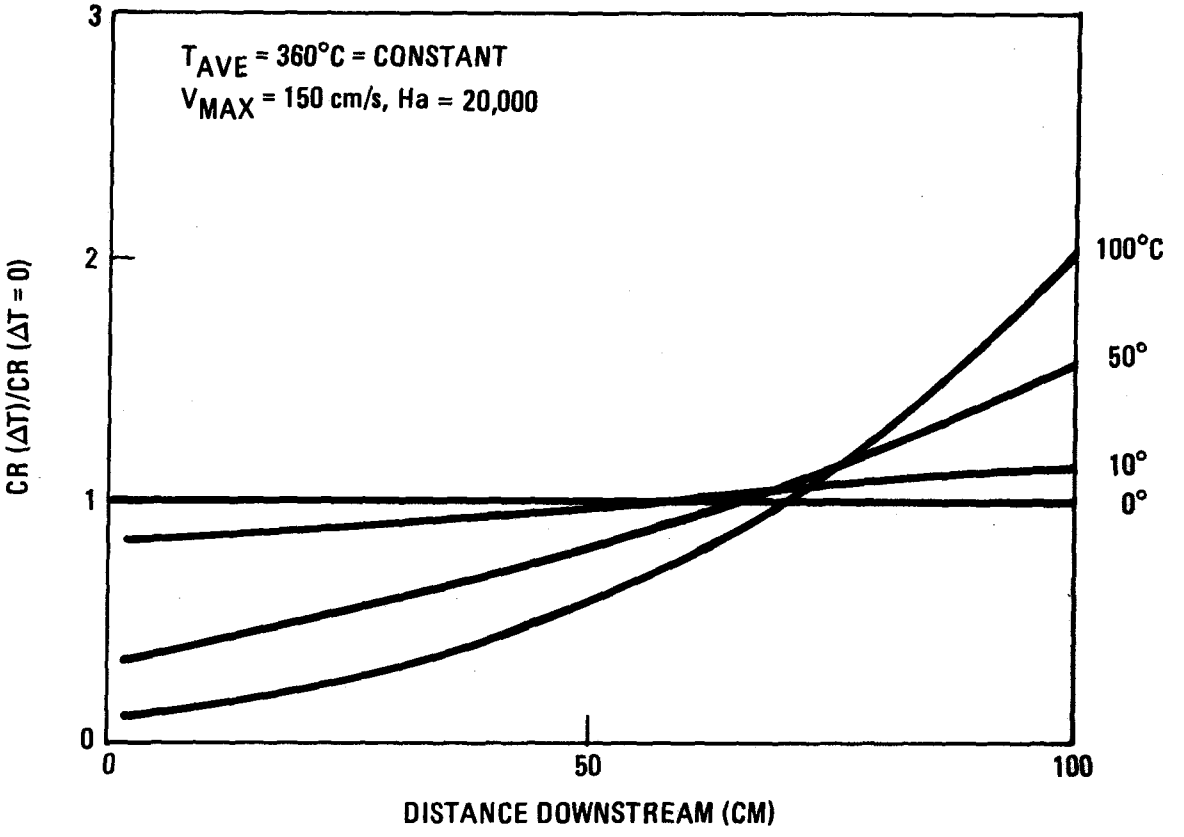

Figure 6.2.3-6 Effect of axial temperature increase on corrosion rate - constant average channel temperature.

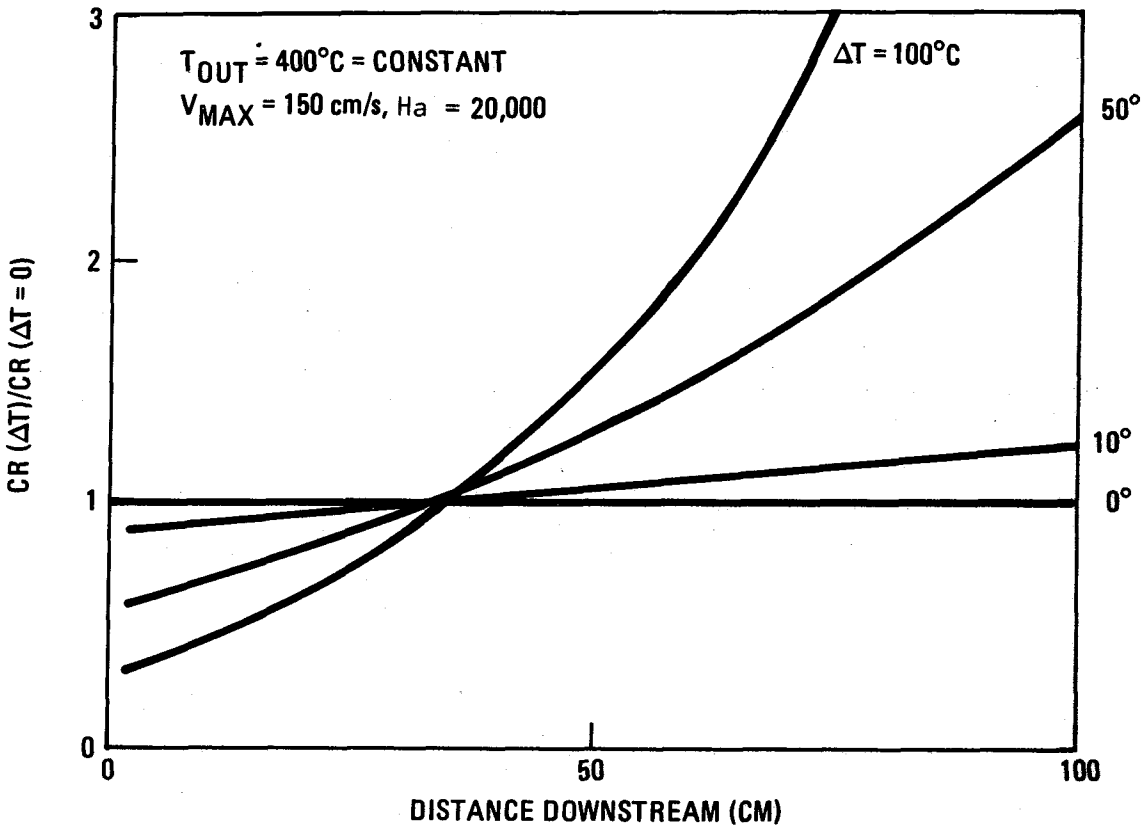

Figure 6.2.3-7 Effect of axial temperature increase on corrosion rate - constant channel outlet temperature.

References for Section 6.2.3

1. M. A. Abdou, et al., "Blanket Comparison and Selection Study," Argonne National Laboratory, ANL/FPP-83-1 (1983).

2. R. L. Ammon, "Vanadium and Vanadium-Alloy Compatibility Behavior with Lithium and Sodium at Elevated Temperatures," International Metals Review, 25, 255-268 (1980).

3. W. D. Bjorndahl and J. Gordon, "MHD Effects on Liquid-Metal Corrosion Product Transfer," Transactions of the American Nuclear Society, New Orleans, 46, LA, June 3-7, 1984.

4. W. M. Kays and M. E. Crawford, Convective Heat and Mass Transfer, 2nd Edition, McGraw-Hill Book Company, San Francisco (1980).

5. J. A. Shercliff, "Magnetohydrodynamic Pipe Flow, Part 2. High Hartmann Number," J. Fluid Mechanics, 13, 513-517 (1962).

6. D. R. Olander, Fundamental Aspects of Nuclear Reactor Fuel Elements, NTIS, Springfield, Virginia (1976).

7. P. F. Tortorelli and J. H. DeVan, "Thermal-Gradient Mass Transfer in Lithium-Stainless Steel Systems," J. Nuclear Materials, 85-86, 289-293 (1979).

8. R. B. Bird, W. E. Stewart, E. N. Lightfoot, Transport Phenomena, John Wiley and Sons, New York (1960).

9. H. R. Konvicka and P. R. Sattler, "LILO-1 -- A Thermoconvection Loop for Studying the Behavior of Stainless Steel Exposed to Liquid Lithium," J. Nuclear Materials, 122-123, 1241-1242 (1984).

6.2.4. Structural Mechanics

6.2.4.1 Overview

A key to the successful design of a fusion blanket is the distribution of the amount of structural material in the first wall of the blanket. The first wall must support dynamic and static mechanical loads and at the same time sustain the thermal gradients and erosion resulting from the plasma heat and particle fluxes. Dynamic and static loads require high flexural rigidity. The most efficient way of increasing rigidity in the first wall region would be to increase the height of the first wall channel, but this dimension is constrained by thermal hydraulics (increasing the height would increase the volumetric flow rate or require decreasing velocity) and possibly by MHD flow profile considerations. Since the first wall temperature is proportional to the thickness of the first wall, thermal stresses require thin first walls, while thick walls are necessary to account for erosion and corrosion. A feasible design must represent an optimal solution satisfying many conflicting requirements.

The structural design of the blanket must not only withstand the steady state operating conditions, but must also meet cyclic conditions due to start-up, shut-down, and pulsed operation. Fatigue of the first wall, crack propagation under cyclic load, and residual stress build-up are the most important issues related to repetitive loading conditions. Another problem arising from the time history of the loads is thermal shock due to power ramps. One also has to consider off-normal situations such as loss of pressure and loss of coolant flow.

Throughout its life, the blanket will be subjected to a radiation environment causing radiation induced creep, swelling, and embrittlement. The relative importance of each of these interactive phenomena depends on the structural material and the design. Although creep has a tendency to relieve high stresses due to thermal gradients, it can cause large displacements which will ultimately lead to failure. Under axially restrained conditions, creep buckling and high stresses due to swelling may be important. The irradiation environment causes an increase in the yield stress and a significant loss of ductility. As a result of these changes, the structure is more likely to fail

by brittle fracture. Satisfactory structural design requires that all the operating conditions and changes in materials properties be allowed for without loss of structural integrity of the system.

The poloidal/toroidal flow lithium cooled tokamak blanket from BCSS and the MARS blanket were selected as reference designs (see Figs. 6.1-1 and 6.1-2, and Appendix D.3). Consequently, the results of the structural analysis are specific to these particular designs, although the scaling relations derived from them have general significance. Section 6.2.4.2 discusses the analysis of the BCSS design and Section 6.2.4.3 discusses the MARS design.

6.2.4.2 Structural Analysis of the Lithium Cooled Tokamak Blanket

Model and Assumptions

To address some of the issues described above and gain some insight into scaling, a model based on technical beam theory and small scale plastic behavior due to creep was developed. The structure is modeled as an assembly of Euler-Bernoulli I-beams. Movement of the shaded surfaces in Fig. 6.2.4-1 is constrained in rotation and in the Z direction in the structure due to symmetry, while these are free edges in the I-beam model. Since the maximum stiffness of the composite plate structure in bending occurs along the axis of the web (e.g., the plate is most stiff in bending about the Z axis), the I-beam model results in a good approximation of the first wall structure.

The composite first wall is supported periodically by the sides of the poloidal coolant channels (see Fig. 6.2.4-1) There is no rotation or transverse translation at these supports due to symmetry. Consequently, built-in conditions are assumed at the ends of the I-beams. It is further assumed that the module is free to extend in the toroidal direction and, thus, the beam ends are unconstrained in the x direction.

The constitutive equation is:

$$\sigma_{xx} = E(\varepsilon_{xx} - \alpha\Delta T - \varepsilon_c) \qquad (6.2.4\text{-}1)$$

where:

σ_{xx} = stress in the x direction

ε_{xx} = total strain in the x direction

E = Young's modulus

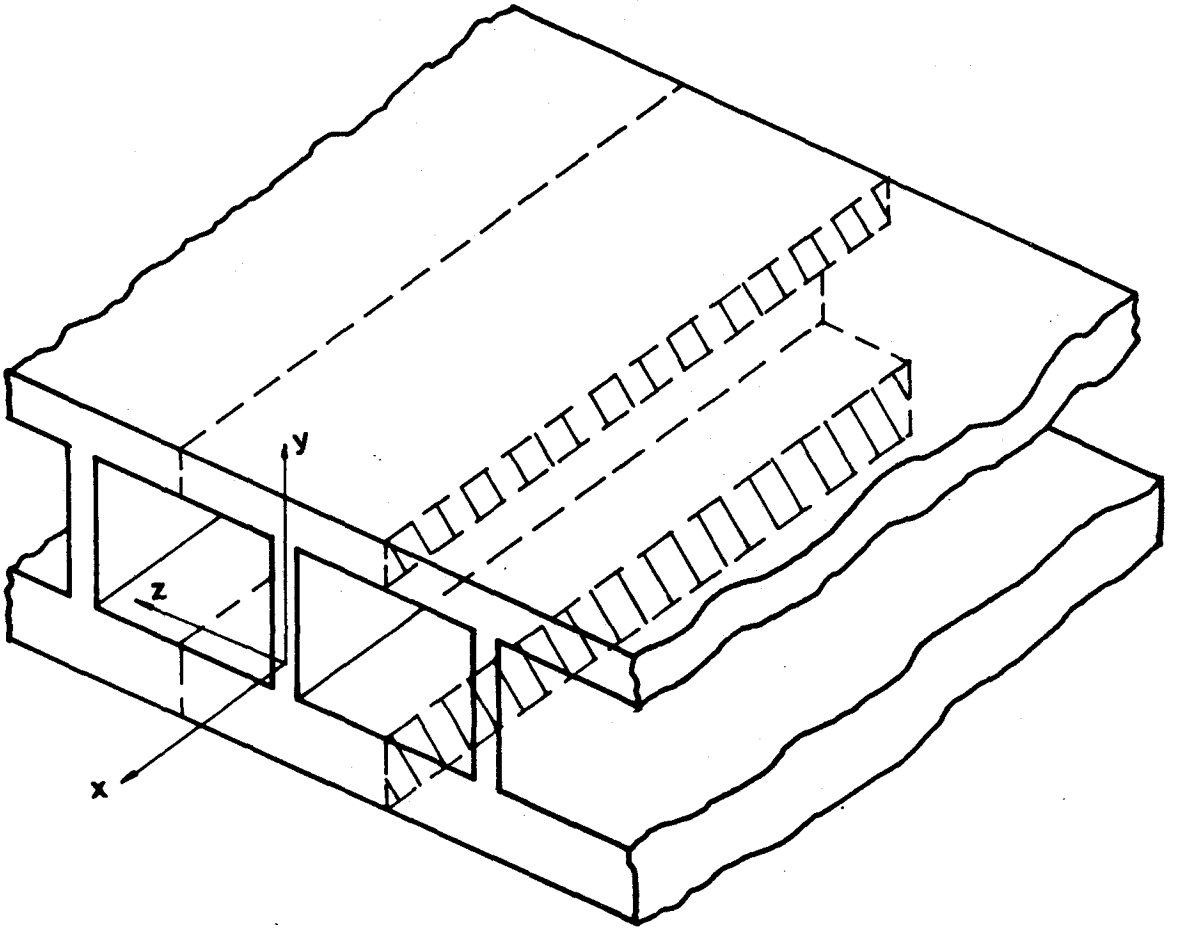

Figure 6.2.4-1. I-Beam model.

α = coefficient of thermal expansion

ΔT = temperature difference from a base temperature

ε_c = irradiation creep strain

The creep law for irradiation creep is taken as:

$$\dot{\varepsilon}_c = B\,|\sigma|^n \text{ sign } (\sigma)\ \phi\eta(y) \qquad (6.2.4\text{-}2)$$

where:

B = creep coefficient

n = creep exponent

$\sigma\eta(y)$ = neutron damage

Further assumptions are that E, α, B and n are constants and that the load is applied as a step function.

Solution Method

The first step in the solution is to assume the displacement field:

$$u(x,y,z) = f_o(x) + yf_1(x) + zf_2(x) \qquad (6.2.4\text{-}3)$$

Then the strain field is

$$\varepsilon_{xx} = f_o'(x) + yf_1'(x) + zf_2'(x) \qquad (6.2.4\text{-}4)$$

Next the creep strain is given by discretizing time. The total creep strain in the i^{th} time interval is:

$$^i\varepsilon_c = {}^{i-1}\varepsilon_c + \frac{1}{2}\,\Delta\,{}^i\varepsilon_c \qquad (6.2.4\text{-}5)$$

where

$$\Delta^i\varepsilon_c = B\,|^i\sigma|^n \text{ sign}(\sigma)\ \phi\eta\Delta t \text{ and } {}^o\varepsilon_c = 0 \qquad (6.2.4\text{-}6)$$

The 1/2 factor in (5) means, that we take the average of ${}^{i}\varepsilon_c$ and ${}^{i-1}\varepsilon_c$ as the accumulated plastic strain in the i^{th} time interval. The stress in the i^{th} time interval is:

$$ {}^{i}\sigma_{xx} = E\left(\varepsilon_{xx} - \alpha\Delta T - {}^{i}\varepsilon_c\right) \qquad (6.2.4\text{-}7) $$

From the equilibrium of a cross section

$$ \int_A {}^{i}\sigma_{xx}\, dA = 0 \qquad (6.2.4\text{-}8) $$

$$ \int_A y\,{}^{i}\sigma_{xx}\, dA = M(x) \qquad (6.2.4\text{-}9) $$

Substitute (4) and (7) in (8) and (9), utilize the fact that x is the centroidal axis, y and z are principal axes. Solve for $f_o(x)$, $f_1(x)$, $f_2(x)$ and substitute them in (7) to obtain:

$$ {}^{i}\sigma_{xx} = -E\alpha\Delta T - {}^{i}\varepsilon_c E + \frac{P_T + {}^{i}P_c}{A} + \frac{M + M_T + {}^{i}M_c}{I}\, y \qquad (6.2.4\text{-}10) $$

where P_T and ${}^{i}P_c$ are equivalent axial forces due to thermal and creep strains, and M_T and ${}^{i}M_c$ are equivalent bending moments:

$$ P_T = \int_A \alpha E\Delta T dA \qquad {}^{i}P_c = \int_A E\,{}^{i}\varepsilon_c\, dA $$

$$ M_T = \int_A \alpha E\Delta T y dA \qquad {}^{i}M_c = \int_A E\,{}^{i}\varepsilon_c\, y dA \qquad (6.2.4\text{-}11) $$

From the analysis of deformation the differential equation of the deflection curve is:

$$\frac{d^2v}{dx^2} = -\frac{M + M_T + {}^{i}M_c}{EI} \qquad (6.2.4\text{-}12)$$

By assuming that $\Delta T = \Delta T(y)$ one can find the deflection:

$$EIv(x) = -(M_o + M_T)\frac{x^2}{2} - V_o\frac{x^3}{6} - q\frac{x^4}{24} + EI(c_o + c_1 x) - \int_o^x (x - \zeta)\,{}^{i}M_c(\zeta)\,d\zeta \qquad (6.2.4\text{-}13)$$

Here V_o and M_o correspond to the reaction force and moment at $x = 0$ and c_o, c_1 represent a rigid body motion. These constants are determined from the end conditions. In the middle of the module, built-in end conditions can be assumed at the supports due to symmetry, where "built-in" is given by

$$x = 0$$

$$v = 0 \quad , \quad \frac{dv}{dx} = 0$$

$$x = \ell$$

$$v = 0 \quad , \quad \frac{dv}{dx} = 0 \qquad (6.2.4\text{-}14)$$

then,

$$c_o = c_1 = 0$$

$$V_o = -\frac{q\ell}{2} - \frac{6}{\ell}\left[{}^{2}\bar{M}_c(\ell) - {}^{1}\bar{M}_c(\ell)\right]$$

$$M_o = \frac{q\ell^2}{12} - M_T + 2\,{}^{2}\bar{M}_c(\ell) - 3\,{}^{1}\bar{M}_c(\ell) \qquad (6.2.4\text{-}15)$$

where

$$\overline{M}_c^{1}(x) = \frac{2}{x^2} \int_o^x (x - \zeta)\ {}^{i}M_c(\zeta)\, d\zeta$$

$$\overline{M}_c^{2}(x) = \frac{1}{x} \int_o^x {}^{i}M_c(\zeta)\, d\zeta \qquad (6.2.4\text{-}16)$$

Scheme For Numerical Solution:

1. Calculate the elastic stress distribution as initial state and initialize the variables; define Δt, Δx, Δy, set $t = 0$, $i = 1$, ${}^{o}\varepsilon_c(x,y) = 0$, $\Delta^{o}\varepsilon_c(x,y) = 0$.
2. Add the current incremental plastic strain field to the current plastic strain field. Determine the values of V_o and M_o;

$${}^{i}\varepsilon_c(x,y) = {}^{i-1}\varepsilon_c(x,y) + \frac{1}{2}\Delta^{i}\varepsilon_c(x,y)$$

   substitute ${}^{i}\varepsilon_c(x,y)$ in Eq. (11). Substitute Eq. (11) in Eq. (16). Substitute Eq. (16) in Eq. (15). Evaluate integrals numerically.
3. Calculate ${}^{i}\sigma_{xx}(x,y,)$ from Eq. (10).
4. Calculate $\Delta^{i}\varepsilon_c(x,y)$ from the incremental form of the creep law Eq. (6).
5. If the values of the incremental strain have not converged then refine them by repeating the process from step 2.
6. Otherwise, the plastic strain field is updated and the next time step is solved.

For the results presented here, the cross section was divided into 12 partitions, and the length of the module was divided into 42 partitions to evaluate the integrals in step 2. Both partitions were refined further to check accuracy. Some representative results can be seen for the reference blanket on Figs. 6.2.4-2 through 6.2.4-6. Fig. 6.2.4-2 shows the stress profiles resulting from the elastic calculations at two locations. Fig. 6.2.4-4 and Fig. 6.2.4-5 give the stress histories due to creep at the

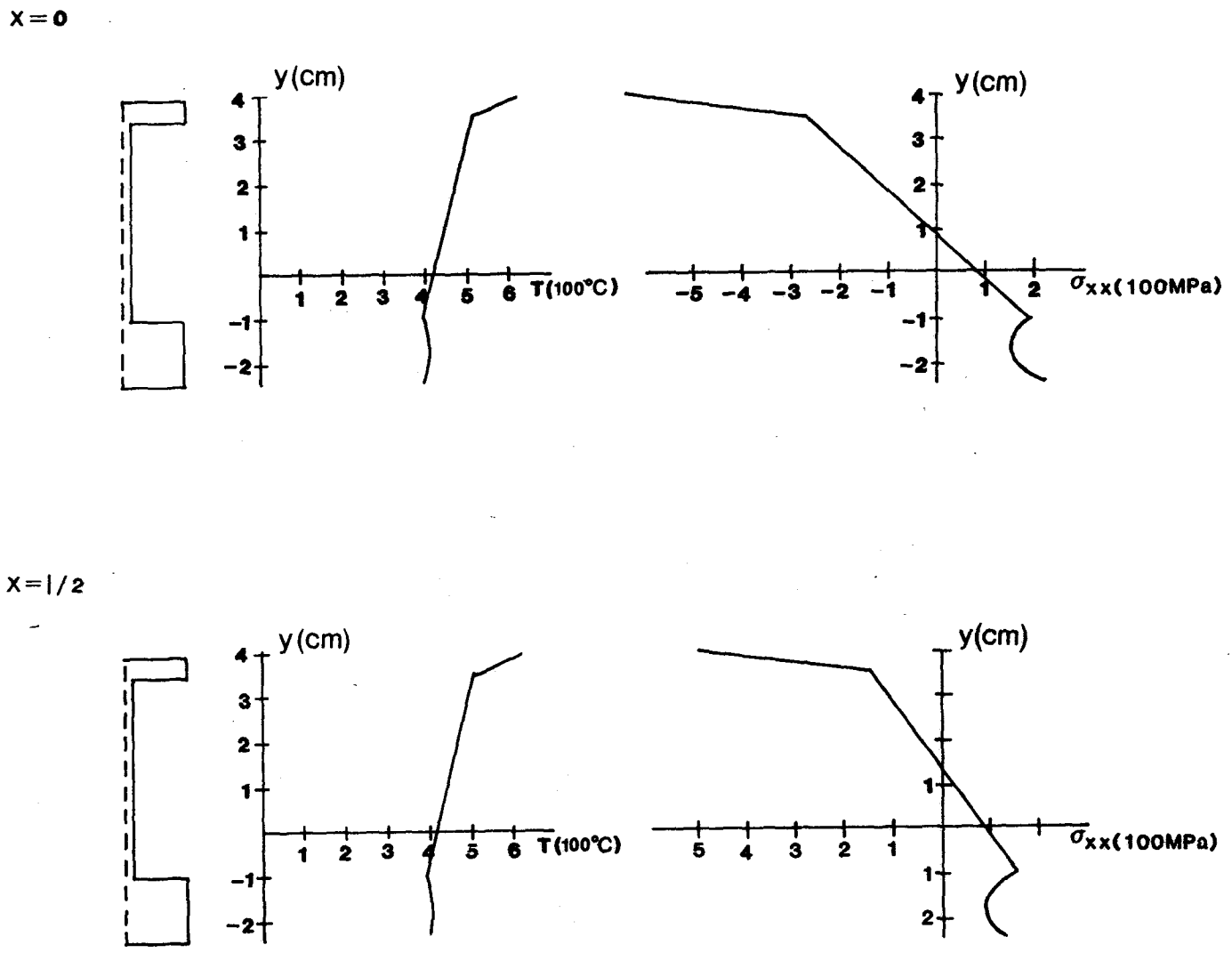

Figure 6.2.4-2. Initial stress and temperature profiles through the I-Beam.

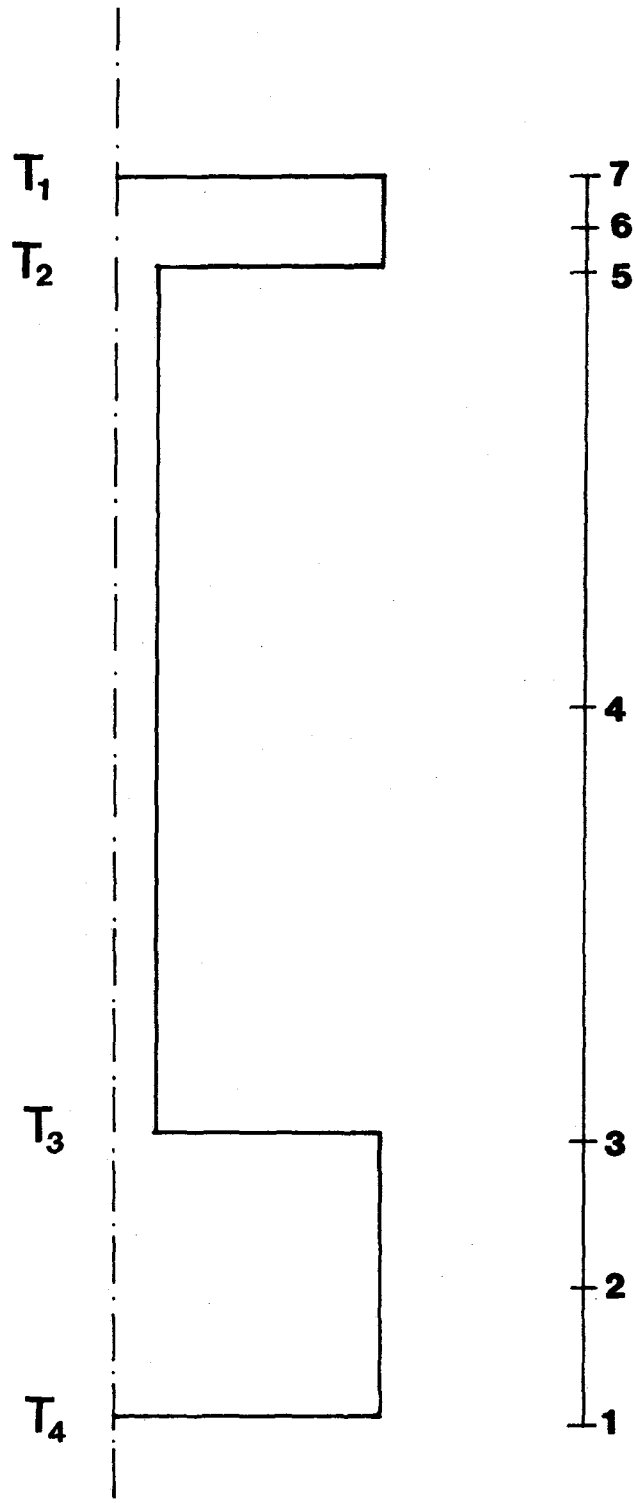

Figure 6.2.4-3. Location of points plotted in Figures 6.2.4-4 and 6.2.4-5.

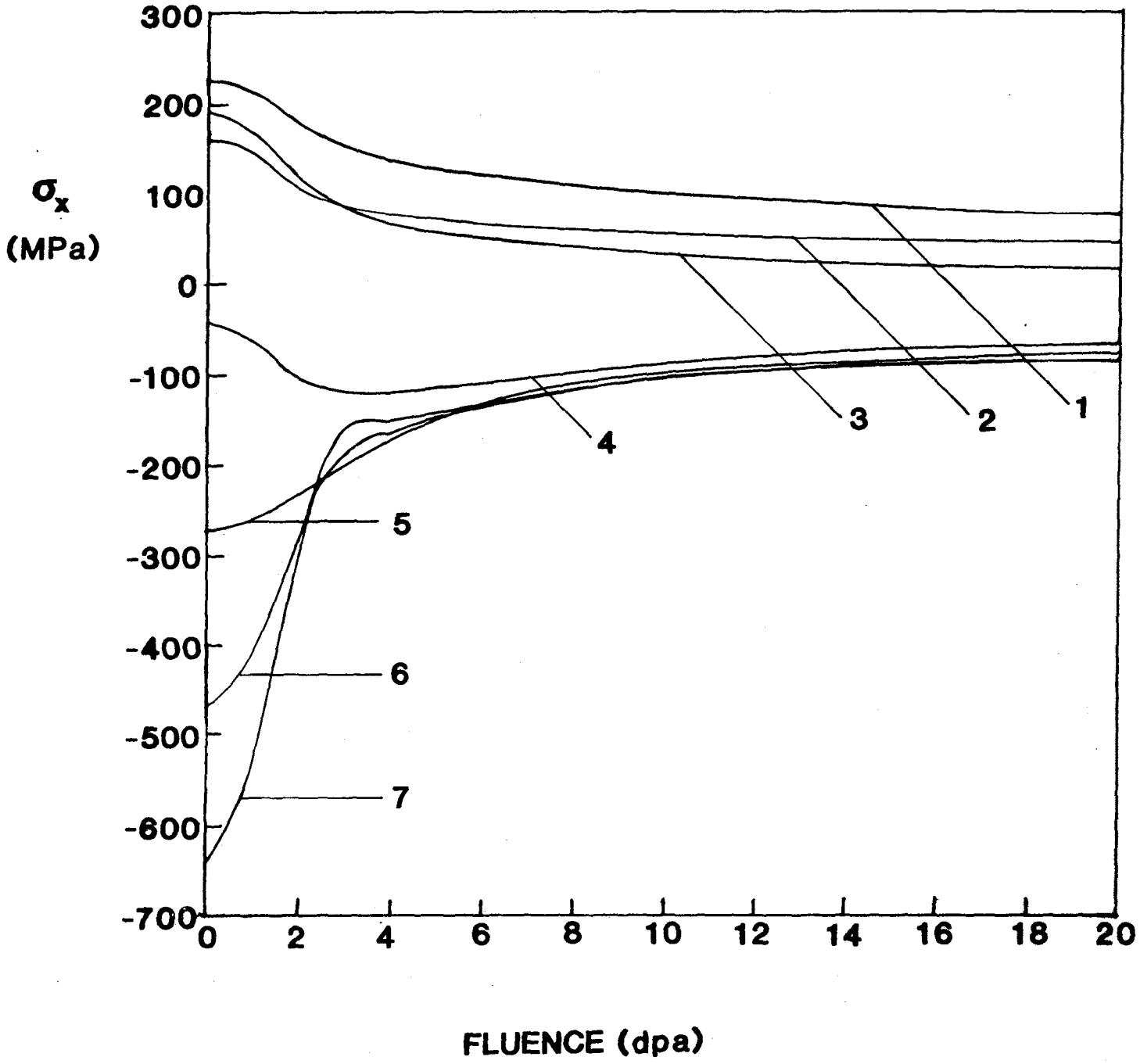

Figure 6.2.4-4. Stress history at the beam end (x = 0) due to creep with the flux gradient included.

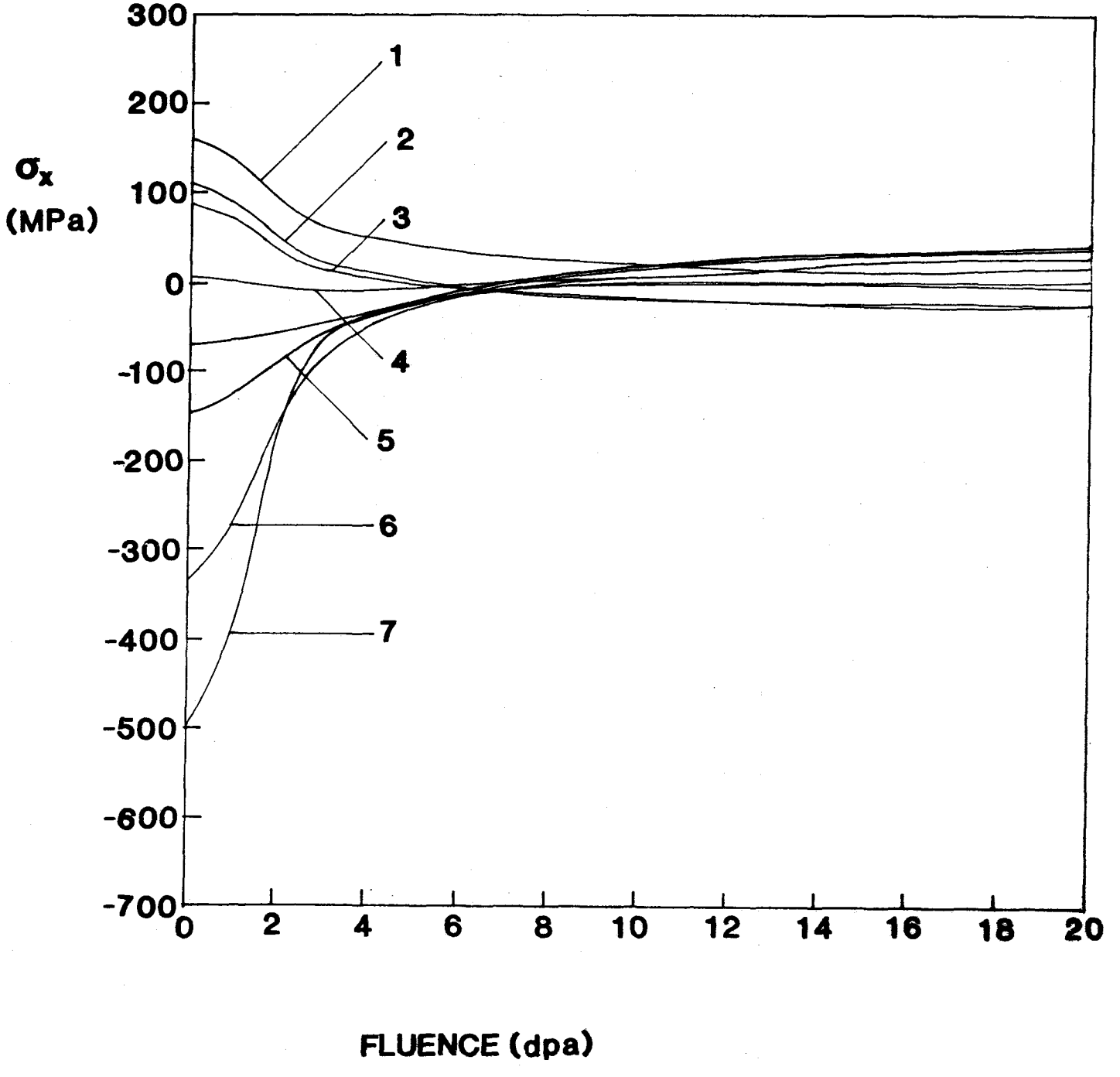

Figure 6.2.4-5. Stress history at the beam center (x = $\ell/2$) due to creep with the flux gradient included.

same locations. In Fig. 6.2.4-6 the displacement patterns are shown as function of time. Material property values used are given in Table 6.2.4-1. More results are presented and discussed below in Section 6.2.4.

Limitations and Uncertainties

Elastic-plastic analysis is necessary to better understand the scaling of geometry, since the stresses exceed the elastic limit. Furthermore, residual stress build-up due to cyclic loading should also be calculated. Material properties indicate that at high temperatures the elastic-perfectly plastic constitutive law could be assumed. Elastic-plastic analysis is the most important subsequent step to be taken in the work begun here.

The length to width ratio of a segment between two supports is not large, (~8:1), consequently, the effect of shear deformations may be important. Since shear deformation is not included in the model, we have taken a preliminary look at it as follows. A virtual work solution using a simple linear factor to approximate distortions of plane surfaces perpendicular to the beam axis results in a 11% contribution to total deformation from shear. This solution is for a concentrated load and does not consider thermal stresses or creep, but it gives an idea of the magnitude of the error introduced by neglecting shear deformation.

As indicated in Fig. 6.2.4-2 the temperature profiles in the first and second wall are parabolic and the temperature in the web is linear. The values chosen are based on thermal-hydraulics analysis (Section 6.2.2) and reference operating parameters. The actual web temperature profile is unknown because of uncertainties in the MHD velocity profiles. Temperature profiles in a test module are discussed in Section 6.4.

The built-in end conditions are not valid at the edges of the blanket module. Also, numerous structural details (inlets, etc.) have been neglected. Inlet and outlet regions may be the most prone to failure because of temperatures (the highest temperature occurring at the outlet), more welds, and possible stress concentrations in these relatively complex portions of the blanket. These regions are very design dependent and do not lend themselves to simplified analysis.

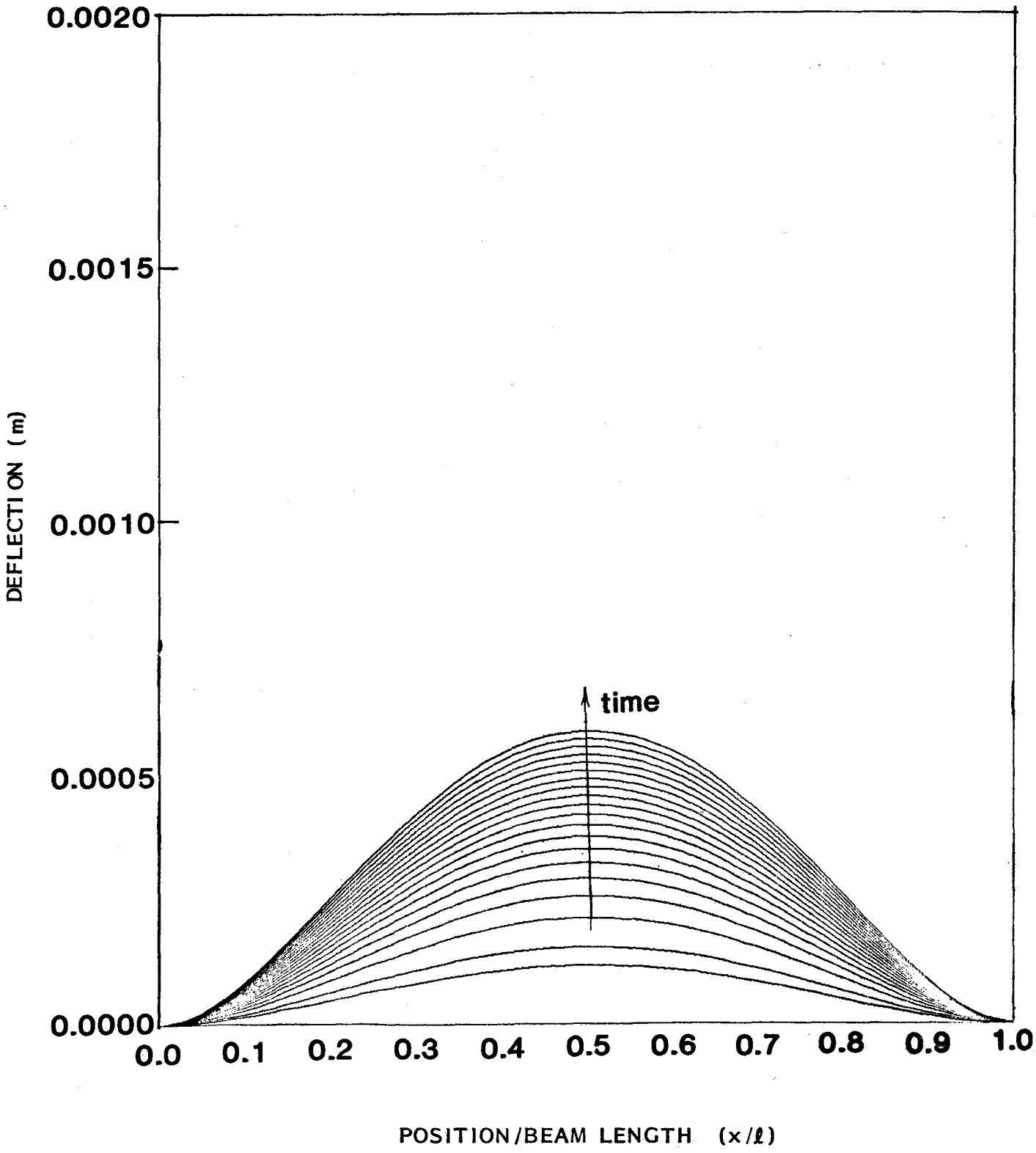

Figure 6.2.4-6. Deflection history due to creep with the flux gradient included.

Table 6.2.4-1. Material Properties Used in the Analysis of the Vanadian Alloy BCSS Reference Design and Test Module

Young's Modulus	120 GPa
Poisson's ratio	0.3
Coefficient of thermal expansion	2.66×10^{-5} 1/°C
Irradiation creep coefficient	2.2×10^{-5}% $MPa^{-1.5}$/dpa
Irradiation creep exponent	1.5

Temperature variation in the axial (x) direction has been neglected because the temperature change is low compared to that in the radial direction (~12°C in the axial direction versus >200°C in the radial direction). Upon taking the average temperature between the supports for the given temperature field, the results should be accurate enough for engineering purposes.

Thermal creep may be an important effect to include depending on the material properties and operating temperature. The effect of misalignments and imperfect geometry was not considered here. These factors play important roles only in structures prone to buckling.

6.2.4.3 Structural Analysis of the MARS Blanket

The analysis in this section considers a type of structural response very different from that of the BCSS design described in the previous section. The MARS design has much lower thermal stresses, and the blanket supports are of fundamental importance in determining the first wall stresses. Plastic deformation is negligible in the MARS design, unlike the BCSS design, because the stresses are below the elastic limit.

Standard beam theory, as used in the ASME Boiler and Pressure Vessel Code,[1] is inadequate in its treatment of radiation effects. This section describes an analysis which extends classical beam theory to account for radiation effects. In addition to elastic strains, the model includes thermal expansion strains, radiation swelling, and both irradiation and thermal creep strains -- all of which are felt to be important to the overall structural response.

Figure 6.1-2 shows the MARS blanket configuration. A hollow beam model, shown in Figure 6.2.4-7, is used to analyze a single cooling pipe from the blanket. Further details on the theory and derivation are provided in reference 2. The major results from the analysis are presented in Section 6.4.

The largest uncertainty regarding the applicability of this analysis is in the materials data. Recent unpublished data indicated that swelling in HT-9 may be negligible, rather than a dominant contributor to end of life stresses. Good materials data is a necessity not only in developing reasonable fusion reactor designs, but also for developing useful integrated tests.

Calculation of End Reactions

The first step in determining the pipe stresses and strains is to find the redundant end reactions which result from the applied strains. A displacement balance equation is developed for the rotation and deflections of the free end of the pipe in the form:

$$\underline{\underline{F}} \cdot \underline{X} + \underline{E} = \underline{D} \qquad (6.2.4\text{-}17)$$

where $\underline{\underline{F}}$ is the flexibility matrix, $\underline{X}$ is the vector of unknown end reactions, $\underline{\underline{F}} \cdot \underline{X}$ represents the elastic displacements due to the end reactions, $\underline{E}$ repre-

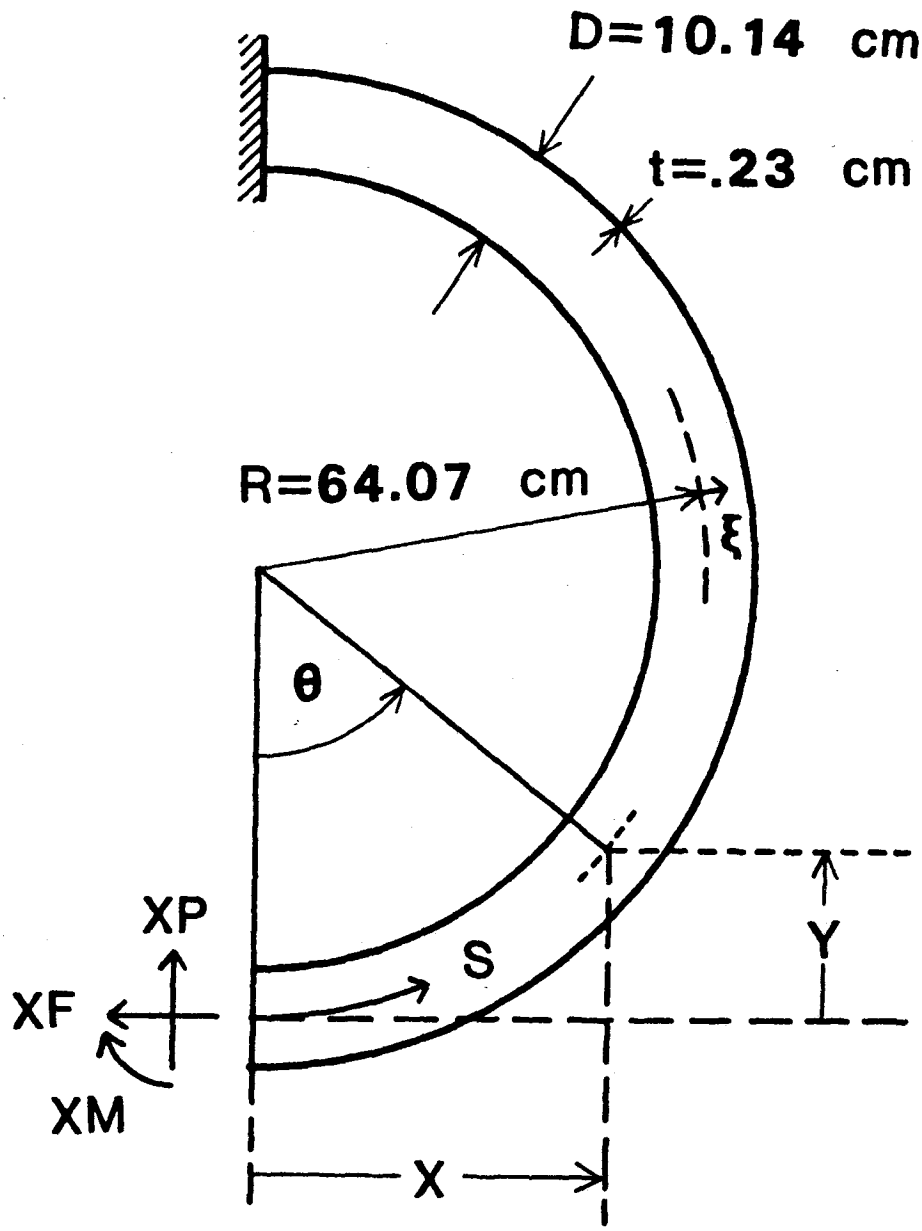

Figure 6.2.4-7. Configuration of the Pipe Model.

sents the displacements due to the inelastic strains (which are calculated from constitutive laws), and $\underline{D}$ is the total deflection determined by boundary conditions. In Figure 6.2.4-7, X_M, X_F, X_P are the unknown end reactions which form the $\underline{X}$ vector, s denotes the position along the pipe, and ξ is the distance from the neutral axis, which also specifies the position on the cross section.

Because the tube is curved and statically indeterminate (due to the external restraints), the axial problem cannot be separated from the radial and rotational problems. The flexibility matrix for the structure is developed using the virtual work principal:[3]

$$\underline{\underline{F}} = \frac{1}{EI} \begin{matrix} R^2\int ds & R\int y\,ds & R\int x\,ds \\ R\int y\,ds & \int y^2 ds & \int xy\,ds \\ R\int x\,ds & \int xy\,ds & \int x^2\,ds \end{matrix} \qquad (6.2.4\text{-}18)$$

The first row of the matrix equation gives the rotations (normalized to R) due to a unit moment, unit axial force and unit radial force, moving from left to right. Similarly, the second row gives the axial deflections and the third row gives the radial deflections due to unit loads at the free end. E is the modulus of elasticity, I is the area moment of inertia of the cross section, and R is the radius of curvature of the pipe.

After performing the integrals, using $y = R(1-\cos\theta)$, $x = R\sin\theta$, and $ds = R\,d\theta$, the flexibility matrix is simplified to:

$$\underline{\underline{F}} = \frac{R^3}{EI} \begin{matrix} \pi & \pi & 2 \\ \pi & 3\pi/2 & 2 \\ 2 & 2 & \pi/2 \end{matrix} \qquad (6.2.4\text{-}19)$$

The deflections due to inelastic strains, contained in the vector $\underline{E}$, are computed from known relations for the inelastic strain, e', which includes thermal strain, void swelling, irradiation creep, and thermal creep. These are discussed in detail in the following subsection. The vector $\underline{E}$ is given by:

$$\underline{E} = - \begin{matrix} R \int w' \, ds \\ \int w'y \, ds - \int \bar{e}' \cos\theta \, ds \\ \int w'x \, ds + \int \bar{e}' \sin\theta \, ds \end{matrix} \qquad (6.2.4\text{-}20)$$

where $\bar{e}'$ is the average inelastic strain

$$\bar{e}' = \frac{1}{A} \int e' \, dA \qquad (6.2.4\text{-}21)$$

and w' is the curvature change due to inelastic strains:

$$w' = - \frac{k_1}{I} \int e' \xi \, dA \, . \qquad (6.2.4\text{-}22)$$

The factor k_1 accounts for the fact that in any curved beam of hollow cross section, the deflection of the beam is related to the deformation of the cross section which occurs as the beam is bent. This non-negligible, nonlinear effect is found to increase the effective flexibility of the beam, resulting in a reduction of the magnitude of the axial stresses, for a problem involving fixed displacements.(4)

If these inelastic deflections are added to the deflections due to the end reactions, one obtains the total resultant end rotation and deflections. The total deflection, $\underline{D}$, is generally determined entirely by the boundary conditions. For example, if both ends of the pipe are clamped, there are no end rotations or deflections and $\underline{D}$ is identically zero.

Assuming $\underline{\underline{F}}$, $\underline{E}$, and $\underline{D}$ are known, the unknown reactions are easily found by inverting the flexibility matrix and solving Eq. 6.2.4-17 for the vector $\underline{X}$.

Calculation of Deflections

Once the end reactions are known, the pipe deflections and axial stresses can be found as a function of toroidal angle. To calculate the displacements at some angle, θ_i, the displacement balance equation, 6.2.4-17 is used. First, the flexibility matrix must be recalculated for a circular pipe of arclength
$\pi - \theta_i$. This is accomplished by substituting $\theta - \theta_i$ for θ in the integrals of equation 6.2.4-4 and integrating from 0 to $\pi - \theta_i$. To find the deflections at θ_i due to the moment and forces at that angle, the vector $\underline{X}$ is filled with the forces obtained from the equilibrium equations, derived from simple statics:

$$M = X_M + x\,X_P + y\,X_F \qquad (6.2.4\text{-}23)$$

$$F = X_F \cos\theta - X_P \sin\theta \qquad (6.2.4\text{-}24)$$

$$P = X_F \sin\theta + X_P \cos\theta \qquad (6.2.4\text{-}25)$$

where M, F, and P are the moment and axial and radial forces on a section at an angle θ. The deflections due to the inelastic strains are then recalculated in a manner identical to the flexibility matrix, and added to the elastic deflections to give the resultant deflections at the desired angle.

Calculation of Stresses

The total strain is represented by the elastic and inelastic components:

$$e = \frac{\sigma}{E} + e' \qquad (6.2.4\text{-}26)$$

In standard beam theory, the total strain in a beam with free ends subjected to bending is proportional to the curvature change for small deformations:

$$e = -\xi w \qquad (6.2.4\text{-}27)$$

This equation is valid only if the beam's cross section remains unchanged during bending. For a hollow pipe, the change in cross section (as discussed above) must be accounted for by replacing the displacement ξ with the actual displacement $(1-k_2\xi^2)\xi$, which depends on the position around the pipe minor axis. This correction is a second order expansion which approximates the cross section as an ellipse.

In addition, because of the added presence of axial loads, the total strain is composed of a component due to bending and an average value at the neutral axis, $\bar{e}$. Then Eq. 6.2.4-27 becomes

$$e = -\xi(1-k_2\xi^2)\,w + \bar{e} \qquad (6.2.4\text{-}28)$$

The total curvature, w, can be replaced by its elastic and inelastic parts:

$$w = -k_1 \frac{M}{EI} + w' \qquad (6.2.4\text{-}29)$$

and the average strain $\bar{e}$ can be obtained by integrating Eq. 6.2.4-26

$$\bar{e} = \frac{F}{AE} + \bar{e}' \qquad (6.2.4\text{-}30)$$

Using Eq. 6.2.4-29 and -30 in Eq. 6.2.4-28 gives us

$$e = \frac{F}{AE} + \bar{e}' + \xi\,(1-k_2\xi^2)\,(k_1 \frac{M}{EI} - w') \qquad (6.2.4\text{-}31)$$

which is substituted into Eq. 6.2.4-26. Using the equilibrium relations given above, all of the terms in Eq. 6.2.4-26 are now defined:

$$\frac{\sigma}{E} = \frac{F}{AE} - (e' - \bar{e}') + \xi\,(1-k_1\xi^2)\,(k_1 \frac{M}{EI} - w') \qquad (6.2.4\text{-}32)$$

This equation for stress is used both in determining the structural response and in the constitutive relations which follow.

Constitutive Equations

The inelastic strains mentioned above are computed using semi-empirical constitutive relations. The total inelastic strain is given by

$$e' = e_T + e^s + e_r^c + e_T^c \qquad (6.2.4\text{-}33)$$

The thermal strains e_T are given by $e_T = \alpha_T T$ where α_T is the thermal expansion coefficient and T is the difference between the operating temperature and the zero-stress temperature. For the swelling strains, e^s, a design equation developed by Ghoniem and Conn for ferritic alloys is used:[5]

$$e^s = \frac{f(Cr)}{300}\,(0.036\ \delta - 0.074)\,\exp\left[-\left(\frac{T-T_p}{\gamma}\right)^2\right] \qquad (6.2.4\text{-}34)$$

where T_p = 425 C for HT-9

γ = 59 K for HT-9

δ = the displacement dose (dpa)

$$f(Cr) = \begin{cases} 0.067\ Cr^2 - 0.457\ Cr + 1.0 & ,\ Cr < 5\% \\ 0.037\ Cr + 0.235 & ,\ Cr > 5\% \end{cases}$$

and Cr is the chromium content of the structural material.

Recent data for the swelling of ferritic steels indicate that voids do not appear in the matrix until some "incubation dose" is reached.[6] This can be accounted for with an equation of the form:

$$e^S = S\left[\phi t + \frac{1}{\beta} \ln\left\{\frac{1 + \exp[\beta(\tau - \phi t)]}{1 + \exp(\beta\tau)}\right\}\right] \qquad (6.2.4\text{-}35)$$

where τ is a measure of the incubation time, ϕt is the neutron fluence, and S is the steady state swelling rate. The parameter β determines the transition to the steady swelling regime after the incubation fluence is reached. The presently available data are insufficient to warrant this type of correlation, but one should be aware of the possibility that the use of Eq. 6.2.4-34 may be an overestimate with a large impact on the conclusions.

Irradiation creep data exist for a limited number of ferritic alloys. Odette[7] compiled such information with a suggested correlation of the form:

$$\dot{e}_r^c = A_c \dot{\delta}\ \sigma \qquad (6.2.4\text{-}36)$$

where A_c is a constant, independent of both flux and temperature. σ is the applied equivalent stress and δ is the irradiation dose (dpa). Reported values of A_c range from 7×10^{-7} to 2×10^{-5} $dpa^{-1}ksi^{-1}$.

As with swelling, other correlations are available for creep. For example, Wolfer, Ashkin, and Boltax[8] recommend a swelling-enhanced equation of the form

$$\dot{e}_r^c = (k_1 + k_2\ S)\ \sigma \qquad (6.2.4\text{-}37)$$

where k_1 and k_2 are constants and S represents the swelling rate. A similar swelling-enhanced creep term has been suggested by Gelles[6] for 2 1/4 Cr-1 Mo. A severe lack of data precludes the use of this type of equation for HT-9 at this time.

For thermal creep, the following equation developed by Amodeo and Ghoniem is used:[9]

$$\dot{e}^{c}_{T} = \frac{7.4\times10^{-3}}{kT} \exp\left(\frac{-1.23}{kT}\right) (\sigma-\sigma_o)^3 \qquad (6.2.4\text{-}38)$$

with σ_o = 198.2 - 0.219 T (ksi), where T is the absolute temperature in Kelvin and σ_o is the back stress. When the stress is less than the back stress, the thermal creep strain is assumed to be zero.

References for Section 6.2.4

1. ASME Boiler and Pressure Vessel Code, Sections I, II, III, and Code Case 1592, "Class I Components in Elevated Temperature Service," (1977).

2. J. P. Blanchard, "Global Inelastic Structural Analysis and Lifetime Estimation for Tubular Fusion Reactor Blankets," UCLA Department of Mechanics and Structures, M.S. Thesis (unpublished), June 1984.

3. Republic Aviation Corporation, "Thermo-Structural Analysis Manual," Framingdale, NY (1964).

4. W. Hovgaard, "The Elastic Deformation of Pipe Bends," Journal of Math. and Physics, 5&6, (1925-1927).

5. N. M. Ghoniem and R. W. Conn, "Assessment of Ferritic Steels for Steady State Fusion Reactors," IAEA Technical Committee Meeting and Workshop on Fusion Reactor Design and Technology, Tokyo, October 15-16, (1981).

6. D. S. Gelles, and R. J. Puigh, "Evaluation of Ferritic Alloy Fe-2 1/4 Cr-1 Mo After Neutron Irradiation -- Irradiation Creep and Swelling," HEDL-7405 (1983).

7. G. R. Odette, "Property Correlations for Ferritic Steels for Fusion Applications," Damage Analysis and Fundamental Studies Information Meeting, October 2-3 (1980).

8. W. Wolfer, M. Ashkin, and A. Boltax, "Creep and Swelling Deformation in Structural Materials During Fast-Neutron Irradiation," ASTM STP-570 (1976).

9. R. J. Amodeo and N. M. Ghoniem, "Constitutive Design Equations for Thermal Deformation of HT-9," to be published, Nuclear Engineering and Design/Fusion (1984).

6.2.5 Neutronics

6.2.5.1 Introduction

In this section, the neutronics behavior of the liquid breeder blanket concept is described. As is shown in Appendix D.2, the neutronics performance of the blanket is characterized by the following parameters: (1) tritium production rate, (2) heat deposition rate, (3) displacement per atom, (4) hydrogen production rate, and (5) helium production rate. The profiles for these parameters are most relevant in this section, because the profile is the most suitable indicator to measure the scaling behavior of the blanket. Detailed data for the overall neutronics performance of the blankets are given in Appendix D.2. Most of this section will be devoted to discussion of the profiles for the above parameters.

The blanket concepts used for the analysis are the liquid Li self-cooled blanket with $V_{15}Cr_5Ti$ structure (Li/Li/V),[1] and the $Li_{17}Pb_{83}$ self cooled blanket with PCA structure (LiPb/LiPb/PCA).[1] The analysis was performed assuming a tokamak fusion reactor as the reference device. A neutron wall load of 5 MW/m^2 was assumed.

6.2.5.2 Calculational Method

The analysis is based on one dimensional cylindrical models of the blankets. The assumed material arrangement of the Li/Li/V reference blanket is shown in Fig. 6.2.5-1. The material composition of each region is the result of homogenization. Natural lithium is used as the breeding material. The vanadium alloy $V_{15}Cr_5Ti$ is used as the structural material in the first and second walls, and the toroidal and poloidal channels. Fe1422 steel is assumed for the reflector and the shield material because its expected activation level is low. The atomic density of each material region is summarized in Table D.2.5-1 of Appendix D.2.

Fig. 6.2.5-2 shows the material configuration of the LiPb/LiPb/PCA reference blanket. Enriched lithium (90% ^6Li) is used to compose $Li_{17}Pb_{83}$. PCA is assumed as the structure throughout the blanket. The ferritic steel alloy Fe1422 is also used in this case as the shield material. A simple configuration is assumed for the first wall; complex structures like the toroidal channels in the Li/Li/V model are not used in the LiPb/LiPb/PCA

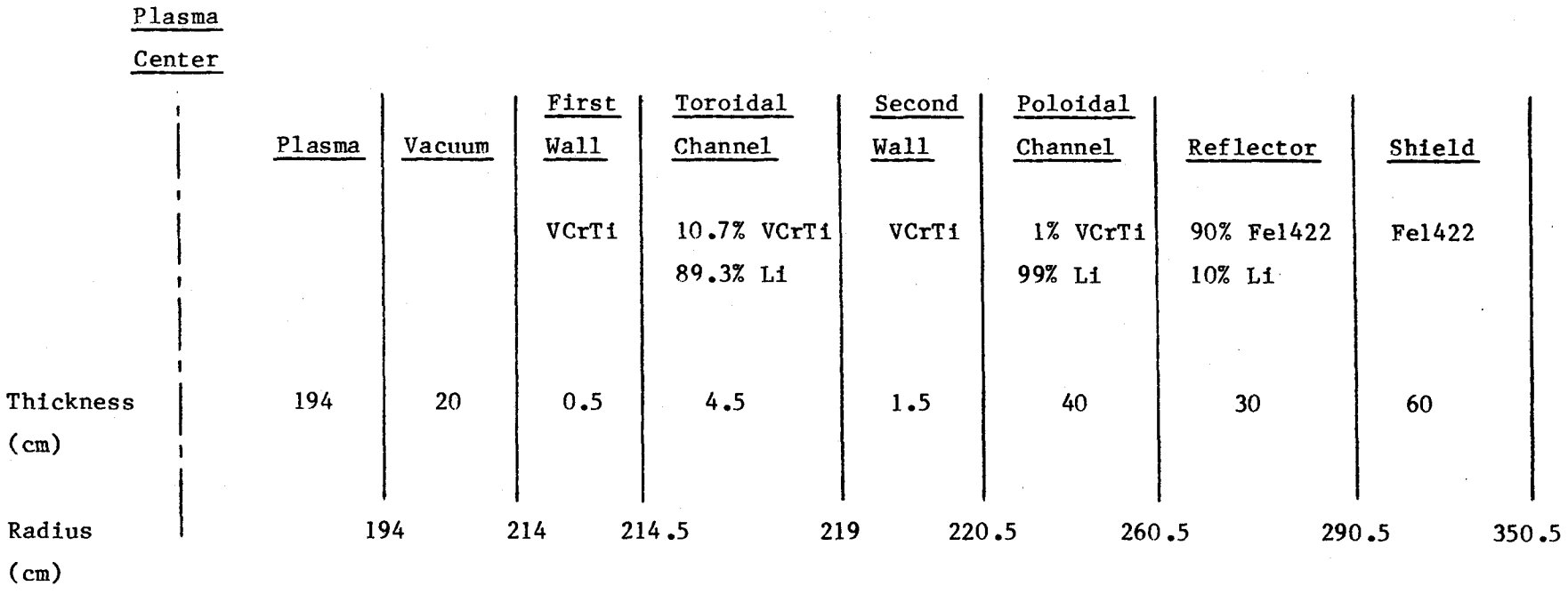

Figure 6.2.5-1. One Dimensional Model for the Lithium Self-Cooled Blanket with V15Cr5Ti Structure (Li/Li/V)

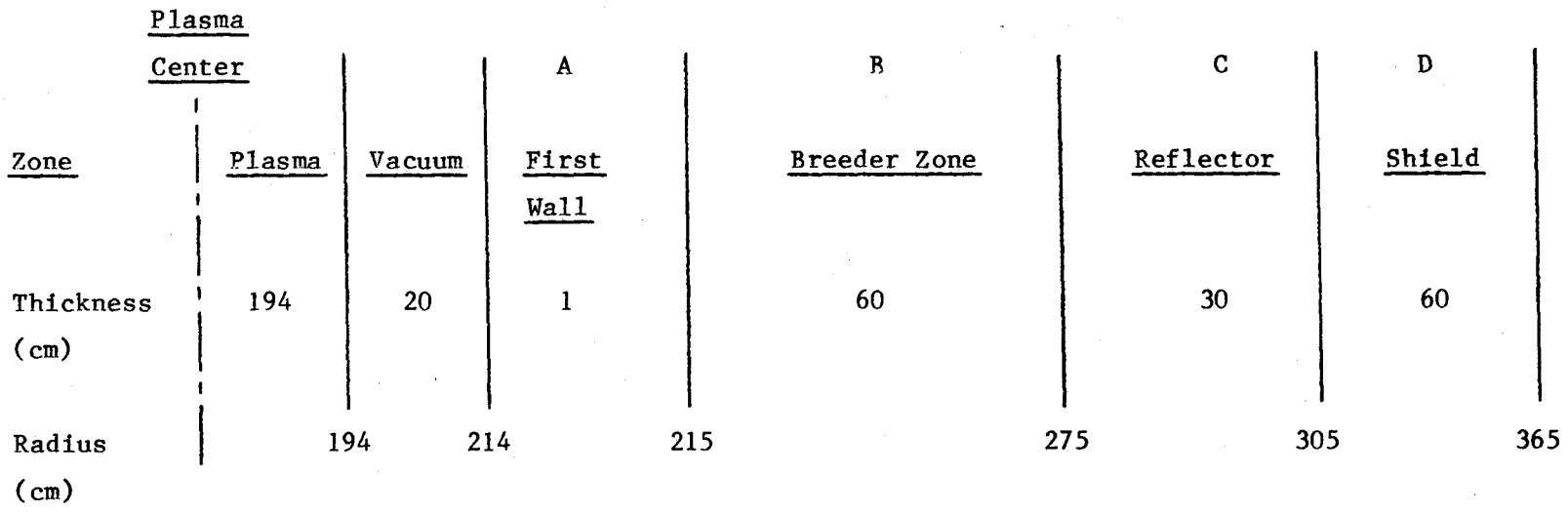

A. 50% PCA, 50% $Li_{17}Pb_{83}$ (90% ^{6}Li)

B. 7.5% PCA, 92.5% $Li_{17}Pb_{83}$ (90% ^{6}Li)

C. 90% PCA, 10% $Li_{17}Pb_{83}$ (90% ^{6}Li)

D. 90 Fe 1422, 10% H_2O

Figure 6.2.5-2 One-Dimensional Model for $Li_{17}Pb_{83}$ Self-Cooled Blanket

model.

The neutronics calculations were performed with the one dimensional discreet ordinates code ANISN[2] using a 41 group (25n-21γ) cross section library based on the ENDF/B-IV data.[3] The library was collapsed from the VITAMIN-C/DLC-41B library.[4] The energy structure of the library is tabulated in Table D.2.1-1 in Appendix D.2. The ANISN calculation was done with a third order Legendre expansion (P_3) and an eight discrete angular mesh approximation (S_8) in cylindrical geometry.

6.2.5.3 Nuclear Heating Rate

The profile for the total nuclear heating rate and the contribution to this profile from both neutron and gamma ray heating are shown in Fig 6.2.5-3 for the Li/Li/V blanket and in Fig. 6.2.5-4 for the LiPb/LiPb/PCA blanket.

The following observations are made for the profiles in the Li/Li/V blanket: (1) Attenuation of the profiles in the lithium layer (the toroidal and poloidal channels) is slow and the profiles are flat. (2) Attenuation of the profiles in the structure (the first and second walls) is large. (3) Neutrons dominate the bulk heating in the lithium layer. (4) The bulk heating in the structure (the first and second walls) is larger than that in the lithium layer, and the main contribution to the heating there is done by gamma rays.

As the lithium layer of the poloidal channel is less effective for high energy neutron attenuation than the structure, the heating rates in the lithium layer vary very slowly with the depth. The decrease in the total heating rate is about 50% from the front edge of the poloidal channel to the back of it. The contribution from neutrons dominates bulk heating in these two lithium layers. The contribution from gamma rays is about 1/20 of that from neutrons. The reason is that lithium is almost transparent to gamma rays because of its low mass number.

Conversely, in the first and second walls, the reflector and the shield, gamma ray heating is about twice as large as neutron heating. Because large amounts of high energy gamma rays are produced from neutron interactions with structure, and these gamma rays deposit their energy in the structure more efficiently than neutrons. This also means that the profile of the heating

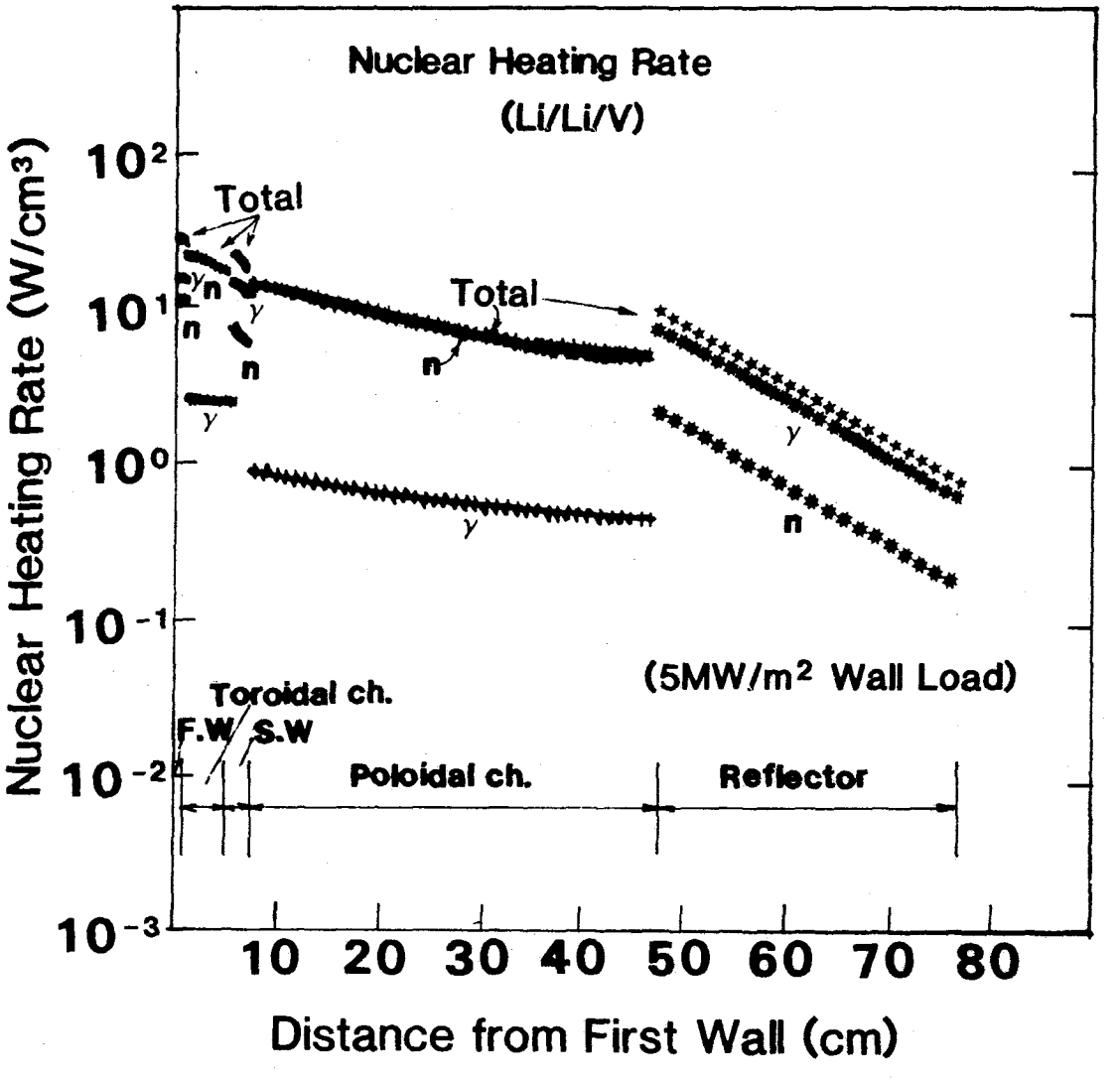

Figure 6.2.5-3 Depth profile of total nuclear heating and the contribution from neutron and gamma ray heating for the Li/Li/V blanket.

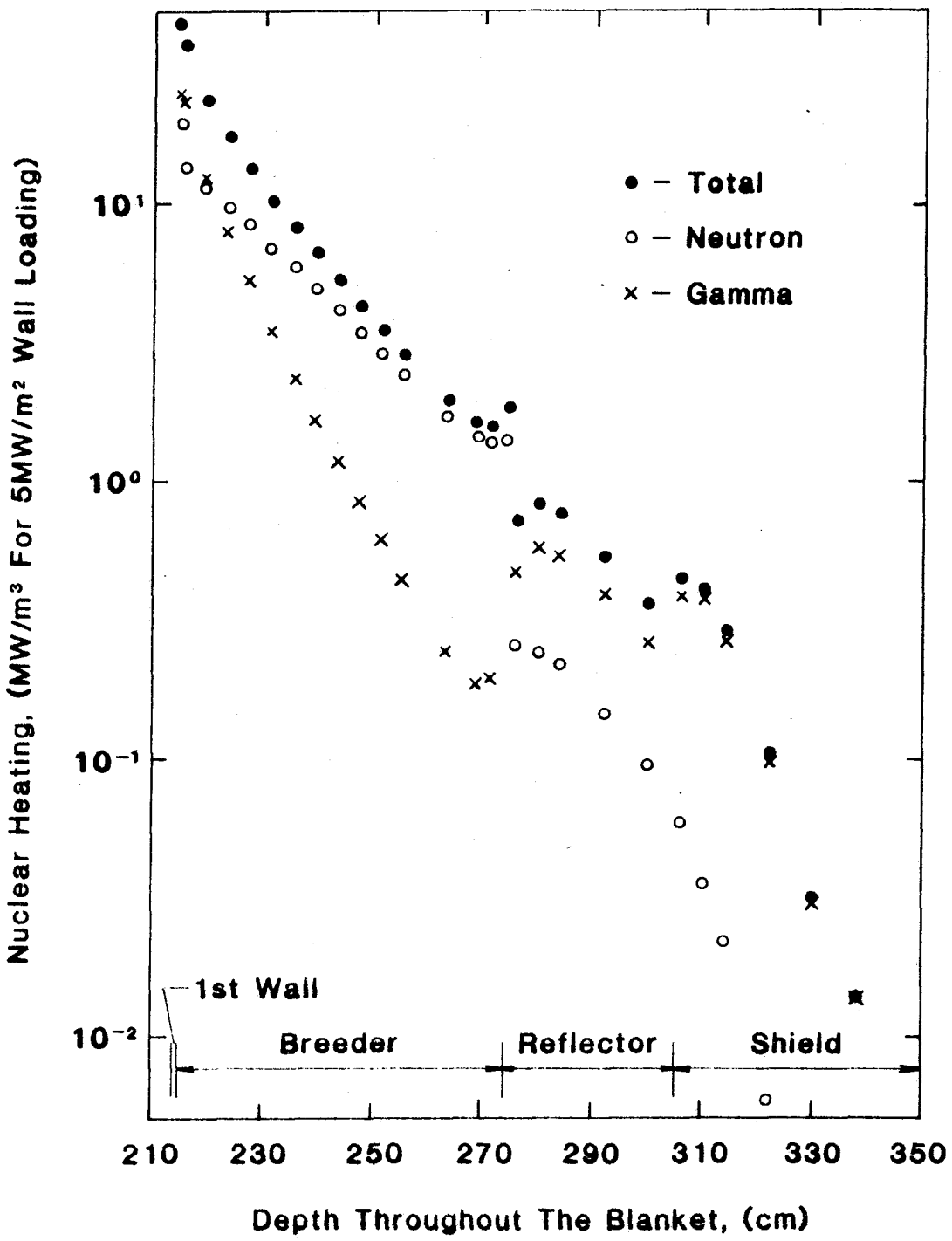

Figure 6.2.5-4 Depth profile of total nuclear heating and the contribution from neutron and gamma ray heating in the LiPb/LiPb/PCA blanket.

rate from gamma rays in the structure is controlled by the profile of the neutron flux. In fact, the profile of the gamma ray heating rate is about proportional to that of the neutron heating rate. The interactions of high energy neutrons take place more frequently in the structure than in the lithium layer, so all the profiles attenuate more quickly in the structure than in the lithium layer.

Regarding the profiles in the LiPb/LiPb/PCA blanket, the following observations are made: The profiles are much steeper than that in the Li/Li/V blanket. The gamma ray contribution is important at the front of the breeder. Neutron slowing down processes through (n,n') and (n,2n) reactions in lead work very effectively in this type blanket, so neutrons are multiplied near the front of the breeding zone. At the same time, many gamma rays are produced in this region. Slowed down neutrons are absorbed by ^{6}Li through $^{6}Li(n,\alpha)T$ reactions. Gamma rays are attenuated by lead quickly because lead has a very high mass number. Because of these processes, very steep profiles were obtained in the breeding zone.

In the LiPb blanket, about 43% of the total heating comes from gamma ray heating. The value was about 28% for the Li/Li/V blanket. For both blankets the maximum heating rate was observed at the first wall. The obtained values are 25 W/cm^3 and 45 W/cm^3 for the Li/Li/V and LiPb/LiPb/PCA blankets, respectively.

6.2.5.4 Tritium Production Rate

The profiles for the total tritium production rate and each contribution from ^{6}Li and ^{7}Li are shown in Figs. 6.2.5-5 and 6.2.5-6 for the Li/Li/V blanket and the LiPb/LiPb/PCA blanket, respectively. The vertical axes of Figures 6.2.5-5 and -6 are expressed in terms of the number of tritium atoms produced per year per lithium atom consumed.

The contribution from ^{6}Li dominates in both blanket types. Especially for the LiPb/LiPb/PCA blanket, about 99.8% of the tritium production comes from the ^{6}Li reactions. There are two reasons for this. One of them is the fact that ^{6}Li was 90% enriched. The other reason is the existence of many lead atoms in the breeder. The slowing down of high energy neutrons proceeds very rapidly in the breeder through Pb(n,n') or Pb(n,2n) reactions, which reduces the ^{7}Li contribution and enhances the ^{6}Li contribution. However, the

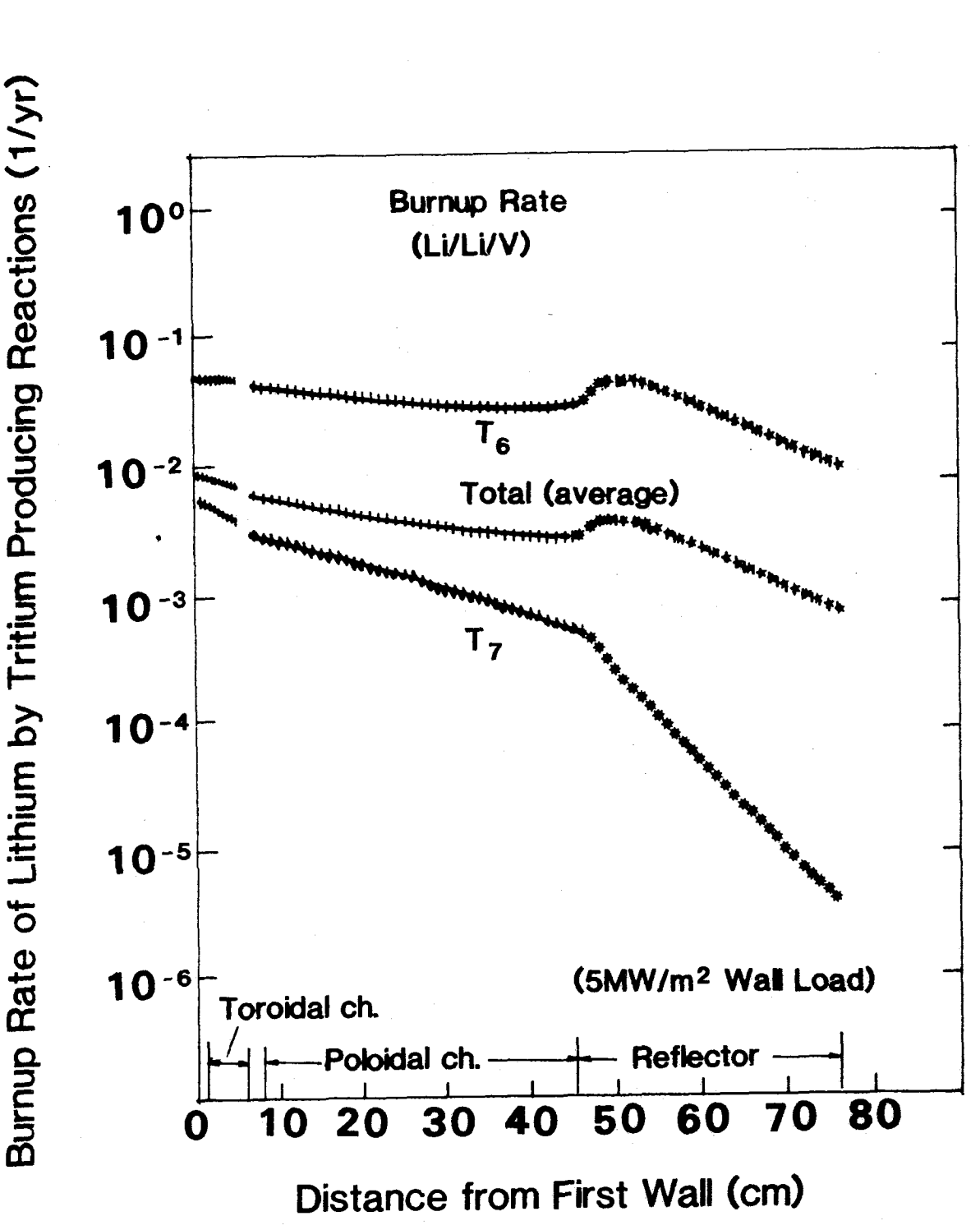

Figure 6.2.5-5 Depth profiles for burnup rate of lithium by tritium-producing reactions in the Li/Li/V blanket.

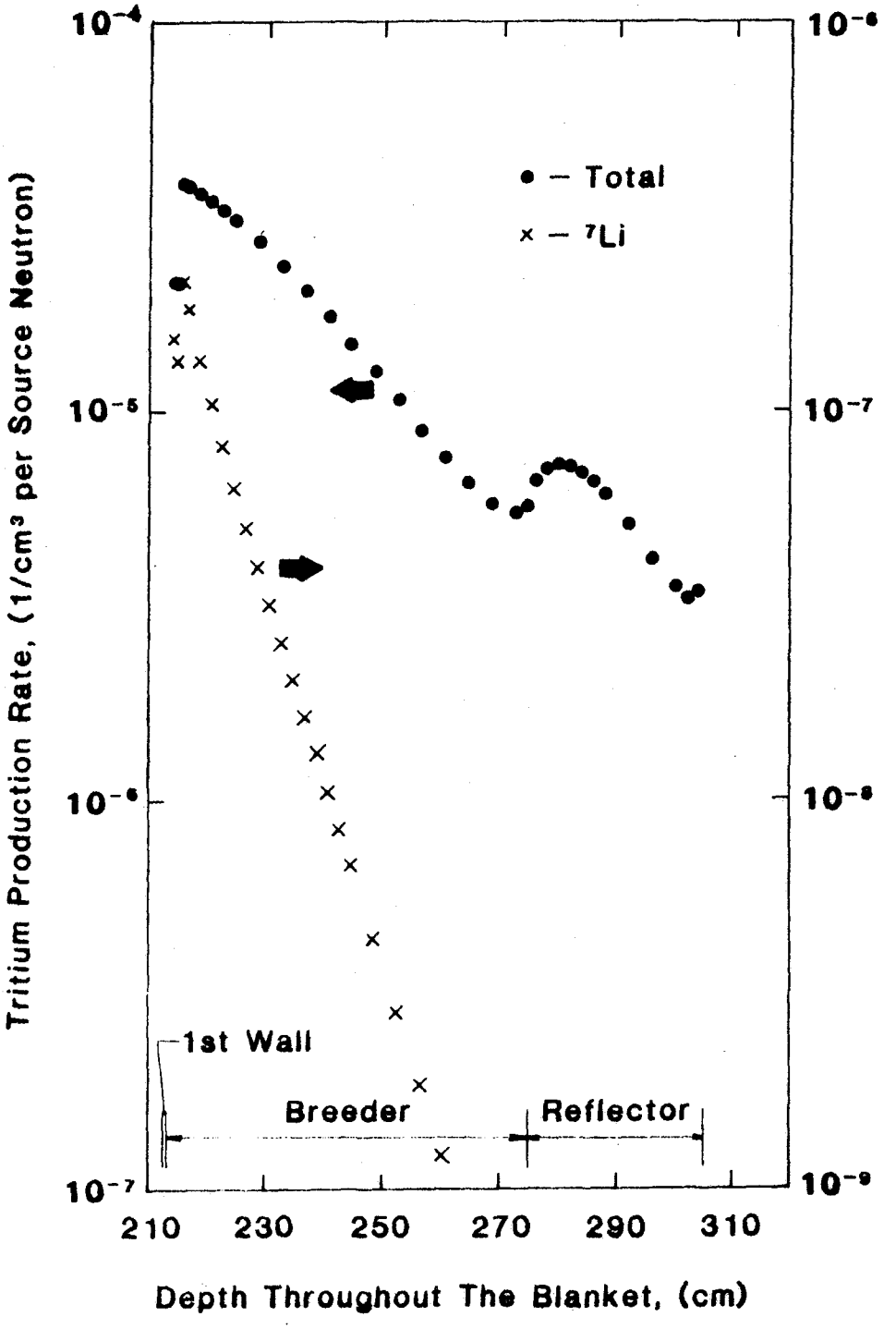

Figure 6.2.5-6 Depth profile of the burnup rate of lithium atoms by tritium producing reactions in the LiPb/LiPb/PCA blanket.

burnup rate of ^{6}Li in the LiPb blanket is small, i.e., 8×10^{-3}/(yr ^{6}Li atom) at the front edge of the breeder. It is small enough that problems arising from breeder burnup need not be considered.

The contribution of ^{6}Li to the total tritium production in the Li/Li/V blanket was 64%. Natural Li was used in the Li/Li/V blanket, so the atomic density of ^{7}Li is about 12 times as large as that of ^{6}Li. This caused the appreciable ^{7}Li contribution. The burnup rate of ^{6}Li atoms is $\sim 6\times10^{-2}$/(yr ^{6}Li atom), which is relatively high. During the operation of the reactor, the reduction of TBR caused by ^{6}Li burnup may be important.

The spatial profile of the Li/Li/V blanket data shows a very flat shape in the toroidal and polodial channels, especially the curve for the ^{6}Li contribution is almost uniform in these regions. Attenuation of high energy neutrons is less in the lithium layer. (See the shape of the T_7 curve.) Moreover, the reflection of slow neutrons from the reflector to the breeder enhances the T_6 values in the region close to the reflector. For these reasons, the total tritium production rate varies very slowly in the poloidal channel; the change in its value is only 25% throughout the poloidal channel. Notice the peak in the profile near the reflector boundary. This shows the buildup of neutron flux there. The reflector is very effective in the Li/Li/V blanket.

The profile of the tritium production rate in the Lipb/LiPb/PCA blanket shows a much higher gradient than that in the Li/Li/V blanket. This is caused by strong neutron slowing down in lead through (n,n') or (n,2n) reactions and by the large capture cross section of ^{6}Li for slow neutrons. Although a slight reflector effect (enhancement of the tritium production) is noticeable near the boundary with the reflector, its magnitude is small.

6.2.5.5 Radiation Damage Indicators

Figs. 6.2.5-7 through 6.2.5-9 show the damage parameters, DPA (diplacements per atom), hydrogen production rate, and He production rate for the main components of the V15Cr5Ti alloy in the Li/Li/V blanket. All the profiles for both the hydrogen production rate and He production rate of all elements resemble one another. Both the hydrogen and He producing reactions are usually high threshold reactions. The reaction rate of these reactions depends strongly on the high energy neutron flux distribution. As is seen in

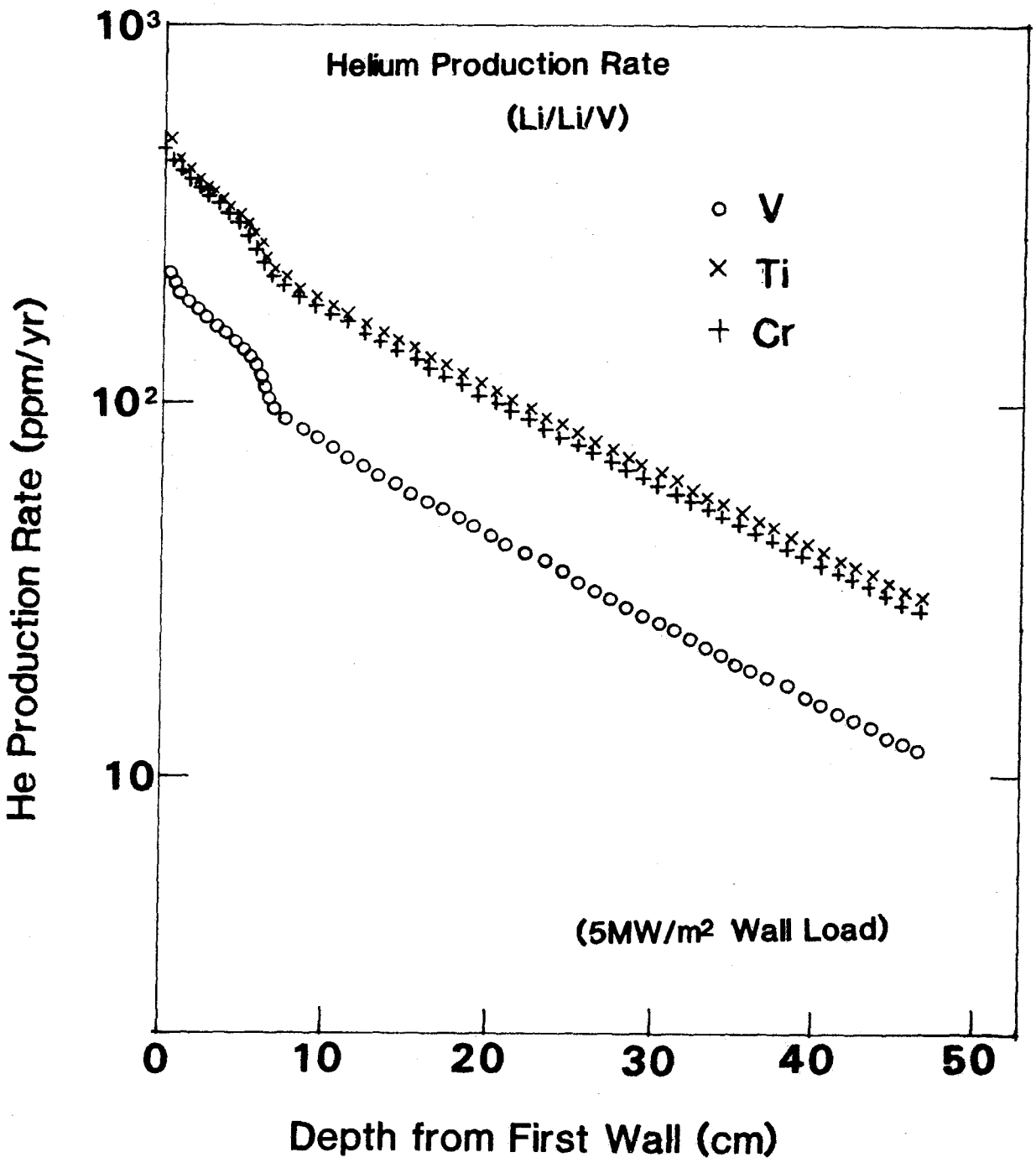

Figure 6.2.5-7 Atomic displacement rate in structure in the Li/Li/V blanket.

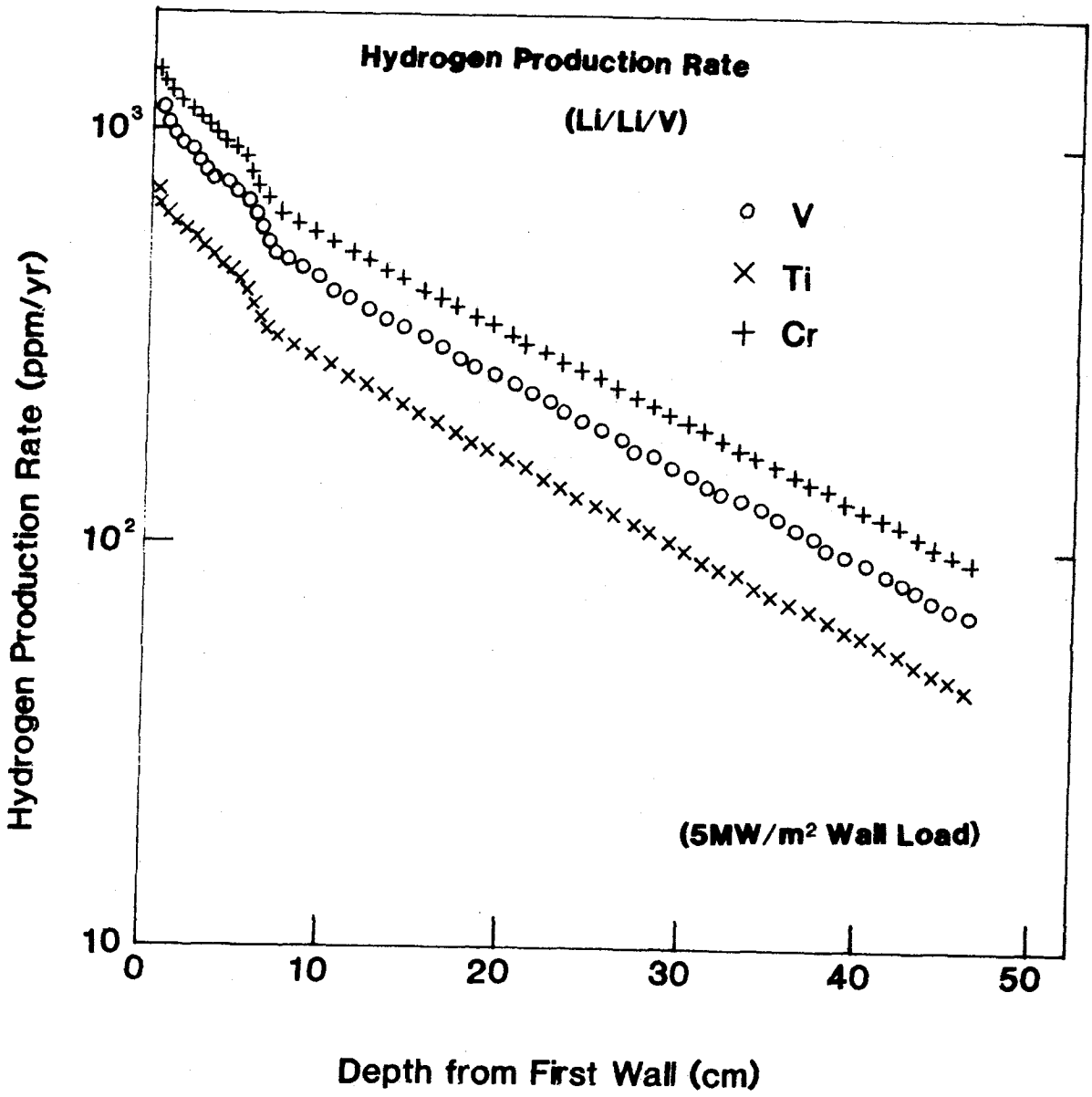

Figure 6.2.5-8 Hydrogen production rate in the structure in the Li/Li/V blanket.

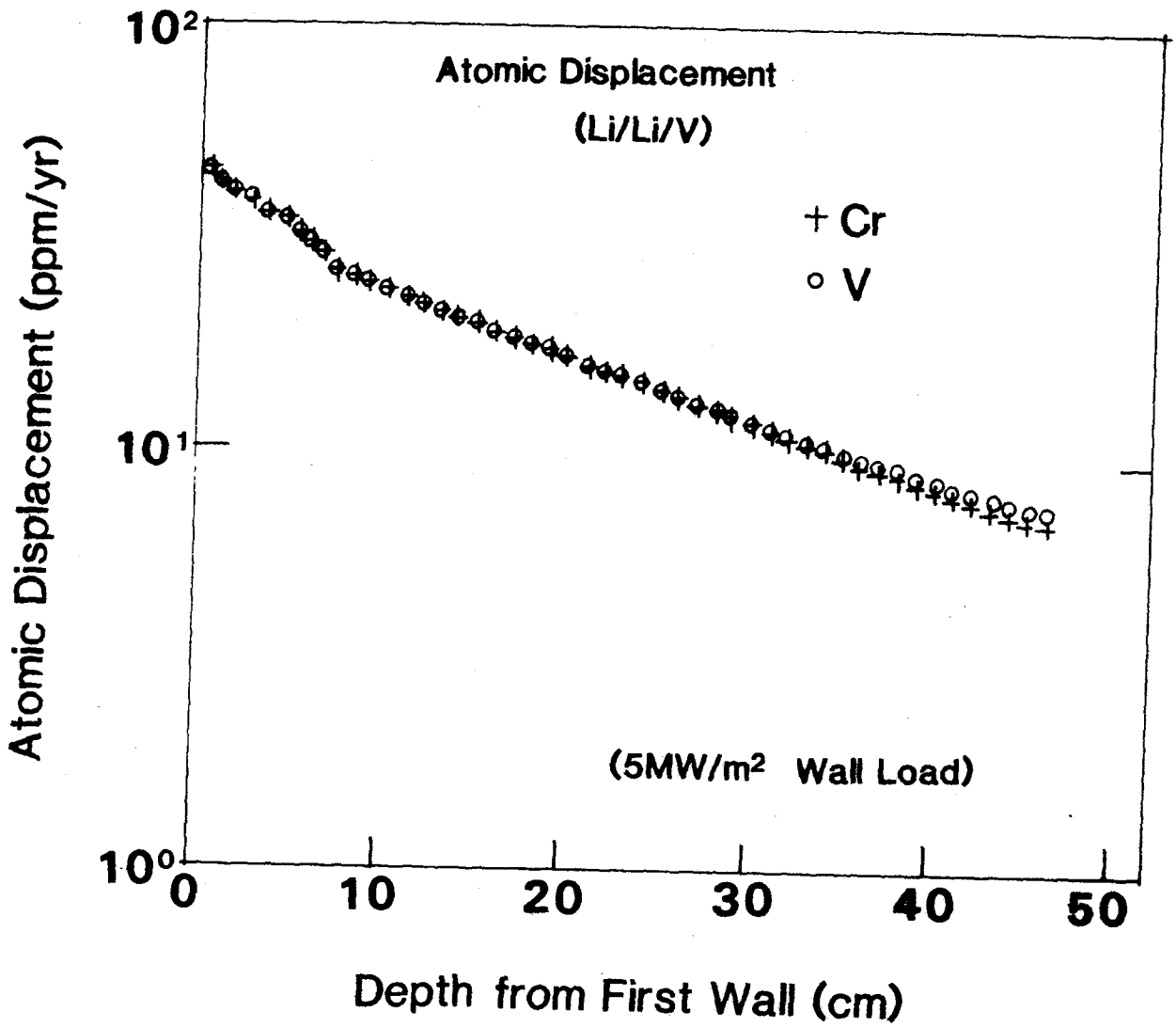

Figure 6.2.5-9 Helium production rate in the structure in the Li/Li/V blanket.

the figure, high energy neutrons are attenuated sharply in the first and second walls and the gradient of the profile is similar in these two regions, because the same material (V15Cr5Ti) is assumed in the walls.

The absolute value of the data depends directly on the reaction cross sections of each element. Among the three elements (V,Cr,Ti) in the figures, chromium shows the highest hydrogen production rate and titanium the highest helium production rate.

The DPA is related to the total energy deposition by neutrons. It depends not only on high energy neutrons, but also on low energy neutrons. The profile of the DPA is more moderate then the other two profiles. The DPA profile of chromium and vanadium resemble each other both in absolute value and in shape.

The maximum displacements per atom, hydrogen and helium production rates are seen at the front edge of the first wall. The values at this location averaged over all the constituents in the V15Cr5Ti alloy are 62 dpa/yr, 1.65×10^3 ppm/yr and 3.85×10^2 ppm/yr for the atomic displacement, hydrogen and He production rates, respectively.

Figs. 6.2.5-10 through 6.2.5-12 show the damage parameter profiles for the main elements (Fe,Ni,Cr) in the PCA alloy for the LiPb/LiPb/PCA blanket. Again the atomic displacement shows very similar profiles both in the absolute value and in the shpae among these elements. As was discussed in sections 6.2.5.3 and 6.2.5.4, neutrons are attenuated quickly in the LiPb/LiPb/PCA blanket. The DPA profile is much steeper in this case as compared to the Li/Li/V blanket.

Regarding the profiles for both the hydrogen production rate and the He produciton rate, the same things which were pointed out for these parameters in the Li/Li/V blanket are observed. Nickel has the largest (n,p) and (n,α) reaction cross sections. It dominates the damage rate in PCA steel. The average value for the hydrogen production rate from Fe, Ni and Cr in the first wall is $\sim 4.8 \times 10^3$ ppm/yr. The corresponding value for the He production and the atomic displacement rates are $\sim 1.55 \times 10^3$ ppm/yr and ~ 80 dpa/yr, respectively.

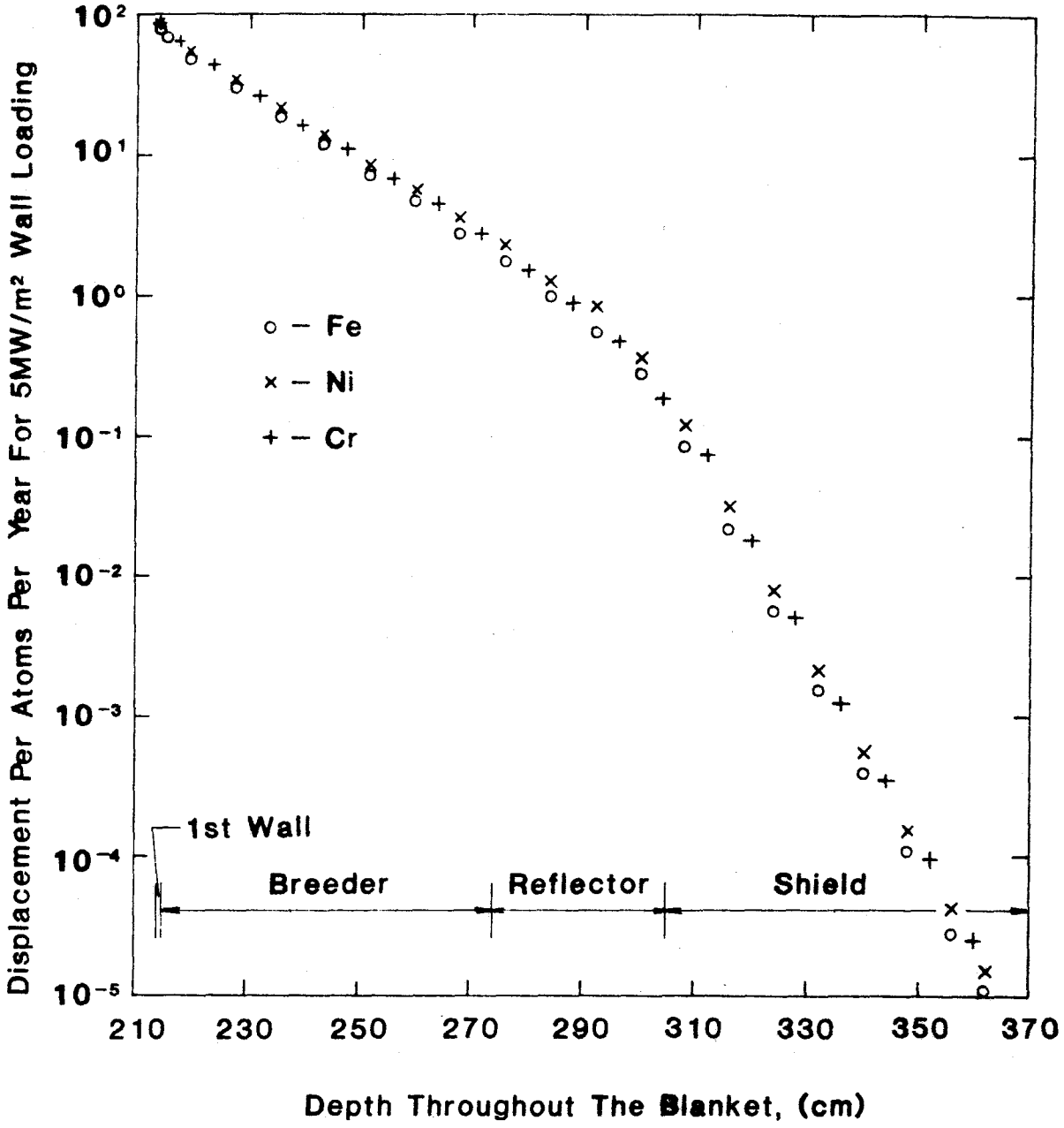

Figure 6.2.5-10 Atomic displacement rate in the structure in the LiPb/LiPb/PCA blanket.

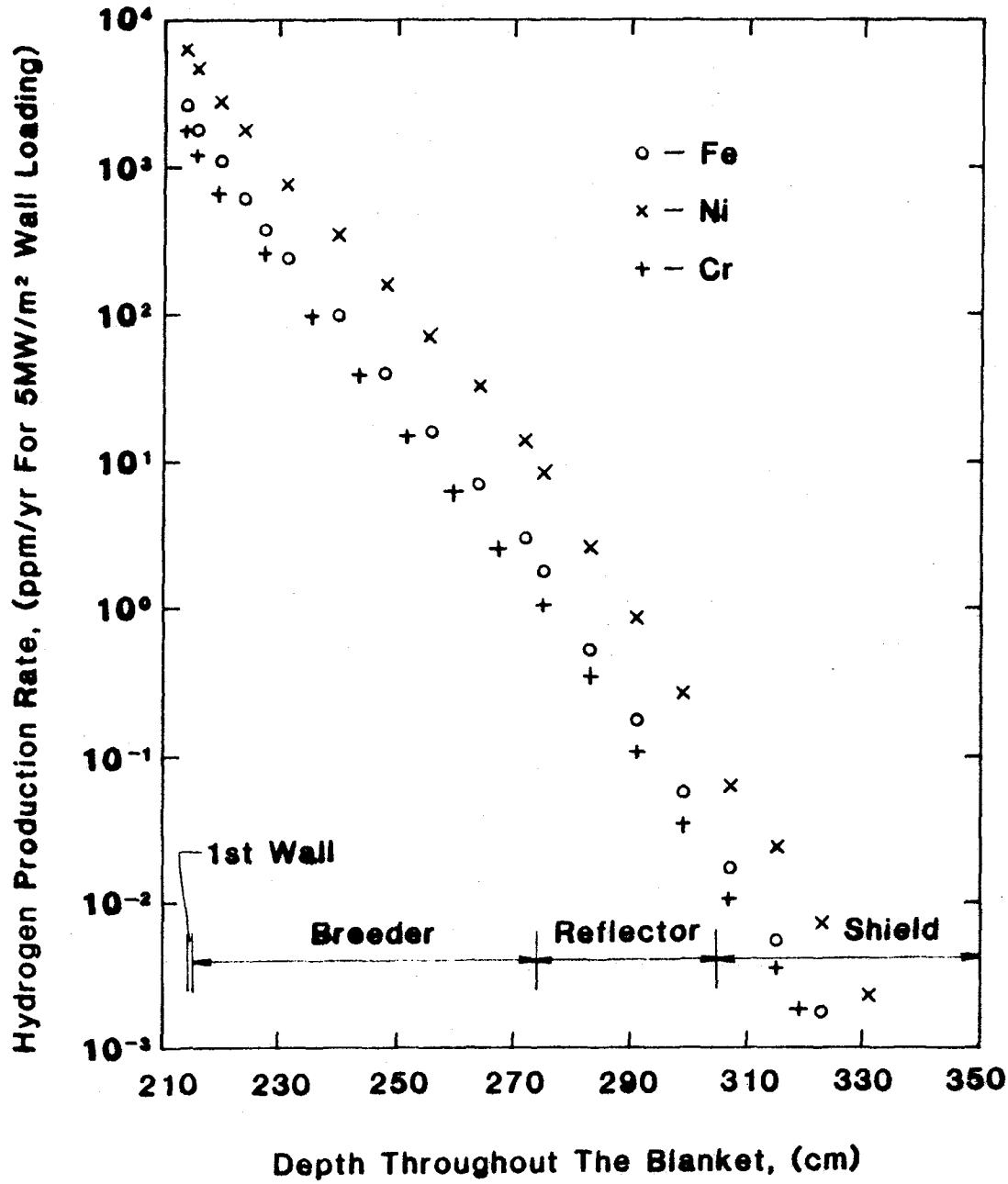

Figure 6.2.5-11 Hydrogen production rate in the structure in the LiPb/LiPb/PCA blanket.

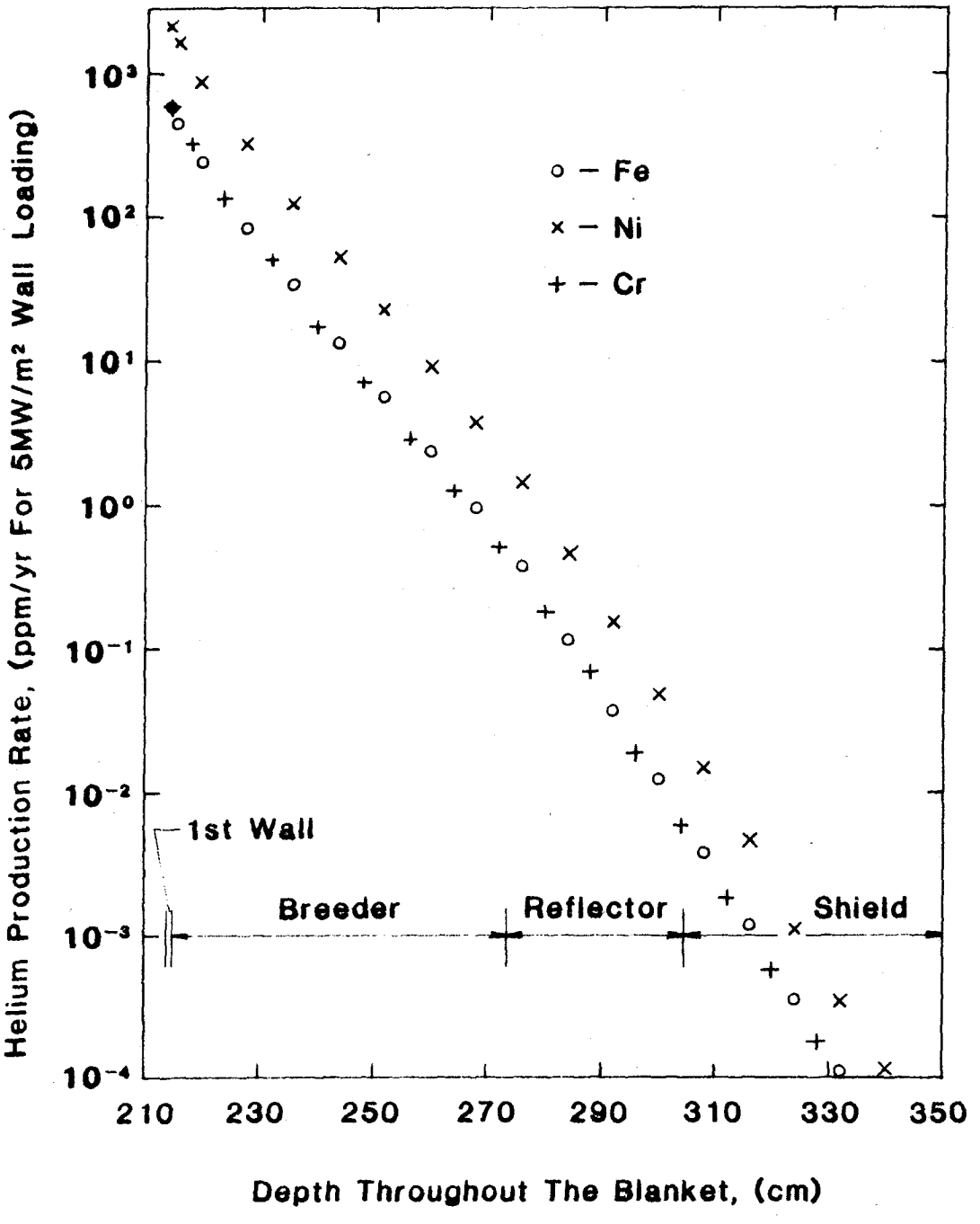

Figure 6.2.5-12 He production rate in the structure in the LiPb/LiPb/PCA blanket.

ratio of the electromagnetic force to the inertial force. It is very large (10^3-10^4) in a fusion reactor blanket, which means that inertia can be neglected. The velocity profile is affected mainly by the electromagnetic force.

In the neighborhood of the wall, viscosity plays an important role. The Hartmann number $Ha=aB\sqrt{\sigma_f/\mu}$ is an important parameter which denotes the square root of the ratio of electromagnetic to viscous forces, where μ is the viscosity. The boundary layer thickness can be expressed as a function of the Hartmann number. In a fusion reactor blanket, the Hartmann number is very large (10^3-10^4), hence the boundary layer is very thin. The boundary layer is important primarily because it affects corrosion.

The large Stuart number and the large Hartmann number mean that the electromagnetic force is dominant. The electromagnetic force is caused by the eddy current, the intensity of which depends both on the electromotive force and on the conductivity of the circuit.

The magnetic Reynolds number $Re_m=Va\sigma_f\mu_m$ denotes the ratio of the induced magnetic field strength to the magnetic field strength, where μ_m is the magnetic permeability of the fluid. If this value is large, we cannot neglect the magnetic field induced by the eddy current. In a fusion reactor blanket, the magnetic Reynolds number is small (10^{-3}-10^{-1}).

As the electromagnetic resistive force is undesirable, a fusion reactor blanket should be designed so that the resistivity of the circuit is high. However, even if it is designed carefully, there may be an unknown current path. Testing will be necessary because of the difficulty in predicting the entire current profile and the importance of induced currents on pressure drop and flow distribution. The test model should be designed so that the distribution of the electromotive force and the characteristic of the circuit are similar to those of the real blanket. The best way to attain similarity is to preserve aspect ratios. Reduction in dimensions causes alteration of the non-dimensional numbers. This may affect the MHD fluid flow and the pressure drop, but the effect seems to be small as long as the electromagnetic force is dominant.

Magnetic field stength and flow velocity can be reduced when the absolute value of the pressure drop is not important. If the pressure distribution

along the channel is important, the absolute value should be preserved, but we can reduce the value for verification of the pressure drop. Flow distribution seems not to depend on the field strength and the velocity as long as the electromagnetic force is dominant. The transition to turbulence should be avoided in a testing model because it is suppressed in a real blanket this requirement can be satisfied easily, because transition to turbulence is over an order of magnitude of field strength away. The requirements on the field strength and the velocity should be discussed quantitatively, but it is very difficult because of the lack of knowledge.

It is recommended that two types of experiments be performed: a verification test on the correlations between the MHD pressure drop or the flow distribution and the non-dimensional numbers, and a model test for the ascertainment of interactive effects such as global current effects. The former test can be made using a simple test section, such as a single bend. But a simulative model is needed with the major components of a real blanket for the latter test. The former type of test should be done before the latter type of test. Nuclear testing should be focussed on the latter type of test, because it is difficult to make many costly experiments.

In the following, requirements for testing the effects discussed in Sec. 6.2.1 are studied.

6.3.1.2 Multiple Channel Effects

One of the special features of the reference liquid metal blanket is the parallel toroidal channels in front of the main blanket. If there are parallel channels in contact with each other, the eddy current flows not only around a single channel but also across several channels. Hence the MHD pressure drop in parallel channels is quite different from the pressure drop in a single channel. If there are parallel channels, the alteration of the velocity profile in a channel affects the pressure drop in the neighboring channels. The whole blanket should be treated in the calculation. In experiments, the test model should be designed so that the eddy current distribution is similar to that of a real blanket. A partial model can be used, but special attention should be paid to the confirmation that there is no current path which crosses the boundary of the model in the real blanket.

The MHD pressure drop is one of the major issues in the liquid metal

blanket design. In a straight toroidal channel, the pressure drop is considered to be expressed as follows:

$$\frac{dp}{dx} = \sigma_f B_p^2 u_b \frac{\phi_w}{1 + \phi_w} \qquad (6.3.1\text{-}1$$

where B_p is the poloidal magnetic field strength and u_b is the mean velocity in the channel. The conductivity ratio ϕ_w is $\sigma_w t_w / \sigma_f a$ where t_w is the half width of the walls normal to B_p, i.e., the half width of the ribs. It should be noted that the effective wall thickness is equal to one half of the physical thickness when two channels share a common wall. The MHD pressure drop is nearly the same with a single channel, because the return current must flow back through the ribs.

The pressure drop in the second wall orifices is entirely different from that in a single orifice as was discussed in Sec. 6.2.1-2. As long as there is some current path across the orifices, global currents flow, which affects the MHD pressure drop. The pressure drop depends on the number of orifices. Global current effects can be examined using a model which has several orifices. As excessive pressure drop should be avoided in the blanket, the orifices may be insulated to some extent. In this case, the coolant is likely to flow near the wall. The pressure drop is affected by the local aspect ratios. The local aspect ratios should be preserved in the testing model. The effect of the Stuart number is not clear. It is desirable to preserve it, but useful information may be obtained from tests with different Stuart numbers. Of course, the Stuart numbers should be much larger than unity. There must be more than three orifices in the test model.

6.3.1.3 Velocity Profile Development

The velocity distribution in the toroidal channel of the reference blanket is important because it affects both the first wall temperature and the corrosion rate of the wall.

The effect of the poloidal field on the velocity profile cannot be neglected. If there is no poloidal field, the fully developed velocity profile may be parabolic because turbulence is suppressed by the toroidal field. In flow parallel to the magnetic field, the flow develops very slowly. The entry length ℓ_e in a duct is given by:

$$\ell_e = 0.16\ aRe_a \qquad (6.3.1\text{-}2)$$

where a is the half width and Re_a is the Reynolds number based on a[1]. The ratio of the lateral (poloidal) magnetic field strength to the axial (toroidal) strength should be preserved in the testing model.

Flow development under angled magnetic field is affected by the ratio of the field strength parallel and perpendicular to the flow as was shown in Sec. 6.2.1.3. Since a rough model was used there, further studies are needed on this problem. It is desired to obtain the entry length by experiment. We should stress that the global current affects the resistive force in the radial direction, thus it affects the entry length. There should be several parallel channels. The local aspect ratios are very important and should be preserved. The Hartmann number and the Stuart number have some effects. The peak velocity in the wall jet in the fully developed flow is affected by the former. The effect of the latter is not clear, but it affects flow development if the field is not angled.[2] Preserving them is desirable. If it is difficult, parametric studies are needed.

6.3.1.4 Necessity of Basic Experiments and Code Development

Many uncertainties are left in thea area of MHD flow in fusion reactor blankets requiring further basic studies, as listed in Table 6.2.1-1. Scaling laws exist, based on the non-dimensional numbers shown above, but our knowledge is so limited that the performance of the real blanket using testing results with scaled conditions cannot be predicted. There is a current need for fundamental tests, such as MHD pressure drop measurements in a bend.

A three dimensional code which can solve the eddy current and flow distribution simultaneously will provide information on the MHD flow problem to a certain extent. Most of the MHD phenomena depend on the design. In the absence of a 3-D code, we cannot predict what happens when aspect ratios are changed. Of course, experiments are needed even if such a code exists. However, we can derive better information from the experiments with the code. It is recommended that development of the code should be done before integrated testing.

6.3.1.5 Summary

MHD eddy currents are a "whole-blanket" phenomena in many tokamak blanket designs. The entire blanket, or a large fraction of it, must be modeled to address channel-to-channel flow distributions and pressure drop. Velocity distributions, temperatures, and thermal and pressure stresses are all related to eddy currents. Aspect ratios appear to be the most critical parameter in maintaining act-alike eddy currents.

Requirements on the magnetic field strength are low if pressure distributions along the channel are neglected. The transition to turbulence is over an order of magnitude away and verification of pressure drop does not appear to require full field strength. It is desired that the non-dimensional numbers N and Ha be preserved. If it is difficult, scaling laws are needed from parametric tests. As they are far larger than unity in real blankets, they must be large in the tests.

Before integrated testing, there is a current need for fundamental tests and an advanced code.

References for Section 6.3.1

1. H. Schlichting, Boundary Layer Theory, 4th edition, McGraw-Hill (1960), p. 171.

2. J.C.R. Hunt and S. Leibovich, "MHD flow in channels of variable cross-section with strong transverse magnetic fields," J. Fluid Mech., 28, 241 (1967).

6.3.2 Liquid Metal Thermal Hydraulics

6.3.2.1 Introduction

Thermal hydraulics analysis of liquid metal blankets is very complex. There are several phenomena in these blankets that are poorly understood and contribute to the need for testing. For example, the liquid metal coolant in the Li/Li/V reference blanket has the following features:

1. The velocity profile for liquid metal flow under magnetic field is not well understood especially for the case of channels where the coolant turns from poloidal to toroidal direction through a bend while crossing magnetic field lines. This will cause peculiar velocity profiles (see Section 6.2.1) which in turn affects the first wall heat transfer.

2. Heat is generated volumetrically throughout the liquid metal coolant. It has been shown (see Section 6.2.2) that this affects the coolant temperature profile and hence the structure temperature.

3. The coolant flows in hydrodynamically and thermally developing regions. As a result, the first wall heat transfer depends on the position in the blanket and on the details of the blanket geometry and operating conditions.

4. The above three phenomena are nonlinearly interactive. That is, their effects are not additive.

One of the objectives of this study is to perform engineering scaling for liquid metal blankets in order to design test modules with which, upon experimentation, the unknown and poorly known phenomena would be revealed and perhaps resolved. A more detailed description of the philosophy of engineering scaling for liquid metal blankets is given in Section 6.1. Engineering scaling of such a complex system is a very elaborate task. The first step, however, is to identify and quantify the importance of device parameters for the many issues that have been recognized to be critical for liquid metal blanket design, operation, and testing.

6.3.2.2 Importance of Device Parameters

Device parameters directly affect the thermal hydraulics of the liquid metal blankets. Temperatures and temperature profiles are the key parameters, since most of the phenomena depend on them. General guidelines for liquid metal thermal hydraulics scaling include:

1. Hydraulics of the blanket should be preserved. This includes the velocity profiles and channel geometry. The effects of nonuniform velocity profiles on heat transfer and corrosion is one of the greatest uncertainties in the liquid metal blankets. Loss of the velocity profiles would therefore seriously limit the usefulness of testing.

2. Temperatures and temperature profiles in the coolant and structure should also be preserved. Temperature profiles affect thermal stress and irradiation damage effects; therefore, failure modes are highly dependent on temperature profiles. Mass transfer has also been shown to depend on both temperature and temperature profiles. The coolant temperature profile is not generally preserved unless item 1 above is satisfied.

3. The reference blanket and the test module should be in the same thermal and hydrodynamic developing region since the heat transfer coefficient in the entrance region varies spatially.

With these in mind, several examples are given of how the device parameters affect the thermal hydraulics of liquid metal blankets and how to maintain these behaviors at reduced device parameters.

First Wall Temperatures

First wall temperatures are very important to many issues such as corrosion and first wall stress. The heat conduction equation may be solved directly to obtain the following:

$$T_1 - T_2 = (\dot{Q}_v \delta_{fw}^2/2 + q_s \delta_{fw})/k_{fw} \qquad (6.3.2\text{-}1)$$

$$T_1 - T_{avg} = (\dot{Q}_v \delta_{fw}^2/6 + q_s \delta_{fw}/2)/k_{fw} \qquad (6.3.2\text{-}2)$$

$$T_{avg} - T_2 = (\dot{Q}_v \delta_{fw}^2/3 + q_s \delta_{fw}/2)/k_{fw} \qquad (6.3.2\text{-}3)$$

Where T_1 and T_2 are plasma and coolant side first wall temperatures respectively, and T_{avg} is the first wall average temperature. There are incentives to preserve the magnitude of the temperatures T_1 and T_2; T_2 for corrosion and T_1 for radiation effects testing. Temperature T_1 also impacts the first wall surface damage mechanisms while T_1-T_2 is important for thermal stresses

As the volumetric heat generation and surface heat flux are reduced by switching from the reference conditions, the first wall thickness may be increased according to Eq. (6.3.2-1) to preserve $T_1 - T_2$. Meanwhile, T_{avg} is not preserved, nor is the thermal stress due to the first wall temperature profile. Figure 6.3.2-1 shows how temperatures vary with the test device parameters, keeping T_1-T_2 constant by varying the first wall thickness. It is seen that the deviations in T_1-T_{avg}, and T_{avg}-T_2 increase as the neutron wall load is decreased.

Thermal Stresses

Thermal stresses at the first wall are also very important. In some designs, the thermal stress is so high that the structure undergoes significant plastic deformation. If this high level of stress is not achieved in the test module, then it is unclear whether any benefit is gained from testing failure modes and the interaction of stresses and deformations. It is believed that the main parameter causing the first wall stresses in the temperature difference between the first and second walls (see Section 6.2.4). From the analysis in Section 6.2.2, this temperature difference may be written as

$$T_{fw} - T_{sw} = \frac{a_c}{k_c} \left[q_{fw} - q_{sw} + \dot{Q}_v a \int_{-1}^{1} d\eta \int_{-1}^{\eta} d\eta (f-1) \right] \qquad (6.3.2\text{-}4)$$

where the first wall heat flux, q_{fw}, is the sum of the surface heat flux and the heat generated in the first wall, and q_{sw} is only the heat generated in the second wall. The integral term in Eq. (6.3.2-4) is due to the interactive effect of the velocity profile and the heat generation. This integral becomes identically zero for symmetric velocity profiles, hence the temperature

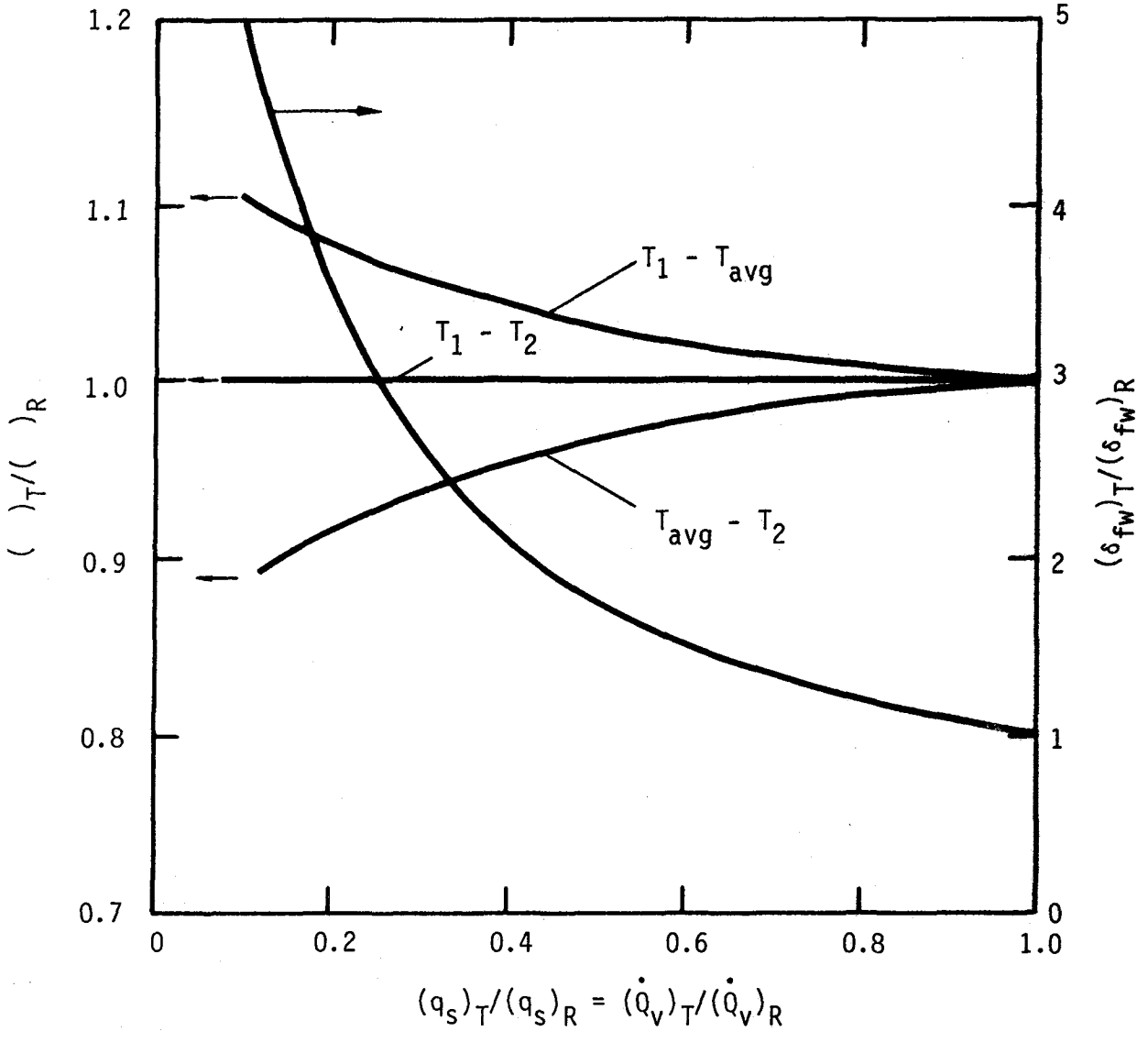

6.2.3-1 First wall temperatures as a function of test device neutron wall load.

difference in Eq. (6.3.2-4) becomes independent of the velocity profile. This, however, is not likely to be the case. There are indications that the coolant velocity profile in the toroidal channels will be nonuniform throughout the entire length of the channel and may exhibit a peak near the second wall.

Figure 6.3.2-2 shows the dependence of the temperature difference between the first and second walls for various velocity profiles. The figure confirms that the first and second wall temperatures are very sensitive to the velocity profile and that the velocity profile should be preserved. Preservation of the velocity profiles depends primarily on maintaining the blanket geometry and magnetic field strength. This issue is further discussed in Sections 6.2.1 and 6.3.1.

Importance of Heat Generation

A question frequently raised is whether a test module may be designed under reduced heat generation. One way is to replace volumetric heat generation with surface heat flux while preserving the total energy input. Figure 6.3.2-3 shows this model. The test module is operated under reduced heat generation ($\dot{Q}_{v,T} = \eta \dot{Q}_{v,R}$) while the heat flux at both surfaces have been increased to compensate for this reduction. The figure shows how the first and second wall temperatures are varied as a function of the fraction η which may also be thought of as the ratio of the test to reference neutron wall load. It is clear that while the total energy input and bulk temperature are preserved, the first and second wall temperatures have increased. Figure 6.3.2-4 shows the coolant velocity profiles for the two cases: with ($\eta = 1$) and without ($\eta = 0$) heat generation. It is seen that the temperature profile is strongly affected by the presence of heat generation.

It is possible to reduce the volumetric heat generation and surface heat flux in order to preserve the wall temperatures. That is, to solve for such q_w^+ and q_w^- that would preserve the wall temperatures. This case is also included in Fig. 6.3.2-4. It is seen that the temperature profile matches very well with that for the reference conditions. There are, however, two concerns. (1) The two wall heat flux have been reduced (at different rates), this alters the temperature profiles in the first and second walls. (2) The total energy input and the bulk temperature is not preserved. One way to deal

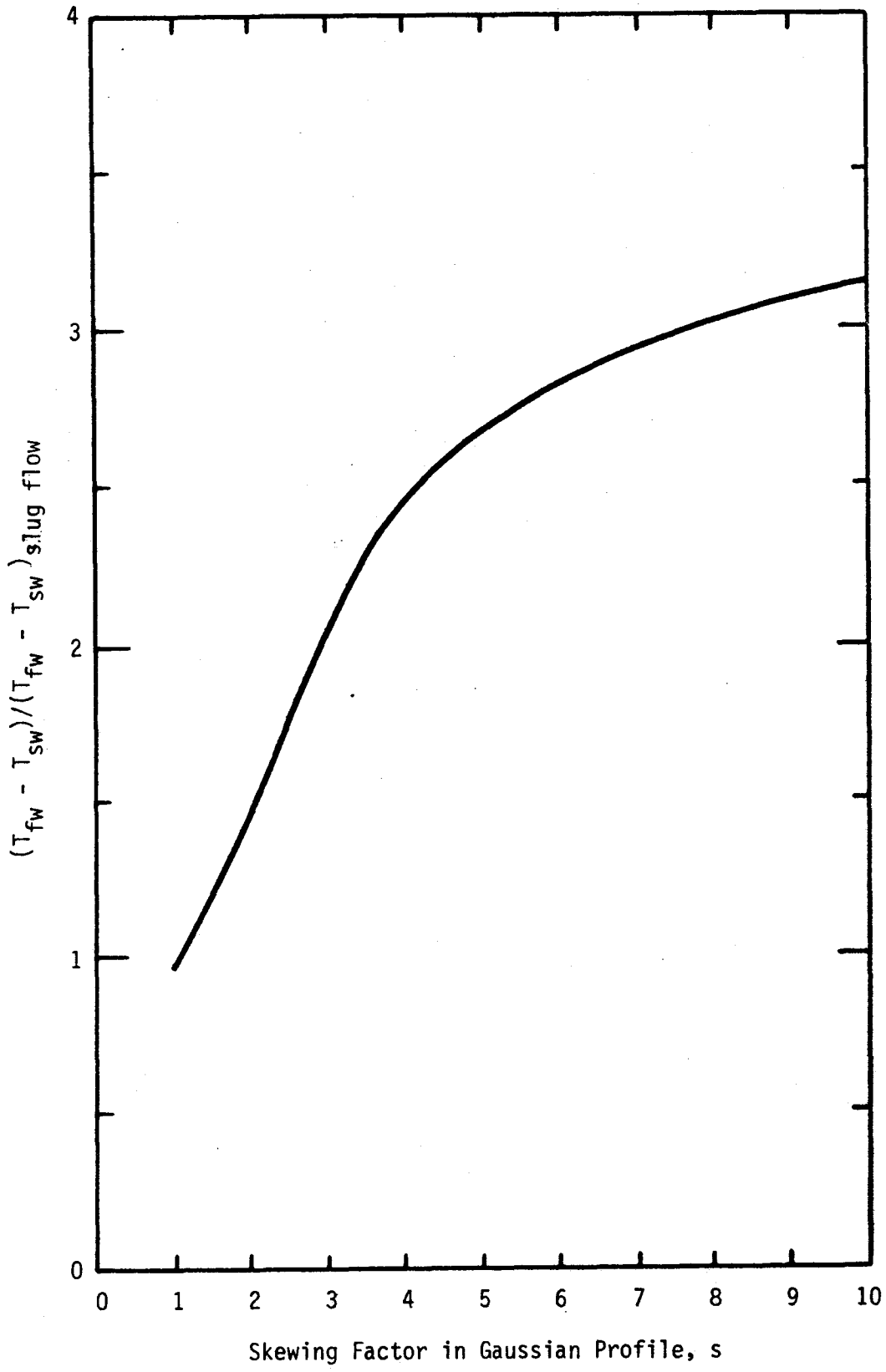

Figure 6.3.2-2 Difference between first and second walls as a function of velocity profiles (for Gaussian velocity profiles, see Fig. 6.2.2-4).

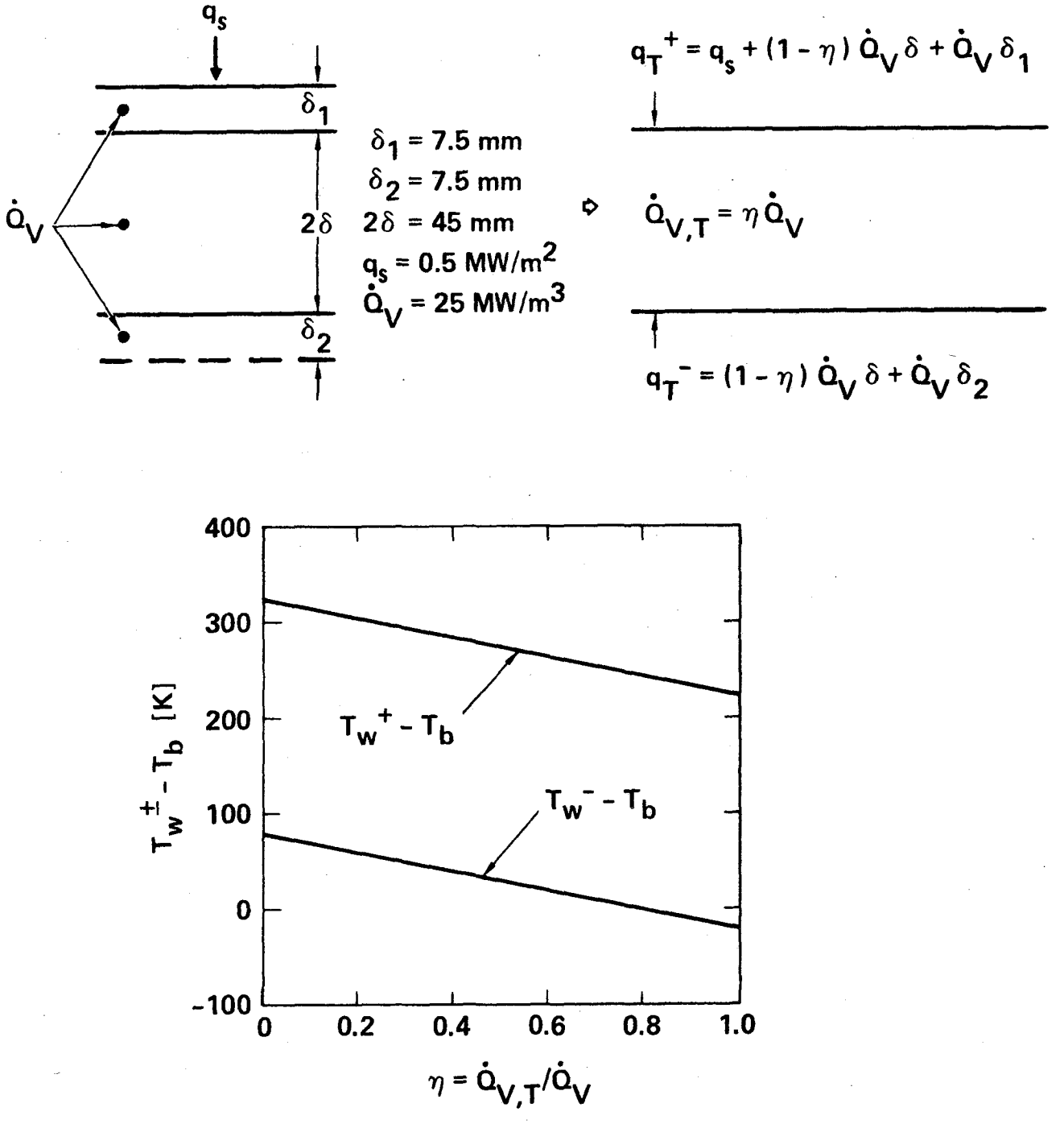

Figure 6.3.2-3 First and second wall temperatures as a function of volumetric heating with total energy input preserved.

	q_w^+ (W/m^2)	q_w^- (W/m^2)	$\dot{Q}_v$ (W/m^3)
Reference ———	7.5×10^5	3.75×10^5	5×10^7
Reference —·—	1.875×10^6	1.5×10^6	0
Modified – – – –	9.493×10^5	5.735×10^5	0

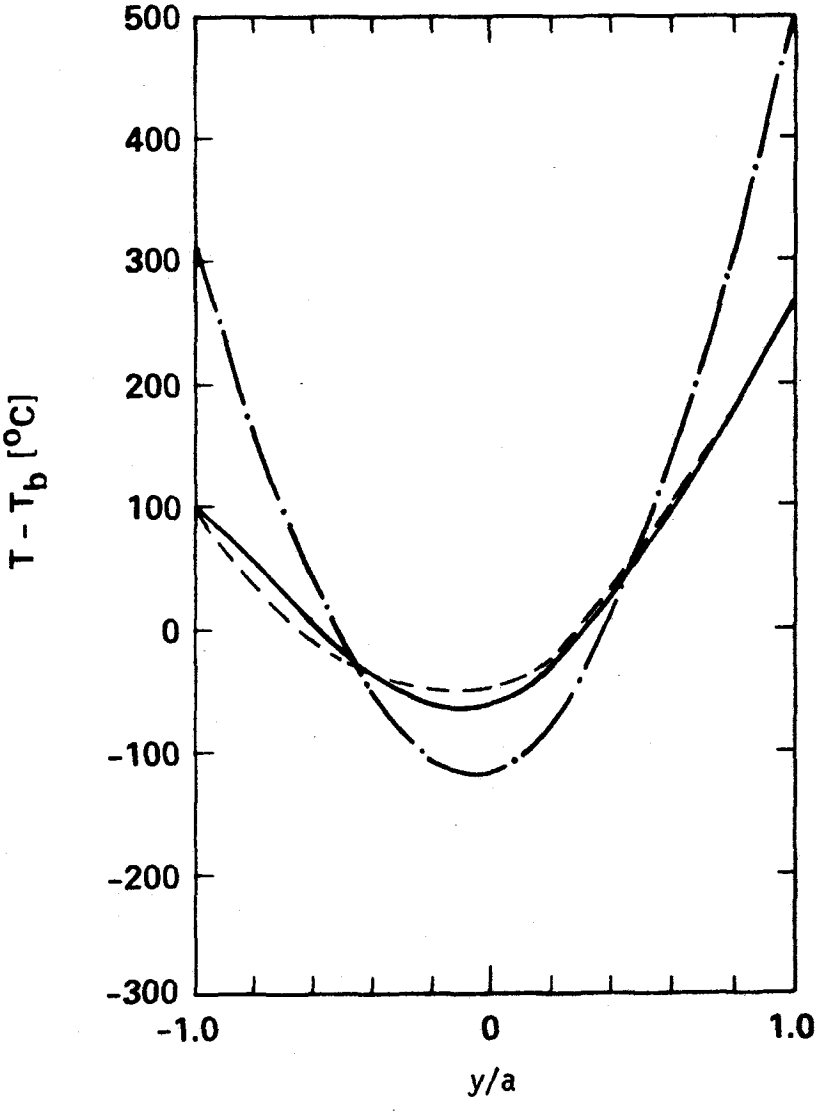

Figure 6.3.2-4 Temperature profiles across the first wall channel for the reference condition (—— with bulk heating, _·_ without bulk heating, and _ _ for modified condition).

with the latter is to decrease the coolant bulk velocity accordingly in order to preserve bulk temperature (e.g. for this case u_b must be decreased by a factor of 2.03). Reduction of the velocity in turn may pose problems of its own, e.g. different fluid regime, pressure drop, etc.

Importance of Velocity Profile

The velocity profile affects the temperature profile as well as the first and second wall temperatures (as seen in Fig. 6.3.2-5). There are many phenomena that depend on temperature profiles, e.g., the coolant heat transfer coefficient and corrosion. Figure 6.3.2-5 compares the two cases of slug flow and gaussian velocity profile. The coolant temperature profile is a strong function of the velocity profile and that to preserve the temperature profile, velocity profiles should also be preserved.

Importance of Size

Size is one of the major device parameters. It sets limitation on the dimensions of the test module. One desires to decrease the size of the test module without changing the thermal characteristic of the blanket. One major consideration is the thermal entry length. It is known that the Li/Li/V reference blanket is entirely in the thermally developing region and enjoys higher than ordinary heat transfer coefficients. The test module should also be designed to operate in the same developing region. To do this, a dimensionless number called the Fourier number should be preserved.

$$Fo = \alpha L/ua^2 \qquad (6.3.2\text{-}5)$$

where L and a are the length and half width of the coolant channel. If L is decreased, a should also be decreased in order to preserve the Fourier number. This is clearly in contradiction to the earlier suggestion of increasing a while the heat generation rate, $\dot{Q}_v$, is decreased. Again, the coolant bulk velocity may be altered to preserve the Fourier number, but (as was earlier discussed) one should consider the preservation of other hydrodynamic effects.

Importance of Burn and Dwell Times

The most important time constant in liquid metal blankets is the coolant

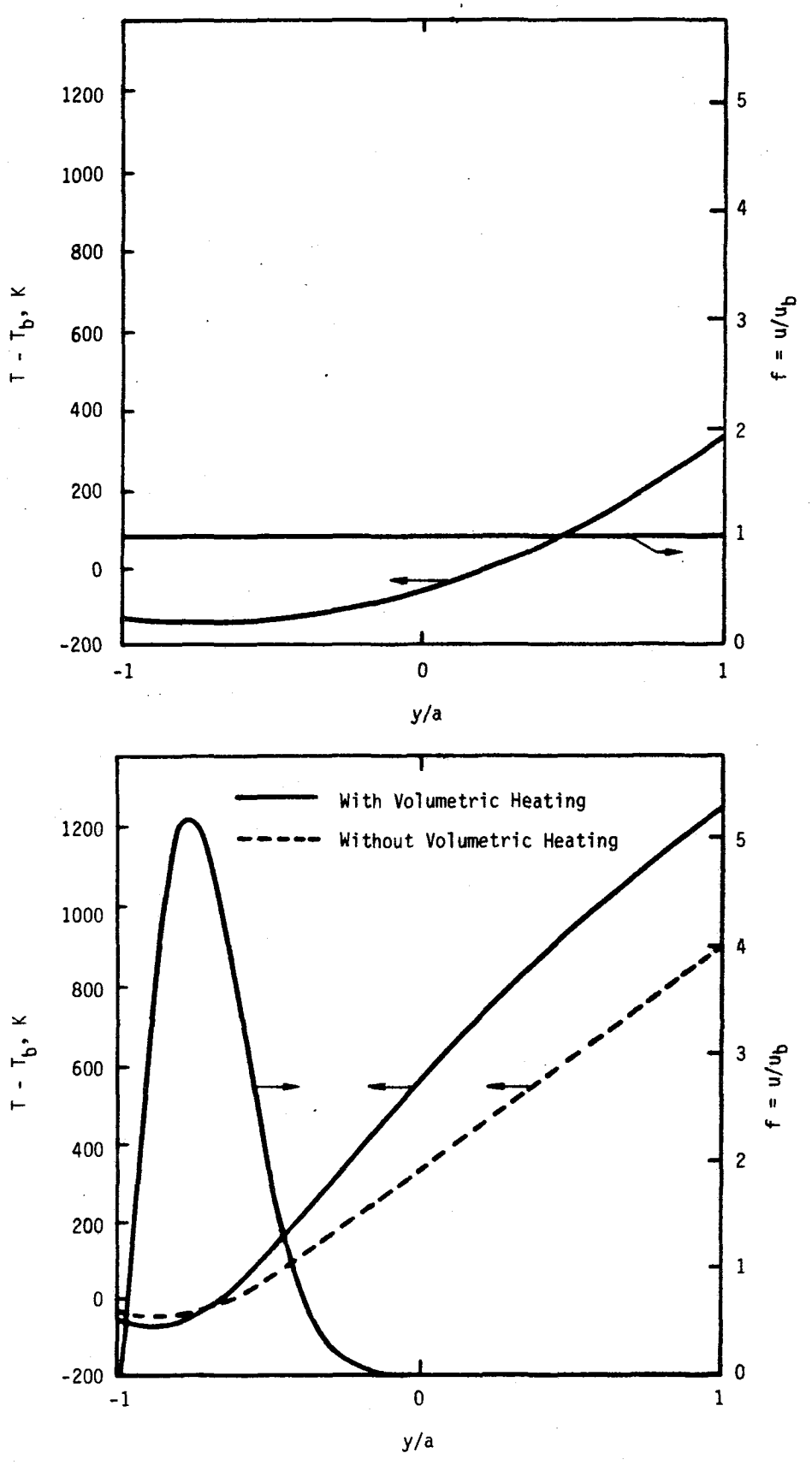

Figure 6.3.2-5 Coolant temperature profiles for various velocity profiles with and without heat generation.

residence time. This is the blanket's thermal characteristic time since any thermal information is completly transfered across the blanket in the residence time. Ideally, one desires very long burn and short dwell times, since the reference condition is that of steady state. Practically, however, one would like to quantify the usefulness of the test module (or the degree of being act-alike, or the information lost) versus the test device burn and dwell time. This, of course, requires extensive and detailed investigation of the thermal hydraulics of the liquid metal blanket. But as a first order approximation, it is desirable to have burn time much greater than residence time. This would limit the thermal transient time (=residence time) compared to the burn time.

6.3.3 Corrosion

6.3.3.1 Overview

The issue of corrosion mass transport affects blanket design and operation in several ways. The ultimate consequence of corrosion is to set upper limits on the blanket temperature design window and to limit the blanket lifetime. These limits can be attributed to three primary aspects of corrosion: (1) removal of structural material from hot regions of the coolant loop (i.e., the blanket cooling channels) results in wall thinning and enhancement of material properties degradation, (2) transport of the corrosion products results in activation of the entire primary cooling system, and (3) redeposition of corrosion products in the cold regions of the coolant loop (i.e., the heat exchanger) results in tube plugging. There are several major uncertainties in our ability to predict corrosion, mass transport, and redeposition. Because this issue sets temperature limits on the liquid metal blanket designs, possibly eliminating the window entirely, it is of critical importance.

Most of our current phenomenological understanding and predictive capabilities of liquid metal corrosion in fusion reactor blankets is based on a small amount of applicable data. The majority of data are from experiments with sodium and stainless steels. Some information is available for lithium and stainless steel systems, but very little information is available for lithium and vanadium systems.

There also is a need for better definition of transport data (molecular diffusivities, solubilities, etc.) for the particular structural species (vanadium, austenitic and ferritic steels) and coolants (lithium and lithium-lead) of interest to fusion. As indicated in Section 6.2.3, it has been necessary to estimate some of the necessary data from sodium information or order of magnitude theoretical predictions in order to model dissolution behavior.

One of the key features of liquid metal blankets which has been absent from corrosion test data is the effect of the magnetic field interactions on corrosion mechanisms. Liquid metal corrosion testing has centered on experimentation with either capsule tests, forced-convection or thermal-convection loops.[1,2,3] Corrosion in MHD induced velocity fields has not been monitored.

The effect of magnetic field on corrosion is an example of a multiple interaction test, which resolves one of the suspected key interactions involving mass transport. A level of uncertainty will remain due to the combined effects of all of the fusion environmental conditions, including: magnetic field, radiation, bulk heating, impurities, and system interactions.

Two of the most important system parameters which affect corrosion are velocity and temperature (both the absolute magnitudes and spatial profiles.) The importance of these parameters has been studied and scaling methods for preserving act-alike behavior determined.

6.3.3.2 Velocity Scaling

For liquid metal flows perpendicular to the magnetic field, the magnetic field tends to retard mass transfer by laminarizing the flow (suppression of turbulence), as compared to that of fully turbulent flow. However, at the same time, mass transfer is enhanced by thinning the momentum boundary layer, similar to turbulent flow. Whether the thinning of the momentum boundary layer by magnetic fields or by turbulence is more severe has not been assessed in this work. The main focus of engineering scaling is to identify significant effects and determine methods of preserving these important phenomena; quantitatively predicting corrosion rates is a secondary concern. It is possible that corrosion will be enhanced in some areas of the coolant loop and reduced in others due to magnetic interactions.

Figure 6.3.3-1 shows the predicted effect of Hartmann number (magnetic field strength or velocity gradient) on the corrosion or dissolution rate. Actually, this figure shows the sensitivity of the mass transfer coefficient to the velocity gradient near the wall. The results do not indicate a direct effect of magnetic field, but rather the impact of the MHD velocity profiles on the relative position of the momentum and concentration boundary layers.

The entrance lengths required for momentum, concentration, and thermal profile development will not in general coincide. Due to the properties of liquid metals, and lithium in particular (low Prandtl number and high Schmidt number), the three profiles will develop at different rates. To obtain act-alike corrosion behavior, the relative positions of the concentration and momentum boundary layers should be maintained between the blanket and the test module. This requirement may preclude complete act-alike behavior in a single

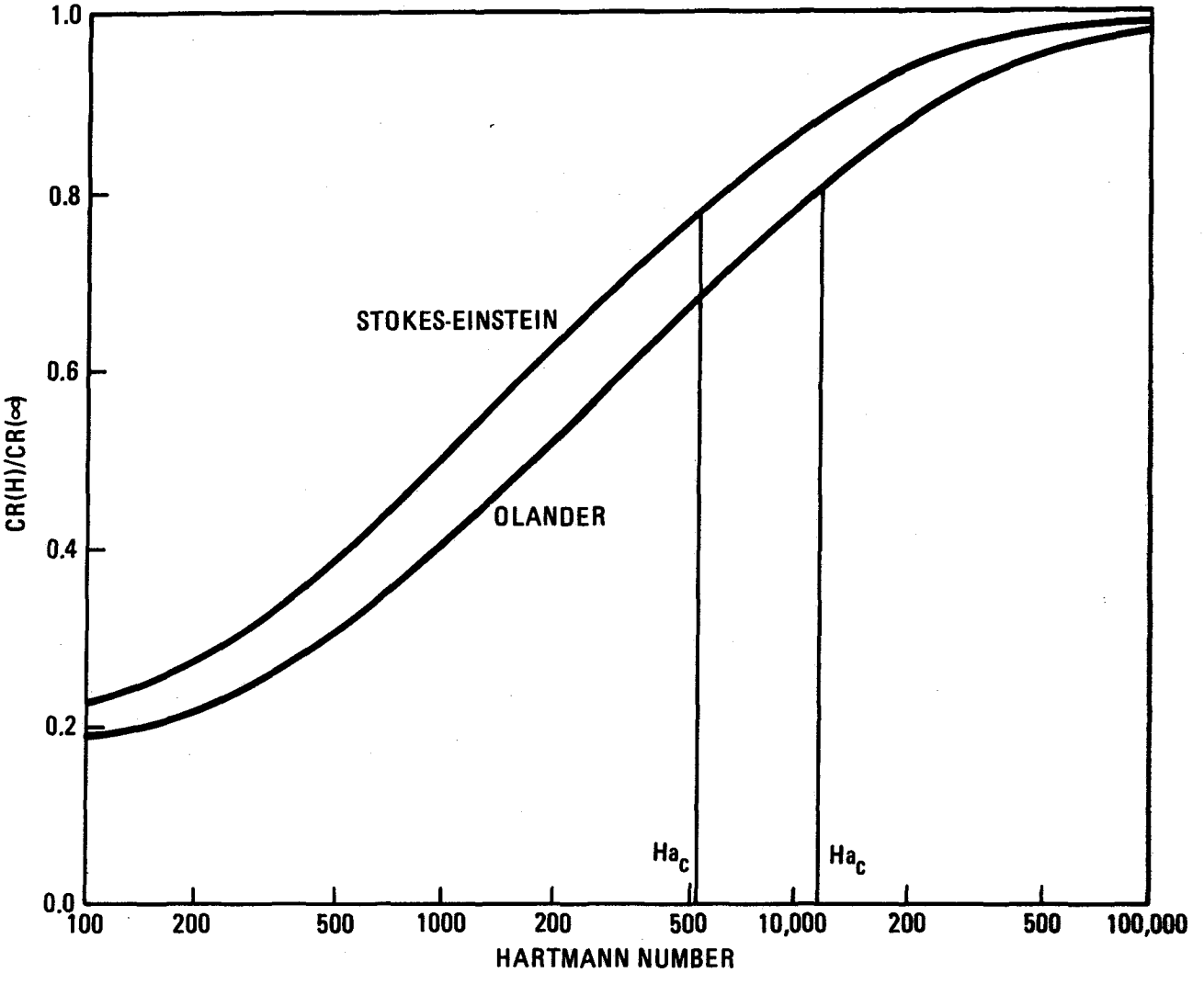

Figure 6.3.3-1 Corrosion rate versus Hartmann number - iron in lithium.

test module if the device parameters are altered — particularly the length of the coolant channels. In addition, geometric nonuniformities (inlets, outlets, flow obstructions) may be important if they delay or interrupt the development of a particular boundary layer.

6.3.3.3 Residence Time

The model presented in Section 6.2.3 indicates that one possible technique for obtaining act-alike corrosion behavior is to maintain the fluid residence time of the system. If the channel length is reduced, then an equal reduction in velocity will result in a good model of the convective/diffusive aspects of corrosion. Figure 6.3.3-2 shows the corrosion behavior with constant residence time, which is obtained by decreasing the velocity and channel length proportionately. Identical corrosion behavior was predicted when the axial position is normalized to the total channel length, indicating that residence time scaling is valid for dissolution behavior.

If the channel lengths are restricted by a reduction in the test module surface area, then reducing the coolant velocity will also maintain the coolant temperature rise. Figure 6.3.3.3 indicates that residence time scaling is still valid in the presence of temperature gradients. This can be interpreted as the result of maintaining the momentum boundary layer (Hartmann number) and wall concentration (temperature) for each corresponding axial position.

6.3.3.4 Temperature Scaling

Both the absolute value and the axial increase in temperature will be important to both the dissolution and impurity interaction processes. The absolute temperature will dominate the kinetics of the interfacial reaction — both impurity and dissolutive. The channel temperature increase will probably affect primarily the dissolutive reaction. In this section, the temperature dependence of the chemical kinetic portion of the interfacial reactions is ignored, although it may be an important contributor to the test requirements on temperature.

If the surface heat flux and bulk heating are reduced, preservation of either the average or the outlet temperature are two possible scaling options. In reactors, the outlet temperature is the most restrictive corrosion limit,

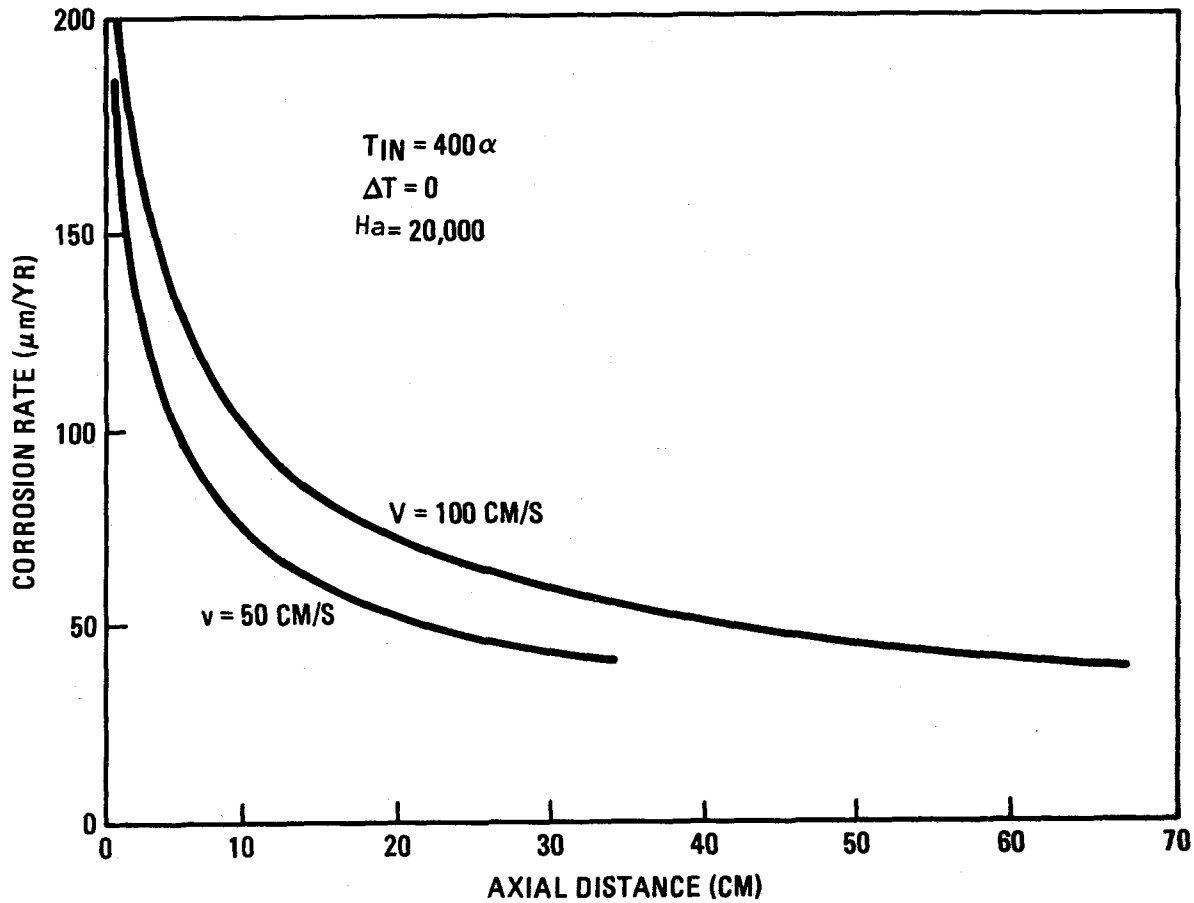

Figure 6.3.3-2 Axial corrosion rate profile with constant residence time.

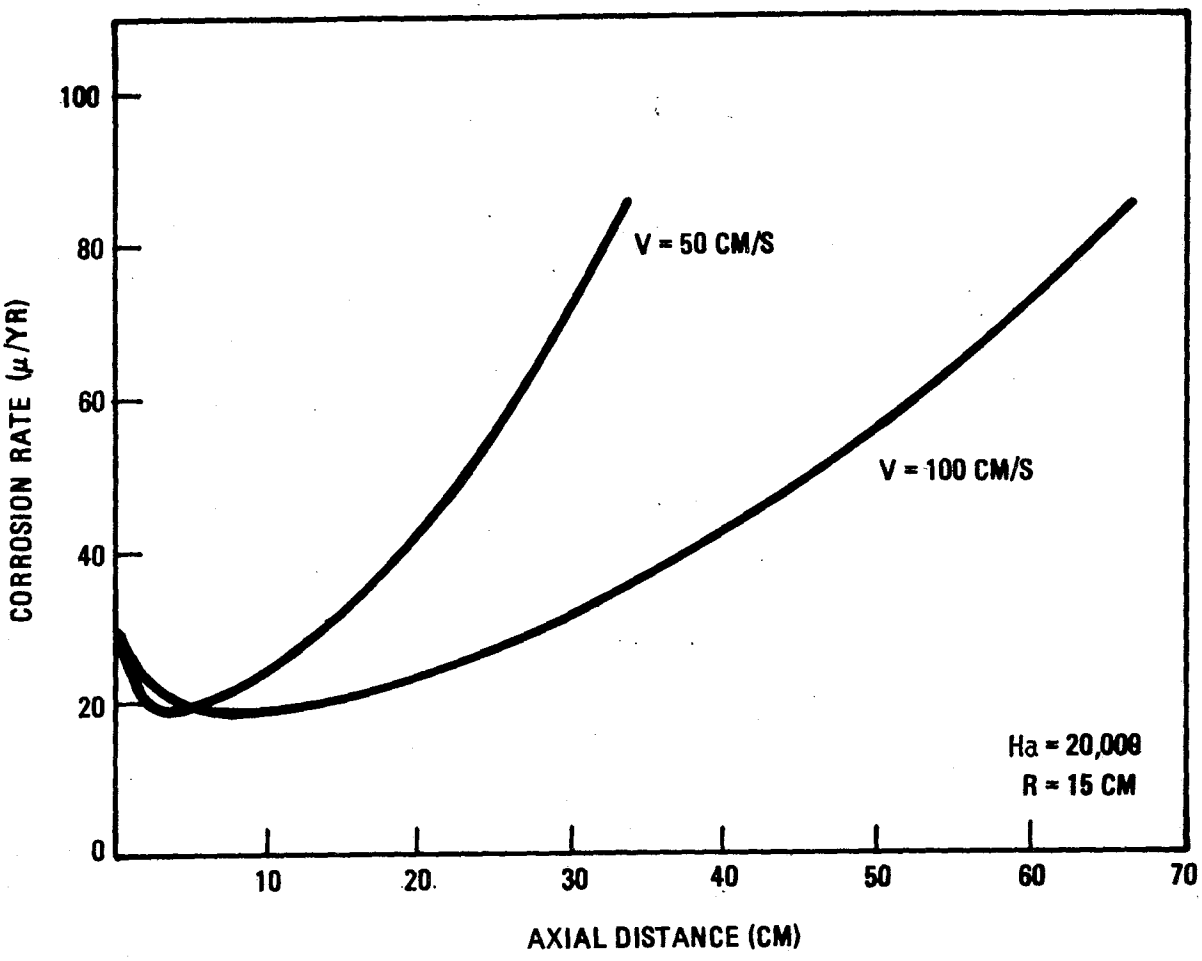

Figure 6.3.3-3 Axial corrosion rate profile with constant residence time and axial temperature increase.

while average temperature may be important for other concurrent testing in a particular test module design. Figure 6.3.3.4 shows the contrasting behaviors obtained with constant average versus constant outlet temperatures.

From a corrosion act-alike standpoint, preservation of both outlet temperature and channel temperature increase is desirable. Loss of channel "absolute temperature" would affect both dissolutive and impurity reactions, while loss of channel temperature increase would primarily affect dissolution.

It has been shown in Section 6.2.3 that three regimes of corrosion occur in a cooling channel with heat input. In the first regime, the concentration near the wall is small compared to the solubility and a fairly high corrosion rate results. After a short distance, the concentration profile develops and the corrosion mechanism begins to saturate. Due to the increase in temperature and solubility at the wall, the corrosion rate overcomes the saturation mechanism and continues to rise according to the behavior of the wall temperature. A loss of temperature rise is tolerable for model verification as long as the three regimes are observed. From Figure 6.3.3.4, it is clear that the coolant residence time should not be reduced by more than about a factor of two, or the corrosion behavior may not be reproduced.

6.3.3.5 System Interactive Effects and Test Requirements

At this time, system interactive effects are probably the least well understood aspect of corrosion. Interalloying of structural material, bulk transport of corrosion products to other system components and impurity movement and control all result from the integrated nature of the blanket and its related systems. The severity of each of these effects is unknown. In addition, there may be other important phenomena not yet discovered.

In the model described in Section 6.2.3, the bulk concentration of corrosion products at the inlet to the channel has been assumed to be negligible. The build-up of corrosion products in the bulk free stream will be extremely important and may cause deposition rather than corrosion at the inlet, and reduced corrosion near the outlet. Studies such as MARS and BCSS have concluded that deposition in the heat exchanger, rather than thinning and wastage in the blanket, are the limiting factor in blanket designs. The effect of corrosion product buildup has not yet been assessed in this study.

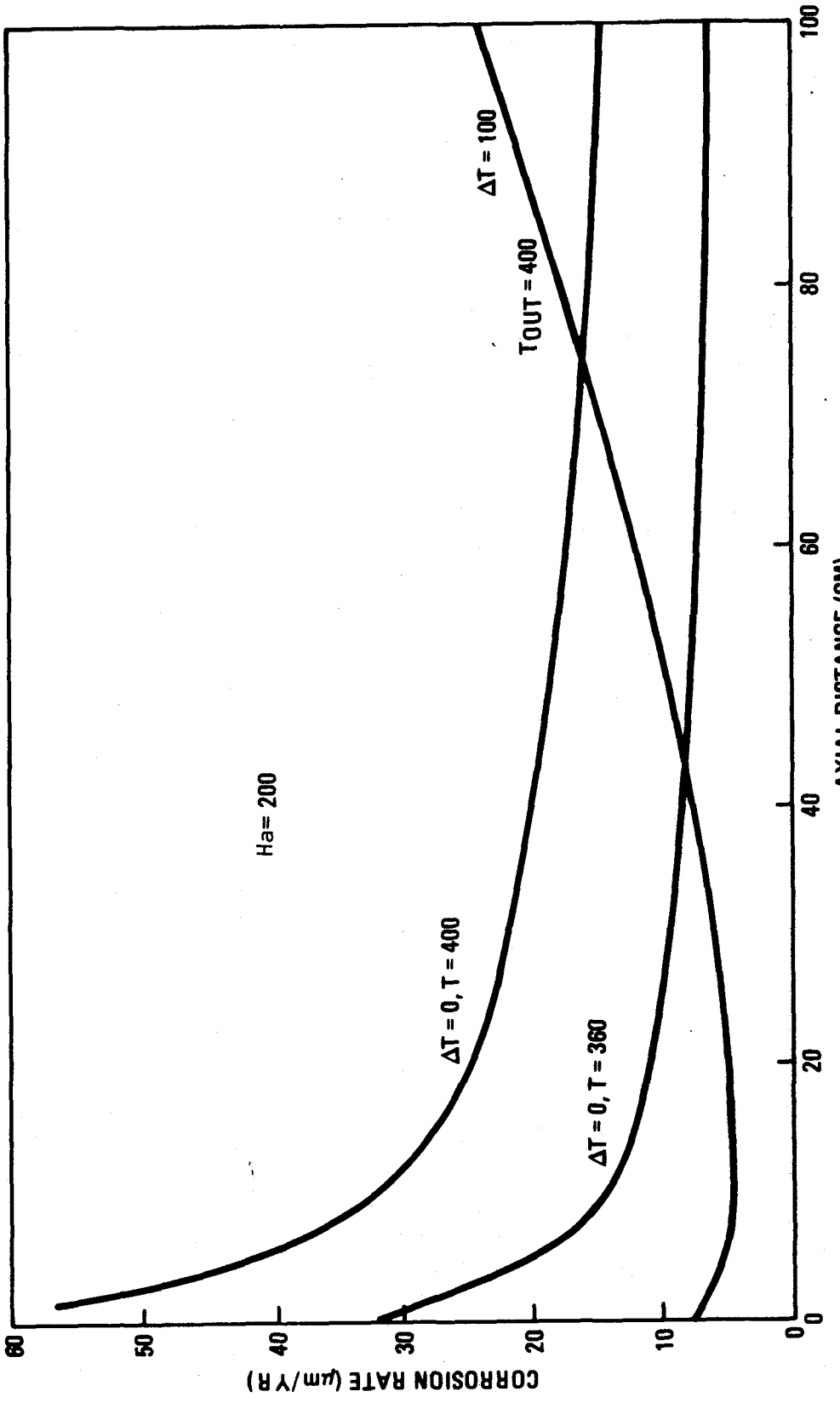

Figure 6.3.3-4 Comparison of corrosion rate profiles with constant average versus outlet temperature.

Ammon[1] has suggested that the most useful scaling technique for certain of these interactive phenomena is to preserve the ratio of surface areas between the hot and cold regions.

6.3.3.6 Summary

The test requirements described in this section are based on a very simple model which relies on a small amount of data to model a very complex process. The modeling performed for the dissolution mechanism of liquid metal corrosion has proven to be the most fruitful for determining test requirements. The results indicate that the relative position of the momentum and concentration boundary layers are important to maintain act-alike behavior. Fluid residence time scaling for convective/diffusive processes appears to be valid.

The behavior of both dissolution and impurity interactions will be affected by changes in absolute and axial increase of channel temperature. Analysis of the diffusive/convective corrosion mechanism suggests that the fluid residence time should be reduced by no more than about a factor of two.

References for Section 6.3.3

1. R. L. Ammon, "Vanadium and Vanadium-Alloy Compatibility Behavior with Lithium and Sodium at Elevated Temperatures," International Metals Review, 25, 255-268 (1980).

2. P. F. Tortorelli and J. H. DeVan, "Thermal-Gradient Mass Transfer in Lithium-Stainless Steel Systems," J. Nuclear Materials, 85-86, 289-293 (1979).

3. H. R. Konvicka and P. R. Sattler, "LILO-1 — A Thermoconvection Loop for Studying the Behavior of Stainless Steel Exposed to Liquid Lithium," J. Nuclear Materials, 122-123, 1241-1242 (1984).

6.3.4 Results and Conclusions of the Structural Analysis

Analyses of the BCSS lithium cooled and MARS lead-lithium cooled reference designs are described in Section 6.2.4. Application of the structural models discussed in Section 6.2.4 to the design of test modules for testing in a tandem mirror device are explored in Section 6.4, below. Some general conclusions are reported in this section.

6.3.4.1 BCSS Reference Blanket

The analysis discussed in Section 6.2.4.2 considers a first wall under high thermal stress which contains the coolant pressure in bending. The high thermal stresses are partly due to the choice of a composite plate structure, which increases the moment of inertia to efficiently contain the pressure, but also increases the average temperature difference through the wall. The composite flat plate first wall is a reasonable design approach for liquid metals because the coolant/breeder can fill and cool the structure (the toroidal channels in the reference design) with no neutronic penalty. This allows the design of a high moment of inertia structure to resist bending with good neutronic performance. The penalty is thermal stress; to increase the moment of inertia the structure should be made deeper (e.g. increase the web in the y direction in Fig. 6.2.4-1) which tends to increase the temperature difference and thus the thermal stress.

In the BCSS reference design the thermal stresses exceed the yield strength of the material, but not the reported allowable value for secondary stresses. The guidelines used in BCSS for allowable stresses are consistent with the ASME code, which allows yielding in some materials due to secondary stresses. However, designing in the plastic regime is subject to some controversy. Problems may arise due to thermal ratcheting agravated by irradiation creep. Since the model considered here does not include initial plastic deformation (plastic deformation due to irradiation creep is included) the effects of high secondary stresses and thermal ratcheting have not been evaluated quantitatively. A fruitful area for future work would be to include initial plastic effects in the model, and to examine designs which contain the coolant pressure in hoop stress and thereby incur lower thermal stresses.

Several useful conclusions can be drawn from the results of our work. Aspect ratio scaling appears to work well for preserving stresses. If a test module is operated at reduced wall loading and surface heat flux, stresses can be made act-alike by increasing all dimensions of the structure in direct proportion such that the temperatures are preserved. Stress response does not appear to be sensitive to small changes in the temperature profile as long as the temperature difference averaged over the area of the structure is preserved. For example, a test module with a thickened first wall and lowered heat flux has a more parabolic profile than the reference blanket. This has a negligible (less than a few percent at a surface heat flux of 20 W/cm^2) effect on stresses according to our calculations (see Fig. 2.4.2-2). Pressure stresses are preserved if the pressure and aspect ratios are preserved, and can be controlled somewhat when aspect ratios are not preserved by adjusting the pressure.

Some experimentation in trying to preserve stresses without preserving aspect ratios was performed. It was found that the model was relatively insensitive to changes in the web connecting the first and second walls. Stress profiles can be made reasonably act-alike (within 10% in a test device operating at 2 MW/m^2 neutron wall loading and 20 W/cm^2 surface heat flux) by increasing the first and second wall thicknesses and retaining the overall depth of the composite wall (decreasing the web height). However, thermal-hydraulic analysis indicates that the channel thickness should increase at reduced heat flux and wall loading to match temperatures (see Section 6.3.2). The best way to preserve stresses is to preserve aspect ratios.

The above conclusions were found to hold when radiation creep was included. No creep data was available for the vanadium alloy at the time of this writing, so values for HT-9 were used for the creep coefficient and creep exponent in equation (2) of Section 6.2.4.2. The results shown in Figs. 6.2.4-4 through -6 indicate two important conclusions: (1) Thermal stresses relax due to irradiation creep after roughly two months (10-12 dpa) of operation in the power reactor. This means that several months of operation will be required in a lower wall loading test device to study stress relaxation. Stresses toward the center of the span reverse (Fig. 6.2.4-5) due to the coolant pressure. Note that dpa rate dependence is not included in the model. Rate dependence may be negligibly small, however, if thermal creep is

significant stress relaxation patterns will be strongly affected by dpa accumulation rates; (2) Deformation appears to continue after the higher stresses have relaxed (see Fig. 6.2.4-6). The continued deformation is presumably due to pressure stresses. This could impose a constraint on blanket life, depending on the amount and impact of deformation in a particular design.

Results of this section and their impact on testing are discussed further in Section 6.4.

6.3.4.2 MARS Reference Blanket

The analysis in Section 6.2.4.3 considers a very different situation than that of the BCSS design in the previous section. The MARS design has much lower thermal stresses, and the blanket supports are of fundamental importance in determining the first wall stresses. The model includes radiation and thermal creep and swelling. The major results of this analysis are that aspect ratio scaling will work if damage (primarily swelling) gradients can be preserved (this may be difficult), and that stresses continue to rise throughout the useful lifetime of the blanket. These results and their impact on integrated testing are discussed further in Section 6.4.

The model described in Section 6.2.4.3 includes all the effects considered to be important to the MARS blanket structural response. Thermal stresses do not exceed the yield strength of the material as they do in the tokamak blanket discussed above. The major uncertainties are in the materials data. Recent, unpublished data indicates that swelling in HT-9 may be negligible, rather than a dominant contributor to end-of-life stresses as indicated by our analysis. Good materials data is a necessity in developing reasonable fusion reactor blanket designs.

6.3.5 Neutronics

6.3.5.1 Introduction

Module tests may be performed in a fusion test device which is smaller in both size and power than a fusion reactor. To simulate the phenomena which take place in the full size reactor blanket under scaled test conditions, the size of the blanket components may need to be changed. Moreover, the module test may be done with a single test module which is surrounded by reflectors and plugs. Since neutronics parameters are sometimes sensitive to the geometrical configuration of the system, scaling the device size or the test module size may affect the neutronics parameters. Also, the very different environment around the module which is expected in single module testing may disturb spatial profiles of the parameters.

The purpose of this section is to demonstrate the influence of neutronics parameters on the effectiveness of blanket testing under scaled conditions. Both the absolute value and the spatial profiles of the neutronics parameters depend on the device size, the module size, and the module environment. Here, these dependences are analyzed and discussion of the results of this analysis is presented.

An overview outline of the results provides the following conclusions: (1) The magnitude of device size effect is ~ 20-30% for both the absolute value and the relative profile of the parameters, provided the device first wall radius is larger than 20 cm. (2) The influence of the module thickness on the neutronics parameters is very small (less than 15%). (3) A change in the first wall thickness gives rise to a 30-50% increase in the heating rate in the first wall. (4) The effect of module width and environment on overall depth profiles is ~ 10%.

These results indicate that the simulation of neutronics behavior of the module will be attained relatively easily under scaled conditions. Note that the conclusions of this section are derived for general blanket testing rather than neutronics testing. The required accuracy in neutronics testing, which is presented in Chapter 7, is very severe; for neutronics testing under scaled conditions, simulation of the blanket behavior requires a more sophisticated treatment than that described in this section.

6.3.5.2 Method of Analysis

The bulk of the neutronics calculations were performed with full coverage geometry around the plasma using the one-dimensional code ANISN.[1] The results were used to analyze the size effects of the device and the test module. The multi-group constants used in the calculations were the same ones already described in Section 6.2.5.

To facilitate the analysis of the geometrical effect which arises from testing a single module in a test port, multi-dimensional calculations were also performed. The pointwise Monte Carlo code MCNP[2] was utilized in the analysis together with its library data. The vertical profiles of the neutronics parameters around the first wall were analyzed using the Monte Carlo results. Although there is no limitation on geometrical modeling for the Monte Carlo calculation, poor statistics sometimes makes it difficult to get accurate profiles at relatively deep locations in the module. The two-dimensional code DOT-4.3[3] was utilized instead of the Monte Carlo code to obtain the depth profiles of the parameters. These calculations were performed based on 23 group (n13 + γ10) constants, which were derived from the VITAMIN-C/-MACLIB-IV library,[4] using a third order Legendre expansion (P_3) and 16 angular mesh (S_4) approximation.

6.3.5.3 Device Size Effect

The effect of the device size on the absolute value and the profiles of the neutronics parameters is considered in this subsection. The analysis was performed assuming that the full size module would be used in three different size devices. Figure 6.3.5-1 shows the material configuration of the full size module. This is identical to the reference module of the self-cooled liquid metal blanket except that V15Cr5Ti alloy is used in the reflector instead of Fe1422 (See Figure 6.2.5-1). The device parameters, i.e., the plasma radius r_p and the first wall radius r_f of the three devices are listed in Table 6.3.5-1.

First Wall Parameters

Table 6.3.5-2 shows the results of the first wall radiation damage indicators, i.e., DPA, hydrogen production rate, and He production rate, as well as the nuclear heating rate. The values in the table are averaged over

	Plasma	Vac.	First Wall	Toroidal Channel	Second Wall	Poloidal Channel	Reflector	Shield
			VCrTi	VCrTi 10.7% Li 89.3%	VCrTi	VCrTi 1% Li 99%	VCrTi 90% Li 15%	Fe1422 90% He 10%
Thickness (cm)	r_p	t_v	0.5	4.5	1.5	40	30	60

Figure 6.3.5-1 One Dimensional Model for the Full Size Module of the Li/Li/V15Cr5Ti Blanket

Table 6.3.5-1 Device Parameters Assumed in the Analysis of Device Size Effect

	r_p(cm)	r_f(cm)
Tokamak	194	214
Mirror	50	60
Test Device	15	25

Table 6.3.5-2 First Wall Parameters Obtained for Three Different Size Devices

	N.H.(a)	DPA(b)	H(c)	He(d)
Test Device	9.02	18.87	523.6	126.8
Mirror	9.16	20.81	547.2	132.0
Tokamak	10.11	22.35	564.5	135.8

Note (i) a. Nuclear Heating Rate in units of w/cm^3.
b. Atomic Displacement Rate in units of dpa/yr.
c. Hydrogen Production Rate in units of a ppm/yr.
d. He production Rate in units of ppm/yr.

Note (ii) $2MW/m^2$ wall load was assumed.

Table 6.3.5-3 Attenuation Coefficient of Nuclear Heating Rate

Region	α (1/cm)
First Wall	0.121
Toroidal Channel	0.0626
Second Wall	0.147

the first wall thickness. The damage indicators were obtained by averaging the data of each element over all elements in the first wall structure. The absolute value of the data in Table 6.3.5-2 shows a general tendency: the smaller size device results in a lower value for every parameter. This means that reducing the device size decreases the parameter value.

As was derived in Section 5.3.1, the total neutron flux at the first wall is expressed as:

$$\Phi^{tot} = \Phi^{uncol} + \frac{4A_{\ell}}{1 - A_{\ell}} J^{uncol}, \qquad (6.3.5\text{-}1)$$

where Φ^{uncol} = the direct neutron flux from the source,

J^{uncol} = the neutron current of direct neutrons,

A_{ℓ} = the albedo value of the blanket system.

The second term accounts for the scattered (low energy) neutron component. Neutronics parameters are proportional to the total flux, Φ^{tot}, while the reactor power is usually expressed by the neutron wall load, which is proportional to J^{uncol}. Therefore, at fixed wall load, the variation in neutronics parameters with geometry can be expressed by the varition in the ratio of the total flux and the uncollided current, or f_s, where

$$f_s = \frac{\Phi^{uncol}}{J^{uncol}} + \frac{4A_{\ell}}{1 - A_{\ell}} \qquad (6.3.5\text{-}2)$$

The data in Table 6.3.5-2 are plotted in Figure 6.3.5-2, where the ratio Φ^{uncol}/J^{uncol} (which is the first term in Eq. (6.3.5-2) and the value of f_s corresponding to the conditions in the Table 6.3.5-1 are also plotted in the same figure. All values in Figure 6.3.5-2 are normalized to 1.0 at the tokamak condition. Although the neutron number albedo was used to estimate the value of f_s, the trend is reproduced well. To get more accurate values, we need to determine more adequate values of A_{ℓ} for each parameter. The value of A_{ℓ} depends on the radius of the first wall r_f, while the first term Φ^{uncol}/J^{uncol} depends on the ratio r_p/r_f, where r_p is the plasma radius. When the aspect ratio r_p/r_f is fixed and the device size is changed, the neutronics parameters will vary as shown in Fig. 6.3.5-3, where the albedo of 0.63 for the tokamak condition was assumed, the dependence of the albedo on the first wall radius was taken from Fig. 5.3.1-8, and $r_p/r_f = 0.906$ was

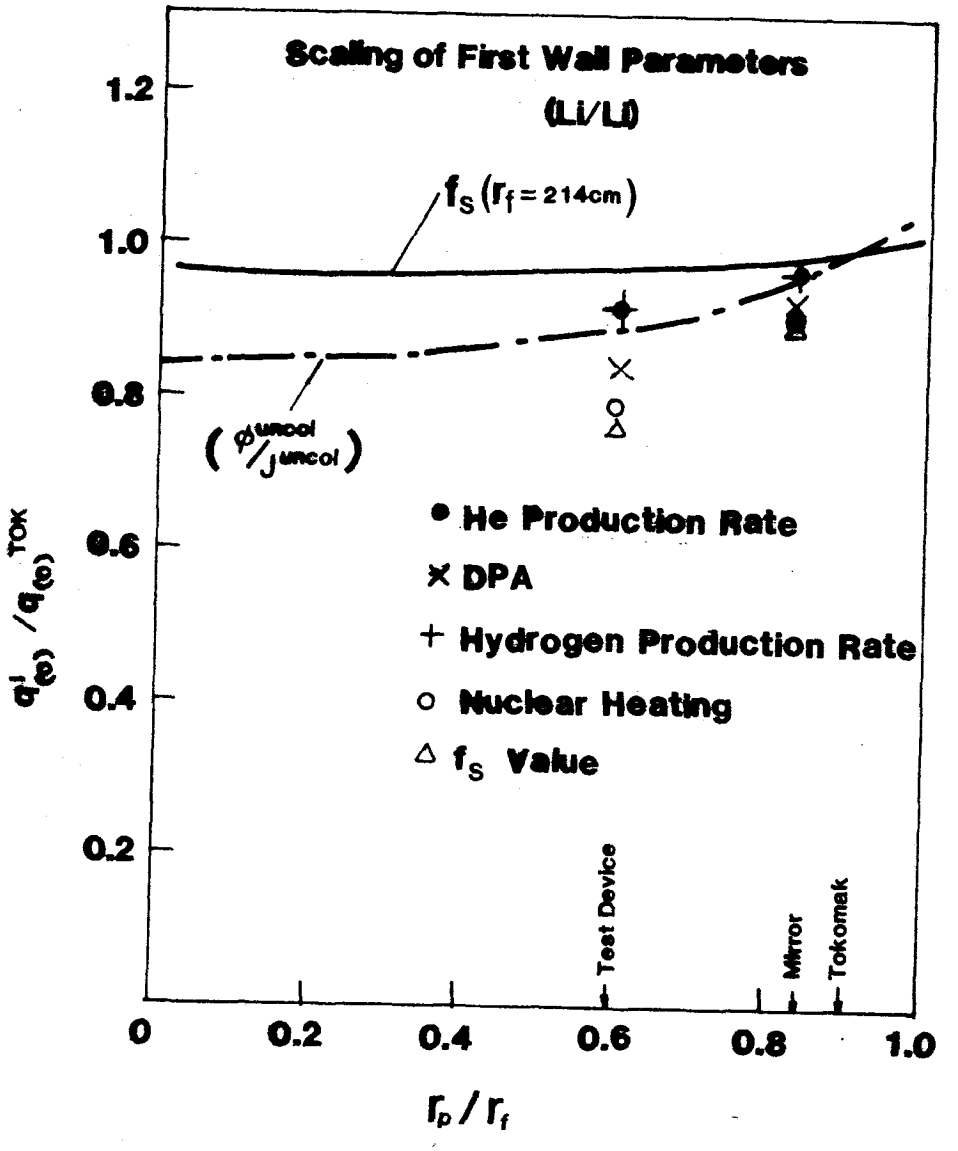

Figure 6.3.5-2 Scaling relation of the first wall parameters as a function of device size.

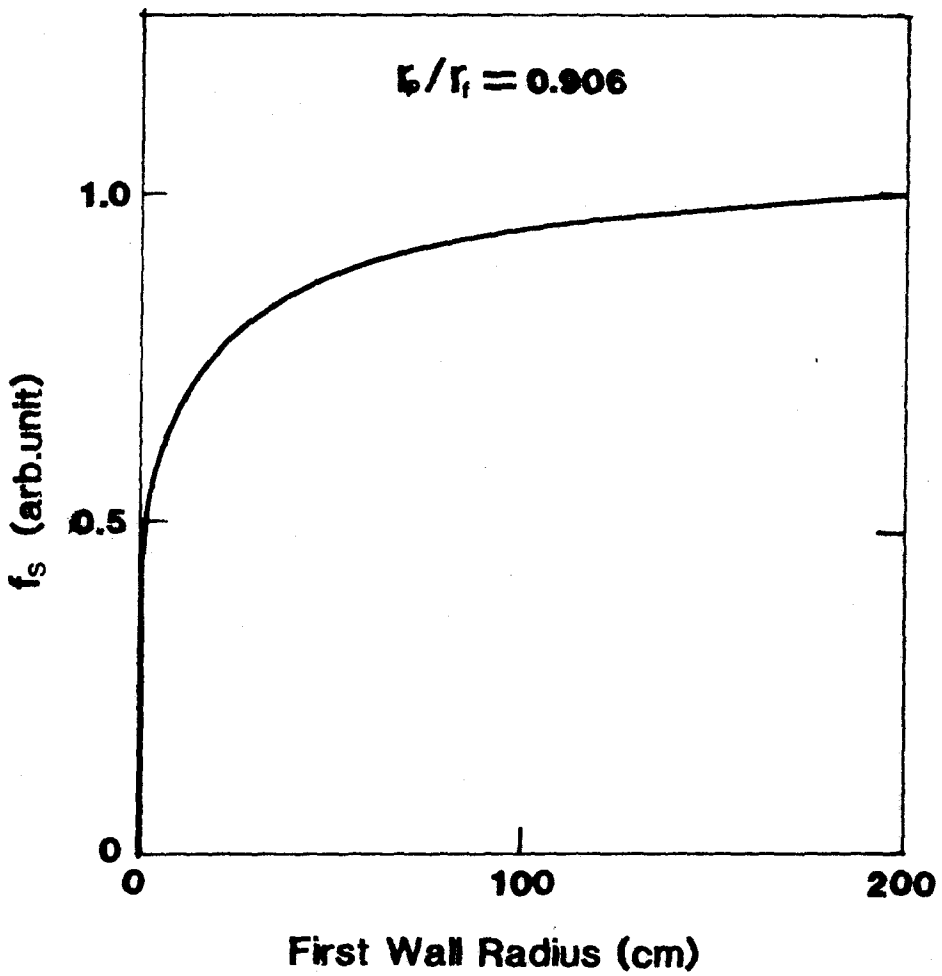

Figure 6.3.5-3 Scaling factor f_s as a function of first wall radius with the condition $r_p/r_f = 0.906$.

assumed. If the radius r_f is fixed, and the ratio r_p/r_f is changed, the neutronics parameters will vary as shown with the solid curve in Fig. 6.3.5-2, as a function of the ratio r_p/r_f. Comparing Fig. 6.3.5-3 with the solid line in Fig. 6.3.5-2, the main component which causes a decrease in the parameter value is the second term in Eq. (6.3.5-2).

The following observations are obtained from the results in Figs. 6.3.5-2, 6.3.5-3 and Table 6.3.5-2:

(1) As the device radius decreases, the parameter values obtained at the same wall load will decrease, especially for very small devices with radius less than 20 cm very small values are obtained (See Fig. 6.3.5-3.)

(2) For the helium and hydrogen production rates, the second term (low energy neutron contribution) in Eq. (6.3.5-2) is not important. So they follow roughly the curve of the ratio Φ^{uncol}/J^{uncol}. Consequently, the device size effect is smaller for these parameters than for other parameters.

(3) The parameters in the test device of Table 6.3.5-2 deviate from those in the tokamak case by about 20% at maximum.

The conclusion of this subsection is that the device size effect on the first wall parameters is within ~ 20% under the same wall load, if the test is performed in a device having a first wall radius larger than 20 cm.

Depth Profiles of Nuclear Heating Rate and Tritium Production Rate

Figure 6.3.5-4 shows depth profiles of the nuclear heating rate and the tritium production rate throughout the whole blanket region. Two things are observed from this figure. As the device size decreases, the absolute value of the data decreases for both parameters. This was already discussed above for the first wall parameters. The shape of the profiles is scarcely changed with the device size, although the gradient of the curves gets slightly steeper as the device size decreases. Rigorous treatment of this problem is very difficult. As the aspect ratio r_p/r_f was changed simultaneously with the device size, the angular distribution of incident neutrons was changed from case to case. But it can be concluded from the results in Figure 6.3.5-4 that the profiles of the neutronics parameters are mainly determined by the neutronic properties (cross sections) of the blanket system, so the effect of the change in the device size is not large.

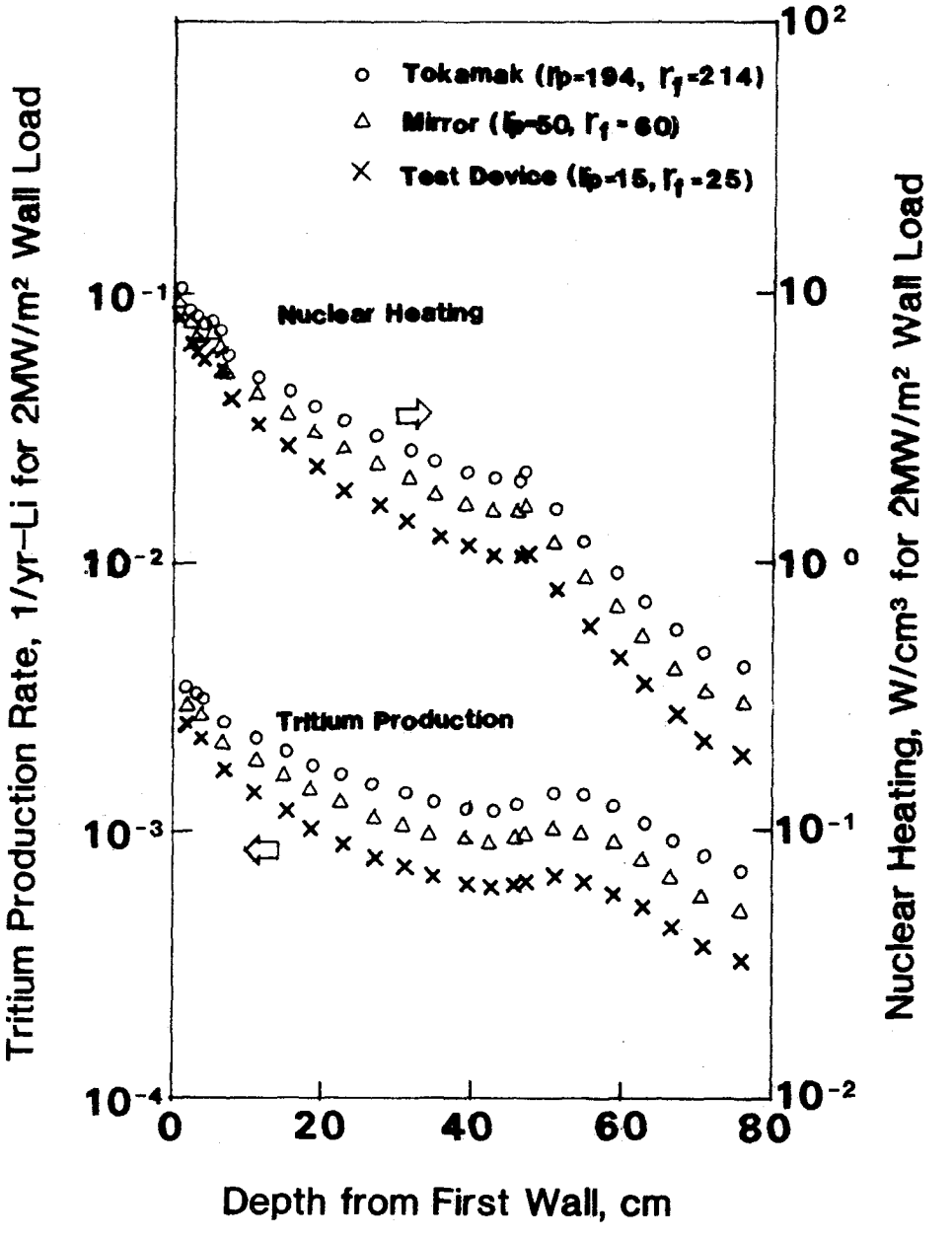

Figure 6.3.5-4 Depth profiles for the nuclear heating rate and the tritium production rate in the Li/Li/V blanket.

To compare the shape of the profiles in more detail, three curves of each parameter in Figure 6.3.5-4 were renormalized to the value of the test device at the top of the poloidal channel, i.e., the point of 6.5 cm depth. The results are shown in Figure 6.3.5-5. In the region from the first wall up to 20 cm deep in the poloidal channel, the profiles are almost the same for the three devices. Even if the whole blanket region is considered, the profiles are in the range of ~ 30% deviation for both parameters.

The conclusion of this subsection is that the effect of the device size on the profiles for the nuclear heating rate and the tritium production rate is small (within 30%).

6.3.5.4 First Wall Thickness Effect on Nuclear Heating Rate

Module testing performed at reduced power, may require the first wall thickness to be increased to achieve the same level of thermal stress. The increased first wall thickness will change the radiation field around the first wall, because high energy neutrons will be attenuated more by the thicker wall and this will give rise to additional low energy neutron production by (n,2n) reactions and also cause more gamma-ray production. The purpose of this section is to consider the effect of the first wall thickness on the nuclear heating rate around the first wall.

Figure 6.3.5-6 shows the material configuration of the test module used in the analysis. The first wall thickness was increased from 0.5 cm, which was the reference case, to 1.34 cm. The second wall was also increased from 1.5 cm to 2 cm, while the thickness of the toroidal channel was kept at the same value. Figure 6.3.5-7 shows the calculated results of the heating rate in comparison with the data for the reference blanket, which were cited from Figure 6.3.5-4. The increase in the first wall thickness resulted in about 30% higher heating rate in the first wall and in the second wall, while the heating in the lithium layer (toroidal channel) was scarcely changed.

The enhancement of the first wall heating was caused by gamma rays, which were produced by the increased wall material, because gamma-ray heating dominates the heating in the first wall, as is seen in Figure 6.3.5-7. The lithium layer is almost transparent to gamma rays, so its heating was not affected, but the transmitted gamma rays to the second wall through the lithium layer deposited additional energy in the second wall.

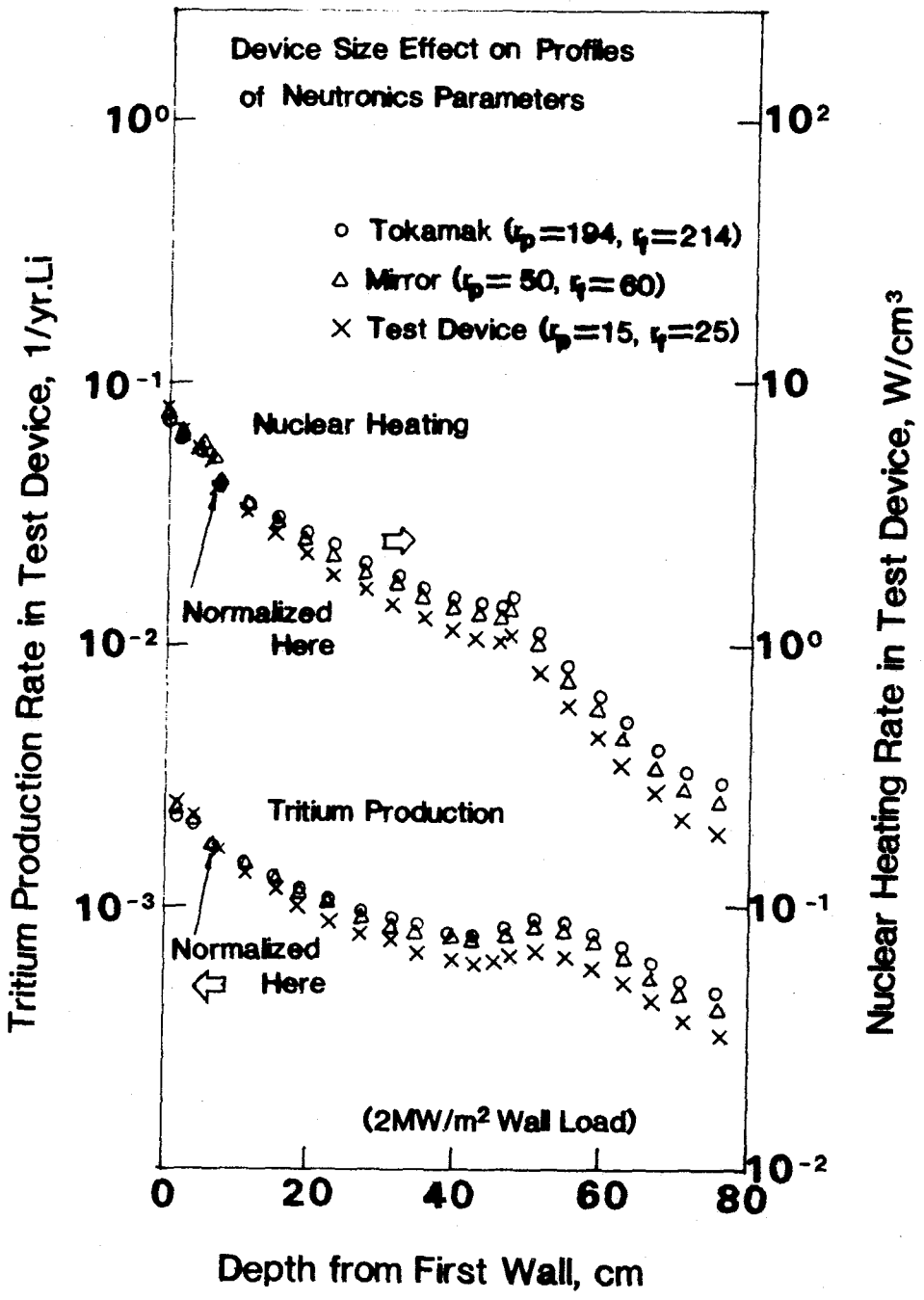

Figure 6.3.5-5 Comparison of the shape of depth profiles among different size devices.

	Plasma	Vac.	First Wall	Toroidal Channel	Second Wall	Poloidal Channel	Reflector	Shield
Thickness (cm)	15	10	1.34	4.5	2	17.16	30	30

Figure 6.3.5-6 Material Configuration of Test Module
Small Size Module

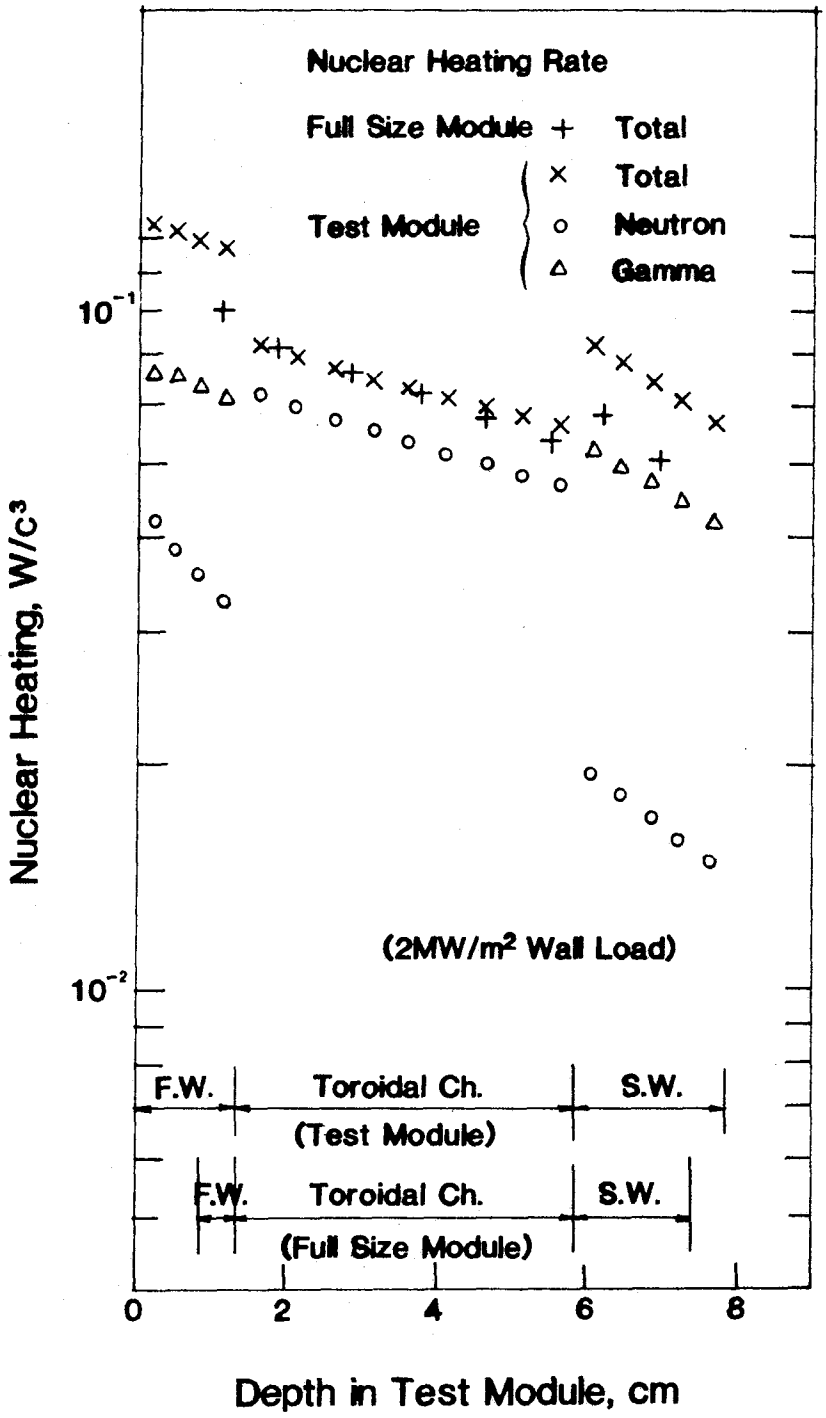

Figure 6.3.5-7 Comparison of heating rate profiles between the test module and the reference module.

High energy neutrons were attenuated by adding to the first wall thickness, but this effect was cancelled by the increase of low energy neutrons produced by neutron multiplication in the first wall. Consequently, the heating in the lithium layer, which was dominated by neutron heating, kept the same values.

The data of the total heating rate in Figure 6.3.5-7 were fitted to an exponential curve,

$$q(x) = q_0 e^{-\alpha x} \quad . \tag{6.3.5-2}$$

The α values of each region were not changed by the first wall thickness. Results of the α value are listed in Table 6.3.5-3.

The derivation of the scaling factor for the coefficient q_0 is very difficult. Very rough assumptions will be used to simplify the derivation. The value of q_0 in the first wall is proportional to the total neutron and gamma ray flux at the front of the first wall, which is written by the albedo, A_ℓ, of the blanket system as

$$\begin{aligned} \Phi_{tot} &= \Phi^{uncol} + \Phi^{col}, \\ &= \Phi^{uncol} + \frac{4A_\ell}{1 - A_\ell} J^{uncol} , \end{aligned} \tag{6.3.5-3}$$

where Φ^{uncol} and J^{uncol} are the flux and current of direct neutrons. We assume that the albedo is proportional to the amount of backscattered fast neutrons from the blanket. Then the blanket is split into two parts; the first wall and the remainder. The number of backscattered fast neutrons is written by an empirical formula as,[5]

$$N_f \sim \gamma_1 (1 - e^{-2\beta x_0}) + \gamma_2 e^{-2\beta x_0}, \tag{6.3.5-4}$$

where x_0 = the first wall thickness,

β = fitting constant,

γ_1 = albedo value at $x_0 = \infty$

and γ_2 = albedo value of the blanket part other than the first wall.

We will make another simplification to the second term in Eq. (6.3.5-3) as

$$\Phi_{tot} \sim 4J^{uncol} (\xi + A_{\ell}), \tag{6.3.5-5}$$

where $$\xi = \frac{\Phi^{uncol}}{4J^{uncol}} .$$

So the q_0 value should be

$$q_0 = \xi + A_{\ell} . \tag{6.3.5-6}$$

From the assumption,

$$A_{\ell} = \gamma_1 + (\gamma_2 - \gamma_1)e^{-2\beta x_0}, \tag{6.3.5-7}$$

the q_0 value is written simply as

$$q_0 = k\{(\xi + \gamma_1) + (\gamma_2 - \gamma_1)e^{-2\beta x_0}\}, \tag{6.3.5-8}$$

or

$$q_0 = \eta + \tau e^{-2\beta x_0}, \tag{6.3.5-9}$$

where $\eta = k(\xi + \gamma_1)$, $\tau = k(\gamma_2 - \gamma_1)$.

We need to determine η, τ, and β in Eq. (6.3.5-9) from known q_0 values at various thickness x_o.

Unfortunately, we have only two cases now for x_o = 0.5 and 1.34. The value of β should be close to the value of the attenuation coefficient of neutrons. The estimated neutron attenuation coefficient is ~ 0.25 using the curve of the neutron heating rate in Fig. 6.3.5-7. So, the β would also be around 0.25. Figure 6.3.5-8 shows the scaling of q_0 value by Eq. (6.3.5-9) with the first wall thickness as a function of β.

The value of q_0 in the toroidal channel should be less sensitive to the first wall thickness as compared to the value of q_0 in the first wall. It was not changed when the thickness was increased from 0.5 cm to 1.34 cm. However,

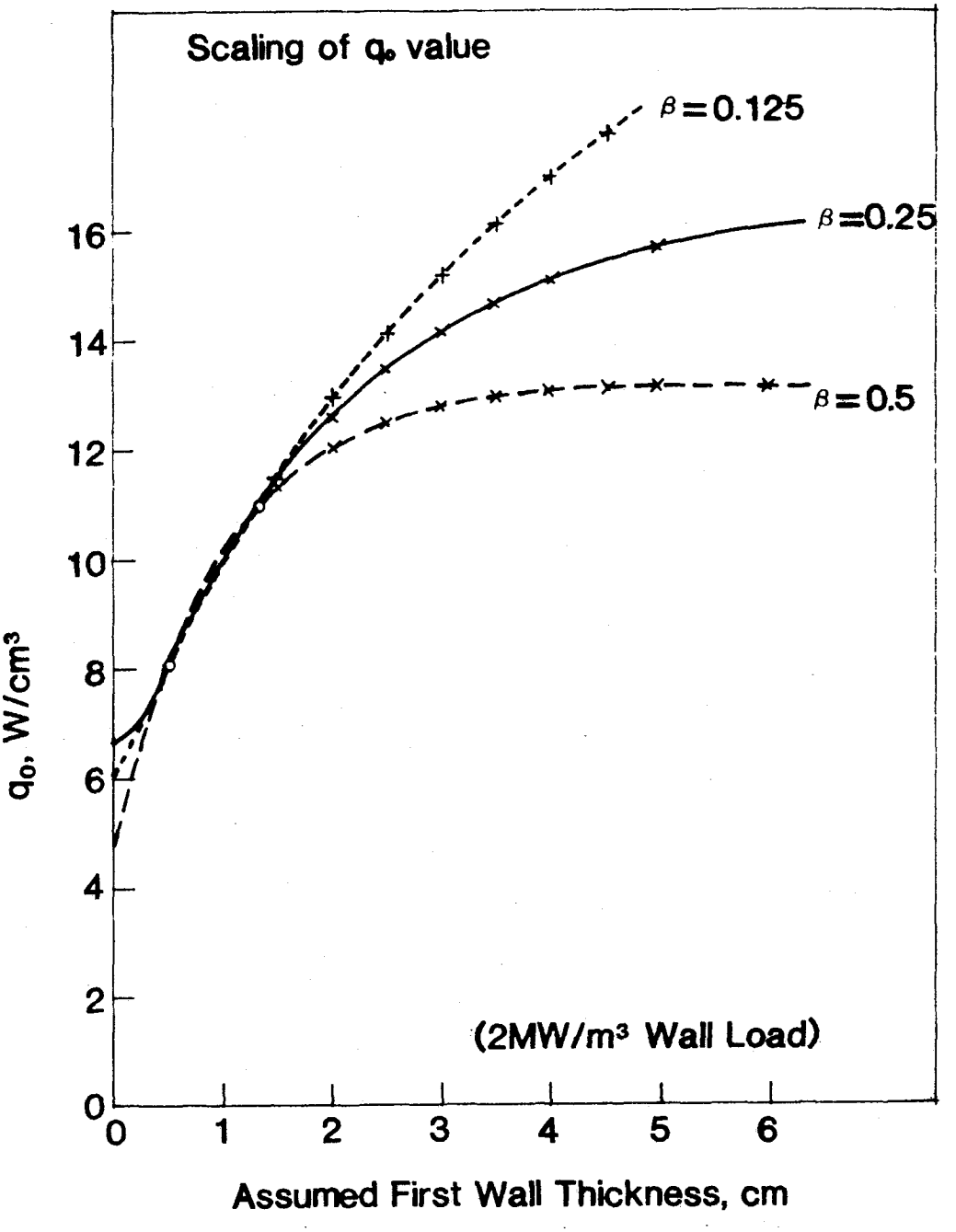

Figure 6.3.5-8 Variation of q_o value of the first wall with the first wall thickness.

it will decrease slowly if the thickness is increased further, because the attenuation of neutrons will dominate the variation of q_0 in the lithium layer for a very thick first wall case.

The value of q_0 in the second channel is controlled mainly by gamma ray flux at the front edge of the second channel because the gamma ray heating dominates the heating in the second wall. Since the lithium layer is less effective for gamma ray attenuation, the gamma ray flux at the second wall should be about the same as that at the bottom of the first wall. Consequently, the value of q_0 in the second wall is roughly expressed as

$$q_0^2 = kq_0^1 e^{-\alpha^1 x_0}, \qquad (6.3.5\text{-}10)$$

where q_0^1, q_0^2 are the q_0 values in the first and second walls, respectively, and k is the normalization constant, x_0 is the first wall thickness, and α^1 is the attenuation coefficient α in the first wall in Table 6.3.5-3.

We can summarize the discussion of this subsection as follows:

(1) An increase of the first wall thickness from 0.5 cm to 1.34 cm gave rise to an increase of ~30% in the first wall heating.

(2) From the scaling of q_0 in the first wall, a very thick first wall may result in very high q_0 value. (See curve of $\beta = 0.25$ case in Fig. 6.3.5-8.) The thickness should not exceed 2 cm to keep a similar heating rate profile.

(3) The first wall thickness effect on the heating rate in the toroidal channel is very small. So its effect on the tritium production rate there will be also small.

(4) The heating rate in the second channel will depend on the first wall thickness in a similar manner as the first wall heating rate when the thickness is not large. But, for a very thick first wall, the increment would be cancelled because of attentuation in the first wall.

(5) The damage parameters usually depend strongly on fast neutron flux. So an increase in the first wall thickness will result in a decrease of these parameters everywhere in the blanket, where the amount of the decrease will be controlled by the α value of the first wall in Table 6.3.5-3.

6.3.5.5 Effect of Module Thickness on Neutronics Parameters

Module testing may be done with a thinner blanket module as compared to the full size module. The thinner breeder will cause additional fast neutron leakage from the breeder zone to the reflector. This will cause more generation of secondary gamma rays, which will change the heating rate throughout the system. Moreover, the neutron reflection effect of the reflector may change of the heating rate profile in the thinner breeder.

One-dimensional radiation transport calculations were performed in cylindrical geometry to analyze the effect on the depth profile of the nuclear heating rate. The geometrical configuration which was utilized in the calculation is shown in Fig. 6.3.5-9, where the module thickness, t, was varied from 5 cm to 35 cm in steps of 5 cm. Only the poloidal channel was considered. None of the first wall, the toroidal channel nor the second wall was considered here to simplify the problem. The module was followed by the 50 cm shield (plug), so the reflector in the reference blanket was not considered either. The albedo boundary condition was imposed on the outer surface of the shield (plug).

Figure 6.3.5-10 shows results of the calculations. As expected, the thinner module gave rise to a higher heating rate in the whole region. But the amount of the increase is uniform throughout the module: the profiles are shifted to a higher value, and the shape of the profiles is scarcely changed. The amount of increase is higher in the thinner module case. This was also expected prior to the analysis. The amount, however, is very small (only 15% in the largest case).

Since the shield works as a neutron multiplier as well as a neutron reflector, the heating rate is enhanced in the region close to the shield. More neutrons are injected into the shield in the thinner breeder cases; the effect is more pronounced in these cases. However, the range over which the profile is affected extends only ~ 5 cm in the distance from the reflector boundary.

The conclusions of this subsection are as follows:

(1) The shape of the depth profile of the heating rate in the breeder is not influenced by the breeder thickness, excluding the region close to the reflector boundary.

1D Neutronics Model (Cylindrical Geometry)

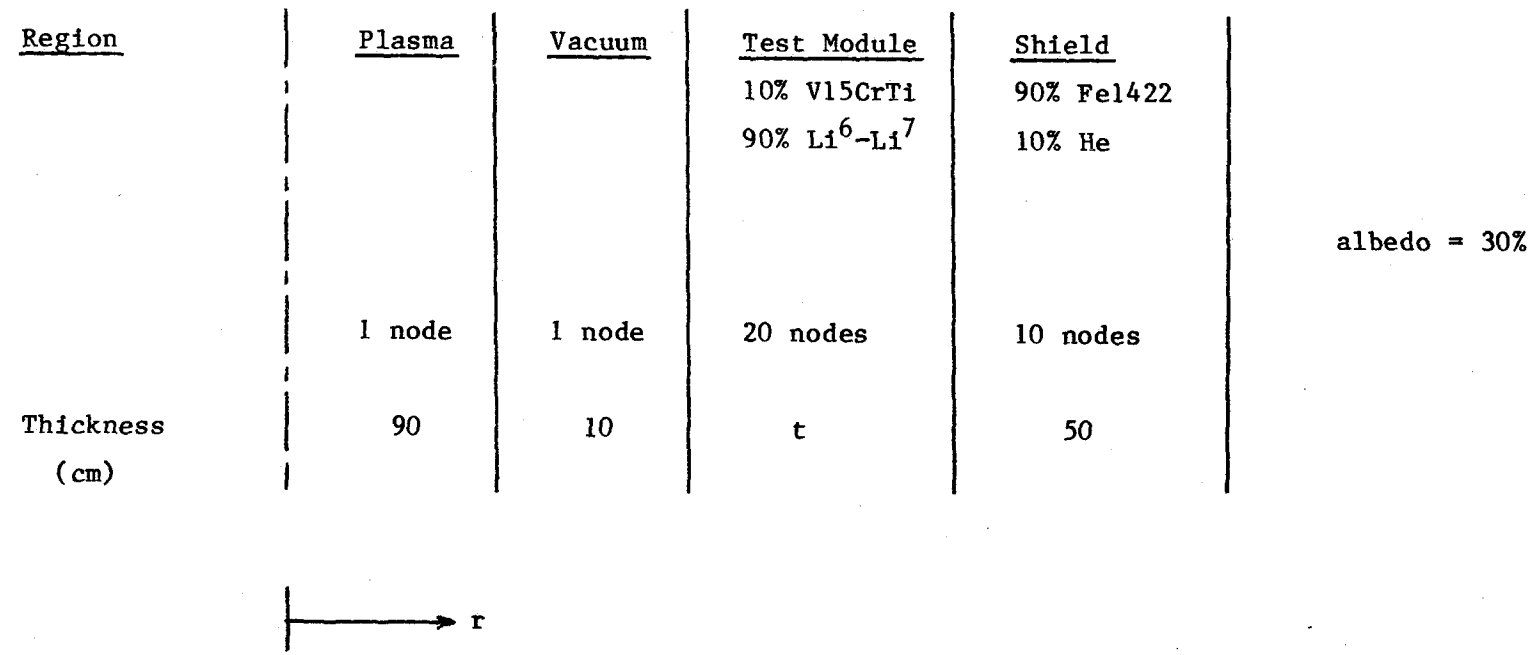

Figure 6.3.5-9 Calculational model assumed in the analysis of the module thickness effect.

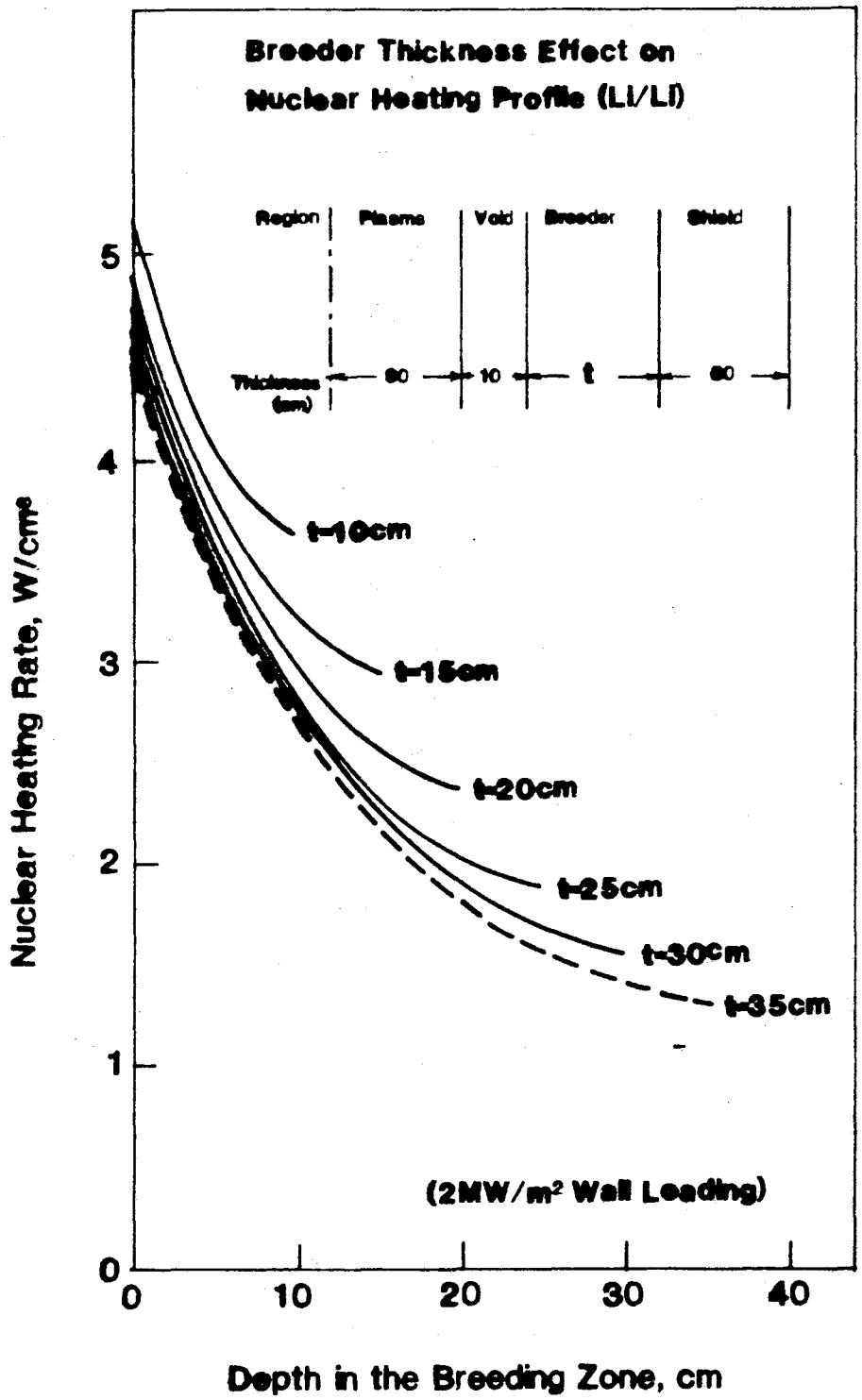

Figure 6.3.5-10 Depth profile of total nuclear heating rate obtained for various module thickness.

(2) The effect of the breeder thickness on the absolute value of the heating rate is very small (within ~ 15%).

(3) The effect of neutron reflection by the shield (plug) on the heating rate profile is noticeable only in the range of ~ 5 cm from the boundary.

These conclusions mean that if the test is done with a module having a breeder zone thicker than 10 cm, and done in the region around the first wall, good simulation of the heating rate will be obtained in both the absolute value (within 15% error) and the profile. To provide a good simulation throughout the entire module, a thicker breeder (more than 25 cm) is required to avoid the influence of the plug (see Fig. 6.3.5-10).

6.3.5.6 Effects Arising from Partial Coverage

For efficient, cost effective testing, test facilities may be configured with multiple test ports. A single test module would be inserted into one of these ports, and the module would be surrounded by reflectors and a plug if necessary. This geometry is significantly different from the full coverage condition of a reactor blanket.

Two problems arise from this test geometry. Profiles of the neutronics parameters in the direction perpendicular to the radial direction will not be uniform because the module width may be comparable to the dimension of the neutron source. A second problem is the possibility of disturbing the radiation field around the module with surrounding materials (reflectors). The analysis of these problems will be given in this subsection.

The analysis was performed by the MCNP Monte Carlo code and the DOT4.3 2-D Sn code, using multidimensional models which simulate the module test condition in the test port.

The schematic drawing of the assumed module test is shown in Fig. 6.3.5-11. The test module is inserted in one of the test ports. The space is surrounded by reflectors (denoted as "shield" in the figure). The location of the module can be selected flexibly, corresponding to the required module size. The test module dimensions assumed here are 50 cm wide by 55 cm thick. The material configuration along the depth direction is the same as that in Fig. 6.3.5-6.

Figure 6.3.5-12 shows calculational models of the test geometry. The

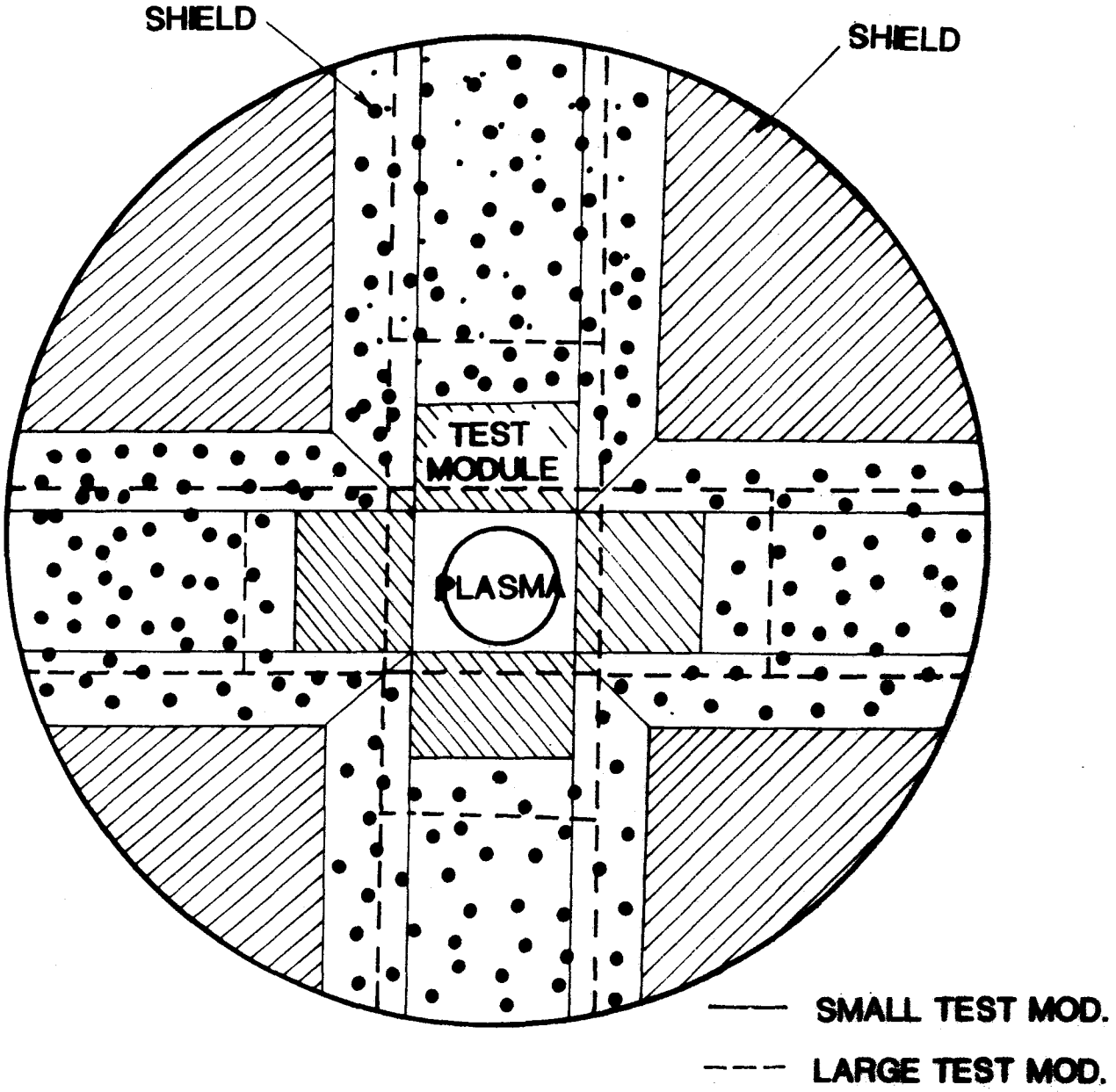

Figure 6.3.5-11 Fusion test device with four test ports for test modules.

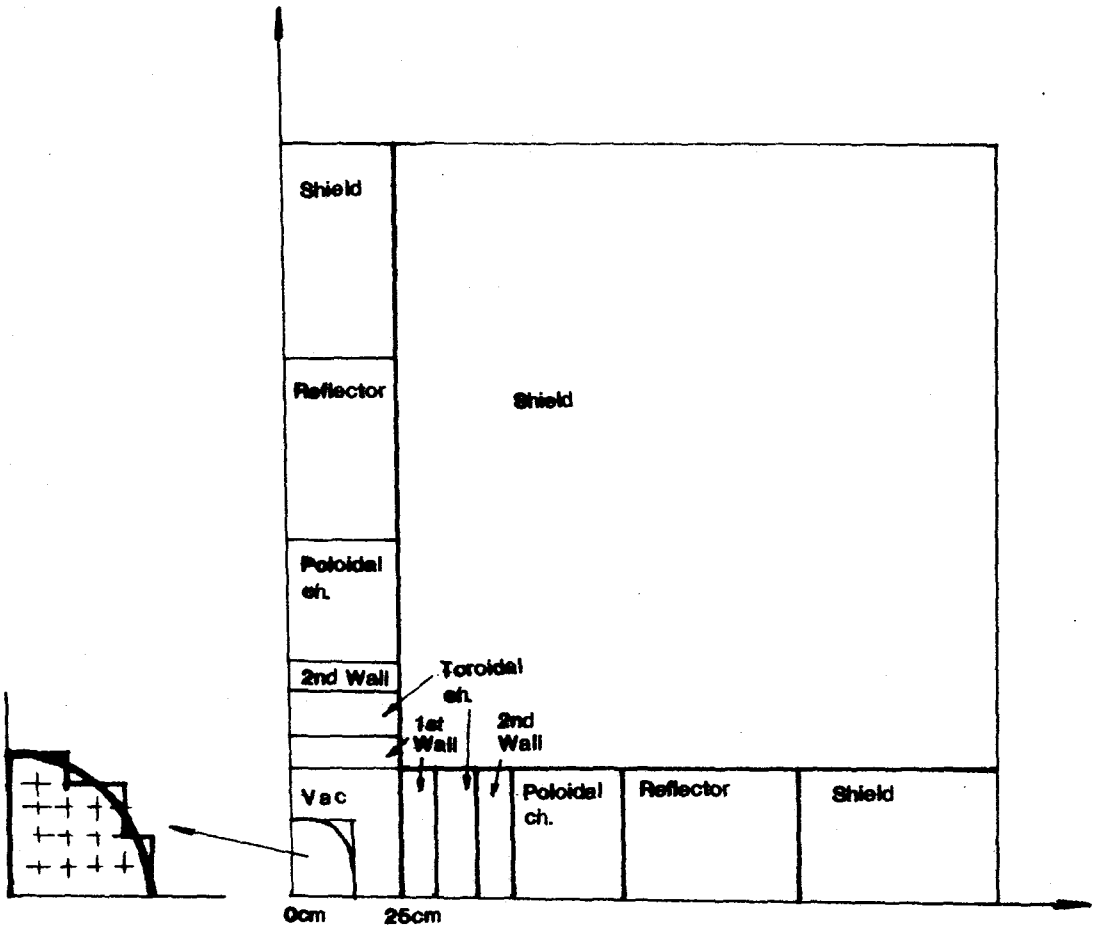

Case (1)

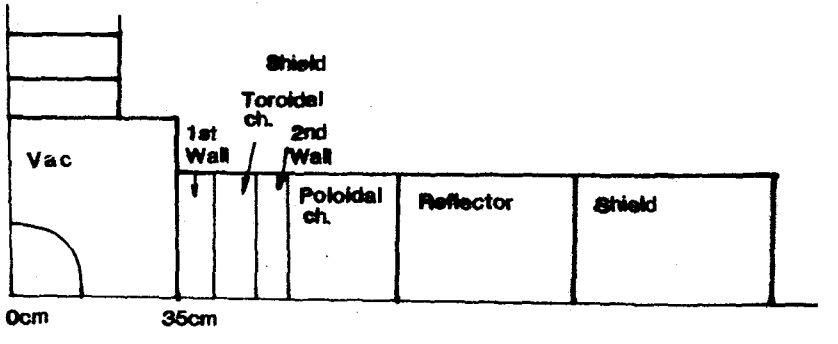

Case (2)

Figure 6.3.5-12 Two dimensional calculation model of module test geometry.

figures show the models for different test locations of 25 cm position [Case (1)] and 35 cm position [Case (2)] from the plasma center line. The geometries were expressed in the x-y coordinates, with the axes being on the module center lines.

Effect of Partial Coverage on Vertical Profiles of Neutronics Parameters

Figure 6.3.5-13 shows calculated results for the vertical profile (in the direction perpendicular to the module center line) of the nuclear heating rate in the first wall and the tritium production rate in the toroidal channel. These were obtained by MCNP in Case (1) (25 cm location) geometry. The nuclear heating rate follows a 1/r distribution, where r is the distance between the plasma center line and where the data were obtained, within the accuracy of statistical fluctuation in the data. The tritium production rate data differ from a 1/r distribution in the region close to the reflector. The tritium production rate was affected by neutron multiplication and neutron reflection from the reflector, which contains iron.

Similar results are obtained for Case (2) (35 cm location case) as compared to Case (1). As Fig. 6.3.5-14 demonstrates, increasing the distance from the plasma to the module moderates the gradient of the profile. For instance, the ratio of the heating rate at the module center to that at the boundary is decreased from 1.42 to 1.20, and for the tritium production rate, the ratio varies from 1.21 to 1.09.

The plasma radius was assumed to be 15 cm for Cases (1) and (2). In order to check the generality of the 1/r behavior which was observed in the profile of the nuclear heating rate, the radius was varied from 1 cm to 25 cm. The Case (1) geometry was used in the analysis. The results are shown in Fig. 6.3.5-15. As was expected, the nuclear heating rate follows a 1/r distribution in all cases. Moreover, the values are almost the same in absolute value except the extreme case of r_p = 25 cm, where the plasma almost touches the module.

The distribution of the neutron heating rate does not always follow the 1/r law as shown in Fig. 6.3.5-16. This implies that the origin of the 1/r distribution is from gamma ray heating. (In fact, the magnitude of gamma ray heating is twice as large as that of the neutron heating.) However, in a very rough approximation, the curves in Fig. 6.3.5-16 may be approximated by a 1/r

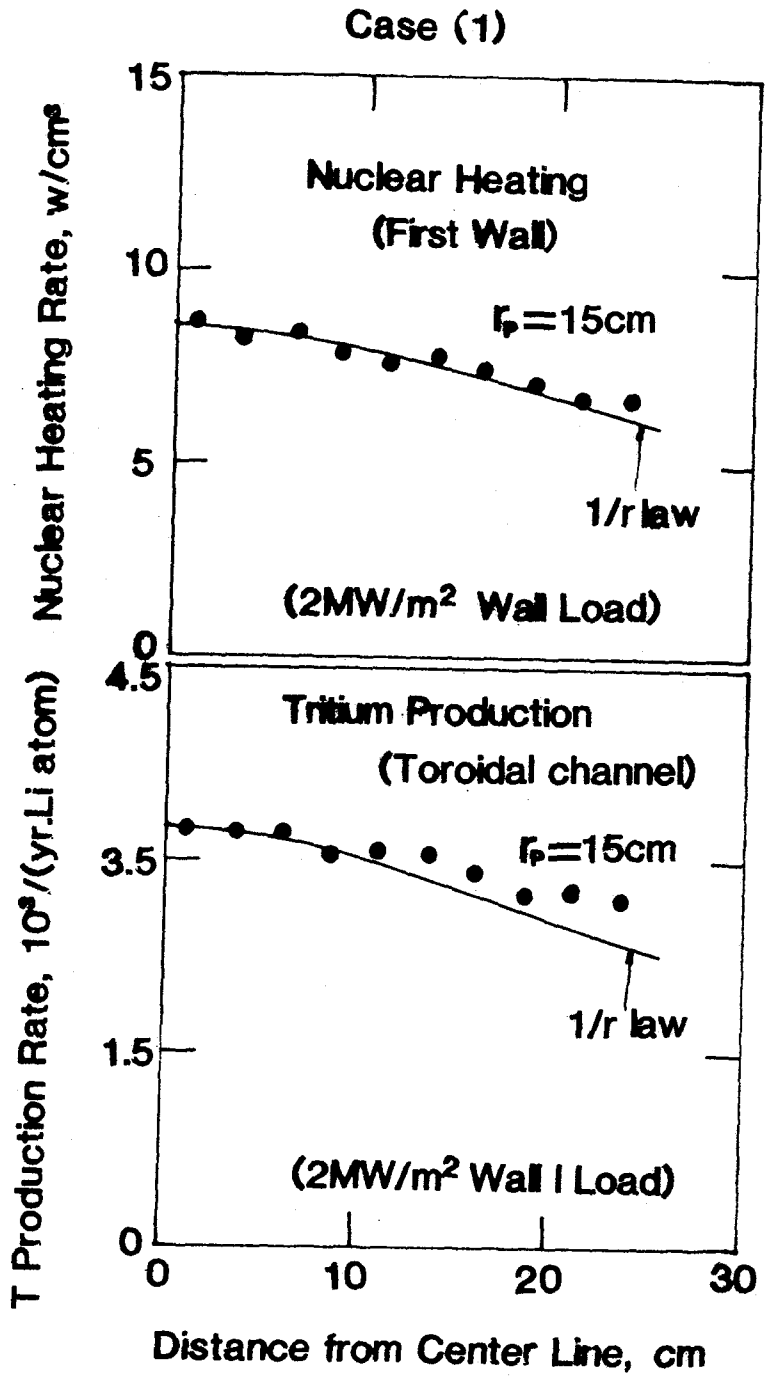

Figure 6.3.5-13 Vertical profiles of nuclear heating rate in the first wall and tritium production rate in the toroidal channel obtained for case (1) (25cm position) geometry.

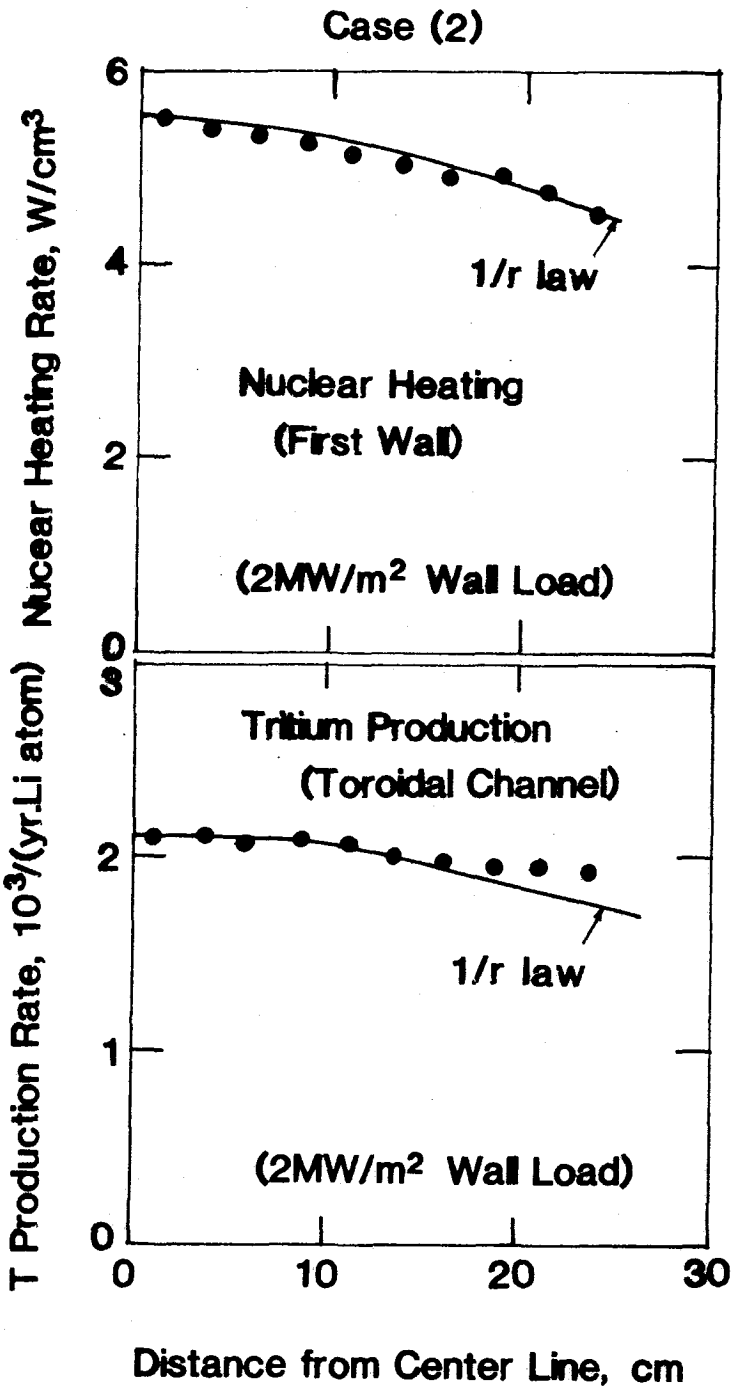

Figure 6.3.5-14 Vertical profiles of nuclear heating rate in the first wall and tritium production rate in the toroidal channel obtained in the case (2) (35cm position) geometry.

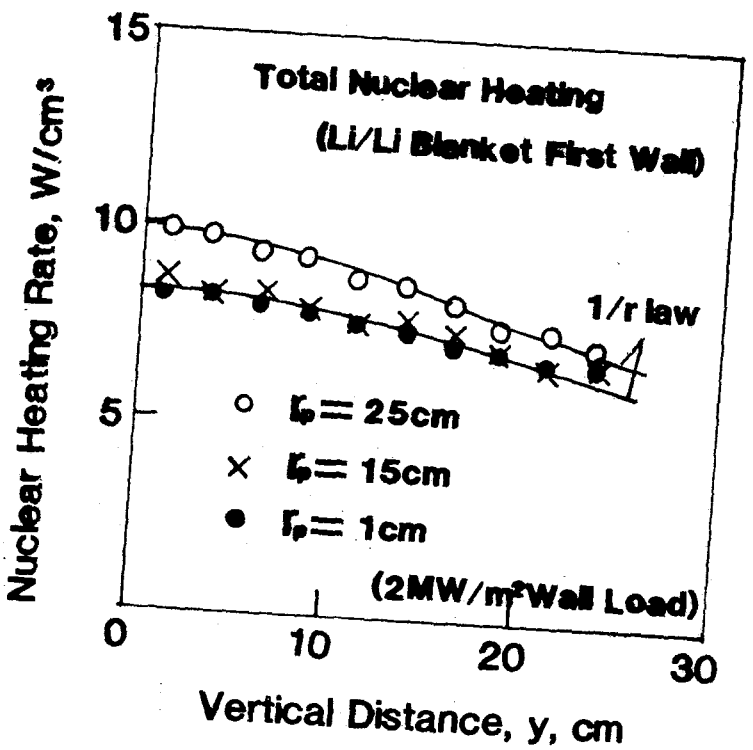

Figure 6.3.5-15 Vertical profiles of total nuclear heating rate for various source conditions.

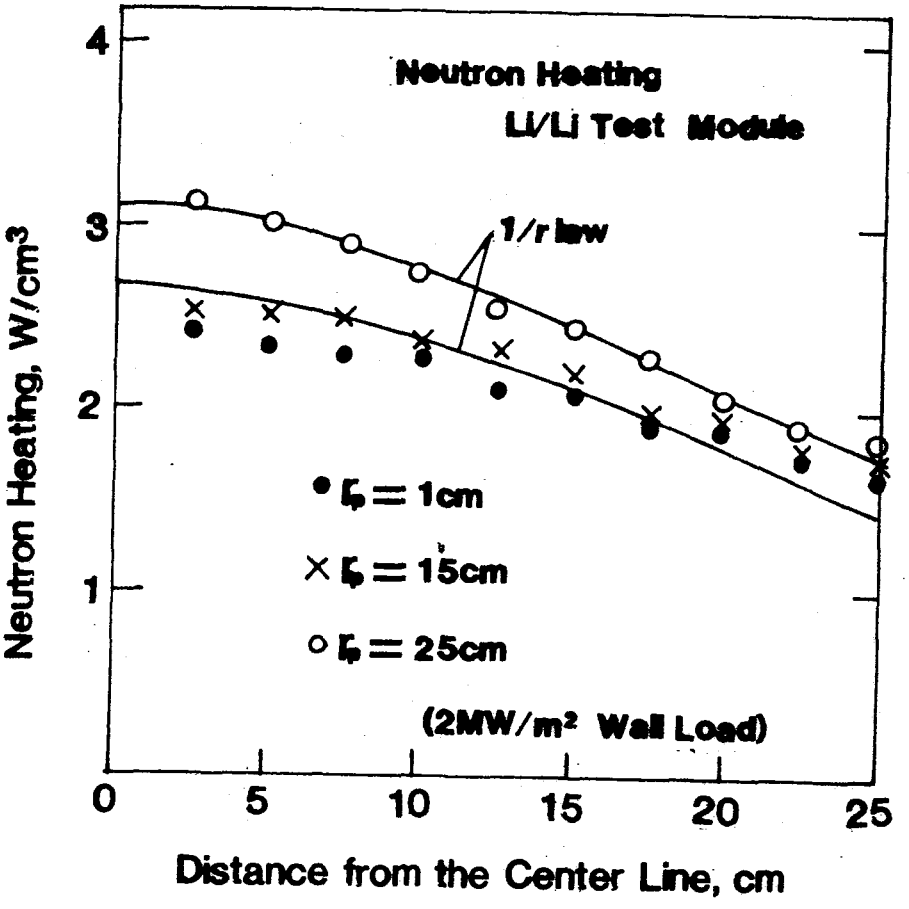

Figure 6.3.5-16 Vertical profile of neutron heating rate for various source conditions.

distribution.

The DPA rate, which was not analyzed here, is closely related to the neutron heating, so the profile of the DPA rate will look like the curves in Fig. 6.3.5-16. Figure 6.3.5-17 shows uncollided 14 MeV neutron fluxes for the three source conditions. The He production rate will show similar distributions because the threshold of the He producing reactions in the structural material is generally very high. Again, the distributions in Fig. 6.3.5-17 are approximated by a 1/r distribution except for a very extreme source condition (r_p = 25 cm).

From the above discussion, the 1/r distribution is generic among the vertical profiles of the total heating rate and the damage parameters (dpa and helium production rate) at the first wall of the test module. A similar 1/r distribution can be expected in the tokamak and mirror reactors for the neutronics parameters discussed above, although the analysis has not been done yet for these reference reactors. If this assumption is correct, the relative profile of the parameters will be similar to Fig. 6.3.5-18, where the same module width of 50 cm was assumed in the estimation of the curves. In the region up to 10 cm from the center, the profile of the test device is within 7% deviation from the tokamak curve. The deviation will increase to 30% at the module edge. From this figure, we may conclude that the test must be done only in the center region to avoid the size effect which will be caused by the difference in the profile.

The conclusions of this subsection are as follows:

(1) Vertical profiles of the total heating rate, and the damage parameters (dpa, helium production rate) follow approximately 1/r distributions in the test module.

(2) The tritium production rate in the toroidal channel shows more uniform distribution than the first wall parameters due to the neutron multiplication effect from the reflector.

(3) If a similar 1/r distribution is assumed in the tokamak and mirror reactors, the value of the neutronics parameters in the first wall will deviate ~ 30% at maximum with the size effect of the devices between the tokamak reactor and the test device for the 50 cm wide module.

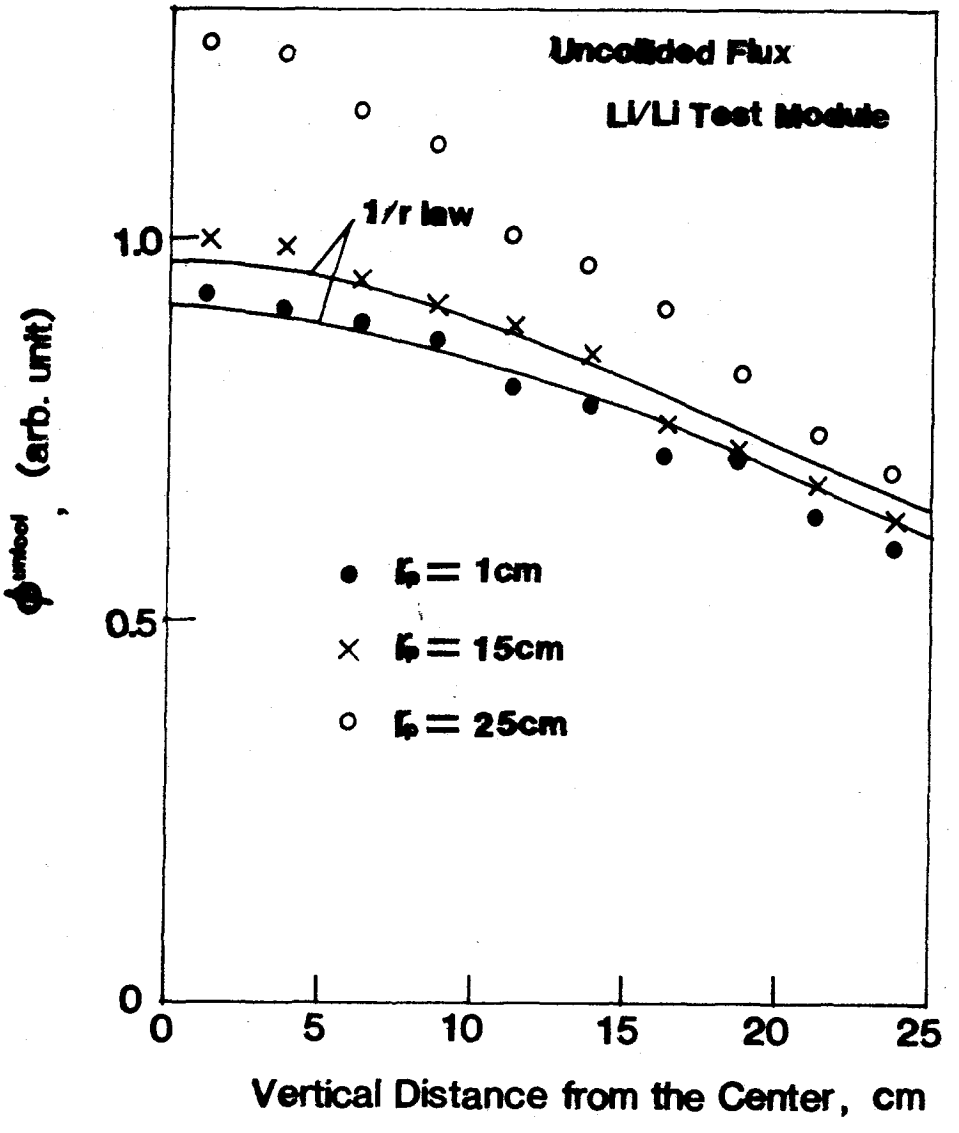

Figure 6.3.5-17 Vertical distribution of uncollided neutron flux for three source conditions.

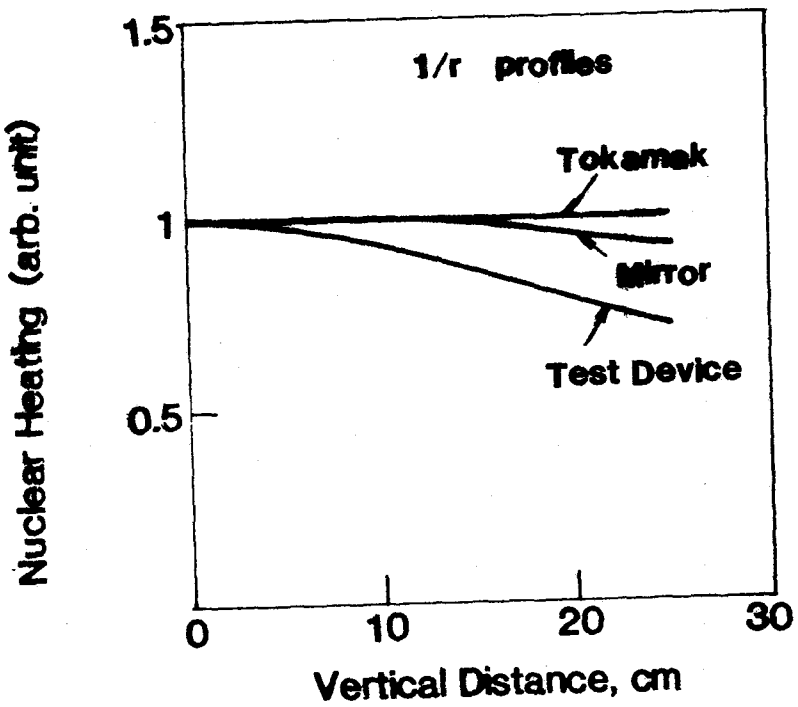

Figure 6.3.5-18 Estimated vertical profiles for neutronics parameters in different size devices.

Effect of Partial Coverage on Depth Profiles of Neutronics Parameters

The geometric effects of testing in a single test module is analyzed here regarding the depth profile of the neutronics parameters. Depth profiles obtained for the 2-D geometry will be compared with those for the full coverage geometry. The calculations were performed by the DOT4.3 code and obtained results were averaged over the module width to get the data at a certain depth.

Figure 6.3.5-19 shows results for the nuclear heating rate and the tritium production rate. Monte Carlo results are also plotted in the figure to check the consistency between the calculations. From the comparison between the DOT4.3 and the MCNP calculations, the consistency of the calculations is confirmed. Comparing the 2-D results with the results for the full coverage geometry, the test geometry gives about 10% lower values for the nuclear heating rate at the first wall. The tritium production in the test geometry is slightly larger than that of the full coverage case. Note that the tritium production rate was lower at the edge of the module than the midpoint in Fig. 6.3.5-13. This means the tritium production is enhanced even at the midpoint by the existence of the reflector. However, the increment is very small (~ 10% at maximum).

The depth profile of the overall tritium production rate in the full coverage geometry is reproduced closely in the test geometry (see Fig. 6.3.5-19). It seems that the drop of the values near the module edge is compensated by the increase due to the neutron multiplication and reflection in the reflector. The same thing can be pointed out for the profile of the nuclear heating rate.

The Case (2) geometry (35 cm location) resulted in ~ 40% decrease in the heating rate at the first wall and ~ 25% decrease in the poloidal channel as compared to the results of the Case (1) geometry (25 cm location). The tritium production was less affected by the module location. It was dropped by ~ 10% in the whole region.

The conclusion of the analysis of the depth profile is that the overall depth profiles for both the heating rate and the tritium production rate are reproduced fairly closely (within 10% deviation) to those in the full coverage geometry with the 50 cm thick test module. If the width is decreased, the

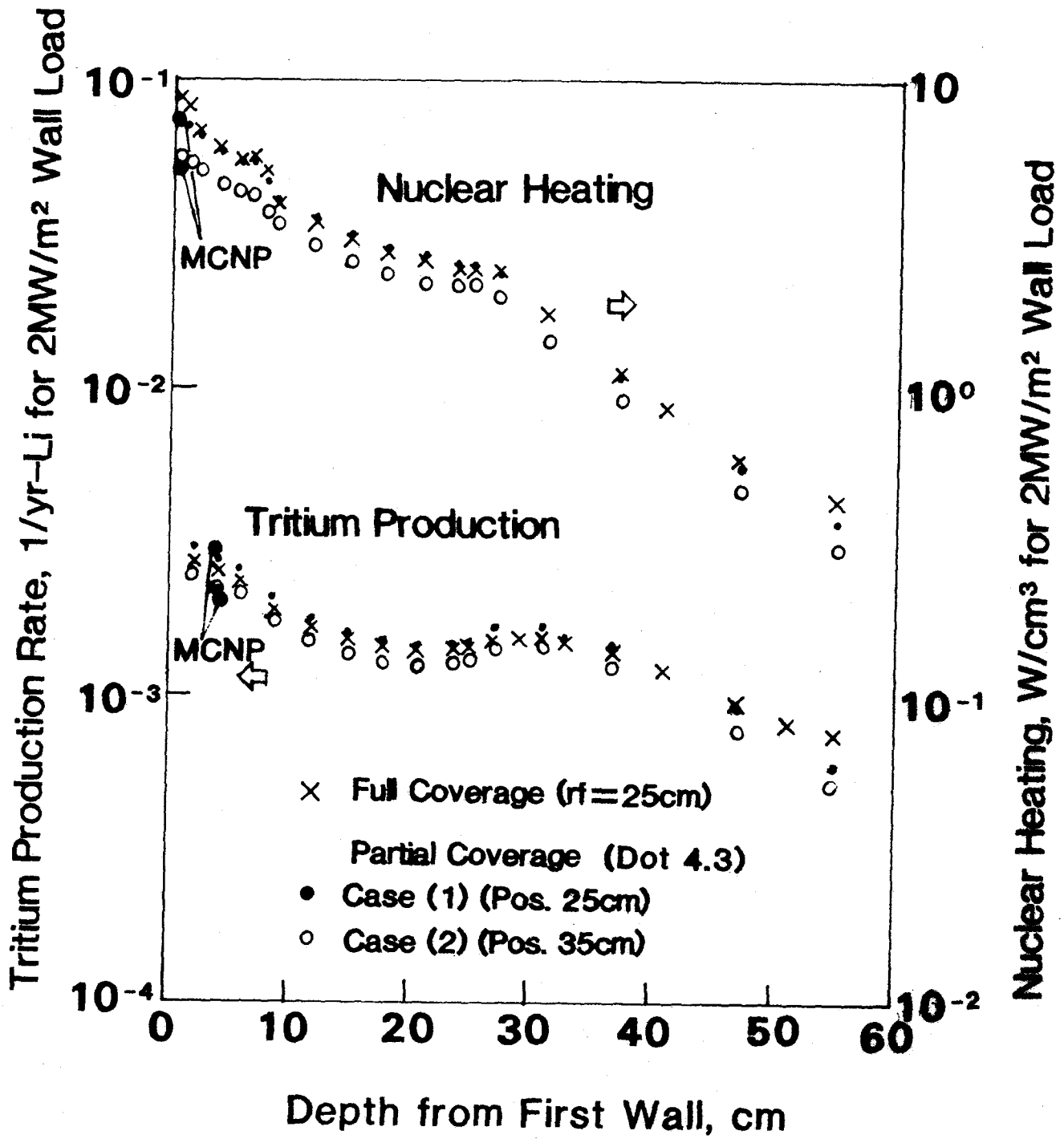

Figure 6.3.5-19 Depth profiles for the nuclear heating rate and the tritium production rate obtained by DOT-4.3 two dimensional calculations.

values will be enhanced, especially near the top of the module, so the heating rate profile will become closer to the full coverage case, while the increase in the test module width will result in the worse profile for the heating rate, i.e., the drop of the values around the first wall. The reverse is true for the tritium production rate.

6.3.5.7 Summary of Conclusions

The conclusions of the neutronics section are as follows:

Device Size Effect

(1) The device size affects the absolute value of the parameters in the first wall by about 20% for the reduction of the size from Tokamak reactor (r_f= 214 cm) to the test device (r_f= 25 cm).

(2) The profiles of the parameters become a little steeper as the device size is decreased, from the Tokamak reactor to the test device. But its influence is very small (within 10%) when the first 20 cm of the blanket is considered. For the whole blanket region, the maximum deviation in the profiles is ~ 30% at the bottom of the breeder zone.

Module Thickness Effect

(1) The module thickness effect on the nuclear heating rate is very small. Its effect on the absolute value of the parameter is within ~15% for the variation of the thickness from 5 cm to 35 cm.

(2) The profile of the heating rate is not affected by the module thickness, except the region close to the reflector.

(3) The influence of the neutron reflection from the plug extends ~ 5 cm from the reflector boundary.

First Wall Thickness Effect

(1) The change in the first wall thickness from 0.5 cm to 1.34 cm increases the heating rate in the first wall by ~ 30%, but it does not have any influence on the heating rate in the toroidal channel (lithium layer). The heating rate in the second wall is increased by ~ 20%. The effect is largest in the first wall.

6.4 Test Module Design

6.4.1 Introduction

One of the ultimate goals of fusion nuclear technology development is to perform integrated fusion blanket testing in fusion test devices. These test devices may operate at lower neutron wall loading, lower first wall heat flux, and smaller size then the power reactor. In the preceeding sections, the effects of scaling these device parameters on act-alike performance have been discussed. In this section, an attempt is made to synthesize our understanding of scaling effects into test module designs that can address several important issues in an integrated and act-alike manner.

The approach in this work has been to concentrate on specific designs and specific issues in a manner that will illuminate generic testing problems and their solutions. A preliminary design, which incorporates consideration of fluid flow, heat transfer, structural analysis, mechanical design and neutronics gives a practical, realistic assessment of the limitations of scaled integrated testing. The work has so far been directed toward testing in tandem mirror test devices, and has concentrated primarily on the BCSS lithium cooled vanadium reference blanket design described in Appendix D.3. Some attention has also been given to testing the MARS lead-lithium cooled ferritic steel design (also described in Appendix D.3). Thermal-mechanical issues have been emphasized because of their importance to the liquid metal designs. The following sections describe the preliminary design and performance of a module for testing the BCSS reference blanket in a tandem mirror (TM) device. Also included is a qualititive evaluation of the test module performance in addressing the issues identified in Chapter 3. Modules for testing the MARS blanket are also briefly considered.

6.4.2 A Module for Testing the BCSS Lithium/Vanadium Blanket in a Tandem Mirror

Thermal and pressure stresses are the primary causes of possible structural failure in the BCSS toroidal-poloidal flow lithium cooled blanket. To preserve thermal stresses, temperature changes throughout structural members

must be preserved. If temperature differences can be preserved, absolute temperatures can generally also be maintained by controlling the coolant inlet or outlet temperatures. As will be discussed below, it appears that temperature matching can be accomplished for a limited portion of the blanket. Matching temperatures will improve the value of the test for many issues. Pressure stresses can also be made act-alike over a limited portion of the blanket by adjusting the inlet pressure, assuming that geometry has been preserved. We have performed a preliminary design of a test module, for testing in a small tandem mirror fusion device, that attempts to reproduce the BCSS blanket stresses and temperatures exactly over a limited region of the composite first wall. This "unit cell" approach is felt to be valid for this blanket design because the local stresses are due primarily to the local loading. Whole-blanket forces are generally supported by the external support structure. Although this work is preliminary and is directed toward a specific design, it results in a few conclusions which appear to be generic for liquid metal cooled tokamak blankets.

6.4.2.1 Configuration

The configuration of the lithium cooled test module is shown in Fig. 6.4-1. The design approach has been to define a minimum structural unit cell and attempt to attain act-alike temperatures, stresses, and velocity profiles within the cell. The test device is assumed to resemble the MFTF Upgrade machine shown in Fig. 13.3-3, operating at approximately 2 MW/m^2 neutron wall loading. Lithium inlet and outlet piping through the shield may need to be large in the test device because of high MHD pressure drops in the vicinity of high field coils which are needed to create the fusion plasma. Four test modules could surround the plasma circumferentially.

The test module first wall is flat to preserve geometry. Curving the wall to follow the plasma radius would result in more even neutron fluxes, but would also significantly stiffen the structure. Neutronics results shown in Fig. 6.4-2 and discussed in Section 6.3.5.6 indicate a reasonably flat flux profile. Axial neutron losses in the tandem mirror device are also significant, and are discussed in Section 6.3.5 and Chapter 13.

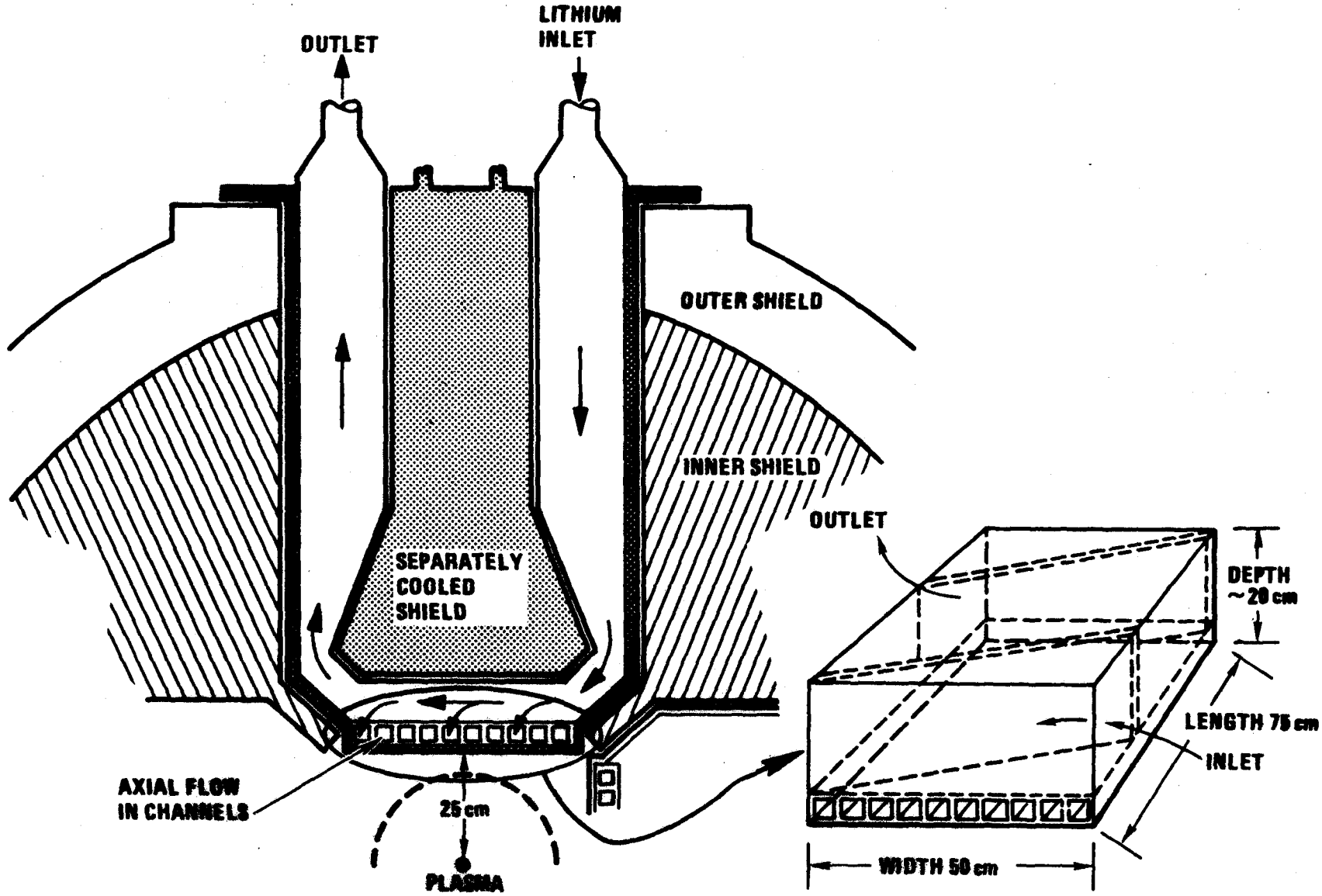

Figure 6.4-1. Lithium cooled vanadium tokamak blanket test module.

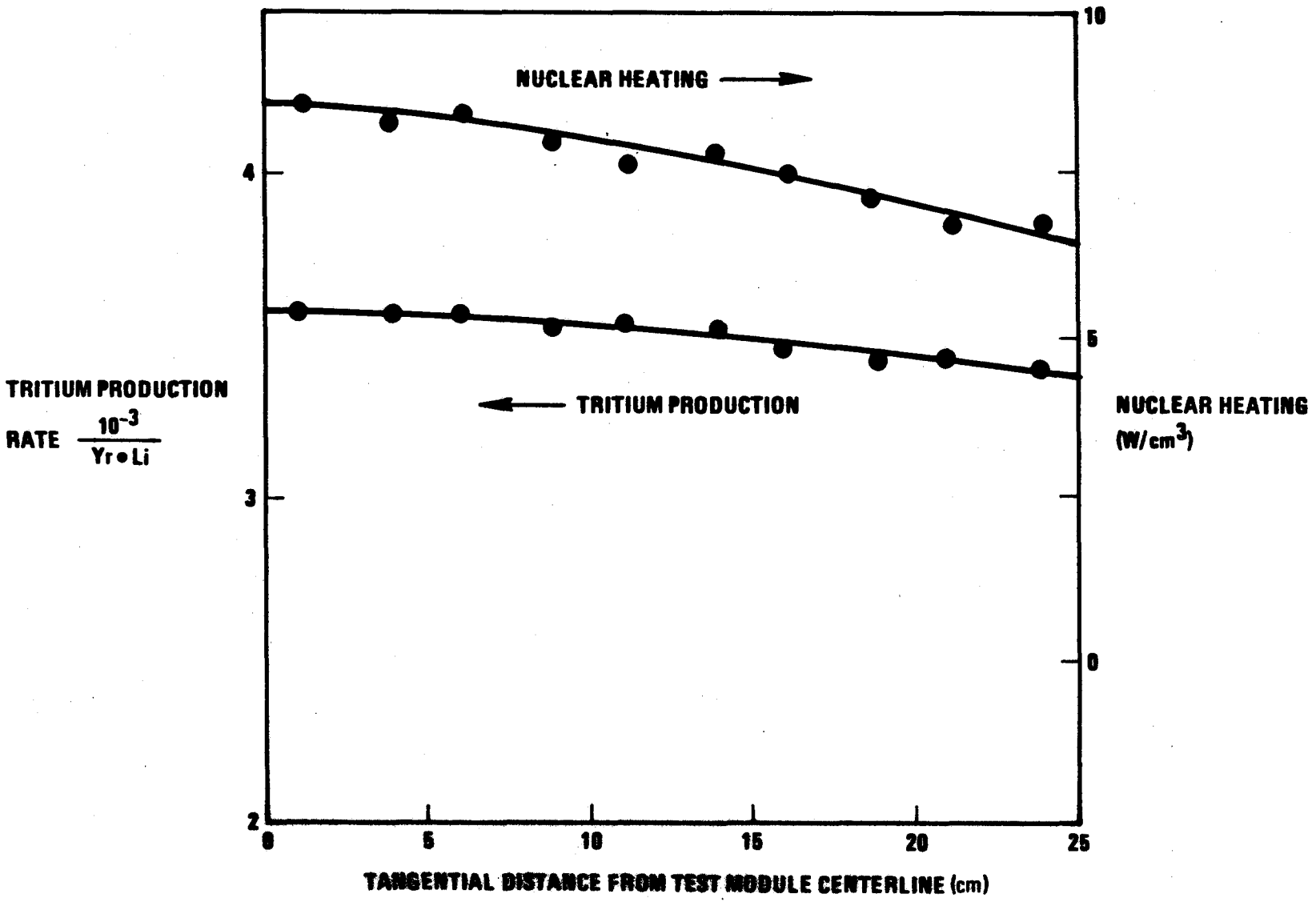

Figure 6.4-2. Poloidal profiles are nearly uniform in the tokamak test module.

The first wall area is based on considerations of the space available and on a minimum structural unit cell. In the axial direction, or the direction that would be toroidal in the tokamak, increasing length is expensive because it requires increasing the power injected to the plasma. One span of a single poloidal channel is the absolute minimum structural unit cell. The difficulty lies in correctly modeling boundary conditions (this will be discussed further below). The module width (see Fig. 6.4-1) is limited here by the requirement of fitting four modules as closely as possible to the plasma. The structural unit cell in this direction is one toroidal channel. Shear and bending boundary conditions can be neglected in all but a few of the outermost channels because of structural damping. The test module first wall area has been determined somewhat qualitatively, but we believe it is reasonably close to a minimum structural unit cell. First wall area is very dependent on the particular blanket design being tested.

Maintaining tokamak first wall heat fluxes can reduce the required size of the test module and may improve the value of the test for reasons discussed below. It may be feasible to artificially heat the first wall in the TM test device with tungsten heating elements. Thin tungsten wires will have little impact on neutronics and can easily supply over 50 W/cm^2 to the first wall by radiation. It may be difficult to achieve 100 W/cm^2 or more by this means because of the required temperature of the heating elements (see Table 6.4-1). The elements will probably have to be replaced after a few months of operating time due to evaporation. Resistive heating of the first wall is discussed further in Chapter 13.

Lithium flows through the three large "poloidal" channels in the same direction. The two end channels provide the inlet and outlet to the first wall "toroidal" channels, while the middle channel is a dummy, providing only cooling to the second wall and some neutron reflection. Velocity profiles in the three large channels may not become the fully developed Hartmann flow expected in the blanket poloidal channels because of the short path length. The test module depth could be reduced to increase flow development in this region. Velocities will be scaled to attempt to achieve act-alike flow in the first wall channels, not the large "poloidal" channels which are felt to have a lesser impact on the thermal and structural response of the first wall. Flow in the first wall channels will be discussed below. As indicated in

Fig. 6.4-1, it may be desirable to configure the test module inlet and outlet so that turn angles are minimized and velocity changes do not occur at the test module edge.

Table 6.4-1. Preliminary Tungsten Filament Results

Number of wires = 90
Filament length - 1 x 360 x module length
Filament temp. = 2487°C K (75% of m.p.)
Filament resistivity = $8.4 \cdot 10^{-7} \Omega \cdot m$
Filament emissivity = 0.323

Filament Radius (mm)	Mesh Transmission Fraction	Net Absorption Efficiency	Average Mesh Thickness (mm)	Surface Heat Flux (W/cm^2)	Filament Power (KW)	Filament Voltage (Volts)	Filament Current (Amps)
(Unoxidized steel wall emissivity = 0.25)							
0.25	0.886	0.846	0.05	32.3	5.69	311	18.1
0.50	0.772	0.725	0.18	55.4	9.70	204	47.5
1.0	0.544	0.536	0.72	<82*	14.3	124	115
2.0	0.084	0.287	2.90	~60**	15.3	64	239
(Strongly oxidized steel wall emissivity = 0.95)							
0.25	0.886	0.941	0.05	35.9	6.28	328	19.2
1.0	0.544	0.766	0.72	117	20.5	1.48	138
2.0	0.084	0.534	2.90	~140**	28.4	87	325

*Neglecting increased emissivity due to expanded wire surface (shadowing).
**Including increased wire emissivity.

6.4.2.2 Elastic Stress Matching

Calculated elastic stress values, primarily due to thermal stress, are above the yield stress in the BCSS lithium cooled vanadium blanket under consideration. This may be generic to tokamaks if both first wall heat fluxes and erosion rates are high. The secondary thermal stresses will be reduced when the material yields and, therefore, will never reach the values obtained using elastic analysis. However, since the local geometry (e.g., thickness-to-length ratios) of the power reactor blanket is preserved in the test module, if the calculated elastic stresses are matched, then the initial plastic stresses and strains should also be matched to a good approximation.

Irradiation and thermal creep, and swelling, also play an important role in stress relaxation, stress buildup, and deformation, and will be discussed in the next section.

The major assumption in this analysis is that the composite first wall can be modeled as an assembly of I-beams, as indicated in Fig. 6.2.4-1. The model and method of analysis is discussed in detail in Section 6.2.4. The model uses a one dimensional temperature profile, as will be discussed below. The major conclusion is that initial elastic stresses can be made act-alike in the test module first wall region over a wide range of wall loadings and first wall heat fluxes as long as all aspect ratios, pressures, and temperatures are preserved. For example, if the first wall thickness must be increased to preserve temperatures and thermal stresses then all other dimensions (e.g., first wall channel width and depth, second wall thickness, etc.) must be increased in direct proportion. Because the span of the first wall across the poloidal channels defines the test module length, the size of the test module must be increased if stresses are to be preserved at lowered first wall heat fluxes. Preserving aspect ratios also aids in preserving temperatures at reduced wall loadings and first wall heat fluxes, as will be discussed in Section 6.4.2.5. However, neutron mean free paths do not scale and, therefore, damage gradients are altered if the blanket thicknesses are changed in the test module. This, together with the linear increase in test module size with decreasing first wall heat flux, indicates that it is desirable to preserve first wall heat fluxes by artificial means.

6.4.2.3 Irradiation Creep and Plastic Behavior

Irradiation creep has been included in the elastic stress model as described in Section 6.2.4. Figs. 6.2.4-5 and -6 show stress relaxation and deflection of the composite first wall due to irradiation creep. Although the model used has some important limitations, three significant conclusions can be drawn: 1) relaxation of thermal stresses due to irradiation creep occurs over a period of a few months, 2) the displacement rate due to irradiation creep under primary (pressure) stresses appears to be constant and, 3) scaling while preserving aspect ratios may be feasible. No irradiation creep data for V-15Cr-5Ti was available at the time of this writing, so HT-9 creep properties were used. The vanadium alloy may have a different steady state creep rate

and relaxation times may change somewhat, but we expect the above conclusions to hold.

A stress relaxation period of a few months can have significant impact on the requirements (and cost) of a fusion test device due to ratcheting. The BCSS lithium cooled tokamak blanket operates in the plastic stress regime. This is primarily due to the combination of high first wall heat flux and erosion rates. Erosion requires thickening the wall with sacrificial material, and the thick wall with a high heat flux creates very high thermal stresses. The stresses will never reach the initial levels shown in Fig. 6.2.4-5 because plastic deformation will reduce the thermal stresses. If the reactor were shut off after irradiation creep relaxed most of the thermal stresses (after a few months of operation), the thermal stresses would reverse and might again enter the plastic regime. The stress distribution at shutdown would be dependent on how long the reactor had been operating and, if plastic deformation occurred, the stress distribution after the reactor was re-started would also depend on how long the reactor had been on. Thus, a unique stress distribution would exist for each start-up/shut-down history.

Thermal creep has also been neglected and is expected to significantly affect the stress distribution by preferentially relaxing stresses where the temperatures are highest. This complicates the situation further, but does not alleviate the fact that long periods (months) of continuous operation may be required of a fusion test device if stresses are to be matched. Note that if stresses do not enter the plastic regime when the test device is shut down, the ratcheting behavior described above would not occur and stress matching could be done in a short duty cycle test device.

Irradiation creep displacements could limit lifetime in some designs. Extrapolating the displacement results shown in Fig. 6.4.2-6 results in a displacement of roughly 5 mm at the center of the I-beam at 150 dpa for the reference blanket. This could have a significant effect on first wall cooling in the magnetic field because of MHD streaming flow. The liquid lithium would have to cross magnetic field lines to travel the 10 mm out to the first wall and back, which could result in flow stagnation and overheating in this region. The magnitude and impact of displacements is a very design dependent phenomena.

The model was applied to the analysis of different size I-beams, with all aspect ratios preserved (all dimensions were scaled in direct proportion). Initial stresses and creep relaxation did not change, and displacements scaled in direct proportion as expected. This is also expected to occur if thermal creep and plastic deformation due to the high thermal stresses are included. The major remaining uncertainty in thermal-mechanical act-alike testing with aspect ratio scaling is crack growth and subsequent failure. Cracks are expected to grow longer in a thicker member with a lower stress gradient and, thus, crack growth scales in the right direction; the dimensions of the crack get larger and smaller with the dimensions of the member. However, failure modes and times to failure due to cracks may not be act-alike. If possible, the original size as well as the geometry of the power blanket should be preserved in the test to remove this uncertainty. This is also another reason for preserving first wall heat fluxes.

6.4.2.4 One Dimensional Temperature Profile Model

The structual analysis discussed above and in Sections 6.2.4 and 6.3.4 employs a one dimensional temperature profile, as shown in Fig. 6.4-3. The justification for and limitations of this approximation are discussed here. The bulk coolant temperature rise in the BCSS power reactor blanket is approximately $30^{o}C/m$ in the toroidal first wall channels and $20^{o}C/m$ in the poloidal channels behind the composite first wall. These temperature changes will lead to significant thermal stresses, probably concentrated near the major blanket supports. The test module design under consideration consists of a unit cell that excludes the major blanket supports (it could be designed to include only one support because of its size), thus, information about these support stresses has been lost.

The I-beam section of the first wall (see Section 6.2.4) experiences a $12^{o}C$ temperature change along its length and $0.1^{o}C$ change across its width due to the bulk $30^{o}C/m$ and $20^{o}C/m$ coolant temperature gradients, respectively. These temperature changes are ignored in the one dimensional model. An analysis of the web connecting the first and second walls indicates that the divergence from the one dimensional approximation is less than $10^{o}C$. In comparison, the temperature difference across the composite first wall is roughly $200^{o}C$. This temperature gradient has the largest effect on the thermal

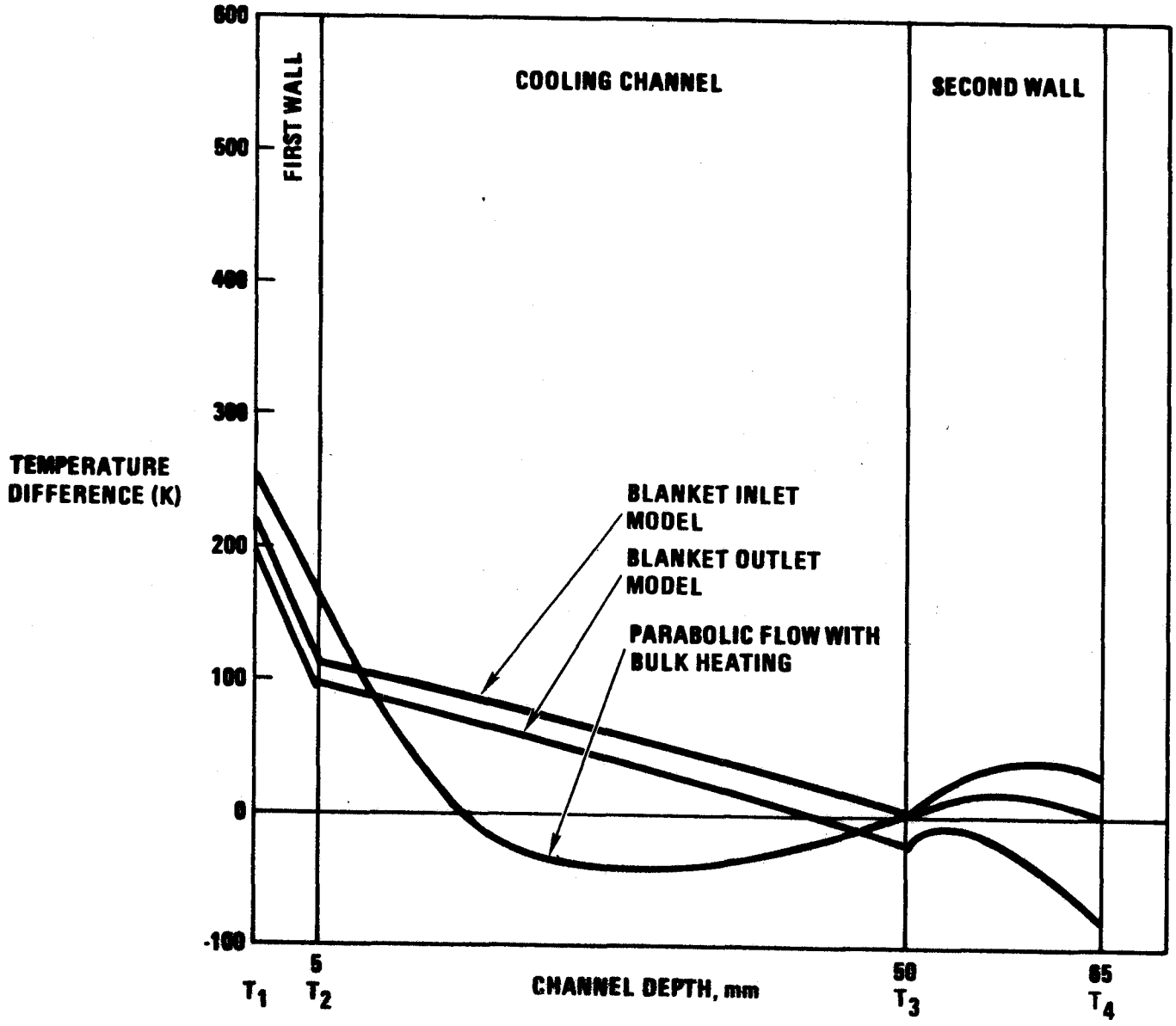

Figure 6.4-3. Temperature profile through the composite wall.

stresses; thus, the one dimensional model has included the most important temperature differences in the local region of the blanket under consideration.

The temperature profiles assumed for the structural analysis are parabolic in the first and second walls and linear in the web joining the two walls. (See Fig. 6.4-3.) Parabolic profiles are imprecise because the heat deposition is not constant, but comparison with exponential profiles indicates that the error is less than 1 percent. The linear profile in the web was taken for convenience in the absence of understanding of the MHD velocity and temperature profiles. Since the heat flux from the web to the coolant is low (less than 1 W/cm^2 away from the first wall) the web interface temperature is expected to closely follow the coolant temperature. Heat generation within the thin (3 mm) web will cause less than a 2^oC temperature rise at 30 W/cm^3. Possible coolant temperature profiles in the toroidal channels are discussed in Section 6.3.2. Using the actual temperature profile in the web (if it were known) would alter the stress profile, but we do not believe it would significantly change the maximum stress unless the temperature difference across the web, as well as the temperature profile, were to change.

6.4.2.5 Temperature Matching

Temperatures in the BCSS toroidal/poloidal flow blanket structure are determined by heat generation in the structure, heat deposition on the first wall, and heat transfer to the coolant. Interactions with the coolant can be represented by the coolant bulk temperature and the heat transfer coefficient. It has been shown in Section 6.2.3 that the heat transfer coefficient is dependent on the first wall heat flux, the heat generation in the coolant and structure, and the fluid velocity profile. Thus, the structural temperatures depend on these operating parameters as well. Unfortunately, the MHD-dominated velocity profiles are not well understood at this time, contributing to large uncertainties in the actual behavior of temperatures and stresses.

In this section we will examine the effect on the structural temperatures of simultaneously varying first wall heat flux, heat generation, and channel size (preserving aspect ratios as discussed above) in the test module. The analysis is as previously described in Section 6.2.3, using parabolic and flat ($n = 2$ and $n = 7$) velocity profiles. It is assumed that velocity and

temperature profile development can both be made act-alike. If the velocity profiles are assumed to be fully developed, then temperature profiles can be made act-alike by preserving the Fourier number, which generally requires slowing the flow rate in the test module. Preserving velocity profiles in shortened channels also requires slowing the flow, but magnetic field effects and end effects are not currently well enough understood to even assess the feasibility of the BCSS design, making analysis of act-alike testing impossible. Some control may be possible by slightly adjusting the orientation of the first wall channels to the magnetic field. Conclusions drawn in this section must be taken with caution since they are based on the tenuous assumption that velocity profiles can be made fairly close to act-alike in the test module.

Aspect Ratios

Channel size (first wall thickness, channel depth, and second wall thickness) is varied with first wall flux and heat generation such that the temperature rise through the first wall is kept constant and aspect ratios are preserved. For example, if the first wall heat flux is lowered, the first wall should be thickened until the temperature rise through it (due to heat flux plus heat generation) is equal to the temperature rise in the BCSS reference design. The other channel dimensions are increased in direct proportion to the first wall. Note that if the test module is a minimum structural unit cell, its size must also increase in direct proportion to the first wall thickness. The Nusselt numbers and temperatures are then calculated as in Section 6.2.3, and the temperatures through the first and second walls are also included.

Since the first wall heat flux results in a linear temperature profile and heat deposition results in a parabolic profile, the scaled temperature profile is, in general, different from the reference case. Fig. 6.4-4 compares profiles for some test module operating conditions with the BCSS reference design. The error is not large unless the first wall heat flux is dropped to very low values. As discussed in Section 6.3.4, profile differences in this region do not appear to greatly impact thermal stresses as long as the temperature difference is unchanged and the profile changes are not large.

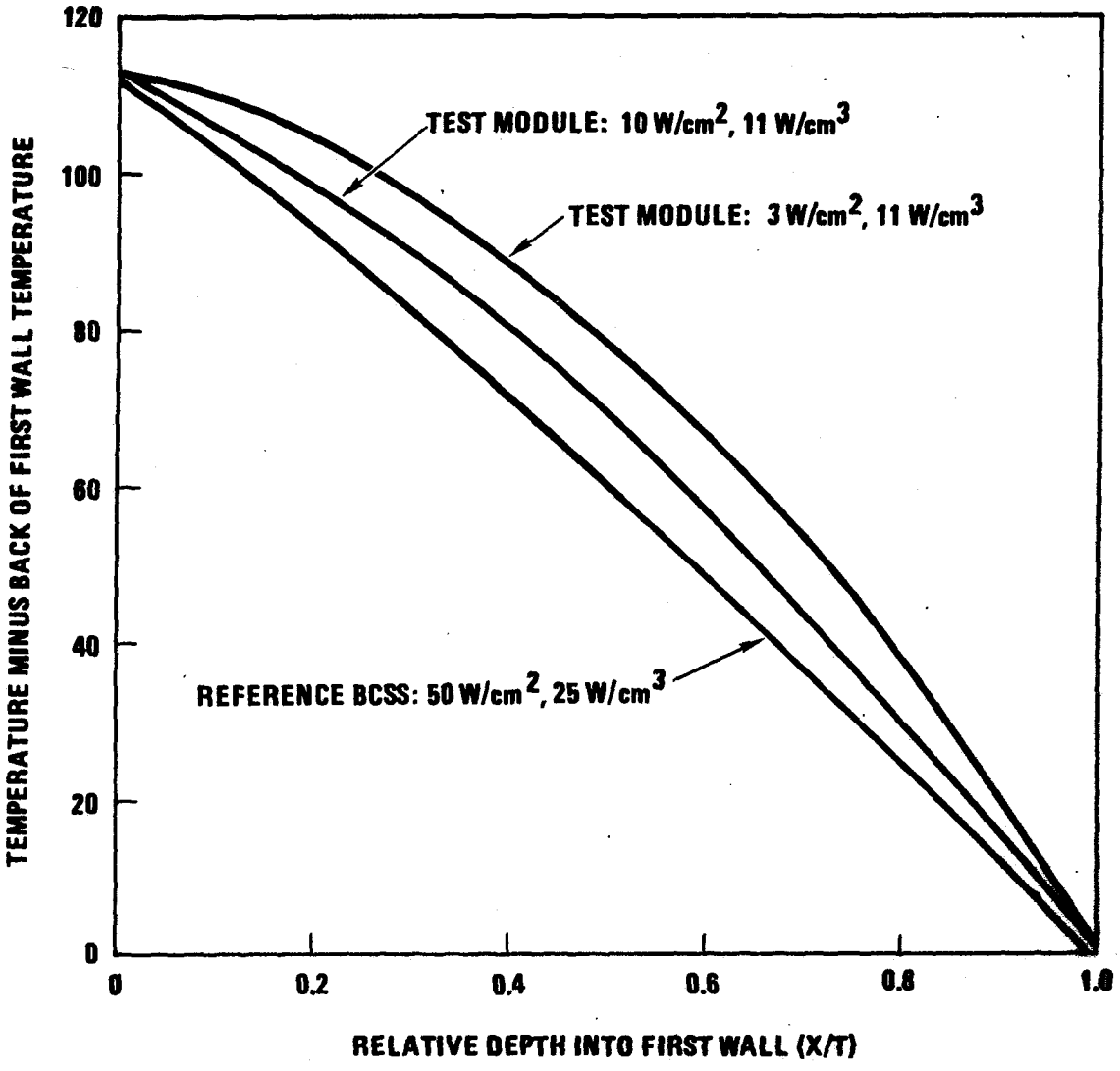

Figure 6.4-4. Temperature profiles through the first wall under various operating conditions.

Second Wall Adiabatic Boundary

The Nusselt numbers calculated in Section 6.2.3 depend on the heat flux from the second wall into the coolant channel, as well as the flux from the first wall and the heat deposited within the lithium. The possible range of variation of this second wall heat flux in the BCSS reference design is discussed here.

Heat deposited within the second wall results in a parabolic temperature distribution within the wall as shown in Fig. 6.4-5. (The actual temperature profile distribution is more complicated, but a simple analysis using an exponential heat desposition profile through the wall has shown that the error is less than 1 percent.) Superimposed on the parabola is a linear temperature profile due to the temperature difference between the front and back of the wall (T_3 and T_4 in Figs. 6.4-3 and 6.4-5). If the maximum of the parabola occurs within the wall, it forms an adiabatic boundary since heat must always flow down the temperature gradient. If the difference between T_3 and T_4 is not too large an adiabatic boundary will occur within the second wall, as appears to be the case throughout the reference design. This is advantageous as it prevents heat from flowing from the toroidal to the poloidal channels.

The first-cut analysis described below confirms that the adiabatic boundary will always occur within the wall, and sets limits of between 3.5e4 W/m^2 and 1.7e5 W/m^2 for the heat flux from the second wall into the coolant in the reference design. Further refinement is possible, but we would not expect these numbers to change significantly.

In the test module it will be possible to adjust the location of the adiabatic boundary as desired by controlling the temperature in the central "poloidal" channel. Flow into this channel does not enter the first wall channels and, thus, can be controlled separately. Since the second wall thickness is determined from requirements on the first wall, it is unlikely that the temperature profile in the test module second wall will match that of the reference blanket at various wall loadings and first wall heat fluxes. However, a good approximation is likely through controlling the central poloidal channel temperature. This approach is based on the idea that the

first wall is most important and should be emphasized, and results in the loss of more information as one gets further from the first wall.

Adiabatic Boundary Analysis

The location of the adiabatic boundary can be found if T_3, T_4, and the heat generation rate are known by setting the derivative of the temperature profile (parabolic plus linear) to zero. The heat generation rate used for the reference design was 17 w/cm^3 from neutronics calculations. Maximum and minimum limits of T_3-T_4 were found as follows.

Near the blanket module inlet the bulk lithium temperature in the poloidal channel is near the 350°C blanket inlet temperature. In the toroidal channels the coolant temperature rise is 87°C in passing the length of the channel. Thus, the maximum bulk fluid temperature difference between the toroidal and poloidal channels (T_3 and T_4) is 87°C. This can occur across the second wall at the point where the poloidal channel enters the blanket and is crossed by the first toroidal channel as it is about to exit. Because we are considering the maximum difference between T_3 and T_4, we can expect a large fraction of the heat deposited in the second wall to flow into the poloidal channel and, thus, expect a film drop temperature between the bulk coolant temperature and T_4. A 10°C film drop temperature would require a Nusselt number of 44, which may be feasible in this entrance region to the poloidal channel. Taking T_4 to be 360°C and the bulk temperature in the toroidal channel to be 437°C, and proceeding iteratively (using the relationships described in Section 6.2.3) to find T_3, results in a T_3 of 415°C and an adiabatic boundary 14 percent of the second wall thickness behind the front of the second wall (see Fig. 6.4-5). The 10°C film drop temperature used to determine T_4 is questionable, but it is unlikely that the adiabatic boundary occurs at less than 10 percent of the thickness.

For finding the maximum distance of the adiabatic boundary behind the front of the second wall, we can assume that the bulk temperatures in the poloidal and toroidal channels are equal. This may occur near the entrances to the toroidal channels, and it is certain that the poloidal temperature cannot exceed the toroidal. Assuming very good heat transfer at the toroidal channel inlet, we take a 1°C film drop temperature to find T_3, and then solve

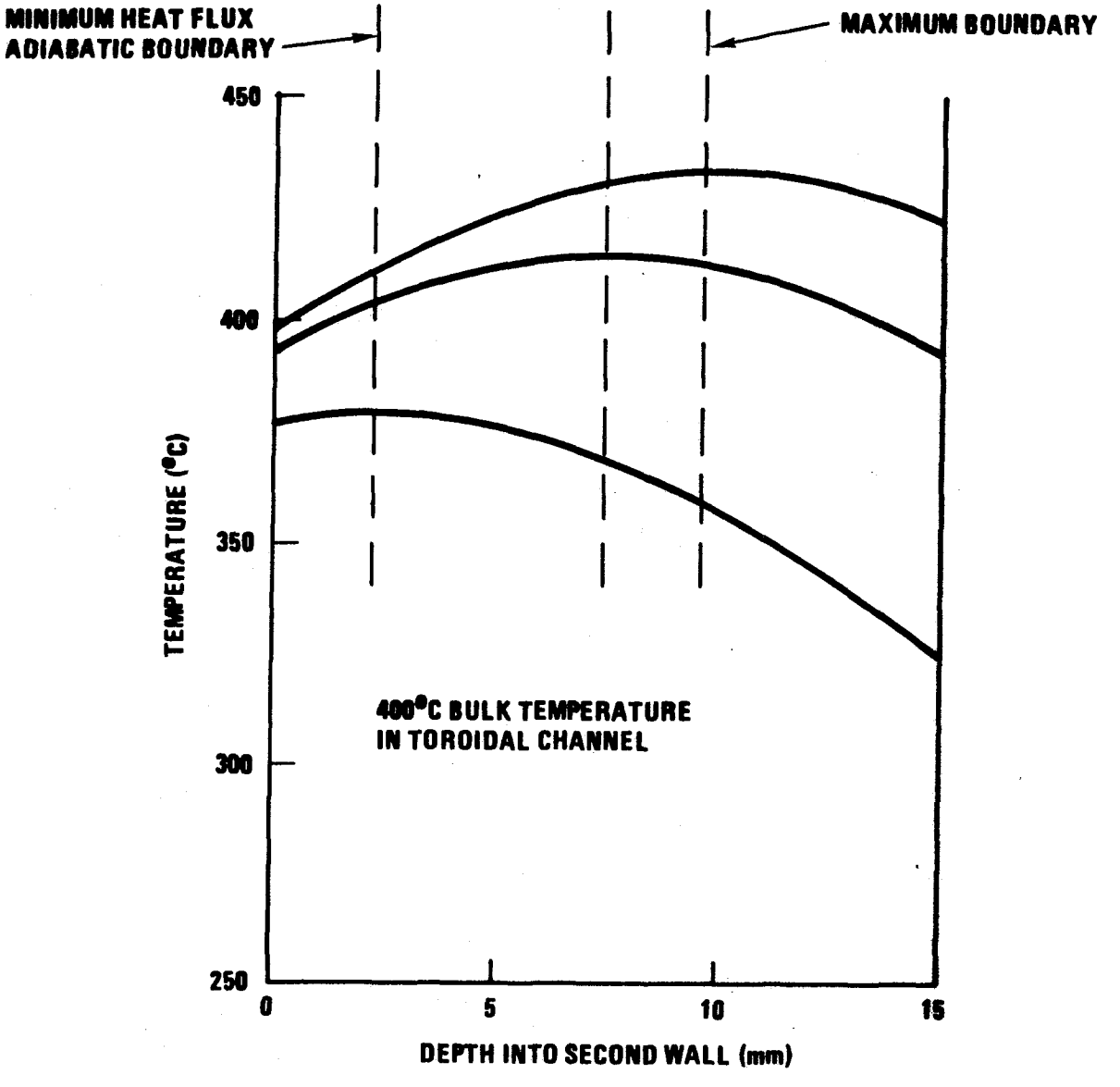

Figure 6.4-5. Second wall temperature distribution and adiabatic boundary.

iteratively for T_4 and the location of the adiabatic boundary. This conservative approach results in the boundary occuring 65% of the way through the wall (see Fig. 6.4-5).

6.4.2.6 Evaluation of Test Module Performance With Respect to Major Issues

The test module discussed here emphasizes thermal-mechanical issues. We have attempted to design a module that will test as many issues as possible in an integrated manner. When conflicts arise, stress and thermal-mechanical issues are given the highest priority. The next step would be to design another module or integrated test that would emphasize the issues on which this module performs poorly. As a beginning point, we have considered MHD testing in a non-nuclear reactor mock-up to address some of the issues not covered by the test module. If we are optimistic about the performance of the test module and the MHD mock-up, they tend to address the issues (as currently understood) in a complementary fashion.

Resolving the issues in integrated tests will mean removing or greatly reducing the final uncertainties. Many smaller experiments will have been completed prior to these tests. It is reasonable to expect that these experiments will have the effect of removing issues, adding issues, or perhaps eliminating the entire blanket concept. Thus, the issues identified in Chapter 3 are not the issues that must be addressed by integrated testing because we are not yet to the integrated testing stage. The conclusions drawn in this section must, therefore, be interpreted with caution.

Our work indicates that it may be feasible to obtain act-alike stresses and temperatures over a small region of the blanket, with different test modules and/or different operating conditions to model different parts of the blanket. We have assumed that the test module will perform as indicated, and that a reasonable number of modules and operating conditions will be sufficient, and have evaluated the benefit of these tests with regard to the issues identified in Chapter 3. This is summarized in Table 6.4-2. Costs, or the feasibility of operating continuously for several months (which may be required) have not been addressed.

MHD effects cannot be made act-alike in this type of test module. The magnetic field strength and geometry in the tandem mirror test device are too dissimilar from those in the tokamak reactor, and the global geometry of the

Table 6.4-2. Test Module Performance Relative to Ten Liquid Metal Blanket Issues Rated Critical and High Priorty.

Issue		Act-Alike	Benchmark(1)	Little Or No Information
A.2.a	Effect of first wall heat flux and cycling in fatique and crack growth related failure	A		B
A.2.b	Premature failure at welds and discontinuities	A		B
A.2.c	Failures due to hot spots	A	B	
A.2.d	Inter. of primary and secondary stresses and deformation	A		B
B.1	MHD pressure drop and pressure stresses	B	A	
B.2	MHD and geometric effects on flow distributions	B	A	
D.1.a	MHD effects on first wall cooling and hot spots	B	A	
D.1.b	Response to cooling system transients	B	A	
D.2.a	Corrosion mass transfer rates and consequences		AB	
F.1.a	Uncertainties in doubling time margin and predictive capabilities		A	B

A = test module, B = non-nuclear MHD mock-up.

1) Benchmarking can generally be provided by various other tests, some of which may be much cheaper.

test module is also too dissimilar from that of the reference blanket. The several MHD-related issues that may require integrated testing will need a different approach. A non-nuclear scale model or mock-up test has been suggested, and deserves further consideration. As yet, no work has been done on an MHD mock-up, but it seems feasible to assume that act-alike (or nearly act-alike) velocity profiles and pressure drops can be achieved in a non-nuclear device. Temperatures are not assumed to be act-alike because of the lack of bulk heating, but act-alike first wall heat fluxes are included. Cost has not yet been considered.

The three columns in Table 6.4-2 provide a qualitative evaluation of the test module performance in resolving the testing issues. The first column is marked if the test is perceived to be act-alike with regard to the issue. For example, if we assume that the test module contains the critical welds and discontinuities, that stresses and temperatures are act-alike, and note that the test is performed in a fusion neutron environment, we can expect act-alike response for issue A.2.b. The second column represents information which can be used to benchmark or verify codes and theoretical models. The test module is not act-alike in MHD flow, but does provide complex liquid metal flow paths in a strong magnetic field. Verification of a prediction of the velocity profiles and pressures in the test module would greatly increase confidence in predictions of blanket performance. If one is less optimistic about the test module's performance, benchmark information may be the best attainable data for all the issues.

Table 6.4-2 summarizes test module performance with respect to several critical and high priority issues from Chapter 3. Only blanket issues were considered. Three critical issues from Chapter 3 do not appear on the list for the following reasons:

A.1 Changes in Properties and Behavior of Materials - This issue was considered to be too general to address with test modules. It is included as a major contributor in all the structural issues listed in the table.

A.2.h.(2) Magnetic Forces Due to Disruptions and Magnetic Transients - This issue should be addressed separately. It is not feasible to test tokamak disruptions and magnetic transients in a tandem mirror device. An approach to addressing this critical issue should be developed.

A.3.a Effectiveness of Tritium Permeation Barriers - This is not an issue within a liquid metal blanket, but is a critical balance of plant issue. A loop test is the most appropriate place to test this issue.

Some high priority issues have also been eliminated for similar reasons.

As discussed above, act-alike stress test module and an act-alike non-nuclear MHD flow mock-up have been postulated in Table 6.4-2. These two tests perform complementary functions with respect to the issues addressed. If we interpret the results of the test module design work optimistically, it appears that we can obtain act-alike stresses, and are limited in addressing the stress issues only by fluence. It appears that the major requirement for neutrons in stress testing is materials damage. Note that materials damage is of primary concern in all four of the stress issues (i.e., structural failure modes) in the table.

Under optimistic assumptions, all but two of the major liquid metal blanket issues identified in this study can be resolved with these two testing approaches. The corrosion and tritium breeding issues will require additional testing methods if benchmarking is inadequate. If we take a less optimistic approach and assume that stresses cannot be made act-alike or that meaningful levels of fluence are too expensive, the test module will give useful information that can be used to benchmark codes and test theories. This is also true of the MHD mock-up. Note that the test module provides benchmark information for the MHD issues, but the MHD test provides no information for most of the stress issues. The test module can provide some information about all the issues listed because it embodies all the conditions and relevant components found in the power reactor.

6.4.3 A Module For Testing the MARS Lead-Lithium Cooled Blanket in a Tandem Mirror

A comparatively small amount of effort has been put into design considerations of a test module for the MARS blanket. Structural and thermal analyses have been performed on a scale model of the MARS design at lowered wall loadings. There are several major differences in the testing issues for the MARS and BCSS designs.

The MARS blanket design (see Fig. 6.1-2) has an obvious minimum unit cell for testing, consisting of one tube in which lead-lithium flows from the top to the bottom of the reactor. Neutronics considerations require that the tube be surrounded by something with a similar neutron albedo, which is most easily accomplished by adding more tubes. This results in a scale model test module. A meaningful test module consisting of a part of a tube is difficult to conceive for this stage of integrated testing in a fusion reactor. As will be discussed below, the MARS scale model has a different set of problems than the BCSS unit cell.

The tandem mirror reactor is expected to have much lower first wall heat fluxes than the tokamak (3 - 10 W/cm^2 vs 50 - 100 W/cm^2). This results in lower requirements on a tandem mirror test device and increases the importance of bulk heating. Because of the low first wall heat flux and erosion rates in the mirror, the initial MARS blanket structural stresses remain within the elastic regime. This greatly simplfies structural analysis and test requirements. (Plastic effects due to swelling and creep occur and are discussed below.) Another significant tokamak/mirror difference is that well defined Hartmann velocity profiles are expected in the MARS design. This allows the calculation of temperature profiles with confidence since the velocity profiles are known and the velocity development length is relatively short.

6.4.3.1 Structural Analysis Results

The structural analysis of the MARS blanket is described in Section 6.2.4.3. The analysis includes thermal expansion, swelling, and irradiation and thermal creep. The swelling model includes both temperature and flux dependence, but does not take into account recent data for HT-9 which indicates that swelling may be negligible. Fig. 6.4-6 shows stresses for the MARS design and a scaled test module as a function of dose. The stress differences after startup are due to the flatter neutron flux across the small test module. This results in lower differential swelling from the front to the back of the smaller tube.

This analysis indicates that, if swelling is present, stresses may increase throughout the life of the blanket and that the blanket thickness must be preserved to preserve stresses. It may be possible to scale swelling gradients by tailoring the neutron spectrum, but this approach has not been

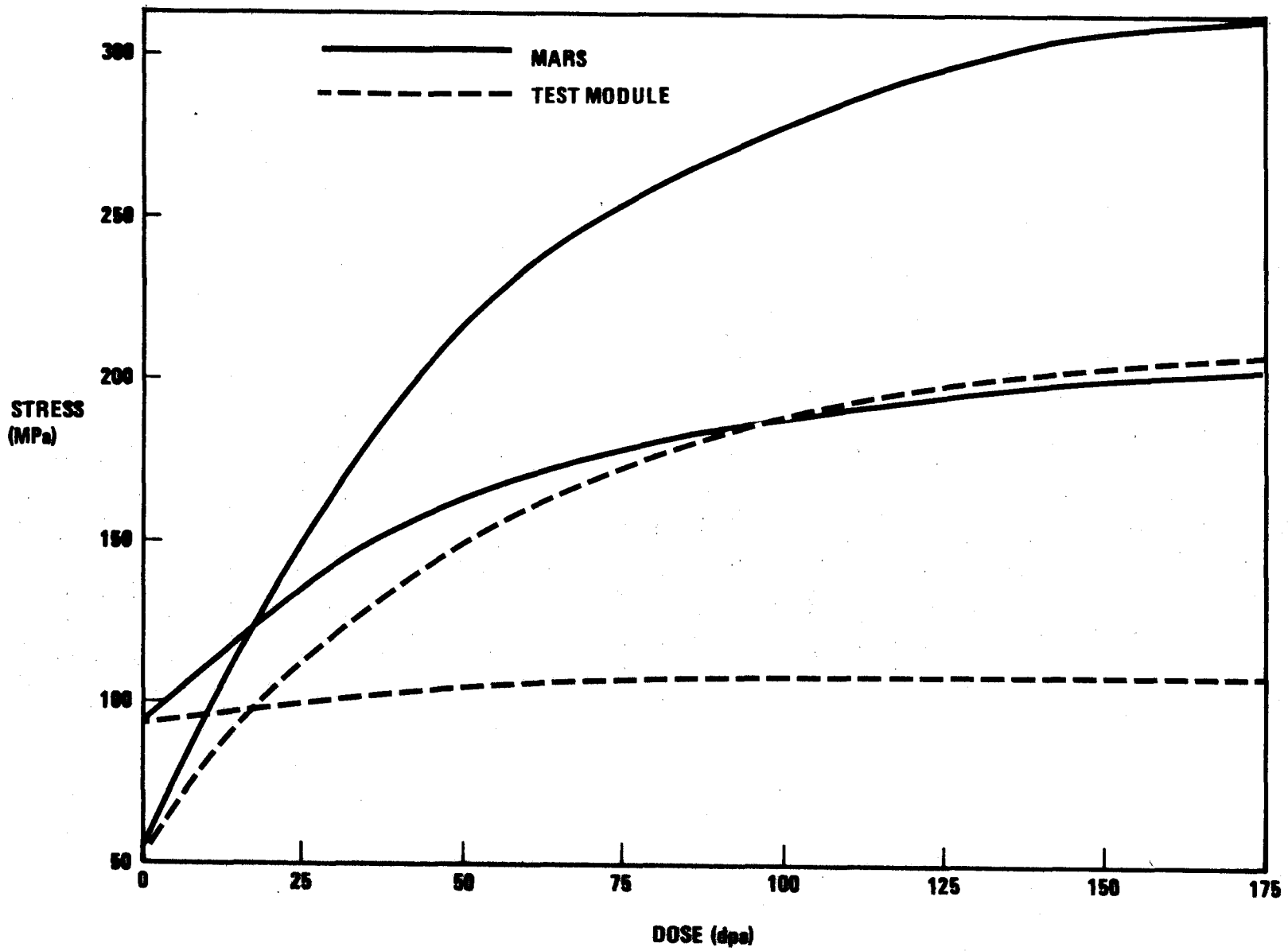

Figure 6.4-6. Stress versus damage.

explored. As for the BCSS design, if stresses are to be preservedin the MARS test module, the ratio of the tube length-to-thickness must also be preserved. The only way to maintain both thickness and aspect ratio in the test module is to make it full size. This results in a significant drop in wall loading, from 2 to 0.83 MW/m^2, because of 1/R effects. The large test module will match stresses well but will accumulate damage at a lower rate and may, therefore, be impractical.

The fact that stresses may increase throughout the life of a fusion blanket has significant implications for both fusion and fusion testing. This is primarily a materials issue, depending on the relative values of the swelling and irradiation creep rates. The creep and swelling equations used in this analysis are somewhat speculative, but these results help to illustrate the importance of good creep and swelling data.

6.4.3.2 Temperature Profile Matching in the MARS Design

As mentioned above, the MARS unit cell for testing consists of one tube in which lead-lithium flows from the top to the bottom of the reactor. Temperature profiles in both the axial direction (along the tube) and the radial direction are important in order to match stresses and corrosion rates. (In the BCSS design, axial temperature gradients were deemed less important than radial temperature gradients.) Matching axial temperatures requires matching inlet and outlet temperatures to those in the power reactor, which can only be done by lowering the coolant velocity if the wall loading is lowered. Matching temperature development in the radial direction requires matching Fourier numbers, which will generally require a higher velocity than that required by matching axial temperatures in a scale model at lowered wall loading. It is, therefore, not possible to simultaneously match the axial temperatures and the Fourier number. Slower flow in the test device, to preserve axial temperatures, results in more fully developed temperature profiles in the tube. A simple analysis has been performed to determine the effects on radial temperature profiles at lowered wall loading when bulk temperatures and temperatures at the front and back of the tube are matched.

The following equation from reference 6.4-1 was used to evaluate the temperature profiles.

$$\theta[(x/R),Fo] = Po_c \left\{ \frac{1}{b}\left(1 - \exp\,[-b]\right) Fo + \sum_{n-1}^{\infty} (1 - (-1)^n \exp[-b]) \right.$$
$$\left. \frac{2b}{(n\pi)^2\left(b^2 + (n\pi)^2\right)} \cdot \cos\,(n\pi)\,\frac{x}{R}\left[1 - \exp\left(-\,(n\pi)^2 Fo\right)\right]\right\} + \phi\left(\frac{x}{R}, Fo\right)$$

where:

$$\phi[(x/R),Fo] = Ki\left[Fo - \frac{1}{6}\,[1 - 3(x^2/R^2) - \sum_{n-1}^{\infty} (-1)^n\, 2/(n\pi)^2 \right.$$
$$\left. \cos\, n\pi(x/R)\, \exp\left(-\,(n\pi)^2 Fo\right)\right]$$

θ = dimensionless temperature, T/T_a

T = temperature

T_a = reference temperature (e.g., average temperature)

x = distance from the back wall

R = distance from the front to the back wall

Po_c = dimensionless power density at the back wall, QR^2/KT_a

Q = volumetric power density

K = thermal conductivity

b = dimensionless spatial power density exponent

Fo = Fourier modulus, $K\tau/\rho C_p R^2$

τ = time

ρ = mass density

C_p = heat capacity

Ki = dimensionless surface heat flux, qR/KT_a

q = surface heat flux at x = R.

A slug velocity profile between parallel plates with an exponential heat deposition rate and a heat flux behind the first wall is assumed. Properties are constant. The heat flux value used is 10 W/cm^2; 4 W/cm^2 from the heat flux on the first wall and 6 W/cm^2 from the heat deposited in the tube wall. The heat deposition rates are based on ONEDANT neutronics calculations for a design similar to MARS. Results are shown in Fig. 6.4-7 an Table 6.4-3.

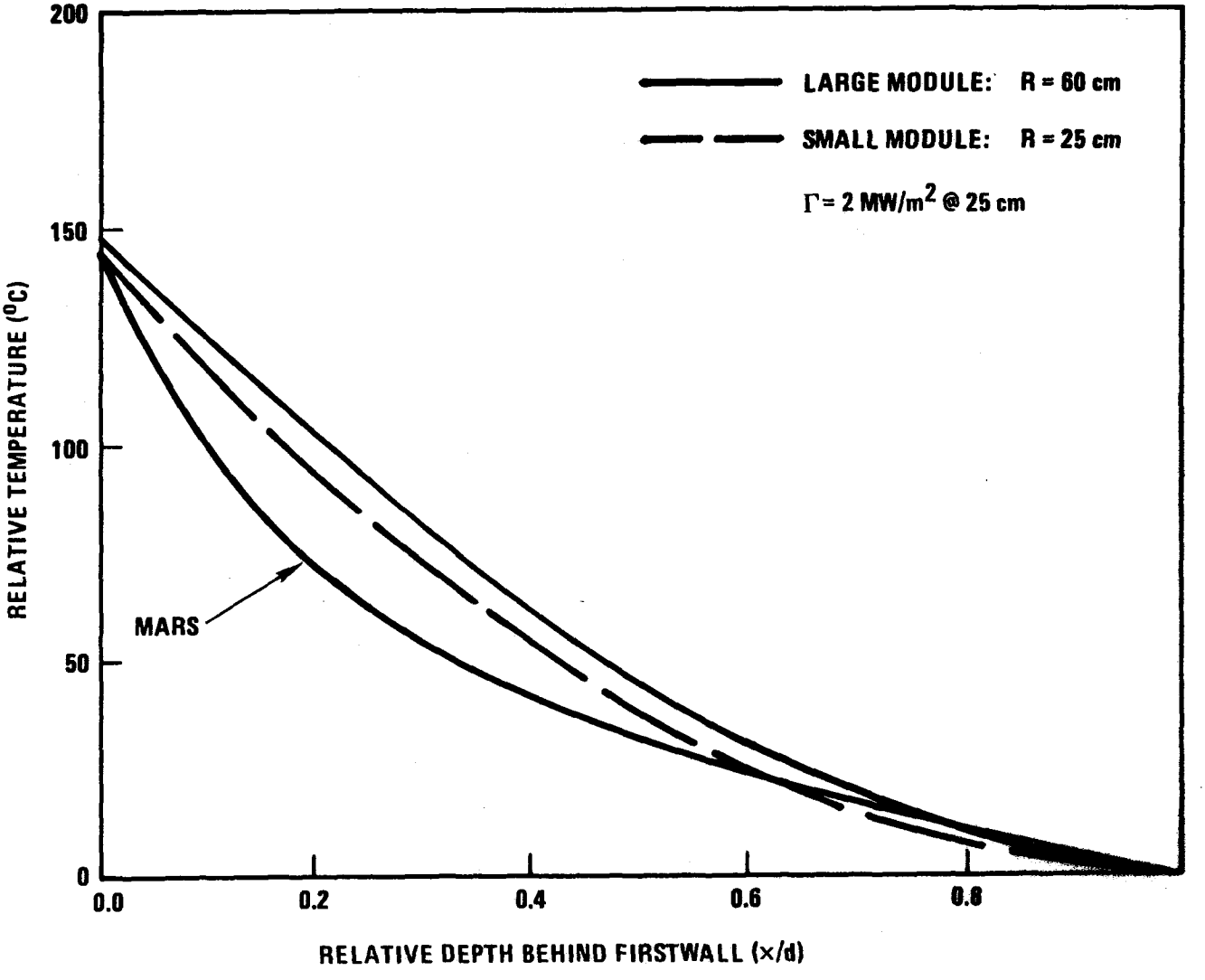

Figure 6.4-7. Matching MARS temperature profiles (temperature profiles at the outlet)

Temperature profiles in both a small and large module were considered. Both modules occupy one meter axially in the test device, are reflected with water cooled stainless steel at both ends, and resemble a one meter piece of the MARS blanket. The test device wall loading is assumed to be 2 MW/m^2 at a radius of 25 cm. It is also assumed that the first wall heat flux can be controlled in the test device. The small module has a 25 cm first wall radius to maximize the wall loading, and is a scale model of the MARS blanket. The large module is simply a segment of the MARS blanket operating at 0.83 MW/m^2, and was explored because of the importance of damage gradients in the tube as discussed in the previous section.

Table 6.4-3. Matching MARS Temperature Profiles

	MARS	Large Module	Small Module
First wall radius (m)	60	60.0	25.0
Tube diameter (cm)	9	9.0	4.16
Heat deposition at back of tube (W/cm^3)	23	3.8	9.02
First wall heat flux (W/cm^2)	10	4.0	10.7
Coolant velocity (cm/s)	17	1.9	2.8

Temperature gradients in the test module are more dominated by conduction from the first wall than those in MARS. The maximum difference in temperature is on the order of 20 percent of the front-to-back temperature change. Actual temperatures will be more complex because of the slab geometry in the model. It appears that a fairly significant error in temperature cannot be avoided when operating at reduced wall loading. Note that to keep the error this low requires control of the first wall heat flux, probably by resistive heating.

Another useful test of the MARS blanket would be to attempt to match velocities and velocity profiles, and thus verify MHD effects, at the expense of not matching temperatures. Such a test could be performed without altering the test module by operating at the proper velocities. This approach has not yet been explored.

6.4.4 Summary and Conclusions

Two different approaches to integrated test module design have been proposed for testing the two reference blankets in a tandem mirror device. For the BCSS design, a minimum unit cell appears likely to yield the most information at near act-alike values. For the MARS design, a scale model approach appears to be necessary. Act-alike structural behavior and failure modes may be attainable in the unit cell test module. However, under realistic operating conditions in an affordable test device it may be difficult to obtain the 10 to 12 dpa damage required to relax thermal stresses, and thus adequately test ratcheting and stress dependent failure modes. It is likely that benchmarking information, rather than proof of component information, will be obtainable.

The unit cell approach ignores global effects to concentrate on local effects, which appear to be more severe in the BCSS design. Global stress will change the local stresses, but this has been assumed to be a second order effect. A more detailed study should assess global effects in the BCSS design.

The scale model approach has limitations primarily because it attempts to assess both local and global effects at the same time. This leads to information loss when requirements conflict. For example, to put the first wall as close as possible to the plasma, and thereby obtain the highest possible wall loading, the module dimensions must all be reduced in direct proportion to the first wall radius. When the blanket thickness is reduced, damage gradient effects are reduced and information is lost.

The unit cell test module appears to perform well in addressing the major issues as currently understood. A non-nuclear MHD test can address most of the velocity profile, flow distribution, and pressure drop issues which may not be resolved in the test module. We were unable to identify alternate fusion test modules for either the MARS or the BCSS design that would perform complimentary roles with respect to the issues. Most of the issues not thoroughly addressed in the structural tests are MHD related, and fusion test module performance is limited by the geometry and strength of the magnetic field in the test device.

Useful blanket tests with act-alike behavior parameters can be performed in a tandem mirror test device at reduced wall loadings. A device capable of achieving over 10 dpa in several test modules would be valuable for testing structural failure modes. (At least 10 dpa is required to relax out thermal stresses, and thus study stress reversal and ratcheting.) The ability to control first wall heat flux in the test device would be extremely useful and will be necessary to match temperatures in some cases. For testing high heat flux tokamak blankets, fluxes equal to those in the power reactor (50 - 100 W/cm^2) will greatly increase the value of the test, and can reduce the required size. For testing TM blankets, the ability to adjust the heat flux (in the range of about 5 to 20 W/cm^2) to control the coolant temperature rise, and temperature profile, would allow the temperatures to approach act-alike values. Methods of controlling the first wall heat fluxes in test devices should receive further attention.

The test module design exercise yields useful general and design specific information. Tieing the scaling studies to a specific design concept tends to reveal interactions that would not otherwise be apparent. The BCSS and MARS blankets proved to offer very different insights into test requirements due to the different geometries and testing issues. Extending the efforts of test module design to other blanket concepts and test devices may further increase our understanding of blanket testing.

Referecence for Section 6.4

1. A. V. Luikov, "Analytical Heat Diffusion Theory," Academic Press, 1968.

6.5 Engineering Scaling

6.5.1 Overview

Engineering Scaling is the science which explores the most effective ways to do integrated testing at scaled conditions. This includes (1) identification of the effects of varying the device parameters, and (2) development of techniques for maintaining the act-alike conditions which allow for adequate resolution of the testing issues characterized above. For interactive phenomena, it is not always possible to devise a single test which incorporates all of the important behaviors. In designing tests, there are many trade-offs which involve the importance of issues and the difficulty of testing. These factors make Engineering Scaling at present somewhat of an art rather than an exact science. There is an obvious need to continue serious efforts to establish the technical foundations for Engineering Scaling because of the complex nature of fusion technology development.

In this section, the elements of Engineering Scaling are presented by summarizing and interpreting the results presented in Sections 6.2 through 6.4. First, the key testing issues for liquid metal blankets are reviewed in order to identify the most important test conditions which should be maintained in integrated tests. Test requirements and engineering scaling techniques are then explored by summarizing the effects of varying the device parameters. By combining the test requirements and the test device parameter ranges, scaling conflicts are uncovered. Scaling conflicts can arise for one of several reasons: (1) when unacceptable restrictions exist on the available device parameters, (2) when proper scaling to retain operating conditions differs for two or more different issues, or (3) when simultaneously changing more than one device parameter makes it impossible to maintain a particular test condition.

6.5.2 Summary of Testing Issues and Important Test Conditions

The results of the previous sections of Chapter 6 indicate that variations in the major device parameters result in changes to the operating conditions within the blanket unless special care is taken to maintain them. The loss of blanket operating conditions may have serious implications on the adequacy of testing to resolve the key testing issues.

For liquid metal blankets, the most critical integrated testing issues belong to one of three categories:

1. Thermomechanical response to the fusion environment, including MHD effects
2. Materials Compatibility
3. Failure Modes and Rates

6.5.2.1 Required Test Conditions for Thermomechanics Testing

There are many uncertainties in the thermomechanical behavior of liquid metal blankets both because the exact loading conditions are unknown and because the response to this loading is complex. One of the largest uncertainties in the loading is related to thermal hydraulics and thermal stresses. It was shown in Section 6.2.4 that even with optimistic assumptions of the temperature profiles at the first wall of a tokamak blanket, the structure will probably deform plastically due to the high thermal stresses. Reliable operation in this regime is highly uncertain. In addition to simple primary and secondary stresses, other complicating features include cycling and the influence of radiation effects, such as materials damage, irradiation creep and swelling.

The effect of the magnetic field on liquid metal flow has been treated in detail in Sections 6.2.1 and 6.2.2. It was shown there that the possibility exists that the actual temperatures at the first wall could be hundreds of degrees higher than the optimistic estimates, and further, that local hot spots are likely to form near geometric complexities where the flow becomes highly nonuniform. These higher temperatures translate directly into the possibility of higher thermal stresses.

Another large uncertainty in loading is due to the MHD pressure drop and associated pressure stresses. The pressure stresses alone are predicted to approach the suggested design limit for the structural materials being considered. Even if this limit is not achieved, there is uncertainty in the level of creep deformation and the possibility of rupture. It is likely that separate effects testing will resolve many of the larger uncertainties with respect to the magnitude of the MHD pressure drop. However, the possibility remains that many of the complex aspects of magnetohydrodynamics will persist, and that reliable engineering data on MHD pressure drop will have to be

obtained from near-integrated tests. This is particularly true if the margin for error in blanket designs continues to be small.

Because of the large uncertainties in the actual loading conditions experienced by the blanket, care should be excersized to maintain as much similarity as possible in the operating conditions which contribute to the loading. The most important conditions include: (1) temperatures, which create thermal stresses, (2) velocity profiles, which control the temperature profiles, (3) MHD pressure drop, which generates pressure stresses, and (4) geometry, which impacts all of the above in addition to magnetic forces and transients.

The other aspect of thermomechanical behavior of the blanket is the response to the applied loading. Some of the concerns include plastic deformation, crack growth, and the effects of swelling and creep on stress concentrations.

As mentioned above, one of the primary uncertainties occurs if any part of the blanket deforms plastically. In this case, in the presence of creep relaxation, reversal of the stresses on shutdown may result in more plastic deformation. It is unknown what amount of cycling the structure can withstand under these conditions. The test requirements for this issue are severe, since obtaining plastic deformation requires that the test module be highly stressed as in the reactor blanket.

Crack growth and fracture mechanics constitutes another large uncertainty in the blanket response. Crack growth depends on a wide variety of factors, including temperatures, cyclic behavior, irradiation, surface conditions, and constraints. Temperature gradients and structure thicknesses may also be important. Because of the strong dependence on irradiation and the many contributing blanket conditions, this issue will be difficult to treat adequately at low fluences and reduced device parameters.

Some irradiation effects occur early in life and therefore may be more easily tested. An example is irradiation creep, which is expected to have a beneficial effect by relieving stresses at areas of high stress concentration.

While many single effects tests can be identified to resolve specific issues regarding the response of structures using simulated loading conditions, highly integrated testing will probably be necessary to verify the

feasibility and thermomechanical performance of liquid metal blankets. In order to maintain a useful integrated test of the total blanket response, geometry and materials must be strictly maintained. Most of the issues of thermomechanical response are very design dependent; in fact, this design dependency also makes it difficult to quantify generic test requirements.

In addition to geometry, a useful verification test should contain the correct loading conditions, as specified above. Whereas true component verification requires complete modeling of the loading conditions, this appears to be impractical in a scaled test. The different loading conditions in a liquid metal blanket vary throughout the blanket in a complex way which is difficult to maintain at reduced volume, surface heat flux, and neutron wall loading. Nevertheless, it is fesible to model the loading correctly over a limited area of the blanket, which results in a limited form of component verification and very useful data for verification of predictive capabilities.

Finally, an ideal thermomechanics test should include irradiation effects. Although some of these effects require a high, end-of-life level of fluence, some irradiation effects on thermomechanical response may be observable at lower fluences, e.g., 1-20 dpa.

6.5.2.2 Required Test Conditions for Materials Compatibility Testing

Materials compatibility influences blanket operation and safety in several ways, including:

1. by imposing limitations on the operating temperatures in the blanket
2. by contributing to the mobilization, transport, and redeposition of activated materials
3. by contributing to materials degradation, limits on lifetime, and failure modes

Corrosion places upper limits on the allowable temperature of the coolant and structure. This temperature limit is a boundary on the design window for blanket operation which, because of the problems with heat removal, is a serious issue in determining the feasibility of liquid metal blankets. Present data rules out liquid metals with austenitic steels and provides only a narrow design window with ferritic steels.

Currently, the most serious concern with corrosion temperature limits is the problem of redeposition in cold areas of the primary cooling loop, particularly the heat exchanger. A good test will require simulation of temperatures throughout the entire primary cooling loop, correct materials, long operating times, and probably the inclusion of coolant impurities which are likely to exist in the reactor blanket. One of the largest contributions to uncertainty in corrosion rates, which is likely to remain for integrated testing, is geometric effects on MHD velocity profiles and temperatures. Both velocity and temperature are critical parameters which affect corrosion rates. Therefore, simulation of the thermal hydraulic behavior of the blanket is important.

Corrosion also contributes to activation product mobilization. The mobilization, transport, and redeposition of activated materials is a high level of concern for safety and maintainance, but is not necessarily a critical factor in determining the feasibility of liquid metal blanket concepts. The same operating conditions listed above are also needed for this issue.

Another concern with materials compatibility is its contribution to structural materials degradation, failure modes, and lifetime. As a lifetime issue, the testing requirements are difficult to meet in a scaled, integrated test. The following section contains more discussion of this class of issue.

6.5.2.3 Required Test Conditions for Failure Modes and Rates

The principal failure modes in liquid metal blanket structural members include:

Early Failures

- brittle fracture
- plastic rupture

Long-Term Failures

- crack growth
- creep rupture

Crack growth is suspected to be the most serious concern for liquid metal blankets. The operating conditions which influence crack growth and other failure modes are very complex, including the detailed loading condition, irradiation, precise materials properties and pre-treatment, cycling, temperatures, impurities, and surface effects. Cracking is expected to be most

serious at welds, where the materials properties are altered from the base material, or at discontinuities, where stress concentrations occur.

Because of the large number of important operating conditions required to adequately address the issue of failure modes, they have not been studied extensively for the engineering scaling of partially integrated test modules. Additional considerations of failure modes are given in Appendix E. For some early failure mechanisms, there may be imformation gained in thermomechanics testing. The desire to observe failure modes in scaled integrated tests provides an added reason to always push the test parameters to levels as close as possible to reactor device parameters.

6.5.3 Review of Device Parameter Scaling

Reductions in the test device parameters away from those of a fusion reactor places limitations on the useful information which can be obtained from integrated testing, for both interactive experiments (data and verification of predictive capabilities) and for component verification tests. For this study, the ability to perform component verification testing was emphasized due to its greater difficulty and more stringent requirements on testing.

The device parameters which are most relevant for liquid metal blanket behavior include surface heat flux, bulk heating, total energy input, magnetic field strength, magnetic field geometry, structure geometry, burn/dwell time, and size (length, width, and depth). The test requirements for each of these is considered in this section.

Beyond understanding and analysis of the issues, the analysis performed here for Engineering Scaling is in an early stage. Trends can be indicated, but precise quantitative conclusions can not be drawn now. An attempt was made to identify the most important behaviors in the blanket and carefully examine these in detail. Due to limitations on time and effort, some important phenomena that may lend different requirements to the testing were either overlooked or intentionally excluded. Therefore, the conclusions on test requirements must be interpreted as a partial list. Known phenomena that have been excluded are discussed.

6.5.3.1 Surface Heat Flux Scaling and Thermal Stresses

The surface heat flux is a primary source of energy input to the tokamak blanket. It dominates the temperature profiles in the area near the first wall; therefore, it also dominates the thermal stresses in the first wall. In order to maintain the contribution of thermal stresses to the structure loading at reduced surface heat flux, the thickness of the first wall may have to be increased in such a way as to keep the temperature drop through the wall constant.

Thickening the first wall has several potential consequences. First, the pressure stresses in the first wall will drop. (This is a design dependent effect; in designs without a separate first wall cooling system, the pressure gradient would increase and pressure stresses would remain constant.) It is possible to control the pressure stress at any point through the use of an external pressurizer, but the spatial distribution of pressure stress throughout the blanket (and therefore the ratio between pressure stress, swelling, etc.) will be lost outside the local area. This is problematic for most designs, because the different types of stresses vary widely throughout the blanket and the location of worst consequences is uncertain. Furthermore, loss of the overall stress distribution will affect global structural behavior. Although the BCSS reference design is thought to be dominated by local responses, other designs may require simulation of the entire distribution of stresses. The net result is that a thickened first wall will allow matching stress distributions over a given local region, but global component verification in a single test suffers greatly.

The second consequence of reduced surface heat flux is related to the need to maintain constant structural aspect ratios for reasons of act-alike structural response and MHD induced eddy current similarity. If the first wall is thickened, then the first wall cooling channel and the second wall must be thickened, the channel support spacing must be widened, etc. This results in two problem: the number of channels which can be modeled in a fixed volume is reduced, impacting fluid flow and thermal issues, and the radiation damage spatial profile is altered. The effects of altered damage profiles is highly uncertain because the basic materials properties changes, such as swelling, are uncertain. If radiation effects are a large contributor to end of life stresses, then increasing the channel dimensions will reduce

one of the most important potential benefits of component testing in a neutron environment. However, testing in this manner may still be very useful for the purposes of some model verification.

Finally, the relationship of first wall thickness to failure modes, such as crack growth and propagation is uncertain. Also, the stress concentrations at welds and discontinuities may be affected. As indicated in the introduction, these are both very important issues for blanket testing.

The net conclusion regarding surface heat flux is that strong incentives exist to keep this vital parameter high. Supplemental resistive heating or artificial methods for enhancing plasma heat flux may be important for testing. This is particularly true if a tokamak blanket is to be tested in a mirror device, because of the high first wall heat fluxes expected in tokamaks.

6.5.3.2 Bulk Heating Scaling

Bulk heating is another primary heat source in the fusion blanket. It has its largest absolute effect near the first wall, but because the surface heat flux dominates behavior at the first wall in tokamaks, the effects of bulk heating are generally considered as more important within the depth of the blanket. In tandem mirrors, bulk heating is important throughout the blanket. Two important effects of bulk heating have been examined in this study, relating to radial and axial temperature profiles. "Radial" refers to the direction perpendicular to the first wall surface; "axial" refers to the direction along the coolant channels.

In Section 6.2.4, the thermal stresses in the BCSS composite first wall were shown to depend strongly on the average temperature in the second wall. Without bulk heating, it would be difficult to achieve the correct temperature in the second wall unless the coolant temperature in the poloidal channels is also controlled. The obvious problem with such active control over the coolant temperatures is that the actual loading conditions of the blanket are achieved artificially. The uncertainties in thermal hydraulic behavior of the blanket are sufficiently large that active control reduces the value of component verification. In addition, not all blanket designs allow such active control over the coolant temperature. For example, in the MARS blanket design, the need for bulk heating to model structure temperatures is much greater.

In the liquid metal blanket, the heat transfer coefficient depends on the temperature profiles. This is due to the fact that conduction dominates the coolant heat transfer in the direction perpendicular to the flow. Therefore, because bulk heating alters the temperature profile in the coolant channels, the surface heat transfer coefficient is also altered. In other words, the presence of bulk heating changes the effect of the surface heat flux. The more asymmetric the velocity profile, the more pronounced is this effect. In the liquid metal blankets, the heat transfer coefficient varies throughout the blanket; hence, the effect of bulk heating contributes to the global temperature profiles. For reasonable assumptions of velocity profile (which is highly uncertain), the effect of bulk heating on the temperature profiles is still secondary in comparison with the surface heat flux (10-20%). Therefore, it is possible to model the temperature profiles for thermomechanical testing without bulk heating. But testing to verify the global blanket thermal hydraulics is limited in the absence of bulk heating, to an extent which depends strongly on the MHD velocity profiles (see Section 6.2.2).

6.5.3.3 Total Energy Input Scaling

The sum of surface heating and bulk heating dictates the total temperature rise along the coolant channels. For thermal and corrosion behavior, it is desirable to maintain the coolant residence time similar to the reference reactor design by varying the coolant velocity. If this degree of freedom on the coolant velocity is removed, then a lower total energy input must result in a lower temperature rise along the channel.

This has two effects. One is that corrosion behavior along the channel will be altered. It is believed that the corrosion rate at any point in the channel depends on the entire history of the mass transport upstream in addition to the local temperature. A different temperature gradient will therfore result in a different axial mass transfer profile. As stated above, the total blanket corrosion rate and redeposition outside the blanket are less sensitive to the spatial details within the blanket, but issues of wall thinning and localized failure rates require attention to the correct temperature profiles.

The second effect of a reduced temperature rise relates to the temperature dependence of radiation damage, such as swelling, creep, embrittlement,

etc. If the axial temperature profile is altered, then the axial damage profile will also be altered. This is considered to be a minor loss in the reference blanket because radial profiles of temperature and stress are felt to dominate the structural response of the blanket. Gradients in the radial direction tend to be over an order of magnitude larger than in the axial direction.

Other blanket concepts, such as the MARS design, will be more seriously affected by the loss of total energy input. If the fluid flow velocity is reduced to account for the reduction of heat input, then the residence time will not be maintained, affecting corrosion, heat transfer, and the MHD pressure drop.

6.5.3.4 Magnetic Field Strength Scaling

The magnetic field governs both the velocity profiles and the MHD pressure drop. Magnetic field effects have been separated into two groups: those which depend on the strength of the field and those which depend on the geometry. The effect of time dependent changes in the magnetic field represents a third group that will be analyzed in the future.

One consequence of reducing the magnetic field strength is the reduction of the Hartmann boundary layer thickness, which scales proportionately with B. The boundary layer is very thin--on the order of microns. Therefore, it has little effect on heat transfer because the thermal diffusion scale length is much larger. However, the mass transfer diffusion scale length is the same order of magnitude as the velocity boundary layer. It is likely that diffusion-dominated corrosion mass transfer will be affected by altering the magnetic field strength. Under conditions of the BCSS reference blanket (but with PCA rather than vanadium), convective/diffusive mass transfer is mass diffusion limited. A reduction by a factor of two or more in the field increases the effect of the velocity boundary layer thickness. Not only does the corrosion rate itself drop, but the rate-limiting process changes as well.

It is speculated that the magnetic field may have other, less well understood effects on corrosion by impeding cross-field diffusion of impurities. In addition, the presence of MHD currents and voltages at the interface could alter the interface corrosion process itself.

Another more obvious consequence of reducing the magnetic field strength is the reduction in MHD pressure drop. The bulk MHD force on the fluid generally scales as B^2. Contributions due to wall friction, thermoelectric effects, and possibly due to flow perturbations scale differently. However, the bulk MHD force by far dominates the pressure drop in most designs. The average value of pressure can be maintained through the use of an external pressurizer. Therefore, the principal loss of information at reduced field strength will be loss of the spatial variation of pressure and pressure stresses.

It is also important to note that not all test devices will have reduced magnetic field strength. For example, the MFTF α+T design has peak fields larger than would be expected in either a tokamak or mirror reactor blanket. This could prove to be an asset for scaling, since the effects of reduction in size and energy input on pressure drop can be somewhat compensated.

6.5.3.5 Magnetic Field Geometry

The geometry of the magnetic field, together with the structure geometry, dominates the velocity profiles in the coolant channels and to a lesser extent the pressure drop. It has been shown that the shape of the velocity profiles can have a large influence on temperature profiles, and therefore on thermal stresses, corrosion, temperature-dependent properties, radiation effects, and failure modes. Because of their overwhelming importance to blanket behavior, close attention must be paid to any effect which alters velocity profiles.

One of the geometric effects which is easiest to identify is the effect of the ratio B_t/B_p on velocity profile development in the toroidal channels. It has been shown that the entry length for velocity profile development scales roughly as $B_t/B_p\sqrt{\phi}$. It is difficult to alter the field itself, although the channel orientation could be changed in such a way as to retain similarity in flow devleopment. In shortened modules, or in a mirror test device, it may be desirable to reorient the channels to keep the ratio of entry length to channel length fixed.

6.5.3.6 Structure Geometry

In addition to the details enumerated above, the blanket dimensions are important because of the existence of large global eddy currents. The shape

and magnitude of these eddy currents depends on the structure aspect ratios. Eddy currents determine interchannel and intrachannel flow distribution, and therefore temperatures, stresses, etc. It is likely that large global eddy currents will not exist in reactor designs because their impacts on pressure drop, flow distribution, and velocity profiles are so severe that any blanket containing large global MHD effects will not be feasible. Nevertheless, even if design solutions are found to resolve the worst problems with global eddy currents, they are likely to remain a partial contributor to uncertainties in blanket behavior.

6.5.3.7 Burn/Dwell Time

Time dependent structural effects can be very difficult to analyze for blankets in which yielding, creep, and crack growth are occuring. Pulsing also may have a large impact on corrosion, which depends intimately on the temperatures throughout the entire heat transport system. If the reference device has inherently pulsed operation, then the test model should also simulate time dependent phenomena. If the reference device is steady state, then a pulsed operation test device must be considered as an option. Testing a steady state blanket in a pulsed system may have serious implications on the value of the tests.

For heat transfer phenomena within the blanket, it was shown in Section 6.2.2 that the time constants are fairly short — on the order of 30 seconds or less in the BCSS reference blanket. These numbers could increase in the test module if the dimensions of the walls and channels are increased (increasing conduction times) or if the coolant velocity is decreased (increasing the residence time). The longest, and therefore most important time constant is felt to be the coolant residence time in the channels, which can be controlled by varying the coolant velocity. It has been shown that residence time scaling can be applied and at the same act-alike time thermal and corrosion behavior retained.

The complex effects of time dependent structural response and corrosion have not yet been studied in detail. The influence of cycling on plastic deformation with irradiation creep appears to be difficult to maintain under altered plasma burn scenarios. This is discussed in more detail in Section 6.4.

6.5.3.8 Length and Width

The most outstanding impact of limitations in the surface area available for testing comes from velocity, temperature, and corrosion product transport. As mentioned earlier, all of these parameters are in the development stage throughout the entire blanket. In this regime, the magnitude of heat, mass, and momentum transport are changing rapidly. Therefore, reducing the channel length for any of the channels could eliminate important regions of the blanket from the modeling. In cases where the most serious consequences occur at channel outlets, for example temperature and corrosion, important failure modes may not be properly modeled.

Another effect of reducing the channel lengths is that the temperature rise in the channels will be reduced. As discussed earlier, this is one phenomenon which can probably be accomodated by maintaining the fluid residence time. However, when the energy input to the blanket is reduced, there is no obvious way of maintaining temperature rises without affecting other phenomena.

Another effect of reduced length is the decrease of MHD pressure drop. The contribution due to straight channel flow is usually the dominant one, so reducing the length substantially will increase the apparent effect of flow nonuniformities, bends, etc. The contribution of this latter type of pressure drop is extremely design dependent. The loss of total pressure drop will result in lowered fluid pressure. Although the base pressure can be raised externally, the pressure gradient cannot.

Finally, limits on the available surface area place minimum requirements on the surface heat flux for thermomechanics testing. For example, if the toroidal width of the BCSS test module is limited to 1 m., then only two full size poloidal channels can be included -- the minimum for maintaining the structural boundary conditions. The surface heat flux in this case could not be reduced from its full value because of the required increase in toroidal width to maintain aspect ratios when the first wall thickness and radial dimensions are increased.

Table 6.5-1 Table of Design Guidelines

Scaled Down Device Parameter	What is Potentially Lost	Scaling Techniques	Comments on Ultimate Consequences
1. Surface Heat Flux	a. First Wall Thermal Stresses	Thicken first wall $\Delta T \sim q\delta$.	Since aspect ratios must be preserved, a thicker wall results in altered radial damage gradient.
	b. Spatial Distribution of Temperature-Dependent Radiation Damage (Radial Temperature and Damage Profiles)	Radiation damage doesn't scale.	Most important if the amount of swelling is high. Only model verification is possible.
	c. Failure Modes and Stress Concentrations	Unknown	Crack growth rate increases with wall thickness; amount is unknown
	d. Pressure Stress and Stress Ratios	Increase B or v	Static pressure can be increased to model localized stresses only.
2. Bulk Heating	a. Heat Transfer Coefficient and Axial Temperature Profiles	Maintain $Q\delta/q$ and velocity profiles.	Secondary concern since effect is not dominant.
	b. Radial Temperature Profiles (Similar to 1.b)	Maintain $Q\delta/q$ and velocity profiles.	Second wall temperature may not be easily modeled without good control of coolant temperature.
	c. First Wall Thermal Stresses	Maintain $T - \frac{\int T\, da}{A}$.	If second wall temperature is not maintained, thermal stresses will be lost.

Table 6.5-1 Table of Design Guidelines (cont.)

Scaled Down Device Parameter	What is Potentially Lost	Scaling Techniques	Comments on Ultimate Consequences
3. Total Energy Input $(q + Q\delta)L$	a. Corrosion Dependence on Temperature Rise	Lower velocity or increase length (preserve ΔT).	Can't be scaled if residence time is fixed.
	b. Radiation Effects due to Axial Temperature Gradient	Lower velocity or increase length.	Not felt to be dominant in BCSS reference design; more important in MARS type design.
4. Magnetic Field Strength	a. Corrosion Boundary Layer Thickness	Constant $\frac{a/H}{\sqrt{DL/u}}$.	Lower field results in lower corrosion rates. Changes of a factor of two may alter regimes from diffusion controlled to velocity profile controlled.
	b. MHD Pressure Drop and Stresses	Increase wall conductivity $\nabla p \sim v B^2 (\sigma_w/a)$ or velocity	Axial pressure gradient effects are likely not to be modeled at reduced field strength.
5. Magnetic Field Geometry (B_t/B_p)	a. Fluid Flow Developing Profiles	$B_t/B_p\sqrt{\phi} \sim L/d$.	Reorient angle of flow.
	b. Velocity Profile Effect on Heat Transfer		Serious concern; local velocity, B-field regime, and geometry must be preserved.
6. Structure Geometry	Eddy Currents (Consequently Velocity Profiles, Pressure Drop, Temperatures) and Structural Behavior	Constant aspect ratios	Interactive testing requires close attention to geometry.

Table 6.5-1 Table of Design Guidelines (cont.)

Scaled Down Device Parameter	What is Potentially Lost	Scaling Techniques	Comments on Ultimate Consequences
7. Burn/Dwell Time	a. Temperature Profile Development	Keep burn time much longer than residence time.	Temperature profiles develop quickly in most LM blankets (<30 sec in BCSS).
	b. Creep/Swelling/ Fatigue/Crack Growth	Uncertain	
8. Length, Width	a. Thermal, Velocity, Concentration Profile Development	$\alpha L/vd^2$ and $\sqrt{C_y/C_x}$ scaling; lowered velocity.	
	b. Temperature Rise for Corrosion Profile Development	Scale residence time L/v.	
	c. MHD Pressure Drop	increase v or B	model verification can probably be done in short modules

Table 6.1 Scaling Conflicts in the Liquid Metal Blankets

1. Thermal Stress/Radiation Damage Profiles
2. Reduced Surface Area/Reduced Heat Flux for Thermomechanics Testing
3. Thermal Stress/Transport Phenomena
4. Thermal Stress/Eddy Currents and Flow Distribution
5. Temperature Rise/Residence Time
6. MHD Pressure Drop/Residence Time

6.5.4 Summary

There are a large number of tests which would (and should) be performed to resolve individual issues, such as pressure drop, heat transfer, thermal stresses, etc. These separate effects tests are relatively easy to design because of the ability to freely choose the device parameters. But many of the most important phenomena in the liquid metal blanket are interactive in nature.

Design of an integrated test under scaled down conditions is difficult for several reasons (see Table 6.1). First, scaling conflicts arise between different phenomena at reduced device parameters. A scaling which would allow addressing one phenomenon may be incompatible with the scaling for another. Integrated tests are possible in which a limited number of multiple interactive effects with similar scaling can be act-alike.

Another conflict arises due to the effects of changing more than one device parameter simultaneously. It may occur that for a given issue, the appropriate response to scaling for one device parameter is contradictory to the response for another. A good example for the liquid metal blankets is the simultaneous loss of surface heat flux and surface area in a fusion test device. The combination of these two places more stringent limitations on the testing because the total energy input is reduced by both.

Another problem arising from integrated testing is the inherent limitations on device parameter flexibility in a large, integrated test. For example, in any neutron producing facility there are restrictions on the total volume and surface area available for testing. Some of the issues — for example MHD pressure drop and flow development -- will be affected even in the absence of scaling conflicts.

A fourth problem in integrated testing is the potential complexity of diagnostics and the difficulty of interpreting results. An integrated test is by definition an attempt to test many things at once. Diagnostic equipment cannot be allowed to interfere significantly with test performance, and must be kept simple enough to achieve high reliability. In the event of a negative result, such as first wall failure, it may be extremely difficult to isolate the cause without extensive further testing. For this reason, integrated testing is probably of little use until separate effect and partially integrated tests are largely completed.

Because of its importance in determining the feasibility of liquid metal blankets, much of our effort has concentrated on studying test requirements for thermomechanical performance. The stress state at any point in the blanket structure is dictated by several factors, including pressure, temperature distribution, swelling rate, thermal and irradiation creep, and geometry. Furthermore, the relative contribution of these factors in the BCSS reference blanket varies from point to point all across the blanket. Reductions in the test volume, surface heat flux, and bulk heating make it impractical to retain all of the loading conditions throughout the entire blanket.

Although no good solution appears capable of preserving the correct stress state throughout the blanket, an approach has been demonstrated which models only a part of the blanket at a time. This "unit cell" approach is capable of structural verification of limited parts of the blanket and provides a very good benchmark for model verification.

The usefulness of this approach is dependent on the resolution of related issues in other tests, including a range from separate effects to integrated tests. The current uncertainties in thermal hydraulic performance of the blanket are very large. Unless the actual blanket temperatures are well characterized, then structural tests with simulated loading will not provide adequate component verification of the blanket. For temperature verification, bulk heating is important to establish the temperatures deep in the blanket and also has a significant effect on the surface heat transfer near the first wall.

Because of our lack of understanding of MHD effects on mass, momentum, and heat transfer, a partially integrated test outside of a neutron environment would have a high benefit to cost ratio. Accurate resolution of the uncertainties in velocity profiles and pressure drop in a large, geometrically correct, partially integrated test would allow for much greater confidence in the results of the unit cell structural verification discussed above (and in Section 6.4).

Finally, there is an obvious need to obtain information on materials behavior under irradiation and in a liquid metal environment. It is difficult even to design a test withoud accurate materials data, much less design a practical fusion reactor blanket.

The design of a thermal mechanical test was described in Section 6.4. Together with a partially integrated MHD test, an integrated thermal hydraulics test, and a large amount of basic materials properites, a large number of the testing issues from Chapter 2 can be resolved. In general, complete component verification in the strict sense cannot be accomplished at scaled device parameters. Even with scaled, integrated testing there will always be some remaining risk involved in the first full-scale fusion reactor built. A strong program of modeling, together with integrated model verification testing, will eliminate most of the uncertainties.

6.6 Summary and Recommendations

In this chapter, a wide array of issues have been addressed regarding the details of blanket operation and specific problems encountered with scaled testing. Much of this work has treated specific, design-dependent behavior, and the results are often difficult to extrapolate into general conclusions. Within the context of these limitations, our results suggest the following.

The Need for Neutrons

In the composite first wall structure of the BCSS reference blanket, bulk heating is of secondary importance as compared to the surface heat flux in determining the heat transfer characteristics and structural response. The thermal stresses can be simulated well by controlling the fluid temperature in the coolant channels. Although analysis on other tokamak blankets has not been performed, bulk heating may be of secondary importance in the first 5-10 cm (closest to the plasma) of liquid metal cooled tokamak blankets in general. Neutrons in tokamak liquid metal blankets are, therefore, needed primarily to match stresses from radiation creep and swelling, and to produce materials damage (properties changes).

In the MARS design, bulk heating was found to be of primary importance for matching temperatures. This is expected due to the low surface heat flux in mirrors.

Preserving the Thermomechanical Response in a Test Module

The most critical integrated testing issue for liquid metal blankets appears to be thermomechanical performance. A good thermomechanics test must preserve the loading conditions as well as act-alike response characteristics. The response depends primarily on the aspect ratios in the structure. It has been shown that both elastic stresses and irradiation creep strains are preserved through aspect ratio scaling.

It has also been shown that if swelling is present in the blanket structure, then stresses may increase substantially throughout the blanket lifetime. For swelling effects, aspect ratio scaling may not be valid because of the importance of damage profiles. The damage gradient depends primarily on materials choices and only weakly on geometric factors. In the event that swelling exists, the damage gradients will be an important parameter to match.

Preserving the Thermal Stresses

As stated above, the thermal loading in a tokamak depends primarily on the surface heat flux. As the surface heat flux is reduced, the first wall thickness may be increased to maintain the temperature rise, and thus the thermal stresses. But problems develop due to tradeoffs between reduced module size, aspect ratio scaling, damage profiles, crack growth, and other failure modes. In order to simulate thermal stresses, there is a high priority on maintaining high first wall heat flux. A method of supplementing the natural surface heat flux with tungsten resistance heating appears feasible; because of the importance of surface heating, this option should be explored further.

Much of the importance of maintaining high thermal stresses results from the assumption that tokamaks may operate in the plastic regime. This assumption has a significant impact on testing. Blankets which don't operate in the plastic stress regime should be emphasized. More effort should be invested into determining whether or not any such tokamak blankets exist.

Bulk heating, rather than surface heat flux, dominates the thermal response in tandem mirror blankets. The analysis and scaling of the MARS design indicates that axial and radial temperature profiles can be preserved (to a first order approximation) if the first wall heat flux can be controlled. The desired first wall heat flux for testing a tandem mirror blanket in a small tandem mirror test device may be lower than the nominal flux in the device. The ability to control surface heat flux in a test device will be of value for both tandem mirror and tokamak blanket testing.

Preserving Corrosion Behavior

Corrosion is a phenomenon which involves the entire primary cooling system. Within the blanket, temperatures and velocities of the coolant are critical parameters -- both their absolute values and their spatial profiles. It has been demonstrated that the magnetic field can have a substantial effect on the corrosion rate due to its impact on the fluid velocity profile near the coolant channel walls. The corrosion rate at high field strength can be an order of magnitude higher than at low field strength. It has also been shown that the spatial profile of corrosion depends on both the residence time in the channel and the temperature rise.

Some of the most critical uncertainties involving corrosion relate to the total amount of structural material mobilized in the blanket and redeposited in the remainder of the primary cooling system. For this type of concern, the magnetic field strength, average blanket temperature, and coolant residence time are the dominant parameters. But corrosion is also a contributor to the degradation of structural material and ultimately to blanket failure modes. In this regard, accurate modelling of the spatial profiles becomes more important. Magnetic field geometry is more important because local velocity perturbations may dominate the local failure rates. Temperature rise along the channel also becomes a factor, since the streamwise corrosion profile is strongly dependent on the temperature profile.

Test Module Benefits and Limitations

For the BCSS tokamak reference blanket, it has been demonstrated that temperatures, thermal and pressure stresses can be made act-alike over a limited region, but it is difficult to model the entire blanket in a single test module. This stems primarily from the conflicts between thermal hydraulics and structural mechanics test requirements.

This limitation is not felt to be catastrophic for the BCSS design because the structural response is dominated by the local conditions. However, the "unit-cell" approach to testing removes much of the value of testing for global eddy currents, MHD velocity profiles, pressure drop and global temperature profiles.

In blankets which possess a more dominant global structural response (e.g., the MARS blanket), this approach does not work as well. In that case, it may be more practical to design a scale model nuclear test rather than a unit-cell type of test. Scaling techniques for thermal hydraulics have been demonstrated for maintaining the thermal response in smaller scale test modules, for example: entry length and residence time scaling.

Because of the difficulty of maintaining both the global MHD and thermal hydraulic behavior in a liquid metal blanket, it is proposed that extensive testing be done outside the fusion environment in a non-nuclear MHD act-alike experiment. The combination of an act-alike (possibly large), MHD experiment together with a small scale nuclear test appears to be nearly inclusive for addressing the testing issues as we now know them.

Nomenclature for Chapter 6:

a	channel half-width or radius
A	area
A_c	creep constant
A_ℓ	neutron albedo
b	pitch (distance between ribs)
B_o	magnetic field strnegth
B_p	poloidal magnetic field
B_T	toroidal magnetic field
c_p	specific heat
C	effective conductivity factor
C_o	value of C at y=0
$\overline{C}$	average value of C
C_x	MHD bulk force coefficient, x-direction
C_z	MHD bulk force coefficient, z-direction
d	toroidal channel depth
d_i	dimension of radial inlet orifice
D	mass diffusion coefficient
$\underline{D}$	total displacement matrix
e	strain
E	modulus of elasticity
$\underline{E}$	inelastic strain displacement matrix
f	non-dimensional velocity, u/u_b
F	axial force
$\underline{F}$	flexibility matrix
Fo	Fourier number, $\alpha L/4a^2 u_b$
h	heat transfer coefficient
Ha	Hartmann number, $aB\sqrt{\sigma_e/\mu}$
Ha_c	critical Hartmann number
i	electric current density
I	area moment of inertia
I_1, I_2	velocity integral expressions
j	mass flux
J	neutron current
k	thermal conductivity
K	surface current density

K_B	Boltzman constant
ℓ_e	entry length for velocity profile development
ℓ_i	dimension of toroidal inlet orifice
ℓ_p	length of insulating partition
ℓ_D	concentration (diffusion) scale length $\sqrt{DL/Ub}$
ℓ_H	velocity (Hartmann) scale length a/Ha
L	channel length or toroidal blanket width
M	moment
n	arbitrary integer parameter
N	Stuart number, or interaction parameter $\frac{Ha^2}{Re}$
Nu	Nusselt number, 4ah/k
p	pressure
P	radial force
Pr	Prandtl number, $c_p\mu/k$ or ν/α
q_w	wall heat flux
q_s	surface heat flux
Q	flow quantity
Q_v	volumetric heat generation rate
r	radial coordinate in channel
R	radius of curvature
Re	Reynolds number, $\frac{\rho va}{\mu}$
Re_m	magnetic Reynolds number, $\mu_o \sigma_e Lv$
s	poloidal arc length ($ds = Rd\theta$)
S	swelling rate
Sc	Schmidt number, ν/D
t	time
t_b	burn time
t_d	dwell time
t_f	channel width
t_p	pseudo-time, x/u_b
t_w	wall thickness
t_R	residence time
T	temperature
T_b	bulk averaged temperature $\frac{\int Tu\ dy}{\int u\ dy}$
T_w	wall temperature
u	toroidal or axial component of velocity
u_b or U_b	bulk velocity

v	poloidal or transverse component of velocity
V	velocity or reaction force
w	radial component of velocity or change in beam curvature
W	blanket width in toroidal direction
W^*	transformed blanket toroidal width
x	toroidal or axial coordinate
X	concentration
y	poloidal or transverse coordinate
y^*	transformed poloidal coordinate, $y\ \sigma_\rho/\sigma_r$
z	radial coordinate in blanket
α	thermal diffusivity, $k/\rho C_p$ or coefficient of thermal expansion
γ	non-dimensional surface heat flux, $q_s\ a/2k$
δ	boundary layer thickness
δ_{fw}	first wall thickness
ε	strain
ε_c	creep strain
ε_h	eddy diffusivity for heat transfer
ε_m	eddy diffusivity for momentum transfer
ζ	non-dimensional axial coordinate, $\alpha x/u_b a^2$
η	non-dimensional y coordinate, y/a
θ	poloidal angle
Θ	temperature increment due to bulk heating
λ	non-dimensional volumetric heating, $Q_v\ a^2/k$
μ_o	permeability of free space
μ	viscosity
ν	kinematic viscosity, μ/ρ
ξ	radial coordinate
ρ	mass density
σ	stress
σ_e	electrical conductivity
σ_f	fluid electrical conductivity
σ_w	wall electrical conductivity
τ	swelling incubation time constant
ϕ_e	electric scalar potential
ϕ_w	wall conductivity ratio
Φ	neutron flux